

---

**Forschungszentrum Karlsruhe**  
in der Helmholtz-Gemeinschaft

---

**Wissenschaftliche Berichte**  
FZKA 6741

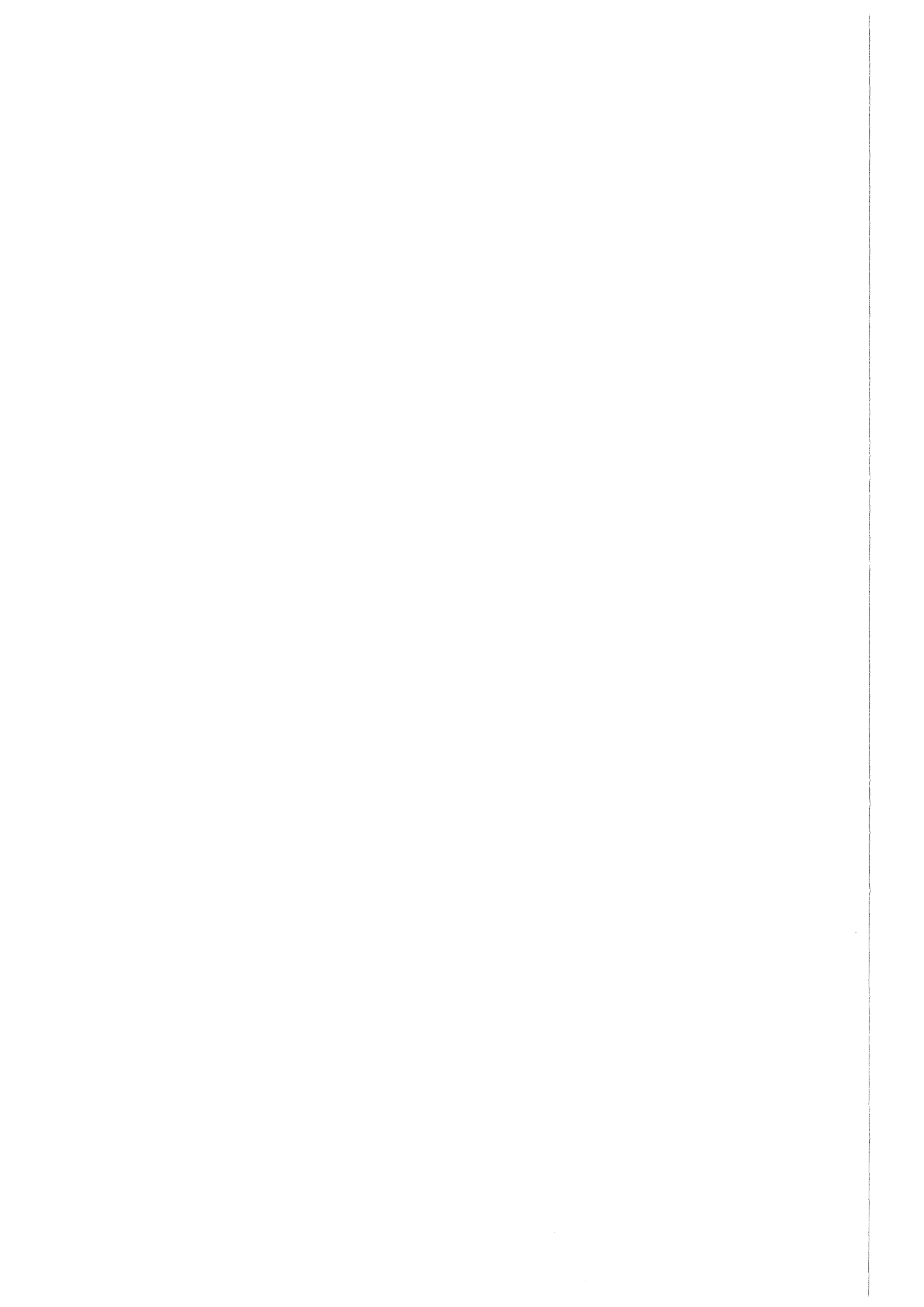
**Programm Nukleare  
Sicherheitsforschung**  
**Jahresbericht 2001**  
**Teil 1**

**B. Mühl (Hrsg.)**

**Programm Nukleare Sicherheitsforschung**

**Juni 2002**

---



# **FORSCHUNGSZENTRUM KARLSRUHE**

in der Helmholtz-Gemeinschaft

Wissenschaftliche Berichte

FZKA 6741

## **Programm Nukleare Sicherheitsforschung**

### **Jahresbericht 2001**

#### **Teil 1**

Herausgegeben von B. Mühl

Programm Nukleare Sicherheitsforschung

Forschungszentrum Karlsruhe GmbH, Karlsruhe

2002

Als Manuskript gedruckt  
Für diesen Bericht behalten wir uns alle Rechte vor

Forschungszentrum Karlsruhe GmbH  
Postfach 3640, 76021 Karlsruhe

Mitglied der Hermann von Helmholtz-Gemeinschaft  
Deutscher Forschungszentren (HGF)

ISSN 0947-8620  
ISSN 1619-9731

## Summary

The R&D work of Forschungszentrum Karlsruhe (FZK) related to reactor safety and the safety of nuclear waste disposal is concentrated in the Nuclear Safety Research Programme (NUKLEAR). In the reporting period 2001, the programme NUKLEAR covered five main topics of work:

Light Water Reactor safety

Innovative systems

Studies related to the transmutation of actinides

Safety research related to final waste storage

Immobilisation of HAW

Numerous institutes of the research centre contribute to the work programme, as well as several external partners. The tasks are coordinated in agreement with internal and external working groups.

The contributions to this report, which are either written in German or in English, correspond to the status of early 2002.

## Zusammenfassung

Die F+E-Arbeiten des Forschungszentrums Karlsruhe (FZK) zur Reaktorsicherheit und zur Sicherheit der nuklearen Entsorgung sind im Programm Nukleare Sicherheitsforschung (NUKLEAR) zusammengefasst. Das Programm NUKLEAR umfasste im Berichtsjahr 2001 die folgenden fünf Arbeitsthemen:

Leichtwasserreaktorsicherheit

Innovative Systeme

Studien zur Actinidenumwandlung

Sicherheitsforschung zur Endlagerung

Immobilisierung von hochradioaktivem Abfall

Die konkreten Forschungsvorhaben innerhalb dieser Arbeitsthemen werden laufend mit internen und externen Fachgremien abgestimmt.

An den beschriebenen Arbeiten sind im wesentlichen die folgenden Institute und Abteilungen des FZK beteiligt:

Institut für Hochleistungsimpuls- und Mikrowellentechnik	IHM
Institut für Kern- und Energietechnik	IKET
Institut für Materialforschung	IMF I, II, III
Institut für Nukleare Entsorgung	INE
Institut für Reaktorsicherheit	IRS
Institut für Technische Chemie	ITC

sowie vom FZK beauftragte externe Institutionen.

Die einzelnen Beiträge stellen den Stand der Arbeiten im Frühjahr 2002 dar und sind entsprechend dem F+E-Programm 2001 nummeriert.

**Inhalt**  
**Contents**

	<b>Seite</b>
<b>Teil 1 (FZKA 6741)</b>	
<b>32.21      <u>LEICHTWASSERREAKTORSICHERHEIT</u></b>	<b>1</b>
<b>32.21.01    <b>Wasserstoffverhalten und Gegenmaßnahmen</b></b>	<b>1</b>
I.    Model Development and Validation of GASFLOW II (G. Necker, J.R. Travis, P. Royl, IKET)	1
II.   CO-H <sub>2</sub> -Air Combustion Tests in the FZK - 7 m - Tube (A. Vesper, G. Stern, J. Grune, W. Breitung, B. Burgeth, IKET)	6
III.  Numerical Simulation of Combustion with COM3D, B0B, Flame3D (U. Bielert, A. Vesper, A. Kotchourko, R. Redlinger, W. Breitung, IKET)	15
IV.  Run-up Distances to Supersonic Flames in Obstacle-Laden Tubes (A. Vesper, W. Breitung, S. Dorofeev, IKET)	27
V.    Das Einmassenschwinger Modell (B. Burgeth, IKET)	38
VI.  On the Load Carrying Capacities of a Spherical PWR Steel Contain- ment under a Postulated Hydrogen Detonation (R. Krieg, B. Dolensky, B. Göller, IRS; W. Breitung, R. Redlinger, P. Royl, IKET)	42
<b>32.21.02    <b>Thermische Wechselwirkung von Kernschmelze und Kühlmittel</b></b>	<b>55</b>
I.    ECO-Experimente zur Energiekonversion bei Dampfexplosionen (G. Albrecht, H. Brüggemann, W. Cherdron, E. Jenes, A. Kaiser, N. Prothmann, D. Raupp, W. Schütz, IRS)	55
II.  Theoretische Arbeiten zur Schmelze-Kühlmittel-Wechselwirkung (H. Jacobs, B. Stehle, E. Stein, IKET; M. Böttcher, U. Imke, D. Struwe, IRS)	63

<b>32.21.03</b>	<b>Versagen des Reaktordruckbehälters und Dispersion der Kernschmelze</b>	<b>71</b>
I.	Experimente zur Dispersion von Corium (M. Greulich, M. Kirstahler, L. Meyer, M. Schwall, E. Wachter, G. Wörner, M. Gargallo, IKET)	71
II.	Rechnungen zur Dispersion der Kernschmelze (D. Wilhelm, IKET)	81
<b>32.21.04</b>	<b>Thermischer Angriff durch Kernschmelze und deren langfristige Kühlung</b>	<b>86</b>
I.	COMET-Konzept (H. Alsmeyer, T. Cron, G. Merkel, S. Schmidt-Stiefel, W. Tromm, T. Wenz, IKET; C. Adelhelm, IMF; H.-G. Dillmann, H. Pasler, ITC-TAB; W. Schöck, IMK; C. Grehl, IMVT; Ing.-Büro G. Schumacher)	86
II.	LIVE (Late In-Vessel Phase) Experiments (B. Eppinger, G. Fieg, W. Tromm, T. Wenz, IKET)	97
III.	KAJET-Versuche (G. Albrecht, H. Brüggemann, E. Jenes, D. Raupp, W. Schütz, IRS)	104
IV.	Spreading on ceramic and concrete substrates (J.J. Foit, IKET)	110
<b>32.21.06</b>	<b>Dynamische Beanspruchung von Reaktordruckbehälter und Containmentstrukturen unter hochtransienten Belastungen</b>	<b>119</b>
	Limit Strains for Severe Accident Conditions (LISSAC) (B. Dolensky, G. Hailfinger, J. Holzinger, T. Jordan, G. Karner, R. Krieg, K.-H. Lux, T. Malmberg, G. Messemer, N. Prothmann, H. Rieger, M. Sidor, E. Stratmanns, IRS; J. Aktaa, E. Diegele, D. Hofer, E. Materna-Morris, R. Schmitt, IMF; H. Plitz, NUKLEAR)	119

<b>32.21.07</b>	<b>Analysen zum Containmentverhalten</b>	<b>131</b>
I.	Quelltermuntersuchungen für schwere Unfälle in Leichtwasserreaktoren (P. Schmuck, IKET)	131
II.	KAREX-Experiments zum radiologischen Quellterm infolge Resuspension (J. Minges, W. Schütz, IRS; M.K. Koch, RUB/LEE)	135
<b>32.21.08</b>	<b>Untersuchungen zur Kernzerstörung</b>	<b>139</b>
I.	Results of the QUENCH-07 Bundle Experiments on the Investigation of Cool-Down Behaviour of Overheated PWR Fuel Rod Simulators (QUENCH-Programme) (A. Miassoedov, D. Piel, L. Sepold, IMF III; M. Steinbrück, L. Steinbock, U. Stegmaier, IMF I)	139
II.	Metallographic Post-test Examination of QUENCH-04 and QUENCH-05 Test Bundles and Phenomenological Interpretation (G. Schanz, M. Heck, IMF III; U. Stegmaier, IMF I)	146
III.	Oxidation kinetics of B <sub>4</sub> C (BOX rig experiments) (M. Steinbrück, A. Meier, U. Stegmaier, L. Steinbock, J. Stuckert, IMF I)	151
IV.	Degradation of B <sub>4</sub> C control rod segments (M. Steinbrück, A. Meier, U. Stegmaier, L. Steinbock, J. Stuckert, IMF I)	157
V.	Einzeleffekt-Untersuchungen zur B <sub>4</sub> C-Oxidation und ihrer modellmäßigen Beschreibung (W. Krauss, G. Schanz, H. Steiner, M. Heck, IMF III)	160
VI.	Modelling of boron carbide oxidation and boric acid formation (H. Steiner, IMF III; M. Steinbrück, IMF I)	168
VII.	Cool-down tests in various atmospheres on the thermal and thermo-mechanical behaviour of Zircaloy-4 cladding (J. Stuckert, M. Steinbrück, U. Stegmaier, IMF I; A. Palagin, IBRAE Moscow)	175

VIII.	Messung optischer Eigenschaften von Reaktorwerkstoffen (L. Steinbock, IMF I)	181
IX.	Severe Accident Investigations (W. Hering, Ch. Homann, W. Sengpiel, D. Struwe, IRS; J.S. Lamy, EDF)	182
<b>32.21.09</b>	<b>Entwicklung von Methoden zur Abschätzung und Minimierung der radiologischen Folgen von Reaktorunfällen</b>	<b>196</b>
	(G. Benz, J. Ehrhardt, F. Fischer, Ch. Haller, I. Hasemann, E. Hesselschwerdt, C. Landmann, A. Lorenz, J. Päsler-Sauer, M. Rafat, W. Raskob, T. Schichtel, IKET)	
<b>32.21.10</b>	<b>Beteiligung am PHEBUS-Projekt</b>	<b>202</b>
I.	Analytical Interpretation of Experimental Results (W. Sengpiel, W. Hering, IRS)	202
II.	Deposition and Revaporisation of Fission Products (G. Henneges, IKET)	208
<b>32.21.11</b>	<b>Untersuchungen zur Reaktor- und Anlagendynamik</b>	<b>221</b>
	Investigations on Reactor and Plant Dynamics (D.C. Cacuci, M. Ionescu-Bujor, W. Hering, V.H. Sanchez, IRS)	221
<b>32.22</b>	<b><u>INNOVATIVE SYSTEME</u></b>	<b>226</b>
<b>32.22.03</b>	<b>Entwicklung von Methoden, physikalischen Modellen und Rechenprogrammen zur Zweiphasenströmung</b>	<b>226</b>
I.	Theoretische Untersuchungen (M. Wörner, M. Ilic, G. Grötzbach, D.G. Cacuci, IRS)	226
II.	Experimentelle Untersuchungen zum Strömungsumfeld aufsteigender Gasblasen in ruhendem Fluid und dessen Wechselwirkung mit dem Aufstiegsverhalten der Blasen (V. Heinzl, H. Sauter, IRS)	234

<b>32.22.04</b>	<b>Strukturelle Integrität</b>	<b>242</b>
I.	Investigations to Size Effects on Deformation and Failure Behavior of Specimens including a Center Hole (J. Aktaa, M. Klotz, M. Pfeifenroth, R. Schmitt, IMF II)	242
II.	Material models for large deformation elasticity and plasticity theories (E. Diegele, R. Elsäßer, D. Hofer, G. Rizzi, IMF II., Ch. Tsakmakis, TU Darmstadt)	244
<b>32.22.06</b>	<b>Untersuchungen zum Brennstoff- und Brennstabverhalten innovativer Systeme</b>	<b>261</b>
I.	Instrumentierung für CABRI-Testeinsätze (P. Norajitra, D. Piel, L. Sepold, IMF III)	261
II.	Theoretical interpretation of results of CABRI experiments (D. Struwe, W. Pfrang, W. Zimmerer, IRS)	262
<b>32.22.08</b>	<b>Oberflächenvergütung mit gepulsten Elektronen- und Ionenstrahlen</b>	<b>263</b>
I.	Behandlung von MCrAlY-Schutzschichten mit Grundlagenuntersuchungen zur Strahlerzeugung (G. Müller, R. Huber, G. Schumacher, H. Bluhm, V. An, D. Strauß, F. Zimmermann, IHM; V. Engelko, Efremov Institute, St. Petersburg)	263
II.	Mikromechanische Modellierung von Wärmedämmschichten (K. Sfar, J. Aktaa, IMF II)	273
<b>32.22.09</b>	<b>High Performance Light Water Reactor (HPLWR)</b>	<b>275</b>
I.	Thermal-Hydraulic Analysis of a Supercritical Pressure Light Water Reactor (X. Cheng, H. Jacobs, T. Schulenberg, , D. Squarer, IKET)	275
II.	Validation of Coupled Neutron Physics and Thermhydraulics Analysis for HPLWR (C.H.M. Broeders, V. Sanchez, A. Travleyev, IRS; E. Stein, IKET)	290

III.	Water Chemistry of BWR's, PWR's and Supercritical Fossil Fuel Power Plants (J. Konys, K. Ehrlich, S. Leistikow, IMF)	301
IV.	Untersuchungen an Strukturmaterialien der Kerntechnik (M. Schirra, P. Graf, A. Falkenstein, S. Heger, E. Materna-Morris, IMF I, L. Heikinheimo, GW)	311
<b>32.23</b>	<b><u>STUDIEN ZUR ACTINIDENUMWANDLUNG</u></b>	<b>314</b>
<b>32.23.01</b>	<b>Neutronenphysikalische Untersuchungen zur Transmutation von Actiniden und Spaltprodukten</b>	<b>314</b>
	Status und Weiterentwicklung des Inventarcodes KORIGEN, der Szenariocodes KORREC und SOLEQ sowie des Nachwärmecodes CALOR (H.W. Wiese, IKET)	314
<b>32.23.02</b>	<b>Abtrennverfahren für Actiniden aus hochradioaktiven Abfällen</b>	<b>318</b>
	(A. Geist, M. Weigl, U. Müllich, K. Gompper, INE)	
<b>32.23.03</b>	<b>Sicherheitsuntersuchungen zum dynamischen Verhalten von Kernen mit Actinidenanteil</b>	<b>326</b>
I.	Improvements of Passive Safety Features of Accelerator Driven Transmutation Systems (W. Maschek, A. Rineiski, S. Wang, X. Chen, M. Mori, E. Wiegner, W. Götzmann, IKET; M. Flad, D.T.I. GmbH)	326
II.	Investigation of Neutron Kinetics Models for ADS Transient Analyses (A. Rineiski, W. Maschek, IKET)	338
III.	Improvements in the SIMMER-III/IV Neutronics Module (G. Buckel, E.Kiefhaber, A. Rinesiky, W. Götzmann, IKET)	361

IV.	Erstellung einer neuen Referenzversion des Programms SAS4A (D. Struwe, W. Pfrang, W. Zimmerer, IRS)	363
<b>32.23.04</b>	<b>Bestrahlungsexperimente zur Transmutation von Actiniden im HFR</b>  (H. Plitz, NUKLEAR)	<b>364</b>
<b>32.23.05</b>	<b>Untersuchungen zu Beschleuniger getriebenen, unterkritischen Anlagenanordnungen (ADS)</b>	<b>366</b>
I.	Thermalhydraulic Investigations into Blanket and Target Design (J.U. Knebel, X. Cheng, R. Stieglitz, M. Daubner, K.J. Mack, F. Fellmoser, C. Pettan, S. Gnieser, IKET)	368
II.	Liquid metal corrosion (G. Müller, A. Heinzl, A. Weisenburger, IHM; J. Konys, O. Wedemeyer, IMF III; A. Rusanov, IPPE; V. Markov, PROMOTEY)	384
III.	Generation of coarse group libraries with the KAPROS procedure COLLIB (C.H.M. Broeders, R. Dagan, IRS)	397
IV.	Entwicklung des Rechenprogramms FLUTAN für thermo- und fluid-dynamische Anwendungen – Numerical analysis of MEGAPIE related thermal and fluid-dynamical problems (G. Grötzbach, C. Panefresco, IKET; L.N. Carteciano, B. Dorr, W. Olbrich, IRS)	404
V.	Werkstoffkundliche Bewertung des Strahlfensters (E. Materna-Morris, A. Möslang, D. Preininger, P. Vladimirov, IMF I)	411
<b>32.23.06</b>	<b>HGF Strategy Fund Project 99/16: Thermalhydraulic and Material Specific Investigations into the Realization of an Accelerator Driven System (ADS) to Transmute Minor Actinides</b>  (J.U. Knebel IKET, G. Müller IHM, J. Konys IMF III, KALLA Team)	<b>417</b>

## Teil 2 (FZKA 6742)

<b>32.25</b>	<b><u>SICHERHEITSFORSCHUNG ZUR ENDLAGERUNG</u></b>	<b>457</b>
<b>32.25.01</b>	<b>Szenariientwicklung und Vergleich von Endlagerkonzepten</b>	<b>457</b>
I.	Thermomechanical analysis of backfilled drifts in a radioactive waste repository (A. Pudewills, INE)	457
II.	Code Development for Modelling of Coupled Effects at Corrosion of Carbon Steel Containers under Repository Conditions (E. Korthaus, INE)	463
<b>32.25.02</b>	<b>Radionuklidrückhaltung durch technische und geotechnische Barrieren</b>	<b>467</b>
I.	Radionuclide retention by secondary alteration products of HLW glass (B. Luckscheiter, M. Nesovic, P. Zimmer, INE)	467
II.	Radiolysis and corrosion of <sup>238</sup> Pu doped UO <sub>2</sub> pellets in chlorine brine (M. Kelm, E. Bohnert, INE)	474
III.	Assessment of the Barrier Disposal Container: Contact corrosion between Ti99.8 and carbon steel (E. Smailos, B. Fiehn, R. Weile, INE)	486
IV.	Chemie und Stabilität der Versatzmaterialien (H. Hofmann, A. Bauer, T. Schäfer, Th. Rabung, INE; F. Claret, E. Ferrage, B. Lanson, Environmental Geochemistry Group, University Grenoble)	491
V.	Solid and surface analysis: Nanoscopic observation of U(IV)-oxide surface dissolution and remineralization by electrochemical AFM (M. Plaschke, J. Römer, INE)	499
VI.	Solid and surface analysis: Untersuchung der Oberfläche von Chlorit mit ADXPS (D. Schild, F. Brandt, INE)	512

<b>32.25.03</b>	<b>Radionuklidrückhaltung in der geologischen Barriere</b>	<b>518</b>
I.	Colloid-Detection in Trace Concentrations by LIBD (C. Walther, C. Bitea, F.J. Scherbaum, INE)	518
II.	Characterization of aquatic colloids by a combination of LIBD and ICP-MS following the size fractionation (H. Geckeis, M. Bouby, Th. Ngo Manh, F. Scherbaum; INE)	525
III.	Fulvate Complexation of tetravalent Neptunium (C.M. Marquardt, A. Seibert, J.I. Kim, INE; V. Pirlet, SCK-CEN Mol)	531
IV.	Iron Oxide/-Hydroxide Colloid Facilitated Americium Migration in Gorleben Groundwater (T. Schäfer, R. Artinger, K. Dardenne, A. Bauer, INE)	540
V.	Actinide Migration Experiment in ÄSPÖ HRL (B. Kienzler, P. Vejmelka, J. Römer, E. Fanghänel, F. Geyer, E. Soballa, M. Fuß, T. Kisely, INE)	546
VI.	Colloid and Radionuclide Retention Experiment at the Grimsel HRL (W. Hauser, H. Geckeis, R. Götz, F. Geyer, Th. Schäfer, Th. Rabung, J.I. Kim, INE)	550
VII.	Initial results on changes in humic colloid content through drainage of wetland in the Gorleben south-east area (G. Buckau, R. Artinger, J.I. Kim, INE; M. Wolf, GSF-IfH, S. Geyer, P. Fritz, UFZ)	559
<b>32.25.04</b>	<b>Aquatische Chemie der Actiniden und langlebiger Spaltprodukte</b>	<b>566</b>
I.	Aquatic Chemistry and Thermodynamic of tetravalent Actinides (V. Neck, M. Altmaier, R. Müller, M. Bouby, Th. Fanghänel, J.I. Kim, INE)	566
II.	Study of Cm(III) Sorption onto $\gamma$ -Al <sub>2</sub> O <sub>3</sub> and clay minerals by Time-Resolved Laser Fluorescence Spectroscopy (Th. Rabung, H. Geckeis, M.-C. Pierret, A. Bauer, R. Klenze, J.I. Kim, INE; Th. Stumpf, Institut für Radiochemie, FZ Rossendorf)	579

III.	In situ Speciation von Actiniden mit Synchrotronstrahlung (K. Dardenne, M.A. Denecke, P. Lindqvist-Reis, J. Rothe, INE)	585
<b>32.25.05</b>	<b>Geochemische Transportmodellierung sowie Untersuchung der Übertragbarkeit</b>	<b>599</b>
I.	Application of geochemical modeling in site selection process for radioactive waste repositories (V. Metz, B. Kienzler, W. Schübler, INE)	599
II.	Comparison of double layer models in transport problems (J. Lützenkirchen, B. Kienzler, INE)	610
<b>32.26</b>	<b><u>IMMOBILISIERUNG VON HOCHRADIOAKTIVEM ABFALL</u></b>  (W. Grünewald, G. Roth, INE)	<b>617</b>
<b>32.26.01</b>	<b>Technologie zur Verglasung der hochradioaktiven Spaltproduktlösungen der WAK in einer Standortverglasungsanlage</b>	<b>618</b>
<b>32.26.02</b>	<b>UKAEA Dounreay Projekt, Verglasung hochradioaktiver Spaltprodukte aus der Schnellbrüterbrennstoff-Wiederaufbereitung</b>	<b>624</b>
<b>VERÖFFENTLICHTE BERICHTE</b>		<b>625</b>

## 32.21 LEICHTWASSERREAKTORSICHERHEIT

### 32.21.01 Wasserstoffverhalten und Gegenmaßnahmen

#### I. Model Development and Validation of GASFLOW II (G. Necker, J.R. Travis, P. Royl)

#### **Abstract**

The 3D CFD code GASFLOW is developed at FZK as an integral analysis tool for the calculation of steam/hydrogen distribution with simulation of mitigation in nuclear reactor containments. This progress report for the year 2001 focuses on developed new documentations for a Lecture Series on GASFLOW and on results from the simulation of hydrogen mitigation by catalytic (THINCAT) foils in a large break LOCA. It then references the ongoing activities for new 3D benchmark calculations and finally discusses the possibilities of a developed new graphical user interface.

#### **1. Lecture Series on GASFLOW**

A GASFLOW workshop has been held both at KAERI (Korean Atomic Energy Research Institute) in Taejon, Korea and in the Institute for Nuclear Engineering Technology (INET) of the Tsinghua University in Beijing, China.

To prepare for these workshops a new GASFLOW code version II.2 has been finalized and remotely implemented on a HP PA-RISC machine in the Korean Atomic Energy Research Institute at Taejon, Korea. Parallel to the implementation over the internet this version II.2 was implemented on a Sun Spark platform and sent to INET on CD prior to the workshop. The new GASFLOW release versions for these two platforms included the full plotting package pscan and its associated libraries with some tailoring specific to the different platforms.

A series of pdf documents was compiled into a CD, that give a comprehensive documentation of the code. Among the pdf documents is a complete set of code manuals (theory, users, and validation manual) and all work reports which have been compiled since the release of the GASFLOW version II. These work reports supplement the common FZK/LANL release version of the code from October 1998

(report FZKA-5994, LA-13357-M) and fully document the new release version II.2. The GASFLOW bibliography has been updated. All recent publications referring to GASFLOW modeling and application in the last 3 years as far as they are available in pdf format are included on this CD with a special reference to these documents given in the bibliography. The workshop comprised 13 lectures, that were delivered in 4 days plus a number of sample cases developed for on line training. An overview of these lectures is given in table 1.

Table 1: Lectures Prepared for the GASFLOW Workshop at KAERI and INET

Lecture	Topic	Lecture	Topic
1	Overview	8	Analysis of HDR Test T31.5
2	Application	9	Large Break Loca GKN-2
3	Fluid Mechanics in GASFLOW	10	GASFLOW Radiation Model
4	Running GASFLOW	11	Managing GASFLOW
5	Structure Modeling	12	Flame Acceleration and Detonation Criteria (simple EPR sample)
6	Evaluation of Time History Data	13	3D Display of GASFLOW results
7	Definition of external Sources		

The CD prepared for this workshop contains the presented viewgraphs from all lectures in one large pdf document and also includes subdirectories of the individual lectures with pdf files of the lecture notes and the discussed input and output. All data from the CD have been put on the server of the Institute fuer Kern- und Energietechnik and can be found directly from the web with the link

<http://www.iket.fzk.de/gasflow-workshop>

## 2. Scoping calculations for hydrogen mitigation in a large break loca with the model for catalytic foils from GASFLOW

The model for catalytic foils in GASFLOW [1], that has been developed in the last year has been applied to simulate the mitigation effect of different catalytic coatings in a 3D scoping analysis of a large break LOCA in a Konvoi type containment [2]. Catalytic coating was applied on the steam generators, pumps, and pressurizer vessels (in total 1744 m<sup>2</sup>, see separate structures in figure 1). The foils result in a stronger overall hydrogen removal than the 62 Siemens recombiner boxes that were originally analyzed for backfitting. Some problems of the catalytic foils became evident during the development of local hot spots on the insulated foils, during

temporary hydrogen accumulations in the dome away from the foils, and from inhomogeneities of the recombination resulting from the interaction with the global containment convection. The operation of such recombiner foils in a region with globally downward directed containment convection needs further investigations. Figure 1 shows the calculated hydrogen source jet in the large break LOCA and the resulting stronger local heating of the foils near the source. A global downward containment convection in the steam generator towers opposite to the source side acts against the developing buoyancy and slows down the local recombination effect in this region.

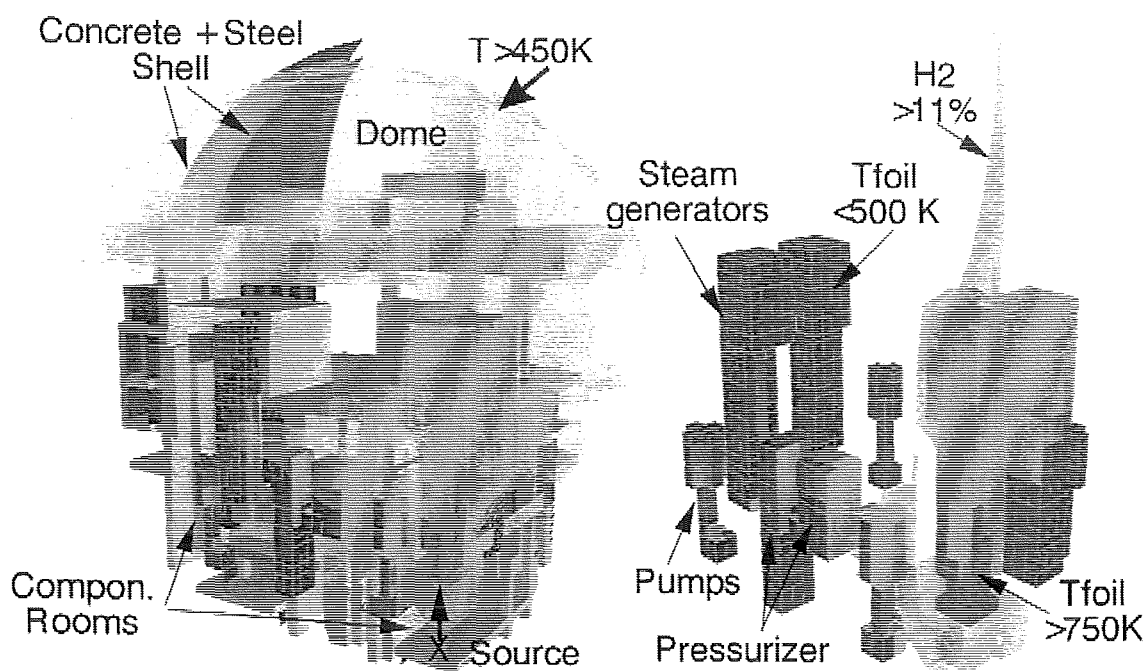


Fig. 1: Temperature of THINCAT foils in component rooms of Konvoi plant and hydrogen cloud during a large break LOCA

### 3. Development of 3D GASFLOW Models for the TOSQAN and THAI facilities

To prepare our participation in the upcoming new round of benchmark calculations with blind pre-calculations for different experiments in the French TOSQAN and German THAI facility we have developed and tested new 3D models for these facilities. The geometry model for the THAI facility has been applied in an open post test simulation of the THAI experiment TH1 [3]. An error in the condensation model was found and corrected, so that the energy balance is rather well fulfilled in the analysis of this test now.

#### 4. Graphical User Interface for the Definition of 3D Cylindrical Models from Scanned Containment Drawings

In November 2001 the Dutch ministerie van "Volkshuisvesting, Ruimtelijke Ordening en Milieubeheer" (VROM) issued a contract to FZK to perform a 3D GASFLOW analysis of hydrogen mitigation in the nuclear power plant Borssele (KCB) during a postulated hypothetical small break LOCA. In preparation for this contract we developed a new graphical user interface (GUI) for defining 3D GASFLOW geometry models. This GUI is of general use for the development of 3D building models also for other cylindrical or spherical reactor containments.

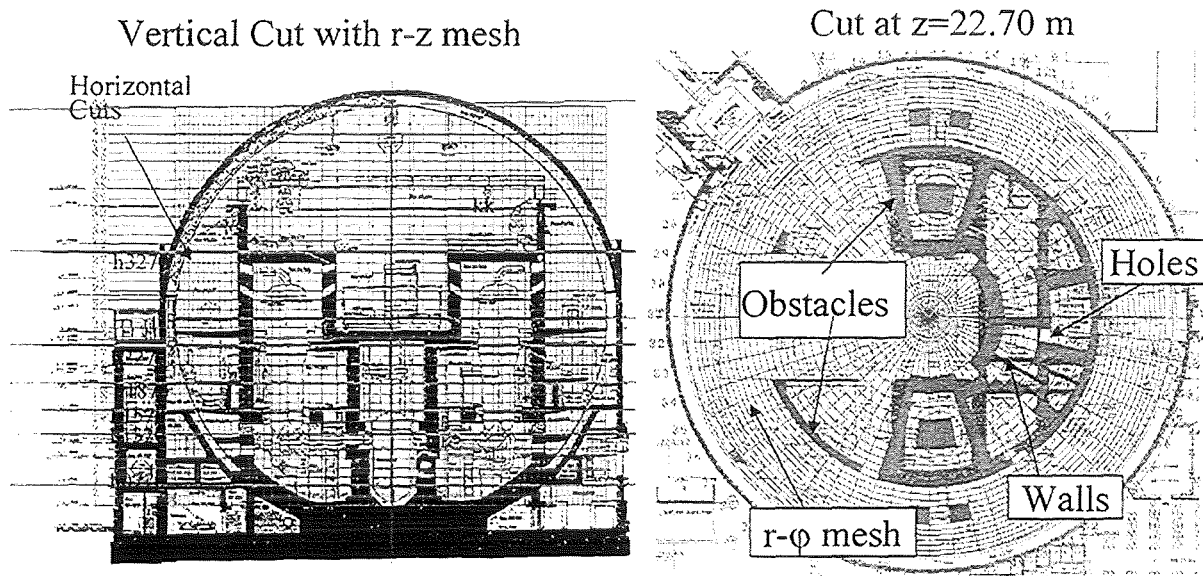


Fig. 2: Graphical User Interface for GASFLOW to Define Obstacles, Walls and Holes on scanned containment drawings in cylindrical coordinates

The GUI makes use of scanned containment drawings. These drawings are defined as bitmap files and put in the background of a graphical window, that is opened in the Speakeasy IV system. Each drawing is then calibrated on the screen with the actual horizontal and vertical containment dimensions. We then superimpose a predefined axial z mesh with the correct scaling in different axial cuts. The left part of figure 2 gives an example with a superimposed axial mesh. Because this cut is centrally located we could also overlay a predefined radial mesh. Excentrical axial cuts in various viewing directions are also scanned but only overlaid with the axial mesh. The axial mesh in each scanned cut defines the discrete axial dimensions of the major components like pump and steam generator and the axial locations of the

various ceilings and walls in the GASFLOW mesh. In the given example we have displayed in the vertical cut as thick green horizontal bars the locations of the 6 horizontal cuts through the containment which were made available to us. One horizontal cut at 22.7 m is displayed in the right part of figure 2. The scanned horizontal cuts are calibrated with the actual outside radius of the containment at this axial location and our scaled r-phi mesh is set up around the center. We then define the corner points of obstacles, walls, and holes in this horizontal slice by cursor input. The GUI automatically transforms the cursor input to the discrete r-phi mesh and it then prompts the user to define the axial mesh range of each obstacle, wall or hole as two numbers that the user must read out from a suitable axial cut like the one given on the left. The user can directly define the relevant structures across their whole length, or he can refine the regions between certain horizontal cuts. Previously defined structures are always redisplayed and give the user orientation during the refining of the geometry model. The coordinates of obstacles, walls, and holes are continuously updated in different files during the cursor input and finally written in a file with mobs, walls and holes input which the user must merge into his input file.

The GUI has also options to define locations for other input like rupture disks, locations of recombiners and sensor locations. Another option included allows to prepare the input for the condensation of rooms inside the 3D mesh. Based on these so-called roomdef statements GASFLOW averages the temperatures, steam-, and hydrogen- concentrations and evaluates the flame acceleration and detonation criteria for each of these defined rooms. These rooms can be defined for physical rooms in the containment or for control volumes of lumped parameter models.

## References

- [1] P. Royl, G. Necker, J. R. Travis: "GASFLOW Simulation of Hydrogen Recombination with Radiation Transport from Catalytic Foils in the Recombiner Foil Test HDR E11.8.1", Procs Jahrestagung Kerntechnik, Dresden, May 15-17, 2001
- [2] P. Royl, J. R. Travis, W. Breitung : „Modeling of Catalytic Foils and Application in 3D Containment Analysis using the 3D CFD Code GASFLOW", IAEA Technical Committee Meeting Cologne, Germany, 18-22 June 2001, IAEA-J4-TC-1181
- [3] S. Schwarz: "Blind Cocosys Calculations for Thai Test TH2", Procs Jahrestagung Kerntechnik 2002, Stuttgart

II. CO-H<sub>2</sub>-Air Combustion Tests in the FZK - 7 m - Tube  
(A. Vesper, G. Stern, J. Grune, W. Breitung, B. Burgeth, IKET)

**Abstract**

To investigate the combustion behaviour of H<sub>2</sub>-CO-air mixtures under different conditions (variation of the initial pressure, tube orientation, ignition location, experiments were made in an explosion tube equipped with orifice plate obstacles. The tube was 7.2m long with an internal tube diameter of 0.1 m. The blockage ratio (BR) of the orifice plates was 0.3 (= fraction of total tube cross section blocked by obstacles).

It was found that for mixtures below 13% (H<sub>2</sub>+CO) fuel the replacement of H<sub>2</sub> by CO leads to less sensitive mixtures. The transition from slow to fast combustion modes is shifted to higher fuel concentrations with increasing CO content. For mixtures above 13% (H<sub>2</sub>+CO) fuel there were no effects of CO on the combustion regime. Also the investigated tube orientation and pressure variation had no effects on the combustion regime.

**1. Introduction**

Carbon monoxide will be produced in severe accidents from ex-vessel interaction of molten core with concrete. Depending on the particular core-melt scenario, the type of concrete and geometric factors affecting the interaction, the quantities of carbon monoxide produced can vary widely. Typical (H<sub>2</sub>+CO) concentrations in the resulting cavity gas range from 5 to 20 vol. % [1]. Carbon monoxide is a combustible gas. The carbon monoxide thus produced is in addition to the hydrogen produced by in-vessel metal-water reactions and by radiolysis. It represents a possibly significant contribution to the total combustible gas inventory in the containment. The assessment of possible accident loads to the containment thus requires knowledge of the combustion properties of CO/H<sub>2</sub> mixtures in the containment atmosphere. Therefore a variety of experiment series were done.

**2. Experimental facility**

The experiments were made in a rectangular explosion tube (Figure 1) equipped with orifice plate obstacles. In Table 1 the initial conditions of these experiments are listed. The initial temperature was  $293 \pm 8$  K. The tube was 7.2 m long with an internal tube diameter of 0.1 m. The tube was equipped with an array of obstacles of a

blockage ratio (BR) 30% and a distance between neighbouring obstacles of 0.1 m. The H<sub>2</sub>-CO-air mixture experiments have been performed in a range of 9 % to 15% (H<sub>2</sub>+CO) fuel gas concentration. The instrumentation consisted of photodiodes to measure flame-arrival times and fast pressure transducers (PCB model 113 and 114) to measure transient pressure loads to the tube walls. The instruments were mounted pairwise at given cross sections of the tube. The measuring places had a distance of 40 cm. A total of 16 photodiodes and 16 pressure transducers were used in the tests.

Table 1 : Table of experiments, 7m tube, BR=30%

Experiment	[Air] vol%	[H <sub>2</sub> ] vol%	[CO] vol%	p <sub>0</sub> [bar]	Tube orientat.	ignition location
R1000_04	89	11	---	1	v (ertical)	bottom
R1000_05	90	10	---	1	v	bottom
R1000_06	88	12	---	1	v	bottom
R1000_07	87	13	---	1	v	bottom
R1000_08	86	14	---	1	v	bottom
R1000_09	85	15	---	1	v	bottom
R1000_10	85	7.5	7.5	1	v	bottom
R1000_11	85	11.25	3.75	1	v	bottom
R1000_12	87	6.5	6.5	1	v	bottom
R1000_13	87	9.75	3.25	1	v	bottom
R1000_14	89	5.5	5.5	1	v	bottom
R1000_15	89	5.5	5.5	1	v	bottom
R1000_16	89	8.25	2.75	1	v	bottom
R1000_17	91	9	---	1	v	bottom
R1000_18	90	10	---	1	v	bottom
R1000_19	90	5	5	1	v	bottom
R1000_20	90	7.5	2.5	1	v	bottom
R1000_21	88	6	6	1	v	bottom
R1000_22	88	9	3	1	v	bottom
R1000_23	86	7	7	1	v	bottom
R1000_24	86	10.5	3.5	1	v	bottom
R1000_25	91	9	---	1	h(orizontal)	tube end
R1000_26	90	10	---	1	h	"
R1000_27	90	5	5	1	h	"
R1000_28	90	7.5	2.5	1	h	"
R1000_29	89	11	---	1	h	"
R1000_30	89	5.5	5.5	1	h	"
R1000_31	89	8.25	2.75	1	h	"
R1000_32	85	15	---	1	h	"
R1000_33	85	7.5	7.5	1	h	"
R1000_34	85	11.25	3.75	1	h	"
R1100_00	88	12	---	1	h	"
R1100_01	88	6	6	1	h	"

Experiment	[Air] vol%	[H <sub>2</sub> ] vol%	[CO] vol%	p <sub>0</sub> [bar]	Tube orientat.	ignition location
R1100_02	88	9	3	1	h	"
R1100_03	87	13	---	1	h	"
R1100_04	87	6.5	6.5	1	h	"
R1100_05	87	9.75	3.25	1	h	"
R1100_06	86	14	---	1	h	"
R1100_07	86	7	7	1	h	"
R1100_08	86	10.5	3.5	1	h	"
R1100_09	88	6	6	1	h	"
R1100_10	91	9	---	0.5	h	"
R1100_11	90	10	---	0.5	h	"
R1100_12	89	11	---	0.5	h	"
R1100_13	88	12	---	0.5	h	"
R1100_14	87	13	---	0.5	h	"
R1100_15	86	14	---	0.5	h	"
R1100_16	85	15	---	0.5	h	"
R1100_17	85	7.5	7.5	0.5	h	"
R1100_18	85	11.25	3.75	0.5	h	"
R1100_19	89	5.5	5.5	0.5	h	"
R1100_20	89	8.25	2.75	0.5	h	"
R1100_21	90	5	5	0.5	h	"
R1100_22	90	7.5	2.5	0.5	h	"
R1100_23	87	6.5	6.5	0.5	h	"
R1100_24	87	9.75	3.25	0.5	h	"
R0301_08	90	10	---	1	v	top
R0301_09	89	11	---	1	v	top
R0301_10	88	12	---	1	v	top
R0301_11	87	13	---	1	v	top
R0301_12	85	15	---	1	v	top
R0301_13	89	8.25	2.75	1	v	top
R0301_14	87	9.75	3.25	1	v	top
R0301_15	87	6.5	6.5	1	v	top
R0301_16	85	15	---	1	v	top
R0301_17	85	7.5	7.5	1	v	top

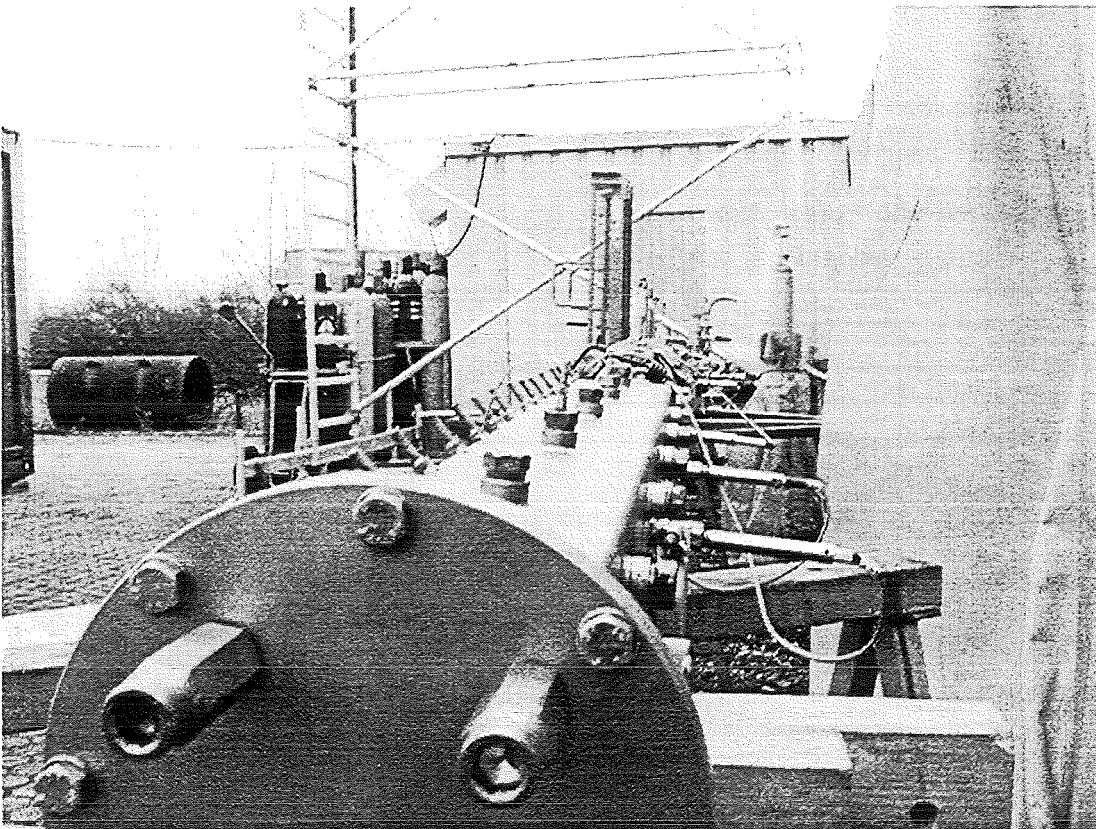
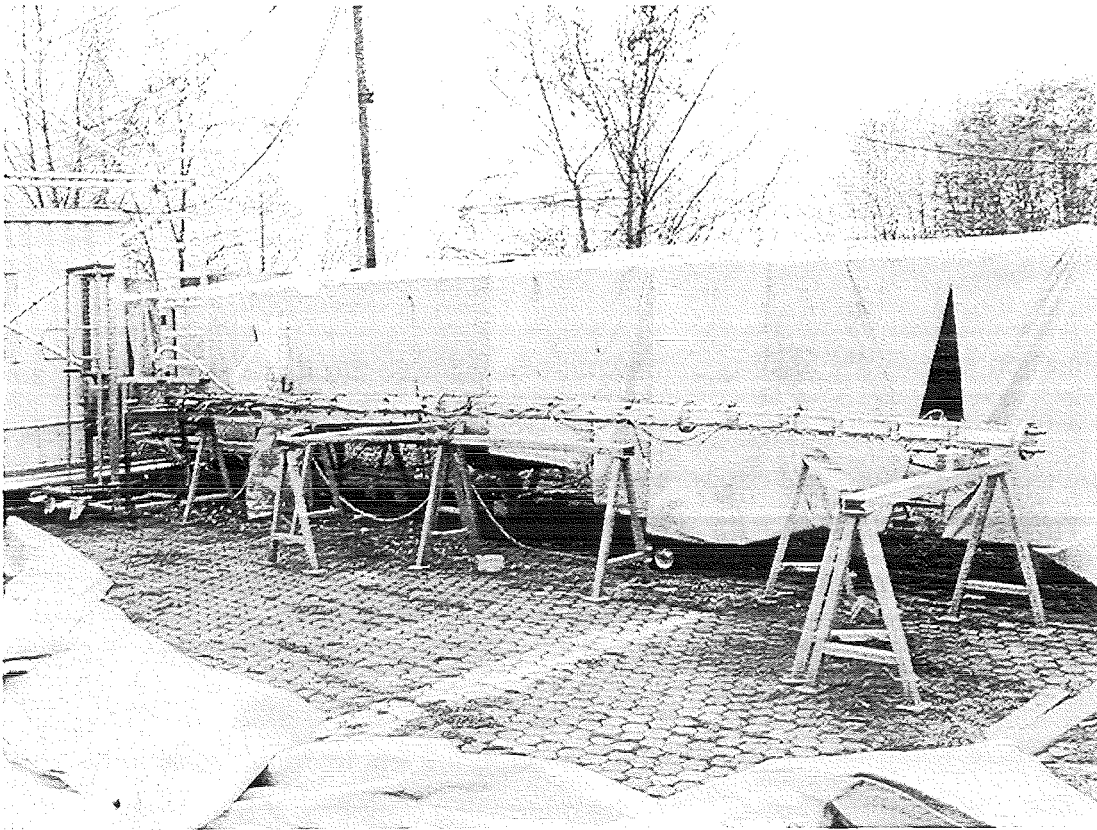


Figure 1: View of FZK 7m- tube in horizontal position. The tube could be orientated vertically with the help of a joint at the left tube end (upper picture). The lower figure shows installed photodiodes and pressure transducers along the tube. Ignition of the mixture was at the left tube end plate (upper picture) by a weak spark.

## Results

The time dependent flame propagation along the tube was analysed using the measured light and pressure signals. Flame velocity-distance diagram for the exemplary concentrations of 9%, 11% and 15% fuel gas are displayed in the Figures 2, 3 and 5.

The situation for the 9% case is somewhat exceptional: the fuel gas consisted solely of pure hydrogen, since any admixture of CO made an ignition of the mixture impossible. Three combustion experiments were performed, one with a vertical position of the 7-meter tube at an initial pressure of 1 bar. The other two have been done in a horizontal position of the tube, but with two different pressures of 1 bar and 0.5 bar (see Figure 2). In all three cases global quenching occurs before the flame front reaches the end of the tube independent of the tube's orientation. Only the pressure seems to have some influence: The quenching at 0.5 bar takes place at 4.5 m (about 60% of the tube length) while at 1 bar the quenching happens at 5.5 m (about 75% of tube length).

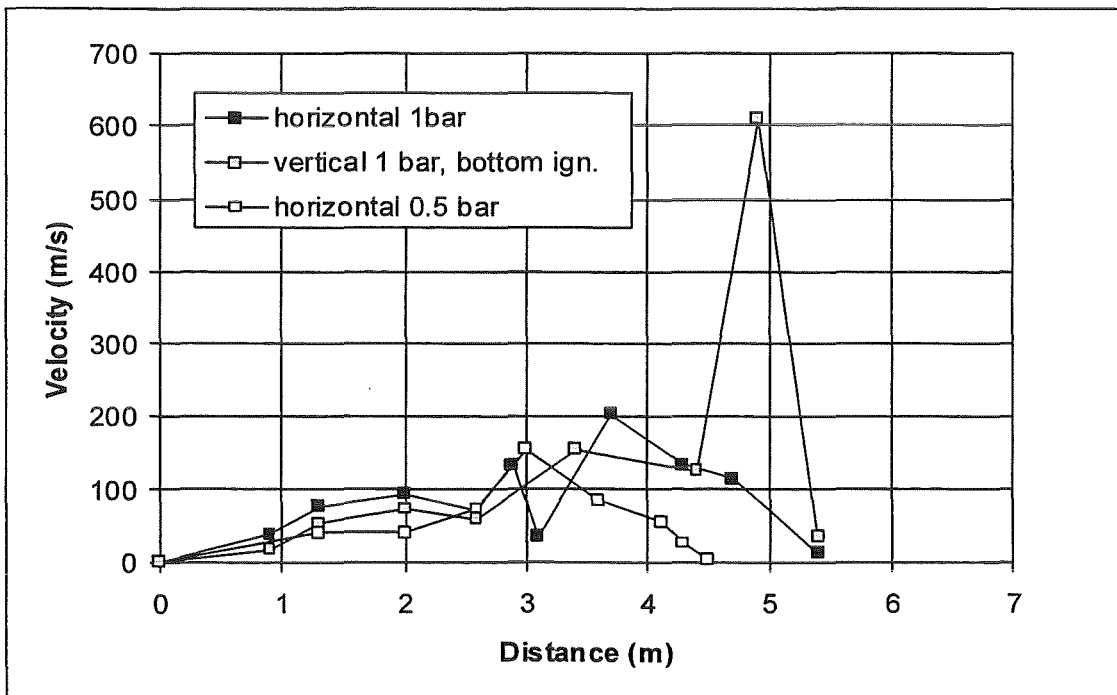


Figure 2: V-x diagram with 9% H<sub>2</sub> in air (flame velocity along the tube), ignition at x=0.

The results of the experiments carried out with 11% fuel gas concentration are depicted in Figure 3. In this case the admixture of CO was actually feasible in the

sense that the fuel gas was ignitable. However, the combustion behaviour depends strongly on the CO-H<sub>2</sub> ratio.

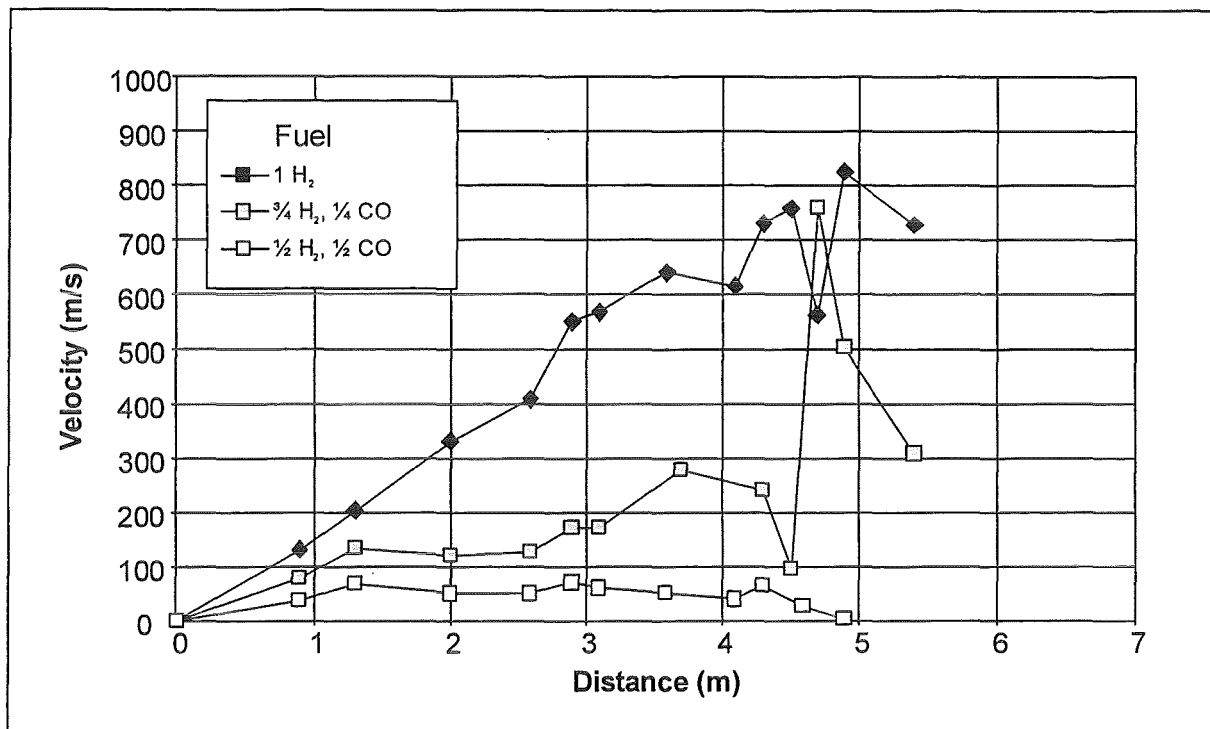


Figure 3: V-x diagram with 11% fuel gas

In the pure H<sub>2</sub> -air mixture acceleration of the flame to the fast supersonic deflagration mode is observed, and the more CO is contained in the fuel gas the slower the combustion progresses. If CO accounts for half of the fuel gas the reaction is globally quenched at about 5 m (70 % of tube length).

The sensitivity of the combustion process to the CO concentration is visible in the associated pressure histories. Fig. 4 shows recorded pressures at 3.8 m.

With pure hydrogen a very pronounced, steep and high pressure peak ( max. 8 bar) is realized. The pressure recordings for fuel gases are the smoother the higher the CO fraction in the fuel gas.

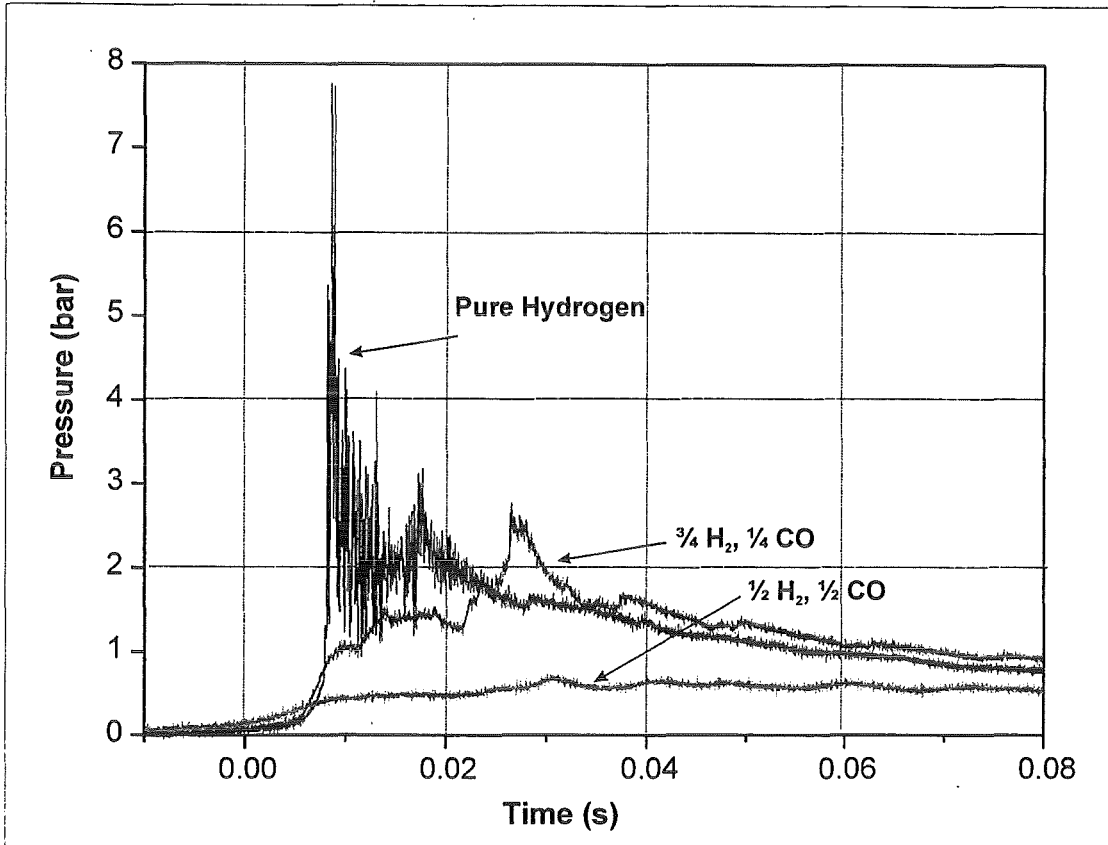


Figure 4: Comparison of measured local pressure histories at the 3.8m position for the three investigated fuel gas mixtures ( $H_2+CO = 11$  vol%).

For mixtures with 15% ( $H_2+CO$ ) the measured flame velocities along the tube (Figure 5) exhibit a greatly diminished sensitivity to the CO concentration. Quenching did not occur, only fast combustion can be observed independent of the CO concentration and of the orientation of the tube (horizontal vs. vertical).

All the experimental results are summarized with respect to the terminal flame velocity against fuel gas concentration in Figure 6. Clearly the terminal velocity depends strongly on the fuel gas concentration for concentrations below 13%. But for higher total fuel gas concentrations the influence of the mixture composition decreases strongly. Comparison of the black and the shaded symbols in Fig.6 demonstrate that the tube orientation had no influence on the terminal flame speed.

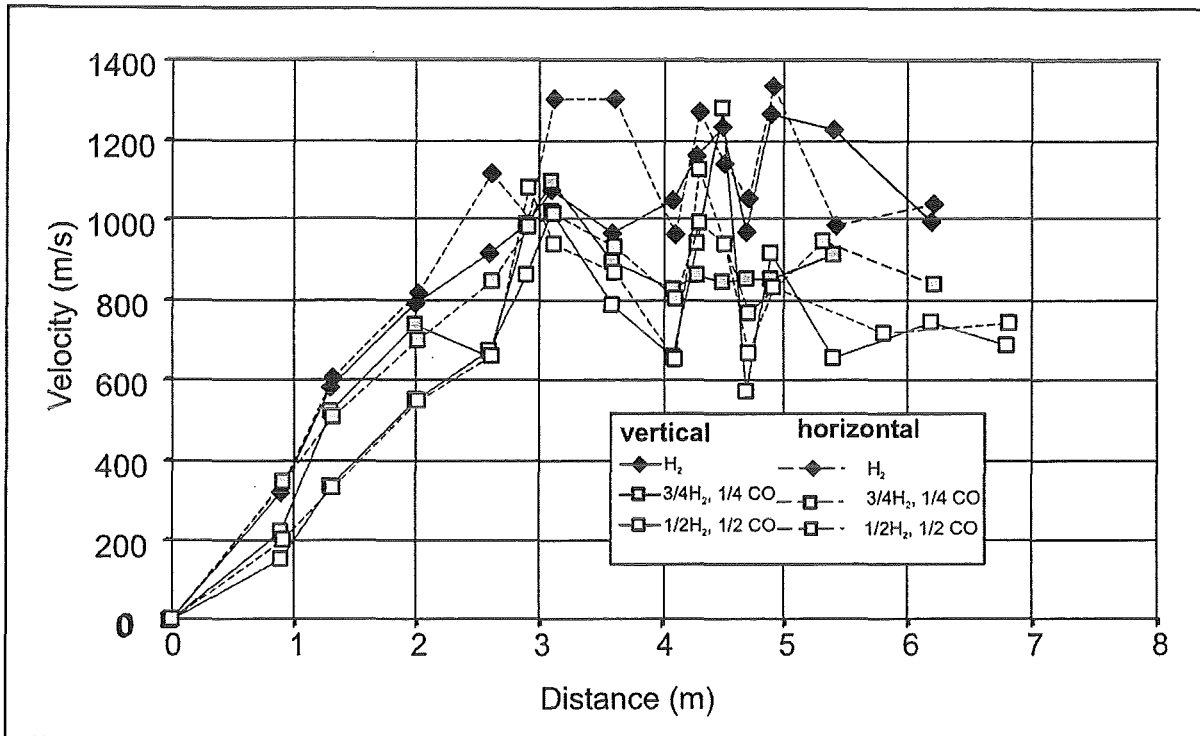


Figure 5: Measured flame velocities in mixtures with 15vol% (H<sub>2</sub>+CO). For such strong mixtures no effect of CO concentration in the terminal flame speed is observed.

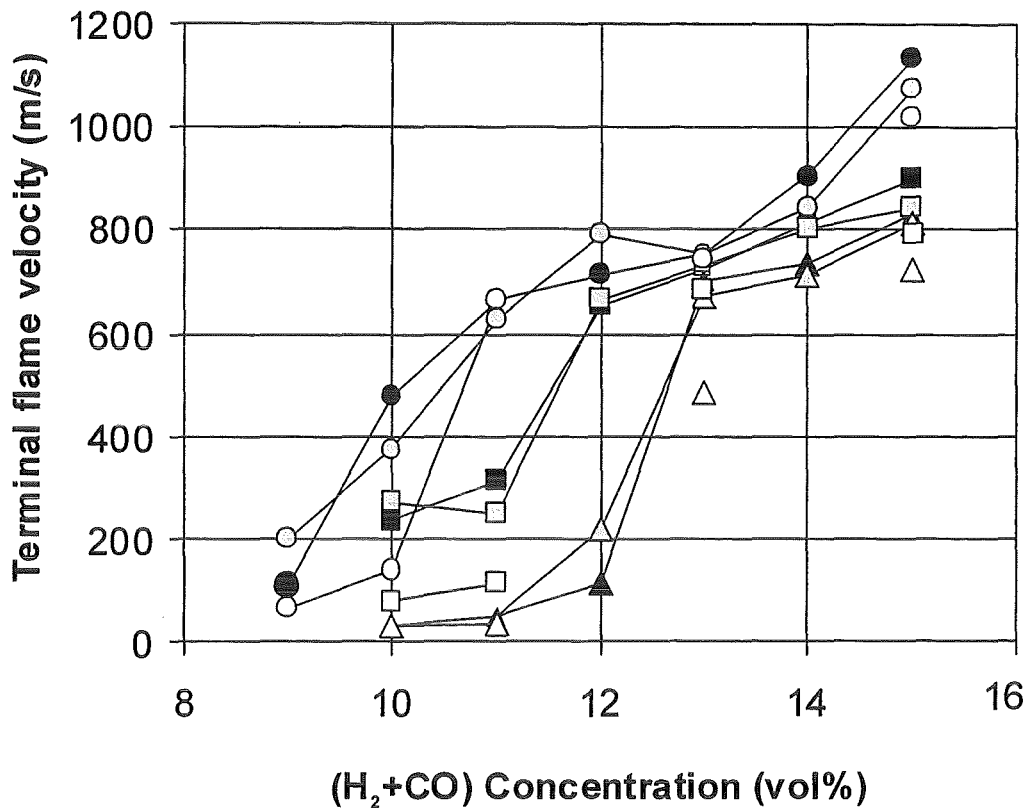
#### 4. Summary

The experiments clearly indicate a strong influence of the CO fraction in the mixture for low total fuel gas concentrations. Compared to pure H<sub>2</sub> the presence of CO hinders fast deflagration and may even lead to global quenching in obstructed flow geometries.

The transition from slow to fast combustion is shifted towards higher fuel concentrations with increasing CO fraction in the mixture.

For total fuel gas concentrations above 13% the influence of CO on the combustion speed is much less pronounced, and can be neglected in the first order (CO equivalent to H<sub>2</sub>)

The results of this study can not be explained with traditional EBU models, which assume that the reaction rate is independent of the mixture composition and solely determined by the turbulent mixing time scale for burned and unburned gases



Orientation	Fuel (H <sub>2</sub> /CO)	Pressure (bar)
●—Horizontal	1.0/0.0	1
■—Horizontal	0.75/0.25	1
▲—Horizontal	0.5/0.5	1
○—Vertical	1.0/0.0	1
□—Vertical	0.75/0.25	1
△—Vertical	0.5/0.5	1
○—Horizontal	1.0/0.0	0.5
□—Horizontal	0.75/0.25	0.5
△—Horizontal	0.5/0.5	0.5

Figure 6: Measured terminal flame velocities of FZK-7m-tube experiments with various fuel-air mixtures, tube orientations and initial pressures. CO has only a significant effect below 13 vol % (H<sub>2</sub>+CO).

### References

[1] R.K. Kumar, G.W. Koroll, M. Heitsch, E. Studer, „Carbon Monoxide-Hydrogen Combustion Characteristics In Severe Accident Containment Conditions”, Final Report, NEA/CSNI/R (2000)10, February 2000.

III. Numerical Simulation of Combustion with COM3D, B0B, Flame3D  
(U. Bielert, A. Veser, A. Kotchourko, R. Redlinger, W. Breitung, IKET)

**Abstract**

In the second year of the project the focus of our work was on pre- and post test calculations of the various experiments performed within the project. Calculations were performed with three different codes: B0B, Flame3D and COM3D. In the following we will present some results of the simulations.

**1. Simulation of small scale tests with B0B**

In the experimental part of the project four different configurations were tested and the details of the different configurations are described in the reports D1 and D2. Results of the experiments are already documented in reports D6, D7 and D8.

For all four configurations simulations were performed with the combustion code B0B. For configurations 1, 2 and 3 the calculations were performed as post test calculations after the

Experiments had been performed, while the simulation for configuration 4 is a pre test calculation performed before the actual experimental data is distributed.

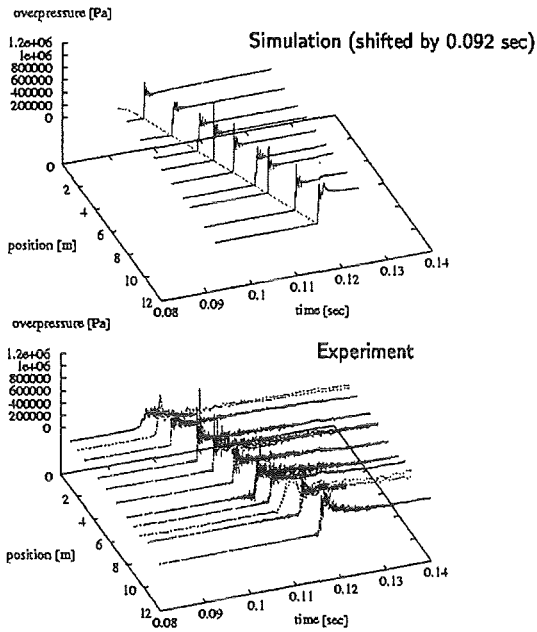
In configuration 1 the effect of ignition location and of venting at the tube end was investigated experimentally. Three cases of the test matrix for this configuration have been simulated with B0B. In all three cases the hydrogen concentration was 13 %. The pressure histories of the simulations are compared to the experimental data in Figure 1. Note that the simulation data is shifted in time by a constant value for each calculation. This is necessary because the initial phase of the ignition process is controlled by random processes not captured in the numerical model.

In test mc012 the mixture was ignited at the end of the tube. The strength of the leading wave changes while it is moving through the tube. The simulation gives similar locations for the pressure peaks as the experiment. A detailed comparison of experiment and simulation shows good agreement at all locations with the largest differences at position 1.18m. Since the numerical model does not include heat losses a constant pressure is predicted after the combustion process is finished. Of

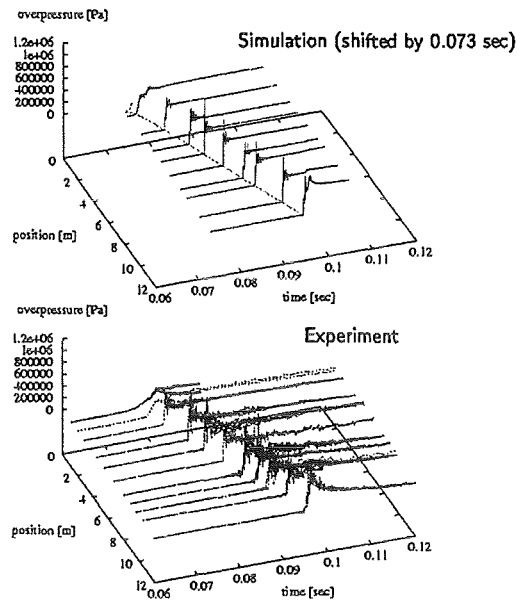
course the losses in the experiment result in a pressure decay after the end of combustion. However, the effect of neglecting heat losses is small during the combustion process.

In tests mc025 and mc028 the mixture is ignited at some distance from the end of the tube. For both tests the experimental and the simulation pressure data are given in figure 1. Again the simulations capture the main features of the flame propagation correctly. The lower right corner of figure 1 shows the flame arrival times and the flame velocities along the tube. Shown are the experimental results as lines and the simulation results as lines with symbols. With the time offsets given in the pressure diagrams a good agreement between experiments and simulations is observed. Only the ignition phase is not covered correctly by the simulation as stated earlier. The diagram of flame velocities shows a somewhat earlier acceleration in the simulations. Also some smaller velocity fluctuations observed in the experiment at later times are not reproduced by the calculations.

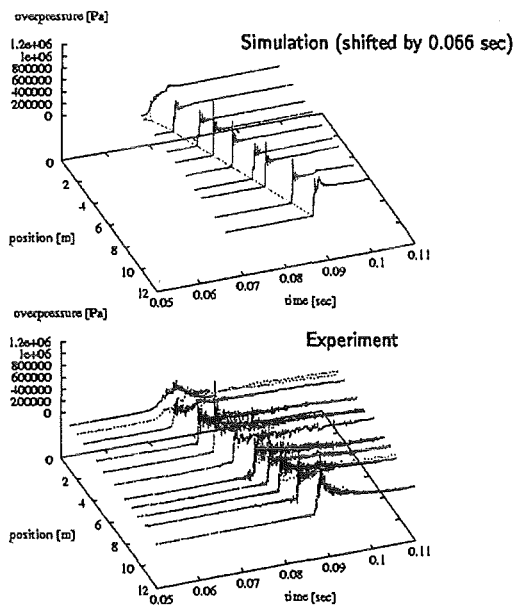
### Configuration 1 Experiment mc012



### Configuration 1 Experiment mc025



### Configuration 1 Experiment mc028



### Configuration 1

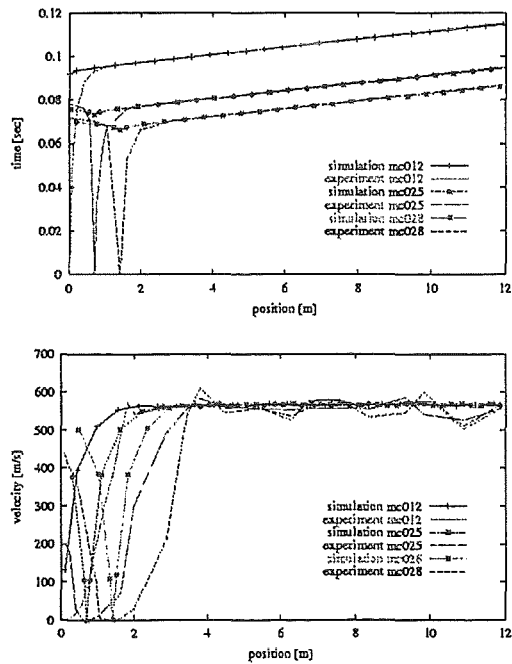


Figure 1: Results for small scale tests in configuration 1

In configuration 2 the effect of change of blockage ratio was investigated. Two experiments with a hydrogen concentration of 13% H<sub>2</sub> were simulated in this configuration. In test mc038 the flame is ignited at the end of the tube section with a blockage ratio of BR=0.3. At the middle of the tube the flame enters into a more confined section with a blockage ratio of BR=0.6. The pressure histories for this case are presented in the top left corner of Figure 2. Some differences between experiment and simulation exist. Namely the peak pressure values and the wave characteristics near the end walls are not predicted correctly.

The second case calculated in this configuration is a flame propagating from a more confined region with BR=0.6 into a less confined region with BR=0.3. This case is shown in the upper right corner of figure 2 as experiment mc042 Here the agreement between experiment and simulation is again good.

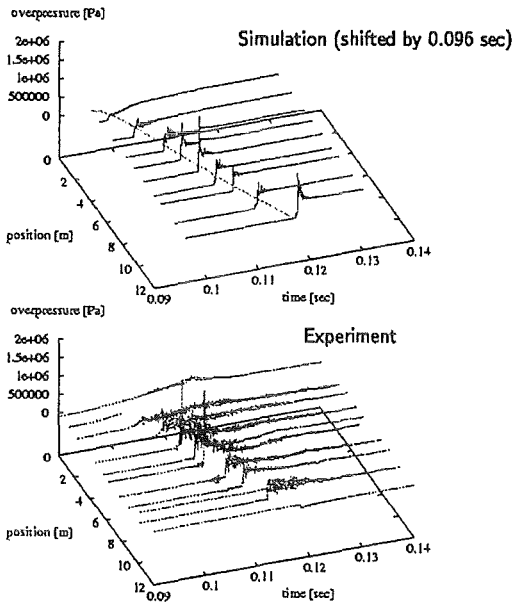
Flame arrival times and flame velocities are shown in the lower part of figure 2. Neglecting the initial phase the flame propagation is correctly described by the simulation. For case mc042 (flame moving into a less confined region) the flame velocities near the change of blockage ratio is predicted qualitatively correct. However, for case mc038, where the flame moves into a more confined region, the calculated velocities are different from the experimental observations. In the experiment the flame accelerations prior to the change in blockage ratio. As the flame enters the more confined section the velocity goes down. In the simulation the velocity in the first section reaches an almost stationary value and drops at the change of blockage ratio. This drop is followed by a velocity peak between 7 and 8 m. This peak is not observed in the experiment.

In configuration 3 the combined effect of change of blockage ratio and change of tube diameter is investigated. For this configuration for simulations were performed with hydrogen concentrations of 13%. These for cases are summarized in the following table:

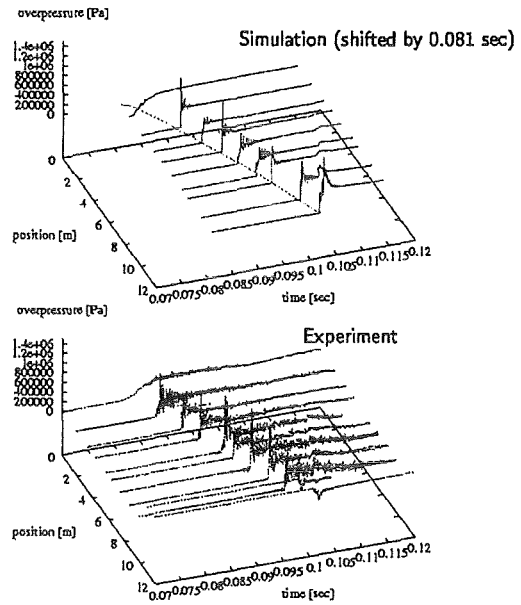
Case	Blockage ratio change	Tube diameter change
HC08	Decrease 0.6 – 0.3	Decrease
HC18	Increase 0.3 – 0.6	Decrease
HC17	Decrease 0.6 – 0.3	Increase
HC27	Increase 0.3 – 0.6	Increase

The pressure histories for all for cases are given in Figure 3. For case HC08 shown in the top left corner the agreement between experiment and simulation is good. For case HC18 the agreement is quite good in the first half of the setup, but the flame propagates to fast in the second section. The simulation of case HC17 shown in the lower left corner is again in good agreement with the experiment. For case HC27 difference between simulation and experiment are observed. From these simulations it seems that the transition from a less confined to a more confined region posses some problems to the numerical model.

**Configuration 2 Experiment mc038**



**Configuration 2 Experiment mc042**



**Configuration 2**

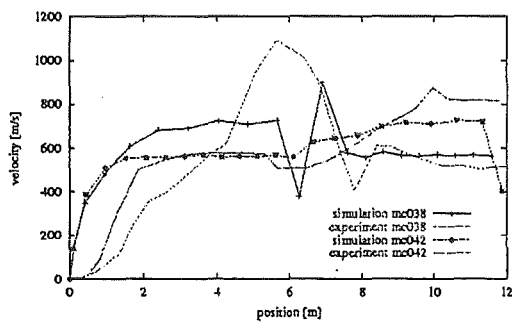
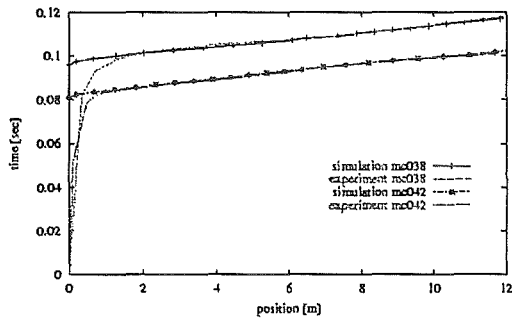
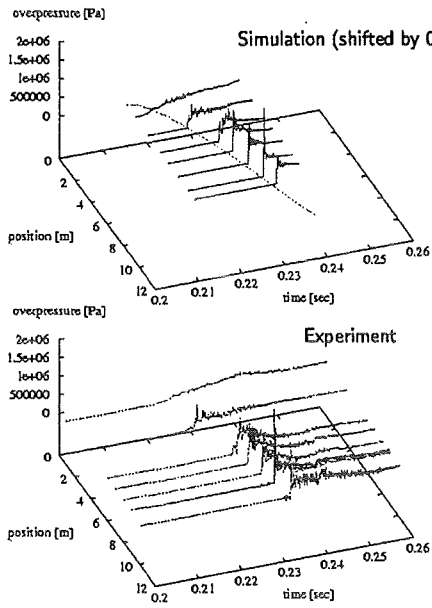
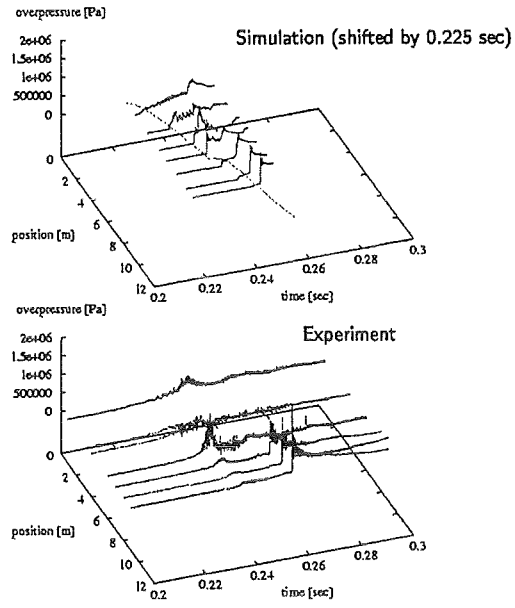


**Figure 2: Results for small scale tests in configuration 2**

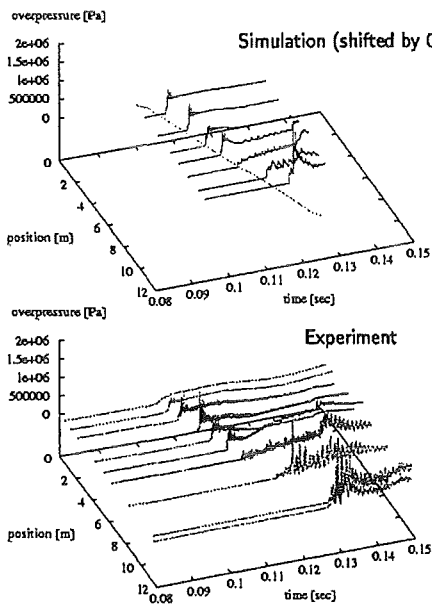
**Configuration 3 Experiment hc08**



**Configuration 3 Experiment hc18**



**Configuration 3 Experiment hc17**



**Configuration 3 Experiment hc27**

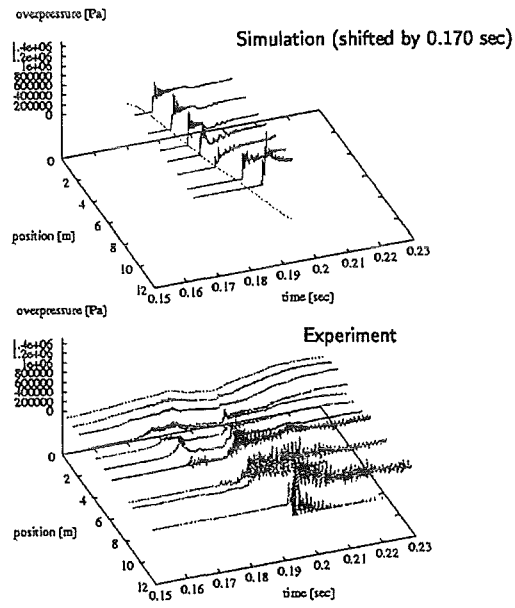


**Figure 3: Results for small scale tests in configuration 3**

The last configuration investigated in the small scale experiments is also a tube with a change in the tube diameter. However, compared to configuration 3 the tube is now twice as long. One case was calculated for this configuration as blind pre test calculation. In the selected configuration a mixture with a hydrogen concentration of 10% is ignited at the end of the larger diameter tube. The blockage ratio in the right larger diameter tube is  $BR=0.6$  and the blockage ratio in the smaller left tube is  $BR=0.3$ . The flame is ignited in the right section of the setup and then propagates into the smaller tube. Figure 4 shows the spatial distribution of temperature, pressure, energy and axial velocity for an instance in time when the flame enters the smaller tube. It can be observed, how the flame still consumes unburned pockets in the larger tube between the obstacles.

In the lower part of figure 4 the calculated pressure histories and the position of the flame as function of time are given. These curves indicate that the combustion is rather slow and now strong overpressures are produced. The next step for this simulation will be a comparison with the experimental data as soon as it becomes available.

## 2. Simulation of large scale tests

For the large scale tests simulations were performed with the fully parallel combustion code Flame3D. Four experiments were calculated with this code as blind calculations.

Case	Hydrogen concentration	Ignition location
HYC11	10 %	Channel
HYC12	11.5 %	Channel
HYC13	10 %	Canyon
HYC14	11.5 %	Canyon

The calculated pressure histories for all four cases are summarized in Figure 5. The slowest combustion is observed for case HYC13 with the lower hydrogen concentration and an ignition location at the bottom of the canyon. In the time period shown in the figure the combustion is not completed and thus the final pressure value has not

yet been reached. Generally the calculations with the same ignition location also have similar dynamics. For each ignition location the case with the higher hydrogen concentration is burning faster, resulting in higher peak pressures and stronger oscillations. For different ignition locations the peak pressures are observed at different locations. Of course this is expected as the flame propagates in opposite directions for the two different ignition locations.

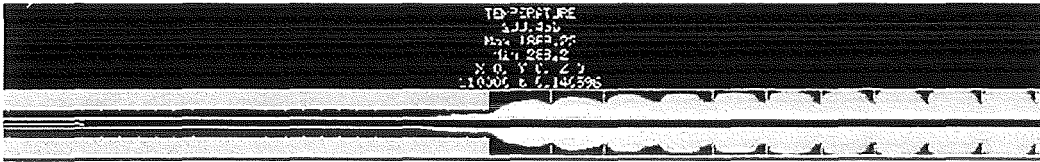
The test case HYC14 was also simulated with the turbulent combustion code COM3D. Results of this calculation are shown in Figure 6. This simulation produced very smooth pressure curves, indicating a slow combustion process with very small pressure waves in the system.

Since the experimental data for the four large scale tests is not yet available, the final evaluation of the pre test calculations must be postponed for the time being.

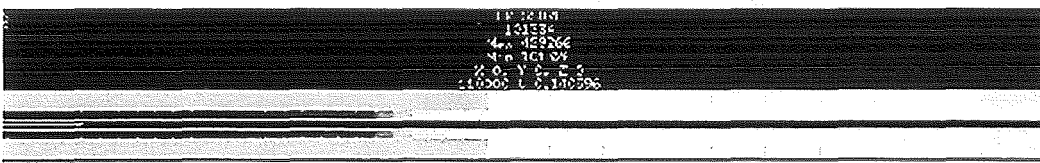
In addition to the simulation results produced at FZK work to compare the simulation results of the different partners is under way and has been partially documented in the reports D3 and D4.

## Configuration 4

Temperature



Pressure



Energy



Z Velocity

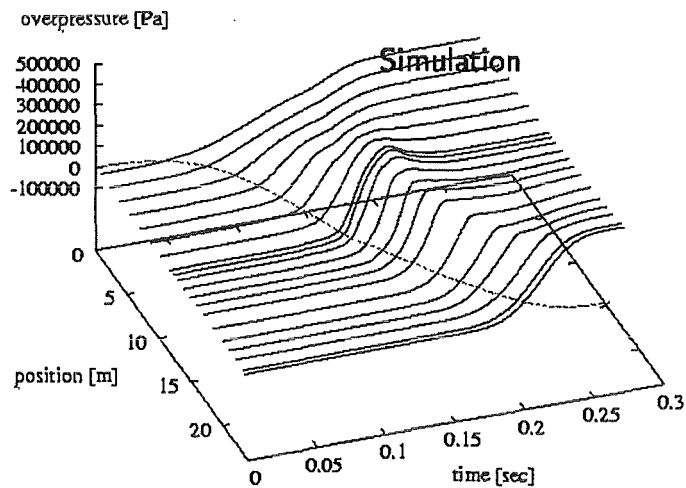
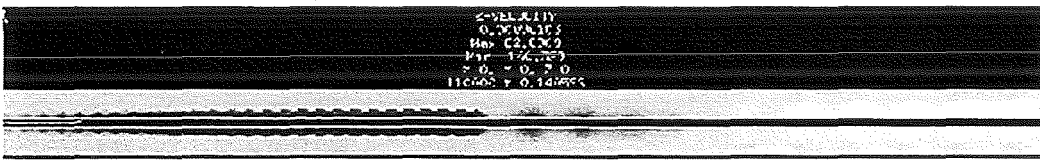
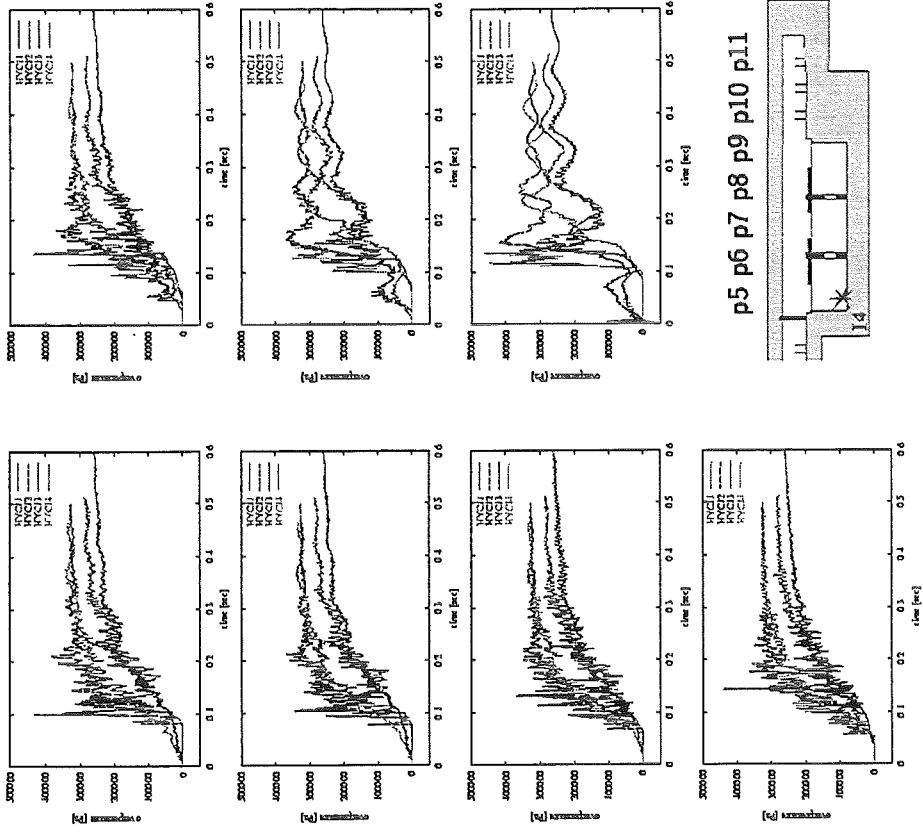


Figure 4: Results for small scale tests in configuration 4

Flame3D: pressure data top row



Flame3D: pressure data bottom row

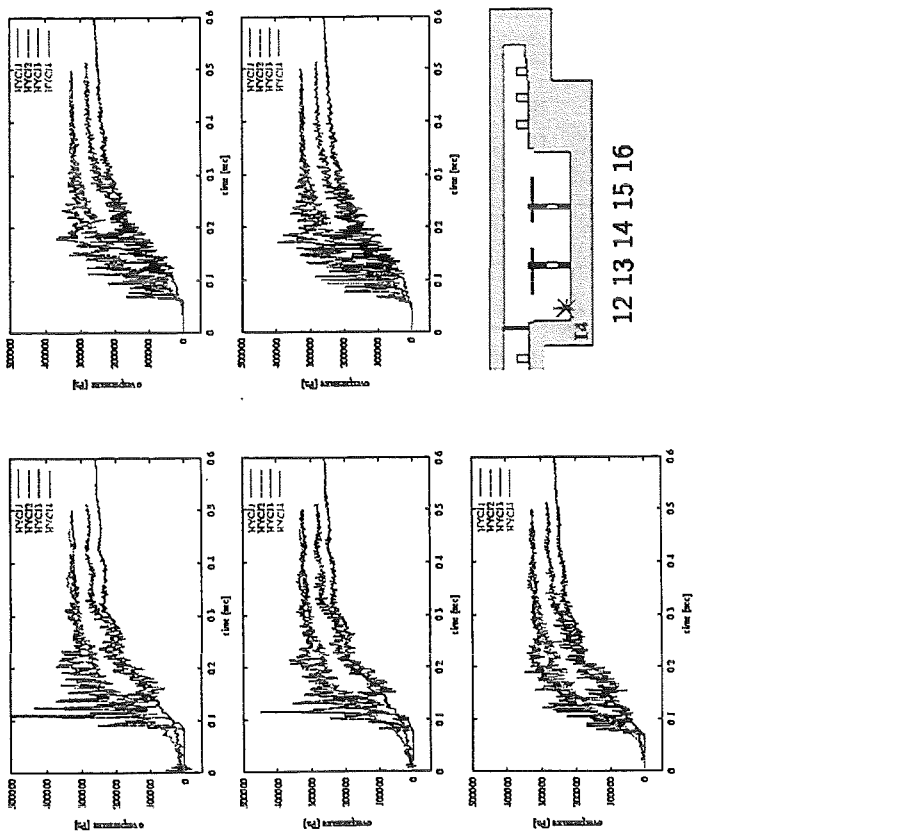
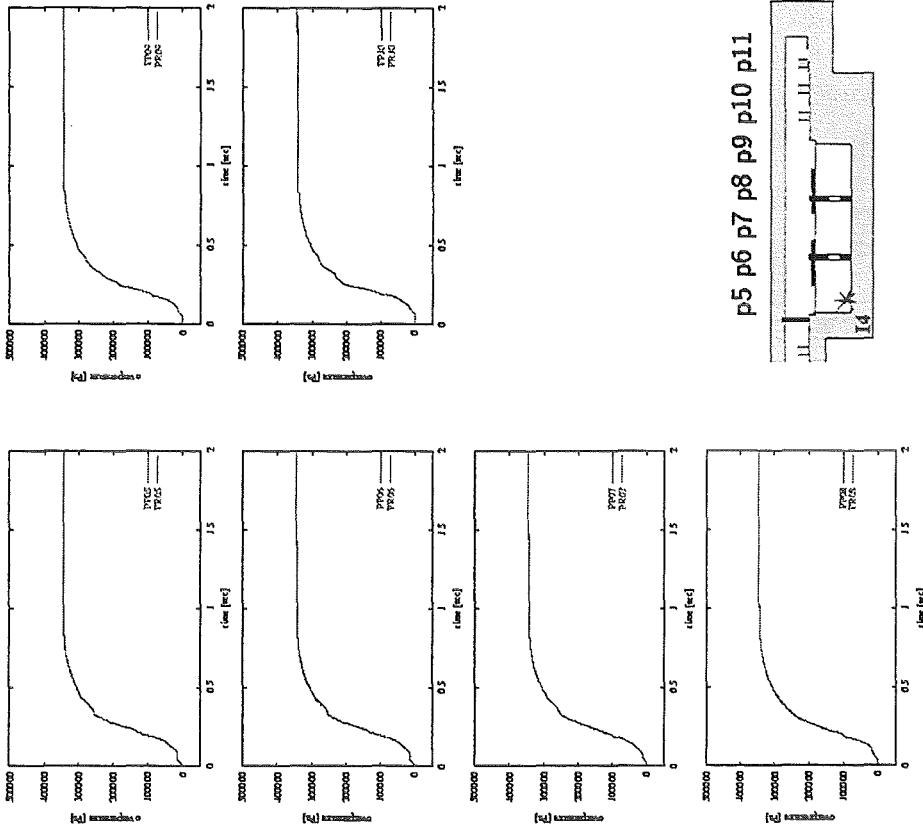


Figure 5: Flame3D calculations for large scale tests

COM3D: HYC14 top row



COM3D: HYC14 bottom row

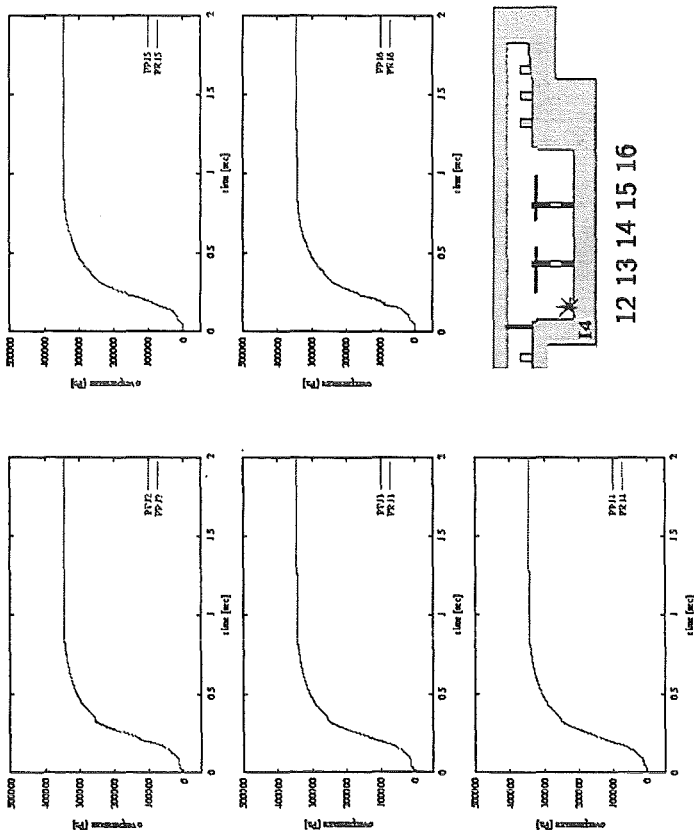


Figure 6: COM3D calculations for large scale tests

#### IV. Run-up Distances to Supersonic Flames in Obstacle-Laden Tubes

(A. Vesper, W. Breitung, S. Dorofeev, IKET)

##### **Abstract**

The problem of the minimum run-up distance for the flame acceleration to supersonic combustion regimes in tubes with obstacles is studied both experimentally and numerically. Experiments were made in an explosion tube equipped with orifice plate obstacles. The tube was of 12-m long with internal tube diameter of 0.35 m. Blockage ratios (BR) of the orifice plates were 0.3, 0.45, 0.6 and 0.75. Hydrogen mixtures were used in the tests. The process of the flame acceleration in a geometry, which is similar to the experimental one, was studied numerically in a series of 3D gasdynamic simulations. It was found both in the tests and in the simulations that characteristic distance of the flame acceleration decreases with the increase of the blockage ratio and with the increase of the mixture reactivity (burning rate). A simple analytical model is proposed, which describes the evolution of the flame shape in the channel with obstacles. The dimensionless flame acceleration distance is determined in the model, which accounts for BR, laminar burning rate, and sound speed in combustion products. The model allows to estimate the minimum acceleration distance necessary for the development of fast flames.

##### **1. Introduction**

Numerous experimental data on combustion of gaseous mixtures in obstacle-laden channels show that three characteristic combustion regimes can be distinguished in this type of geometry. These regimes include slow subsonic deflagrations, fast deflagrations, and quasi-detonations. Generally, cases of fast deflagrations and detonations can result in significantly high values of overpressures, which can be dangerous for integrity of confining structures. Considering practical applications for safety analyses, two important problems should be solved. The first one concerns the possibility of development of the fast combustion regimes in a particular mixture and geometry. If the fast deflagrations and quasi-detonations are principally possible, the second problem should be solved: evaluation of the minimum run-up distance for development of these fast combustion waves. While the first problem can be addressed with application of criteria for different combustion regimes (see, e. g., [1]), the second one should generally require application of a model for time-dependent

simulation of the flame acceleration process. The problem of the minimum run-up distance for the flame acceleration to supersonic combustion regimes in tubes with obstacles is studied in the present work both experimentally and numerically.

## **2. Experimental**

Experiments were made in an explosion tube equipped with orifice plate obstacles. The tube was of 12-m long with internal tube diameter of 0.35 m. Blockage ratios (BR) of the orifice plates were 0.3, 0.45, 0.6 and 0.75. Hydrogen-air mixtures with 11 to 20 vol. % of hydrogen and stoichiometric hydrogen-oxygen mixtures diluted with argon and helium were used in the tests. Experiments were made at normal initial conditions ( $t = 20\text{ C}$ ,  $P = 1\text{ atm}$ ). A weak electrical spark was used to ignite the mixtures at one end of the tube. Fast-response piezoelectric pressure transducers and photo-diodes were used to measure pressure and flame time-of-arrival.

## **3. Numerical Model**

The process of flame acceleration in a geometry, which is similar to the experimental one, was simulated numerically with 3D gasdynamic code B0B [2]. It was assumed that the effective turbulent burning rate is constant during all the process of the flame acceleration. This means that from two main factors responsible for the flame acceleration: increase of the flame surface due to interactions of gas flow with obstructions and increase of the burning rate with the increase of turbulence level, only the first one was accounted for in the simulations. The value of the effective turbulent burning velocity,  $S_T$ , was varied from 3.4 m/s to 17.4 m/s. This range represents the maximum achievable turbulent burning velocity for typical fuel-air mixtures, which is usually of the order of 10 times the laminar burning velocity. Thermodynamic properties corresponded to those of the mixture of 13 % vol. of hydrogen with air in all the calculations.

## **4. Results**

### **4.1. Experimental results**

Figures 1, 2, 3, and 4 show examples of experimental data on flame propagation velocities versus distance along the tubes. Examples are shown for hydrogen-air mixtures. Data for BR = 0.3 presented in Fig. 1 show the flame acceleration can result in a variety of the flame propagation velocities. In two mixtures (9 and 10% H<sub>2</sub>)

the flames achieve velocities well below the sound speed in reactants. In other mixtures the flame accelerates to supersonic velocities relative to a fixed observer. Data of Figs. 2, 3, and 4 show only fast supersonic flames. Some of these supersonic flames accelerate to a velocity, which is roughly equal to the sound speed in combustion products. This is known as the “choked flame” regime [3, 4]. In other cases the flame achieves a speed just below the theoretical CJ detonation velocity. This propagation regime is commonly referred to as “quasi-detonation.”

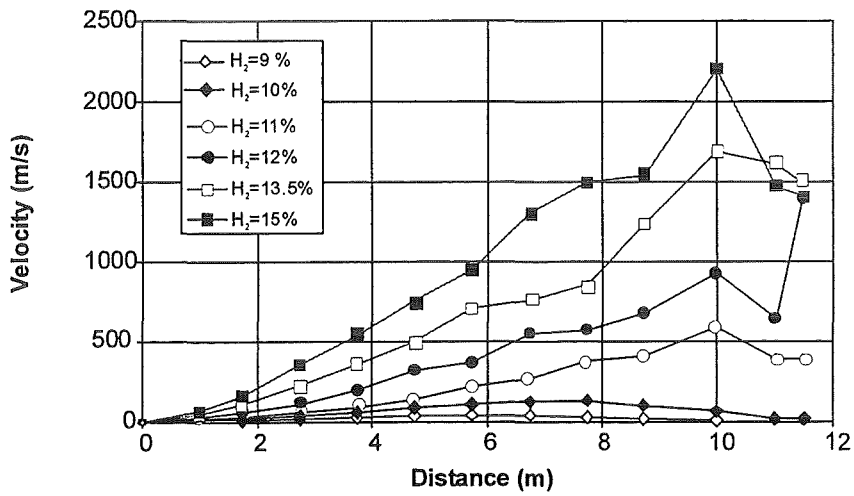


Figure 1. Flame velocities versus distance in hydrogen-air mixtures with BR = 0.3

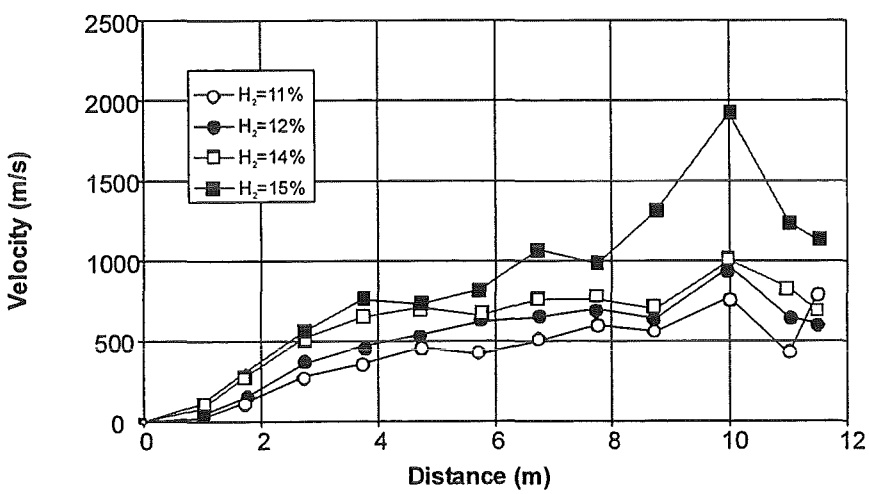


Figure 2. Flame velocities versus distance in hydrogen-air mixtures with BR = 0.45

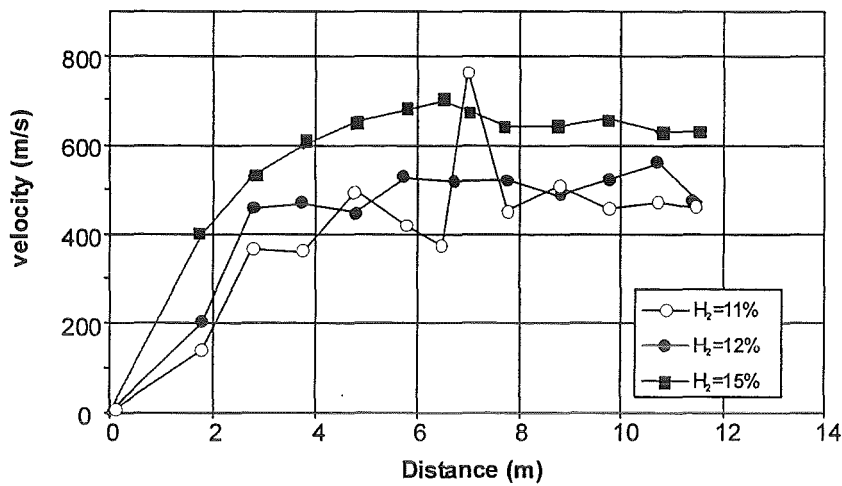


Figure 3. Flame velocities versus distance in hydrogen-air mixtures with BR = 0.6

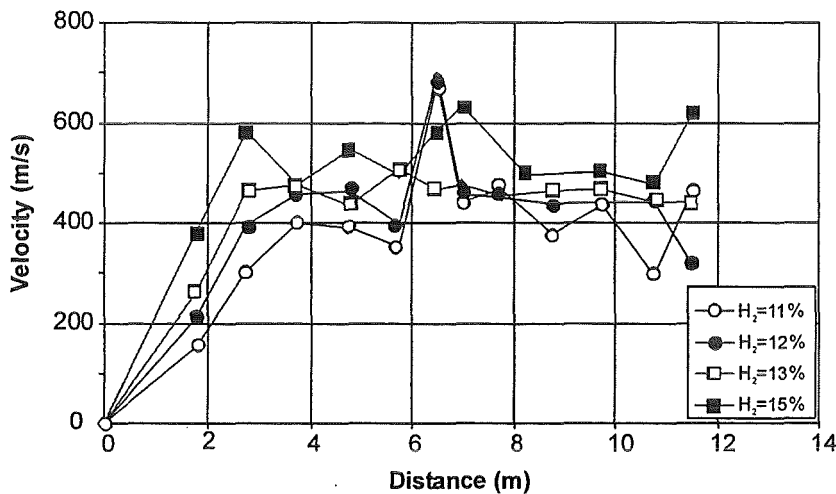


Figure 4. Flame velocities versus distance in hydrogen-air mixtures with BR = 0.75

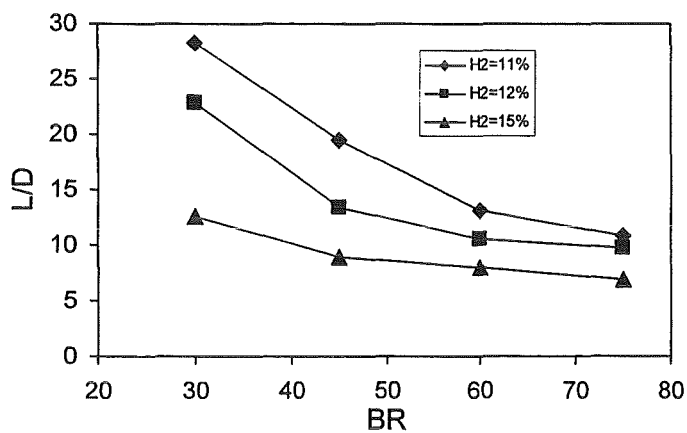


Figure 5. Run-up distances for flame acceleration over tube diameter L/D versus BR

In cases the flame acceleration to the supersonic combustion regimes was possible, a characteristic run-up distance,  $L$ , was determined from the experimental data. It was defined as a distance, where the flame speed reaches the value of 95% of the choked flame speed for each value of BR (close to the sound speed in combustion products). Figure 5 shows as an example the dimensionless flame acceleration distance as a function of BR for three hydrogen-air mixtures. It is seen that  $L/D$  decreases with increase of BR and with increase of the mixture energetic.

#### 4.1. Numerical results

Flame shapes in the obstructed tubes for two different time moments are presented in Fig. 6. Examples of calculations with BR = 0.6 are given with the turbulent burning velocity  $S_T$ , equal 3.4 and 17.4 m/s. The dependences of the flame speed versus distance are shown in Figs. 7 and 8. The values of the maximum Mach numbers in the flow versus flame propagation distances are also presented in Figs. 7 and 8. The run-up distance was determined in a similar way as in the analysis of the experimental data. It was found that at the distances where the flame acceleration is completed and a steady-state flame speed is approached, the maximum local Mach number in the flow reaches unity.

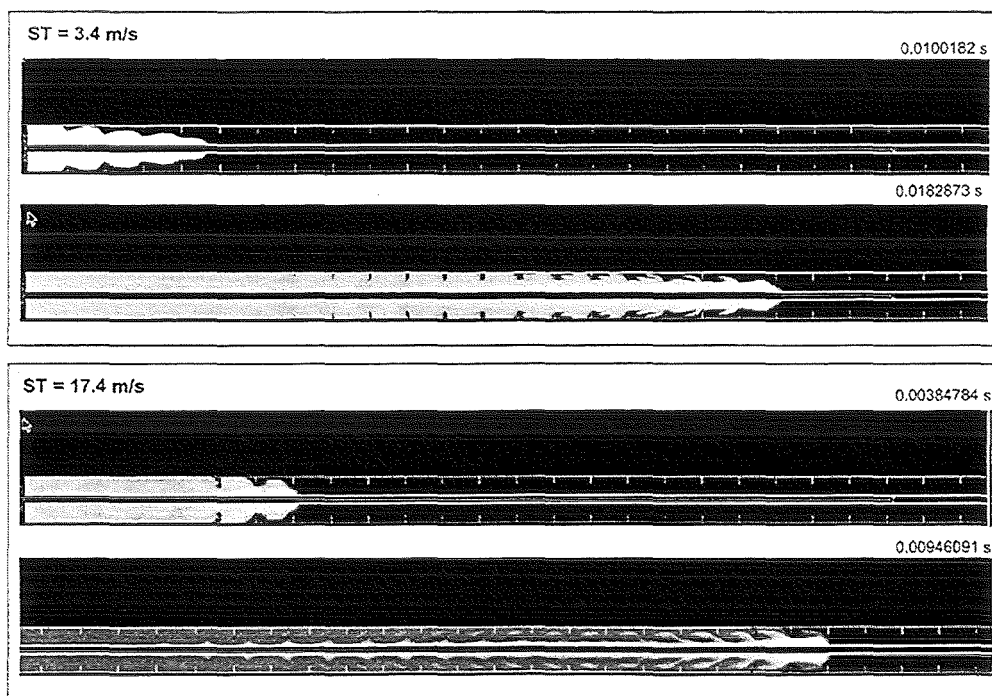
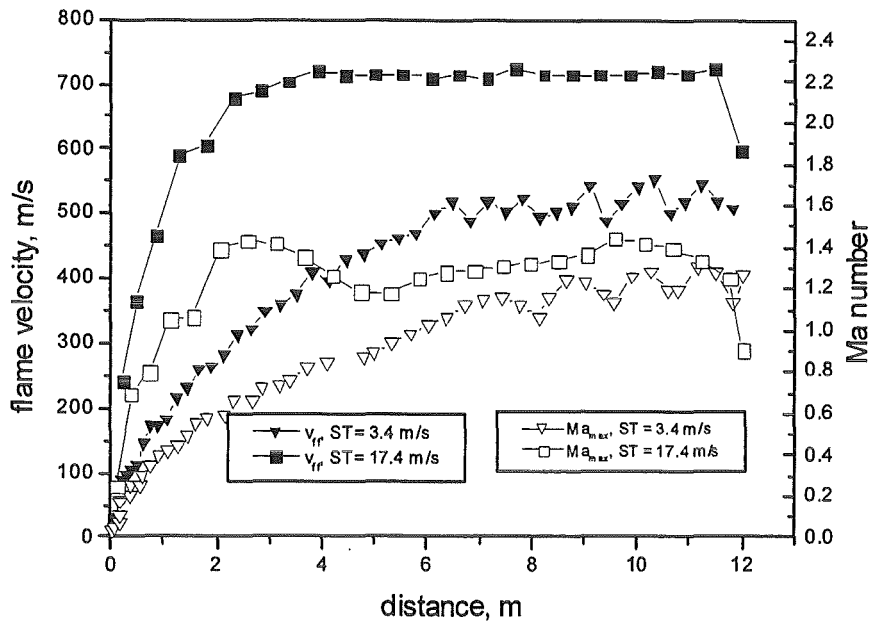
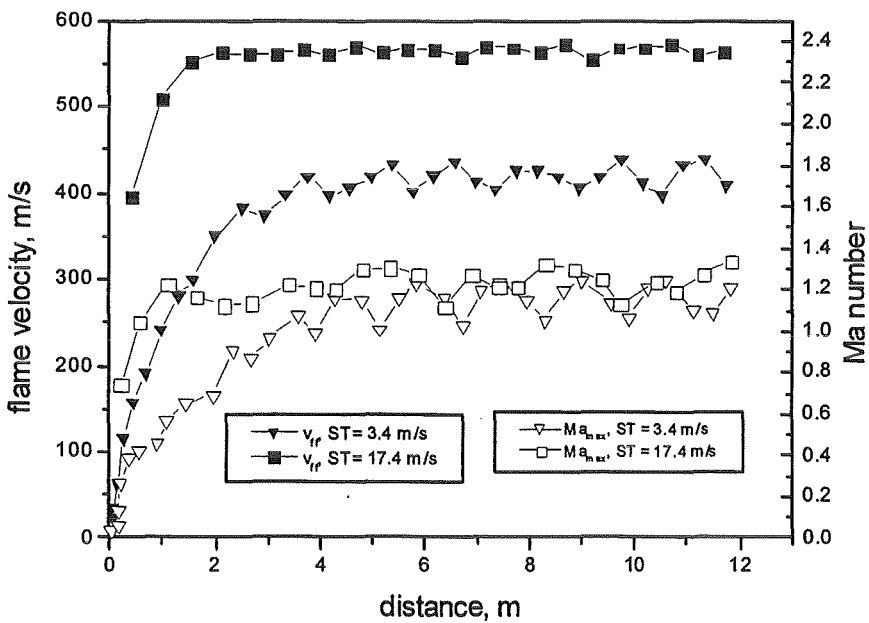


Figure 6. Temperature distributions showing the shape of the flame front.



**Figure 7.** Flame velocities and maximum flow Mach number versus distance of flame propagation. Results of simulations with BR = 0.3, D = 0.174 m



**Figure 8.** Flame velocities and maximum flow Mach number versus distance of flame propagation. Results of simulations with BR = 0.6, D = 0.174 m.

Characteristic run-up distances determined from the results of simulations are presented in Fig. 9. Similar to the experimental results, it was found that characteristic distance of the flame acceleration in the simulations decreases with the increase of the blockage ratio and with the increase of the mixture burning velocity.

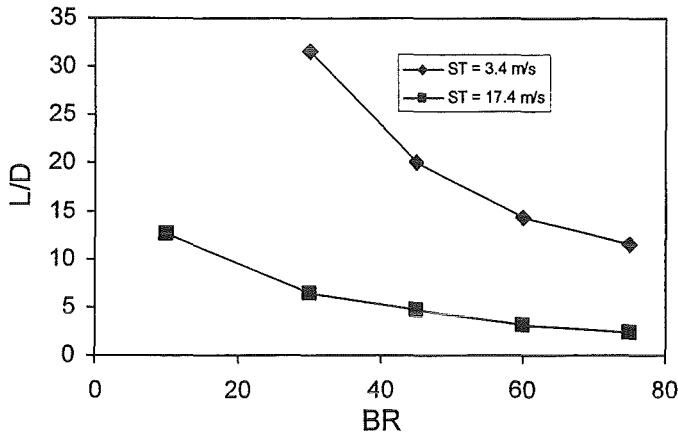


**Figure 9.** Run-up distances for flame acceleration over tube diameter L/D versus BR. Results of simulations.

## 5. Discussion

A comparison of Fig 5 and Fig. 9 shows that the results of simulations reproduce correctly the flame acceleration distance found experimentally, if the effective turbulent burning velocity,  $S_T$ , in calculations is chosen to be 10 times the laminar burning velocity. This suggests that in the channel geometry with dense obstructions, with BR from 0.3 to 0.75, the geometrical factor (increase of the flame surface) is mainly responsible for the flame acceleration.

On this basis a simple analytical model may be suggested, which describes the evolution of the flame surface and visible flame speed in the channel with obstacles. A schematic illustration of the flame shape in a tube with orifice plates is presented in Fig. 10. At the moment when the head of the flame reaches a distance  $X$ , the flame surface,  $\Omega$ , can be estimated from the following expression.

$$\Omega = \pi R X + b \pi R X \cdot BR = \pi R X (1 + b \cdot BR) \quad (1)$$

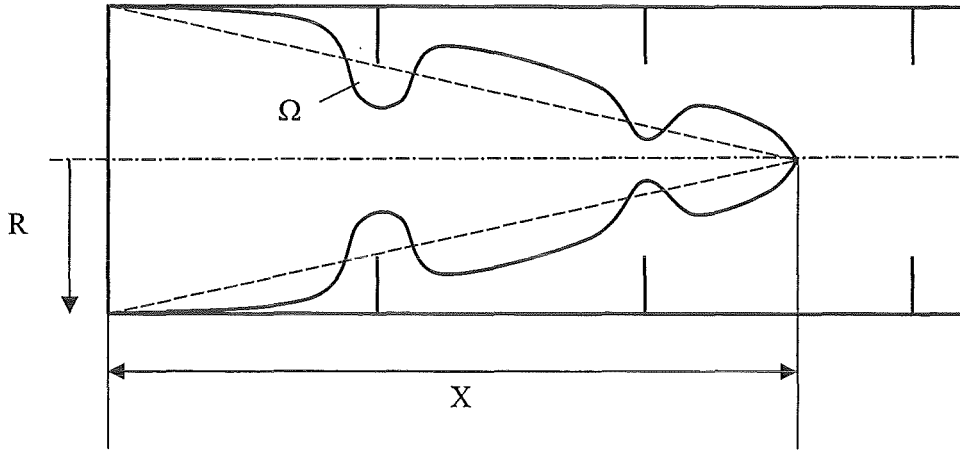


**Figure 10.** Schematic for estimation of flame surface in tube with orifice plates.

The first term in the sum of Eq. (1) corresponds to the surface of the cone shown by dashed lines in Fig. 10. The second term describes the contribution of the bended part of the flame surface near the orifice plates. The relative weight of this contribution is given by the coefficient  $b$ , which should be of the order of unity.

The speed of the flame generated flow,  $U$ , through the orifice of the obstacle plate with an area  $s$  can be estimated as:

$$U \approx S_T(\sigma - 1) \frac{\Omega}{s} = S_T(\sigma - 1) \frac{X}{R} \frac{1 + b \cdot BR}{1 - BR}, \quad (2)$$

where  $\sigma$  is the ratio of densities of the reactants and products (expansion ratio). The flame speed relative to a fixed observer will be given by the sum  $U + S_T$ . At the distance,  $L$ , when the flame speed approaches the sound speed in combustion products,  $c_p$ , the flow speed,  $U$ , will be close to  $c_p$ , as well, because  $c_p \gg S_T$ . Thus, one can obtain the following estimate for the run-up distance  $L$ :

$$\frac{L}{R} \approx \frac{c_p}{S_T(\sigma - 1)} \frac{1 - BR}{1 + b \cdot BR}. \quad (3)$$

At the stage when the flame approaches the choking regime, the turbulent burning velocity should be close to the maximum one, which corresponds to a high turbulence level. This velocity is expected to be about 10 times the laminar burning

velocity  $S_L$ , or at least to be proportional to  $S_L$ . Taking this into account, the expression for the run-up distance can be rewritten as:

$$\frac{L}{R} \frac{10S_L(\sigma - 1)}{c_p} \approx a \frac{1 - BR}{1 + b \cdot BR}, \quad (4)$$

where  $a$  is a coefficient, which is expected to be of the order of unity. The left-hand side of Eq. (4) represents a dimensionless run-up distance, which accounts for the mixture properties. This dimensionless distance is expected to be a function of the blockage ratio.

One can evaluate the validity of the above approach by correlating the experimental data using the dimensionless run-up distance from the left-hand side of Eq. (4). Such a correlation is presented in Fig. 11. The data from the present study are supplemented by data from different tubes [5] in Fig. 11. Data were taken for the mixtures with hydrogen concentrations in air ranging from 11 to 20 %. The corresponding variations of  $S_L$ -values are quite large, from about 0.3 to 1.5 m/s. The data for mixtures with Ar and He dilution give a possibility to include cases with a wide range of  $c_p$ , from 640 to 1900 m/s.

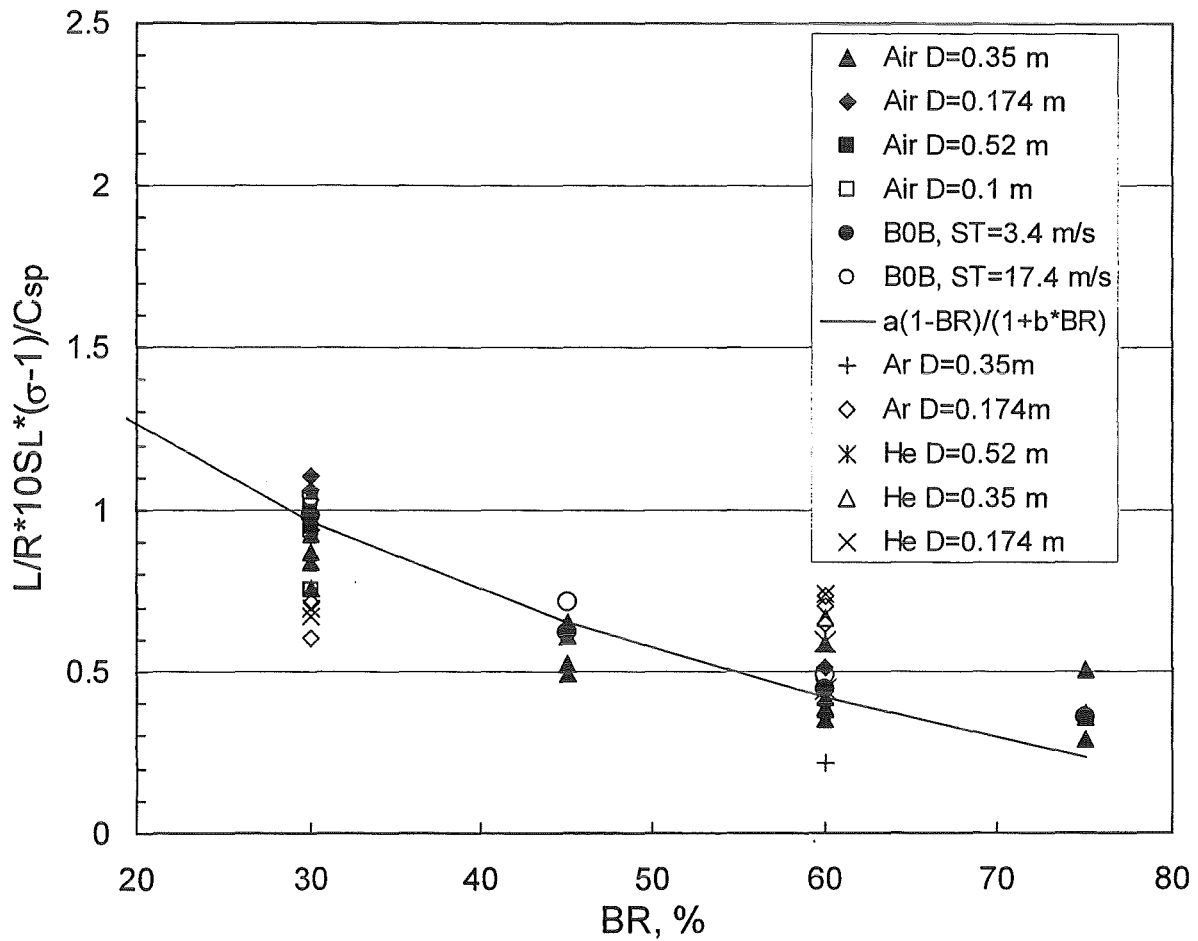


**Figure 11.** Dependence of dimensionless run-up distance for flame acceleration on BR. Data of experiments in different tubes ( $D$  is tube diameter) and results of simulations (B0B). Mixtures: hydrogen-air, hydrogen-oxygen-argon and hydrogen-oxygen-helium.

Fig. 11 shows that application of the dimensionless combination for the run-up distance gives a possibility to group the points for different mixtures with the relative accuracy of about  $\pm 25\%$ . The data from simulations, where  $S_T$  was used directly instead of  $10S_L$ , appear to be inside the experimental points. The function on the blockage ratio defined by the right-hand side of Eq. (4) is also shown in Fig. 11 with  $a = 2$  and  $b = 1.5$ . It is seen that such a simple model gives rather good description for the dimensionless run-up distance within the range of BR from 0.3 to 0.75.

## 6. Conclusions

We have presented results of experimental and numerical study aimed at determination of the minimum run-up distance for the flame acceleration to

supersonic combustion regimes in tubes with obstacles. Experiments were made in a tube equipped with the orifice plate obstacles with blockage ratios of 0.3, 0.45, 0.6 and 0.75. Geometry similar to the experimental one was studied numerically in a series of 3D simulations.

It was found both in the tests and in the simulations that run-up distance for the flame acceleration decreases with the increase of the blockage ratio and with the increase of the mixture reactivity (burning velocity). A simple analytical model is proposed, which describes the evolution of the flame shape and flame speed in the channel with obstacles. The dimensionless flame acceleration distance is determined in the model, which accounts for mixture properties, such as the laminar burning velocity and sound speed in combustion products. This dimensionless distance is expressed as a function of the blockage ratio.

The predictions of the model were found to be in a good agreement with experimental data obtained for a wide variety of mixtures in different tubes. The model allows estimating the minimum acceleration distance necessary for the development of fast flames as function of mixture properties and geometrical parameters.

## References

1. S. B. Dorofeev, M. S. Kuznetsov, V. I. Alekseev, A. A. Efimenko, and W. Breitung. Evaluation of limits for effective flame acceleration in hydrogen mixtures. *Journal of Loss Prevention in the Processes Industries*, vol/14/6, pp. 583-589, 2001
2. A. A. Efimenko and S. B. Dorofeev. CREBCOM code system for description of gaseous combustion. *Journal of Loss Prevention in the Processes Industries*, vol/14/6, pp. 575-581, 2001
3. Lee J.H., R. Knystautas, C.K. Chan, Turbulent flame propagation in obstacle-filled tubes, 20th Symposium (Int.) on Combustion, The Combustion Institute, Pittsburgh, PA, pp 1663-1672, 1984
4. Peraldi O., R. Knystautas, J. Lee, 19th Symposium (International) on Combustion, The Combustion Institute, p. 1629, 1986.
5. Kuznetsov M.S., V.I. Alekseev, A.V. Bezmelnitsyn, W. Breitung, S.B. Dorofeev, I.D. Matsukov, A. Vesper, and Yu.G. Yankin Effect of obstacle geometry on behavior of turbulent flames. Preprint IAE-6137/3, RRC "Kurchatov Institute", Moscow, 1999, Report FZKA-6328, Forschungszentrum Karlsruhe, Karlsruhe, 1999

V. Das Einmassenschwinger Modell  
(B. Burgeth, IKET)

Die bei Bauwerken oder technischen Strukturen auftretenden Schwingungsphänomene lassen sich in vielen Fällen als freie oder fremderregte *lineare* Schwingungen auffassen. Insofern kann der Einmassenschwinger als ein einfaches, konservatives Modell dienen, um das Verhalten von Bauwerken bei zeitabhängig einwirkenden Kräften zu untersuchen.

Dieses Modell wurde herangezogen um die schädigende Wirkung von Druckwellen, wie sie z.B. bei explosionsartigen Verbrennungen auftreten, auf Baustrukturen abzuschätzen. Ein Einmassenschwinger, charakterisiert durch seine Eigenfrequenz  $\nu$  [Hz] und dem häufig verwendeten dimensionslosen Lehr'schen Dämpfungsmaß  $D$  wird beschrieben durch die gewöhnliche Differenzialgleichung

$$\frac{1}{4\pi^2\nu^2}\ddot{r}_{\nu,D}(t) + \frac{D}{\pi\nu}\dot{r}_{\nu,D}(t) + r_{\nu,D}(t) = \underbrace{\text{interpolation}[(t_1, p_1), \dots, (t_N, p_N)]}_{=: p(t)}$$

Die rechte Seite dieser Gleichung, der Zwangsterm, ist gegeben durch viele hundert oder sogar einige tausend Datenpunkte, die im Kontext dieser Untersuchungen aus CFD-Rechnungen, aus Experimenten oder Abtastwerte von analytischen Funktionen stammen. Nach einer geeigneten Interpolation dieser Daten werden komplizierten aber genauen semi-analytischen Lösungen  $r_{\nu,D}(t)$  für beliebige  $\nu$  und  $D$  berechnet. In einem angeregten, schwingenden Feder-Masse-System entspricht  $r_{\nu,D}(t)$  der Last, mit der die Feder beansprucht wird, wenn auf die Masse die Last  $p(t)$  zur Zeit  $t$  einwirkt.

Das entwickelte Verfahren zum Lösen der DGL ist hinreichend genau, wie eine Fehlerbetrachtung im Falle der Testfunktion

$$\tilde{p}(t) = 1 - e^{-10t}, t \geq 0, \quad (1)$$

als Zwangsterm zeigt (Abb. 1a). Diese Testfunktion wird an 100 Punkten äquidistant abgetastet und zu dem entstehenden Datensatz für verschiedene  $\nu$  (aber  $D=0$ ) die semi-analytischen Lösungen  $r_{\nu,0}(t)$  berechnet. Schließlich vergleicht man diese approximativen Lösungen mit den exakten analytischen  $\tilde{r}_{\nu,0}(t)$  mittels der Berechnung des Spektrums des absoluten maximalen Fehlers im Intervall  $[0,10]$  (Abb. 1b):

$$e(\nu) := \max_{0 \leq t < 10} |r_{\nu,0}(t) - \tilde{r}_{\nu,0}(t)|. \quad (2)$$

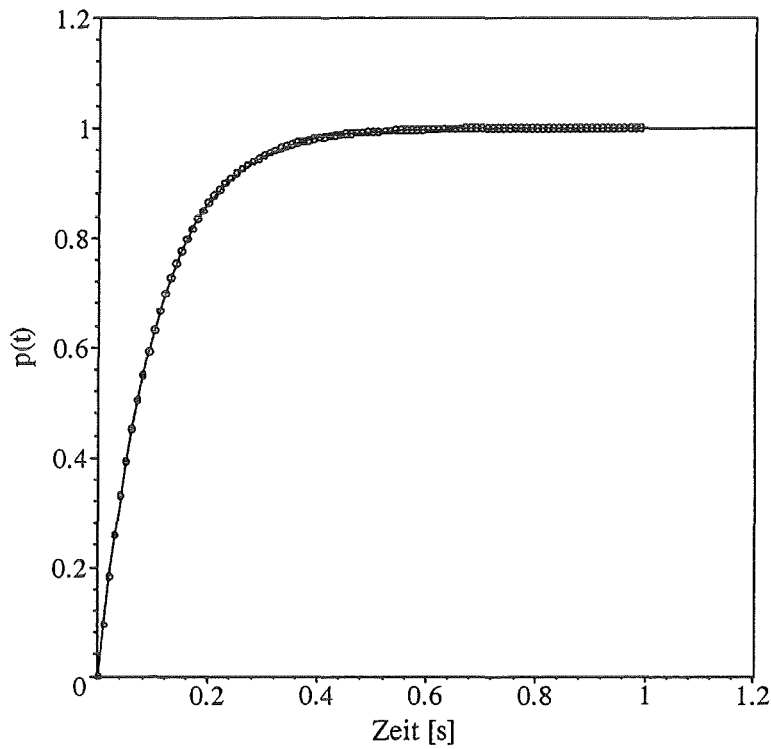


Abb. 1a: Die Testfunktion  $\tilde{p}$  aus (1) und die 100 äquidistanten Abtastwerte für seine stückweise lineare Interpolation  $p$ .

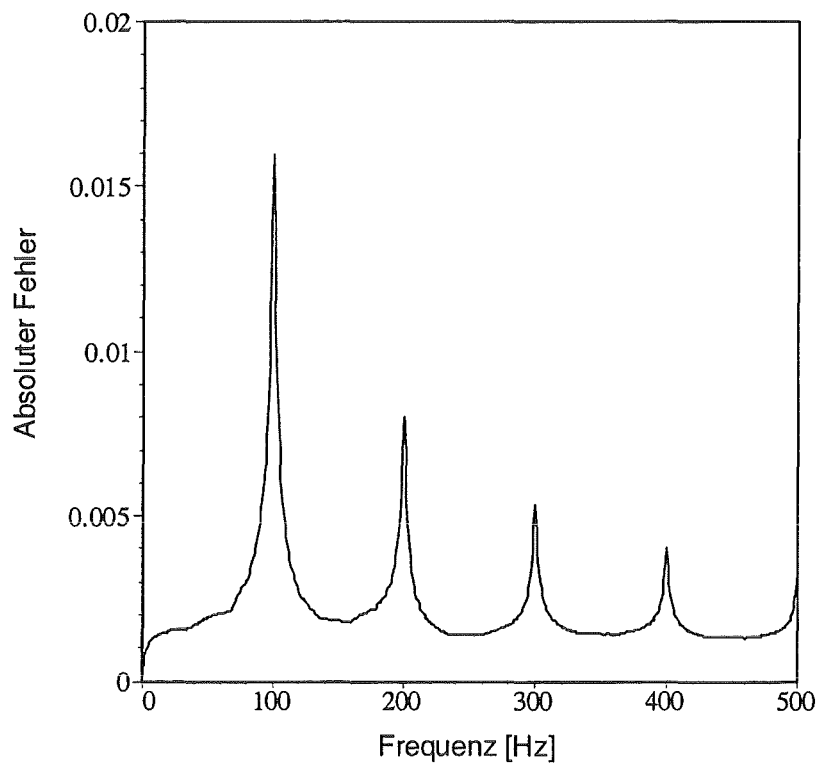


Abb.1b: Das Spektrum des zugehörigen maximalen absoluten Fehlers  $e(\nu)$  aus (2), aufgetragen in Abhängigkeit von  $\nu$ .

In der Strukturdynamik sind die folgenden Größen von Bedeutung:

$R_{v,D}^{\max} := \max_{t \in [0, t^*]} r_{v,D}(t), t^* \gg 1$ , die maximale effektive (statische) Last. Und

$R_{v,D}^{\min} := \min_{t \in [0, t^*]} r_{v,D}(t), t^* \gg 1$ , die maximale Zuglast. Die Berechnung dieser Größen als

Funktion von  $v$  und  $D$  ist numerisch aufwendig, da die Lösungen der Differenzialgleichungen für variable  $v$  und  $D$  über ein großes Zeitintervall hin bekannt sein müssen.

In einem Anwendungsbeispiel (Abb. 2a) wird ein Druckschrieb aus der CFD-Simulation einer 20% H<sub>2</sub>/Luft-Verbrennung ( $T_0=298\text{K}, p_0=10^5 \text{ Pa}$ ) untersucht.

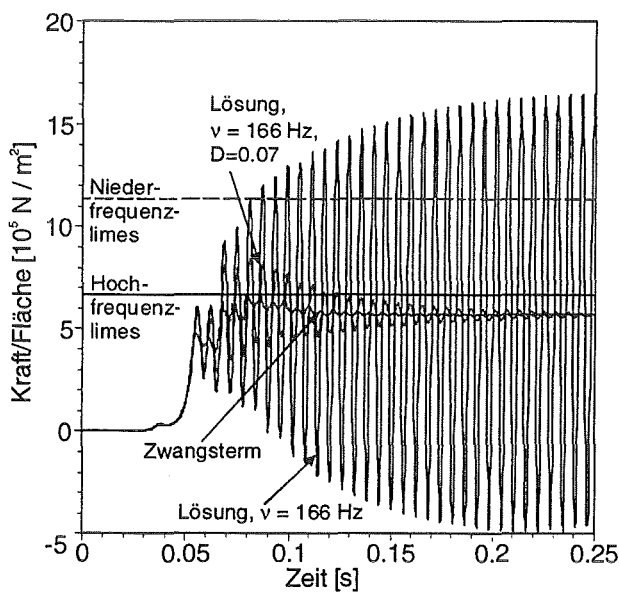


**Abb. 2a:** Eine typische transiente Drucklast aus einer CFD-Rechnung dargestellt zusammen mit der Lösung  $r_{v,D}$  für die Parameterwerte  $v=166$ ,  $D=0.0$  and  $0.07$

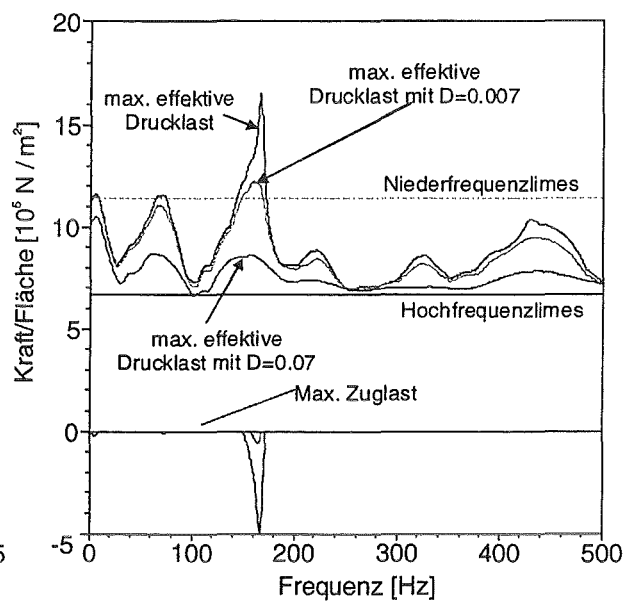


**Abb. 2b:** Die entsprechenden Spektren der maximalen effektiven Lasten  $R_{v,D}^{\max}$  und  $R_{v,D}^{\min}$  für die Parameter  $D=0.0, 0.007$  und  $0.07$ .

Das Einmassenschwinger Modell ist sehr sensitiv. Das entwickelte Lösungsverfahren trägt dieser Sensitivität Rechnung. In der Ingenieurspraxis werden oft geglättete, idealisierte Daten verwendet, um dadurch die Lösbarkeit der DGL zu gewährleisten. Die Benutzung geglätteter Daten kann aber zu Fehlinterpretationen führen wie das folgende Beispiel zeigt (Abb. 3).

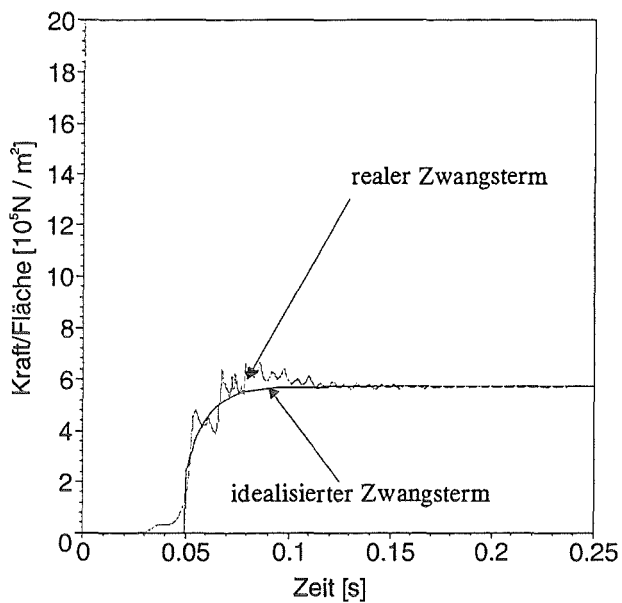


**Abb. 3a:** Der originale Druckschrieb aus Abb. 2a und seine idealisierte Approximation, die eine exakte analytische Lösung der DGL zulässt.

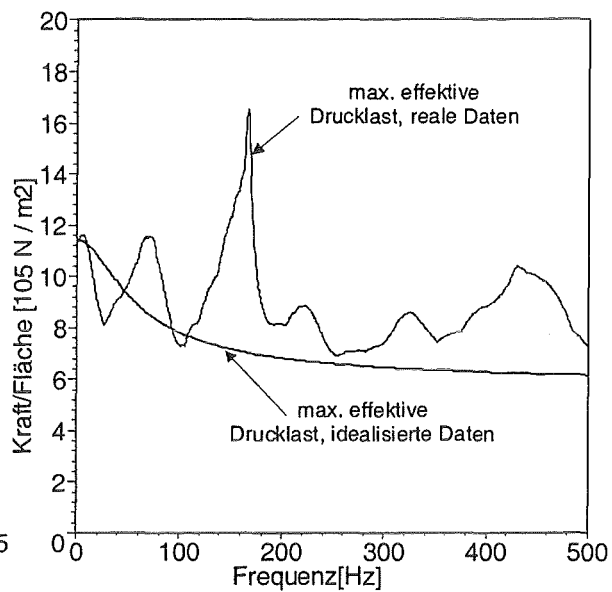


**Abb. 3b:** Die entsprechenden Spektren von  $R_{v,0}^{\max}$  jeweils für den originalen Druckschrieb und seine idealisierte Variante.

Das angesprochene Verfahren scheint in dieser Form neu zu sein. Es erlaubt die korrekte Anwendung des Einmassenschwinger Modells auch auf Zwangsterme, die zuvor dieser Art des post-processings nur bedingt zugänglich waren.

VI. On the Load Carrying Capacities of a Spherical PWR Steel Containment under a Postulated Hydrogen Detonation

(R. Krieg, B. Dolensky, B. Göller, IRS; W. Breitung, R. Redlinger, P. Royl, IKET )

**1. Introduction and Objectives**

To reduce the risk of early containment failure from hydrogen deflagrations or detonations, the existing German Konvoi nuclear power plants have been, or will be soon, equipped with a system of passive auto-catalytic recombiners (PAR's). However, due to the low hydrogen removal capacity per module (few g H<sub>2</sub>/s) these PAR systems are only effective in scenarios with relatively low hydrogen release rates (e.g. <0.5 kg H<sub>2</sub>/s for 1300 MWe units). In case of high release rates, as they occur e.g. during the reflood of an overheated core (several kg H<sub>2</sub>/s), the recombiners have no significant effect on the short term hydrogen inventory in the containment and the formation of burnable mixtures.

The purpose of this investigation is to quantify the load carrying capacities of the 38 mm thick steel shell to fast hydrogen combustion events by performing a sequence of mechanistic 3d calculations. Earlier scoping calculations with simplified structural dynamics models for the steel sphere indicated substantial resistances against global dynamic loads (4-8 MPa for 5 ms duration, [1]). The 3d structural response of the sphere to space and time dependent combustion pressure loads and the containment integrity has not been investigated so far.

The approach taken in this study consists of three main steps:

- a) calculation of the hydrogen and steam distribution in the spherical Konvoi steel containment, using the 3d code GASFLOW,
- b) transfer of the computed gas distribution to the 3d detonation code DET3D and calculation of local detonation pressure loads to the containment shell, and
- c) transfer of local gas-dynamic loads to the structural mechanics code ABAQUS, calculation of stresses, strains and deformations in the spherical steel shell, and evaluation of the results using appropriate experimental findings.

In steps a) and b) quite conservative assumptions are applied to achieve an example for limiting dynamic loads and bounding deformations of the steel sphere.

## 2. Hydrogen and steam distribution

A small break loss of coolant accident (SB-LOCA) with delayed depressurization of the secondary system was selected as accident scenario in a typical German Konvoi plant. The steam and hydrogen source was taken from conservative scoping simulations in which the hydrogen release was maximized and the steam release was reduced due to depressurization of the secondary system.

The three-dimensional fluid dynamics code GASFLOW [2] was used to simulate the steam and hydrogen distribution in the spherical Konvoi containment. A detailed 3D Cartesian geometry model with 184 320 computational cells has been applied. The geometry model and the initial conditions are documented in [3]. The assumed break location for the steam and hydrogen injection is in the lower part of one steam generator compartment.

The blowdown and the release of superheated steam inject about 290 000 kg of steam and water over a total time of 10 000 s. The steam injection rates are rather low, therefore only a few rupture disks fail in the roof of the steam generator towers and allow for a continuous pressure equilibration between the component and the operating rooms as the steam-hydrogen injection continues. The fast hydrogen release phase from the reflood starts at 7800 s. It reaches peak injection rates of 7 kg/s and enters 885 kg in about 300 s (Fig. 1). The most sensitive mixture occurs at 7950s, when about 550 kg of hydrogen have been released and the rate of further hydrogen release slows down rapidly. The recombiner system which is also modeled in this simulation has practically no effect as hydrogen sink on these time scales.

Figure 2 displays the calculated steam and hydrogen distribution from GASFLOW. The isosurface in space corresponding to 15 vol% hydrogen is given in dark grey. Inside this isosurface hydrogen concentrations greater than 15 vol% exist. The left hand side of the figure displays the clouds together with the major containment structures. On the right hand side the clouds are displayed without structures to show the hydrogen trapped inside the steam generator towers and the missile protection cylinder.

### 3. Detonation

The distribution calculation predicted detonable mixtures during the time of the rapid H<sub>2</sub>/steam release phase (near 8000 s). To calculate the transient gas-dynamic pressure loads in the containment from a presumed hydrogen-air detonation, a simple geometry model of the PWR Konvoi reactor was used. It consists of the spherical containment shell, the missile protection cylinder with three openings in the lower part, and a concrete block filling most of the bottom of the containment (Fig. 3). To bound approximately the results of the distribution calculation of section 2, the whole containment was filled with a gas mixture consisting of 5 vol% hydrogen, 40 vol% steam and 55 vol% air at a pressure of 2.25 bar and a temperature of 403 K. Inside the missile protection shield a cylindrical domain was filled with hydrogen rich gas consisting of 40 vol% steam plus stoichiometric hydrogen-air at the same pressure and temperature (Fig. 4). The detonable mixture contains about 550 kg of hydrogen.

For the numerical simulation of the hydrogen-air detonation occurring in this quite conservative situation, the 3d computational fluid dynamics code DET3D [4] was used. This is an explicit, finite difference program that solves the reactive Euler equations of compressible gas dynamics. The code was verified on 1 d analytical solutions and 3 d detonation tests, ranging in scale up to 35 m length and 250 m<sup>3</sup> volume. For the Konvoi calculation, an equidistant discretization of the above described model containment with a mesh size of 40 cm and a total of about 2.2 million numerical cells was used.

The sensitive mixture was detonatively ignited in the lower left corner of the cylindrical cloud (Fig. 4, top, left) because this ignition location causes the highest impulse to the dome, a strong reflection into the lower containment region including focussing effects, and a large dynamic load to the unprotected shell near the openings in the missile shield. The calculated transient pressures on the outer containment shell from the initial detonation phase and the subsequent shock wave reverberations were recorded at about 8700 locations (numerical "pressure gauges").

Typical peak reflected over-pressures from the incident detonation wave at the shell are 2-4 MPa, typical impulses from the detonation wave are in the range of 10 to 30 kPas. Focussing effects in the lower region of the containment between missile protection cylinder and steel sphere lead to local over-pressures up to 6.6 MPa.

#### 4. Structural Dynamics Response of the Spherical Steel Shell

For the structural dynamics calculations the spherical containment shell has been represented by the finite element model shown in Fig. 5. The finite element code ABAQUS has been applied. Increased shell stiffnesses and masses at nozzles, ports, and other penetrations were not considered.

In order to describe the propagation of bending waves in a satisfying way, the adequate ABAQUS element size has been assessed from the decay length  $\lambda$ , well known in shell theory [6], which gives  $\lambda = 0.8\text{m}$ .

The ABAQUS thin shell element (STR165) with quadratic interpolations and mid sides nodes gives a maximum distance between neighbouring nodes of 0.7 m. Thus the propagation of bending waves can be modeled adequately. The number of finite elements turned out to be 9000, the number of nodes to be 9221, and the number of degrees of freedom is 44682.

For symmetry reasons only half of the shell was modelled. At the meridian angle  $\varphi = 128^\circ$  the shell has been assumed to be perfectly clamped (Fig. 5).

The shell load consists of a uniformly distributed static pressure of 0.225 MPa and the superimposed non-uniformly distributed local gas-dynamic pressures caused by the hydrogen detonation as described in section 3. The 8700 dynamic pressure loads calculated in DET3D were used as input to the ABAQUS analysis.

Fig. 6 presents an example for the time and space dependent gas-dynamic pressure loads to the steel shell. The static pressure component (0.225 Mpa), which causes a uniformly pre-stressed state of the steel sphere, is not included. Fig. 6 shows local gas-dynamic loads in a meridional plane, vertical to the equator. The north pole of the sphere is located at  $\varphi = 0$  and the meridian extends in both direction to  $\pm 128^\circ$ . The detonation front impacts the dome region first near  $\varphi \approx -50^\circ$ . Locations with  $\varphi \leq -50$  are shielded by the missile protection cylinder. The region from  $\varphi = -50^\circ$  to  $0^\circ$  is directly loaded by the primary detonation front (see Fig.4). The group of high pressure peaks near  $\varphi = +90^\circ$  represents shocks transmitted through the missile cylinder openings. The largest pressure peak (4.33 MPa) is created at  $\varphi = +128^\circ$  by focussing effects in the converging gap between sphere and missile protection cylinder. The second major group of pressure peaks ( $>100$  ms) is caused by the detonation wave reflected in the dome. Many more minor pressure waves travel throughout the containment volume, which are however of less significance for the ultimate sphere deformations.

The constitutive relations of the containment steel are described by the stress-strain diagram shown in Fig. 7. It is based on both, classical uniaxial tension tests and biaxial membrane tests with specimens made from sheets of the original Konvoi containment material having the same thickness as the sheets used to build the containment (38 mm, [5]). The applied strain rate in these tests was moderate. The material resistance under the high strain rate caused by the detonation load can be expected to be somewhat stronger. Thus the application of the diagram in Fig. 7 is likely to overestimate the deformations slightly.

Calculated horizontal shell displacements versus time are shown in Fig. 8 for the pole of the shell ( $\varphi = 0^\circ$ ), for the location of the material port ( $\varphi = +90^\circ$ ), and for the opposite location at the same height in the containment ( $\varphi = -90^\circ$ ). At the pole the horizontal displacement is larger than at the location of the material port and at the opposite location. Considering that in the region of the material port the inner cylinder has big openings, while at the opposite location the inner cylinder is protecting the shell from the detonation loads, it is obvious that at the location of the material port the horizontal displacement is larger than at the opposite location. The faster horizontal displacement of the shell near the material port, compared to the other two locations, is due to the earlier arrival and the near normal reflection of the primary detonation shock wave. Fig. 8 indicates clearly that mainly plastic deformations occur since after the maximum deformations have been reached between 160 and 180 ms, the reductions of the displacements are rather small. The deformations obtained for times later than 300 ms are representative for the remaining plastic deformations of the steel shell (200 to 400 mm).

A quantitative overview of the resulting deformations is given in Fig.9. Note that the displacements are magnified by a factor of 5 for better visibility. Rather strong deformations occur close to the lower clamping below the material port because the detonation wave reflected from the dome area is focussed in this part of the containment, causing local gas- dynamic pressure peaks up to 6.6 MPa. Large deformations are also observed near the material port because this part of the shell is not shielded from the gas-dynamic forces by the missile protection cylinder.

The most important result of the ABAQUS calculation is the strain distribution in the spherical shell. The equivalent strains in the mid-plane of the shell (membrane strain) are shown in Fig. 10. The maximum strain of 4.6 % occurs close to the lower

clamping region below the material port. Relatively high strains up to about 2.5 % occur also close to the pole in the particular detonation scenario considered here. Very important are the strains in the region of the material port because of the complicated geometry at this location in the original containment design. Here the maximum value is about 2 %.

## **5. Evaluation of the Structural Response**

The calculated equivalent membrane strains up to about 5 % can certainly be sustained in the undisturbed shell regions without any fractures. In earlier membrane tests where the containment steel was machined to a thickness of 2 mm, much larger equivalent strains have been obtained before failure [5]. Furthermore it will be shown in scaled tests in a current research program that the specimen size has only moderate influence on the failure strains [6]. Even for weldings and shell regions with cracks of several millimeter depth the failure strains were found to be significantly higher than 5 % [7,8].

Also penetrations through the containment shell (nozzles, etc.) do not present much weaker positions. Around the penetrations the shell thickness is increased such that the strains in these zones are smaller than at other positions. At the thin shell regions close to the thickened zones the strain concentrations have been shown to be insignificant in scaled tests [9, 10, 11].

The bolted connection for the large material port represents a more critical location. In previous tests with sections of the bolted connection, it was found that strains in the thin shell region close to the bolted connection may reach 4.1 % without causing failure of this connection [9]. Thus strains up to 2 % as calculated for the location of the material port should not be a problem. However, it has to be emphasized that the plant specific details such as the increased stiffness and the mass concentrations due to the material port which has not been considered in the present finite element model, might increase the strain level somewhat. Consequently, for a final assessment of the local containment integrity, the application of a refined plant specific finite element model is necessary.

Finally, it should be mentioned that other containment details as e.g. the bellows connected to some of the nozzles, the tightness of the electrical penetrations, as well as the tightness of the material port and of the other penetrations have also to be investigated for definite conclusions. Of course, these local details will be plant

specific, but severe difficulties are not expected, because the Konvoi containment represents a well balanced structural design against high static pressure loads.

## **7. Conclusions**

The results of the presented analysis indicate that the spherical steel containments of German PWR Konvoi plants have an excellent capacity to withstand large gas-dynamic pressures loads from fast hydrogen combustion events.

Despite of combined conservative assumptions for H<sub>2</sub>-source, distribution and detonation parameters, the computed equivalent membrane strain distribution in the steel shell suggests that the shell should withstand the high detonation loads without leakage. The scoping calculations presented here suggest that the German Konvoi containments maybe able to resist gas-dynamic hydrogen combustion loads from low-pressure severe accidents. If this finding can be substantiated and supported with further refined studies, the foreseen Konvoi hydrogen mitigation system (PAR's) in combination with the excellent load carrying capabilities of the steel containment can provide a complete and passive hydrogen control, even for beyond-design basis accidents with rapid and large hydrogen generation. With respect to hydrogen management the existing German Kovoil plants may be capable of fulfilling already now the stringent requirements for new future plants.

For final assessment of some remaining local integrity issues a more refined finite element model including plant specific details about containment penetrations is necessary. Furthermore, additional accident scenarios with more realistic (and less conservative) hydrogen release rates and total masses should be investigated. For most cases global turbulent combustions instead of global detonations are expected, which would lower the peak pressures to the containment shell and the resulting deformations, compared to the discussed case.

Based on the present results very good chances exist to prove by fully mechanistic calculations that hydrogen control for severe accidents in German Konvoi plants can be achieved by the fully passive approach "catalytic recombiners + containment resistance".

## References

- [1] Deutsche Risikostudie Kernkraftwerke- Phase B, Verlag TÜV Rheinland (1990), ISBN 3-88585-809-6, p.679
- [2] J.R. Travis, J.W. Spore, P. Royl, K.L. Lam, T.L. Wilson, C. Müller, G. Necker, B.D. Nicols, R. Redlinger, E.D. Hughes, H. Wilkening, W. Baumann, G.F. Niederauer; GASFLOW a computational Fluid Dynamics Code for Gases, Aerosols and Combustion, Reports FZKA-5994 and LA-13357-M, October 1998
- [3] P. Royl, J.R. Travis, W. Breitung; Ergebnisse der GASFLOW Analysen für einen hypothetischen Kühlmittelverlustunfall mit kleinem Leck (Small break LOCA) im Kernkraftwerk Neckarwestheim-2 mit sekundärseitigem Abfahren der Dampferzeuger, Internal report FZK IKET-Nr. 3/00, February 2000
- [4] R. Redlinger; Numerische Simulation von Gasedetonationen in komplexen 3D-Geometrien, FZK-Nachrichten 32 (2000), 243-249
- [5] R. Krieg, et al.; Spherical Steel Containments of Pressurized Water Reactors under Accident Conditions, Investigation Program and First Results, Nucl. Eng. Des. 82, 77, 1984
- [6] R. Krieg, et al: Limit Strains for Severe Accident Conditions, Description of an European Research Program and First Results, SMiRT 16, Washington 2001, paper P01/2
- [7] Staatliche Materialprüfungsanstalt Stuttgart; Zugversuche mit geschweißten Großplatten aus dem Werkstoff 15MnNi63, Internal Report, 1978
- [8] S. Müller and D. Munz; Versagen von großen plattenförmigen Zugproben mit Oberflächenrissen, FZK-IMFII Internal Report, 1985
- [9] B. Göller et al; On the Failure of Spherical Steel Containments under Excessive Internal Pressure, Nucl. Eng. Des. 100, 205, 1987
- [10] R. Krieg, et al; Failure Pressure and Failure Mode of the Latest Type of German PWR Containments, Nucl. Eng. Des. 104, 381, 1987
- [11] B. Göller, et al; Failure Pressure and Failure Mode of the Bolted Connection for the Large Component Port in German PWR Containments, Nucl. Eng. Des. 106, 35, 1988

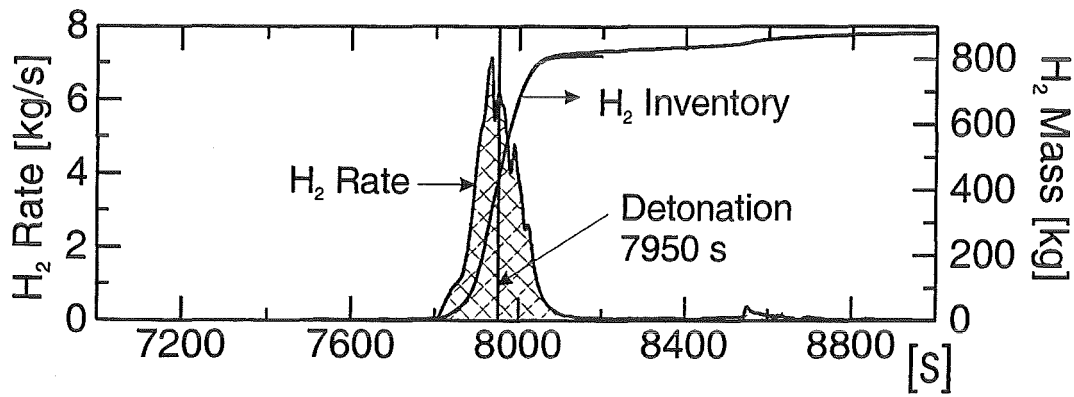


Fig. 1: Hydrogen source for Small Break LOCA simulation with GASFLOW.

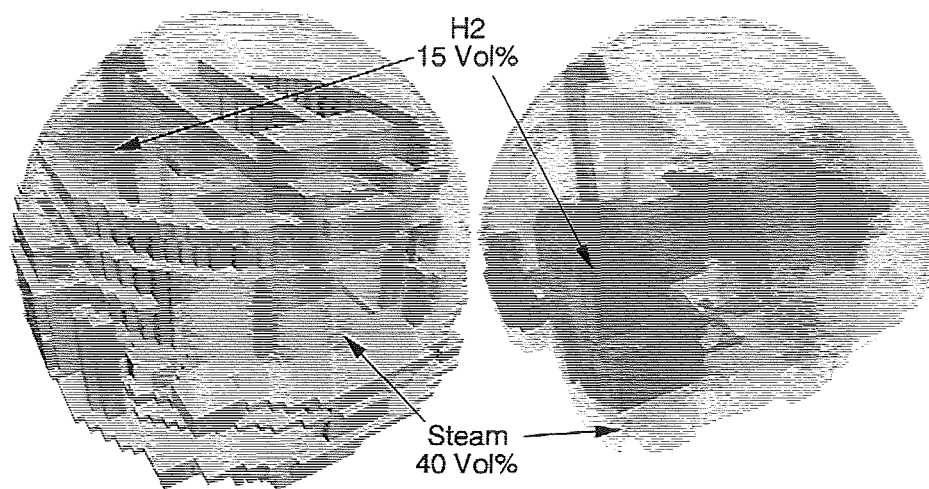


Fig. 2: Steam and hydrogen distribution from GASFLOW at the switch-over time to the detonation simulation (7950 s).

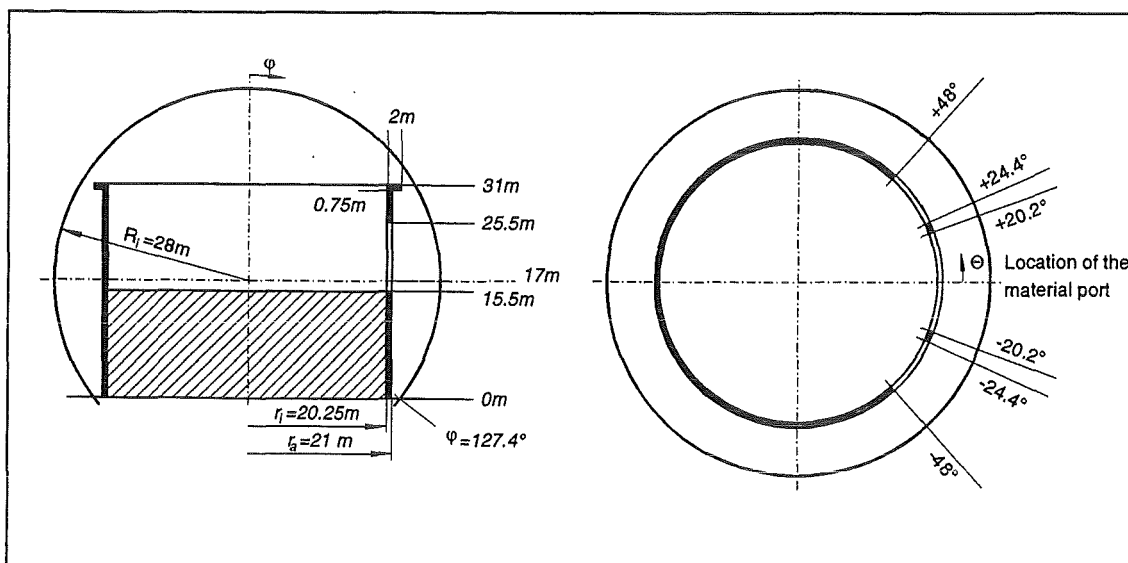


Fig. 3: Geometrical dimensions used for the calculation of hydrogen-air-steam detonation loads in a Konvoi containment.

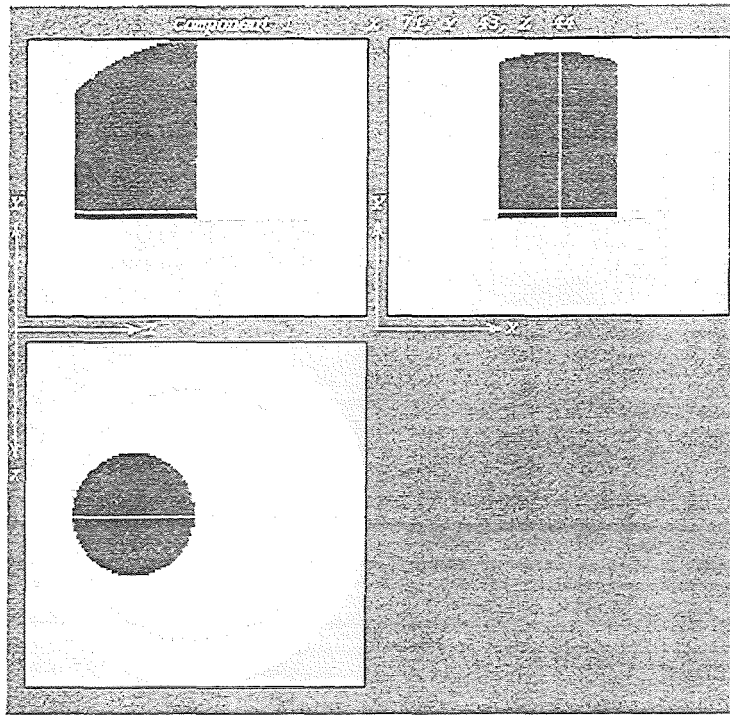


Fig. 4: 2d cuts from the DET3D graphical user interface showing the containment model geometry (in light grey) and the cylindrical domain filled with detonable hydrogen-air-steam mixture (in dark grey). The total hydrogen inventory in the detonable mixture is 550 kg.

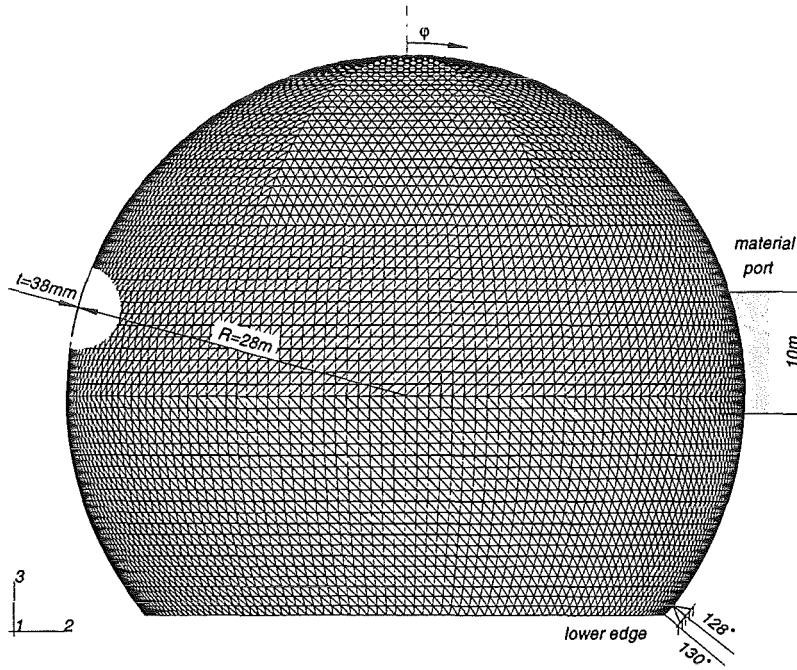


Fig. 5: 3d finite element model of the containment shell with 9000 elements.

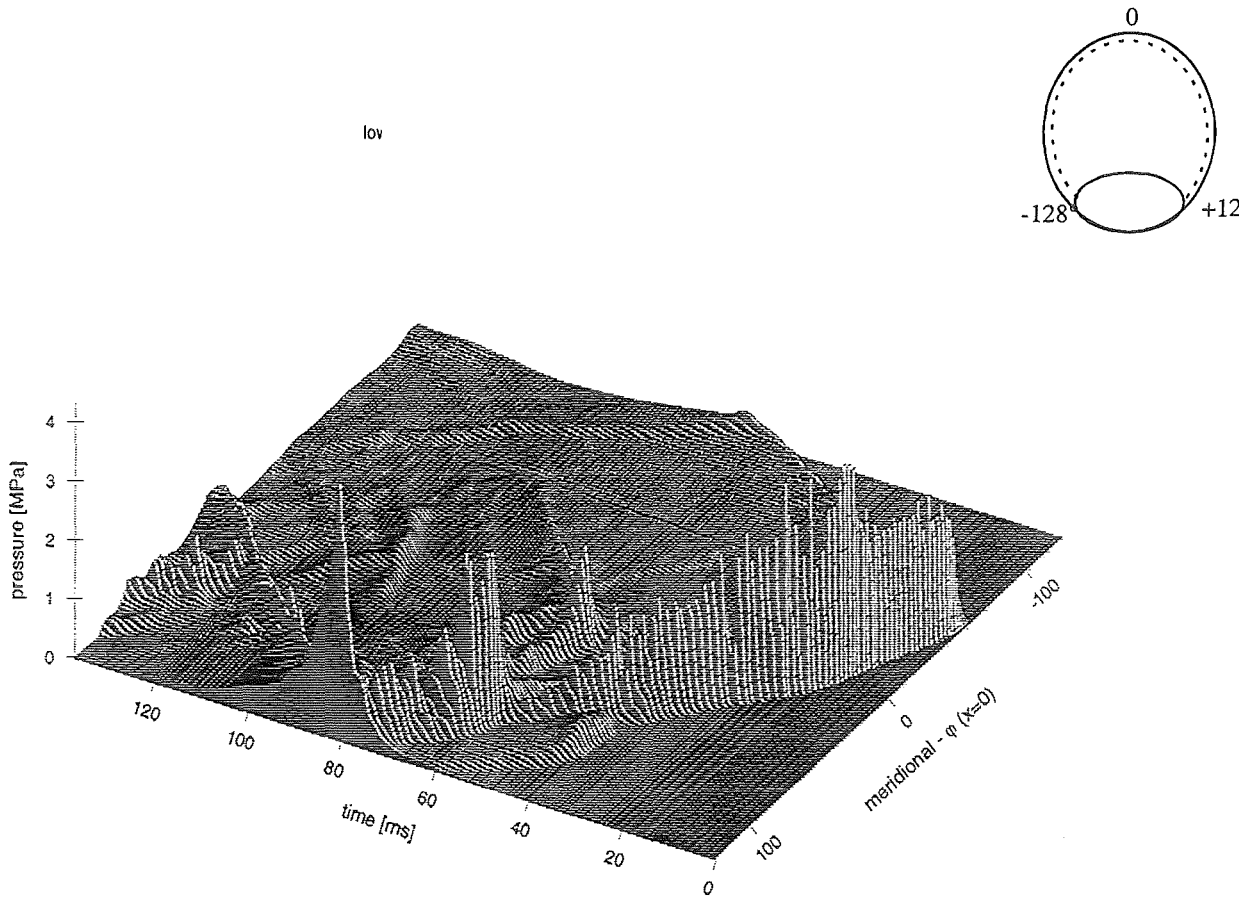


Fig. 6: Local gas-dynamic pressure loads to the spherical steel containment, shown are locations on a meridian of the sphere ( $-128^\circ \leq \varphi \leq +12^\circ$ )

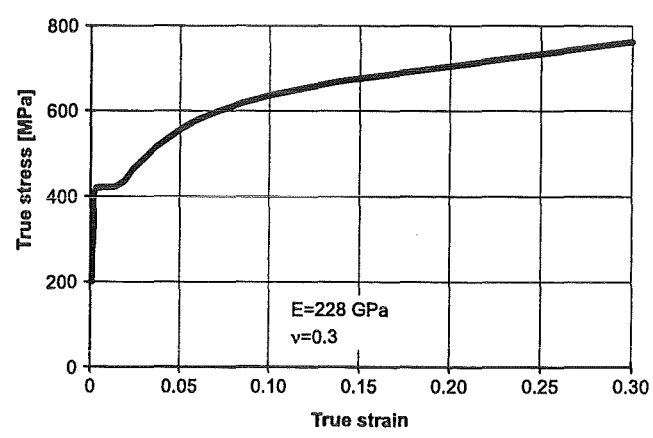


Fig. 7: Stress-strain diagram of the containment steel shell material 15MnNi63.

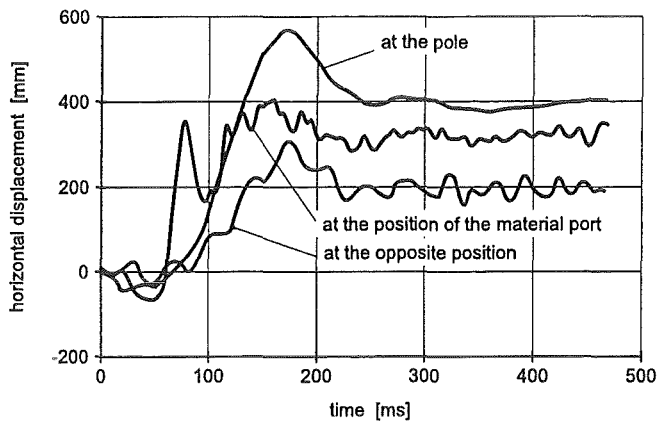


Fig. 8: ABAQUS results for calculated horizontal displacements versus time for different positions on the steel shell.

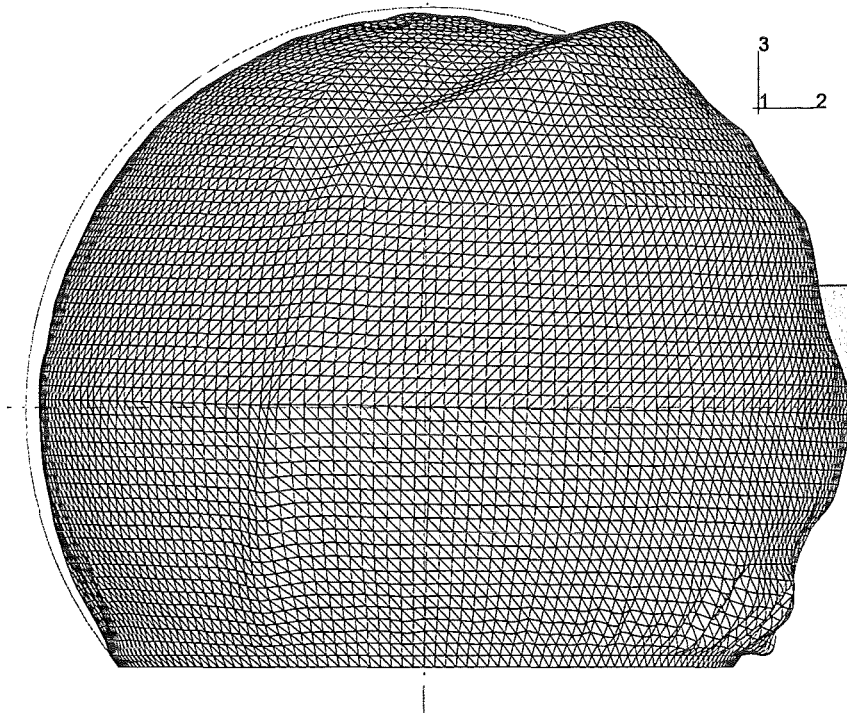


Fig. 9: Computed shell deformations magnified by a factor of 5, together with initial shell location. The gas detonation was located on the left hand side of the sphere, leading to strong deformations near the material port (shaded region) and the clamping region.

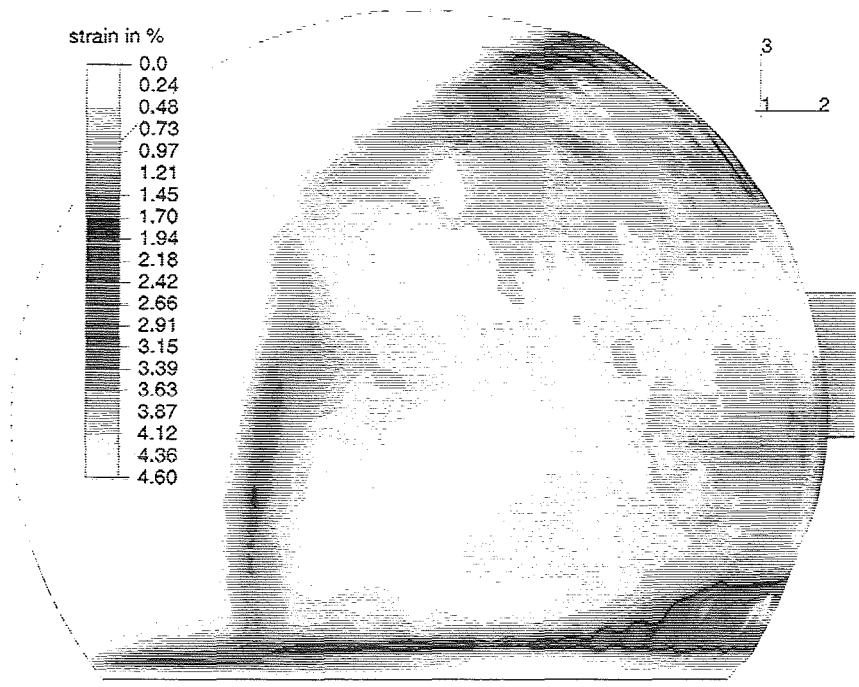


Fig.10: Computed equivalent membrane strain distribution in the spherical steel shell, corresponding to Fig. 9 top.

## 32.21.02 Thermische Wechselwirkung von Kernschmelze und Kühlmittel

### I. ECO-Experimente zur Energiekonversion bei Dampfexplosionen

(G. Albrecht, H. Brüggemann, W. Cherdron, E. Jenes, A. Kaiser, N. Prothmann, D. Raupp, W. Schütz, IRS)

#### **Abstract**

The ECO experiments have been launched in 2000 to measure the conversion of thermal into mechanical energy in confined steam explosions under well-defined conditions. The design of the facility is such that mechanical work done on quite resistant surroundings is directly measured. Aluminum oxide is used to simulate the core melt. The internal dimensions of the test facility as well as major test conditions are similar to the previous PREMIX tests. The facility consists mainly of a cylinder and a piston enclosing the melt generator and the test volume. Under the action of an increased pressure, the piston can move downwards against a stepwise increasing force provided by crushing material.

Two exploratory tests (ECO-01 and ECO-02) were carried out in 2000. In the first test, an artificially triggered explosion occurred, whereas it was a self-triggered explosion in the second tests. The energy conversion was very small in both cases, i.e. below 0.1 percent.

Two further tests (ECO-03 and ECO-04) were carried out in 2001. To reduce the risk of a spontaneous explosion, the pool water was preheated and the system pressure was elevated to 0.25 MPa. A triggered explosion occurred in ECO-03. However, due to malfunction of a valve, only a small part of the melt ( $\approx 1$  kg) was released into the water. The mechanical work was near the lower detection limit. ECO-04 was performed with two significant modifications: 1) To establish a rather compact melt jet with full cross section immediately after beginning of release, a second explosive-driven valve was installed below the melt-through foil of the exit nozzle. 2) To reduce the 'active' water volume and the steam condensation potential, a steel pipe with 30 cm  $\varnothing$  was axisymmetrically installed in the 60 cm  $\varnothing$  test vessel. By these two measures, almost 10 kg of melt were released into the water pool until trigger and explosion, and the piston moved downward by 6.5 cm. This corresponds to an efficiency in the one-percent range. The report is limited mainly to a presentation of ECO-04.

## 1. Introduction

In case of a steam explosion, special interest is being devoted to the part of the thermal energy of the melt that is converted into mechanical work. Under unfavorable conditions, a steam explosion may occur in the sequence of a core melt accident.

One precondition for the occurrence of a steam explosion is a coarse premixing of the hot melt in a cold volatile liquid. In this state, the melt fragments are separated from the liquid by a stable thin layer of steam. Another one is a strong trigger pressure event which leads, via collapse of the steam layer and instability of the surface of the melt fragments, to a fast fragmentation. The increase in the total surface gives rise to flash evaporation going along with very steep pressure increases.

The ECO experiments are being performed to measure the mechanical work under well-defined conditions. In these tests, alumina from a thermite reaction is used as a simulating material instead of corium. Two exploratory tests (ECO-01 and ECO-02) were carried out in 2000. In the first test, an artificially triggered explosion occurred, whereas it was a self-triggered explosion in the second test. The energy conversion was very small in both cases, i.e. below 0.1 percent. For more details, see the Annual Report of 2000, FZKA 6653.

Two further tests (ECO-03 and ECO-04) were carried out in 2001. To reduce the risk of a spontaneous explosion, the pool water was preheated and the system pressure was elevated to 0.25 MPa. A triggered explosion occurred in ECO-03. However, due to malfunction of a valve, only a small part of the melt ( $\approx 1$  kg) was released into the water. The mechanical work was near the lower detection limit.

A significant progress has been achieved with ECO-04. It was our first test that showed a conversion factor in the one-percent range. So, the following report is limited to a presentation of ECO-04 performance and results.

## 2. Test facility, Instrumentation and Performance of ECO-04

The ECO facility (Fig. 1) was designed to measure energy conversion ratios up to 20%. In principal, the facility consists of a piston/cylinder system, while, under the pressure forces developing in the water pool due to the steam explosion, the test vessel (=piston) moves downwards against the resistance of the underlying crushing material. The melt generator providing the melt is part of the cylinder.

The pool has 590 mm in diameter. An important change was made in the ECO-04 test conditions: to reduce the amount of water involved in the condensation processes during the premixing and explosion periods, a concentric steel cylinder (300 mm in diam.) was mounted in the vessel. Holes drilled into the cylinder wall allowed the transfer of pressure waves from the mixing region to the vessel wall where most of the pressure transducers were located. The instrumentation is copious:

*Pressures* are measured in the bottom and at several axial levels by piezo type as well as by strain gauge type transducers (e.g., PK17 and PK08 in Fig. 1).

*Void probes* mounted on horizontal lances (e.g., V08) indicate changes in the local phase conditions. These give, together with *thermocouples* mounted at the ends of the lances, information about the axial and radial growth of the mixing zone.

Six *strain gauges* measure the axial force, two *displacement transducers* the movement between piston and cylinder. The deformation of *crushing material* gives information about the force exerted by the downward movement of the vessel. The latter is observed by video cameras.

The essential test conditions of ECO-04 are given in Table 1, where comparison is made with a former test, ECO-01.

The melt is being produced by the exothermal reaction of a thermite powder which results in liquid alumina and iron. During the chemical reaction, iron separates from the oxide by gravity and is retained in the crucible. The melt released consists of >90 wt.% of oxides and <10 wt.% of iron; the temperature is estimated to be 2600 K. The melt release occurs through the nozzle tube after opening of the upper slide valve. This valve was installed for the first time in ECO-04 to establish a fairly compact jet with full cross section from the start of release on. The pressure in the melt generator is being controlled to compensate the one expected in the vessel due to the melt/water interaction. Since the melt release rate can not be measured, it is estimated on a simple numerical model which is based on a momentum equation that describes forced flow of melt in a vertical pipe with varying cross sections.

### 3. Results

#### *General course of events*

The origin of the time scale used in this report is the time when the signal of the melt detector (see Fig. 1) indicated the arrival of the melt front at the end of the nozzle tube. For that time, an actual speed of the melt of about 12 m/s is calculated.

The penetration of the melt in the water in axial and radial directions is given in Fig. 2 with the time as a parameter. The initial growth rate in the radial direction is remarkable. After about half of the melt release time, the mixing zone came close to the confinement set by the inserted steel cylinder. We deduce from this event that the melt front consisted of scattered fragments. The axial penetration rate, which was reduced compared to the above release rate, increased with time. Farther down, the mixing zone was more narrow while the pressure in the vessel increased surprisingly fast.

When the melt front reached the height of the V01 sensor (see Fig. 2), the lower valve was closed and the trigger capsules located in the vessel bottom were ignited. The steam explosion started.

#### *Pressure measurements*

The pressures due to the steam explosion are shown in Fig. 3. The measurements, locally obtained in the water at various axial heights, present a sequence of three major pressure events lasting a total of 0.016 s.

The first one started in the lowermost part of the pool at 0.139 s. The very first, needle-shaped peak in PK01 (7 MPa) is attributed to the trigger pressure. The pressure, having a peak of 28 MPa and a width of 3 - 4 ms, is seen to propagate into the upper axial direction losing its intensity with time.

The second pressure event started in the uppermost part of the water pool 5 ms after the first one. We conclude from the magnitude of the PK08 pressure peak that the water in the outer ring had increased to a height larger than that of the pick-up at that time. Again, the pressure is seen to lose intensity on its way down.

The third pressure event started at 0.151 s, again in the lowermost part of the pool.

#### *Evaluation of the energy transferred*

The important quantity to be determined in ECO is the mechanical work,  $W$ , performed via kinetic energy due to the steam explosion. To obtain the energy con-

version factor,  $\eta = W/Q$ , the work is related to the quantity of  $Q$ , the heat content of the melt. In ECO-04, the heat content is estimated to be 34.3 MJ, based on 9.6 kg and an enthalpy of 3.57 MJ/kg which is the difference in the enthalpies of the melt at initial and boiling water conditions, 2600 K and 373 K, respectively.

The mechanical work is being determined by three independent methods. While doing so, the first two are regarded to be the more reliable ones: (1) the deformation of the crushing material, (2) the strain gauge and displacement measurements, (3) the pressure measurements.

1. The deformation of the uppermost layer of the crushing material was measured to be 64 millimetres giving a work of  $W = 0.183$  MJ. This corresponds to an energy conversion factor of  $\eta = 0.53\%$ .

2. Work from the strain gauges (Fig. 4) amounts to 0.350 MJ at 0.170 s which gives a conversion factor of  $\eta \approx 1.0\%$ . The evaluation of the displacement data gives a maximum value of 65 mm at 0.172 s.

3. The work (not shown here) calculated from pressure and L displacement data includes a certain error since the pressure record is always a local value. Moreover, the result does not account for the work due to the acceleration of the water situated above or below the pressure transducer referred to. This aspect is illustrated in Fig. 4 in the shift in time between  $F_{PK01}$  and  $F_{DMS}$ .

### ***Post test examinations***

After the experiment, a total mass of melt fragments of 9.6 kg was found. At a first glance, the overwhelming portion of the mass has been finely fragmented. Further examinations, e.g. of the particle size distribution, are under way.

## **4. Summary and Conclusions**

Alumina melt of about 9.6 kg and 2600 K was released into water of around 360 K within 0.150 s. The system pressure was 0.25 MPa. The mixing zone grew rather rapidly in radial direction initially; after about half of the melt release time, it came close to the confinement set by the inserted cylinder. The speed of melt penetration increased with time; further down, the mixing zone was more narrow while the pressure increased steeply.

The steam explosion initiated by a trigger pressure event presented itself as a sequence of three individual pressure events lasting a total of about 0.016 s. The peak pressures were of the order of 30 MPa with a duration of up to two milliseconds. The large reduction of the amount of water taking part in the premixing and heat exchange processes by installing an inner cylinder proved to be successful in achieving a larger energy conversion factor, little less than about one percent, than in the preceding tests. At present, all results including those of the previous experiments are being analysed in more detail to understand what was going on in the test and eventually, to find an explanation for the increase in efficiency.

During 2001, ECO results were published in refs. /1/ and /2/. The final report of PREMIX was presented in ref. /3/.

## 5. References

- /1/ W. Cherdron, A. Kaiser, W. Schütz, H. Will,  
ECO Steam Explosion Experiments on the Conversion of Thermal into  
Mechanical Energy,  
Jahrestagung Kerntechnik, Dresden, May 2001
- /2/ G. Albrecht, W. Cherdon, U. Imke, H. Jacobs, A. Kaiser, W. Schütz, H. Will  
Experiments on melt-coolant interaction processes, including steam explosions.  
Matzen, V.C. [Hrsg.]  
Transactions of the 16th Internat. Conf. On Structural Mechanics in Reactor  
Technology (SMIRT 16), Washington, D.C., August 12-17, 2001,  
Madison, Wis.: Omnipress, 2001 CD-ROM Paper 1383
- /3/ A. Kaiser, W. Schütz, H. Will  
PREMIX experiments PM12-PM18 to investigate the mixing of a hot melt with  
water,  
Wissenschaftliche Berichte, FZKA-6380 (Juli 2001)

**Table 1:** Major test conditions in ECO-04, compared to ECO-01

		ECO-04	ECO-01
<b>Melt source</b>			
Mass released	kg	9.6	5.76
Initial crucible pressure	MPa	0.95	0.35
Nozzle diameter	m	0.06	0.045
Speed at nozzle outlet	m/s	12.5	7.4
Release time	s	0.15	0.168
<b>Water pool</b>			
Temperature	K	336-369	293
Volume <sup>1</sup>	m <sup>3</sup>	0.072	0.273
Initial system pressure	MPa	0.25	0.1

<sup>1</sup> available for mixing

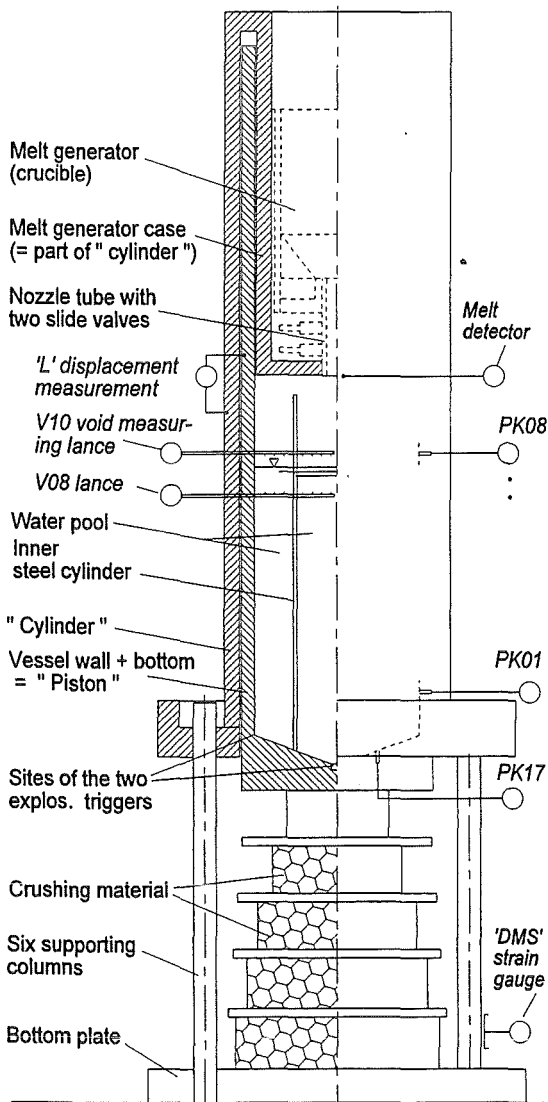


**Fig. 1** ECO test facility,

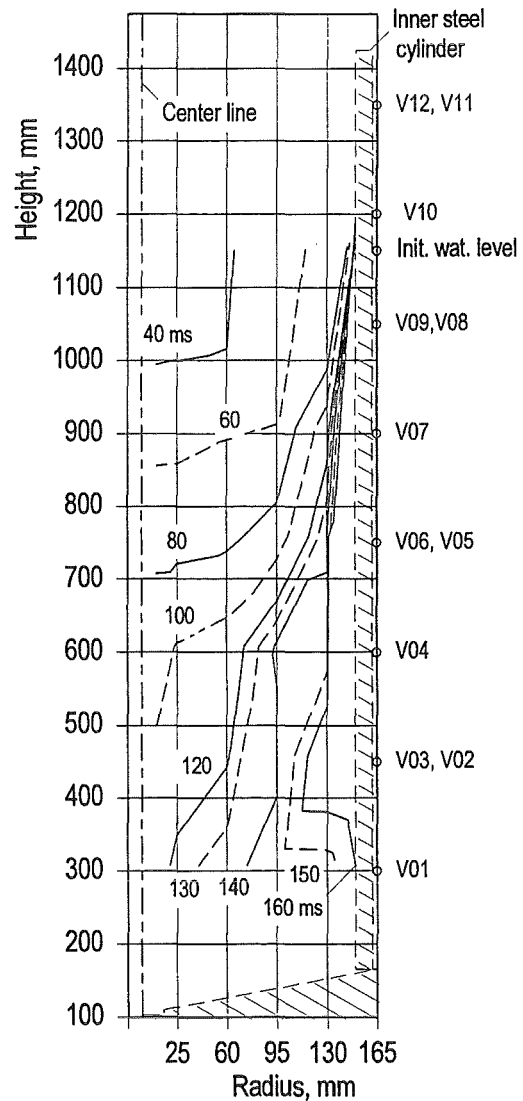


**Fig. 2** Progression of the mixing zone in the volume set by the inner cylinder. The time is taken as a parameter. ECO-04

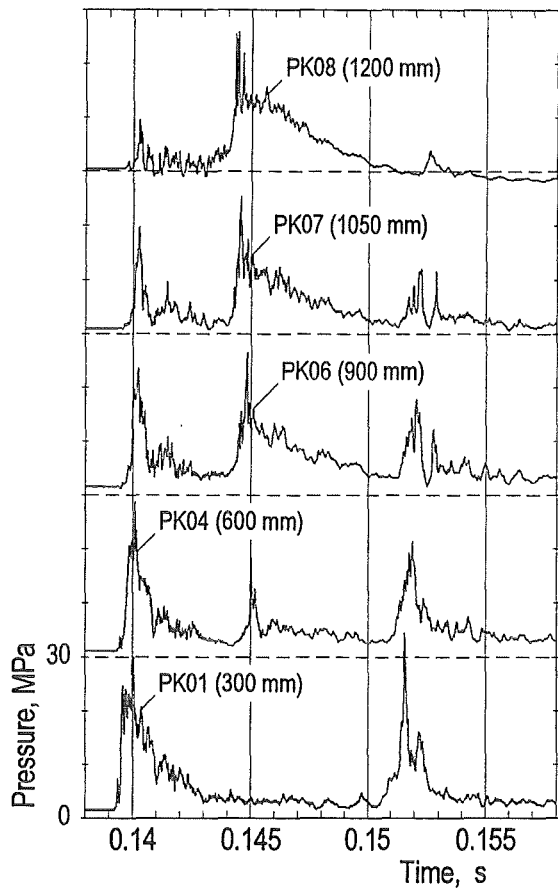


**Fig. 3** Pressure data obtained in the water at various heights. ECO-04.

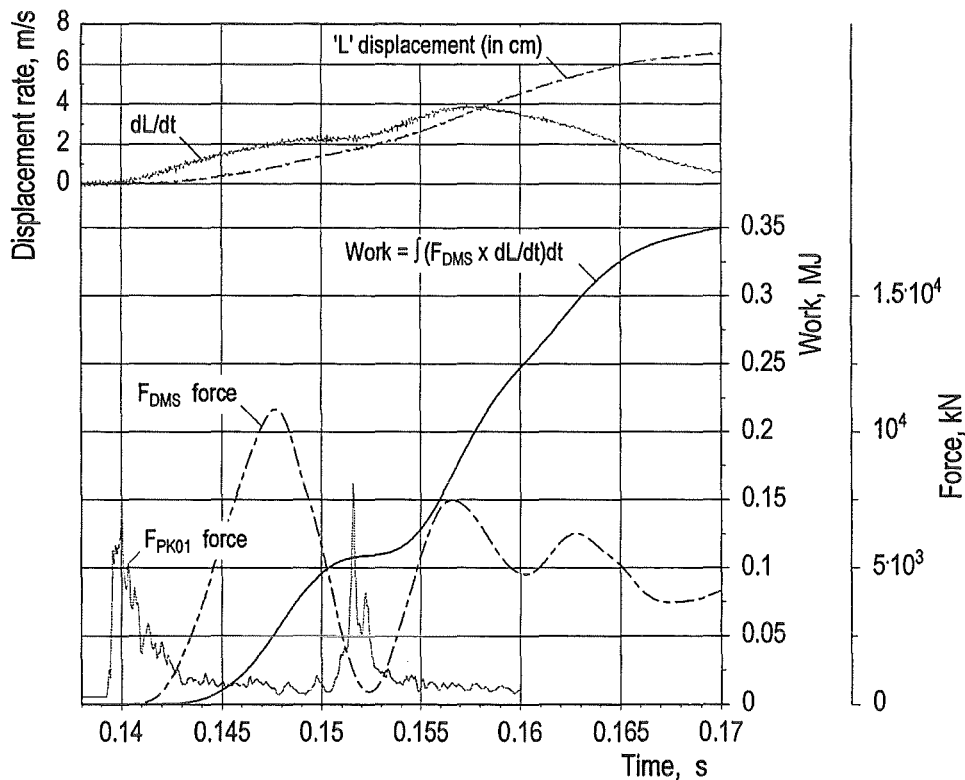


**Fig. 4** Work from DMS strain gauge and displacement data. The force based on PK01 (= pressure x area of vessel) is shown for comparison.

- II. Theoretische Arbeiten zur Schmelze-Kühlmittel-Wechselwirkung  
(H. Jacobs, B. Stehle, E. Stein, IKET; M. Böttcher, U. Imke,  
D. Struwe, IRS)

### **Abstract**

Work in 2001 concentrated on further development and a special application of MATTINA as well as the implementation and adaptation of the new version of MC3D.

### **Zusammenfassung**

Im Jahr 2001 konzentrierte sich die Arbeit auf die weitere Entwicklung sowie eine spezielle Anwendung von MATTINA und die Implementierung und Anpassung der neuen Version von MC3D.

#### **1. Evaluation of the pressure development in a vacuum system due to the thermal interaction between liquid lead-bismuth and water with MATTINA**

The MEGAPIE target is being developed in a large international collaboration [1] for the Spallation Neutron Source SINQ at Villigen in Switzerland (see also 32.23.05). It is also a demonstration facility on the way to accelerator driven subcritical reactor systems, which are under consideration for the transmutation of nuclear waste. But in contrast with the design of such transmutation devices, the proton beam in SINQ comes from below. So the target container is essentially a tube (almost 4 m long, 188 mm inner diameter) with a hemispherical cap at its lower end hanging within the vacuum tube (inner diameter 220 mm) in which the beam is delivered. It is filled with a liquid lead bismuth eutectic (PbBi) that flows downward in an annular gap formed by a tube inside the target container and rises towards a heat exchanger inside that tube. The liquid metal serves at the same time as spallation source and as coolant for the 'beam window,' i.e. the area in the center of the lower hemisphere through which the beam enters the target, and it carries away the important energy deposited by the beam (about 1 MW). So, its temperature varies between about 520 K at the inlet and 620 K beyond the volume with energy deposition. In order to prevent contamination of the beam line with the highly activated liquid metal in case of a leak of the target container, this one is enclosed by a safety hull which is a double walled structure with (heavy) water flowing inside (down on one side and up on the other) to

cool the area at the apex where the beam passes. In case that both, target container and safety hull should fail, this opens the possibility that the hot liquid metal might come into contact with water and the thermal interaction between them might produce pressures that might jeopardise the surrounding structures (vacuum tube and cover gas region of the target).

However improbable the above scenario is, it must be treated in the safety report of MEGAPIE and this requires an estimate of the pressure that might develop as a consequence. To this end a 'base case' was defined assuming a leak size of 2 cm diameter in both structures together with the release of up to 7.5 ℓ of water and all of the 90 ℓ of PbBi available. In the presence of the large free volume inside the vacuum tube, a complete exchange of heat between the two masses would lead to a pressure of only 0.65 MPa, which doesn't pose any threat. This result is largely due to the fact that PbBi, besides its high density (about 10.7 kg/m<sup>3</sup>), has a very low heat capacity of only 146 J/(kgK). Actually the pressure would remain even lower because much of the steam would condense on the cold walls of the vacuum tube. This would probably lead to a complete separation of water and PbBi before thermal equilibrium were reached and to a pressure below 0.1 MPa. But still the question remains which pressures may be reached during the transient, especially in smaller subvolumes of the system as e.g. the 'inner gap,' i.e. the narrow space between target container and safety shroud or the target if water should get there. This largely depends on the masses of water and PbBi that go into the individual volumes and on the rate of heat exchange between them. These processes have been studied by a numerical simulation of the system with MATTINA [2].

Figure 1 shows a rough sketch of the accident situation with the breaks in target container and safety hull indicating the leaks. Their axial position is at about 0.68 m. The dark blocks below height zero indicate the upper and intermediate collimator blocks that may play a role in limiting the volume available. This situation was modelled with MATTINA assuming axial symmetry. The technical structures are modelled with the help of impermeable cell boundaries. In this way, no fine details of their (round) shapes can be represented. The proper width of the gaps between the shells

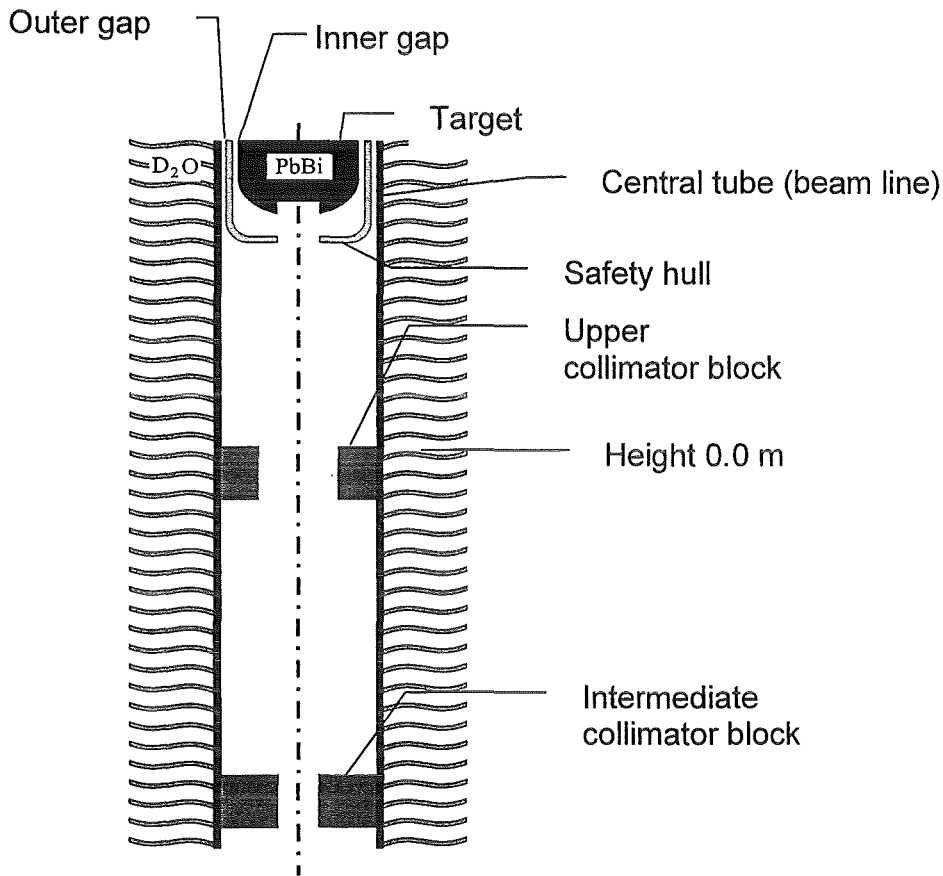


Figure 1: Schematic sketch of the accident situation (not to scale).

was taken into account by assuming appropriate porosities in these areas. The calculation area essentially involved the area from the upper collimator block up to and including the lower part of the target container. The flow of the materials towards the failure locations was modelled with the help of pressure boundary conditions. The (small) free volumes in the inner and outer gaps outside the area were modelled directly without conserving their shapes. The large free volume below the upper face of the upper collimator block was modelled by a space 0.4 m deep below that face that also opened radially to a large volume (about  $1 \text{ m}^3$ ) surrounding the whole configuration. In order to promote the thermal interaction of the fluids in a conservative way, a vessel of 0.3 m height and 0.4 m diameter was assumed below the opening in the upper collimator. In the true geometry, only small amounts of them would come together within the collimator and larger masses would only accumulate in a collecting tank about 10 m further down and correspondingly later. The initial pressure within the vacuum tube is close to zero and cannot be modelled with MATTINA. So the initial pressure was assumed to be 10 hPa (10 mbar).

The leak rates following from the given pressure conditions and leak sizes are nearly constant: 20.8 kg/sec of PbBi and 2.9 kg/sec of water. The water that flows out of the safety hull at a temperature of 40 °C has a vapour pressure of about 74 hPa. So some of it evaporates spontaneously but at the same time it cools down. Thus, in the large space within the central tube, the initial fast pressure rise reaches only 30 hPa within about 0.04 sec. After that, the pressure rises only due to heat transfer from the PbBi to the water and this results in a gradual pressure rise to about 0.06 MPa (0.6 bar) after 10 sec, see Figure 2. The important result here is the almost complete absence of pressure transients due to violent evaporation (steam spikes), to say nothing of steam explosions. All that occurs are a small step of the pressure by about 15 hPa early in the process and a faster pressure rise after about 9 sec.

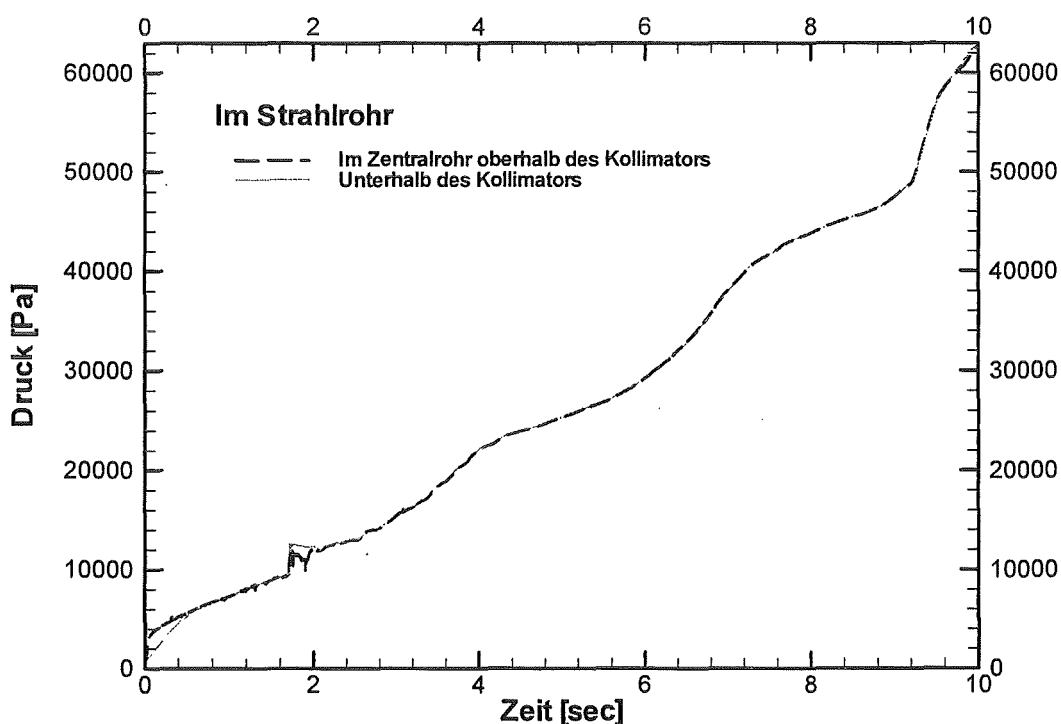


Figure 2: Pressure development in the central tube

In the beginning, a large portion of the PbBi ( $\approx 60\%$ ) and a small fraction of the water ( $\approx 3\%$ ) accumulate in the inner gap between target container and safety hull. In this narrow space, the pressure jumps to almost 70 hPa within 0.02 sec and then rises quickly to reach 0.35 MPa (3.5 bar) after 6 sec, see Figure 3. But even this pressure is still lower than the operating pressures of target container and safety hull. And this

pressure is self-limited: after it has reached about 0.2 MPa, it starts to push out the liquids that have collected at the bottom of the gap. Therefore, after 6 sec, the pressure quickly drops to about 0.1 MPa at 10 sec. All the time, the hydrostatic pressure at the bottom of the target container is much higher than the pressure in the gap so that the PbBi flows out continuously and there is no possibility of water getting into the target container. So, in summary, the base case is far from causing the risk of further mechanical damage to the target or the central tube (beam line).

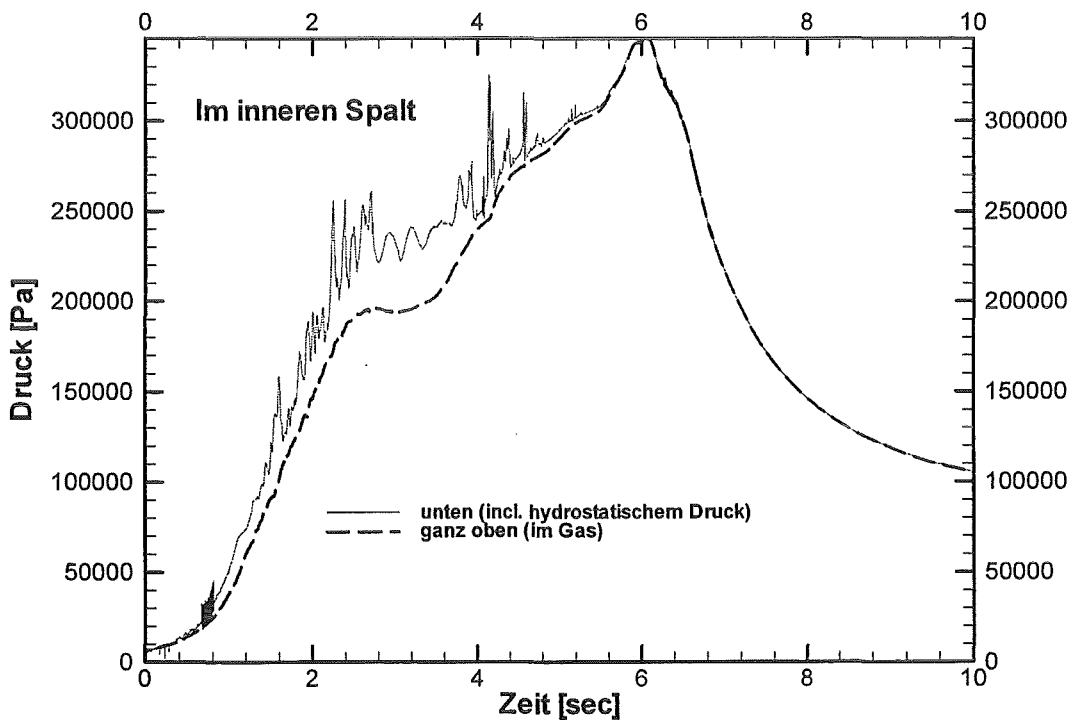


Figure 3: Pressure development in the inner gap

In order to cover conservatively the uncertainties in the definition of the accident, a conservatively aggravated case has been considered as well. It assumes that all openings in the intermediate collimator block are blocked completely by debris from the target structures. This very much reduces the available free volume and means higher pressures. But even this case is still no danger for the central tube. However, during such a case, small quantities of water might penetrate into the target container and lead to pressure transients up to possibly 2 MPa there. So it appears to be prudent to provide the cover gas container of the target (design pressure 1 MPa) with a safety valve that limits the gas pressure to an uncritical value.

## **2. Implementation of the new version of MC3D**

In the beginning of 2001 the Version 3.3 of MC3D was released from CEA-Grenoble. The new version is based on a combination of the programming languages C++ and Fortran, whereas the old interpreter language Esope was substituted by C++. The new data structure is built in an object oriented manner with an interface to the procedure oriented Fortran part. The implementation of the HP-based version on our IBM/RISC6000 system was extremely difficult due to the bad portability properties of the new code. Our computer centre (HIK) helped to remedy these problems, which mainly arise from the different compiler behaviour and a different handling of the Fortran – C++ interface. Some problems could not be resolved completely and it was necessary to remove parts of the source code to get the new version running. Some test calculations were performed and the results were compared with results from CEA at Grenoble leading to the conclusion that the deleted parts are not used in our kind of simulations. In the new version several physical models like boiling and fragmentation are revised or are totally new. Unfortunately most of the modifications implemented by the Forschungszentrum Karlsruhe in the version 3.2 to get useful simulations of low pressure premixing and explosions starting from those premixing situations were not adopted and implemented. First calculations for the PREMIX experiments showed much too low evaporation rates and nearly no fragmentation of large melt droplets released into the water. In addition some programming bugs were detected.

## **3. Modelling adaptation for the new version MC3D 3.3**

To get better results for the simulation of the PREMIX experiments [3] some changes were made to the heat transfer, fragmentation and drag modelling. In general the new heat transfer models create less evaporation than the correlations used in the older versions. The melt droplet - water droplet heat transfer model that we introduced a long time ago was implemented incorrectly in the new version and the source coding had to be corrected. In addition we put in again the option to have no reduction of radiation heat transfer dependent on the water volume fraction in droplet flow. The transition temperature of saturated boiling to strongly sub-cooled boiling was shifted from 1 degree to 5 degree of sub-cooling to get stronger evaporation around the saturation point. A simplified drag correlation for droplets and bubbles under fragmentation was introduced in combination with a simplified fragmentation

model. A main problem in the new version are strong pressure instabilities due to condensation effects, which depend on the vapour bubble size, which itself is a function of drag and fragmentation of bubbles. As the effect of inert gas on condensation processes is not considered the newly implemented condensation scaling factor can improve premixing results. In general the new version runs most stable using constant bubble and droplet diameters for water and melt assuming a pre-fragmented shower of melt droplets or a compact melt jet to be fragmented into droplets of fixed final size. The shape of the compact melt jet is calculated much better than in the earlier version and seems to be more stable numerically. Figure 4 shows the calculated pressure curve and Figure 5 the vapour production for the PREMIX 13 experiment simulated with the modified 3.3 version compared to the measured values. For that case the compact melt jet option is not used and 5 mm melt droplets, which do not further fragment, are released into the water. At the start of the melt coolant interaction the vapour production is overestimated, whereas the long term behaviour is well calculated. CEA announced patches for the new version to put it into a better state. In the next steps we will investigate the code behaviour of the explosion module and the interface from the final premixing state to the first time step in the explosion calculation. Due to the very complicated new data structure and

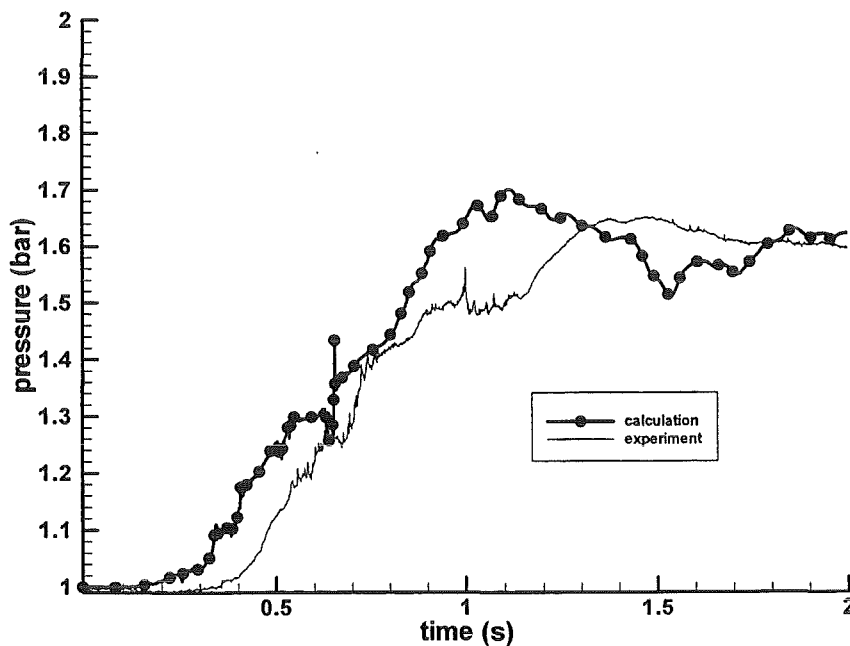


Figure 4: Calculated and measured pressure for PREMIX 13.

the mixing of programming languages the implementation of model modifications is a very time consuming fault-prone task.

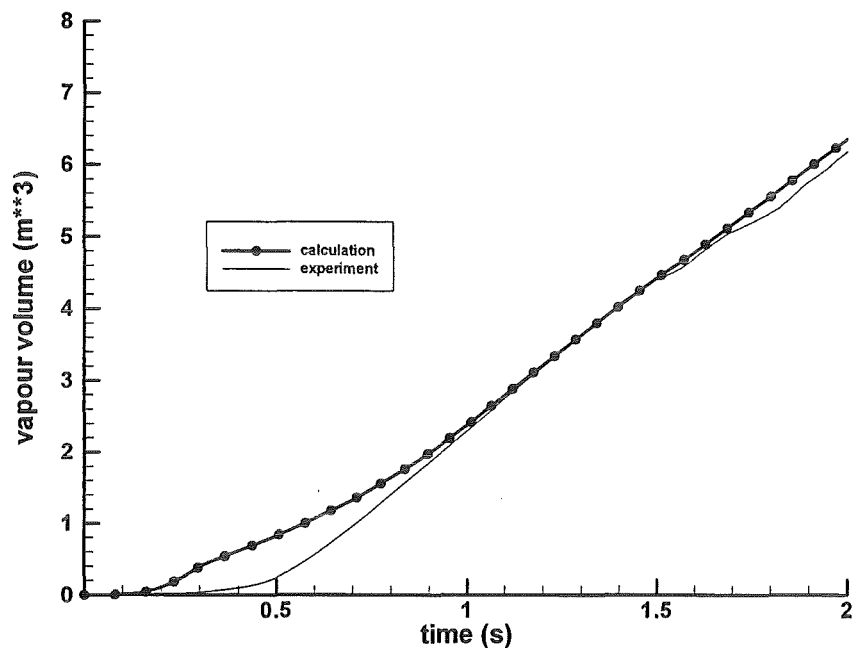


Figure 5: Calculated and measured vapour production for PREMIX 13.

### Acknowledgement

We thank Mrs. L. Obholz (HIK) for her extensive support in implementing the new C++ version of MC3D on the IBM/RISC6000 system.

### References

1. G. S. Bauer, M. Salvatores and G. Heusener, MEGAPIE, a 1 MW Pilot Experiment for a Liquid Metal Spallation Target, J. Nucl. Mater. 296 (2001) 17-33
2. H. Jacobs, Untersuchung zum Sicherheitskonzept des MEGAPIE Targets in der Spallations-Neutronenquelle SINQ: Druckentwicklung im Strahlrohr der Anlage in dem angenommenen Störfall 'Bruch der Strahlfenster an Targetbehälter und Sicherheitshülle,' Forschungszentrum Karlsruhe Report, FZKA 6637, to be published
3. Kaiser, W. Schütz, H. Will, PREMIX Experiments PM12-PM18 to Investigate the Mixing of a Hot Melt with Water, FZKA-6380, 2001.

### 32.21.03 Versagen des Druckbehälters und Dispersion der Kernschmelze

#### I. Experimente zur Dispersion von Corium

(M. Greulich, M. Kirstahler, L. Meyer, M. Schwall, E. Wachter, G. Wörner, M. Gargallo; IKET)

#### **Abstract**

The DISCO-H Test Facility at Forschungszentrum Karlsruhe was set up to perform scaled experiments that simulate melt ejection scenarios under low system pressure in Severe Accidents in Light Water Reactors (LWR). These experiments are designed to investigate the fluid-dynamic, thermal and chemical processes during melt ejection out of a breach in the lower head of a LWR pressure vessel at pressures below 2 MPa, and various failure modes with an iron-alumina melt and steam.

The test facility models the reactor pressure vessel the reactor cavity, compartments and the containment. If the melt is dispersed out of the reactor pit, the mechanisms of efficient melt-to-gas heat transfer, exothermic metal/oxygen reactions, and hydrogen combustion produce a rapid increase in pressure and temperature in the cavity, compartments and containment. In the frame of these Direct Containment Heating (DCH) phenomena the following issues are addressed: (i) final location of corium debris, (ii) loads on the containment in respect to pressure and temperature, (iii) amount of hydrogen produced, (iv) loads on reactor pit and support structures, and (v) impact on safety components.

Main components of the facility are: (i) Containment pressure vessel (14.0 m<sup>3</sup>, 1 MPa, 200°C), (ii) RPV-RCS pressure vessel (0.08 m<sup>3</sup>, 2 MPa, 220°C), (iii) 1:18 scaled cavity, (iv) Steam accumulator (0.08 m<sup>3</sup>, 4 MPa, 250°C).

Standard results are: (i) pressure and temperature history in the RPV, the cavity, the reactor compartment and the containment, (ii) post test melt fractions in all locations with size distribution, (iii) video film in reactor compartment and containment (timing of melt flow and hydrogen burning), (iv) pre and post test gas analysis in the cavity and the containment.

The test facility was set up and instrumented, all systems were checked and scoping tests were performed.

## 1. Introduction

In a severe accident special pressure relief valves in the primary circuit of German Pressurized Water Reactors (PWR) will transfer a high pressure accident into a low pressure scenario. However, there may be a time window during late in-vessel re-flooding scenarios where the pressure is in the order of 1 or 2 MPa at the moment of the reactor vessel rupture. A failure in the bottom head of the reactor pressure vessel, followed by melt expulsion and blowdown of the reactor cooling system, might disperse molten core debris out of the reactor pit, even at such low pressures. The mechanisms of efficient debris-to-gas heat transfer, exothermic metal/oxygen reactions, and hydrogen combustion may cause a rapid increase in pressure and temperature in the reactor containment and may endanger its integrity. This complicated physical and chemical process is known as Direct Containment Heating (DCH). Investigating the DCH-issue a number of problems have to be addressed: (i) final location of corium debris, (ii) loads on the containment in respect to pressure and temperature, (iii) amount of hydrogen produced, (iv) loads on reactor pit and support structures, and (v) impact on safety components. The knowledge of these points can lead to realize additional safety margins for existing or future plants. DCH phenomena have been investigated intensively for cavity designs with large instrument tunnels, high melt ejection pressures and small holes centered at the lower head. Only few works have studied these phenomena and melt ejection scenarios at low pressure with an annular cavity design, where the only large pathway out of the reactor pit is the narrow annular gap between the RPV and the cavity wall [1-3]. Therefore, our experimental program is aimed at low failure pressures, diverse failure modes and larger breach sizes together with an annular cavity design.

At FZK the test facility DISCO-C has been built for performing dispersion experiments with *cold* simulant materials in a scale 1:18 based on a 1200 MW PWR. The fluids employed were water or a bismuth alloy (Wood's metal) instead of corium, and nitrogen or helium instead of steam. In the DISCO-H facility selected experiments in the same scale will be performed with thermite melt, steam and a prototypic atmosphere in the containment. These experiments are designed to investigate the fluid-dynamic, thermal and chemical processes during melt ejection out of a breach in the lower head of a LWR pressure vessel at pressures below 2 MPa, and various failure

modes. The test facility models the reactor pressure vessel (RPV), the volume of the reactor cooling system (RCS), the reactor cavity, pump and steam generator compartments and the containment.

## 2. Description of the experiment

The containment model is heated over a time period of approximately 10 hours by filling with steam additional to the atmospheric air until the vessel pressure reaches 0.2 MPa. The condensate water is drained at the bottom of the vessel from time to time. The average gas temperature and the wall temperature inside the vessel is 373 K (100°C) at the end of the heat-up. A metered amount of hydrogen gas (3 mol%) are added to the vessel at the end of heat-up while fans are running inside the vessel. A gas sample is taken just before the start of the experiment.

The pressure vessel modeling the RPV and RCS volume, that is inside the containment vessel, is electrically heated to the saturation temperature of the planned burst pressure, e.g. to 453 K (180°C at 1.0 MPa). It contains nitrogen at that temperature at 0.1 MPa.

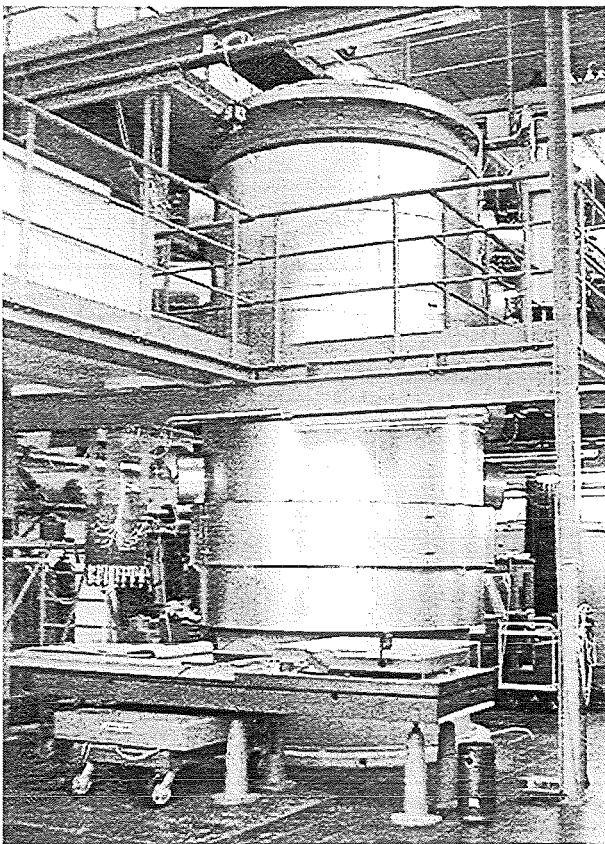


Fig. 1. The test facility DISCO-H

The steam accumulator is outside of the containment vessel. It is heated electrically to the saturation temperature of twice the planned burst pressure, e.g. 486 K (213°C at 2.0 MPa). The accumulator is filled with a measured amount of water by a high pressure metering pump to reach that pressure. The RCS pressure vessel and the accumulator are connected by a 25 mm diameter pipe with an electro-pneumatically actuated valve.

The model of the RPV, that is directly flanged to the RCS pressure vessel, is filled with aluminum-ironoxide thermite. The experiment

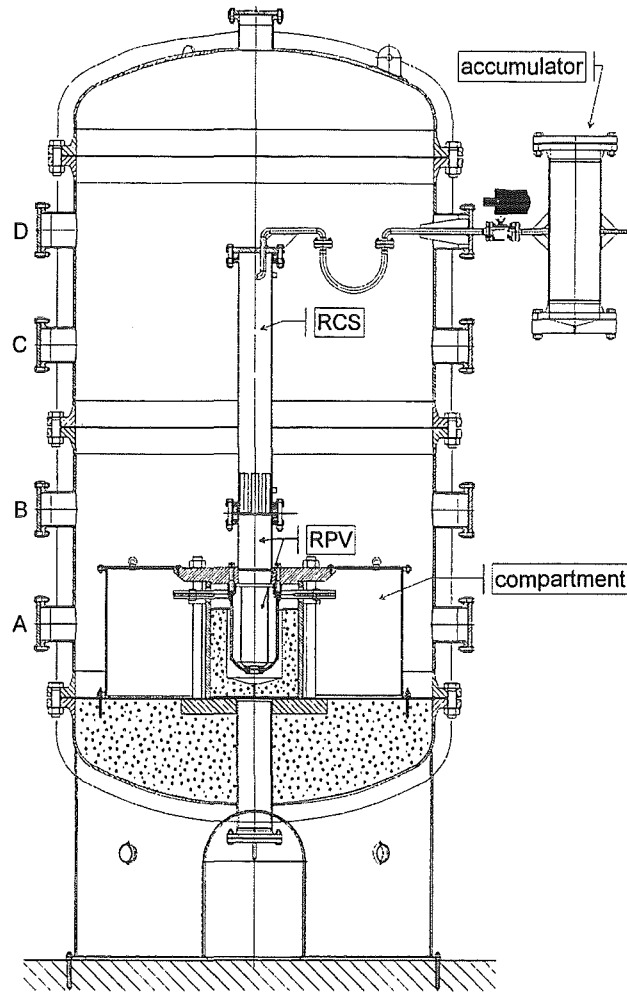


Fig. 2. Scheme of the test facility DISCO-H

is started by igniting the thermite electro-chemically (Pyrofuzer<sup>®</sup>) at the upper surface of the compacted thermite powder. When a pressure increase in the RPV-RCS pressure vessel verifies that the thermite reaction has started, the valve in the line connected to the accumulator is opened and steam enters the pressure vessel. When the pressure has reached a preset value the valve is automatically closed again. The amount of steam that is initially in the RCS-RPV pressure vessel is determined by the amount of steam originally in the accumulator minus the steam left in the accumulator. The steam flow takes approximately one second. During that time and thereafter the thermite reaction progresses until it reaches the bottom of the RPV vessel. Approximately 10 seconds after ignition the brass plug at the bottom of the RPV vessel is melted by the 2400 K hot iron-alumina mixture. That initiates the melt ejection. By that time the pressure in the RCS-RPV pressure vessel will be higher than the preset value due to radiation heat transfer from the hot melt to the steam. The melt is driven

out of the breach by the steam and is dispersed into the cavity and the containment. Due to the melt-to-gas heat transfer, exothermic metal/oxygen reactions, and hydrogen combustion the pressure and temperature in the containment pressure vessel will rise up to an estimated 0.6 MPa and 900 K, for a short time (less than a minute).

### **3. Components of the test facility**

#### **3.1 *The containment pressure vessel (CPV)***

The containment pressure vessel is a TÜV-approved cylindrical pressure vessel made of 15 mm steel and is rated at 1.0 MPa and 200°C. It has an outer diameter of 2.20 m and a height 4.60 m; with the pedestal and the top port its total height is 5.80 m (see Fig. 1 and 2).

The pressure vessel consists of two segments and a lower and an upper head. Each segment has six instrument penetration ports at two levels. One of the ports is closed with a safety rupture disk (diameter 200 mm), with a burst pressure of 1 MPa. The lower head is filled with concrete that forms a level floor. All internal structures are bolted to that floor. At the center of the floor is a large vertical pipe that contains the condensate draining piping and has a connection to the bottom port. The entire vessel is insulated against heat loss on the outside by a 100 mm thick fiberglass insulation. The empty volume of the containment vessel is 14.18 m<sup>3</sup>, the total freeboard volume including the subcompartment is 13.88 m<sup>3</sup>.

#### **3.2 *Subcompartment***

The subcompartment is an annular space around the cavity with a volume of 1.74 m<sup>3</sup>. The flow path from the cavity into the subcompartment is along the eight stubs modeling the main cooling lines (total flow cross section is 0.0308 m<sup>2</sup>). The top cover has four openings with a diameter of 130 mm, that are covered by a mesh to prevent melt to enter the containment.

#### **3.3 *The pressure vessel modeling the RCS and RPV volume***

The RCS-RPV pressure vessel models the volumes of both the reactor cooling system (RCS) and the reactor pressure vessel (RPV) and has a total volume of 0.076 m<sup>3</sup>. A disk holding 8 pipes (46 mm I.D., 255 mm length) separates the two partial volumes. This arrangement models the main cooling lines with respect to the flow

constriction between RCS and RPV. The cylinders (inner diameter 0.20 m) modeling the RCS and RPV are heated electrically, and are insulated over the hole length and on the top.

### 3.4 The RPV model

The RPV model, that serves as crucible for the generation of the melt, is bolted to a plate carrying the RCS-RPV pressure vessel (Fig. 3). An insulation material of magnesium oxide (MagneRam®) is filled between the outer shell of the RPV model and an inner steel liner, that contains the thermite powder. The hole at the bottom of the melt generator is formed by a graphite annulus. It is closed with a brass plate.

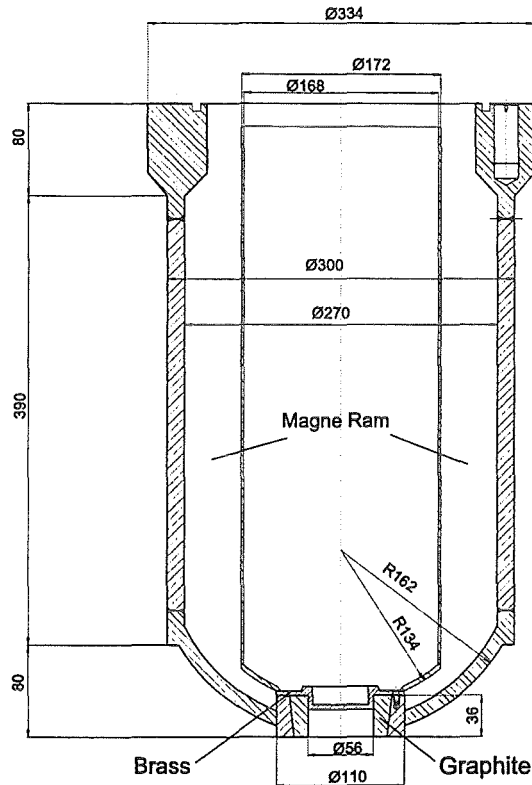


Fig. 3. The RPV model; crucible for the thermite melt

### 3.5 The reactor pit

The cavity and RPV-holddown were designed to withstand a pressure of 10 MPa with a safety factor of 2 to yield. The reactor pit is made of concrete (Fig. 4) and is installed inside a strong steel cylinder (30 mm thick walls). This cylinder is clamped by 8 bolts (56 mm diameter) between a base plate and a top plate, both 90 mm thick. Besides the flow path along the main cooling lines there is the option of a flow out of the cavity

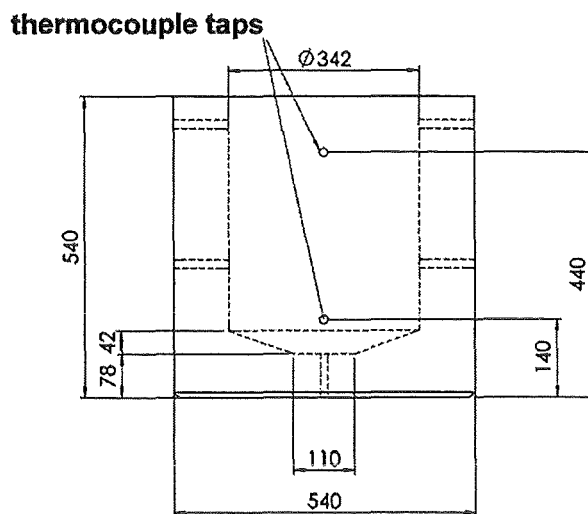


Fig. 4. The reactor pit made of concrete

straight up into the containment through eight openings with a total cross section of 0.052 m<sup>2</sup>. Depending on the reactor design that is to be investigated this cross section is a variable.

### **3.6 Steam accumulator**

The steam accumulator is a TÜV-approved cylindrical pressure vessel placed outside of the containment pressure vessel with approximately the same volume (0.082 m<sup>3</sup>) as the RCS-RPV pressure vessel and is rated at 2.0 MPa and 250°C (Fig. 2). Both vessels are connected by a 25 mm diameter pipe with an electro-pneumatically actuated valve. The vessel is electrically heated from the outside and is insulated by fiberglass. A high pressure metering pump is connected to the accumulator that can inject very accurate amounts of water into the heated and pressurized vessel.

### **3.7 Steam generator**

The steam generator serves for heating up the containment vessel and providing the steam for the initial containment atmosphere. It has a capacity of 42 kg/h steam, (32 kW) at 1 MPa. The steam generator is also used to vent the steam accumulator of air.

## **4. Instrumentation**

### **4.1 Temperature**

Initially, only type-K thermocouples (chromel-alumel) are installed in the facility. They are steel sheathed thermocouples with insulated wires. The outer diameter of the sheath is generally 0.35 mm. It is planned to use some high temperature thermocouples at selected positions in later experiments. A large number of thermocouples is installed at the outside of the steam accumulator tank and the RCS-RPV pressure vessel to control the electric heaters. These temperatures are monitored at the heater control board.

The data acquisition system records the signals of the 22 thermocouples at a rate of 2000 samples per second per channel. The steam temperature in the accumulator tank is measured by two thermocouples, one near the top and one near the bottom. There is one thermocouple within the draining pipe at the bottom to measure the water temperature, if water is present. There are two thermocouples within the RCS-

RPV pressure vessel, one in each compartment (RCS and RPV). A total of 11 thermocouples are located at different levels in the containment pressure vessel (CPV) to measure the bulk gas temperature. Two of them are within the subcompartment, one is at the floor and the rest is either close to the wall or in the space between the RCS-RPV pressure vessel and the containment wall.

Six thermocouples are at two locations near or inside the concrete wall of the cavity (positions see Fig.4). The thermocouple sticking 2 mm out of the wall will measure the arrival of the melt. It will be destroyed by the melt. Later experiments will have a high temperature thermocouple there. The thermocouples placed at two different depths within the concrete will serve to measure the transient heat flux entering the concrete.

#### **4.2 Pressure**

A total of 15 strain gauge-type pressure transducers (Kulite) with ranges of 0–1.7 MPa, 0–3.4 MPa and 0–7.0 MPa were used to measure steam and gas pressures. The compensated operating temperature range is 27°C – 232°C, with a thermal drift of +/- 5% of full scale output. The transducers are being adjusted at the operating temperature just before the start of the experiment. The data acquisition system recorded data at a rate of 2000 data points per second per channel. All gages were mounted in tapped holes that were connected gas tight with the outside atmosphere at their backsides. In case of the transducers in the RCS-RPV pressure vessel, the compartment, and the cavity this connection was achieved by flexible steel hoses. The gages in the containment pressure vessel were mounted in the blind flanges of the ports at different levels.

#### **4.3 Gas composition**

Ten pre-evacuated 500-cm<sup>3</sup> gas grab sample bottles will be used to collect dry-basis gas samples at three positions, in the cavity, in the subcompartment, and in the upper part of the containment. The sample lines and the sample bottles will be cold, thus the bottles will be filled with noncondensable gases only. One pretest sample will collect background information just prior to the start of the melt ejection. One sample at all three stations will be taken during the blow down and one 20 seconds after the

blow down. The gas samples will be analyzed at the Engler-Bunte-Institut at the University Karlsruhe.

#### **4.4 Additional measurements**

Three video cameras will be used in the experiment. One camera looks down from the dome into the containment, one is installed at the level B port looking at the top of the subcompartment and the openings in the top plate (not shown in Fig.2), that represent the direct path from the cavity into the containment. A third camera looks into the compartment from the side by means of an endoscope.

Breakwires were placed across the RPV exit hole and at the annular gap exit. The breakwires were intended to give timing information on entry of debris into and out of the cavity.

The total debris mass dispersed into the DISCO vessel and the debris mass in specific locations will be determined by a posttest debris recovery procedure. A posttest sieve analysis of the debris recovered from different locations will be performed for each test.

### **5. Thermite Burn Scoping Test**

Two thermite burn tests were performed outside of the DISCO Test Facility. The goal of the burn tests was to determine the time to melt plug failure (from ignition) and to verify that the melt plug failed as expected [4].

The tests were performed with the RPV-RCS pressure vessel connected to the RPV-model. The vessel contained nitrogen at 1 bar at room temperature prior to ignition. The crucible (RPV-model) contained 11.5 kg of aluminum-ironoxide thermite. In the first test the inner diameter of the crucible was 220 mm and the density of the thermite was 1.17 g/cm<sup>3</sup>. The time from ignition to melt plug failure was 4.3 seconds, with a burn rate of 6.5 cm/s. The pressure increased to 0.61 MPa inside the RPV-RCS-vessel. Because the time was too short to safely fill the vessel with steam before melt plug failure, the parameters were changed in the second test. The diameter of the crucible was reduced to 168 mm, and the density was increased to 2.28 g/cm<sup>3</sup> by applying a higher compacting pressure. Although the height of the thermite was approximately the same as in the first test, the time to melt plug failure increased to 10.1 seconds, which meant a burn rate of 2.8 cm/s. The pressure increase was less

with 0.460 MPa, compared to the first test, probably because of the smaller surface area of the melt pool.

The melt plug was filmed by a high speed camera (500 frames/s) from below and the side. From these pictures we can infer, that the melt plug is fully open within 2 ms. Posttest inspection of the melt plug exit area determined that the exit hole was round, fully open, and with a diameter of about 55 mm. A 0.5 mm thick film of melt coated the carbon ring that formed the exit hole. A thin film of melt also coated most of the interior steel liner. Some of the steel liner had melted exposing the MgO insulator, particularly at the bottom of the liner.

The test facility has been set up and is instrumented. The heat up of the containment vessel by steam was tested. Also the experiment control and data acquisition systems have been extensively checked. The test facility is ready for the first experiment.

### **References**

1. M. L. de Bertodano, A. Becker, A. Sharon, R. Schnider, "DCH Dispersal and Entrainment Experiment in a Scaled Annular Cavity," *Nucl. Eng. Des.*, **164**, 271-285, (1996).
2. T. K. Blanchat, M.M. Pilch, R.Y. Lee, L. Meyer, and M. Petit, "Direct Containment Heating Experiments at Low Reactor Coolant System Pressure in the Surtsey Test Facility," *NUREG/CR-5746, SAND99-1634*, Sandia National Laboratories, Albuquerque, N.M., (1999).
3. S.B Kim, R.J. Park, H.D. Kim, Chevall and M.Petit, "Reactor Cavity Debris Dispersal Experiment with Simulant at Intermediate System Pressure," *SMiRT15 Post Conference Seminar on Containment of Nuclear Reactors*, Seoul, Korea, August 23-24, (1999).
4. L. Meyer, M. Greulich, M. Kirstahler, M. Schwall, E. Wachter, G. Wörner, "DISCO-H Thermit Brenntest", Interner Bericht 32.21.03, Forschungszentrum Karlsruhe, IKET-Nr. 7/01, NUKLEAR: 3358, (2001)

## II. Rechnungen zur Dispersion der Kernschmelze ( D. Wilhelm, IKET )

### **Zusammenfassung**

Die Rechnungen des letzten Jahres zur Coriumdispersion wurden mit dem für dieses Problem erweiterten Fluidynamik-Code fortgesetzt. Der Code beschreibt den Auswurf von geschmolzenem Kernmaterial aus dem Druckbehälter eines Leichtwasserreaktors in die angrenzenden Räume und den Dom des Sicherheitsbehälters. Die Thermit-Experimente im Massstab 1:10 wurden im Rahmen einer internationalen Übereinkunft im Sandia National Laboratory, U.S.A., durchgeführt. Sie werden fortgesetzt im DISCO Programm des Forschungszentrums Karlsruhe. Die Extrapolation auf den Reaktorfall wurde abgeschlossen. Die Studie zeigt, dass wichtige experimentelle Resultate gemäss allgemeiner Skalierungsgesetze auf den Reaktorfall übertragen werden können, aber dass es Abweichungen vor allem beim Übergang von Thermit auf Corium gibt. Zusätzliche Daten liegen für Coriummischungen vor, für die der Eisenanteil erhöht wurde.

### **1. Introduction**

In the event of a core melt-down of a pressurized water reactor, the molten metals and oxides may collect in the lower head of the pressure vessel. Two scaled-down thermite experiments [1] were performed at the Sandia National Laboratory, Albuquerque, which simulated the discharge of the melt through a given breach of the lower head driven by steam at a moderate pressure of 1.1 MPa. The present program focuses on low and medium pressure levels in the vessel. When focussing on where and when the melt is being dispersed, it became obvious that it was necessary to resolve, different to the previous studies [2], details of the geometry close to the breach. The present program not only seeks to provide results for the melt dispersion, but also for the time sequence of hydrogen generation, in-vessel pool behavior in the lower head, and impact of the melt on safety components.

## 2. Recalculation of the experiment

The experimental program is being accompanied by calculations with a CFD code. To a code of the SIMMER family [3], models were added which were found necessary to describe the phenomena during melt dispersion. Fig. 1 shows an sketch of the reactor pressure vessel and the adjacent structures and an artist's view of the melt during dispersion. The phenomena under investigation are listed close to the location where they occur.

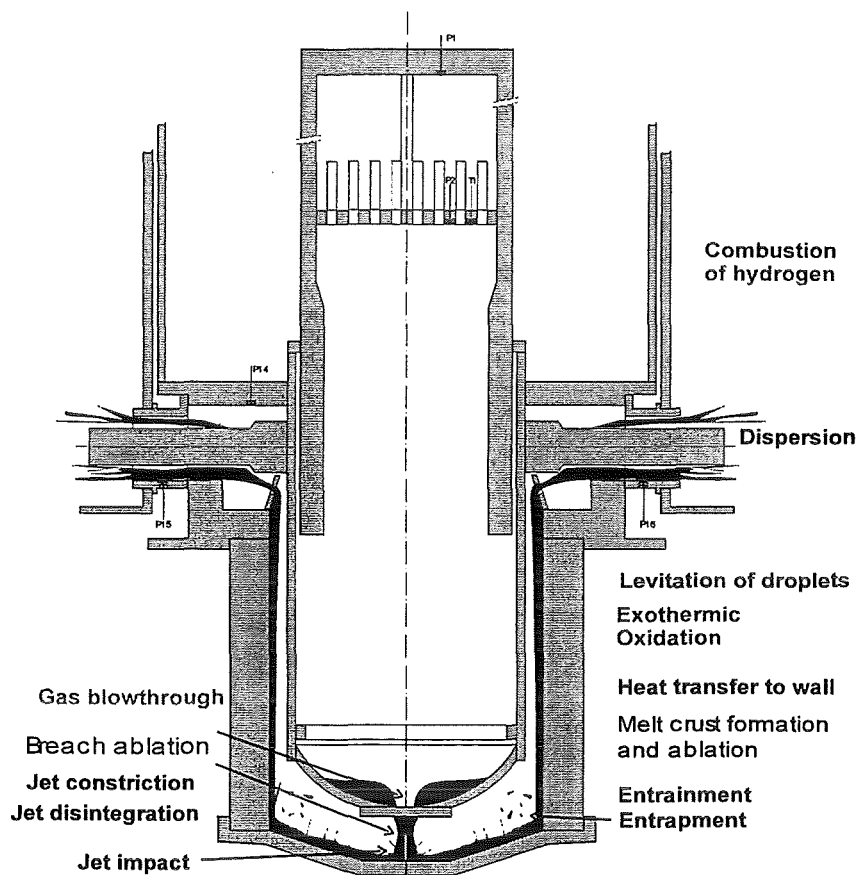


**Fig.1:** Sketch of a model of a reactor with symmetric cavity and dominant phenomena

The code was successfully used to recalculate the two Sandia experiments. Besides the achievement of a good agreement of the pressure transients, the main findings of the post-test analyses of the experimentalists were confirmed, as there are a steam limited oxidation of metal in the cavity, a further oxidation in the containment, a constant hydrogen burning, and the limited amount of thermite dispersed beyond the cavity.

### **3. Extrapolation to prototypic conditions**

After recalculation of the experiments, an attempt was made to extrapolate to prototypic condition [4]. This was done in two steps, first to prototypic scale, and then from thermite to corium. While the geometric scale-up revealed only small differences to the experiment, especially in the dynamics, the change to corium showed new sensitivities. These depend on the specification of the melt, and are thus subjected to the history of the accident. By and large, the relevant results scale as predicted, the pressures look similar to the experiment except for the cavity pressures which are higher, the relative amount of hydrogen generated depends strongly on the melt mass and the metal content in the melt, and the fraction of melt discharged into the containment is lower but rather close to what has been measured.

### **4. Variation of the metal content**

The definition of the corium composition used in the prototypic calculations is based upon the Sandia specification which was taken from the Calvert Cliffs scenario V upper bound limits presented in [2]. The only metal taken into account is zirconium with a mol fraction of 0.062, see Table I. If more metal was found in the corium the chemical reaction would increase. Therefore, a study was added to the reference calculation to identify the influence on the fraction of melt dispersed out of the cavity. The additional metal is supposed to be iron which may represent molten structures inside the pressure vessel. The total melt mass of 119400 kg is not changed, except for the two cases with 130000 kg. The surface tension and all other thermophysical quantities are being kept constant, but the mixture density has been adjusted. The relative mol fractions of the original corium plus zirconium, relative to the corium part alone, have been kept constant.

Given the mol fraction of the added iron which is the parameter of the new runs, the number of mol hydrogen produced per mol melt has to be evaluated. The specific reaction yields a stoichiometric potential of 2 mol hydrogen produced per mol zirconium, and 1 mol hydrogen per mol iron if the iron is oxidized to FeO, a reaction which is dominant given the short time in which it may take place. The hydrogen generation rate of the corium mixture is now the sum of the product of the mol

fraction and the stoichiometric hydrogen potential. Table I shows the parameters used in this analysis.

case	initial melt mixture quantity (kg↔kmol)	mol fractions				reaction energy of mixture (MJ/kg)	thermal energy of mixture (MJ/kg)	fraction of melt dispersed
		Zr	Fe	UO <sub>2</sub>	ZrO <sub>2</sub>			
no metal	119400 ↔ 512	0	0	.7523	.2477	0	1.33	0.52
standard corium	119400 ↔ 531	.062	0	.7056	.2323	0.16	1.33	0.65
iron added	119400 ↔ 662	.0458	.2626	.5203	.1713	0.15	1.38	0.59
iron added	130000 ↔ 721	.0457	.2627	.5202	.1714	0.15	1.38	0.44
large iron mass	130000 ↔ 1216	.0187	.7016	.2098	.0699	0.12	1.57	0.33

**Table I** Standard corium in 1:1 geometry compared with cases of less or more metal

The reaction is exothermic and the energy released for the corium mixture including zirconium of a mol fraction of 0.062 is 37.1 MJ/kmol, see also [1], where the specific reaction energy is 598 MJ/kmol for zirconium. With iron, only a small specific reaction energy of 1.97 MJ/kmol is added to the mixture. Therefore, as shown in Table I, the reaction energy does not change much when adding iron. For the last case, the mol fraction of zirconium is reduced considerably which has an effect on the reaction energy. The energies listed exclude the part produced by hydrogen combustion in the reactor dome because this does not relate directly to the dispersion. The thermal energy is calculated with the assumption that all energy stored in the melt when heating it up from 280 K to 2800 K is available, and the mass affected is the total initial melt mass.

The last column of Table I shows that there is less dispersion, compared to the standard corium case, if there is no oxidation in the cavity. The cases with standard corium and iron added, both with 119400 kg of melt, yield nearly the same dispersions. When increasing the melt mass, the calculated dispersed fraction decreases. The case with the large iron mass yields the smallest fraction of melt being dispersed.

The results of the dispersion and hydrogen generation, including the recalculation of the experiment, are collected in Table II. The table shows that the dispersion is successively reduced when going from the experiment to more prototypic conditions, and even beyond when more iron due to molten in-vessel structures is added to the melt. Because the code is limited to calculate oxidation only in the cavity, hydrogen generation data need to be compared to the reference recalculation.

case	scale	initial melt mass (kg)	dispersed melt mass (kg)	dispersed melt fraction (%)	H <sub>2</sub> produced at half time (kg)	ratio H <sub>2</sub> produced to max. amount possible
<b>experiment</b>	<b>1:10</b>	<b>62</b>	<b>48</b>	<b>78</b>	<b>( 0.89 )</b>	<b>( 0.70 )</b>
reference recalculation	1:10	62	48	78	<b>0.44</b>	<b>0.34</b>
standard corium	1:1	119400	77600	65	106	0.80
corium, no metal	1:1	119400	62100	52	0	0
corium, iron added	1:1	119400	70400	59	201	0.43
corium, iron added	1:1	130000	57200	44	177	0.34
corium, large iron mass	1:1	130000	42900	33	285	0.16

**Table II** Integral results of the present study  
 (...) = post test assessment of total amount at full time

## References

- [1] Blanchat T.K., Pilch M.M., Lee R.Y., Meyer L., Petit M., 1999, Direct Containment Heating Experiments at Low Reactor Coolant System Pressure in the Surtsey Test Facility, Sandia National Laboratory report NUREG/CR-5746, SAND99-1634, July 1999
- [2] Pilch M.M., Allen M.D., Klamerus E.W., 1996, Resolution of the Direct Containment Heating Issue for All Westinghouse Plants with Large Dry Containments or Subatmospheric Containments, Sandia National Laboratory report NUREG/CR-6338
- [3] Bohl W.R., Wilhelm D., 1992, The Advanced Fluid Dynamics Model Program: Scope and Accomplishment, *Nuclear Technology*, 99, 309-317
- [4] Wilhelm D., Analysis of a Thermite Experiment to Study Low Pressure Corium Dispersion, report FZKA 6602, Forschungszentrum Karlsruhe, August 2001

## 32.21.04 Thermischer Angriff durch Kernschmelze und deren langfristige Kühlung

### I. COMET - Konzept

(H. Alsmeyer, T. Cron, G. Merkel, S. Schmidt-Stiefel, W. Tromm, T. Wenz, IKET; C. Adelhelm, IMF; H.-G. Dillmann, H. Pasler, ITC-TAB; W. Schöck, IMK; C. Grehl, IMVT; Ing.-Büro G. Schumacher)

### **Zusammenfassung**

Zur Kühlung der Kernschmelze im Fundamentbereich eines LWR wird das COMET-Konzept entwickelt, bei dem Kühlwasser passiv von unten in die Schmelze eintritt und die Schmelze in poröser, gut kühlbarer Form erstarren lässt. Die Verwendung einer porösen, wasserführenden Betonschicht im Kühlkonzept CometPC zur Injektion des Kühlwassers wurde nach Abschluss der entsprechenden Versuchsreihe bewertet. Die gute Stabilität und Kühlfähigkeit dieses Konzepts soll durch Vorgabe von diskreten Strömungswegen weiter verbessert und die entstehende Porosität in der Schmelze gleichmäßig werden. Dies geschieht mit dem erweiterten Kühlkonzept CometPCA, für das ein erstes Großexperiment mit nachbeheizter Schmelze beschrieben wird. Kurzzeit- und Langzeit-Kühlbarkeit wurden erfolgreich nachgewiesen, unter Einschluss des Langzeitbetriebs mit dem nur schwachen Wasserzufluss, der sich durch Rücklauf des kondensierenden Dampfes im Sicherheitsbehälter ergibt. Weitere Experimente sollen dieses Konzept vertiefen und seine Verwendung für größere Schmelzenhöhen prüfen.

### **Summary**

The COMET concept is under development to cool a core melt in the area of the basement of a LWR. The concept is characterised by passive injection of coolant water to the bottom of the melt which is subsequently solidified as a porous matrix of good coolability. The use of a porous, water filled concrete layer in the CometPC concept from which the coolant water is injected, was assessed after completion of the relevant test series. The good stability and cooling capacity of this concept shall be further improved by discrete flow channels allowing a more homogeneous porosity formation in the melt. This is achieved by the advanced concept CometPCA for which the first large scale experiment is described with sustained heated melt.

Coolability over short-term and long-term conditions was demonstrated, taking into account also the small, long-term coolant water flow which results from the condensation of steam in the containment. Further experiments are planned to verify the concept and to investigate its use for enlarged melt heights.

## **1. Einleitung**

Bei extrem unwahrscheinlichen Unfallabläufen kann eine Kernschmelze den Reaktordruckbehälter durchschmelzen und auf das Betonfundament des Sicherheitsbehälters austreten. Die Stabilisierung und Kühlung einer solchen "ex-vessel" Kernschmelze ist - wie auch im Evaluierungsbericht des BMWi erwähnt - ein wichtiges Ziel, damit die Integrität des Sicherheitsbehälters erhalten und die Freisetzung von radioaktiven Materialien in die Umgebung gering bleiben.

Allein durch Wasseraufgabe von oben auf die mehr als 50 cm hohe Schmelze können eine ausreichende Kühlung der Schmelze und der Stopp der Erosion des Betonfundaments nicht sicher erreicht werden. Daher verfolgt das COMET-Konzept das Ziel, durch passive Injektion von Kühlwasser von unten die Schmelze in eine poröse Struktur aufzubrechen und damit eine schnelle Kühlung und vollständige Erstarrung der Schmelze zu erzielen. Unter diesen Bedingungen bleibt das Betonfundament und die angrenzenden Strukturen so kalt, dass sie ihre volle Barrieren- und Sicherheitsfunktion behalten.

## **2. Kühlung nach dem CometPC - Konzept**

Als eine technisch attraktive Lösung zur Realisierung des COMET-Konzepts wurde das CometPC- Kühlkonzept untersucht [1]. Dabei erfolgt der Zutritt des Kühlwassers in die Schmelze aus einer unten liegenden, porösen Betonschicht (PC = Porous Concrete), die mit Wasser bespeist wird. Der Wasserzutritt in die Schmelze geschieht passiv unter dem Druck des Wasserreservoirs, nachdem eine obere Opferschicht von etwa 10 cm Höhe von der Schmelze erodiert wurde.

Die Untersuchungen zu dieser Kühlungsvariante wurden im Berichtszeitraum abgeschlossen. Das abschließende Großexperiment CometPC-H5 mit einer Schmelzen-

masse von anfangs 800 kg wurde entsprechend dem Nachwärmeniveau durch Induktionsheizung mit typisch 300 kW beheizt. Die zylindrische Geometrie der Versuchsanordnung mit einem Durchmesser der Schmelze von anfangs 670 mm hat eine 3-dimensionale Erosion und entsprechende Kühlvorgänge zugelassen. Obgleich in diesem Experiment nach kurzzeitiger Erhöhung des Flutwasserdrucks ein sicherer Stop und die stabile Kühlung und Erstarrung der Schmelze erreicht wurden, zeigt die Nachuntersuchung der erstarrten geschnittenen Schmelze Zonen mit stark unterschiedlicher Porosität und entsprechend guter oder eingeschränkter Kühlbarkeit. Die Ausbildung so unterschiedlicher Porositäten ist Folge der Zuströmbedingungen des Flutwassers, die sich nach zufälligen Prozessen einstellen. Offenbar konzentriert sich der Wasseraustritt aus der porösen Betonschicht überwiegend auf wenige Hauptströmungswege durch die Schmelze. Die erwünschte, gleichmäßige Durchströmung der Schmelze ist dagegen bei der nicht strukturierten Porösschicht erschwert, da sie mit einem höheren Druckverlust des Kühlmediums verbunden ist.

Die Ergebnisse für das CometPC - Konzept lassen sich daher mit den Beobachtungen aus den großskaligen Experimenten wie folgt zusammenfassen:

Die Kühlungsvorgänge bei Flutung aus der porösen Betonschicht verlaufen ausreichend langsam, so dass keine schnellen Druckspitzen durch das verdampfende Wasser entstehen. Insbesondere kommt es nicht zu energetischen Wechselwirkungen zwischen Schmelze und Wasser, die einer Dampfexplosion entsprechen.

Die wasserführende, poröse Betonschicht besitzt eine hohe Stabilität gegenüber dem Angriff der heißen Schmelze und stoppt daher das Vordringen der Schmelze. In seltenen Fällen kann jedoch die Porösschicht angegriffen werden, wenn der Wasserzutritt lokal begrenzt ist.

Die Durchströmung der Schmelze und die Ausbildung einer porösen Struktur sind weniger gleichmäßig als dies bei Austritt des Kühlwassers aus einem Feld diskreter Strömungskanäle im ursprünglichen COMET-Konzept beobachtet wurde. Die Folge sind Zonen geringerer Kühlbarkeit mit der Möglichkeit der nachträglichen Verlagerung noch flüssiger Restschmelzen.

Die Kühlung der Schmelze ist jedoch trotz der erwähnten Nachteile erfolgreich. Weniger poröse Bereiche der Schmelze weisen dabei eine längere Dauer der Erstarrung auf, da in diesem Fall für den Wärmeentzug im wesentlichen die Wärmeleitung bestimmend ist. Eine spätere Verlagerung von noch flüssigen Teilbereichen der

Schmelze kann jedoch eventuell negative Auswirkungen auf die lokale Kühlbarkeit haben.

### **3. Kühlung nach dem verbesserten Konzept CometPCA**

Um die Kühlung von Kernschmelzen durch Wasserzufuhr von unten in seiner technischen Ausführbarkeit und Anwendbarkeit weiter zu verbessern, wurde die Erweiterung zum CometPCA- Kühlkonzept (Comet Porous Concrete Advanced) vorgenommen. Wichtiges Ziel ist die gleichmäßigere Durchströmung der Schmelze, um eine homogenere Porosität und Erstarrung zu erreichen und spätere Umverlagerungen von noch nicht erstarrter Schmelze auszuschließen. Durch Einbau von Kanälen in die poröse, wasserführende Betonschicht in einem regelmäßigen Raster soll erreicht werden, dass die Schmelze gleichmäßiger durchströmt wird und damit über die gesamte Kühlfläche ausreichend schnell erstarrt, siehe Abb. 1. Dieses erweiterte Konzept soll damit die Vorteile des ursprünglichen COMET-Konzepts mit Schmelzstopfen [2] mit der hohen Beständigkeit einer wasserführenden Porösbetonschicht gegen Schmelzenangriff vereinigen. Zu untersuchen ist nun, ob durch Einfügen definierter Strömungswege eine ausreichend homogene Fragmentierung und Kühlung der gesamten Schmelze erreicht wird und ob dann auch größere Schmelzbadhöhen kühlbar sind. Nachdem erste Experimente mit nicht nachbeheizten Thermiterschmelzen im 50 kg Maßstab das Konzept erfolgreich bestätigt haben, wurde das erste großskalige Experiment mit nachbeheizter Schmelze durchgeführt, das im Folgenden beschrieben wird.

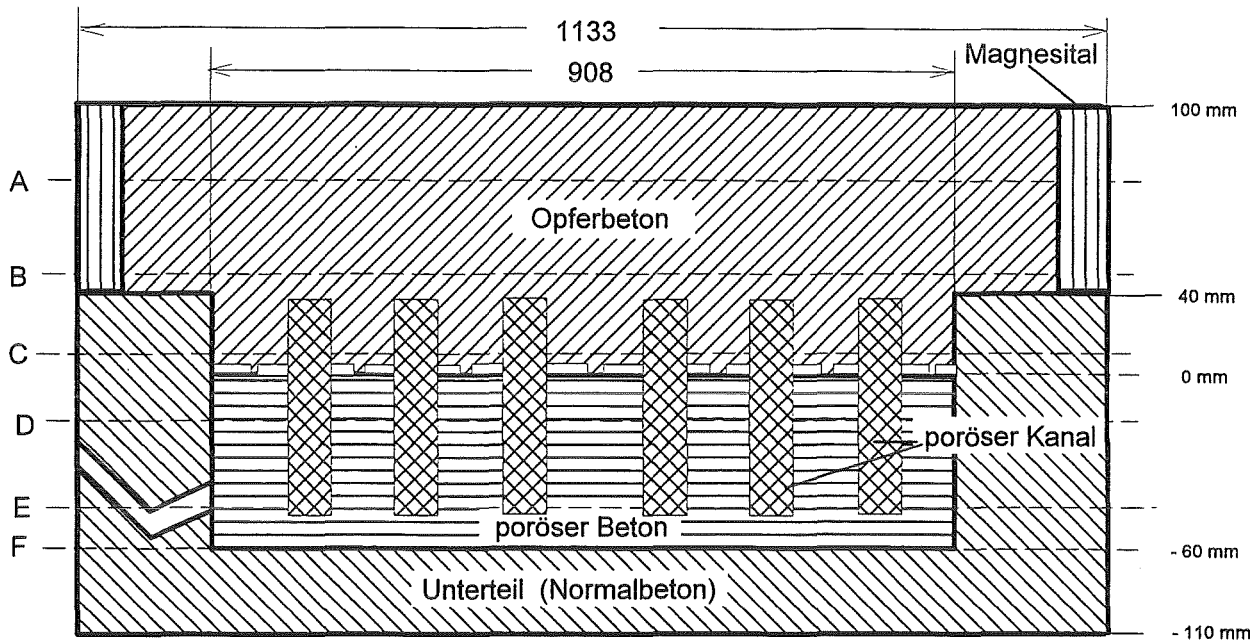


Abb. 1: Aufbau des Kühleinsatzes mit Betonopferschicht

#### Versuchsaufbau

Das Experiment ist nach folgendem Prinzip aufgebaut (s. Abb. 1): Die ebene, 1-dimensionale Kühlvorrichtung stellt einen Ausschnitt aus der größeren Anordnung in einem Reaktor dar. Die seitliche, zylindrische Berandung besteht aus einer Keramik als Isolationsschicht. Die Betonopferschicht aus Glasbeton von 10 cm Höhe dient zur Abkühlung und Konditionierung der Schmelze, darunter befindet sich die wasserführende Schicht aus Porösbeton von 6 cm Höhe. Diese Schicht ist wie in den vorangegangenen Experimenten durch eine Lage von Steinzeugkacheln abgedeckt, die den Wasserzutritt durch ihr spezifisches Versagen durch Bruch verbessern. Von dieser Schicht ragen 24 Kanäle (im quadratischen Raster von 150 mm Abstand, siehe Abb. 2) in die Beton-Opferschicht hinein. Diese Kanäle werden als erste von der erodierenden Schmelze kontaktiert und stellen damit die wesentlichen Wasserzu-

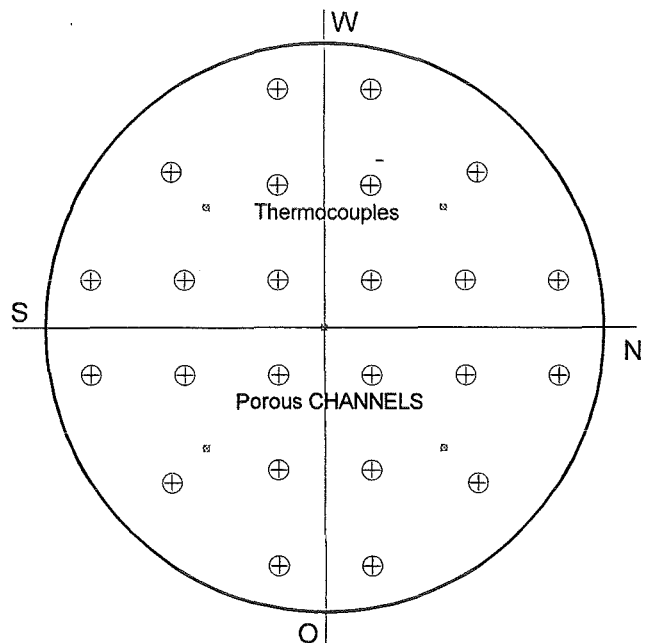


Abb. 2: Aufsicht auf die Betonschicht mit den porösen Betonkanälen

trittswege dar. Sie sind mit grobporösem Beton verfüllt, um den Wasserdurchfluss zu begrenzen und den Durchtritt von Schmelze nach unten zu verhindern.

Die Wasserzuführung von unten erfolgt mit einem Überdruck gegenüber der Schmelze von 0,1 bar. Die erzeugte Thermitschmelze von insgesamt 800 kg besteht aus 358 kg Fe mit 15 % Ni und 442 kg  $Al_2O_3+CaO$ . Die Schmelzbadhöhe ohne Leeranteil beträgt zu Beginn 31,7 cm, davon 8,3 cm Metall unten und 23,4 cm Oxid oben. Zur Simulation der Nachwärme wird die Schmelze kontinuierlich durch die Induktionsheizung mit einer Nettoleistung von 300 kW beheizt. Diese Heizleistung entspricht einem hohen Nachwärmeniveau mit einer Flächenbelastung der Kühleinrichtung von  $430 \text{ kW/m}^2$ . Das Experiment untersucht damit den gesamten Kühlprozess, beginnend mit der Erosion der Opferschicht aus Glasbeton durch die Schmelze, über das Einsetzen der Wasserkühlung durch den passiven Wasserzutritt von unten, bis zur Stabilisierung und vollständigen Erstarrung und Überflutung der Schmelze durch das Flutwasser. Damit ist auch eine sichere Beurteilung der Langzeitwärmeabfuhr und der langfristigen thermischen Belastung aller Strukturen gegeben.

#### Versuchsablauf CometPCA-H1

Zum Zeitpunkt 0 s wird die gesamte Schmelzenmasse von 800 kg mit einer Temperatur von  $1900 \text{ }^\circ\text{C}$  in den Versuchstiegel abgegossen. Dieser Vorgang und die erste Phase der Betonerosion sind begleitet von einer starken Schmelzbadbewegung, wodurch sich auch die starken Schwankungen der durch

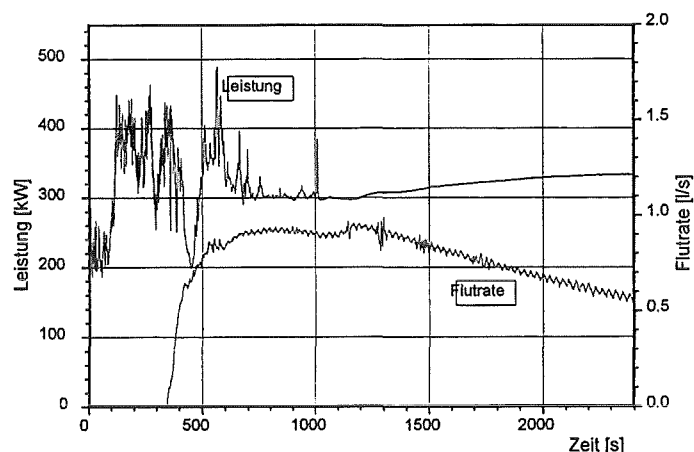


Abb. 3: Nachwärmeleistung und Flutrate durch passiven Wasserzutritt

Induktionsheizung simulierten Nachwärmeleistung erklären, s. Abb. 3. Bis 345 s erfolgt die Erosion der Betonopferschicht. Mit Erreichen der Poröskanäle setzt dann die Kühlung der Schmelze durch den passiv erfolgenden Wasserzutritt von unten ein. Zunächst treten ca.  $0.5 \text{ l/s}$  Wasser in die Schmelze ein, innerhalb kurzer Zeit

steigt dieser Wert durch Öffnen weiterer Kanäle auf ca. 1 l/s an (s. Abb. 3). Nach 660 s hat die Oberfläche der Schmelze eine stabile, durchgängige Kruste ausgebildet, die 20 s später auch überflutet ist. Nach 950 s ist die Schmelze auch in ihrem Inneren vollständig erstarrt, erkennbar an dem vollständigen Erliegen von Schwankungen der

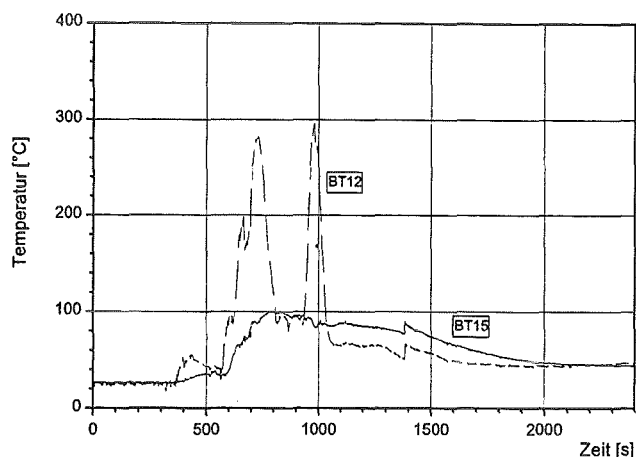


Abb. 4: Temperaturen in der Betonschicht, BT 12: +20 mm Ebene, BT15: +10 mm Ebene

simulierten Nachwärme. Dieser stabile Zustand der Schmelze bleibt bis zum Ende des Experiments erhalten. Die Schmelze ist durch den einsetzenden Wasserzutritt von unten bei einer Höhe von +10 bis +20 mm oberhalb der eigentlichen Porösbetonschicht gestoppt und vollständig erstarrt, die darunter liegenden Betonschichten sind kalt (s. Abb. 4). Die Simulation der Nachzerfallswärme wird während dieser Phase konstant mit 300 kW aufrechterhalten. Der Wasserzustrom von unten fällt in dieser Phase von etwa 0,9 l/s auf 0,6 l/s, da sich mit Zunahme des Wasserstands über der Schmelze der wirksame Überdruck des Flutwassers vermindert. Mit dem Nachweis der sicheren Kühlung der Schmelze wurde diese Versuchsphase damit erfolgreich abgeschlossen.

### Nachttest CometPCA-H1

Nach Erreichen der sicheren Kühlung durch die poröse Erstarrung der Schmelze wurde das Experiment am folgenden Tag fortgesetzt, um die Stabilität der Langzeitkühlung zu untersuchen: Bei reduzierter Heizleistung (200 kW zur Reduzierung der bodennahen Wärmeentbindung) wird der Zustand in der Kaverne eines Kernreaktors simuliert, wie er langfristig zu erwarten ist: Die Schmelze ist überflutet und porös erstarrt. Die Wasserspie-

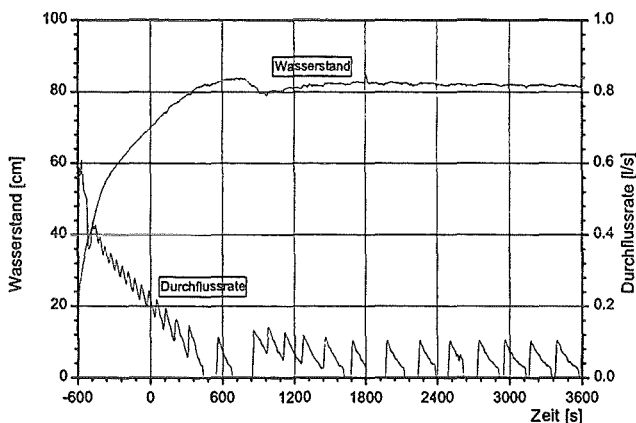


Abb. 5: Durchflußrate und Wasserstand im 92Nachttest zu CometPCA-H1

gel über der Schmelze und im Wasservorratsbehälter gleichen sich aus, so dass keine Druckdifferenz mehr herrscht, um Wasser der Schmelze von unten unter erhöhtem Druck zuzuführen. Demzufolge wird dann lediglich das verdampfende Wasser aus dem Wasservorratsbehälter von unten nachgespeist. Dies ist der langfristig stationäre Zustand, bei dem der Wasservorrat im Vorratsbehälter entsprechend den Kondensationsvorgängen im Sicherheitsbehälter ergänzt und dadurch auf annähernd konstanten Niveau gehalten wird. Dieses konstante Niveau wird auch im Experiment durch Nachspeisen des verdampften Wassers beibehalten.

Im Experiment wurde die interne Beheizung mit 200 kW zum Zeitpunkt 0 s wieder aufgenommen. Der Wasserstand über der Schmelze war zu diesem Zeitpunkt vom Anfangswert 20 cm auf nahezu 80 cm, das heißt Gleichstand mit dem Vorratsbehälter, angestiegen, siehe Abb. 5. Nach 730 s sind erste Siedevorgänge zu beobachten, ab 1000 s ist ein stationärer Zustand erreicht, der

durch eine kontinuierlichen Dampfabströmung und periodisches Nachlaufen des verdampften Wassers gekennzeichnet ist. Die Nachspeisung aus dem Wasservorratsbehälter beträgt im Mittel ca. 0,1 l/s, siehe Abb. 5. Damit entspricht die abströmende Dampfmenge genau der Heizleistung. Wasser und Dampf besitzen dabei die gleiche Strömungsrichtung. Da die Temperatur des aus dem Vorratsbehälter nachgespeisten Wassers bei 16 °C liegen, bleiben die Temperaturen im Porösbeton mit 20 bis 50 °C unterhalb der Siedetemperatur. In der Betonschicht dicht unterhalb der Schmelze liegen sie mit 90 °C (BT12) bzw. 80°C (BT15) (s. Abb. 6) nur wenig höher als im Hauptversuch in Abb. 3 bei wesentlich höherem Wasserzutritt. Dieser Zustand ändert sich über den Zeitraum von einer Stunde bis zum Ende dieser Versuchsphase nicht, und trotz der kontinuierlichen Beheizung erwärmen sich die porös erstarrte Schmelze und die umgebenden Strukturen nicht weiter. Mit Erreichen dieses

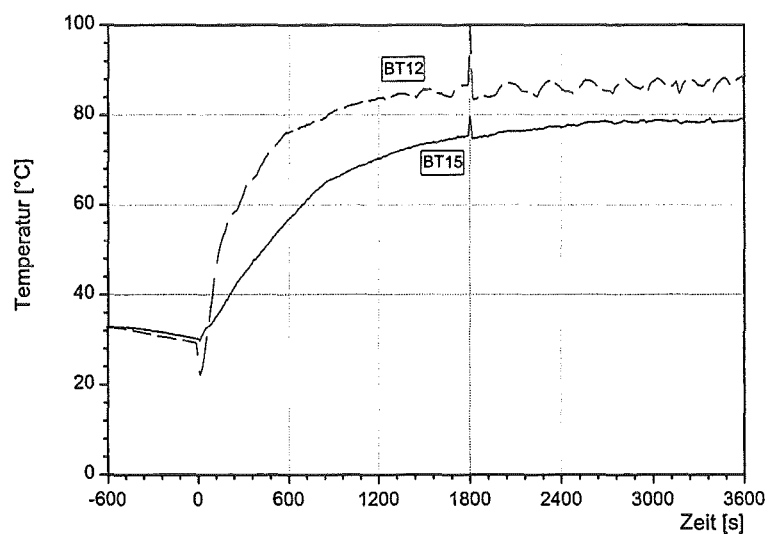


Abb. 6: Temperaturen in der Betonschicht

stationärer Zustand erreicht, der durch eine kontinuierlichen Dampfabströmung und periodisches Nachlaufen des verdampften Wassers gekennzeichnet ist. Die Nachspeisung aus dem Wasservorratsbehälter beträgt im Mittel ca. 0,1 l/s, siehe Abb. 5. Damit entspricht die abströmende Dampfmenge genau der Heizleistung. Wasser und Dampf besitzen dabei die gleiche Strömungsrichtung. Da die Temperatur des aus dem Vorratsbehälter nachgespeisten Wassers bei 16 °C liegen, bleiben die Temperaturen im Porösbeton mit 20 bis 50 °C unterhalb der Siedetemperatur. In der Betonschicht dicht unterhalb der Schmelze liegen sie mit 90 °C (BT12) bzw. 80°C (BT15) (s. Abb. 6) nur wenig höher als im Hauptversuch in Abb. 3 bei wesentlich höherem Wasserzutritt. Dieser Zustand ändert sich über den Zeitraum von einer Stunde bis zum Ende dieser Versuchsphase nicht, und trotz der kontinuierlichen Beheizung erwärmen sich die porös erstarrte Schmelze und die umgebenden Strukturen nicht weiter. Mit Erreichen dieses

stationären Zustandes wurde die sichere Langzeitwärmeabfuhr bei Ersatz des verdampfenden Wassers aus dem Wasservorratsbehälter nachgewiesen.

Nach einer Stunde Versuchsdauer wurden die Kühlbedingungen folgender Weise geändert: Bei weiterhin konstanter Heizleistung von 200 kW wurde die Wasserzufuhr zum Wasservorratsbehälter abgesperrt. Da somit kein Wasser von unten nachströmt, muß Wasser aus dem gefüllten Tiegel selbst im Gegenstrom zum Dampf nach unten strömen. Dieser Gegenstrombetrieb erschwert die Kühlung im Vergleich zum Gleichstrombetrieb, wie aus Untersuchungen an porösen Partikelbetten bekannt ist. Tatsächlich zeigt sich auch für die hier vorliegende porös erstarrte Schmelze, dass ca. 300 s nach Abschalten der Wasserzufuhr die Temperaturen in der Mitte der Kühlfläche langsam ansteigen. Nach 900 s werden 190 °C erreicht, nach 1500 s 320 °C und etwa weitere 200 s später versagen einige Thermoelemente im Zentralbereich durch zu hohe Temperaturen. Ebenso weisen schwache Schwankungen der Induktionsleistung auf ein lokales Wiederaufschmelzen des Metalls im Zentralbereich hin, und ein Teil der Schmelze dringt langsam in die poröse Betonschicht vor. Ursache für die lokal verringerte Wärmeabfuhr ist vermutlich ein kleines Dampfpolster im Porösbeton, das nicht durch zuströmendes Kühlwasser kondensiert wird. Als nach 1900 s nach Beginn dieses Gegenstrombetriebs der Wasserzutritt aus dem Vorratsbehälter wieder geöffnet wird, setzt sofort ein Kühlwasserstrom ein, der den Gleichstrombetrieb wiederherstellt. Über weitere 1400 s wird die Schmelze gekühlt und das Vordringen der Schmelze bleibt gestoppt. Das Experiment wird planmäßig beendet mit Abschaltung der Nachwärmesimulation etwa 2 Stunden nach Beginn der Versuchsphase 2 und vollständiger Auskühlung der Schmelze.

Als Ergebnis dieser zweiten Versuchsphase zur Langzeitkühlbarkeit der porös erstarrten Schmelze ist festzuhalten:

Nach Ausgleich der Wasserspiegel über der erstarrten Schmelze und im Vorratsbehälter reicht der schwache Wasserzufluss aus dem Vorratsbehälter entsprechend der Verdampfungsrate, um im Gleichstrom von Wasser und Dampfströmung die Kühlung zu sichern. Diese Betriebsweise ist der Normalbetrieb, der sich durch den Rückfluss des im Sicherheitsbehälter kondensierten Dampfes in den Wasservorratsbehälter ergibt.

Die vollständige Unterbrechung des Wasserzustroms aus dem Vorratsbehälter sollte jedoch vermieden werden.

Durch den dann einsetzenden Gegenstrom von Wasser und entstehendem Dampf im Naturumlauf ist die Kühlung weniger wirksam und kann bei höherem Nachwärmeniveau zu einem erneuten, lokalen Temperaturanstieg führen.

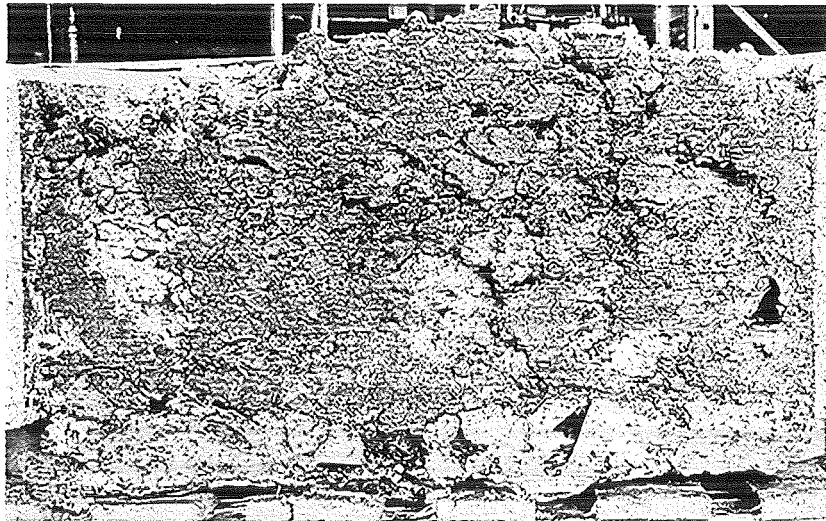


Abb. 7: Schnitt durch die erstarrte Schmelze

#### Nachuntersuchungen

Der Tiegelschnitt (siehe Abb. 7) zeigt, dass die Schmelze porös erstarrt ist. Der oxidische Teil der Schmelze weist eine gegenüber den CometPC-Experimenten vergleichmäßigte, erhöhte Porosität auf. Die verbesserte Porosität und Kühlbarkeit ist damit die Folge der gleichmäßigeren Kühlwasserzufuhr durch die porösen Kanäle. Auch in der Metallschmelze haben sich oberhalb der porösen Kanäle Strömungswege gebildet, die das zuströmende Wasser hinreichend gleichmäßig in die Schmelze leiten und damit schnell abkühlen und erstarren lassen.

In Abb. 8 ist der Schnitt durch die poröse wasserführende Betonschicht zu sehen. Deutlich zu erkennen ist, dass die Schmelze die darüberliegende Opferbetonschicht bis auf die Höhe der Poröskanäle erodiert hat und dort durch den einsetzenden Wasserzutritt gestoppt wurde. Lediglich nach Abschalten der Wasserzufuhr, d.h. während dem Nachttest bei dem Betrieb der langzeitigen Gegenstromkühlung, konnte im Mittenbereich zwischen den zentralen Poröskanälen lokal ein kleiner Teil der Schmelze weiter vordringen.

Es erscheint möglich, dass sich diese Zone bei weiterem Vordringen in die poröse, wasserführende Betonschicht stabilisiert hätte und wieder erstarrt wäre. Trotzdem sollte diese Betriebsart nicht vorgesehen werden, sondern die normale Bespeisung aus dem Vorratsbehälter beibehalten werden.

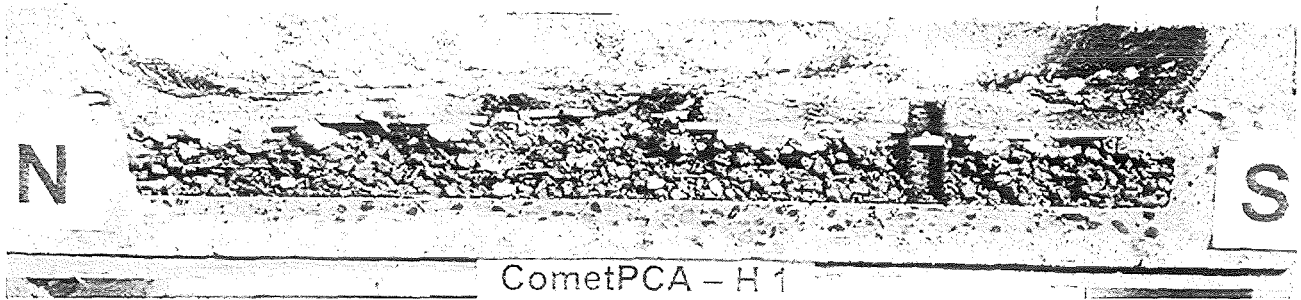


Abb. 8: Schnitt durch die Porösbetonschicht

#### 4. Ausblick

Nach dem erfolgreichen Nachweis der sicheren Kühlung der Schmelze durch die Wasserzufuhr von unten im Kurzzeit- und Langzeit-Betrieb sollen für das CometPCA-Kühlkonzept die Untersuchungen fortgesetzt werden zur Absicherung des Konzepts auch für größere Schmelzbadhöhen. Eventuell sollen auch für weitere Szenarien eines Kernschmelzenunfalls, wie z.B. mit frühem Fluten von oben über den zerstörten RDB, untersucht werden.

#### Literatur

- [1] W. Tromm et al: Experimente zur Kühlung von Kernschmelzen durch das CometPC-Konzept, Jahrestagung Kerntechnik 2001, Dresden, Deutschland, 15-17 Mai 2001
- [2] H. Alsmeyer et al: Corium Cooling by Bottom Flooding: Results of the COMET Investigations, OECD Workshop on Ex-Vessel Debris Coolability, Karlsruhe, Germany, 15 –18 Nov. 1999

## II. LIVE (Late In-Vessel Phase) Experiments (B. Eppinger, G. Fieg, W. Tromm, T. Wenz, IKET)

### **Abstract**

Several experimental and theoretical investigations have been performed to describe the in-vessel evolution of a severe accident. But up to now the experimental database for core melt relocation and the knowledge regarding structure and behaviour of the molten pool is still limited. Therefore, the LIVE experiments (Late In-Vessel Phase Experiments) have been defined taking into account the existing knowledge of core melt down sequences. The experiments will investigate important phenomena during the phase of transient melt relocation to the lower plenum of the RPV and the formation of molten pools in the lower head of the vessel. The experiments are carried out with different simulant materials with temperatures up to 1000 °C. An important condition is that the simulant materials have a similar behaviour with regard to solidification and formation of crusts as the oxidic core melt. The experimental facility consists of a 1:5 scaled RPV of a typical German nuclear power plant. First operation of the experimental facility is foreseen in spring 2003, first small scale experiments with simulant materials will start mid 2002.

### **Zusammenfassung**

Es existieren verschiedene experimentelle und theoretische Arbeiten zum Ablauf eines schweren Unfalls im Reaktordruckbehälter. Bis heute ist der Kenntnisstand über die Verlagerung der Kernschmelze und das Wissen über die Struktur und das Verhalten des Schmelzensees begrenzt. Daher wurden unter Berücksichtigung des bestehenden Kenntnisstandes der Kernabschmelzprozesse die LIVE-Experimente (Late In-Vessel Phase Experiments) definiert. Die Experimente sollen wichtige Phänomene während der transienten Verlagerung der Kernschmelze in die Bodenkalotte des Reaktordruckbehälters und der Ausbildung von Schmelzseen untersuchen. Die Experimente werden mit verschiedenen Simulationsschmelzen mit Temperaturen von bis zu 1000 °C durchgeführt. Dabei ist eine wichtige Bedingung, dass die Simulationsschmelzen im Hinblick auf Erstarrung und Krustenbildung ein ähnliches Verhalten aufweisen wie die oxidische Coriumschmelze. Die Versuchsanlage besteht aus einem 1:5 skalierten Reaktordruckbehälter eines typischen deutschen Kernkraftwerkes. Die Versuchsanlage soll im Frühjahr 2003 ihren Betrieb aufnehmen,

erste kleinere Versuche mit Simulationsschmelzen sollen im Sommer 2002 gestartet werden.

## 1 Introduction

In case of a hypothetical core melt down accident, the in-vessel evolution of a severe accident is characterised by core uncover and heat-up, core material oxidation and melting, molten material relocation and melt behaviour in the lower plenum until possible vessel failure. Principally, the in-vessel core melt progression involves a large number of physical and chemical phenomena that may depend on the severe accident sequence and the reactor type under consideration. The experience gained e.g. from the TMI-2 accident constitutes an important source of data. The understanding of core degradation processes are necessary to evaluate initial conditions

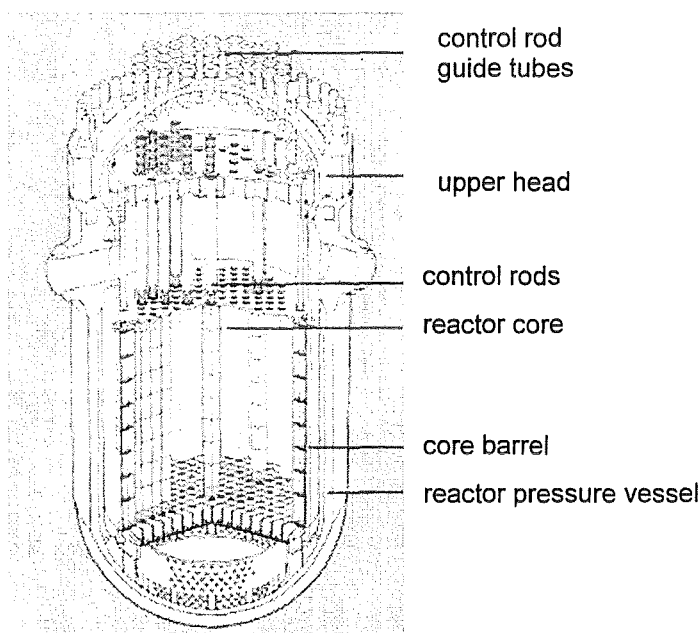


**Figure 1: Reactor Pressure Vessel of a typical German PWR**

for subsequent phases of the accident and define accident management strategies and mitigative actions for operating reactors [1]. In Figure 1 a reactor pressure vessel of a typical German PWR is shown.

The in-vessel core melt progression can be divided into two different phases: the "early and the "late phase". The so-called "early phase" refers to the damage occurring be-

tween the initial fuel and control rod damage and the melting and relocation of metallic materials. The "late phase" is characterised by the melting of ceramic material, loss of core geometry, and molten material relocation to the lower head of the reactor vessel and formation of melt pools [2].

The current knowledge concerning the early phase is mainly derived from numerous experimental programs such as the PHEBUS experiments conducted in France [3] and the CORA and QUENCH experiments [4, 5] conducted at FZK.

The different issues regarding the late phase of core degradation relate to in-core melt pool formation and spreading, crust failure and molten material relocation to the lower plenum, and the debris and melt pool behaviour in the lower head of the reactor vessel.

There is a lack of detailed experimental investigations related to the formation, the stability and the relocation of melt pools as well as to the formation and re-melting of crusts. The experimental database for core melt relocation and the knowledge regarding structure and behaviour of the in-core molten pool crusts is still limited. Further investigations are needed to evaluate molten pool crust behaviour and melt interactions with core surrounding structures, which may influence the pouring rate and the transfer mode of molten material to the lower head of the vessel. Debris and molten pool behaviour in the lower head of the vessel has been analysed in experimental studies. Nevertheless, limitations of most of the experiments are e.g. the 2-dimensional geometry [6, 7].

Therefore, the LIVE experiments (Late In-vessel Phase Experiments) have been defined taking into account the existing knowledge of core melt down sequences. The experiments will investigate important phenomena during the phase of transient core melt relocation to the lower plenum of the RPV and the formation of molten pools in the lower head of the vessel. The experiments are carried out with simulant materials. In the first phase of the experiments, salt mixtures were chosen with a similar phase diagram as the  $\text{UO}_2\text{-ZrO}_2$  melt, but a temperature range of about 400 °C. In a second phase, oxidic melts with temperatures up to 1000 °C will be used with a phase diagram and material properties close to the  $\text{UO}_2\text{-ZrO}_2$  melt. The volumetric heating of the melt is achieved by heat conductors with a net power input of more than 20 kW.

First operation of the experimental facility is foreseen in spring 2003, although first small scale experiments with simulant materials will start mid 2002.

## 2 Objectives of the LIVE experiments

In the first phase, the experiments will concentrate on the behaviour of a melt pool in the lower head in a 3-dimensional geometry. Important phenomena to investigate are: the 3-d heat flux distribution to the lower head and possible resulting crust formation depending on the power density and the external cooling; gap formation between the vessel wall and the melt crust; solidification behaviour including phase segregation of a non-eutectic melt under variation of external cooling modes; debris bed formation under presence of water in the vessel.

Another important objective of the LIVE investigations is the influence of the melt relocation mode to the lower head on melt pool formation and heat flux distribution. Principally, two different scenarios can be subdivided: Coherent melt relocation or gradual melt release. Although the coherent melt relocation is much more likely to occur, the released melt mass can vary in a large range. This leads to different heat flux distributions to the vessel wall, which is one of the important failure criteria. The LIVE facility will investigate this item by a separate heating furnace with a pouring device which enables different charging modes to the lower head, Figure 2.

## 3 Experimental facility

Core of the experimental facility is a 1:5 scaled RPV of a typical German nuclear power plant. Accordingly, the hemispherical bottom of the RPV has an inner diameter of 1 m and a wall thickness of 30 mm. The volume of the total core inventory is 0,1066 m<sup>3</sup> and the total height of the melt pool in the lower head is 290 mm. The power density and the average heat fluxes to the RPV wall are scaled with the Rayleigh- and Nusselt-number, respectively. The Rayleigh number of about 10<sup>13</sup> allows the transfer to realistic conditions (turbulent heat transfer). The cooling of the wall at the outside is possible with air or water according to the experimental objectives.

On the left side in Figure 2 the planned setup of the LIVE facility with all important components is shown and on the right side an enlarged picture of the lower head of the RPV. The instrumentation of the LIVE facility contains thermocouples for temperature measurements in the melt and the structures, heat flux sensors in the wall of the lower head and visual observation of the melt surface and crust formation in case of the transparent salt mixture. Furthermore, weighing cells detect quantitatively the melt relocation and melt samples are extracted during the experi-

ments. The thickness of the melt crust at the wall is detected with mechanical sensors. The power input into the melt is also recorded.

The capability of the melt furnace is up to about 250 l volume which can be heated to more than 1000 °C. Due to different openings in the upper lid of the lower head of the RPV, all scenarios of crust failure locations in the upper core region can be investigated.

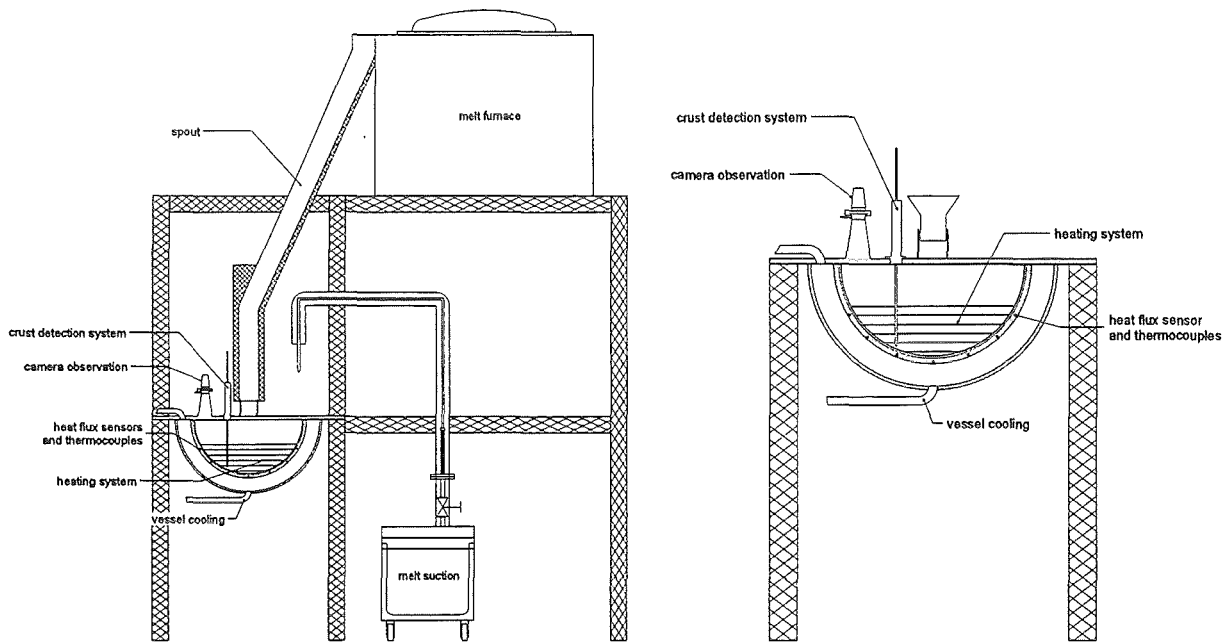


Figure 2: Setup of the LIVE facility and the lower head of the RPV

To investigate the crust formed during the experiment at the wall of the lower head, a suction device is able to suck out the residual melt in the vessel to a special tank. Material probes can be taken from the melt and the formed crust at different levels to determine material composition and structure depending on the spatial distribution.

#### 4 Layout of the volumetric heating of the melt

The melt is continuously heated by heat conductors, which allow a temperature of up to 1000 °C. They are spirally formed with a distance of less than 50 mm and located in 6 different elevations in the lower head of the RPV to realise a homogeneous volumetric heating of the melt. The heating elements are shrouded electrical resistance wires of small diameter located in a special cage to ensure the correct position of each heating element. The distance to the lower head wall is about 10 mm to guarantee that there is no direct contact of the heating to the vessel. All heating

planes together can provide a power of about 28 kW, but each plane can be regulated separately.

### 5 Selection of simulant materials

An important condition is that the simulant materials have a similar behaviour with regard to the solidification and the formation of crusts as the oxidic corium melt. Therefore the simulant melt has to be a non-eutectic mixture of several components with a distinctive solidus-liquidus area (~ 100 K). The temperature range of the simulant melt should not exceed 1000 °C distinctively because of the technical

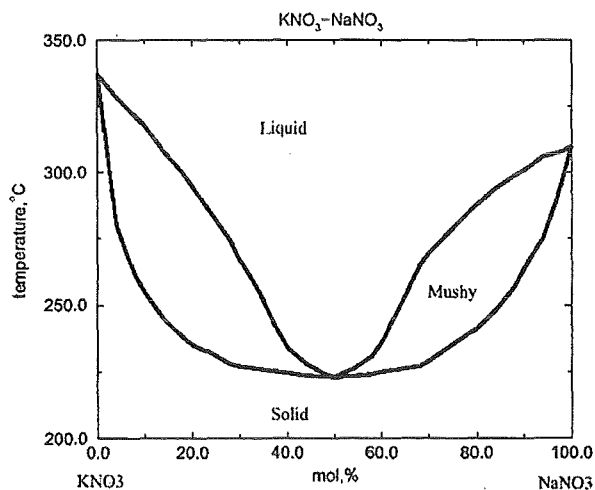


Figure 3: Phase diagram of the binary mixture of NaNO<sub>3</sub> – KNO<sub>3</sub>

handling of the melt and the selection of a volumetric heating system. Several non-eutectic oxides and salts have been investigated as a possible candidate for a simulant melt. Important factors for the investigation are the thermodynamic and thermohydraulic behaviour but also the toxicity of the melt. For the first series of experiments a binary mixture of NaNO<sub>3</sub> and KNO<sub>3</sub> has been selected, Figure 3. This mixture has already been used in different experiments at RIT/Sweden and the material properties are therefore well known [8]. The phase diagram of this mixture has a good similarity to the phase diagram of a UO<sub>2</sub>-ZrO<sub>2</sub> mixture, Figure 4. The 50-50 Mol% NaNO<sub>3</sub>-KNO<sub>3</sub> mixture has an eutectic temperature of 225 °C and the maximum temperature range of about 60 K between the solidus and liquidus temperature is achieved for a 80-20 Mol% NaNO<sub>3</sub>-KNO<sub>3</sub> mixture. This simulant melt is used under dry conditions due

handling of the melt and the selection of a volumetric heating system. Several non-eutectic oxides and salts have been investigated as a possible candidate for a simulant melt. Important factors for the investigation are the thermodynamic and thermohydraulic behaviour but also the toxicity of the melt.

For the first series of experiments a binary mixture of NaNO<sub>3</sub> and KNO<sub>3</sub> has been selected, Figure 3. This mixture has already been used in

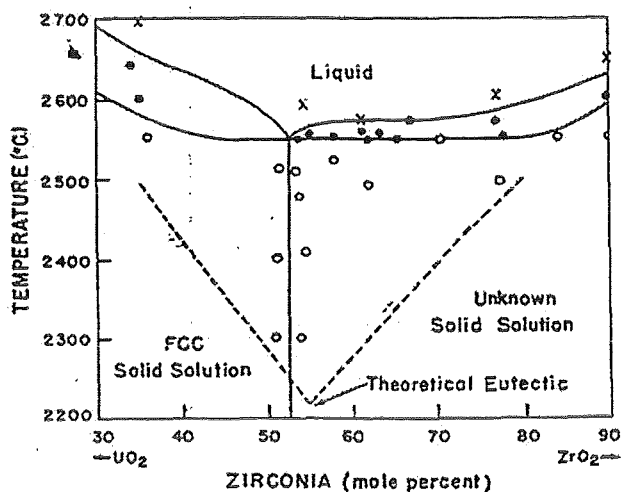


Figure 4: Phase diagram of UO<sub>2</sub>-ZrO<sub>2</sub>

to water solubility of the melt. The internal Rayleigh-number of this melt is some  $10^{13}$ . Several different oxides are at the moment under investigation. The objective is to select oxidic melts with a similar phase diagram as the  $\text{UO}_2\text{-ZrO}_2$  melt and a temperature range of about 800 – 1000 °C to allow a simplified handling of the melt without imposed material restrictions. Binary phase mixtures with  $\text{V}_2\text{O}_5$  as one of the melt constituents are possible candidates. Most of these mixtures are above 700 °C completely liquid. The eutectic temperature is in the range of 600 °C and the liquidus temperature of the pure  $\text{V}_2\text{O}_5$  melt is 660 °C. The internal Rayleigh-number of such a melt is in the range of  $10^{10}$  to  $10^{11}$ .

## References

- [1] Synthesis Paper prepared by G. Bandini in collaboration with the NEA Task Group on Degraded Core Cooling, "Status of Degraded Core Issues", NEA/CSNI/R(2001)5, October 2000
- [2] G. Bandini, R.O. Gauntt, T. Okkonen, K.Y. Suh, I. Shepherd, T. Linnemann, "Molten Material Relocation into the Lower Plenum: A Status Report", NEA/CSNI/R(97)34, September 1998
- [3] G. Gonner, G. Geoffroy, B. Adroguer, "PHEBUS-SFD Programme: Main Results", A.N.S. Meeting, Portland, July 1991
- [4] G. Schanz, M. Steinbrück, U. Stegmaier, A. Miassoedov, "Post-Test Examination Results of the Water-Quenched Bundles QUENCH-01, QUENCH-02 and QUENCH-03, Proceedings of the Annual Meeting on Nuclear Technology 2001, Dresden, 15-17 Mai 2001, pp 197-202
- [5] S. Hagen, P. Hofmann, G. Schanz, L. Sepold, "Essential results of the CORA program", 3rd Internat. Quench Workshop, Karlsruhe, December 2-4, 1997
- [6] L. Bernaz, J.M. Bonnet, B. Spindler, C. Villermaux, "Thermalhydraulic Phenomena in Corium Pools: Numerical Simulation with TOLBIAC and Experimental Validation with BALI", Proceedings of the Workshop on In-Vessel Core Debris Retention and Coolability, Garching, 3-6 March 1998, NEA/CSNI/R(98)18, pp 185-193
- [7] S. Abalin, I. Gnidoi, V. Semenov, V. Strizhov, A. Surenkov, "The Results and Analysis of the RASPLAV Salt Tests", Rasplav Seminar 2000, Munich, Germany, 14-15 November 2000
- [8] B.R. Sehgal, V.A. Bui, T.N. Dinh, J.A. Green, G. Kolb, "SIMECO Experiments on In-Vessel Melt Pool Formation and Heat Transfer with and without a Metallic Layer", Proceedings of the Workshop on In-Vessel Core Debris Retention and Coolability, Garching, 3-6 March 1998, NEA/CSNI/R(98)18, pp 205-213

### III. KAJET-Versuche

(G. Albrecht, H. Brüggemann, E. Jenes, D. Raupp, W. Schütz, IRS)

#### **Abstract**

During a hypothetical core melt accident, the bottom of the reactor pressure vessel (RPV) may be attacked and penetrated by the melt. In case of a localised failure of the RPV, the melt expulsion into the reactor cavity may be as a compact jet for a short period, followed by a dispersed release after gas break-through. The KAJET experiments are related to the short initial phase of a compact jet. The main objective of the experiments is to establish a compact jet under driving pressures up to 2 MPa and to study its interaction with different substratum materials. The molten corium is simulated by an alumina-iron thermite melt. The gas break-through is avoided by sharply reducing the driving pressure.

In the reporting period, two KAJET experiments (KJ06, KJ07) were performed. Samples of borosilicate glass concrete were used as substratum materials in both experiments. Each melt phase (iron/alumina) was exposed to a separate sample due to a revolving mechanism. In KJ06, 54 kg of iron and 61 kg of alumina were released at about 2100°C under a maximum driving pressure of 0.4 MPa. Corresponding values for KJ07 are 71,5 kg, 80,5 kg, 2100°C and 0.8 MPa. The concrete samples as well as the zirconia nozzles were instrumented with an array of thermocouples to measure the erosion rates caused by the melt jets.

In co-operation with Ruhr-Universität Bochum, a theoretical interpretation of the experiments is under way.

#### **1. Einleitung**

Im Verlauf eines hypothetischen Kernschmelzeunfalls kann die Bodenkalotte des Reaktordruckbehälters (RDB) durch die Schmelze angegriffen und in ungünstigen Fällen auch durchschmolzen werden. Bei örtlicher thermischer Ungleichverteilung in der Wärmeübertragung von der Schmelze in das RDB-Wandmaterial ist ein lokales, punktuell Versagen möglich. Abhängig vom Unfallablauf kann zu diesem Zeitpunkt das Primärsystem unter Überdruck stehen, so dass der Schmelzeausstoß durch die

RDB-Öffnung in die Reaktorgrube zunächst in Form eines kompakten Strahles erfolgt. Diese anfängliche Phase wird aber nur von sehr kurzer Dauer sein, da sich zum einen die Versagensstelle durch Wechselwirkung mit der Schmelze aufweitet und zum anderen beim Unterschreiten einer kritischen Schmelzepoolhöhe im RDB ein Durchbruch des treibenden Gases einsetzt. Dieser Durchbruch beendet die Phase des kompakten Strahls und führt zu einem dispergierenden Strahl. Die Wirkung des kompakten Strahls auf Auskleidematerialien der Reaktorgrube bewirkt Erosionsprozesse, deren quantitative Erfassung notwendig erscheint. Demgegenüber sind die Auswirkungen des dispergierenden Strahls eher geringfügig.

Das KAJET-Programm bezieht sich auf die (kurze) Anfangsphase des Schmelzeaustrags, während der möglicherweise ein druckgetriebener kompakter Strahl auftritt. Bei den Experimenten wird ein Schmelzestrahls mit treibendem Druck bis zu 2 MPa erzeugt und – neben der Charakterisierung des Strahls – die Wirkung auf unterschiedliche Auskleide- und Opfermaterialien untersucht. Die Kernschmelze wird simuliert durch eine Thermiterschmelze aus Eisen und Aluminiumoxid. Der Einfluss der metallischen und der oxidischen Phase kann getrennt untersucht werden. Der Gasdurchbruch wird künstlich vermieden durch rasche Reduktion des Treibdrucks am Ende des Schmelzeaustrags. In früheren Versuchen zur Untersuchung des Strahlverhaltens (VJ01-VJ07 und KJ01) wurde die für die anschließenden Erosionsversuche zu verwendende Düsengeometrie bestimmt (Zirkonoxid, Austrittsdurchmesser 12 mm, Düsenwinkel 90 °, Auslaufstreckenlänge 25 mm). Mit dieser Geometrie konnten von 0-1,5 MPa sowohl mit der Eisenschmelze als auch der oxidischen Schmelze kompakte Strahle erzeugt werden.

Im Berichtszeitraum wurden zwei Erosionsversuche durchgeführt (KJ06, KJ07). Als Probenmaterial wurde in beiden Fällen Borosilikatglas-Beton verwendet. Die eingesetzten Schmelzemengen betragen (Eisen/Oxid) 54 kg/61 kg bei KJ06 und (Eisen/Oxid) 71,5 kg/80,5 kg bei KJ07. Die Treibdrücke betragen 0,4 MPa (KJ06) und 0,8 MPa (KJ07). Bei beiden Versuchen wurden außer den Probekörpern auch die Austrittsdüsen aus Zirkonoxid ( $ZrO_2$ ) mit Thermoelementen instrumentiert. So konnte die Betonerosion und im zeitlichen Zusammenhang dazu auch die Düsenaufweitung erfasst werden.

In Zusammenarbeit mit der Ruhr-Universität Bochum werden die Experimente theoretisch interpretiert, die zugrundeliegenden Szenarien analysiert und die Extrapolation auf Reaktorbedingungen vorbereitet.

## 2. Erosionsversuche KJ06 und KJ07

Die Versuchsbedingungen sind in Tabelle 1 aufgelistet. Bild 1 dient zur Erklärung des Versuchsablaufes. Durch eine Thermitreaktion im Schmelzgenerator entstehen zwei Schmelzphasen, Fe und  $Al_2O_3$ . Wegen der höheren Dichte sammelt sich die Eisenschmelze im unteren Teil des Generators an, die oxidische Schmelze sammelt sich über dem Eisen, dadurch ist die Austrittsreihenfolge physikalisch vorgegeben. Die Eisenschmelze wurde in einem Ringraum innerhalb des Generators aufgefangen. Unter dem Generator ist eine

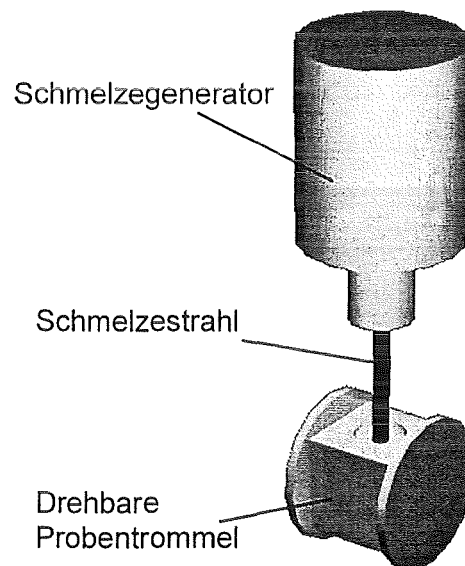


Bild 1. Schema der Versuchsanlage

drehbare Probentrommel angebracht, auf der zwei Betonproben rechtwinklig zueinander angeordnet sind. Die Schmelze tritt unter Druck aus, trifft nach 270 mm Fallstrecke auf den ersten Probekörper und erodiert diesen. Kurz vor dem berechneten Austrittsende der Eisenphase wird die Probentrommel um  $90^\circ$  gedreht und somit die zweite Probe in den Strahlbereich gefahren. In der Zwischenzeit hat der Austritt der oxidischen Schmelze begonnen, die nun die zweite Probe beaufschlägt.

In beiden Versuchen wurden je ein 100 mm dicker Probekörper pro Schmelzephase aus Borosilikatglas-Beton eingesetzt. Die Probekörper sind mit Thermoelementen instrumentiert, um eine zeitliche Zuordnung der Erosion zu ermöglichen. Je acht Thermoelemente (NiCr-Ni) waren in acht horizontal angeordneten Gruppen (Abstand 5 mm) schlangenförmig unter der Auftreffoberfläche angeordnet. Erreichte die Schmelze ein Thermoelement, wurde durch über-/unterschreiten des Ausgangsmesssignals der Kontakt angezeigt.

### 3. Ergebnisse

Die Schnitte in den Bildern 2 und 3 zeigen für KJ06 die vom Fe-Schmelzestrahls ( $\varnothing$  65x75 mm, Tiefe 38 mm) und Oxid-Schmelzestrahls ( $\varnothing$  90 mm, Tiefe 13 mm) erodierten Kavernen. Die abgetragenen Volumina betragen 92 ml (Fe) und 59 ml (Oxid). Die ermittelten Erosionsraten, bezogen auf den Fortschritt in die Tiefe, betragen 5,2 mm/s (Fe) und 2,8 mm/s (Oxid). Die Bilder 4 und 5 zeigen die Schnitte durch die Probekörper nach dem Versuch KJ07. Der Fe-Schmelzestrahls erodierte die Probe auf einer Fläche von 50x60 mm und ca. 45 mm tief. Die durch den oxidischen Schmelzestrahls erodierte Kaverne hat einen Durchmesser von 90 mm und eine Tiefe von 20 mm. Die erodierten Volumina betragen 95 ml (Fe) bzw. 110 ml (Oxid). Die Erosionsraten betragen 8 mm/s (Fe) und 5,1 mm/s (Oxid). Die Erosionsraten waren über die gesamte Einwirkdauer der Schmelzestrahls annähernd konstant.

	KJ06 Eisen / Oxid
Eingesetzte Schmelzenmasse (kg)	115
Eisen (kg)	54
Oxid (kg)	61
Düsendurchmesser	
Austrittsbeginn (mm)	12
Austrittsende (mm)	28
Beaufschlagungsdauer (s)	7,3 / 4,6
Temperatur des Schmelzestrahls (°C)	2100
Max. treibender Druck (MPa)	0,4
Max. Strahlgeschwindigkeit (errechnet) (m/s)	8,5 / 12,5
Horizontale Ausbreitung der Erosion (mm x mm)	75x65 / $\varnothing$ 90
Erosionstiefe (mm)	38 / 13
Erodiertes Volumen (ml)	92 / 59
Mittlere vertikale Erosionsrate (mm/s)	$\approx$ 5,2 / 2,8

Tabelle 1. Bedingungen und Ergebnisse des Versuchs KJ06

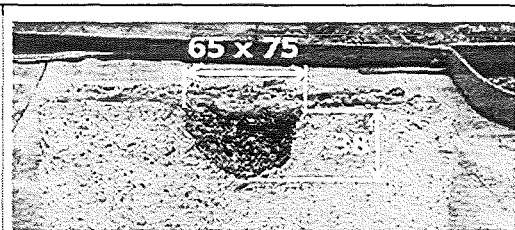


Bild 2. Schnitt durch den vom Fe-Schmelzestrahls erodierten Probekörper

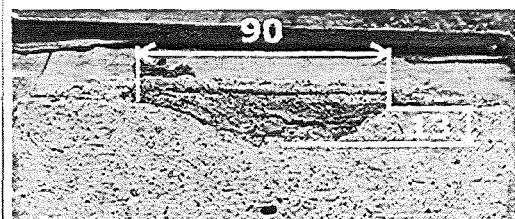


Bild 3. Schnitt durch den vom Oxid-Schmelzestrahls erodierten Probekörper

Bei beiden Versuchen wurden die Austrittsdüsen instrumentiert. Bei KJ06 konnten die Signale nicht aufgezeichnet werden, da die Thermoelemente gleich zum Versuchsbeginn durch die austretende Schmelze zerstört wurden. Bild 6 zeigt die aufgezeichneten Signale des Versuchs KJ07, sowie die Nachrechnung zur Interpretation des Versuchsablaufes. Die Streuung der zu einem Durchmesser gehörenden Signale ist relativ gering. Hieraus lässt sich folgern, dass die Aufweitung der Düse ziemlich gleichmäßig erfolgte und die runde Struktur im wesentlichen erhalten blieb.

	KJ07 Eisen / Oxid
Eingesetzte Schmelzenmasse (kg)	152
Eisen (kg)	71,5
Oxid (kg)	80,5
Düsendurchmesser	
Austrittsbeginn (mm)	12
Austrittsende (mm)	29
Beaufschlagungsdauer (s)	6,3 / 3,9
Temperatur des Schmelzestrahls (°C)	2100
Max. treibender Druck (MPa)	0,8
Max. Strahlgeschwindigkeit (errechnet) (m/s)	12,4 / 18,0
Horizontale Ausbreitung der Erosion (mm x mm)	50x60 / Ø90
Erosionstiefe (mm)	45 / 20
Erodiertes Volumen (ml)	95 / 110
Mittlere vertikale Erosionsrate (mm/s)	≈ 8 / 5,1

Tabelle 2. Bedingungen und Ergebnisse des Versuchs KJ07

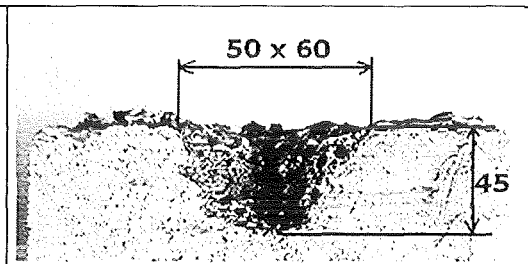


Bild 4. Schnitt durch den vom Fe-Schmelzestrahl erodierten Probekörper

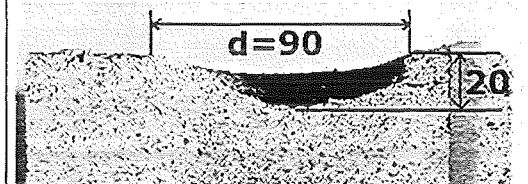


Bild 5. Schnitt durch den vom Oxid-Schmelzestrahl erodierten Probekörper

Bei beiden Versuchen trat während der Betonwechselwirkung mit der Oxidschmelze eine beachtliche Flammenentwicklung auf, die offensichtlich auf die Entstehung brennbarer Gase zurückgeführt werden muss. Die Ursache ist noch nicht verstanden (man hätte eher bei der Wechselwirkung mit Eisen eine Flammenentwicklung durch die Erzeugung von Wasserstoff erwartet).

#### 4. Theoretische Begleitung

In Zusammenarbeit mit der Ruhr-Universität Bochum werden die Experimente modelltheoretisch interpretiert. Dies schließt auch eine Erfassung der Unfallszenarien ein sowie Untersuchungen zur Übertragbarkeit auf Reaktorbedingungen. Die Arbeiten im Berichtszeitraum bezogen sich auf einfache quasi-stationäre Ansätze zur Ermittlung der Erosionsgeschwindigkeit und die Untersuchung der dazu erforderlichen Nu-Korrelationen.

Die KAJET-Versuche KJ06 und KJ07 sind Bestandteil eines Arbeitspaketes im EU-ECOSTAR-Projekt "Ex-Vessel-Core Melt Stabilisation Research" innerhalb des 5. Rahmenprogramms.

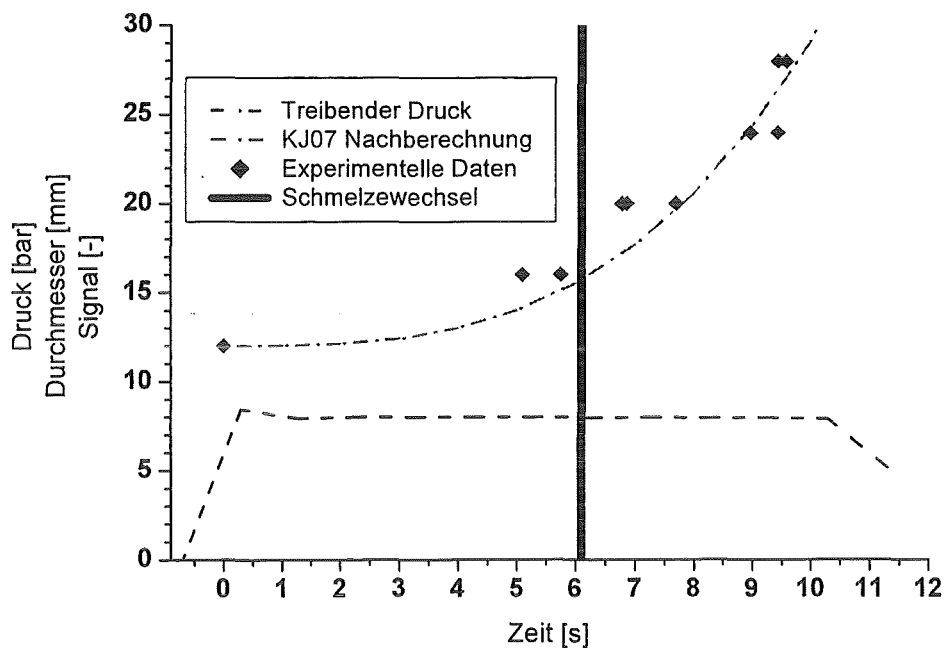


Bild 6. Aufweitung der Austrittsdüse bei KJ07

#### IV. Spreading on ceramic and concrete substrates

(J. J. Foit, IKET)

##### **Abstract**

Spreading on a concrete substrate is influenced by a gas release from the decomposed concrete, which changes viscosity and mixes the surface boundary layers into the interior of the spreading oxide melt. The latter process cools the bulk of the melt. The effects of bubbles on flow rheology are not well understood. The rheology of bubbly suspensions depends on the volume fraction of bubbles and the amount of deformation.

##### **Zusammenfassung**

Die Ausbreitung von heißen Schmelzen auf Beton wird durch die aus dem Beton durch thermische Einwirkung freigesetzten Gase beeinflusst. Dieser Gasstrom führt zu einer Vermischung der sich herausbildenden thermischen Grenzschichten mit dem Inneren der Schmelze und trägt damit zu einer effizienten Kühlung der ganzen Schmelze bei. Zusätzlich wird die Viskosität durch die in der Schmelze enthaltenen Blasen verändert. Die Art der Veränderung hängt vom Gasgehalt und der Stärke der Deformation der Blasen ab. Dieser Prozess ist noch nicht vollständig verstanden.

##### **1. Introduction**

Spreading under gravity has received much attention in the field of nuclear safety research. A variety of spreading experiments were performed within various projects, such as CORINE (CEA, France) [1], KATS (FZK, Germany) [2], COMAS (Siempelkamp, Germany) [3], VULCANO (CEA, France) [4], FARO (JRC, Italy) [5]. The experiments performed can be classified in accordance with melt release conditions:

- a) A given volume of the melt was poured into a cavity at a given volume flux. As soon as the cavity was filled, the melt began to spread.
- b) The melt was gathered in a container, and spreading was initiated by opening a gate. Consequently, a linear decrease of the volumetric flow rate in time during melt release was obtained.

These initial conditions and boundary conditions are more complex than the ideal conditions for which explicit self-similar solutions are known [6,7,8]. However, the asymptotic property [9] allows approximate solutions to be constructed which can be used to analyse the experiments performed or make reasonable predictions for melt front propagation or estimate the viscosity from measured front position as a function of time [8].

## 2. Spreading with gas release from the substrate

### 2.1. Short analysis of the CORINE experiments

To investigate the influence of gas release from the substrate caused by thermal erosion of the underlying concrete by a corium melt on spreading, a series of experiments using water [10] and a non-Newtonian, shear-thinning hydroxyethyl cellulose (HEC)-water mixture [11] were carried out in a 19° angular sector. The effects of bubbles on flow rheology are not well understood [12]. The rheology of bubbly suspensions depends on the volume fraction of bubbles, bubble size and the amount of deformation. For the water experiments, a viscosity increase by a factor of 11 to 18 (Fig. 1) has been observed for spreading in the presence of a gas flux through the spreading surface. This viscosity increase depends on the water inflow volume flux as well as the superficial gas velocity [8], and it is consistent with the model used by Jaupart and Allegre [13] to obtain a fit to the experimental data of Sibree [14]. The estimated gas content in the water of approx. 50%-55% during the spreading is consistent with measurements for the corresponding quiescent water layers [10]. The spreading experiments performed with HEC-water mixtures show a complex influence of bubbles on rheology. The viscosity of the fluid with 12% HEC decreases with increasing superficial gas velocity (Fig. 2) [8]. The 5% HEC-water mixture shows a different influence of gas flow on rheology. During the late phase of spreading without a gas flow through the bottom plate, i. e. for  $t \gg t_{inf}$ , the estimated viscosity is a factor of 2 higher than the viscosity estimated from the experimental data during the melt release period, i. e.  $t \leq t_{inf}$ . For the low superficial gas velocity of 0.01 m/s, the motion of the front is governed by a viscosity which is about 1.6 times

higher than the viscosity estimated from the front positions for  $t \leq t_{inf}$  obtained from the experiment performed without a gas release. In the experiment with the highest superficial gas velocity of 0.1 m/s, the front motion throughout the time of spreading is governed by an effective viscosity estimated from the experiment without a gas flow for  $t \leq t_{inf}$  [8].

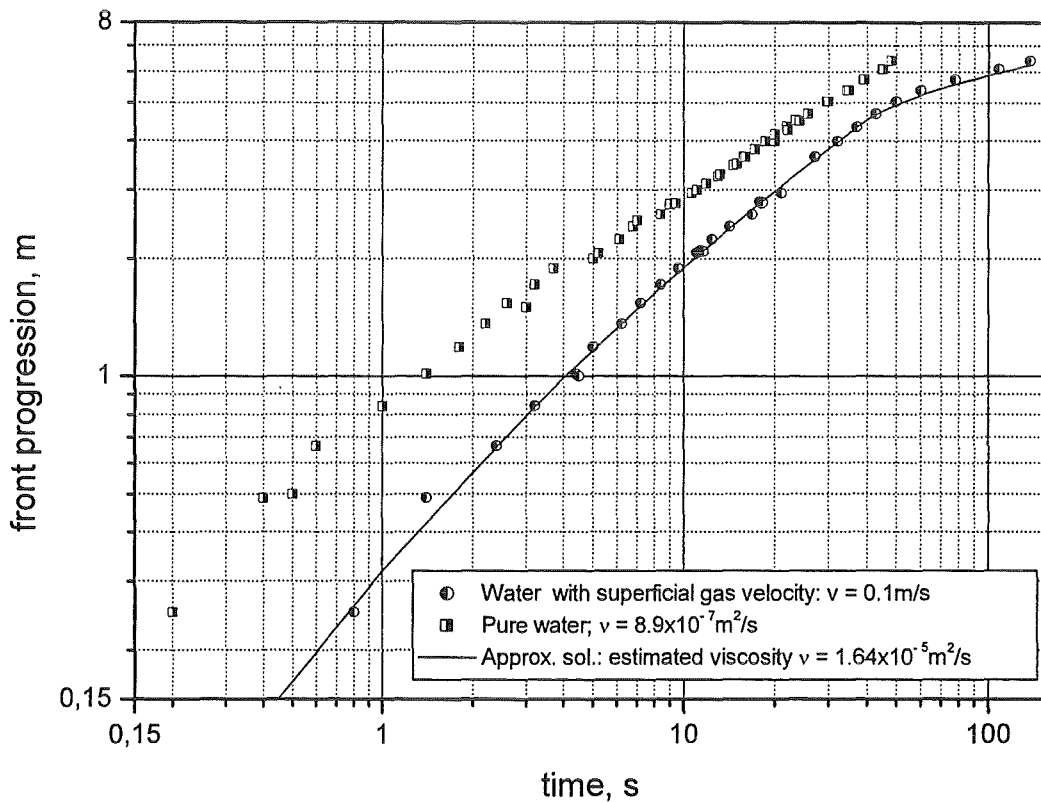


Fig. 1: Spreading of water ( $\dot{V} = 1.4 \times 10^{-3} \text{ m}^3/\text{s}$ ,  $r_0 = 1 \text{ m}$ ) with and without a gas flow through the spreading plate.

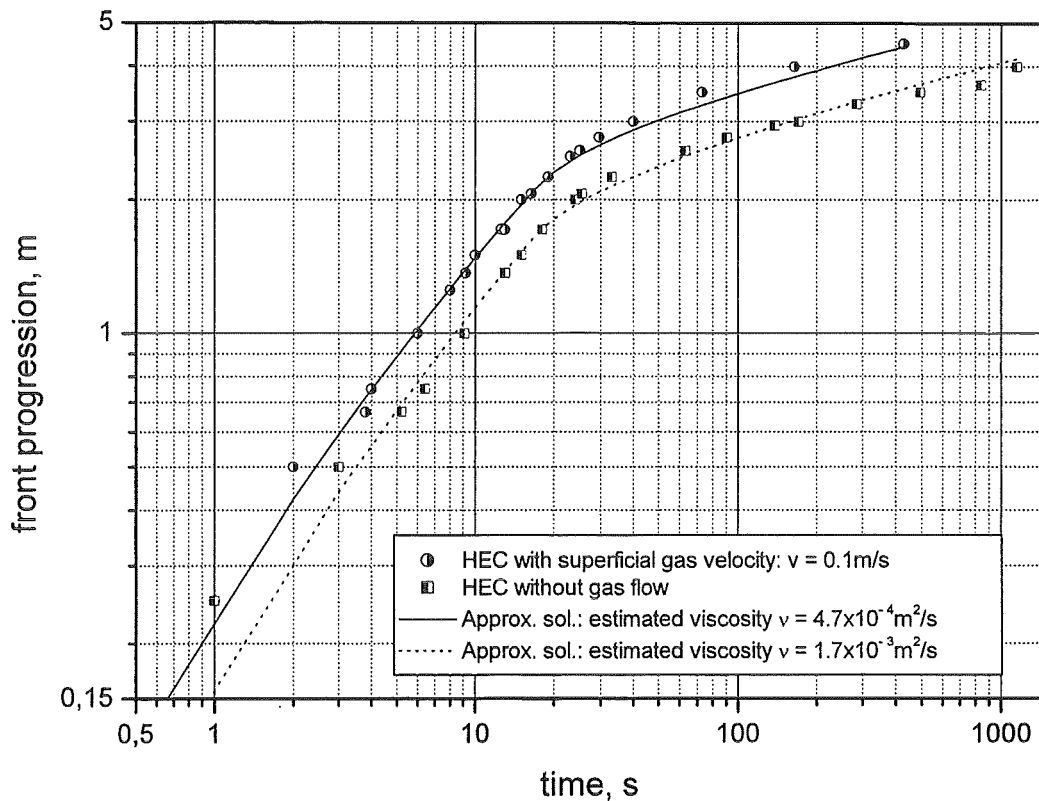


Fig. 2: Spreading of the 12% HEC-water mixture with and without a gas flow through the spreading plate.

## 2.2. Application to spreading on concrete in KATS 13 experiment.

According to the findings of the CORINE experiments spreading on a concrete substrate is influenced by a gas release from the decomposed concrete, which increases or decreases the viscosity and mixes the surface boundary layers into the interior of the spreading oxide melt. The latter process cools the bulk of the melt. There is no model available to estimate the effect of mixing on the spreading behaviour. The final spreading length in KATS-13 was about 30% shorter than observed in an analogous experiment, KATS-12, on a ceramic substrate [2]. In both experiments  $6.6 \times 10^{-2} \text{ m}^3$  of an oxide melt with a nearly the same composition and initial temperatures of 2303 K in KATS-12 and 2328 K in KATS-13 was released into a channel of 0.25 m width under conditions described in (b) (Section 2.1). The melt

release time,  $t_{inf}$ , was estimated to be 10.4 s [2]. For an instantaneous melt release the transition time, i. e. the time at which the inertial forces and the viscous forces are equal, is given by

$$\tau_{tr} \approx \left( \frac{V^4}{\xi_f^{10} g^2 \nu^3} \right)^{\frac{1}{7}}, \quad (1)$$

where  $V$  is the melt volume per channel width,  $\nu$  the kinematic viscosity,  $g$  the gravity constant and

$$\xi_f = \left[ \frac{3}{10} \right]^{-1/5} \left[ \frac{1}{5} \pi^{1/2} \frac{\Gamma\left(\frac{1}{3}\right)}{\Gamma\left(\frac{5}{6}\right)} \right]^{-3/5}. \quad (2)$$

For  $t > \tau_{tr}$  the spreading is dominated by viscous forces. In case of the KATS-12 experiment  $\tau_{tr} \approx 12$  s  $> t_{inf}$ , therefore, the upper bound for the measured front position,  $x_f$  can be obtained for  $t > \tau_{tr}$  from

$$x_f(t) = \xi_f \left( \frac{gV^3}{3\nu} \right)^{1/5} \left[ (t + t_0)^{1/5} - t_0^{1/5} \right] \quad (3)$$

with

$$t_0 = \left( \frac{x_0}{\xi_f} \right)^5 \frac{3\nu}{gV^3}, \quad (4)$$

where  $x_0$  is the coordinate of the gate [8].

The boundaries of the spreading melt are cooled by radiation and by heat conduction into the substrate, producing thermal and rheological boundary layers. For laminar flows as observed in all KATS experiments on a ceramic substrate, the temperature of the interior melt is close to the initial melt temperature during spreading. Due to the fairly large Péclet number, the spreading oxide melt develops only a thin thermal and rheological boundary layer at the cooled boundaries. The most pronounced

rheological changes with temperature occur at temperatures between 1983 K and 1963 K, for which crystallinity passes through the critical range of 40 vol. %-55 vol. %. As the viscosity of the oxide KATS melt is only a weak function of the temperature above the liquidus temperature,  $T_{liq} = 2138$  K, considerable retardation of the advance of the front flow takes place late in time in KATS-12 (Fig. 3). In the early phase of spreading, i. e. approximately during the first 6 s, a similar front propagation was observed in both experiments. The slowing of the front motion in KATS-13 for  $t \approx 6$ s (Fig. 3) indicates a strong viscosity increase and, consequently, a change from the gravity-inertial phase of motion to gravity-viscous spreading. That viscosity increase which is mainly caused by an increased gas volume fraction in the melt cannot be determined from the Jaupart-Allegre correlation because the gas content in the melt during spreading is not known. Furthermore, it is in principle not clear whether the above mentioned correlation can be applied to the oxide melt used in the KATS experiments. The mixing process destroys the developing viscous boundary layers which hinder the melt spreading. In contrast, the bulk cooling caused by that mixing leads to a viscosity increase which slows down the melt front motion. The latter contribution, however, is negligible because of a high melt overheat and a small variation of the viscosity with temperature above the liquidus temperature. Assuming that the front motion in KATS-13 can be estimated by Eq.(3) in a time interval contained in  $(t_{inf}, t_{stop})$ , the bulk viscosity can be estimated from

$$\tilde{\nu} = 1/n \sum_{i=1}^n \frac{1}{3} \xi_f^5 g V^3 [x_{f;exp}^5(t_i) - x_0^5]^{-1} t_i, \quad (5)$$

where  $x_{f;exp}(t_i)$  is the measured front position at time  $t_i$ . For KATS-13 data at  $t_i \in [10.8s, 13.2s]$  [2] Eq. (5) gives  $\tilde{\nu} = 1.56 \times 10^{-4}$  m<sup>2</sup>/s. Using this estimated viscosity the approximate isothermal solution (Eq. (3)) agrees very well with the experimental findings (Fig. 3) for all  $t \in [6.4s, t_{stop}]$ ,  $t_{stop} = 14.4s$ , i. e. the spreading is almost isothermal until the stop of the front motion. There is no significant retardation of the front motion as observed in all KATS experiments performed on a ceramic substrate [15]. The transition time estimated from Eq. (1) is  $\tau_{tr} \approx 6.4$  s. The mean viscosity,  $\tilde{\nu} = 3.5 \times 10^{-5}$  m<sup>2</sup>/s, obtained from Eq. (5) from the KATS-12 front positions at

$t \in [12.23 \text{ s}, 23 \text{ s}]$  is equal to the viscosity estimated from the available measurements for the initial melt temperature of 2303 K [16]. Assuming that the Jaupart and Allegre correlation is valid for the oxide melt under consideration, the estimated increase of the viscosity by a factor of 4.3 is consistent with a gas volume fraction of about 0.35. A post test analysis, i. e. after the complete solidification of the melt, gave a total porosity of about 0.51 [2]. This value is certainly higher than the gas content in the melt during spreading, because of the ongoing concrete ablation during the cooling process. Thus, the Jaupart-Allegre correlation seems to be applicable to the considered oxide melt.

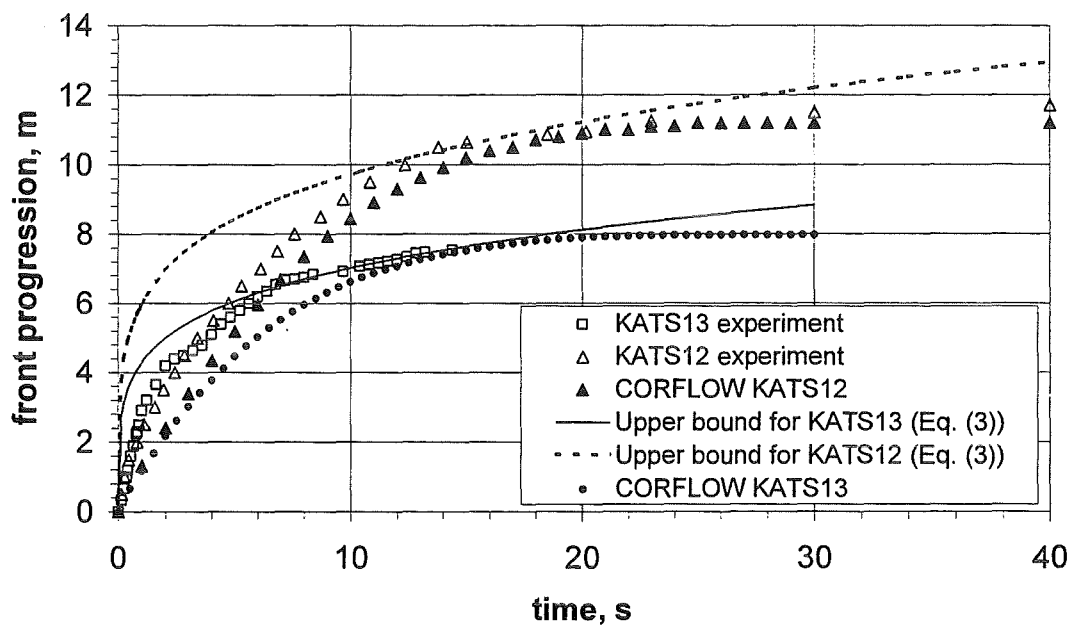


Fig. 3: Spreading on a ceramic substrate (KATS-12) and a concrete substrate (KATS-13).

### 3. Conclusions

The time behaviour of the solutions describing spreading of a fluid droplet with a rather arbitrary initial shape allows approximate solutions to be constructed which describe the spreading of a constant fluid volume with a time dependent flux release. These approximate solutions can be used to analyse the large-scale experiments

performed within the framework of nuclear safety research or to estimate the viscosity from the measured front propagation. The effect of bubbles on rheology in spreading experiments with water and HEC-water mixtures is investigated. The viscosity increase of water-air mixtures during spreading was described by the model proposed by Jaupart and Allegre. Even though the initial melt temperature in the high-temperature oxide melt spreading experiments, such as VULCANO VE-U1 and FARO L-32S, is far below the liquidus temperature, the advance of the flow front can be estimated by the isothermal solution for a sufficiently long period of time. This allows the consistency of the experimental boundary conditions and initial conditions (melt release volume flow rates, initial melt temperature) to be proved if a sufficiently qualified database of material properties is known (COMAS 5a, FARO L-32S).

The performed analyses of KATS experiments show that the variable viscosity model used in the CORFLOW code [17] is adequate for simulations of non-isothermal spreading on ceramic substrates. Although the CORFLOW simulation of the KATS-13 experiment using the estimated viscosity provide a reasonable prediction of the final spreading length, the time at which the melt front stops is predicted to be much longer (26 s) than detected in the experiment (14.4 s) (Fig. 3). The underprediction of the front propagation during the melt release phase is due to the used experimental melt release condition. This melt release mode ((b), Section 1) does not allow the inflow melt volume flux to be estimated with needed precision [18]. The model presented in this paper is suitable for a design and an analysis of the experiment which will be performed within the framework of the ECOSTAR program.

## References

- [1] J. M. Veteau et al., Note STR/LETC/94-164 (1994).
- [2] B. Eppinger et al., FZKA-Report 6589, Forschungszentrum Karlsruhe (2001).
- [3] W. Steinwartz et al., in FISA 99 EU Research in Reactor Safety, EUR 19532 EN, ed. G. Van Goethem et al. (1999).
- [4] G. Cagnet et al., in Proceedings of the OECD workshop on Ex-Vessel Debris Coolability, Karlsruhe, FZK-Report 6475 ed H. Alsmeyer (2000).
- [5] W. Tromm, J. J. Foit, in Proceedings of the OECD workshop on Ex-Vessel Debris Coolability, Karlsruhe, FZK-Report 6475 ed H. Alsmeyer (2000).
- [6] G. I. Barenblatt, *Prikladnaya Matematika i Mechnika*, vol. 16, 67 (1952).

- [7] H. E. Huppert, *J. Fluid Mech.*, 121, 43 (1982).
- [8] J. J. Foit, to be published.
- [9] A. Friedman, S. Kamin, *Trans. Amer. Math. Soc.* 262, No. 2, 551 (1980).
- [10] M. Samaille, Note SETEX/LTEM/-182 (1999).
- [11] M. Samaille, J. M. Veteau, R. Fournet, Note SETEX/LTEM/00-226 (2000).
- [12] M. Manga, J. Castro, K. V. Cashman, M. Loewenberg, *Volcanol. Geotherm. Res.* 87 (1998).
- [13] C. Jaupart, C. J. Allegre, *Earth Planet. Sci. Lett.* 102 (1991).
- [14] J. O. Sibree, *Trans. Faraday Soc.* 30 (1934).
- [15] J. J. Foit, FZKA-Report 6260, Forschungszentrum Karlsruhe (1997).
- [16] G. Fieg, F. Huber H. Werle, FZKA-Report 6605, Forschungszentrum Karlsruhe (1997).
- [17] R. Wittmaack, *Nuclear Technology* 119 (1997).
- [18] J. J. Foit, *Proceedings of the Annual Meeting on Nuclear Technology* (2001).

## **32.21.06 Dynamische Beanspruchung von Reaktordruckbehälter und Containment-Strukturen unter hochtransienten Belastungen**

### Limit Strains for Severe Accident Conditions (LISSAC)

(B. Dolensky, G. Hailfinger, J. Holzinger, T. Jordan, G. Karner, R. Krieg, K.-H. Lux, T. Malmberg, G. Messemer, N. Prothmann, H. Rieger, M. Sidor, E. Stratmanns, IRS; J. Aktaa, E. Diegele, D. Hofer, E. Materna-Morris, R. Schmitt, IMF; H. Plitz, NUKLEAR)

#### **Abstract**

Local failure strains for different specimens of a ferritic steel used for nuclear reactor pressure vessels are investigated. The specimens have design typical holes or notches. Different temperatures are considered. Also the size of the specimens is varied, in order to find possible size effects. The determination of the very local failure strains required the development of the so-called "vanishing gap procedure" which is based on post test examinations of the geometry of the fracture surfaces and subsequent finite element analyses. First results yield rather high local failure strains between 70 % and 140 %. The decrease of the failure strains with increasing specimen size is moderate.

#### **1. Introduction**

The limit strains which can be accepted under accident conditions have a strong effect on the impact load which structures can carry. If only small strains mainly in the elastic range are accepted, the impact loads must be quite small. If, however, under accident conditions large plastic strains are accepted, much higher impact loads can be carried. Thus the question arises, what are the local failure strains of structures? If material or model tests are carried out with specimens smaller than the real structures, the additional question arises, whether the failure strains are size dependent?

To answer these questions for structures of ferritic steel used for nuclear reactor pressure vessels, an extensive research program LISSAC (Limit Strains for Severe Accident Conditions) with 13 European partners sponsored by the European Community has been launched. It consists mainly of test families with different

specimen shapes containing design typical holes or notches under uniaxial and biaxial static and dynamic loads at room temperature, at 400°C and at 850°C. Within one test family the specimen shapes and the other conditions are the same, but the size is varied from specimen thicknesses or diameters of a few millimetres up to more than 100 millimetres. A more thorough description of the research program may be found in [1].

To date only results from uniaxial specimens under static loads have been evaluated. However, from a previous research program also sponsored by the European Community [2, 3] it can be concluded that dynamic effects will not change the overall picture significantly.

## 2. Test Program

To provide a solid basis for the test program, the locations of the different specimens within the cylindrical section of an unused reactor pressure vessel (material: 22NiMoCr37) has been carefully selected. The locations were determined such that specimens belonging to the same test family are grouped together as closely as possible. In this way the influence of spatial variations of the material properties on the results within one test family is minimized.

In addition, specimens which need only a fraction of the wall thickness  $t$  of the pressure vessel were located in the distance  $t/4$  from the outside surface of the reactor pressure vessel. Thus the reduced material strength usually found in the middle of the wall and the enhanced material strength at the surfaces of the wall do not appear in the smaller specimens; that means, the influence of variations of the material properties through the wall thickness of the pressure vessel has been minimized, too.

Nevertheless, the homogeneity of the mechanical material properties has been carefully studied by a large number of material qualification tests including standard tension and Charpy impact tests for specimens taken from different locations of the material. This work was performed by Framatome in France and Equipos Nucleares, S.A. (ENSA) in Spain. From the results available it can be concluded that the scatter of the material properties is rather moderate. Its effect on the material strength within

one test family is expected on the order of magnitude of  $\pm 1\%$ ; its effect on the material ductility is expected to be in the range of  $\pm 5\%$ .

The different test families are shown in Fig. 1. The flat specimens with a hole tested under six load and temperature conditions define six test families. The flat specimens with a bigger hole are tested only under static loading and at room temperature and therefore, define just one test family. All together the tests listed in Fig. 1 comprise 23 test families.

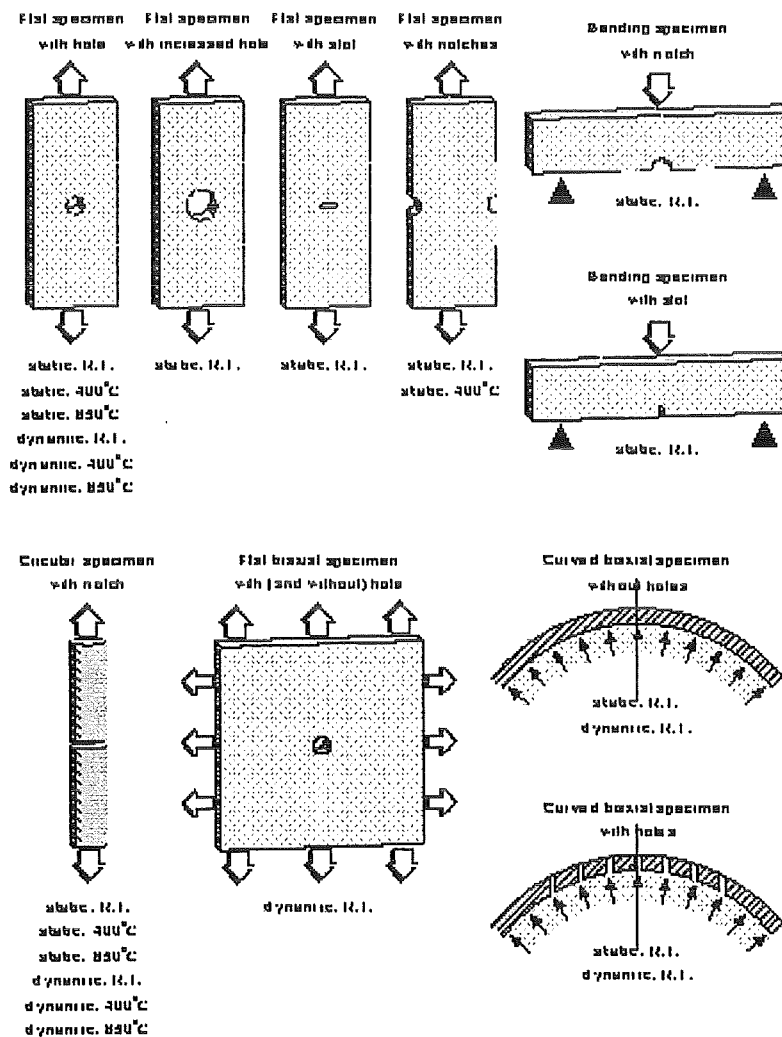


Fig. 1: The specimen shapes and load conditions define 23 test families.

The first test family of the flat specimens with a hole under static loading at room temperature includes five specimen sizes starting with a wall thickness of 4 mm up to a thickness of 200 mm which is almost the wall thickness of the reactor pressure vessel. Recently one partner has added two smaller specimen sizes of 0,2 and

0,8 mm wall thickness. Thus, the size scale (length scale) covers a factor of 1000! This is illustrated in Fig. 2.

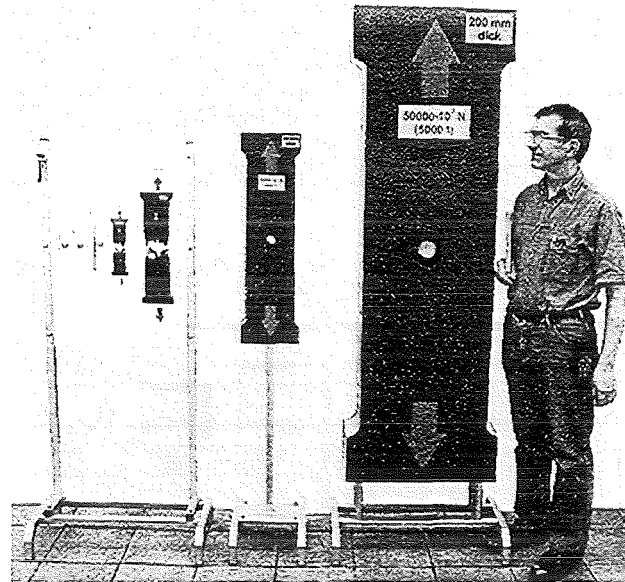


Fig. 2: Flat specimens with holes to be tested statically at room temperature. The smallest specimen has a wall thickness of 0,2 mm, tension force in the range of 50 N. The largest specimen has a wall thickness of 200 mm, tension force in the range of  $50 \cdot 10^6$  N.

The other test families cover a smaller size range. The largest specimen thickness is 80 mm, the largest diameter is 150 mm. The biaxial tests include only two different specimen thicknesses, 4 or 5 mm and 20 or 25 mm.

As already mentioned, special attention is given to design typical strain concentrations. The flat specimens with holes can be interpreted as structural elements of the pressure vessel head. The flat and curved biaxial specimens are steps towards the real geometrical shape of the vessel head. Of course, the real size and temperatures could not be approached at the same time. The specimens with notches have been introduced to study other structural elements, for instance the transition between different component cross sections.

### 3. First Test Results

Results will be discussed here for test families with static, uniaxial loads:

Flat specimens with holes,	R.T.;	thicknesses: 4, 20, 40, 80 mm
Circular specimens with notches,	R.T.;	diameters: 20, 150 mm
Circular specimens with notches,	400°C;	diameters: 20, 150 mm
Circular specimens with notches,	850°C,	diameters: 20, 150 mm

Only the tests with flat specimens of 4 mm thickness have been carried out by FZK, the others have been carried out by MPA Stuttgart.

The maximum local strains of the specimens at failure are of interest. Thus, the best representation of the results would be to show the tension forces versus the growing maximum local strains which occur in the holes or notches of the specimens. However, the direct measurement of these local quantities was not possible. Here it is important to note that the growing maximum local strains are well related to the growing openings of the holes or notches of the specimens. The determination of these integral quantities has turned out to be possible with the available measuring system.

Thus, as results, the nominal stresses, i.e. the tension forces divided by the smallest initial cross-sections of the specimens are shown versus the growing opening of the holes or notches, divided by the initial sizes of the holes or notches. For the flat specimens with holes refer to Fig. 3. A typical fracture surface of such a specimen is shown in Fig. 4. For the circular specimens with notches refer to Fig. 5.

If no size effect would occur, the curves for the tests belonging to the same family would be identical. The figures show that this is approximately true for the ascending and plateau parts of the curves. However, the descending parts (softening regimes) of the curves seem to be size dependent: For larger specimens the fall-offs occur at smaller hole or notch deformations.

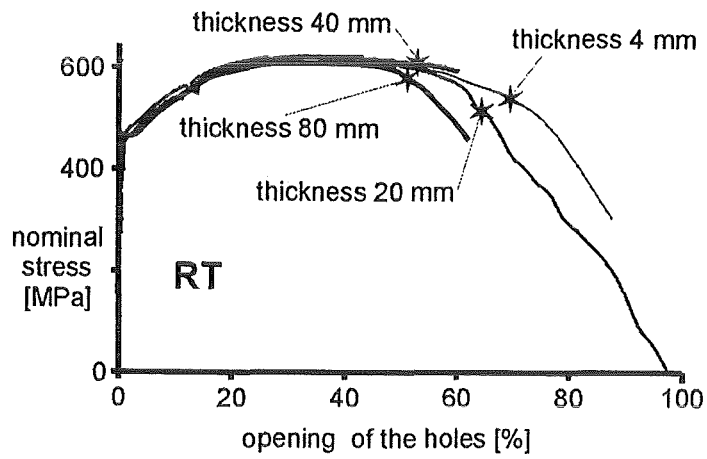


Fig. 3: Results for the test family of flat specimens with holes, static load, room temperature.

The stars denote the states where macroscopic cracks occur.

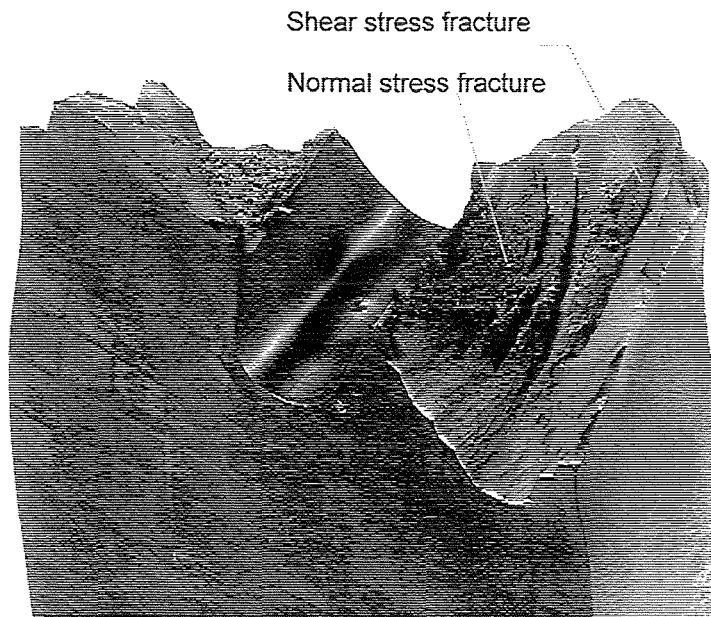


Fig. 4: Fracture surface of a broken flat specimen with a hole.

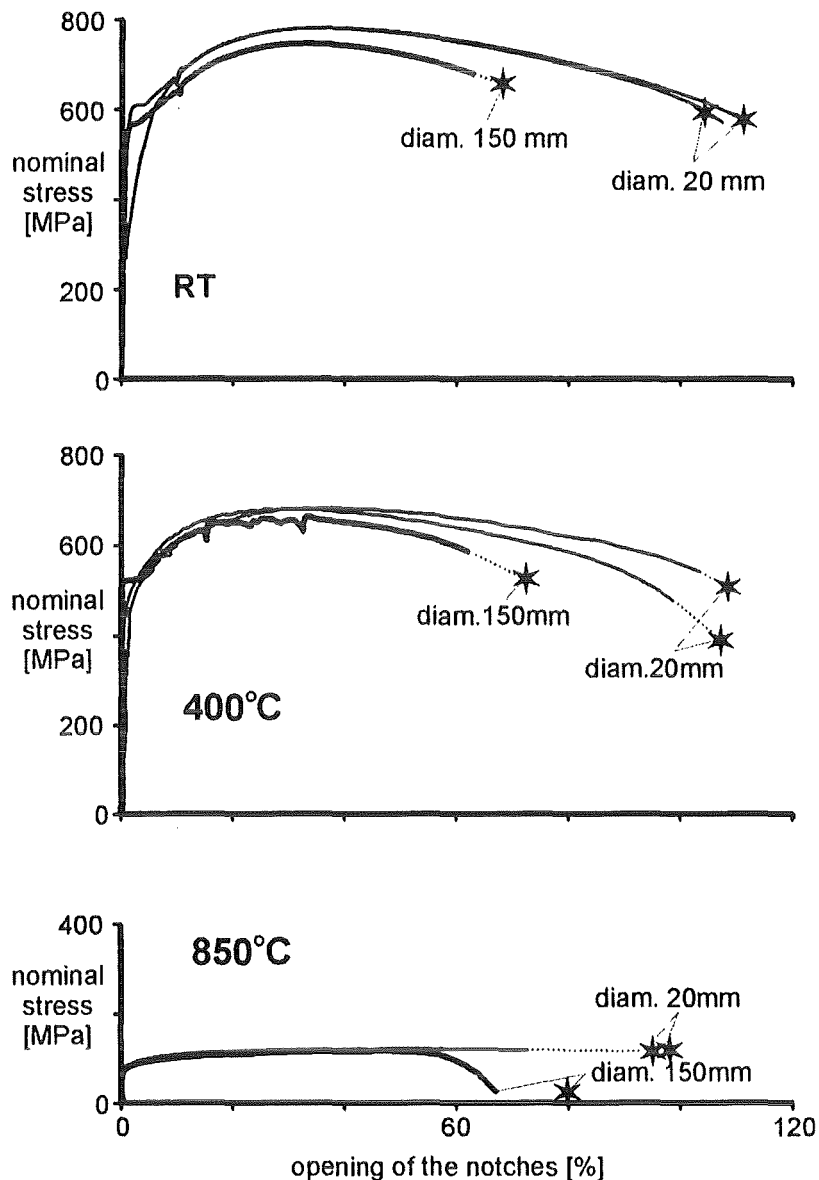


Fig. 5: Results for the test families of circular specimens with notches, static load, different temperatures.

The stars denote the states where macroscopic cracks occur.

#### 4. Determination of the Failure Strains

The first problem is the definition and determination of the deformation of the holes or notches at failure of the specimens. It should be preferably the deformation when a macroscopic crack starts to develop. This is reasonable from a safety point of view, since the load carrying capacity of structures during the subsequent crack propagation is not very reliable and should be excluded.

However, for the flat specimens with holes, for instance, the curves shown in Fig. 3 may include also the process of crack propagation from the location of the initial crack at or close to the holes to the outer surfaces of the specimens. To exclude this later phase, the following so-called “**vanishing gap procedure**” was used:

- The opening of the hole has been measured in a post test examination after the broken parts had been put together.
- Then the maximum crack opening, i.e. the maximum gap width between the crack surfaces was subtracted, Fig. 6.

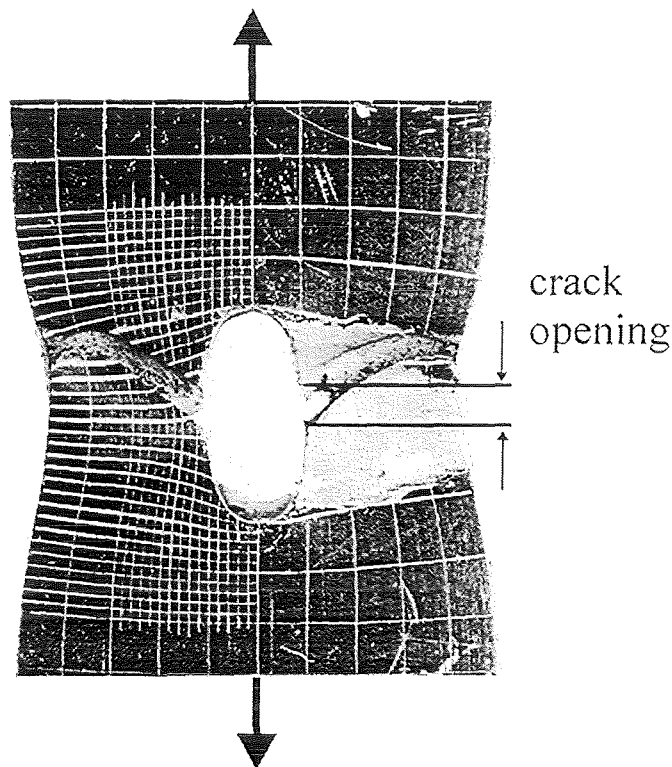


Fig. 6: Application of the “vanishing gap method” for the evaluation of a flat specimen with hole.

The resulting values must approximately correspond to the openings of the holes when the macroscopic crack has formed and starts to grow, since afterwards vertical displacements of the crack surfaces relative to the corresponding parts of the specimens will hardly take place. The values, i.e. the openings of the holes at failure, have been marked by stars in Fig. 3.

A similar procedure has been used for the circular specimens with notches and the resulting openings of the notches at failure have been marked by stars in Fig.5.

The determination of the maximum crack opening requires special measuring techniques, because of the irregular shapes of the crack surfaces, refer to Fig. 4, for instance.

Three measuring techniques have been applied:

- Generation of a negative mock-up of the gap between the crack surfaces with plastic material used in dentistry. Then measuring of the maximum thickness of the mock-up using a micrometer.
- Measurement of the shapes of the crack surfaces using a three-dimensional measuring machine.
- Measurement of the shapes of the crack surfaces using a scanning microscope.

The last technique is mainly applicable for small specimens.

The next problem is to determine the very local strain fields and the maximum local strains (the maximum equivalent strain and the three corresponding principle strains) at failure which belong to the openings of the holes or notches at failure. This has been done by finite element calculations, where the tension force is continuously increased. The results can be used to find relations for the maximum local strains versus the opening of the holes or notches. The inevitable uncertainties in the constitutive equations cause only minor errors, since the calculated strain fields and the given openings of the holes or notches are mainly connected by cinematic relations where the load has not direct influence. This has been checked by analyses with slightly different constitutive equations.

The relations between the maximum local strains and the opening of the holes or notches have remarkable properties:

- The maximum local strains increase almost linearly with the increasing opening of the holes or notches.
- The relations are almost the same for both, the test family of flat specimens with holes and the test family of circular specimens with notches. (Of course, the relations are exactly the same for all specimens of different size belonging to the same test family.)

The relations between the maximum local equivalent strains  $\varepsilon_{\text{equ}}$  and the relative openings  $\delta$  of the holes or notches read (approximately):

$$\varepsilon_{\text{equ}} = 1.42 \delta.$$

Using this equation the maximum local strains at failure can be easily determined for the openings of the holes or notches at failure of the specimens. In other words, the maximum local strains at failure can be determined for each specimen yielding the marked points (triangles, crosses, etc.) in the diagram of Fig. 7. The curves between the marked points for the circular specimens are very vague. To confirm these curves additional tests yielding intermediate points would be necessary.

## 5. Discussion of the Results and Conclusions

Despite of the small number of tests evaluated, Fig. 7 demonstrates that the local failure strains are rather high. For the considered test families the failure strains are between 70 % and 140 %. The decrease of the failure strains for increasing specimen thickness or diameter beyond 20 mm is moderate. Figure 7 indicates also a certain dependence of the failure strains on the specimen shape. The reason may be that for the flat specimens with holes the maximum strains occur in a point type of zone while for the circular specimens with notches the maximum strains are reached in a ring zone.

The failure strains for smaller specimen thicknesses or diameters and for other test families with different specimen shapes, loading conditions and temperatures are still under investigation. They will certainly extend the view considerably. Additional theoretical investigations will help to improve the understanding of the phenomena. However, it is expected that the main trend of the result will not be changed considerably. This is especially expected for tests with dynamic loads.

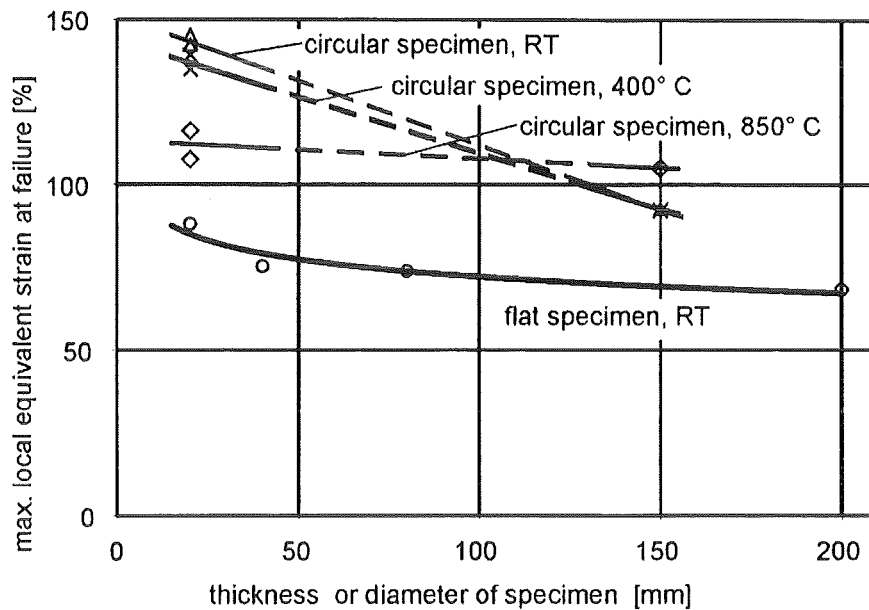


Fig. 7: Failure strains versus size.

On the other hand, if for impact problems a certain fraction of the above failure strains is accepted as the limit strain or the admissible strain of the structures, considerable loads can be carried. They will be higher than most of the admissible loads following the current design rules.

## References

- [1] Krieg, R., Julisch, P., Kalkhof, D., Talja, H., Aifantis, E., Cizelj, L., Caroli, C., Fokkens, J., Bhandari, S., Veròn. P., Schramm, K., Kieselbach, R., Limit Strains for Severe Accident Conditions (LISSAC), *Proc. of the Symposium FISA-2001, Luxembourg, Nov. 2001*, European Commission, pp. 396-407
- [2] Devos, J., et al., Reactor vessel integrity in severe accidents (REVISA), *Proc. of the Symposium FISA-1999, Luxembourg, Nov./Dec. 1999*, European Commission, pp. 256-265
- [3] Malmberg, T., Krompholz, K., Kalkhof, D., Solomos, G., Aifantis, E.C., Size Effects in Deformation and Fracture of a Ferritic Reactor Pressure Vessel Steel, *Proc. of the 16<sup>th</sup> Int. Conf. on Structural Mechanics in Reactor Technology, Washington 2001, division F*

- [4] Jordan, T., Malmberg, T., Failure Strain of the Reactor Pressure Vessel Head under Impact Loading, *Proc. of the 15<sup>th</sup> Int. Conf. on Structural Mechanics in Reactor Technology, Seoul 1999, division L*
- [5] Malmberg, T., Krompholz, K., Solomos, G., Aifantis, E.C., Investigations on Size Effects in Ferritic and Austenitic Materials, *Proc. of the 15<sup>th</sup> Int. Conf. on Structural Mechanics in Reactor Technology, Seoul 1999, division L*
- [6] Malmberg, T., Tsagrakis, I., Elefteriadis, I., Aifantis, E.C., *On the Gradient Plasticity Approach to Size Effects, Part I: Reviews*, Forschungszentrum Karlsruhe, Scientific Report FZKA 6321, March 2001

## 32.21.07 Analysen zum Containmentverhalten

- I. Quelltermuntersuchungen für schwere Unfälle in Leichtwasserreaktoren  
(P. Schmuck, IKET)

### Abstract

The goal of the work presented here is the development and application of methods to determine the internal and external radiological source term for severe accidents in light water reactors. On the one hand we develop detailed methods to improve conservative evaluations usually done earlier (e.g. by accounting more exactly the retention of fission products in the various systems of the reactor). On the other hand we aim to support the emergency management during a severe accident by developing a fast running code system for the prediction of the source term in case of accidental events in European reactors. This last task is performed in cooperation with partners from the EU and is supported by the EU Commission in the 5<sup>th</sup> Framework Program.

### MELCOR

Für detaillierte und genaue Simulation von Unfällen wird das Rechenprogramm MELCOR herangezogen, welches im Sandia National Laboratory (SNL) als NRC Referenzcode für Quelltermberechnungen entwickelt wird. FZK/IKET nimmt über die MCAP (*MELCOR Cooperative Assessment Program*) Initiative Einfluss auf diese Entwicklung. Im Jahr 2001 wurden die Versagensmodelle für die Kerntagplatte und den Reaktor Druckbehälter näher untersucht und Vorschläge zur genaueren Berechnung des Versagens erarbeitet.

Die neue MELCOR Version 1.8.5 wurde auf verschiedenen (Windows NT und Unix) Plattformen implementiert und getestet. Die Code Patches 1 und 2 wurden ebenfalls implementiert und erwiesen sich als sehr wichtig für die Reaktorapplikationen. Auf ein und demselben Standard-PC zeigten sich nur geringe Laufzeitunterschiede zwischen der Windows- und der LINUX-Implementierung. Für einen LOOP (Loss of Offsite Power) Fall in einem DWR konnten ohne spezielle Optimierung Rechenzeiten schneller als Echtzeit (bis etwa 10.000 Sekunden Problemzeit) erreicht werden.

Für die Zusammenarbeit FZK/CEA (WG3) wurden MELCOR Unfallrechnungen für den EPR in bezug auf die Wasserstoff-Quellen neu ausgewertet. Diese wurden für LOOP und LBLOCA (Large Break LOCA) Unfallsequenzen für das Primärsystem und für das Containment über einen Zeitraum von 12 Stunden ermittelt. Die berechneten Werte waren (soweit direkt vergleichbar) größer als die in früheren Studien von SIEMENS ermittelten.

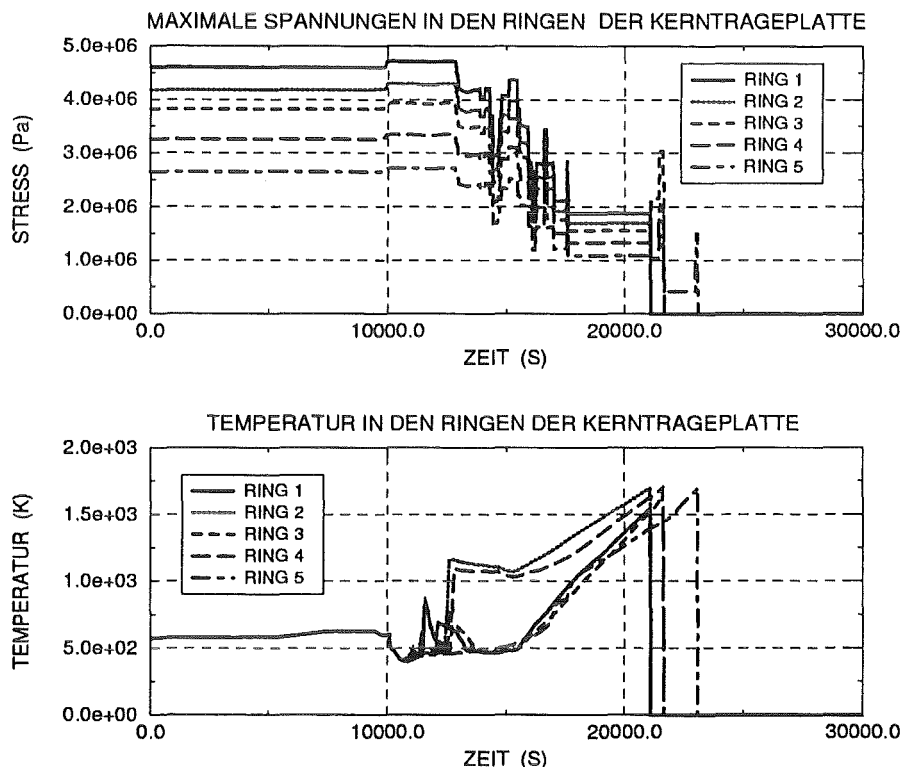


Abbildung 1: Versagensmodus der Kernttrageplatte: Zu hohe Tangentialspannungen und Temperaturen in den fünf Ringen eines DWR

## ASTRID

Mit dem Akronym ASTRID (*Assesment of Source Term for Emergency Response Based on Installation Data*) wird ein EU Projekt zur Entwicklung eines Quellterm-Codes bezeichnet, der für das Krisenmanagement bei Unfällen in allen LWRs der EU verwendet werden soll. Im 5. EU Rahmenprogramm wird ASTRID als Nachfolger des EU Codes STEPS (siehe Abb. 2) entwickelt, der bei aktuellen Unfallsituationen in europäischen (inkl. osteuropäischen) LWRs den radiologischen Quellterm realis-

tisch und rasch voraus berechnet (wesentlich schneller als Echtzeit), um frühzeitig Entscheidungen für das weitere Vorgehen (z.B. Accident Management Maßnahmen) treffen zu können. In solche Rechnungen fließen direkt gemessene Daten aus der beschädigten Anlage ein, um damit die rechnerischen Vorraussagen möglichst realistisch und genau zu erstellen. Dieses datengetriebene Vorgehen stellt einen wesentlichen Unterschied zu herkömmlichen Unfallrechnungen dar. Im Jahr 2001 wurde die Planungsphase zusammen mit den EU Partnern abgeschlossen und der EU Vertrag (Nr. FIKR-2001-00171) ausgearbeitet, in welchem die einzelnen Arbeitspakete definiert sind. Die Koordination dieser Projektarbeiten wird von IPSN in Fontenay-aux-roses (Abteilung DPEA/SECRI) wahrgenommen. IKET hat die Leitungsfunktion bei drei Arbeitspaketen übernommen und wird auch an anderen wichtigen Projektarbeiten mitwirken, z.B. an der Entwicklung eines Pakets für das Schmelzen des Reaktorkerns, die Verlagerung der heißen Debris in das untere Plenum, das Durchschmelzen des Reaktordruckbehälters und den Transport in das Containment.

Die folgenden drei Arbeitspakete werden unter Verantwortung des IKET erstellt:

- Quantification of releases in the diagnostic phase  
Die radioaktiven Freisetzungen werden in der Diagnosephase unter der Benutzung von gemessenen Unfalldaten rechnerisch ermittelt.
- Location of the break  
Ausgehend von gemessenen Daten wird der Ort und die Größe eines Lecks bestimmt.
- Automated transfer of source term estimations  
Hier geht es um die Übertragung der berechneten Quellterme an andere Computer, die - wie z.B. das RODOS System - Unfallkonsequenzen in der Umgebung ermitteln.

Beim Kick-Off Meeting Anfang November 2001 wurde das weitere Vorgehen für die Jahre 2001 bis 2004 im Detail festgelegt. Mit den Vorarbeiten zu den genannten Themen wurde bereits Ende 2001 begonnen.

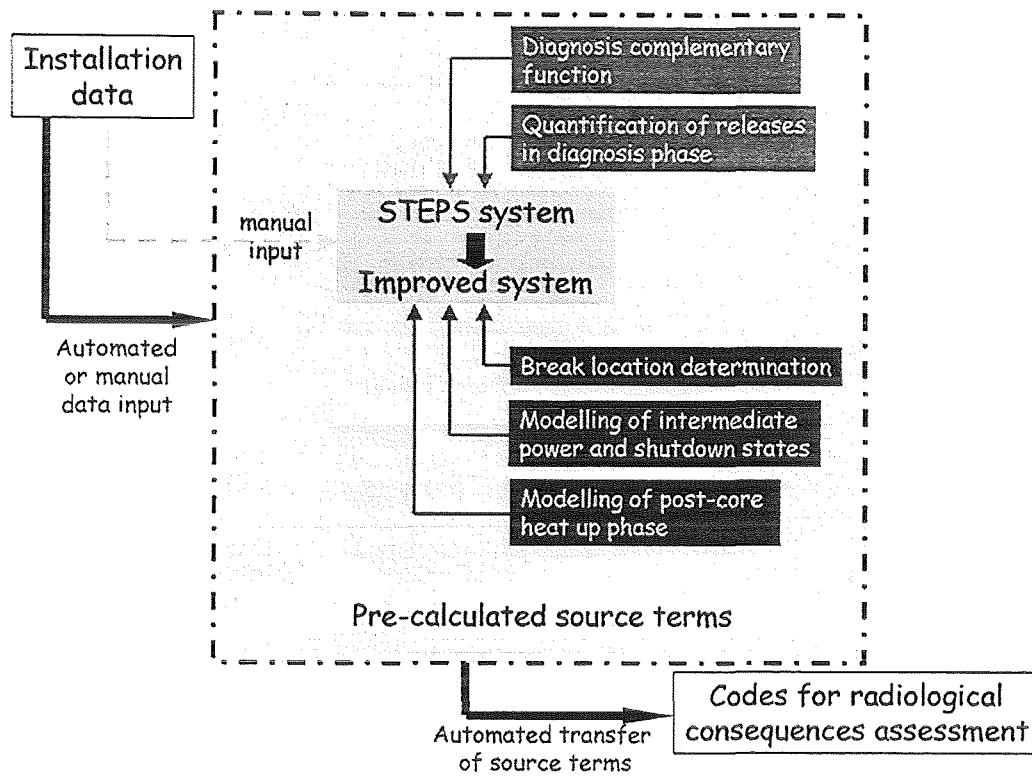


Abbildung 2: Die Entwicklung des Systems ASTRID: das existierende STEPS System als Basis und weitere Komponenten

## II. KAREX-Experimente zum radiologischen Quellterm infolge Resuspension

(J. Minges, W. Schütz, IRS; M.K. Koch, RUB/LEE)

### **Zusammenfassung**

Die Wiederfreisetzung schwerflüchtiger Substanzen aus Flüssigkeiten (nasse Resuspension oder Reentrainment) kann als Langzeitbeitrag zum radiologischen Quellterm nach einem Unfall mit Kernzerstörung, zum Beispiel aus dem gefluteten Core Catcher, eine wichtige Rolle spielen. Im Rahmen des KAREX-Programms wurden Laborversuche, Versuche im technischen Maßstab und modelltheoretische Entwicklungen zu dieser Thematik durchgeführt. Das Programm wurde im Jahr 2001 beendet.

Die Tröpfchenbildung beim Aufplatzen von Gas- oder Dampfblasen an der Phasengrenze ist von besonderer Bedeutung für die Resuspension. Im Berichtszeitraum wurden noch mehrere Experimente zur Messung von Tropfengröße und -geschwindigkeit im Abgasstrom durchgeführt.

Die theoretische Begleitung der KAREX-Experimente durch die Ruhr-Universität Bochum (RUB), in erster Linie mit dem Rechencode SUSANA, wurde fortgesetzt, aber zum Jahresende 2001 ebenfalls beendet.

### **1. Überblick**

Bei der Betrachtung radiologischer Quellterme nach einem schweren Störfall sind Kurzzeit- und Langzeitbeiträge zu beachten. Normalerweise gilt das Interesse den „intensiven“ Kurzzeitbeiträgen. Die Langzeitbeiträge haben meist geringe Massendichten, aber sie können über lange Zeiträume (Monate, Jahre) aktiv sein und deshalb eine besondere Bedeutung erlangen. Die Resuspension (Wiederfreisetzung) sowohl gelöster als auch schwerflüchtiger Substanzen (Spaltprodukte) aus Flüssigkeiten wie z. B. dem Sumpfwasser oder dem gefluteten Core Catcher kann als Langzeitbeitrag zum radiologischen Quellterm nach einem Unfall mit Kernzerstörung eine wichtige Rolle spielen.

Im KAREX-Programm wurden Experimente zur Resuspension aus Wasservorlagen durchgeführt. Eine dominante Rolle spielen dabei Gas- und Dampfblasen, die beim Aufplatzen an der Oberfläche Tropfen bilden. Geringe Gas- oder Dampfvolu-

ströme setzen Tropfen beim Zerplatzen einzelner Blasen (Filmtropfen, Jettropfen) frei. Bei hohen Volumenströmen dagegen beruht die Freisetzung überwiegend auf der Flüssigkeitsabscherung mit Tropfenbildung von den Phasengrenzen zusammenhängender, an der Oberfläche aufbrechender Gaskanäle. In allen Fällen können die Tröpfchen als Träger des beigemischten partikelförmigen bzw. löslichen Materials dienen.

Das KAREX-Programm des IRS bestand aus Laborversuchen und Versuchen im technischen Maßstab. Begleitende modelltheoretische Arbeiten wurden vorwiegend an der Ruhr-Universität Bochum durchgeführt.

Das experimentelle Programm wurde Mitte 2001 beendet. Die Versuchsaufbauten wurden bis Ende 2001 außer Betrieb genommen und zerlegt. Ebenso wurde Ende 2001 die theoretische Begleitung durch RUB beendet.

## **2. Abschließende experimentelle Untersuchungen**

Im Berichtszeitraum wurden noch mehrerer Experimente zur Messung von Tropfengröße und -geschwindigkeit im Abgasstrom des KAREX-Versuchsstandes durchgeführt. Dazu wurde ein Inline-Partikel-Prozessmeßsystem (IPP) eingesetzt. Das Messsystem ermittelt gleichzeitig die Größe und Geschwindigkeit von Partikeln, die das Messvolumen der Sonde durchlaufen. Grundlage des Systems ist ein patentiertes faseroptisches Ortfrequenzfilter-Verfahren, bestehend aus einer Gitteranordnung von Glasfaser-Lichtwellenleitern auf der einen Seite und einer Laserbeleuchtung auf der anderen Seite mit Echtzeit-Datenauswertung. Die Sonde hat den Vorteil, inline bei 100 °C und erhöhtem Druck messen zu können.

Abb. 1 zeigt den schematischen Aufbau der Versuche. Die Messungen wurden bei verschiedenen Heizleistungen (21/25,5/30 kW) und verschiedenen Pool- bzw. Gasraumhöhen durchgeführt. Das gemessene Tropfenspektrum lag im Bereich von 5 µm bis 800 µm. Die gemessenen Dichteverteilungen der Tropfendurchmesser dominieren unterhalb 100 µm. Die Häufigkeitsverteilungen der Tropfendurchmesser haben Maximalwerte bei etwa 180 µm. Die Mittelwerte (50 Prozent-Werte) liegen im Bereich von 100 µm.

Eine signifikante Abhängigkeit von Heizleistung und Covergashöhe (d. h. Höhe des Gasraums) ist nicht zu erkennen. Abb. 2 zeigt die gemessenen 50 Prozent-Werte in Abhängigkeit von Heizleistung und Gasraumhöhe.

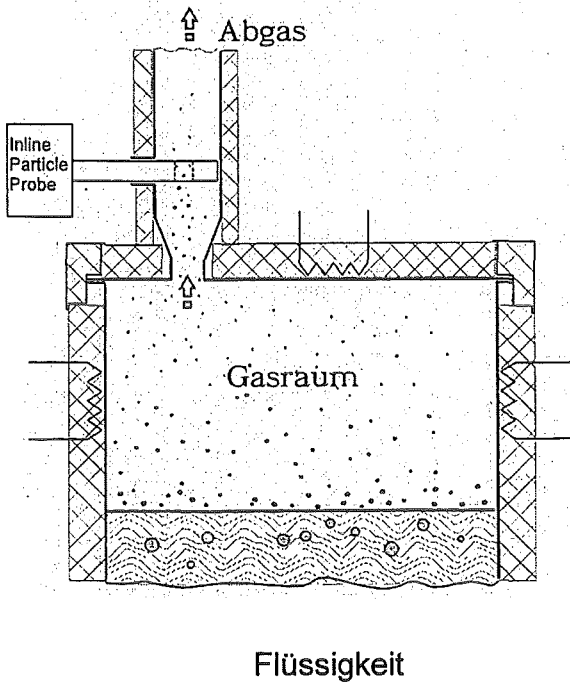


Abb. 1 Verfahrensschema der Messanordnung zur Tropfengrößenbestimmung.

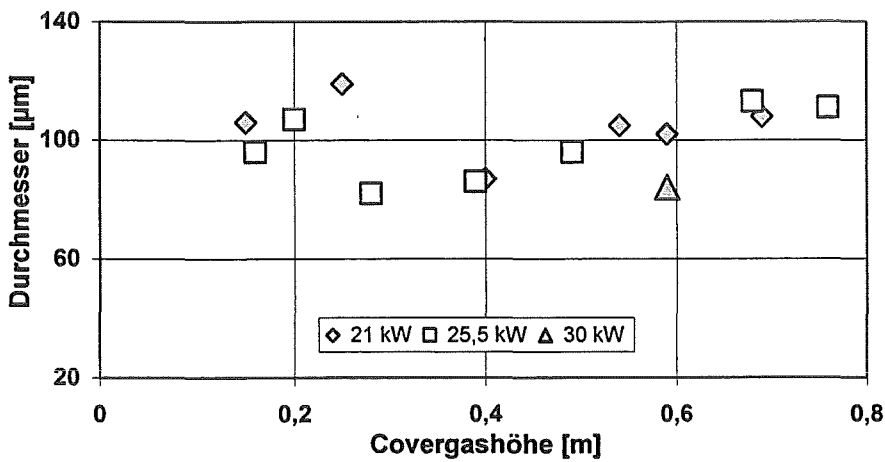


Abb. 2 Tropfendurchmesser (50 Prozent-Werte der Häufigkeitsverteilung) in der Abdampfleitung in Abhängigkeit von Heizleistung und Höhe des Gasraumes.

### 3. Validierung des Codes SUSANA anhand ausgewählter KAREX-Experimente

Zur Berechnung der Tropfenfreisetzung und der damit gekoppelten Radionuklidfreisetzung wurde bei RUB das Programm SUSANA (Sump water resuspension Source term ANalysis) erstellt. Zur weiterführenden Validierung des Programms SUSANA wurden die Experimente der KAREX-Versuchsreihe gesichtet und analysiert. In Abstimmung mit den Experimentatoren wurden zur Validierung geeignete Experimente der KAREX-B- und C-Versuchsreihen (siehe /1/) ausgewählt und weitere benötigte Versuchsdaten ergänzend aufbereitet /2/.

Unter Bezug auf die Vorgaben der Experimente wurden Variationsrechnungen durchgeführt. Die Ermittlung der Lamellendicke für sehr kleine Gasblasendurchmesser ist als kritisch zu erachten und erfordert weiteren experimentellen und theoretischen Forschungsbedarf. Zudem sind weitere Messwerte zum mittleren Durchmesser und zur Größenverteilung der Gasblasen wünschenswert. Für die Nachrechnung der KAREX-Versuche wurde hier ein literaturbasierter mittlerer Durchmesser gewählt.

Ein direkter Vergleich der KAREX-Messwerte mit den SUSANA-Rechnungen ist nur durch Extrapolation möglich, da durch SUSANA die Freisetzung unmittelbar an der Wasseroberfläche berechnet wurde. In den Versuchen erfolgte die Probenahme mit Abständen von 0,03 m – 0,06 m zur Wasseroberfläche.

#### LITERATUR

/1/ J. Minges, W. Schütz

KAREX-Experimente zur Resuspension schwerflüchtiger Substanzen aus siedendem Wasser

Interner Bericht IRS-Nr. 7/00 - PSF-Nr. 3337, März 2000

/2/ N. Reinke, M. K. Koch, H. Unger

Validierung des Codes SUSANA anhand ausgewählter KAREX-Experimente.

Jahresbericht 2001 von RUB/LEE an FZK

## 32.21.08 Untersuchungen zur Kernzerstörung

### I. Results of the QUENCH-07 Bundle Experiment on the Investigation of Cooldown Behaviour of Overheated PWR Fuel Rod Simulators (QUENCH-Programme)

(A. Miassoedov, D. Piel, L. Sepold, IMF III; M. Steinbrück, L. Steinbock, U. Stegmaier, IMF I)

#### **Abstract**

This report describes the test conduct and main results obtained in the bundle experiment QUENCH-07

#### **Zusammenfassung**

In diesem Bericht werden die Versuchsparameter und die wichtigsten Ergebnisse des Bündelexperimentes QUENCH-07 vorgestellt.

#### **Introduction**

Cooling of an uncovered, overheated PWR (Pressurised Water Reactor) core by water is the main accident management measure for terminating a severe accident transient. But, before the water succeeds in cooling the fuel elements, its injection can, under certain circumstances, cause renewed oxidation of the Zircaloy fuel rod cladding, giving re-heating of the rods, a sharp increase in hydrogen production and rod failure followed by the release of additional fission products. The additional hydrogen might threaten the containment, and the increased fission product release increases the source term. Evidence for these effects has been obtained from the analysis of the TMI-2 accident, in in-pile experiments such as LOFT LP-FP-2, and in out-of-pile CORA experiments. The reasons for this enhanced oxidation are not yet fully understood but it is believed that the cracking of oxide layers due to the thermal shock and subsequent exposure of fresh Zircaloy to steam are significant factors.

Because of the importance of understanding the in-vessel hydrogen source term that results during quenching, the QUENCH test facility [1] is being operated at Forschungszentrum Karlsruhe to investigate the physico-chemical behaviour of overheated fuel elements under different flooding conditions, to improve the understanding of the effects of water addition at different stages of a degraded core and to create a data base for model development and code improvement. The main

parameters of the test program are: quench medium, i. e. water or steam, fluid injection rate, extent of pre-oxidation at onset of quenching, and the starting temperature at initiation of quenching or cool-down. Up to now seven experiments have been successfully performed [2-6]. In the following experimental results of the QUENCH-07 experiment are given. This test was the first in the QUENCH series with a B<sub>4</sub>C absorber rod. The main objectives of the test were the investigation of the impact of B<sub>4</sub>C and stainless steel on bundle degradation and composition of the gaseous reaction products formed during oxidation of the B<sub>4</sub>C and B, C-containing melts.

### **Test QUENCH-07**

Major objective of QUENCH-07, performed at the Forschungszentrum Karlsruhe on 25 July, 2001, was to provide information on the B<sub>4</sub>C/SS interactions (absorber rod failure), on the formation of gaseous reaction products during the absorber rod degradation and B<sub>4</sub>C oxidation, in particular of H<sub>2</sub>, CO, CO<sub>2</sub> and CH<sub>4</sub>, and on the impact of control rod degradation on surrounding fuel rods. The test conduct was broadly similar to previous QUENCH experiments, but with the inclusion of a phase designed to examine B<sub>4</sub>C absorber rod degradation. As in PHEBUS FPT3 the control rod parameters are representative of commercial nuclear plants. Main test phases were as follows:

- Phase I Heat-up to ~873 K. Facility checks.
- Phase II Heat-up with 0.3 – 0.5 K/s to ~1720 K. Failure of B<sub>4</sub>C control rod leading to B<sub>4</sub>C-SS-Zry melt formation and relocation.
- Phase III Oxidation of the test bundle at a temperature of ~1720 K for ~15 min.
- Phase IV Heat-up with a rate of 0.35 – 0.45 K/s to a maximum temperature of ~2300 K. Delayed oxidation of B, C - containing compounds at high temperature.
- Phase V Cooldown of partially degraded bundle. Exposure of still non-oxidised B, C-containing materials to steam.

Local perturbation of the control rod temperature followed by helium detection in the off-gas indicated the control rod failure during the Phase II already at ~1585 K (Fig. 1). Formation of C and B containing gaseous reaction products was observed shortly afterwards.

During the Phase III (constant maximum temperature of ~1720 K) the production rates of CO, CO<sub>2</sub> and H<sub>2</sub> were approximately constant. Some methane was observed

but in a much smaller quantity (Fig. 2). Metaboric and orthoboric acids were also detected by the mass spectrometer. At the end of Phase III one of the corner rods was removed from the bundle in order to check the extent of oxidation. The oxidation was strongest in the region between 900 and 1000 mm with a maximum oxide layer thickness of  $\sim 230 \mu\text{m}$  at 950 mm elevation (Fig. 3).

Phase IV was started by ramping the power at 6 W/s. During this phase most of the surface-mounted thermocouples located in the hot zone failed. The increase in temperature was accompanied by a significant increase of all gaseous reaction products except methane. Up to the end of test phase IV the atmosphere consisted of flowing argon (3 g/s) and steam (3 g/s).

Phase V (cooldown) was initiated by switching the injection to cold steam at a rate of 15 g/s (argon flow was kept unchanged) when the two shroud thermocouples at 950 mm had exceeded 2073 K. Power ramp was continued for  $\sim 20$  s and then was reduced from 18.5 to 4 kW in 15 s and kept constant for  $\sim 150$  s to simulate decay heat level. The electrical power was then shut off but the steam injection continued until cooldown to  $\sim 473$  K had been achieved.

Within the heated zone immediate cooling was detected by all surviving thermocouples up to the centre of the heated zone (Fig. 4). A very different behaviour was observed at elevations above the top of the heated zone during the period shortly after beginning of the cooldown phase. Temperature escalation started there, heatup rates of more than 40 K/s were exhibited and temperatures up to  $\sim 2000$  °C were measured (Fig. 5). Associated with this escalation an increased release of all gaseous species was observed. The evaluation of the mass spectrometer data resulted in 198 g of hydrogen release in total, most of which (136 g) was produced during the cooldown. In addition, there were large increases in generation of CO, CO<sub>2</sub>, and boric acids, small amount of methane was also detected. The evaluation of CO and CO<sub>2</sub> release indicates that about 40 % of the boron carbide in the central rod was oxidised during the whole test.

Test bundle and shroud appear severely damaged in the region from  $\sim 750$  mm elevation upwards. In this region the shroud and the bundle were partially molten. The major part of the shroud above the heated zone relocated to the region below 1000 mm. Another damage zone is apparent at the level of the topmost grid spacer, i.e. at 1450 – 1500 mm.

## References

- [1] P. Hofmann, C. Homann, W. Leiling, A. Miassoedov, D. Piel, L. Schmidt, L. Sepold, M. Steinbrück: "Results of the QUENCH Commissioning tests". FZKA 6099, Forschungszentrum Karlsruhe, 1998.
- [2] P. Hofmann, W. Hering, C. Homann, W. Leiling, A. Miassoedov, D. Piel, L. Schmidt, L. Sepold, M. Steinbrück: "QUENCH-01. Experimental and Calculational results". FZKA 6100, Forschungszentrum Karlsruhe, 1998.
- [3] P. Hofmann, C. Homann, W. Leiling, A. Miassoedov, D. Piel, G. Schanz, L. Schmidt, L. Sepold, M. Steinbrück: "Experimental and Calculational Results of the Experiments QUENCH-02 and QUENCH-03". FZKA 6295, Forschungszentrum Karlsruhe, 2000.
- [4] A. Miassoedov, P. Hofmann, W. Leiling, D. Piel, L. Schmidt, L. Sepold, M. Steinbrück, W. Hering, C. Homann: "Flooding experiments on the investigation of the hydrogen source term (QUENCH test results Jahrestagung Kerntechnik 2000, Bonn, 23.-25.Mai 2000, Bonn : INFORUM GmbH, 2000 S.203-06.
- [5] L. Sepold et.al. "Investigation of Cool-Down Behavior of the Overheated PWR Fuel Rod Simulators". FZKA 6412, Forschungszentrum Karlsruhe, 2002.
- [6] G. Schanz, M. Steinbrück, U. Stegmaier, A. Miassoedov: "Post-Test Examination Results of the Water-Quenched Bundles QUENCH-01, QUENCH-02 and QUENCH-03." Proc. "Annual Meeting on Nuclear Technology 2001", Dresden, May 15 – 17, 2001, pp 197 –201.

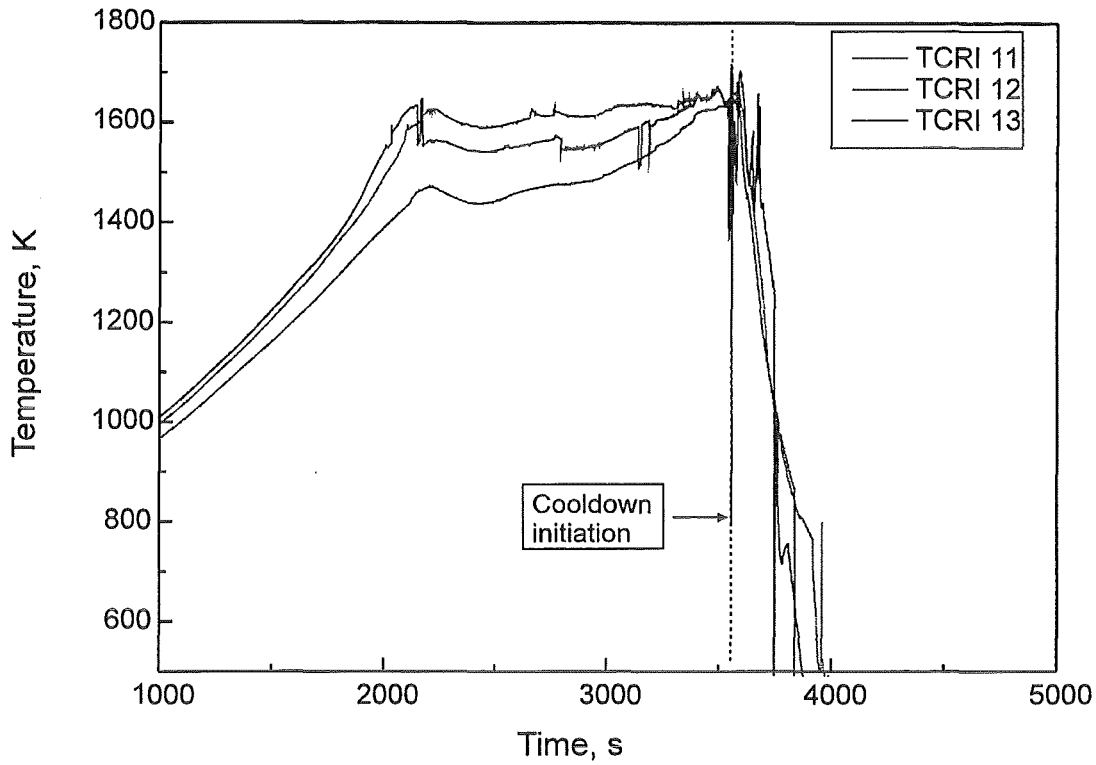


Fig. 1: Control rod failure in QUENCH-07 test.

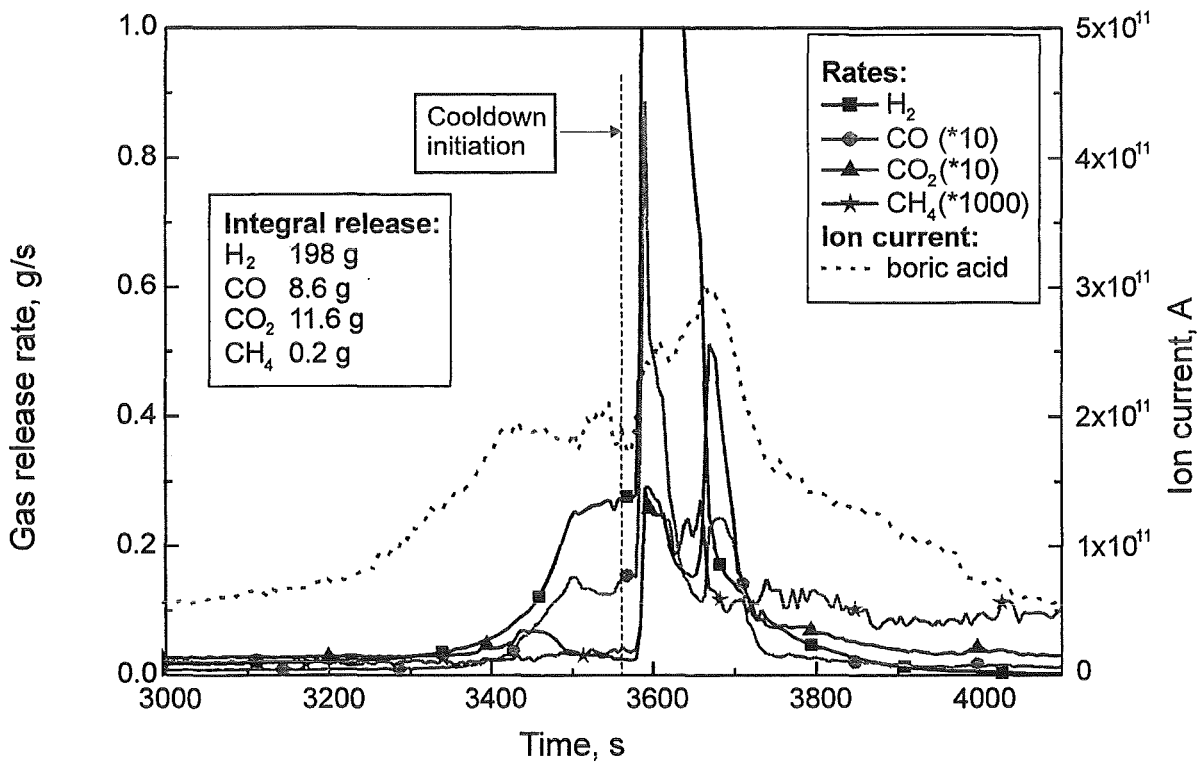


Fig. 2: Gas release rates of carbon- and boron-containing species in QUENCH-07 test.

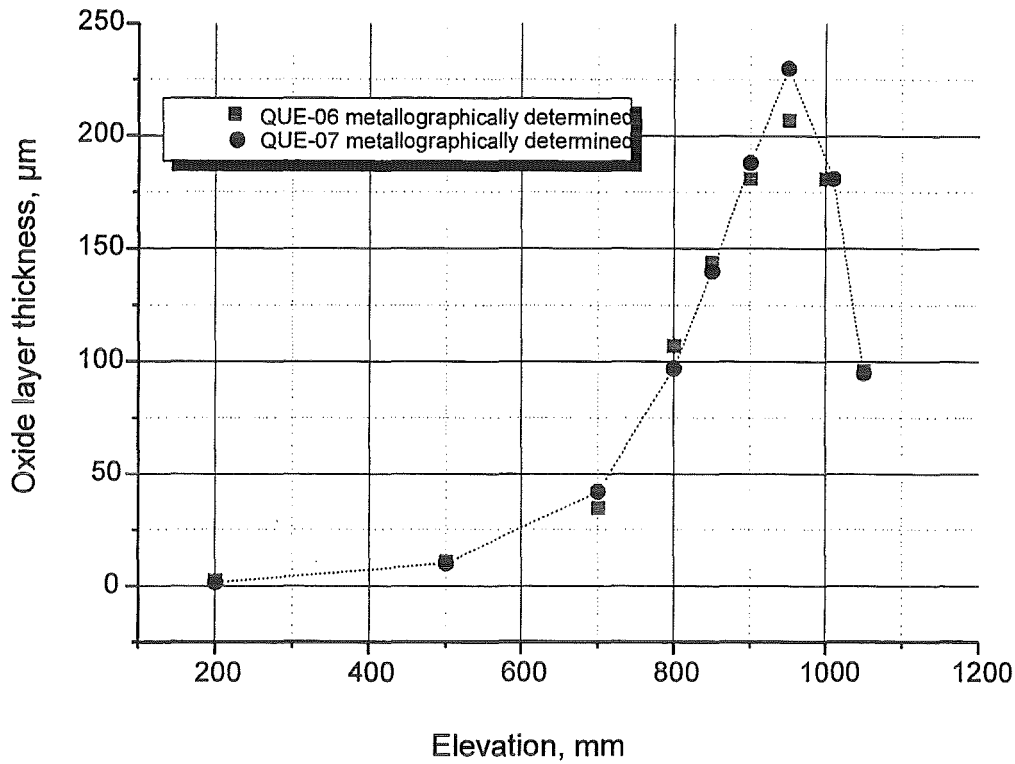


Fig. 3: QUENCH-07; Oxide layer thickness profile of corner rod B (withdrawn from the bundle before the transient) compared to test QUENCH-06.

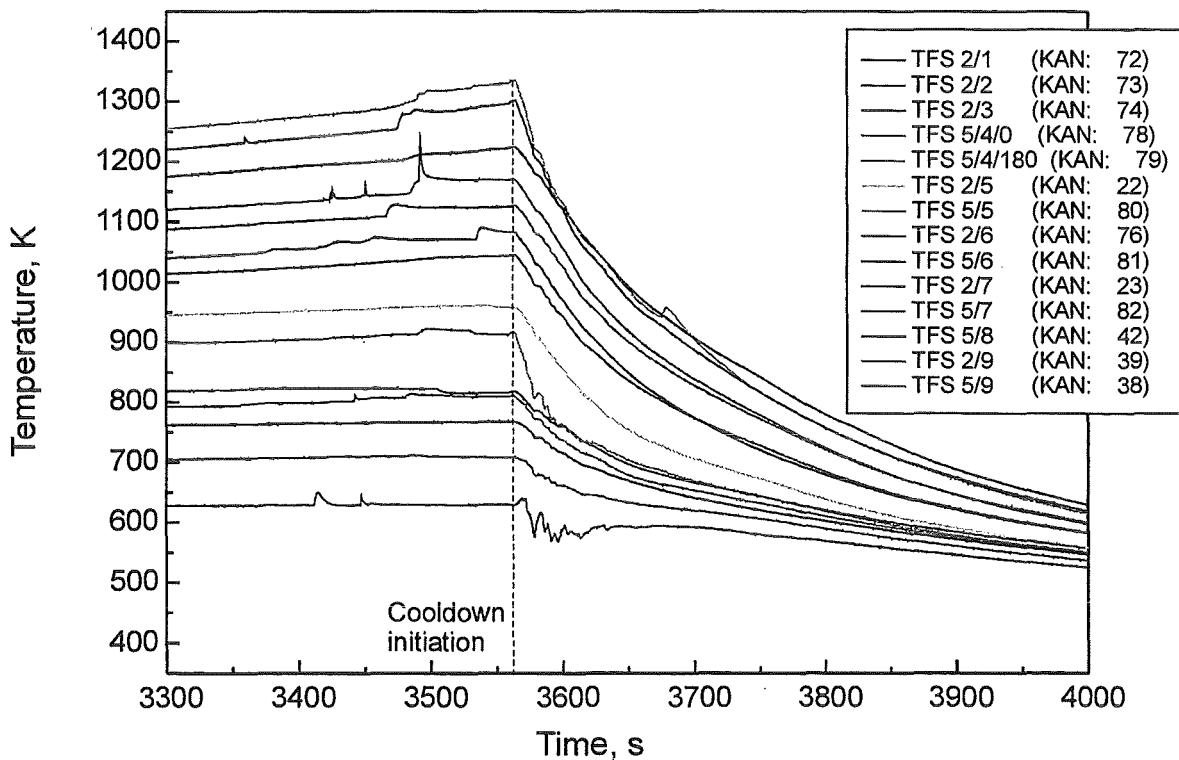
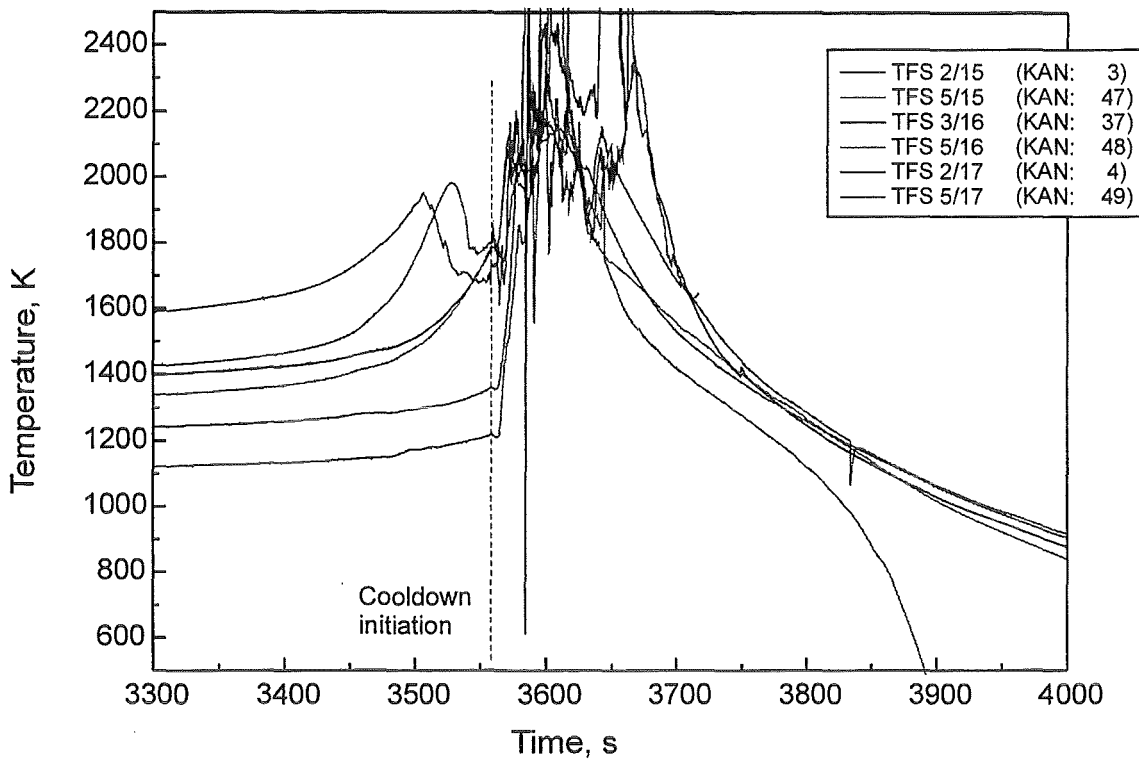


Fig. 4: QUENCH-07; Cladding temperatures at lower bundle elevations (-250 to 550 mm).



**Fig. 5:** QUENCH-07; Cladding temperatures at highest bundle elevations (1150 - 1350 mm).

II. Metallographic Post-test Examination of QUENCH-04 and QUENCH-05 Test Bundles and Phenomenological Interpretation  
(G. Schanz, M. Heck, IMF III; U. Stegmaier, IMF I)

**Abstract**

Main results of the destructive Post-test Examination of the bundles QUENCH-04 and QUENCH-05 are summarised in a phenomenological interpretation of the mechanisms of bundle oxidation and components interaction. Facilitated by the fast response of both bundles to the effective cool-down by steam the temporal development of damage can be mostly deduced from the final state. Crack surface oxidation turns out to have played a minor role, as cracking and cladding fragmentation took place mainly during late stages of cool-down. Though considerable rod-internal melting occurred in both bundles, some melt penetration to the flow channels was observed only for QUENCH-05.

**Zusammenfassung**

Wesentliche Ergebnisse der zerstörenden Nachuntersuchung der Bündel QUENCH-04 und QUENCH-05 werden mit einer Beurteilung der Mechanismen der Bündel-Oxidation und der Wechselwirkung der Komponenten zusammengefasst. Begünstigt durch das schnelle Ansprechen beider Bündel auf die Dampf-Abkühlung kann die zeitliche Entwicklung der Schädigung weitgehend aus dem Endzustand abgeleitet werden. Die Bedeutung der Oxidation von Riss-Oberflächen hat sich als gering herausgestellt, weil Riss- und Fragment-Bildung hauptsächlich während später Phasen der Abkühlung auftraten. Obwohl in den Stäben beider Bündel in beträchtlichem Umfang Schmelze gebildet wurde war nur für QUENCH-05 das Durchdringen von etwas Schmelze in die Kühlkanäle festzustellen.

**Introduction**

After metallographic preparation of selected cross sections of the two bundles a comprehensive microscopic investigation and a detailed photo documentation, including high magnifications, were performed. The oxidation state of the bundles was quantified by systematic scale thickness measurement at all polished cross sections and along the removed bundle components, and combined to axial profiles. Since the lower half of the bundles did not follow the escalation, the series of cross

sections, selected for the post-test evaluation, was restricted to the upper bundle half.

On this basis a description of the final state of the bundles and a discussion of their behaviour in time dependence and as result of simultaneous phenomena and competing mechanisms is given. The state at lower elevations can be understood to largely represent interim states of the higher elevations, at which the phenomena have proceeded at higher temperature. This is why it was helpful to evaluate in upward direction. Thus, the mechanisms and their temporal development were identified and described by thematically composed illustrations.

Eventual cool-down related phenomena, the formation of through-wall cracks in the cladding tubes, the oxidation of the crack surfaces and the steam exposed areas of the inner cladding surface deserved special interest.

It is mentioned that corner rod B was pulled during test QUENCH-04 before the final escalation and the quench phase, whereas fuel rod simulator No. 19 was removed from the bundle after the test, before embedding into epoxy resin. During QUENCH-05 corner rod B, and after the test, the upper fragment of rod No. 15 were removed. This allowed separate analysis of oxidation status and hydrogen uptake for the removed components. For bundle QUENCH-05 the final state of the W-Re type thermocouples was included, with the aim to deduce their degradation mechanisms; as this test began with a pre-oxidation phase (after the usual temperature equilibration), relatively strong oxidative attack and mechanical loading was expected for the TCs.

Detailed information could be deduced from the post-test examination and the accompanying measurements and analyses. Helpful for the description and the phenomenological interpretation or discussing argumentation was the fact that the bundles responded quickly to the fast cool-down with steam and thus retained their state at temperature as far as physico-chemically and mechanically possible.

Detailed results and illustrations of the Post-test Examination are given in the Final Reports on both experiments, which will be published soon [1, 2].

#### **QUENCH-04**

Growth of regular, protective oxide scale with even self-healing tendencies proceeds according to the pronounced axial temperature profile along the bundle. Internal cladding interaction with the ZrO<sub>2</sub> pellets in dependence of contact develops with fair

simulation quality for UO<sub>2</sub> pellets. Depending on the resulting through-wall oxygen profile melting of the cladding can occur. Melt spreading or rod-internal melt relocation is determined by the further increase of temperature in competition with the oxidation process. Oxide scale morphology and melting indicate peak temperature levels above 1800 K and 2100 K, respectively.

Scale de-lamination or spalling processes play an unimportant role. Some through-wall cracking of strongly oxidised cladding at temperature exposes the crack surfaces and the internal surfaces only near to the steam ingress positions, since the steam consumption limits its distribution. Strong internal steam oxidation tends to confine residual metallic melt by crucible formation and thus helps to prevent melt penetration to the flow channels. Characteristic features of melt oxidation can be studied under such conditions. As residual metal gets only locally exposed to steam during cool-down, no corresponding hydrogen signal is observed. Late crack formation at relatively low temperatures plays a major role in determining the final bundle state, as deduced from the typically observed absence of crack surface oxidation.

In general the thermocouple instrumentation is found in sufficiently good condition to have given reliable recordings. This holds especially for the oxidation state of the duplex sheath and the clamp fixing procedure. However, the contact between the TC and the surface of the wall is often found weakened. Arguments for discussion of possible improvements or erroneous readings are the oxidative consumption of the thin clamps (detachment risk) and the possibility of sheath-oxidation related TC excursion in de-coupled status.

The shroud failure is discussed to have resulted from overheating by close rods, tearing under oxidation-related hoop stress, leak formation and steam leakage, continued deformation during external oxidation, melt formation and oxidation. However, the interpretation is not claimed to be complete. At the upper spacer grid the special morphology of long-term oxidation [3] developed at moderate temperature.

#### **QUENCH-05**

The axial oxidation profile reflects the pronounced temperature dependence of Zircaloy-4 / steam oxidation. Generally, this reaction proceeded in the well-known kinetics controlled by growth of protective scale. Favourable conditions for

breakaway-related growth anomalies [3] during the pre-oxidation phase of the experiment at lowest and highest elevations did not influence the transient test phase. In the peak temperature range below the upper electrode zone strong oxidative conversion of the fuel rod simulator cladding was accompanied by chemical interaction with the  $ZrO_2$  pellets at positions of solid-state contact. In total, however, the corresponding oxygen transfer to the cladding remained relatively unimportant in comparison to the effect of the external steam oxidation. No indications for early mechanical cladding failure at temperature were found.

Melting of cladding matrix volumes, melt confinement by the “crucible effect” of the oxygen-enriched surrounding structures, rod-internal melt relocation and resulting agglomeration and gap-filling at expense of void formation was observed in local variability at many positions.  $ZrO_2$  precipitates of dendritic morphology indicate the existence of melt pools at temperature. Cladding failure according to the “chemical thinning process” could not be observed. However, the limited amount of external melt, found in form of oxidised lumps on some rod surfaces, is interpreted to result from metallic cladding residues.

Cladding through-wall cracking, breach formation, steam ingress and internal steam oxidation under supply limitation conditions have to be correlated mainly to the cool-down phase of the experiment. Some  $ZrO_2$  precipitation within the prior  $\beta$ -Zr phase matrix, some spot-wise scale growth from crack surfaces and crack-filling by  $ZrO_2$  growth are attributed to oxidation at high temperature. However, the fact that most of the crack surface network remained non-oxidised, indicates its formation at a late stage, i.e. at low temperature. This interpretation of the oxidation state of the bundle supports the unimportant signal of measured hydrogen release.

The systematically documented state of the thermocouples reflects in general the influence of the strong steam oxidation during the pre-oxidation and the following test phases. The TC fixing procedure, using spot-welded Zr-clamps, is seen to provide safe rod contact until total clamp oxidation. The oxidation of the external part of the duplex TC sheath (zirconium / tantalum) is characterised by formation of some deep wedge-shaped and axially elongated scale cracks and consequently premature splitting, which does not yet limit the TC function. However, tantalum oxidation proceeds extremely fast, so that the TC structure should have been degraded soon after steam exposure of the inner sheath. TC fragmentation and relocation of broken

segments was observed, in relation to the experimental conditions and subsequent handling. Temperature escalations at 750 and 850 mm elevation, registered by TCs, are in contradiction to the more moderate oxidation state of the rods, and seem to be due to thermal decoupling of TCs. This important result deserves further attention.

## References

- [1] L. Sepold, P. Hofmann, C. Homann, W. Leiling, A. Miassoedov, D. Piel, G. Schanz, L. Schmidt, U. Stegmaier, M. Steinbrück, H. Steiner, Investigation of an Overheated PWR-Type Fuel Rod Simulator Bundle Cooled Down by Steam. Part I: Experimental and Calculational Results of the QUENCH-04 Test, FZKA 6412 (2002)
- [2] L. Sepold, C. Homann, W. Leiling, A. Miassoedov, D. Piel, G. Schanz, L. Schmidt, U. Stegmaier, M. Steinbrück, H. Steiner, Experimental and Calculational Results of the QUENCH-05 Test, FZKA 6615, to be published
- [3] G. Schanz, S. Leistikow, Microstructural Reasons for Mechanical Oxide Degradation (Breakaway Effects) and Resulting Kinetic Anomalies of Zircaloy-4 / Steam- HT-Oxidation. Proc. 8<sup>th</sup> Intern. Congress Metallic Corrosion, Mainz, F.R. Germany, 6-11 Sept. 1981, Vol. II, pp 1712-1717

### III. Oxidation kinetics of B<sub>4</sub>C (BOX rig experiments)

(M. Steinbrück, A. Meier, U. Stegmaier, L. Steinbock, J. Stuckert, IMF I)

#### **Abstract**

New results on the oxidation kinetics of B<sub>4</sub>C in steam at temperatures between 800 and 1600 °C are presented. The oxidation rate is determined 1) by the formation of a liquid B<sub>2</sub>O<sub>3</sub> barrier scale and 2) by its loss due to the formation of volatile boric acids and direct evaporation. The properties of the specimens, in particular its porosity, affects the kinetics only at the very beginning of the oxidation. But, the oxidation kinetics is strongly influenced by the surrounding conditions, especially by the steam flow rate.

#### **Zusammenfassung**

Es werden neue Ergebnisse zur Oxidation von B<sub>4</sub>C in dampfhaltiger Atmosphäre bei Temperaturen zwischen 800 und 1600 °C vorgestellt. Die Oxidationsrate wird bestimmt 1) durch die Bildung einer B<sub>2</sub>O<sub>3</sub> Schicht, die als Diffusionsbarriere wirkt und 2) deren Abdampfung durch Reaktion mit Dampf unter Bildung von flüchtigen Borsäuren. Die Probeneigenschaften, insbesondere deren Porosität beeinflusst die Reaktionsgeschwindigkeit nur zu Beginn der Oxidation. Die Oxidationskinetik wird eher durch die äußeren Randbedingungen, vor allem durch die Wasserdampf-konzentration und -strömungsrate bestimmt.

An extensive test series on the oxidation kinetics of boron carbide was performed in the BOX Rig. This experimental set-up, which was designed, constructed and put into operation within 2000, consists of a sophisticated supply system for argon, hydrogen and steam, a tube furnace ( $T_{\max} = 1800$  °C) and a mass spectrometer for the analysis of the gaseous reaction products. The test arrangement was continually improved, especially the sample support was modified 1) to obtain an axially uniform oxidation of the specimens and 2) to prevent or at least to reduce interactions of the sample with the support structures. The kinetics of the B<sub>4</sub>C oxidation is mainly evaluated using the hydrogen release rates. Further gases of interest are CO, CO<sub>2</sub>, CH<sub>4</sub>, and boric acids.

Four types of B<sub>4</sub>C specimens were investigated: 1) commercial pellets used in French PWRs (Framatome), 2) pellets of Russian origin used in the CODEX tests

with boron carbide control rod (CODEX), 3) dense absorber pellets without open porosity obtained by Elektroschmelzwerk Kempten, Germany (ESK) and 4) B<sub>4</sub>C powder as formerly used in German BWRs and obtained by the same company (ESK powder). The different species were chosen to investigate the influence of the sample (state, geometry, density, porosity etc.) on the oxidation behaviour. Table 1 summarises the main properties of the different samples.

**Table 1:** B<sub>4</sub>C specimens used in BOX experiments

	<b>Pellet Framatome</b>	<b>Pellet CODEX</b>	<b>Pellet ESK</b>	<b>Powder ESK</b>
<b>diameter</b>	7.47 mm	7.5 mm	12.25 mm	10.95 mm
<b>height</b>	14.0 mm	10.3 mm	9.4 mm	3.0 mm
<b>mass</b>	≈ 1.1 g	≈ 0.82 g	≈ 2.6 g	≈ 0.46 g
<b>density</b>	1.8 g/cm <sup>3</sup>	1.8 g/cm <sup>3</sup>	2.34 g/cm <sup>3</sup>	1.6 g/cm <sup>3</sup>
<b>geometric surface</b>	3.724 · 10 <sup>-4</sup> m <sup>2</sup>	2.87 · 10 <sup>-4</sup> m <sup>2</sup>	4.8 · 10 <sup>-4</sup> m <sup>2</sup>	0.942 · 10 <sup>-4</sup> m <sup>2</sup>
<b>volume</b>	6.136 · 10 <sup>-7</sup> m <sup>3</sup>	4.55 · 10 <sup>-7</sup> m <sup>3</sup>	1.11 · 10 <sup>-6</sup> m <sup>3</sup>	2.825 · 10 <sup>-7</sup> m <sup>3</sup>
<b>BET surface</b>	3.5-4.0 m <sup>2</sup> /g 4 m <sup>2</sup>			0.07 m <sup>2</sup> /g 0.03 m <sup>2</sup>
<b>surface/volu me</b>	607 m <sup>-1</sup>	631 m <sup>-1</sup>	432 m <sup>-1</sup>	333 m <sup>-1</sup>
<b>grain size</b>				14 mesh
<b>supplier</b>	Framatome	Russia	ESK	ESK

The different specimens were chemically analysed and an X-ray diffraction phase analysis was performed. The CODEX pellets showed a relatively high content of impurities (2.3 Ma%: Fe, Cr, Ni, Al etc.) and a low content of free carbon. The other materials are pure B<sub>4</sub>C with low amounts of impurities.

Isothermal test series were performed to investigate the oxidation kinetics in the temperature range between 800 and 1600 °C. As an example Fig. 1 shows the conduct of one test at 1100 °C. The specimens were heated in a pure argon flow (50 l/h) to the predefined temperature level, then usually for 30 min 30 g/h steam were added leading to a steam partial pressure of 42755 Pa. Finally, the specimens were cooled down in inert atmosphere. The Framatome pellets were used as reference material, tests have been performed between 800 and 1600 °C in 100 K

steps. The test program for the other specimens was restricted to experiments at 800, 1000, 1200, and 1400 °C.

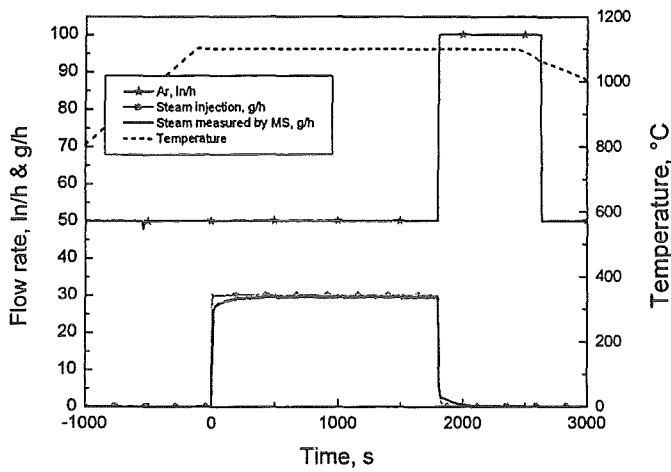


**Fig. 1:**  
Isothermal oxidation of B<sub>4</sub>C;  
Test conduct

The methane production was very low in all tests, only at the lowest test temperature of 800 °C significant amounts of CH<sub>4</sub> were formed.

Figures 2-4 summarise the hydrogen release rates as a measure for the B<sub>4</sub>C oxidation kinetics, measured in the test series with porous Framatome pellets, dense ESK pellets and ESK powder. The results obtained with the CODEX pellets were comparable to those for the Framatome material.

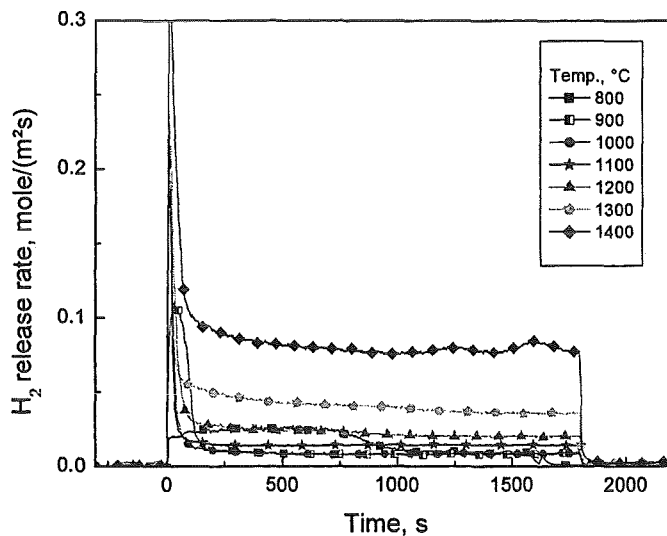


**Fig. 2:**  
Hydrogen release during  
isothermal oxidation in  
steam/Ar  
Framatome pellets (70 %td)

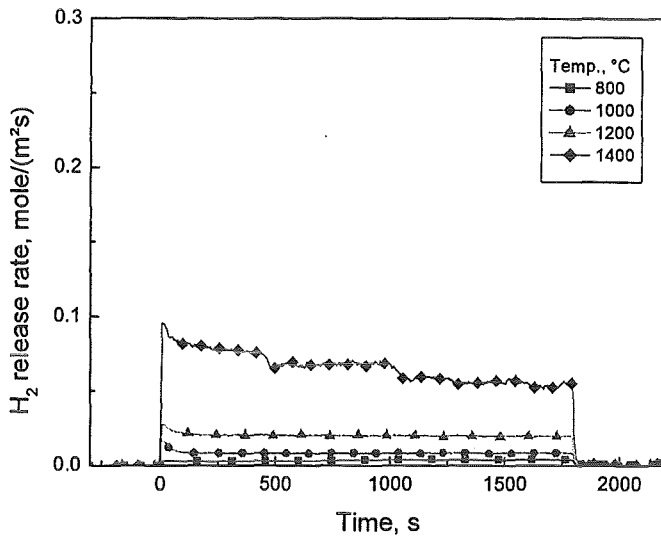


**Fig. 3:**

Hydrogen release during isothermal oxidation in steam/Ar

ESK pellets (95 %td)

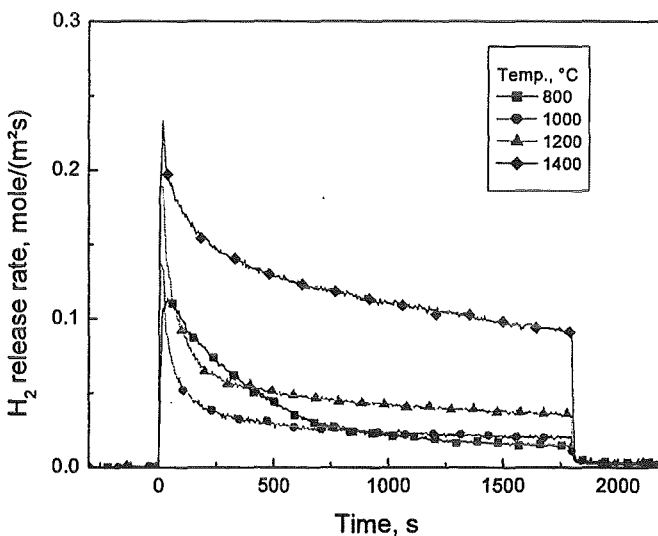


**Fig. 4:**

Hydrogen release during isothermal oxidation in steam/Ar

ESK powder

A peak hydrogen production (and thus oxidation rate) was measured at the initiation of the steam injection in all tests and could be explained by two processes. First, at that time, the bare surface of the specimens allows the direct access of the steam to the specimen. Later on, a liquid B<sub>2</sub>O<sub>3</sub> barrier scale is formed and the oxidation rate is determined by the diffusion of steam/oxygen and reaction products through that layer. The equilibrium thickness of the barrier scale is determined on the one hand by its parabolic growth and on the other hand by its reaction with steam to form volatile boric acids or by direct evaporation of the boron oxide. Second, the initial peak oxidation rate is most pronounced for the porous Framatome pellets. Obviously, the active surface strongly decreases during the initial phase of the tests, e.g., by

clogging of the pores. After that first phase, the oxidation rates are more or less constant and determined by the evaporation rate of the boron oxide scale from the (geometric) surface. The results obtained for the pellet specimens correspond to one another.

Oxidation rates were calculated based on the hydrogen release during the constant phase and the geometric surface of the specimens. A comparison of FZK BOX results (together with a fitted correlation for its temperature dependence between 800 and 1400 °C) with literature data is presented in [Fig. 5](#).

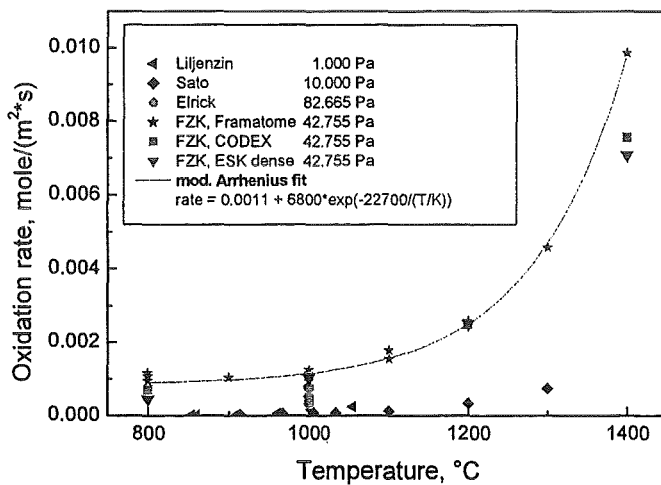


**Fig. 5:** Oxidation of B<sub>4</sub>C pellets in steam; comparison of new FZK results with literature data

The FZK data are significantly higher than most of the literature results. This can be explained by the different experimental conditions in the various experiments. The lower literature data were obtained based on the evaluation of integral mass changes at lower steam partial pressures.

[Figure 6](#) shows that the oxidation rate is strongly influenced by the steam injection rate due to its effect on the B<sub>2</sub>O<sub>3</sub> evaporation. In that BOX experiment, the steam injection was stepwise increased from 5 to 70 g/h at a constant Ar flow (50 l/h) at 1200 °C which led to a more intense oxidation of the specimen.

Summarising the results obtained in the BOX experiments, one can say:

- The understanding of the mechanism of the B<sub>4</sub>C oxidation has been considerably improved.
- Only negligible amounts of methane are released during high temperature oxidation of boron carbide.

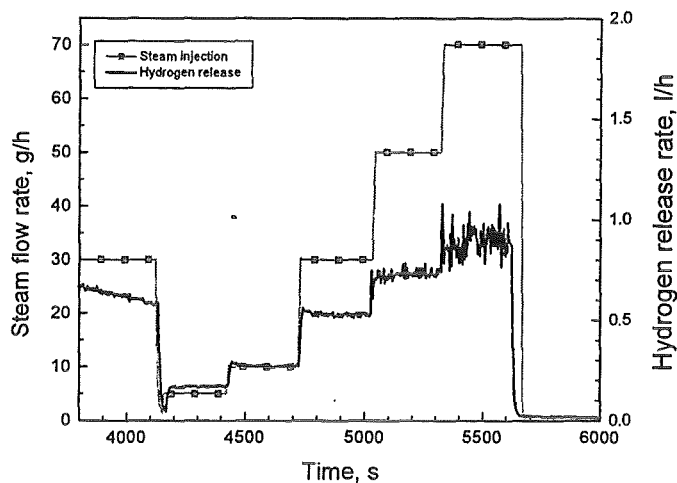


**Fig. 6:**

Oxidation of  $B_4C$  pellets in steam/Ar; dependence of oxidation kinetics on steam flow rates

- The overall oxidation rate is strongly influenced by the steam flow rate due to its effect on the  $B_2O_3$  evaporation.
- The porosity of the specimen strongly affects the oxidation rate at the initiation of the process, later on only the geometric surface does play a role.
- A large amount of data is now available for model development and validation.

The BOX activities within the EU COLOSS project will be completed by experiments on the oxidation of B and C containing melts. Furthermore, selected tests will be performed on request by modellers.

## References

- [1] B. Adroguer et al.  
Core loss during a severe accident (COLOSS)  
FISA-2001 Symp. on EU Research on Severe Accidents and Post-FISA-2001  
Workshop Session, Luxembourg, L, November 12-15, 2001
- [2] M. Steinbrück, A. Meier, U. Stegmaier, L. Steinbock, J. Stuckert  
Oxidation of  $B_4C$  at high temperatures.  
Jahrestagung Kerntechnik 2001, Dresden, 15.-17.Mai 2001 Bonn : INFORUM  
GmbH, 2001 S.193-96

#### IV. Degradation of B<sub>4</sub>C control rod segments

(M. Steinbrück, A. Meier, U. Stegmaier, L. Steinbock, J. Stuckert, IMF I)

##### **Abstract**

First test on the degradation of B<sub>4</sub>C control rod segments have been performed. The degradation is strongly influenced by the surrounding atmosphere. An outer ZrO<sub>2</sub> oxide scale prevents the control rod from early failure, in spite of the formation of eutectic melts inside the specimen.

##### **Zusammenfassung**

Ersten Versuchen haben gezeigt, dass die Degradation von B<sub>4</sub>C Kontrollstabsegmenten stark von der umgebenden Atmosphäre beeinflusst wird. Eine unter oxidierenden Bedingungen gebildete äußere ZrO<sub>2</sub>-Schicht verhindert ein frühzeitiges Versagen der Probe, trotz Bildung von eutektischen Schmelzen im Inneren.

To investigate the degradation and failure of the B<sub>4</sub>C control rod during temperature transients and to measure the oxidation of the produced B and C containing melts, first tests have been performed 1) with 1-pellet-size control rod segments in the BOX Rig and 2) with 10 cm long control rod segments in the single rod QUENCH Rig. Figure 1 shows two types of specimens for the BOX Rig tests. The specimens for the experiments in the QUENCH Rig were of the same design as the short ones with metal plugs, but filled with six B<sub>4</sub>C pellets. All materials are commercial control rod materials used in French PWRs.

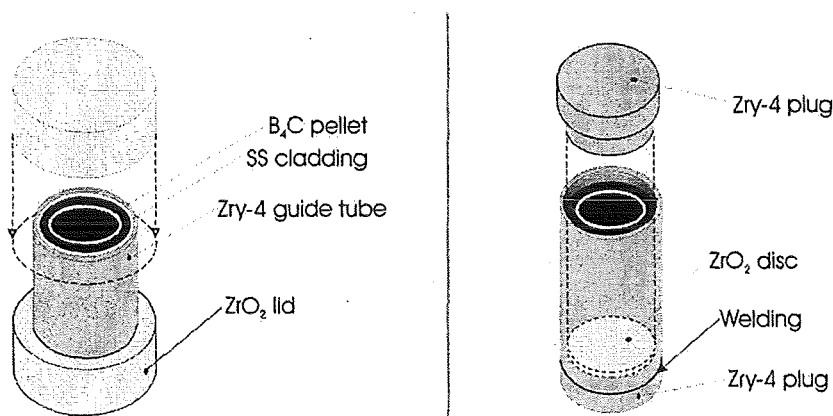


**Fig. 1:** B<sub>4</sub>C control rod segments for separate-effects tests; left: with ceramic caps, right: with metal plugs

The degradation of the control rod is strongly dependent on the atmosphere. This was seen in two transient tests with short CR specimens between 800 and 1500 °C; one in inert and one in oxidising atmosphere. The specimen completely degraded in inert gas due to the eutectic interactions between B<sub>4</sub>C and stainless steel cladding as well as between stainless steel and Zircaloy-4 guide tube (Fig. 2) whereas the specimen heated up in steam/Ar atmosphere did not fail due to the formation of a ZrO<sub>2</sub> scale at the outside of the guide tube.

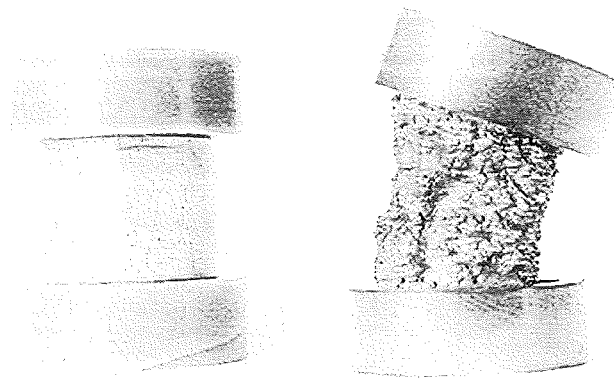


**Fig.2:** B<sub>4</sub>C control rod segments after transient tests between 800 and 1500 °C, left: in steam/Ar, right: in pure Argon atmosphere

In an isothermal test series, specimens with metal plugs were kept at temperatures from 800 to 1700 °C for one hour in steam/argon atmosphere. Up to 1000 °C, no interaction at all took place between the components. At 1200 °C, small interactions between B<sub>4</sub>C and SS as well as between SS and Zircaloy were observed. Significant melt formation was seen at 1400 °C and higher temperatures (Fig. 3).

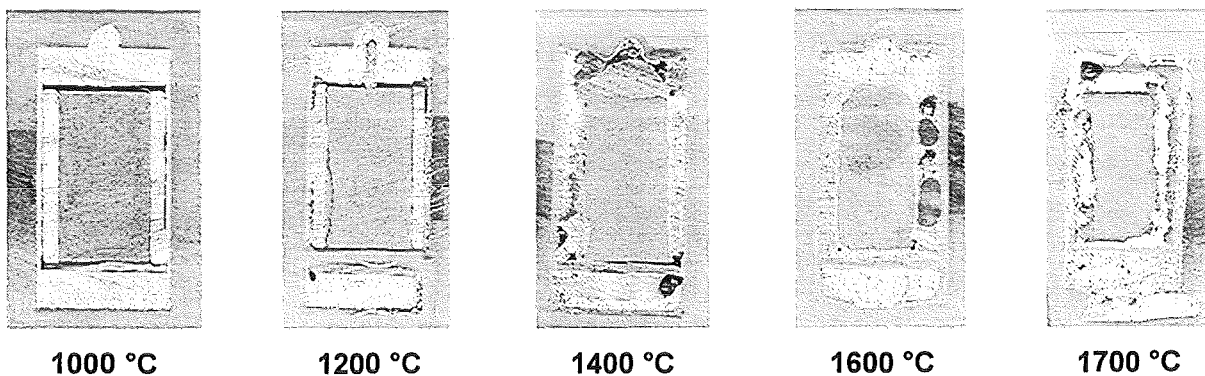


**Fig. 3:** Cross sections of short B<sub>4</sub>C control rod segments after isothermal tests for one hour at the specified temperature

The formation of an outer  $ZrO_2$  scale prevented the specimens from early failure. Only in the 1700 °C test, the sample failed after ca. 40 minutes accompanied by a strong formation of CO and  $CO_2$  and additional hydrogen, as can be seen in Fig. 4.

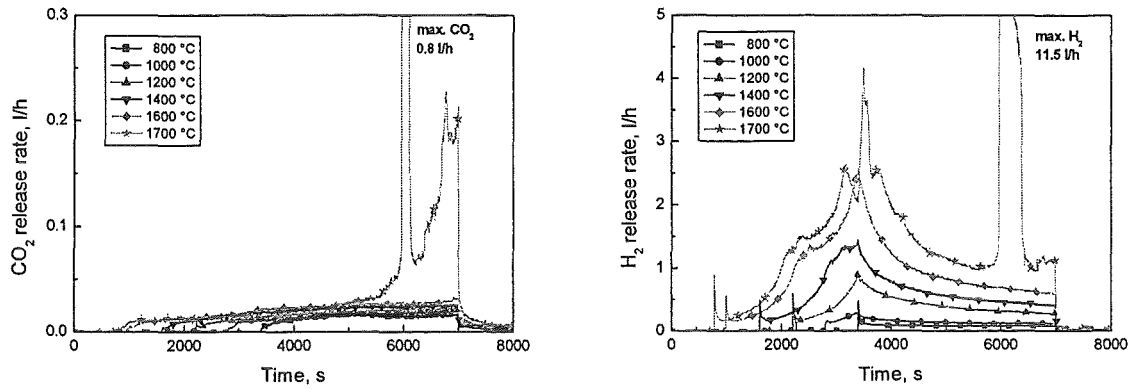


**Fig. 4:** Gas release during isothermal oxidation of short  $B_4C$  control rod segments

Future work will be devoted to the metallographic analysis of the specimens and further tests with longer segments under various boundary conditions.

V. Einzeleffekt-Untersuchungen zur B<sub>4</sub>C-Oxidation und ihrer modellmäßigen Beschreibung

(W. Krauss, G. Schanz, H. Steiner, M. Heck, IMF III)

**Zusammenfassung**

Das experimentelle Programm zu Einzeleffekt-Untersuchungen wurde weitergeführt mit den Schwerpunkten Untersuchung des Oxidationsverhaltens von B<sub>4</sub>C und Modellentwicklung zur mechanistischen Beschreibung der auftretenden Phänomene und Bestimmung der Reaktionskinetik. Die Tests zur B<sub>4</sub>C Oxidation einschließlich der Untersuchung der dabei auftretenden Reaktionsprodukte wie z.B. B<sub>2</sub>O<sub>3</sub> erfolgten bei isothermer Versuchsführung im Temperaturbereich bis 1300°C in der Thermowaage in Ar, Ar/O<sub>2</sub> und Ar-H<sub>2</sub>O gesättigter Atmosphäre. Diese Arbeiten wurden begleitend zum laufenden EU-Projekt COLOSS durchgeführt [1]. Sie ergänzen parallel dazu ausgeführte Untersuchungen in den Anlagen BOX-Rig und QUENCH-Rig des IMF I, decken jedoch andere Atmosphärenbedingungen ab und liefern auch bei niedrigen Temperaturen (500 - 1200 °C) über das Massensignal zusätzliche und für die Modellentwicklung notwendige Datensätze. Diese Einzeleffekt-Untersuchungen einschließlich ihrer modellmäßigen Beschreibung und kinetischen Auswertung befassen sich mit den aktuell interessierenden Störfall-Bedingungen zur Oxidation von B<sub>4</sub>C und B<sub>4</sub>C / Cr-Ni-Stahl / Zircaloy hinsichtlich der Produktion von Methan und der Problematik Jodchemie. Des weiteren dienen die Einzeleffekt-Untersuchungen der Vorbereitung und Auswertung von Integralexperimenten (QUENCH, CODEX, PHEBUS - Tests) und dem Aufbau einer internationalen Werkstoffdatenbasis.

Das Reaktionsverhalten von B<sub>4</sub>C wird durch mehrere konkurrierende Reaktionsmechanismen bestimmt, die zur Ausbildung temperaturabhängiger Regime führen. Der diese Regime definierende Faktor ist die Bildung von passivierenden B<sub>2</sub>O<sub>3</sub> Schichten und das stark temperatur- und atmosphärenabhängige Verdampfungsverhalten von B<sub>2</sub>O<sub>3</sub> einschließlich der Bildung von Borsäure und deren Transport im Gasraum.

Bei niederen Temperaturen (800 °C) und Atmosphären mit geringem Dampfgehalt (Ar/O<sub>2</sub>, Ar-H<sub>2</sub>O gesättigt bei 20 °C) folgt die Oxidation einem parabolischen Zeitgesetz und bei den TG-Tests tritt eine kontinuierliche Massenzunahme mit fallender Zuwachsrates auf. Dagegen liegt oberhalb von 1100 °C in dampfgesättigter Ar Atmosphäre fast keine Passivschicht mehr vor und es wird eine Massenabnahme

mit konstanter Rate, d.h. stationäre Oxidation von  $B_4C$  und Abtransport von Borsäure, beobachtet. Komplexere Reaktionspfade treten auf, wenn statt dichter  $B_4C$  Formkörper poröse, reaktortypische Pellets in den Tests verwendet werden.

Die Modellentwicklung zur Beschreibung und Interpretation der  $B_4C$  Oxidation dichter Formkörper wurde aufgenommen unter der Annahme, dass diese Reaktion überwiegend durch die beiden, sowohl temperaturabhängigen als auch atmosphäre-abhängigen, Teilprozesse der  $B_2O_3$  Schichtbildung durch  $O_2$  Diffusion (parabolische Kinetik) und der Verdampfung von  $B_2O_3$  bzw. gebildeter Borsäure (lineare Kinetik) bestimmt wird. Bereits mit dieser einfachen Annahme konnten die Teilreaktionen eindeutig interpretiert und die reaktionskinetischen Parameter aus den transienten und isothermen Tests bestimmt werden. Des Weiteren lassen sich damit sowohl TG und BOX Tests simulieren und somit auch verschiedene Testmethoden miteinander vergleichen. Durch Integration der Reaktionsgleichgewichte lassen sich auch die Anteile der gebildeten gasförmigen Reaktionsprodukte wie  $H_2$  oder  $CO/CO_2$  bestimmen.

Eine Übertragung der  $B_4C$  Reaktionsabläufe auf Bündelversuche (QUENCH-Tests) ist neben dem Übergang auf reaktortypische Reaktionsoberflächen naheliegendes Ziel. Dazu sind entsprechende Einzelleffekt-Tests auszuführen, so dass die notwendige Datenbasis (Poreneffekte, Atmosphärenzusammensetzung, Strömungseinfluss) bereitsteht und die Modellansätze verifiziert werden können.

### **Introduction**

The separate-effects test program on the oxidation of boron carbide, using the Thermal-balance (TG) test system, was continued with extension to higher test temperatures and by including additional modelling work for better understanding of the ongoing oxidation mechanisms and more detailed evaluation of test data concerning reaction kinetics.

The parameters for the TG test series were oriented on the requirements of the COLOSS project and on the demands for interpretation of the complex oxidation behaviour of  $B_4C$  and evaluation of the test results by modelling. The test series included, besides the examination of  $B_4C$  reactions in wet atmospheres (steam partial pressure up to 0.2 bar), tests in non-prototypical  $Ar/O_2$  atmosphere as well as the examination of basic components as e.g.  $B_2O_3$  under different environment conditions. The advantage of the use of the thermal balance technique is the simultane-

ous measurement of sample temperature and mass changes in time dependence under transient as well as under isothermal conditions. Most of the tests were performed with a heating rate of 20 K/min. The used atmospheres were pure Ar, Ar/O<sub>2</sub> with a volume ratio of 80 to 20, and 'wet' Ar, realised by saturation in a water bath at temperatures between 20 and 60 °C.

**Evaporation and oxidation tests in dry Ar or Ar/O<sub>2</sub> atmosphere:**

Tests on the oxidation of B<sub>4</sub>C and the evaporation of B<sub>2</sub>O<sub>3</sub> were performed in flowing dry Ar or Ar/O<sub>2</sub>. The interests in these test series were to analyse the material behaviour under simple and different environment conditions, to interpret the observed reaction paths and mechanisms detected in wet atmospheres, or to reduce the influence of secondary effects to a negligible level.

Fig. 1a shows the mass change signal of a dense B<sub>4</sub>C pellet which was isothermally oxidised at 800 °C in flowing Ar/O<sub>2</sub> after transient heating. The mass increase

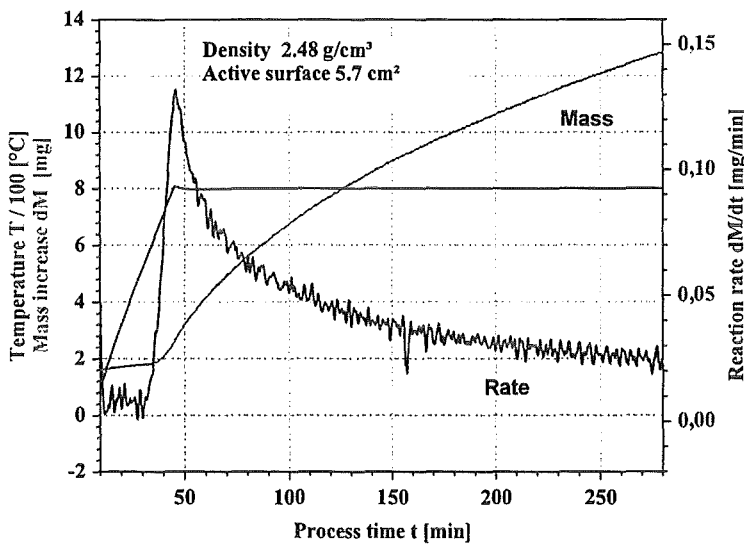


**Fig. 1a:** Oxidation of dense B<sub>4</sub>C in Ar/O<sub>2</sub> atmosphere at 800 °C after transient heating. During the whole test duration a continuous mass increase was detected, however with a decreasing reaction rate.

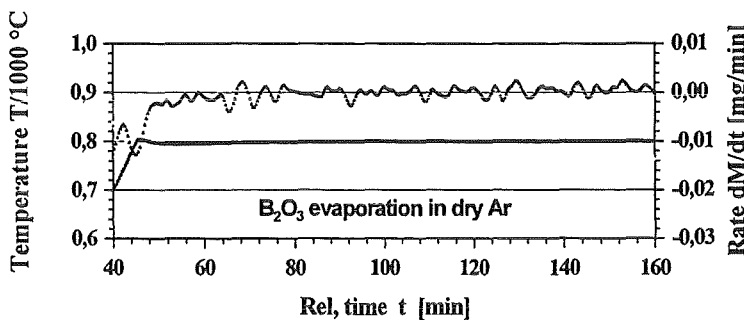


**Fig. 1b:** Evaporation of B<sub>2</sub>O<sub>3</sub> in flowing dry Ar atmosphere. During a test period of 2 hours no significant mass change by evaporation could be detected, as indicated by the rate signal equal to zero.

represents the amount of formed  $B_2O_3$  minus C loss by  $CO/CO_2$  formation and the knowledge, that  $B_2O_3$  evaporation is negligible at 800 °C. The corresponding TG test on  $B_2O_3$  evaporation was conducted under similar conditions and is given in Fig. 1b.

### Oxidation tests in wet (steam containing) Ar atmosphere

Oxidation tests on  $B_4C$  in wet Ar atmosphere were performed with 3 different types of samples a)  $B_4C$  powder in  $Y_2O_3$  crucibles, b) porous  $B_4C$  pellets (reactor grade, Framatome), and c) dense  $B_4C$  pellets. Powder and reactor grade samples show at least during transient heating a complex behaviour (several maxima in rate signal) compared to dense specimens. At the moment we assume that this differences are caused by surface effects. In contrast to these test pieces dense  $B_4C$  samples exhibit more simple oxidation behaviour which can be correlated to basic reaction mechanisms and paths.

The whole test series with dense samples oxidising in wet Ar atmospheres ( $H_2O$ -saturated Ar gas with  $T \leq 60$  °C ) show the same characteristic of first a mass increase to a maximum value and second a linear mass decrease for the rest of the test duration. The maximum can lie in the transient or isothermal test segment depending on test temperature and environment conditions. Fig. 2 shows the TG-diagram (mass and rate signal) for a reaction test at 1000 °C. The mass curve profile can be explained by two counteracting mechanisms the first is the formation of a passivating scale and the second the evaporation of  $B_2O_3$  scale in wet environment with a constant rate. The last one will govern the reaction at stationary conditions.

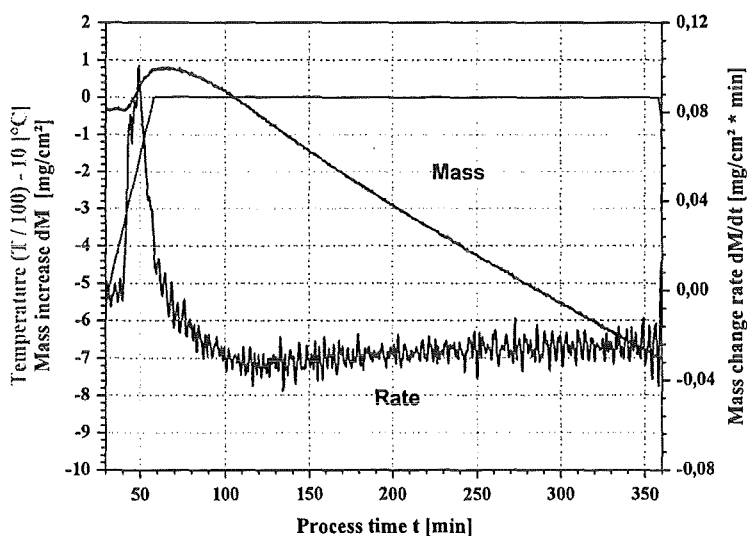


**Fig. 2:** Reaction behaviour of dense  $B_4C$  in wet Ar atmosphere. The Ar gas was saturated by  $H_2O$  in a water bath with 60 °C. The mass signal of the oxidising sample passes a maximum shortly after starting the isothermal test period.

## Model development

The test series performed with the TG-system and the BOX rig indicated that evaluation of reaction kinetics parameters for the complex B<sub>4</sub>C oxidation behaviour as well as comparison of test results obtained by different test methods will be rather difficult or insufficient without modelling support. Caused by these experience the SET program was extended by including model development. Only by modelling support a good exploration of the whole potential of the SET tests as well as an effective transfer of the SET results to bundle tests will be possible.

In the first approach modelling development was started by assuming that parabolic B<sub>2</sub>O<sub>3</sub> scale formation and linear B<sub>2</sub>O<sub>3</sub> evaporation are superposed and will govern the B<sub>4</sub>C oxidation. The used differential form is:

$$\frac{dm_{OX}}{dt} = \frac{a}{m_{OX}} - b$$

with  $m_{ox}$  = specific mass of oxide film (g/cm<sup>2</sup>)

$$a = A_0 * e^{-A/T}$$

$$b = B_0 * e^{-B/T}$$

However, the detailed evaluation of the SET data shows, that b has to be replaced by a more general form e.g.  $b = f(T, v_{gas}, C_{H2O})$

A preliminary evaluation of the TG tests leads to the following value for a:

$$a = 0.102 * 10^{-3} \exp(-1.298 * 10^4/T)$$

and for parameter b, extracted from BOX rig tests, of:

$$b = 9.612 * 10^{-4} \exp(-5.19 * 10^3/T) \quad \text{for } T < 1430 \text{ K}$$

$$b = 3.62 * 10^{-0} \exp(-1.722 * 10^4/T) \quad \text{for } T > 1430 \text{ K}$$

With this approach a simulation of BOX rig and TG tests was performed. Fig. 3 gives a comparison of an experimental and simulated TG test at 1300 °C.

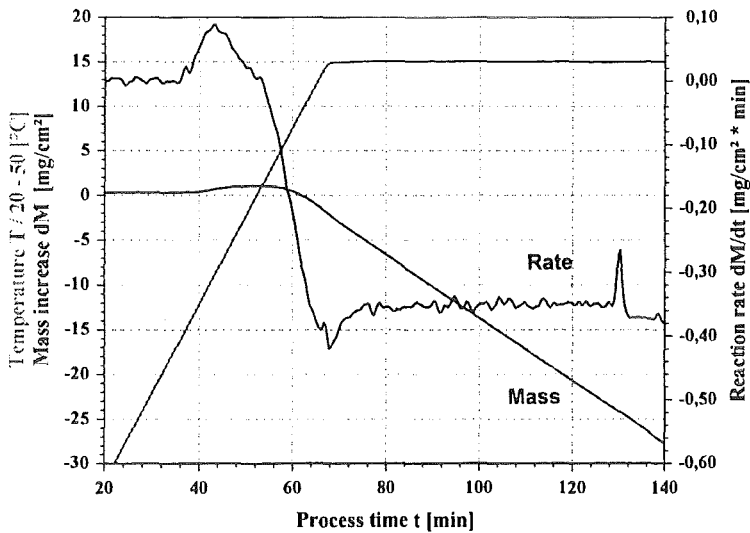
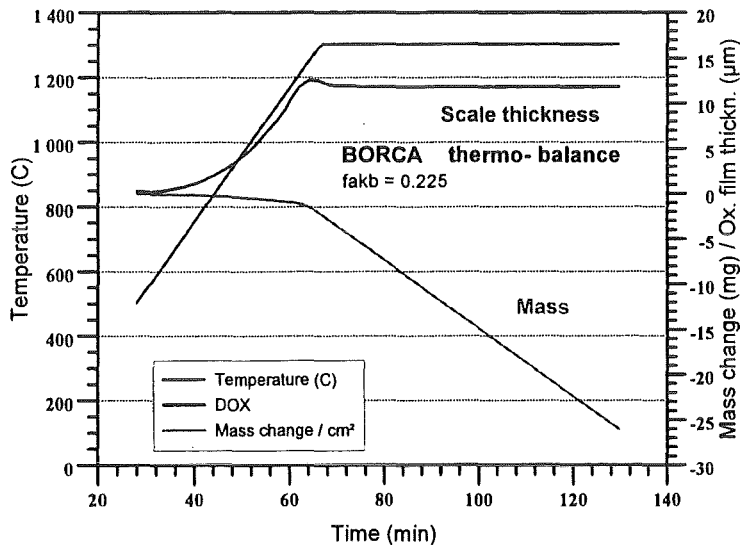


**Fig. 3:** Comparison of thermo-balance test with developed BORCA model for oxidation behaviour of dense  $B_4C$  in wet Ar atmosphere at  $1300\text{ }^\circ\text{C}$ . Measured and simulated mass changes are in good agreement, which can be deduced from the same slopes of the mass curves.



### Reactions under special environment conditions

TG tests performed with varied  $H_2O$  saturation levels in the Ar atmosphere show that  $B_2O_3$  evaporation increases with steam concentration. Both, TG and BOX rig experiments show similar behaviour. However, a modelling of this dependency has not been performed up to yet.

In contrast to the oxidation of  $B_4C$  in steam atmospheres, where a constant scale thickness is formed by the equilibrium between oxidation and evaporation, this equilibrium can not be reached in Ar/ $O_2$  atmosphere at high temperatures. Under these conditions (perhaps also under extreme steam starvation conditions) the formed scales are too thick and a flow down of the scale appears (Fig. 4).

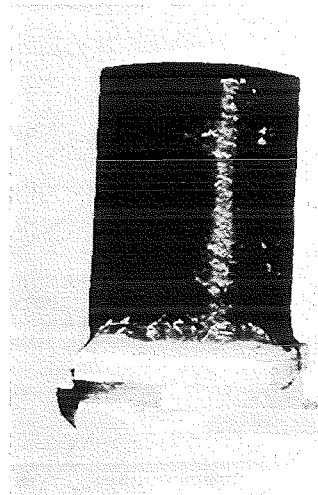
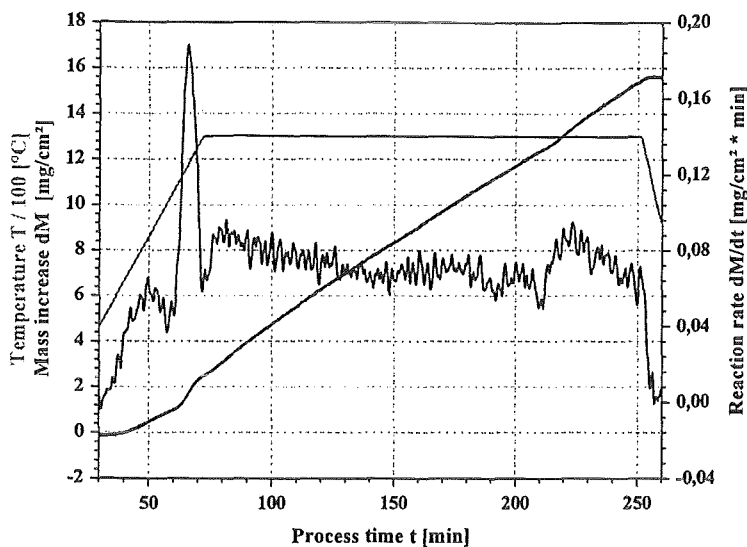


**Fig. 4:** Oxidation behaviour of  $B_4C$  at  $1300\text{ }^\circ\text{C}$  in  $\text{Ar}/\text{O}_2$  atmosphere. A continuous mass increase takes place caused by formation of  $B_2O_3$  and its flowing down to the sample support. The glassy phase can be seen on top of the white support piece. Sample dimensions:  $\varnothing = 10.51\text{ mm}$ ,  $h = 14.5\text{ mm}$ ,  $\rho = 98\text{ \% TD}$

#### Summarised results obtained from TG tests and modelling

- The  $B_4C$  oxidation is much more sensitive to environment conditions compared e.g. to  $ZrO_2$  oxidation.
- Simple test conditions (not severe accident typical) are necessary to identify counteracting mechanisms for determination of reaction kinetics.
- In steam containing atmospheres the oxidation rate of  $B_4C$  is governed by the evaporation of  $B_2O_3$ , the formation of boric acid and the transport in the vapour phase.
- The TG and BOX tests show similar and consistent reaction behaviour.
- Both SET methods are necessary by providing complementary results and a broader data base.
- Some of the occurring reaction mechanisms could be identified and separated.
- Modelling support is necessary for determination of reaction kinetics parameters and for verification of mechanisms.
- First modelling tools were developed and can describe, both, TG and BOX results.

- The inclusion of modelling efforts, performed in parallel to the experimental programs, has contributed to an advanced interpretation of the phenomena and the determination of the kinetics data.

TG tests will be continued with respect to complete the produced reliable data set on B<sub>4</sub>C oxidation and to provide additional results required by modelling.

The work on model development will continue with the interest of transferring the knowledge to bundle tests.

## References

- [1] B. Adroguer et al., Core loss during a severe accident, Proc. FISA-2001 EU research in reactor safety, Luxembourg, 12 - 14 Nov. 2001, p 350.

VI. Modelling of boron carbide oxidation and boric acid formation  
(H. Steiner, IMF III; M. Steinbrück, IMF I)

**Abstract**

An empirical parilinear model for boron carbide oxidation ( $B_2O_3$ ) and the ensuing boric acid formation has been developed for forced convective flow conditions. It depends on two rate parameters  $a$  and  $b$ , which could be determined with the help of experimental data from the thermo-balance and BOX tests done at IMF. The main implication of the model is the existence of an equilibrium oxide film thickness, determined by the loss rate due to boric acid formation. Calculations with the recently developed code BORCA gave encouraging results.

**Zusammenfassung**

Es wurde ein empirisches paralineares Modell zur Beschreibung der Oxidation von Borkarbid ( $B_2O_3$ ) und der darauf folgenden Bildung von Borsäure entwickelt unter der Randbedingung erzwungener Konvektionsströmung. Das Modell hängt von den beiden Parametern  $a$  und  $b$  ab, welche mit Hilfe von experimentellen Daten aus Tests am IMF in der Thermowaage und in der BOX Anlage bestimmt wurden. Das neue Modell bedingt, dass sich nach einer gewissen Zeit ein Gleichgewichtswert bei der Oxidschichtdicke einstellt, welcher im wesentlichen von der Verlustrate  $b$  durch Borsäureproduktion abhängt. Rechnungen mit dem neu entwickelten Rechencode BORCA brachten ermutigende Ergebnisse.

**Introduction**

Different processes contribute to the formation of oxide films on  $B_4C$  samples, like diffusion of boron and carbon ions, the uptake of oxygen, and formation and release processes as oxide vaporisation and boric acid formation. Rate determining are most probably the diffusion of boron ions and volatile boric acid formation under wet atmosphere conditions.

In the following we will develop a model for high density boron carbide samples, which depends on two rate parameters. In case of low density material the so-called pore effect is observed. Due to the presence of open porosity the active surface of the sample is considerably increased. But the boundary conditions for oxidation and boric acid formation within the pores may, of course, be also different from that

prevailing on the surface. In any case, we need a detailed knowledge of the open porosity, like porosity histograms if we want to describe the oxidation within the open pores. For the time being, this information is not available.

### Model development and first results

Thus, we assume that the evolution of the specific mass of the oxide film  $m^{ox}$  can be described by the following rate equation:

$$\frac{dm^{ox}}{dt} = \frac{a}{m^{ox}} - b \quad (1)$$

$$m^{ox} = \rho^{ox} \delta^{ox} \quad (2)$$

whereas the production rate of boric acid is given as:

$$\frac{dm^{b.a.}}{dt} = f_{ox/b.a.} F^{act} b \quad (3)$$

$\rho^{ox}$ = oxide density	$F^{act}$ = active surface of the sample
$\delta^{ox}$ = oxide film thickness	$f_{ox/b.a.}$ = mass conversion factor

The equations (1) and (3) are viewed to hold in case of forced convection flow conditions. If we have stagnant flow conditions, as might be the case in pores, the rate should be determined by the boric acid partial pressure. According to the mass action law, this parameter should tend to an equilibrium value determined by the steam partial pressure:

$$K(T) = \frac{P_{b.a.}^{eq^2}}{P_{H_2O} P_{B_2O_3}} \quad (4)$$

$$\frac{dm^{ox}}{dt} = k(T) (p_{b.a.}^{eq} - p_{b.a.}) \quad (5)$$

No experimental data are available for the validation of equation (5). Therefore the non-prototypical situation of stagnant flow condition is not further investigated.

The first term on the right-hand side of equation (1) describes the effect of the diffusion processes leading to the formation of a  $B_2O_3$  layer and the second term is a

loss rate, which represents either oxide vaporization in dry atmosphere or boric acid formation in wet atmosphere.

The rate parameters  $a$  and  $b$  depend certainly on the temperature but probably also on other test parameters like the steam flow rate, but they should not depend explicitly on the time  $t$ . The differential equation (1) has only for  $b = 0$  a parabolic solution. But one important feature of the solutions can easily be deduced, namely that the oxide film thickness tends to a limiting value  $\delta_{lim}^{ox}$ , which is determined by the condition:

$$\frac{dm^{ox}}{dt} = 0. \quad (6)$$

and  $\delta_{lim}^{ox}$  is given as:

$$\delta_{lim}^{ox} = \frac{a}{b p^{ox}} \quad (7)$$

In this case the mass increase due to diffusion is just balanced by the losses and the oxide film is in an equilibrium condition.

Thus, the hydrogen production rate, for example, will become constant. The equilibrium value  $\delta_{lim}^{ox}$  is approached asymptotically, but depending on its value, the hydrogen production rate becomes fairly constant after a certain lapse of time. In this way the rate parameter  $b$  is determined by the oxidation rates measured by different authors under wet conditions (see Table 1). Of course, under dry atmosphere we would obtain other correlations for this parameter.

The rate parameter  $a$  could be determined with the help of a test in the thermo-balance under dry atmosphere with a temperature ramp going up to 800 °C. It was found that oxide vaporisation was unimportant under these conditions and the measured mass increase was fairly parabolic. Boric acid seems to be a volatile substance and in view of the rather high temperatures, we do not expect that a film of boric acid is deposited on the oxide surface. Therefore we hold that the rate parameter  $a$  is also valid under wet conditions. But, of course, experimental evidence in this respect would be very helpful.

In order to apply the newly developed model in simulations of tests done with boron carbide samples, the computer code BORCA was developed. In the following we will

discuss some results of such code calculations. As a first point, results for  $\delta_{lim}^{ox}$  as obtained for the oxidation rates of different authors are plotted in Fig. 1 versus the temperature T. The big differences in film thickness are due to the differences in oxidation rates. But at temperatures above 1700 to 1800 K the curves based on data of M. Steinbrueck /1/ and Liljenzin-Omtweldt /4/ come fairly near together. There are indications from the literature /2/ that under certain test conditions no oxide film is formed for temperatures under 600 to 700 °C. Such a behaviour may be rather well simulated by the curve due to the data from the BOX tests done at FZK but not by the other two curves. It remains to be clarified experimentally, under what conditions of steam partial pressure and/or steam injection rates the formation of oxide films is indeed suppressed at low temperatures. Also the differences in the oxidation rates seem to be due to different conditions in these test parameters.

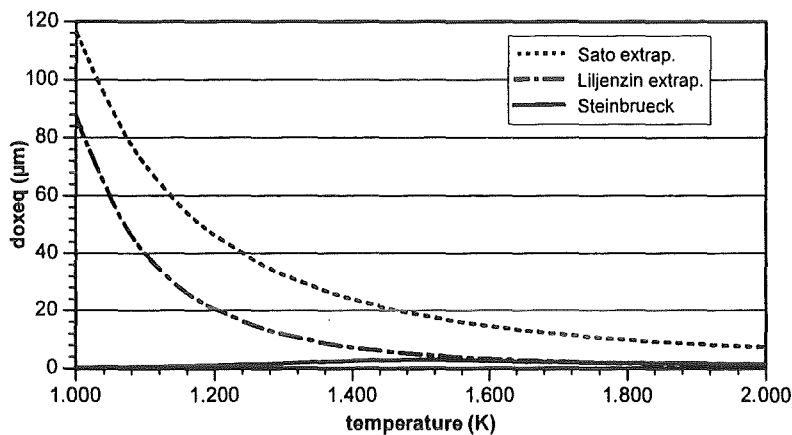


**Fig. 1:** Equilibrium values of oxide film thickness

In the FZK BOX tests the influence of the steam injection rate has been investigated with the help of a test where the Ar flow has been kept constant and the steam injection was varied. In Fig. 2 we have plotted the oxidation rate versus the steam injection rate as obtained from this BOX test. Thus, up to values of 70g/h for the steam injection rate, the oxidation rate increases in a fairly linear manner. Therefore the rate parameter b can be represented in the following way as a function of the steam flow rate:

$$b = b_0 + b_1 \dot{m}_{st} \quad (8)$$

The term  $b_0$  is caused by gas diffusion and by natural convection effects, whereas  $b_1$  is due to forced convection. Unfortunately there are only experimental data for 1200 C. Therefore we cannot establish a correlation for  $b_0$ . But even if such a correlation were available, it could not be applied to other experimental environments, as this parameter depends on temperature gradients and on the geometrical conditions of the test setup.

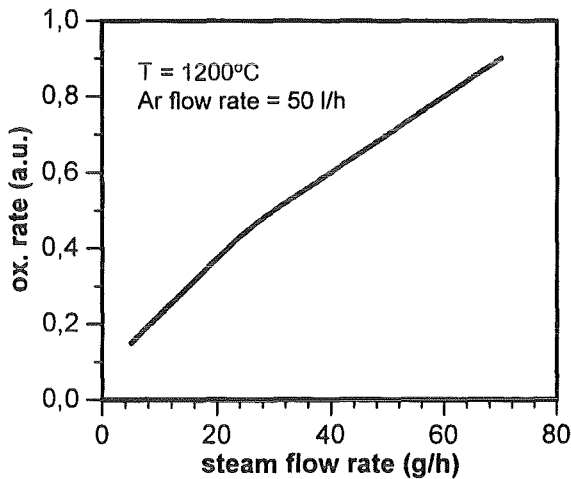


Fig. 2: Oxidation rate versus steam flow rate

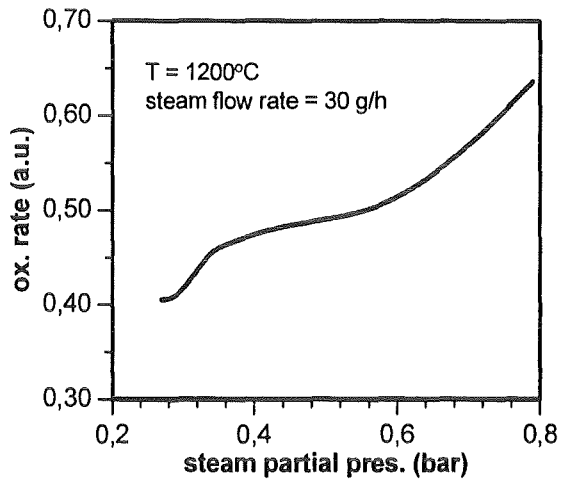


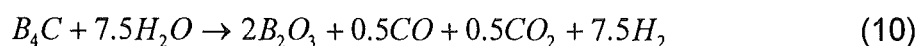
Fig. 3: Oxidation rate versus steam partial pressure

The rate parameter  $b$  depends also on the steam partial pressure  $p_{st}$ , as demonstrated by the data shown in Fig.3, which have been obtained in a BOX test done under a constant steam flow rate and varied Ar flow leading to a variation of the steam partial pressure. Thus, if we neglect the term  $b_0$  the rate parameter  $b$  can tentatively be approximated by:

$$b = b_1 \dot{m}_{st} (1 + 0.86 (p_{st} - 0.43)) \quad (9)$$

For the time being, we have experimental data only for 1200 C. In order to substantiate the proposed correlations tests at other temperatures would be very helpful.

The oxidation of boron carbide in a steam environment is a complex process. But the experimental data obtained in the FZK BOX tests and also data from QUENCH-07 suggest that  $CH_4$  production is rather unimportant and can be neglected to a first approximation. Therefore we take into account only the main reactions at high temperatures:



In equation (10) we have assumed without much loss of generality that CO and CO<sub>2</sub> are produced at equal parts. This assumption has no influence on the hydrogen production rate. We have also assumed that all carbon, which is liberated upon boron oxidation, is released quantitatively from the sample.

In Fig. 4 are plotted the production rates of H<sub>2</sub>, CO, and CO<sub>2</sub> as obtained with the code BORCA together with the evolution of the mass change of a steady-state BOX test done at 1000 C with a high density sample. The production rates reach their stationary values after about 50 s. The transient phase at the beginning is due to the build-up of the oxide film. The high rates are a consequence of the fact that a rather low value of the initial oxide film thickness has been taken in the calculation. Fig. 5 shows a comparison of measured and calculated values of the overall mass change on high density samples at the end of steady-state BOX tests. The agreement is rather convincing. The code BORCA predicts values of the mass change also at higher temperatures. This could be checked with the help of further tests.

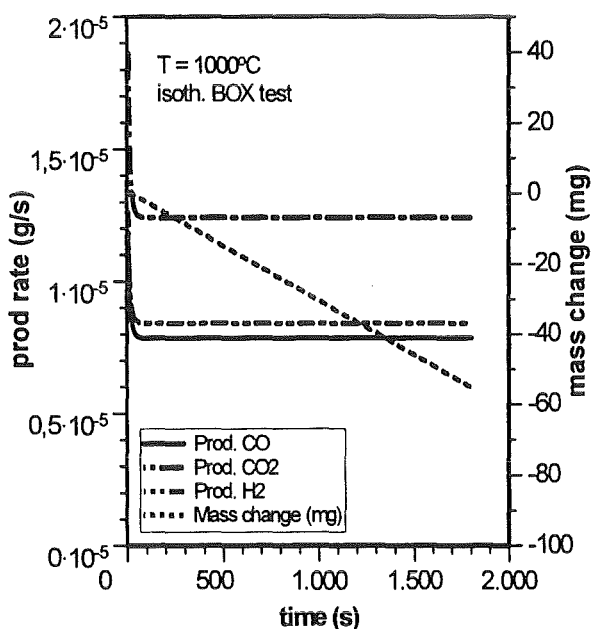


Fig. 4: Evolution of production rates and mass change of a high density sample for a BOX test at 1000 C

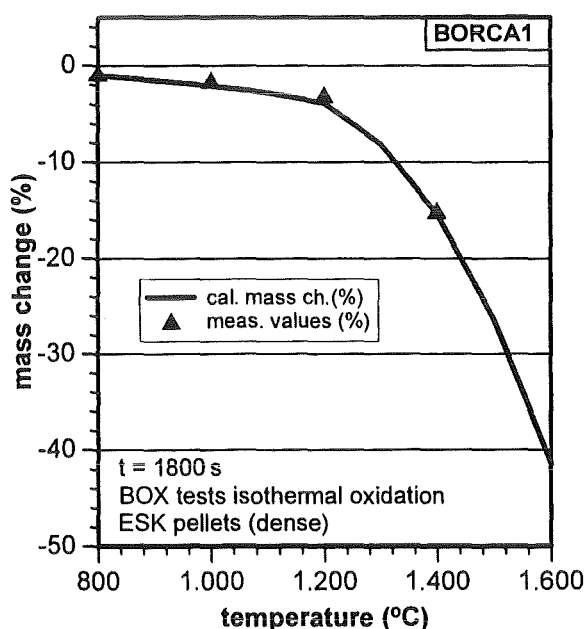


Fig. 5: Mass change of high density samples at the end of steady-state tests versus the temperature

## Conclusion

The recently developed code BORCA, where a parolinear model for the oxidation of boron carbide is implemented, gives rather encouraging simulations of steady-state BOX tests done at IMF I with high density samples. The extrapolation to other test conditions could easily be done. With such tests the code could be further validated.

## References

- /1/ M. Steinbrueck, et al, Oxidation of B4C at high temperatures, Contribution to the 6<sup>th</sup> Intern. QUENCH Workshop, Oct. 2000
- /2/ L.M. Litz and R.A. Mercuri, Oxidation of boron carbide by air, water and air-water mixtures at elevated temperatures, Journ. of the electrochemical Soc. Vol.100 No 8, 1963
- /3/ T. Sato, et al, Oxidation of nonoxide Ceramics by Water Vapour at High Temperatures, Fac. Eng. Tohoku Univ., Sendai, Japan. Zairo (1988), 37(412), 77-82
- /4/ R. Alenljung, et al, The influence of chemistry on melt core accidents, Final report of the NKA Project ATKI-150, Sep. 1990
- /5/ W. Krauss, G. Schanz,  
Thermogravimetric analysis towards B4C oxidation, Contribution to the 6<sup>th</sup> Intern. QUENCH Workshop, Oct. 2000

**Table 1:** Different correlations for the rate parameters a and b

$a = 0.102E-3 * e^{-1.298E4/T}$	W. Krauss /5/ thermo-balance, dry atmosphere
for $T \leq 1430$ K :	} M. Steinbrück /1/ BOX tests, wet atmosphere
$b = 9.612E-4 * e^{-5.19E3/T}$	
for $T \geq 1430$ K :	
$b = 3.62 * e^{-1.722E4/T}$	
$b = 1.429 * e^{-1.852E4/T}$	T. Sato /3/ wet atmosphere
$b = 4.57E1 * e^{-2.17E4/T}$	Liljenzin /4/ wet atmosphere

T in K, a in g<sup>2</sup>/cm<sup>4</sup>/s, b in g/cm<sup>2</sup>/s

- VII. Cool-down tests in various atmospheres on the thermal and thermo-mechanical behaviour of Zircaloy-4 cladding  
(J. Stuckert, M. Steinbrück, U. Stegmaier, IMF I; A. Palagin, IBRAE Moscow)

### **Abstract**

Results of recent separate-effects tests within the scope of the QUENCH Program are presented. The aim of the work was the validation of heat transfer module of SVECHA code. The influence of the different gas mixture in the gas channel on the temporary temperature development of the cladding tube surface was investigated. The results of these tests allow also the calculation of the emissivity of metallic and oxidised Zircaloy tube surface.

### **Zusammenfassung**

Es werden die Resultate von neuen Einzeleffektuntersuchungen innerhalb des QUENCH-Programms dargestellt. Das Ziel der Arbeit war die Validierung des Wärmeübertragungsmoduls des SVECHA-Codes. Es wurde der Einfluss der unterschiedlichen Gasmischungen im Gaskanal auf die zeitliche Temperaturentwicklung der Hüllrohroberfläche untersucht. Die Resultate dieser Versuche haben auch die Bestimmung der Emissivität der metallischen und oxidierten Rohroberfläche ermöglicht.

### **Test performance and results**

For the modelling of the cladding tube behaviour at high temperatures the exact description of gas mixture properties, the cladding surface emissivity properties and thermo-mechanical properties of cladding are very important. For a clear understanding of those phenomena a series of 30 cool-down tests in inert, oxidised and hydrogen-contented atmospheres was performed.

The experimental facility used for the cool-down tests was FZK QUENCH rig. The empty rod specimen (sometimes filled with ZrO<sub>2</sub> pellets) of a length of 150 mm (non-oxidised Zry rod) or 105 mm (oxidised Zry rod) was suspended inside a quartz rod.

In the case of tests without oxidation the Zry rod was heated up to a certain temperature (1200 °C measured by the TC located at the outer surface in the middle of the rod; temperature at the upper and lower ends was smaller by 50-100 degrees),

kept at this temperature for 60 second and, after switching off the power, cooled down in Argon flow (102 l/h or 0.046 g/s).

In the case of tests with oxidation the Zry rod was pre-oxidised at the temperatures 1300-1500 °C during different time intervals in an Argon/Oxygen mixture (30/6 l/h or 0.0135/0.00216 g/s for first series and 20/20 l/h or 0.009/0.0072 g/s for second series) with resulting oxide thickness from 4 µm to 40 µm (first test series) and from 60 µm to 600 µm (second series). The Zry rod was cooled down after switching off the power without change of the gas mixture. The Zry tube for the tests from the first series was hermetically sealed, in the second series the tube had the hole (diameter 1 mm) on the bottom.

The temperature of the rod outer surface was continuously measured. In the case of non-oxidised rod tests three Pt/Rh TCs located at 20 mm, 75 mm and 130 mm elevations were used; TCs were insulated from metallic cladding surface by means of a thin Rhenium film.

In the case of oxidised rod tests one TC located in the middle of the rod (52 mm) was used. Before the tests the specimens have been pre-oxidised to a small extent to prevent eutectic interactions between thermocouples and cladding surface. This thin oxide scale was also formed in the QUENCH rig by exposing specimens with temperature 1000°C in argon/oxygen (40/10 l/h or 0.018/0.0036 g/s) atmosphere for one minute.

The cool-down process was filmed during each test. The films were digitised and synchronised on the time point of cool-down beginning for comparison of different tests.

The [Fig. 1](#) shows the comparison of three cool-down tests performed in argon, argon-hydrogen and helium-hydrogen gas mixtures. In the case of helium-hydrogen cooling the cladding cool-downs faster because of higher thermal conductivity of helium ( $\lambda_{\text{He}}=429.9 \text{ mW/m}\cdot\text{K}$  and  $\lambda_{\text{Ar}}=49.2 \text{ mW/m}\cdot\text{K}$  at 1000°C). At the same time, there is an increase of the hydrogen solubility in Zircaloy. The influence of different axial distribution of hydrogen uptake is shown in [Fig. 2](#). The parts of the tube with the higher hydrogen content are more brittle and intensively cracked because of thermal strength by cool-down.

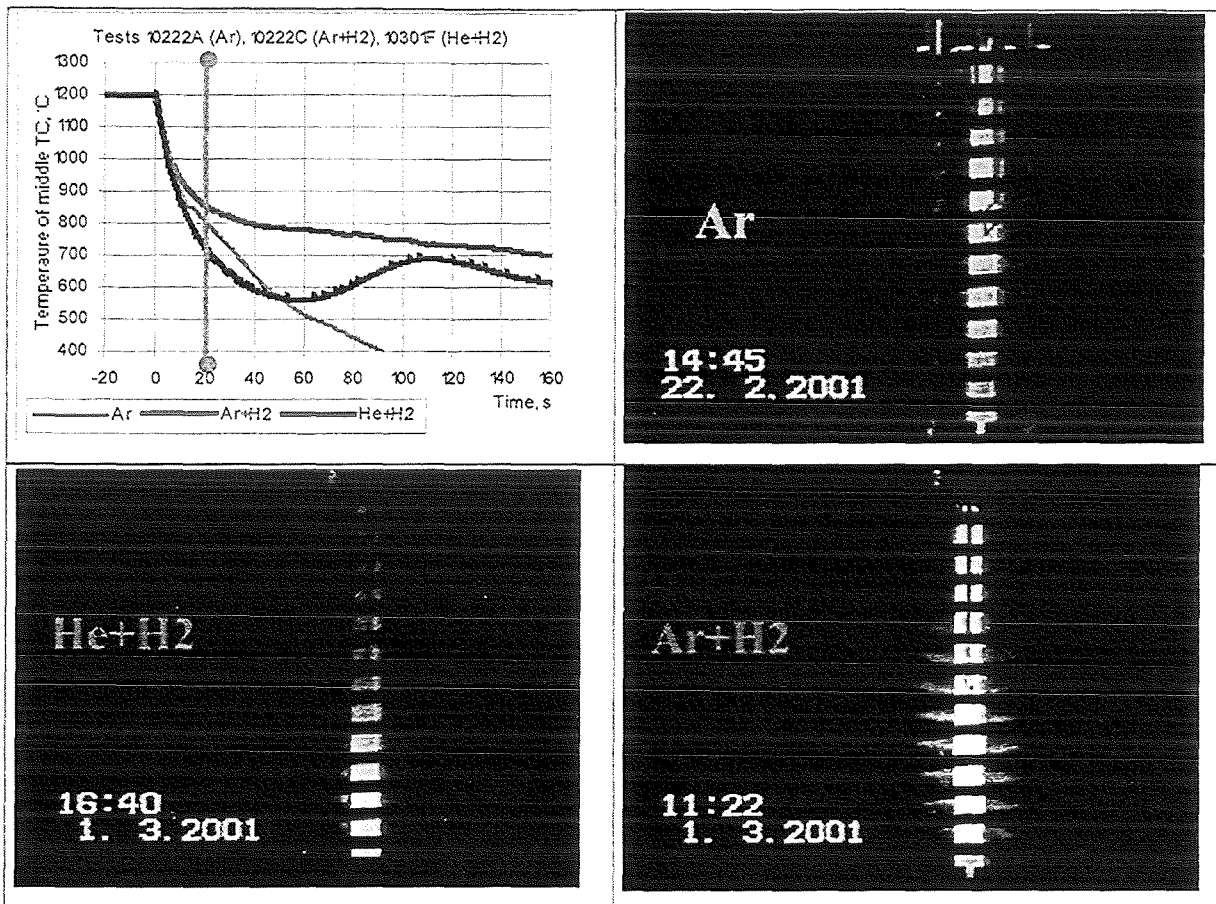


Fig. 1: Frame of synchronised film corresponding to 20 sec in the cool-down phase

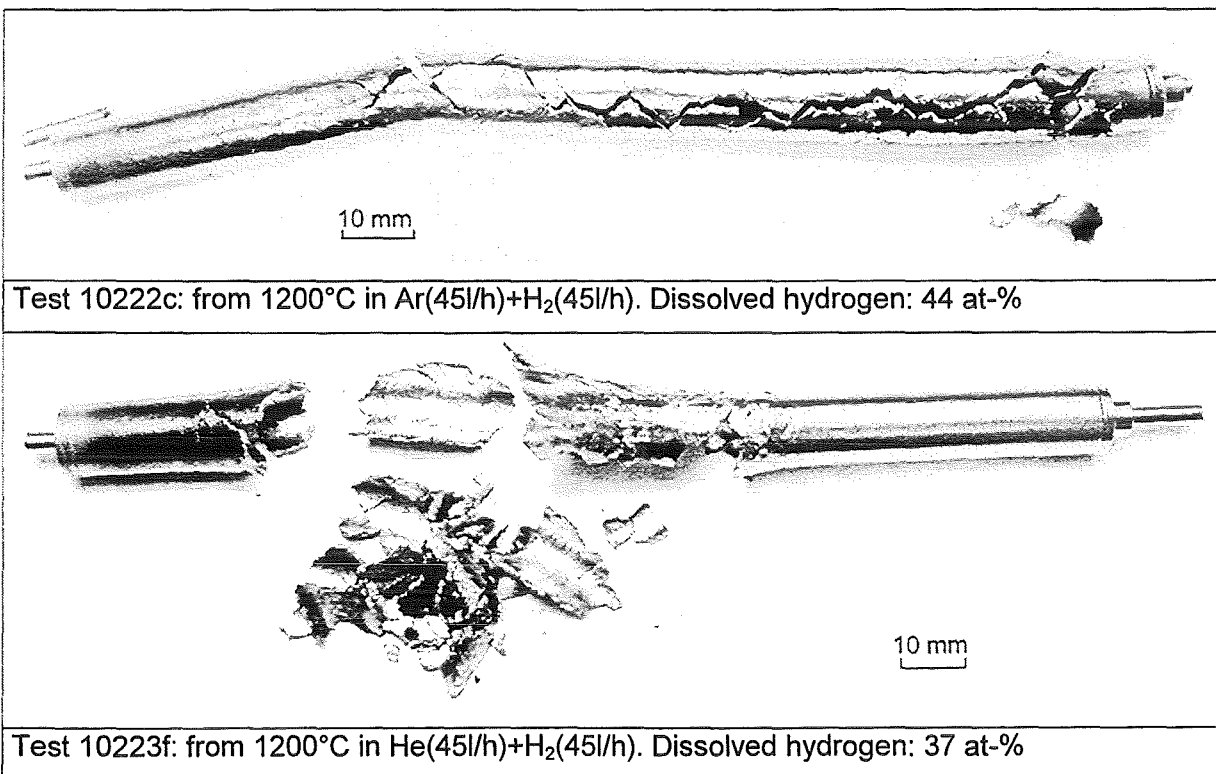


Fig. 2: Influence of the gas composition on the behaviour of the specimens. The cool-down in He occurs quicker and the cladding absorbs the H<sub>2</sub> axially inhomogeneously.

A third factor influencing the cool-down process is the convection properties of different gas mixtures. This factor depends from individual geometry of gas channel and must be precisely tuned by modelling. SVECHA code (mechanistic code used for the modelling of quench phenomena) was previously verified with the pure argon flux in the QUENCH rig. The corresponding mass transfer Nusselt number was  $Nu \approx 3$ . With this value the modelling of cool-down tests was performed. Fig. 3 shows a comparison of calculational results with experimental data.

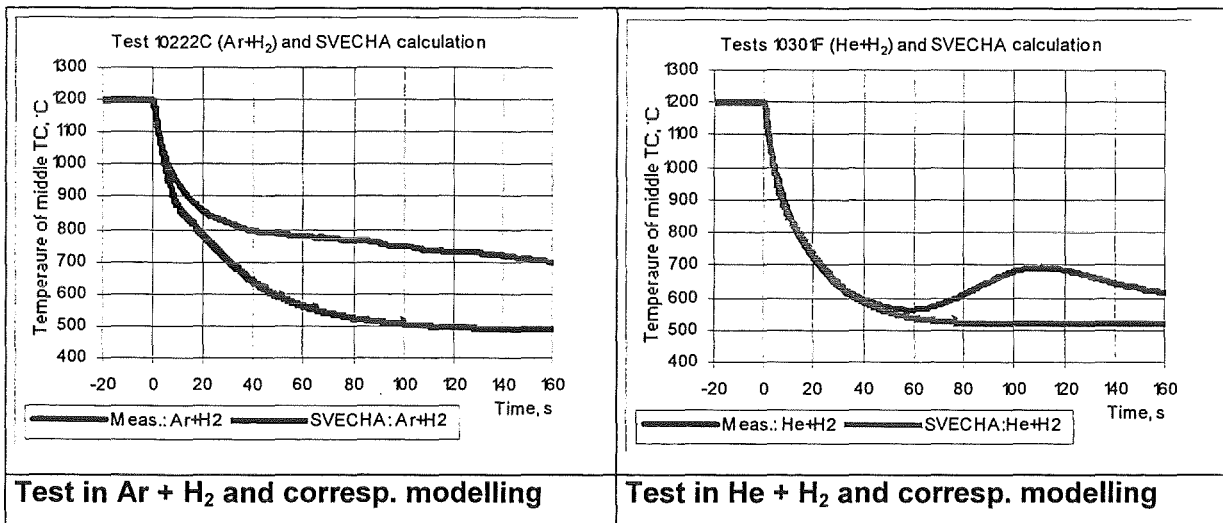


Fig. 3: Comparison of test results with corresponding SVECHA calculation for two different gas mixtures

### Stability of cladding tube

Some tests on the cool-down of the light oxidised cladding tube were performed with hermetic sealed rod. That circumstance causes an unexpected effect. By the heating up to 1400°C the tube collapsed. The schematic explanation of the effect is shown in Fig. 4.

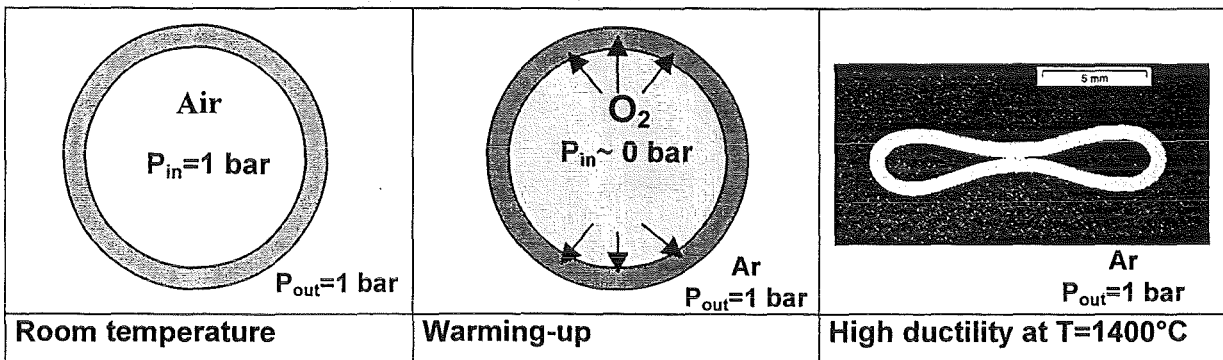


Fig. 4: Collapse at 1400°C with the air filled and sealed Zry-cladding rod

## **Determination of Zr and ZrO<sub>2</sub> emissivities using experimental data of empty rods cool-down tests**

The emissivity is an important property of reactor-related materials. Under severe accident conditions the temperature of the core may reach 1500-2000 K or even more. At such high temperatures radiative heat flows play the main role in heat exchange. In order to describe adequately the temperature distribution inside the core and predict the evolution of severe accidents it is necessary to know the temperature dependence of the emissivity of the materials used in reactor design. The most important are the cladding material zirconium and zirconium dioxide, which appears as a result of cladding oxidation in steam atmosphere.

It should be noted that existing data concerning Zr and ZrO<sub>2</sub> emissivity at high temperatures cannot be characterised as complete. Thus, in the SCDAP/RELAP5 code materials properties database MATPRO only ZrO<sub>2</sub> emissivity is cited, based on works published before 1977. Zr emissivity data are absent in MATPRO.

At high temperatures radiative heat flow from the surface of a body exceeds considerably heat flow to the surrounding gas. By calculating the heat flow from the surface using measured surface temperature evolution one can estimate the value of emissivity. Additional accounting for the heat flow to the gas improves the accuracy of such estimation.

In the present report the first results of the determination of Zr and ZrO<sub>2</sub> emissivity on the basis of temperature data obtained in cool-down tests with empty rods are described. The calculations of the heat flow from the rod surface were performed using the SVECHA/QUENCH code (S/Q). The data used cover the temperature range between 700-1800 K.

The value of the emissivity was estimated on the basis of four cool-down tests with non-oxidised Zr rod and 9-parameters fitting curves for its temperature dependence were proposed ([Fig. 5](#)). The value of ZrO<sub>2</sub> emissivity was also estimated using five cool-down tests with oxidised Zr rod. However, due to large scattering of the data, no fitting curve was proposed ([Fig. 6](#)).

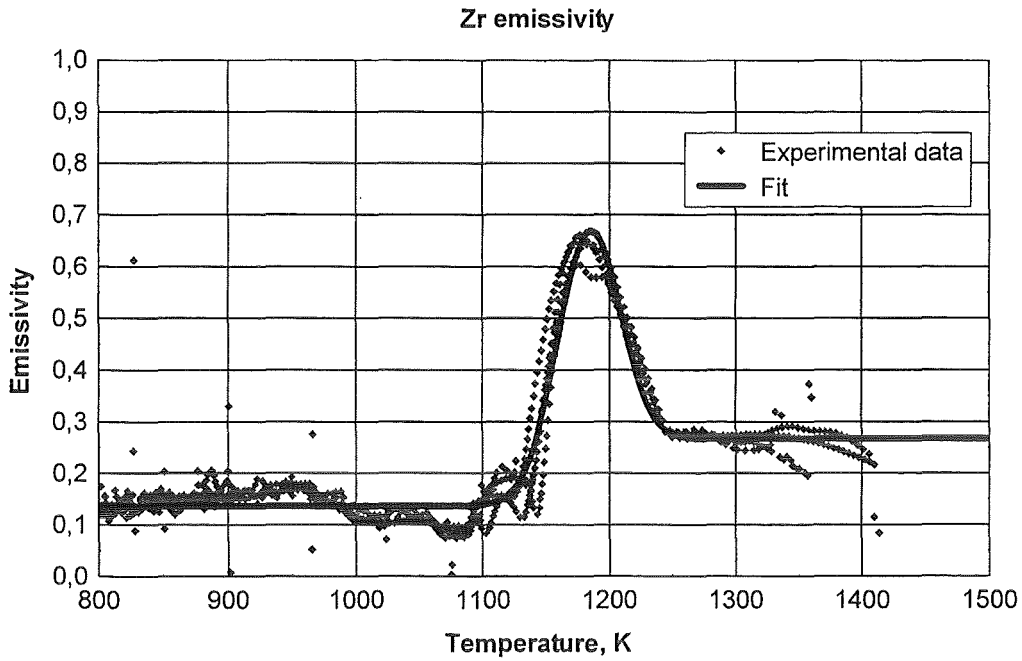


**Fig. 5:** Zr emissivity experimental data and fitting curve

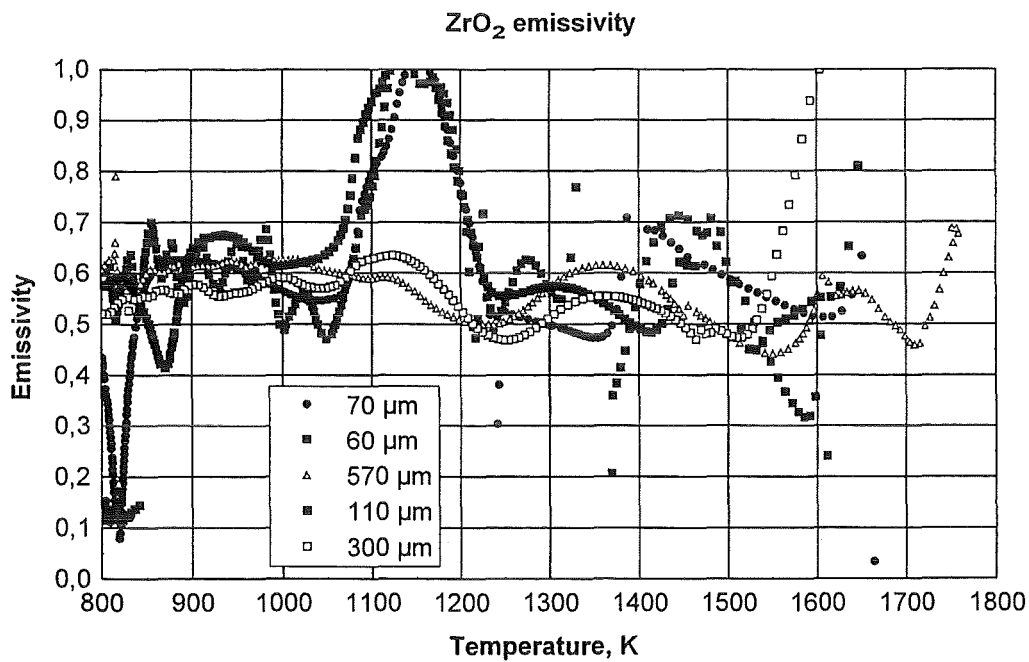
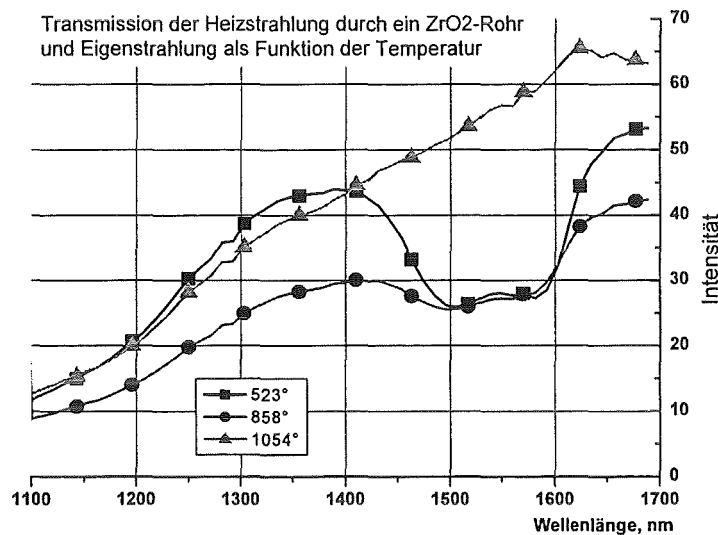


**Fig. 6:** ZrO<sub>2</sub> emissivity coefficient calculated on the basis of smoothed temperature curves for tests with different oxide layer thickness

VIII. Messung optischer Eigenschaften von Reaktorwerkstoffen  
(L. Steinbock, IMF I)

Zusätzlich zum VIS-NIR-Spektrometer (500-1000 nm) wurde ein NIR-Spektrometer (1100-1700 nm) in Betrieb genommen, mit dem die Transmission und Reflektivität von  $ZrO_2$ -Rohren gemessen wurden. Damit können nun optische Eigenschaften zwischen 500 und 1700 nm gemessen werden.

Die Messung der Transmission als Funktion der Temperatur zeigte, dass im NIR-Bereich zwischen 1500 und 1600 nm ein Absorptionsband liegt, das mit steigender Temperatur verschwindet.



Diese Verhalten wurde bereits früher im NIR zwischen 750 und 900 nm beobachtet.

## IX. Severe Accident Investigations

(W. Hering, Ch. Homann, W. Sengpiel, D. Struwe, IRS; J.S. Lamy, EDF)

### **Abstract**

At the Forschungszentrum Karlsruhe (FZK) the Institute for Reactor Safety (IRS) performs accident analyses with severe core damage code systems such as SCDAP/RELAP5, ICARE2 and the thermal-hydraulic code RELAP5.

Main topic is the support of the QUENCH experiments at FZK/IMF. All test were supported by pre- and post test calculations, in this way enhancing effectively understanding of the experiment and separation of physical and facility based effects. In 2001 the main activity was focussed on the management and performance of the International Standard Problem No. 45 (QUENCH-06) of the OECD/NEA/CSNI, especially the analyses of the blind phase calculations delivered by 21 participants from 13 nations.

### **Zusammenfassung**

Im Institut für Reaktorsicherheit (IRS) des Forschungszentrums Karlsruhe (FZK) werden Unfallanalysen mit den Kernschmelzcodes SCDAP/RELAP5 und ICARE2 sowie mit dem Thermohydraulik Programm RELAP5 durchgeführt. Der Schwerpunkt der Arbeiten liegt in der Unterstützung der QUENCH Versuche im FZK/IMF. Für alle Versuche werden Vorausrechnungen und Versuchsanalysen durchgeführt, um mit einem optimal angepassten Anlagenmodell ein verbessertes Verständnis des Experiments und die Separation von Anlagen- und physikalischen Effekten zu erreichen.

Im Jahr 2001 konzentrierten sich die Aktivitäten auf die Durchführung des Internationalen Standardproblems der OECD/NEA/CSNI Nr. 45, basierend auf dem Experiment QUENCH-06. Hierzu wurden die Ergebnisse der Blindrechnungen von 21 Teilnehmern aus 13 Staaten verglichen und dokumentiert.

### **1.1 Accident analyses with SCDAP/RELAP5**

As part of the 5<sup>th</sup> Framework Program COLOSS of the European Union (EU) accident analyses for code comparison among severe accident codes were performed with the in-house version of SCDAP/RELAP5 /1/. They will also be used for

code comparison within the EVITA program to contribute to ASTEC code validation. For this purpose the improvement of the S/R5 B<sub>4</sub>C control rod model is foreseen. So far, material properties are implemented and a simple B<sub>4</sub>C oxidation model is formulated, based on recommendations of the experimental work at FZK/IMF. First results will be expected in 2002.

## **1.2 The OECD International Standard Problem No. 45 (QUENCH-06)**

Despite of great efforts in determining the hydrogen release, when the overheated core of a nuclear reactor is flooded as part of an accident management measure (AMM), knowledge is still too limited to predict this source term sufficiently well with computer programs. The International Standard Problem No. 45 (ISP-45) of the OECD/NEA is initiated to extend the database for such situations, in particular to identify key phenomena and to encourage an extended code validation so that the accuracy and reliability of the codes can be assessed, and, if necessary, improved. The ISP-45 is based on the out-of-pile experiment QUENCH-06 /6/, performed at Forschungszentrum Karlsruhe, Institut für Materialforschung (IMF), on December 13, 2000 to investigate fuel rod bundle behaviour up to and during reflood/quench conditions without severe fuel rod damage prior to reflood initiation /5/. For the ISP-45 both, experimental work (IMF) and analytical task (IRS), is managed by FZK.

In the blind phase 21 participants from 13 nations used detailed mechanistic (d) and integral (I) codes as indicated in Tab. 1. Additionally, FZK post-test analyses were performed with the in-house version of SCDAP/ RELAP5 mod3.2 /3/. About 400 variables were requested for the comparison; the most informative of them are published in /7/, others were requested to facilitate our interpretation of the results.

The data for the blind phase calculation is defined in /5/ and the QUENCH-06 experiment is described in detail in /6/, whereas the results of the blind phase exercise are documented in /7/. From the assessment of the results and the individual participant statements, a ranking of the user experience was established. The user experience covers less experienced (G), experienced users (E), and code developers (D), as given in Tab. 1.

Tab. 1 List of codes and participants plus estimated state of user experience during blind phase exercise

Code	Type	Token	Organization	State of experience	
				Nation	↓
ATHLET-CD	d	GRS	Gesellschaft für Anlagen- und Reaktorsicherheit (GRS), Cologne	Germany	E
		RUB	Ruhr-University Bochum; Institut for Energy Systems and Energy Economics	Germany	D / E
GENFLO	d	VTT	VTT Energy	Finland	G
ICARE/ CATHARE	d	DRS	IPSN/DRS/SEMAR/LECTA	France	D / E
		ENE	ENEA, Bologna	Italy	E
IMPACT/ SAMPSON	d	NUP	NUPEC (Nuclear Power Engineering Corporation), Tokyo	Japan	D / E
MAAP 4.04	I	EDF	Electricité de France (EDF), Paris	France	E / D
		FRA	Framatome-ANP, Paris	France	E
MELCOR <i>incl. reflood</i>	I	REZ	Nuclear Research Institute, Rez near Prag	Czech Rep.	E
		SES	Studsvik ECO & Safety AB	Sweden	G
		SNL	Sandia National Laboratories	USA	E / D
MELCOR	I	IJS	Institut Jozef Stefan, Ljubljana	Slovenia	G
		NK2	NSI of RRC "Kurchatov Institute", Moscow	Russia	G
SCDAPSIM	d	CMX	Nat. Commission of Nuclear Safety and Safeguards (CNSNS)	Mexico	G
		DMM	University of Pisa	Italy	E
		ISS	Innovative Systems Software, Idaho Falls	USA	D / G
		NEH	Nuclear Engineering, University Hacettepe, Ankara	Turkey	G
		NK1	NSI of RRC "Kurchatov Institute", Moscow	Russia	G
		SIE	Framatome-ANP, Erlangen	Germany	E
		UZA	University of Zagreb	Croatia	G
SCDAP-3D	d	INL	Idaho National Engineering and Environmental Lab., Idaho Falls	USA	D / E
S/R5.irs	d	FZK	Forschungszentrum Karlsruhe, Karlsruhe	Germany	E

D Code developer  
E More experienced user  
G Less experienced user

### 1.2.1 Energy balance

Based on the data of the blind calculations, some basic consistency checks were performed such as fluid mass and enthalpy as well as energy balance. In this context some participants show difficulties, which are caused by either limitations of their code system or inconsistencies in the modelling of the QUENCH out-of-pile conditions.

In Figure 1 the remaining power is given calculated by data delivered by the participants of power sources (electrical, exothermal) and power sinks (through shroud, convective losses). During the final stage of the pre-oxidation phase (3000 –

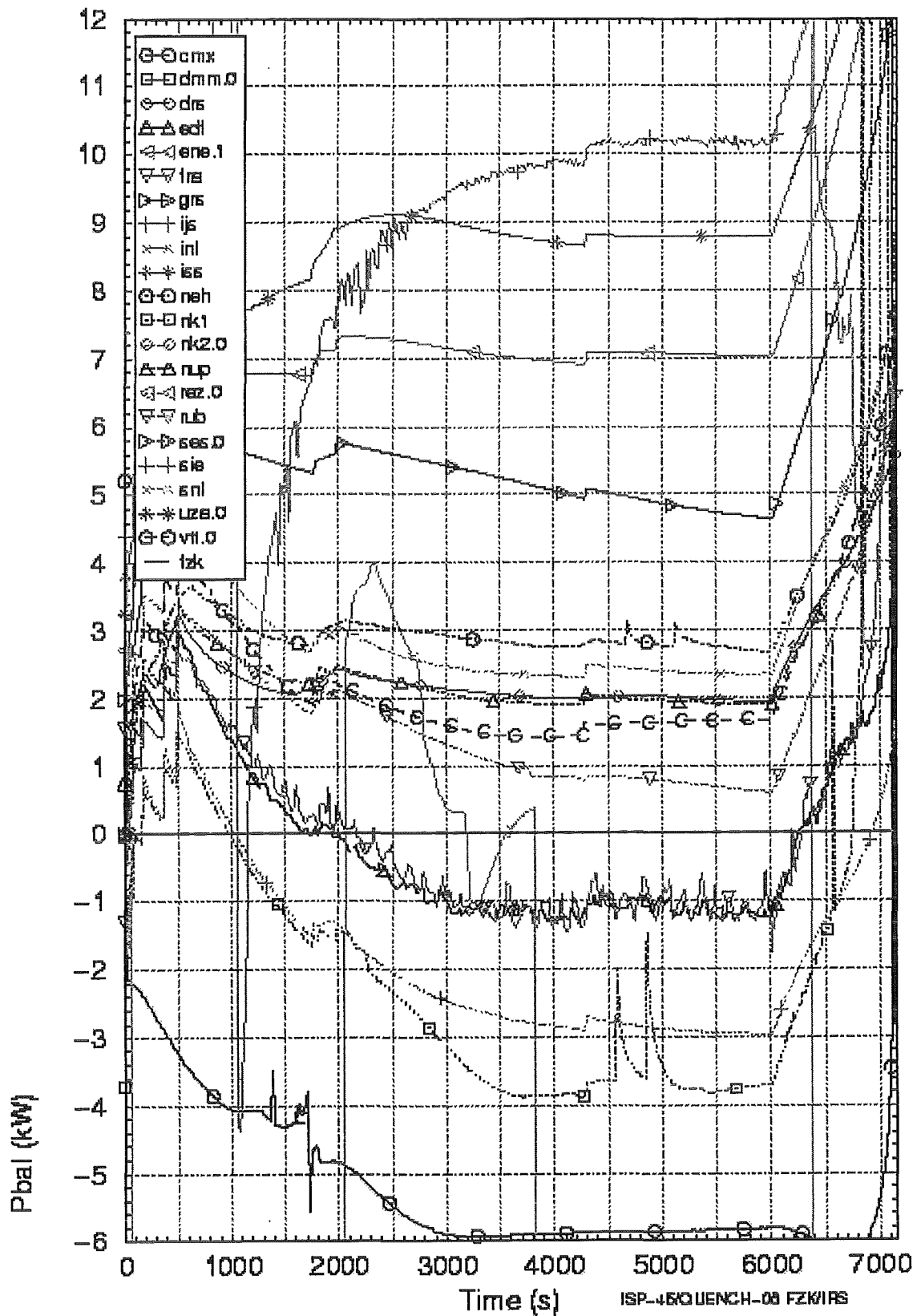


Figure 1 Coarse power balance for the QUENCH test section excluding losses by axial heat conduction in the electrodes calculated by the participants and compared to post-test calculations with S/R5 mod 3.2.irs.

6000 s), the electrical power input was kept stationary so that the storage term should be negligible, so that only the axial heat losses remain, which amount to app. 2 kW. Therefore, we defined the range of reasonable values of  $2 \text{ kW} \pm 40 \%$  as described in Tab. 2 /7/. This high uncertainty in the energy balance originates due to the difficulties in modelling convective losses in the upper electrode zone. But that cannot explain the high deviations of app. 300 – 500 %.

However, nearly all participants calculated the thermal-hydraulic conditions prior to reflood fairly well, except those who had difficulties in simulating the axial power distribution in the heater rods or to model the radiative heat transfer in the annular gap between shroud and cooling jacket in the upper electrode zone.

In order to quantify the results a so called mainstream was defined which includes participants within a certain bandwidth around the experimental data or if not available around the result of the post-test calculation using S/R5 mod3.2.irs.

### **1.2.2 Hydrogen production**

The main topic of the ISP-45 was the hydrogen release during reflood processes of an overheated light water reactor core. Such a situation might occur if safety systems fail but can be reactivated after some hours. In previous experiments (CORA-12, CORA-13, ISP-31, LOFT FP-LP) a large release spike of hydrogen was found, whose origin was quite unclear.

So far the basic physical process was considered to be the cracking or spalling of protective oxide layers allowing unlimited steam access to fresh metal surfaces at high temperatures. To simulate such a behaviour most of the codes have an user defined option which artificially strips the protective oxide scales more or less. As a consequence these codes can calculate that high hydrogen release as can be seen in Figure 2 (top). In the QUENCH-06 experiment, however, only 10 % hydrogen was measured after reflood initiation. This amounts approximately to normal hydrogen release due to oxidation plus some additional hydrogen produced in cracks through the protective oxide layer.

In the mainstream the variation in the hydrogen release increases from app.  $\pm 15 \%$  prior to reflood to  $\pm 40 \%$  afterwards (Figure 2 bottom). Additionally, radiation heat transfer was switched off in some codes, so that unrealistic high surface temperatures were calculated.

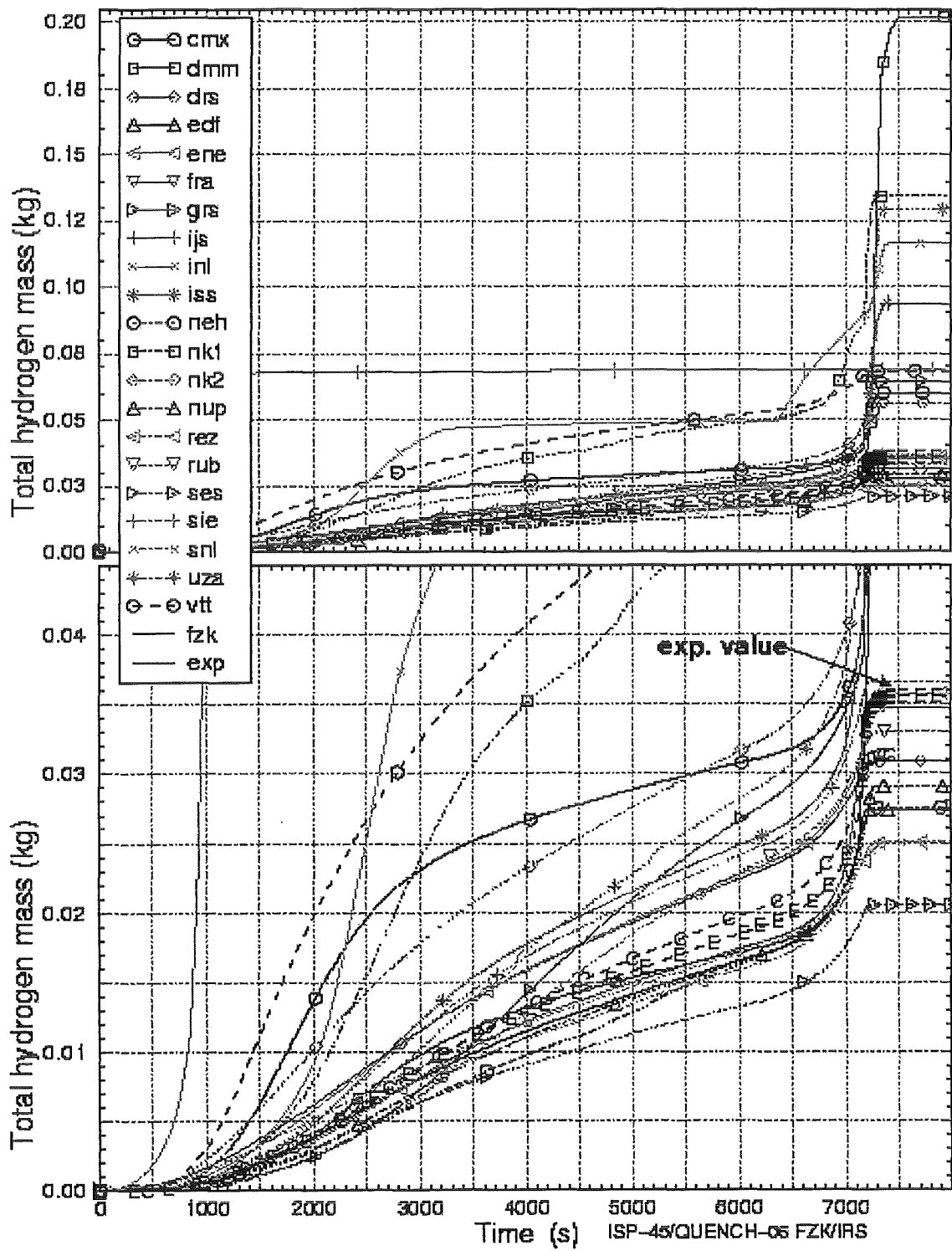


Figure 2 Top: Calculated total hydrogen mass compared to experimental data (-E-), bottom: magnified scale.

### 1.2.3 Summary of blind phase

The outcome of the ISP-45 blind phase was discussed by the organizers and the participants during the Comparison Workshop in December 2001. In Tab. 2 a summary of the blind phase findings with respect to the code performance is shown /7/. It also includes FZK experiences with the S/R5 mod 3.2.irs code.

Tab. 2 Summary of the ISP-45 blind phase calculations

Code	Input source	Code variants	Energy balance	Thermal-hydraulics		Bundle degradation		User experience	Remarks
				heat-up	reflood	heat-up	reflood		
ATHLET-CD	GRS	GRS	± OK	± OK	++	± OK	--	D/E	missing mechanical model
	RUB	"			±OK		++		E
GENFLO	VTT	VTT	--	± OK	±OK	n/a	n/a	G	only static axial power profile
ICARE/ CATHARE	DRS	DRS	±OK	± OK	± OK	±OK	±OK	E/D	No shattering
	ENE	"	++			n/a	n/a		E
IMPACT/ SAMPSON	NUP	NUP	± OK	±OK	±OK	±OK	n/a	D/E	similar to SR5 shattering option
MAAP 4.04	EDF	EDF	--	± OK	± OK	n/a	n/a	E/D	No shattering
	FRA	FRA	--			± OK	MR		E
MELCOR (R)	REZ/ SNL	SNL	± OK	± OK	± OK	±OK	± OK	E D	No shattering
MELCOR (-)	NK2 IJS	"	++	++	++	MR (IJS)	n/a	G	No reflood model
SCDAPSIM	ISS	ISS	++	++	++	n/a	++	D/G	R5 reflood model
	SIE	"	--	±OK	±OK	±OK	±OK		E
SCDAP-3D	INL	INL	/	++	++	±OK	±OK	D/E	outdated USNRC heater rod model
S/R5.irs	16 ax 32 ax	FZK	± OK	± OK	- ± OK	B B	-- ± OK	E	0.1 m nodalization insufficient for reflood

Confidence range: ± 40% ± 15% ± 40% ± 15% ± 40%

results reasonable ± OK

underpredicted --

overpredicted ++

oscillating /

n.a. no sufficient information

B ballooning with clad rupture

MR early melt relocation

D: code developer

E: more experienced

G: less experienced

The main open issues of the ISP-45 were expressed during Comparison Workshop as follows:

- clad failure is still a user parameter. It varies between 2300 K and 2900 K and strongly influences the course of the accident
- reflood thermal hydraulics are not yet sufficient, the sharp temperature drop is often not visible

- quench initiated oxidation modelled only for intact rods, model for melt / debris missing
- Some codes include an option which enhance strongly the hydrogen release during fast cool-down. This option originates mainly from ISP-31 where a tremendous hydrogen peak during reflood was measured, but at that time the influence of the enhanced (Zr-U)O melt oxidation was unknown.

From the present point of view the results of the blind exercise were affected more by user errors than by code errors. The participants agreed in following statements:

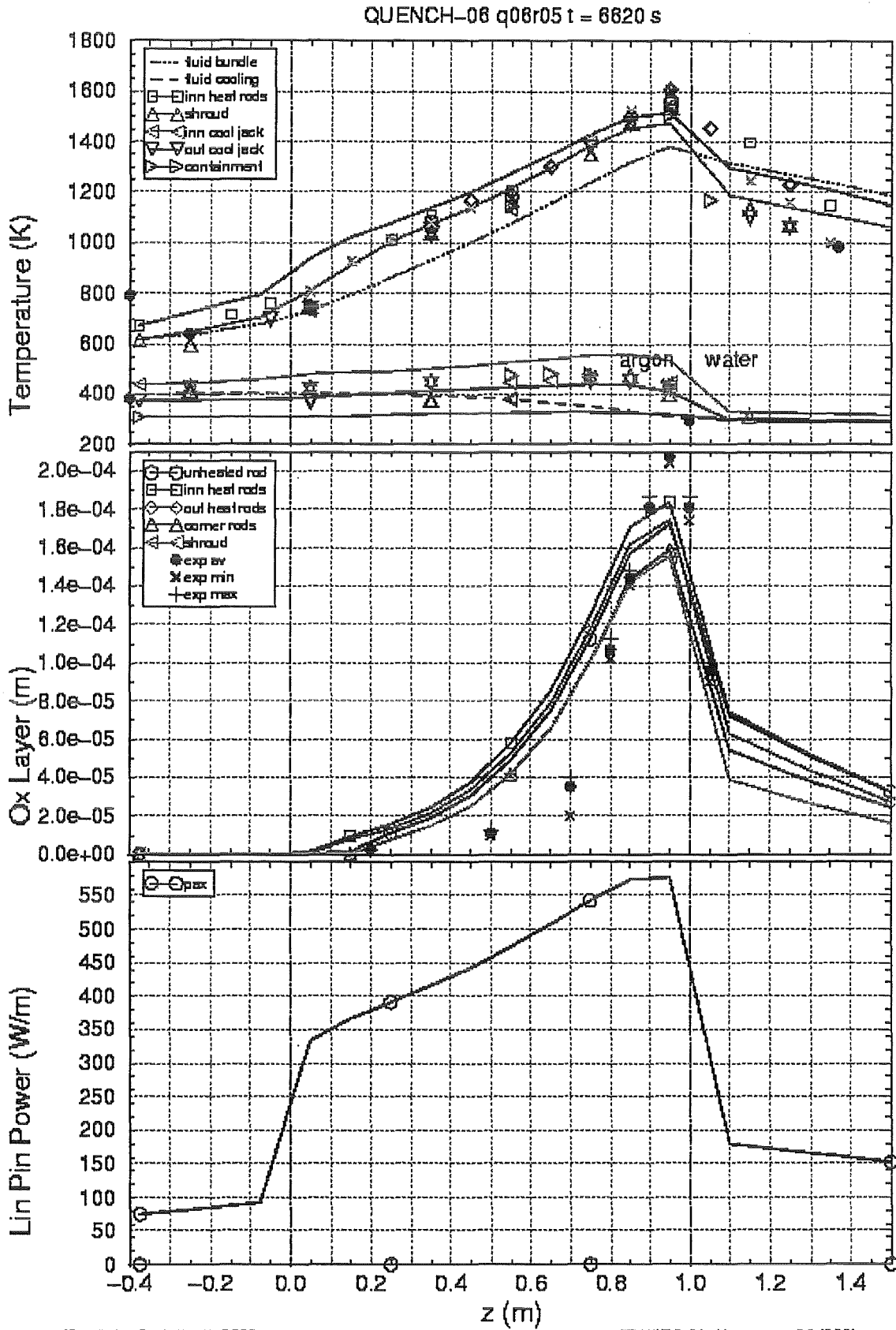
- ISP-45 contributes significantly to the validation of SA computer codes
- Participation in ISP-45 leads to enhanced user qualification. This qualification is absolutely necessary for such a work
- Information given in the specification report may be extended by user guidelines to simulate the facility
- Benefits for plant applications:
  - recommendations for nodalisation, not only during reflood
  - uncertainty in plant reflood analysis reduced to scenarios with melt and/or debris.
- Missing models for melt oxidation during reflood
- A final workshop will be hold in Petten (March 18, 2002) together with an informal meeting about ISP-46 (March 19, 2002).

### **1.3 Support of QUENCH experiments**

The experiments in the QUENCH facility at FZK/IMF aim at investigating the physico-chemical processes during quenching of overheated rod bundles with water or fast cool-down with steam. At IRS these experiments are supported by numerical analyses before and after the tests, mainly with S/R5 mod 3.2. Except for smaller improvements our work concentrated on QUENCH-06 (ISP-45) and QUENCH-07.

#### **1.3.1 QUENCH-06**

Post-test calculations compare quite well with experimental results. As an example measured and calculated temperatures and oxide layer thickness at the time, when one of the corner rods was withdrawn are shown. The oxide layer thickness is overestimated in the lower half of the heated zone. Several reasons may contribute to this finding, so the inadequate modelling of oxidation for low temperatures which are not of special interest in a severe accident code, and locally also the enhanced heat transfer in the vicinity of the grid spacer at 550 mm.



Tue Feb 19 10:36:29 2002

FZK/IRS Ch. Homann ar32.1036i.x

Figure 3 Measured and calculated temperatures, oxide layer thickness, and linear fuel rod power for QUENCH-06

Underestimation of the maximum value may also be due to a code error in post-processing the values calculated in the main part of the code. The axial profile of linear pin power demonstrates the necessity of an adequate model for the electrical heater, taking into account the positive feedback of local power input with temperature.

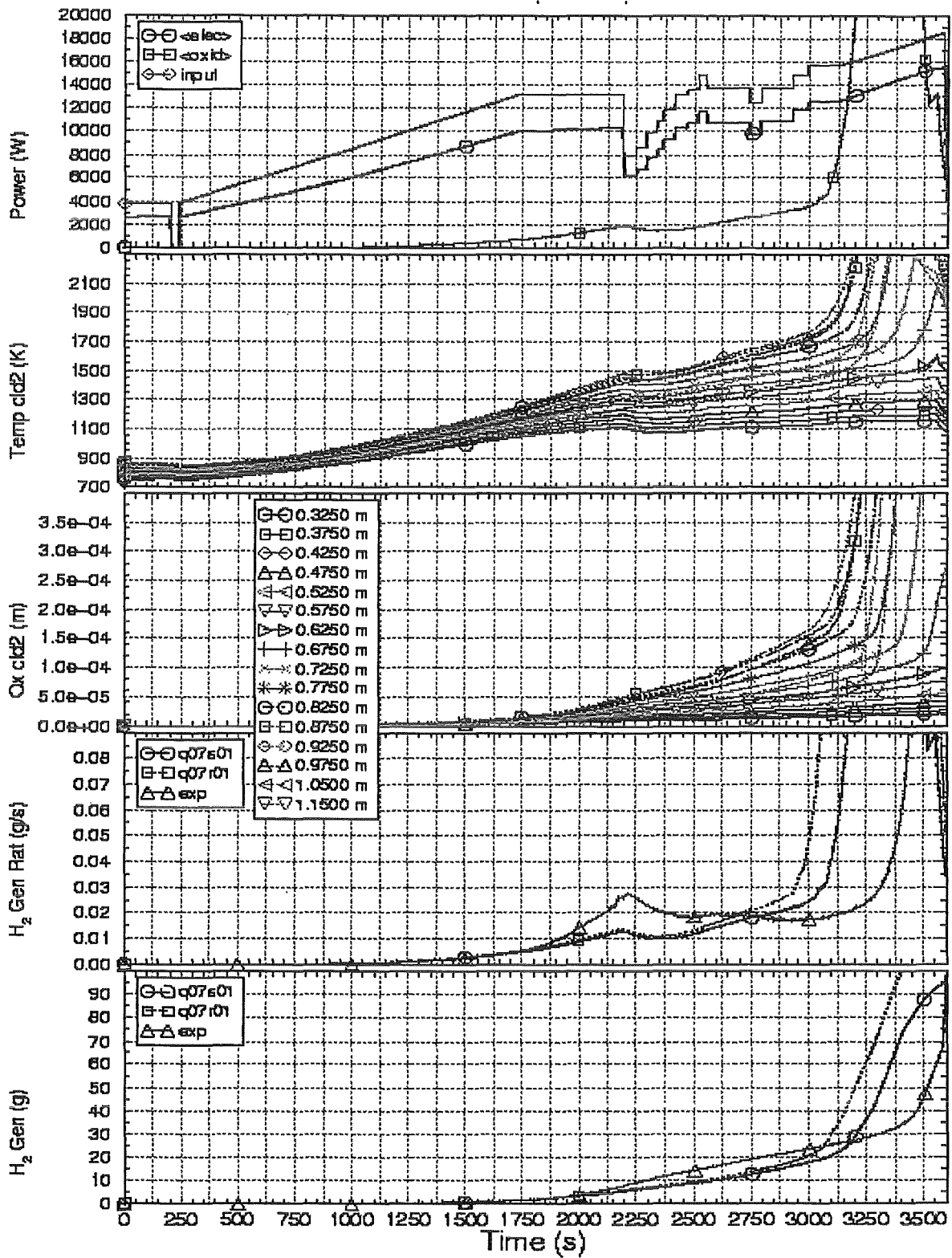
When quench water is switched off, 31.7 g of H<sub>2</sub> are calculated to be produced in comparison to 35.5 g in the experiment. Filling of the bundle during quenching is calculated quite well in comparison to other ISP-45 for the lower half of the bundle, but afterwards a code error leads to unacceptably high mass errors and physically wrong results.

Besides, our calculations have been used as a reference for special issues of ISP-45, e. g. to get a more detailed understanding of the begin of the quench phase, an information which is indispensable for ISP participants: Due to the malfunction of a valve near the pump, the quench water pipe was partly voided, but the extent of this voiding was unknown. To derive the most likely mass flows at bundle inlet in the quench phase, the inlet region was modelled more accurately than for standard calculations, and the mesh lengths in the bundle were reduced to one half of the standard values. To speed up the calculations, the facility has only been modelled up to and including the water and argon cooling flow adjusting radial heat losses out of the bundle on the basis of standard calculations. With this version temperature escalation in the heated zone is overestimated. A complete flooding of the bundle is calculated, but in a shorter time than observed in the experiment.

### **1.3.2 QUENCH-07**

This test is supported in the COLOSS project of the 5th EU framework program. Originally it was intended to be run similarly to Phebus test FPT3, dedicated to investigate degradation of B<sub>4</sub>C absorber rods and production of gaseous reaction products, especially of H<sub>2</sub> and CH<sub>4</sub>. For this reason a phase should be included in the test with a small steam mass flow a bundle temperature as high as 1800 K for about 20 min. Extensive pre-test calculations showed, however, that not only the various experimental aims are difficult to fulfil at the same time, but also that for such conditions the facility reacts rather sensitively to changes of physical parameters. Therefore another test conduct was proposed, more similar to previous test conducts, essentially with a nominal steam mass flow rate of 3 g/s. Even for these

conditions the determination of the test conduct was a tedious work because of the high temperature and hence small safety margin for the facility.

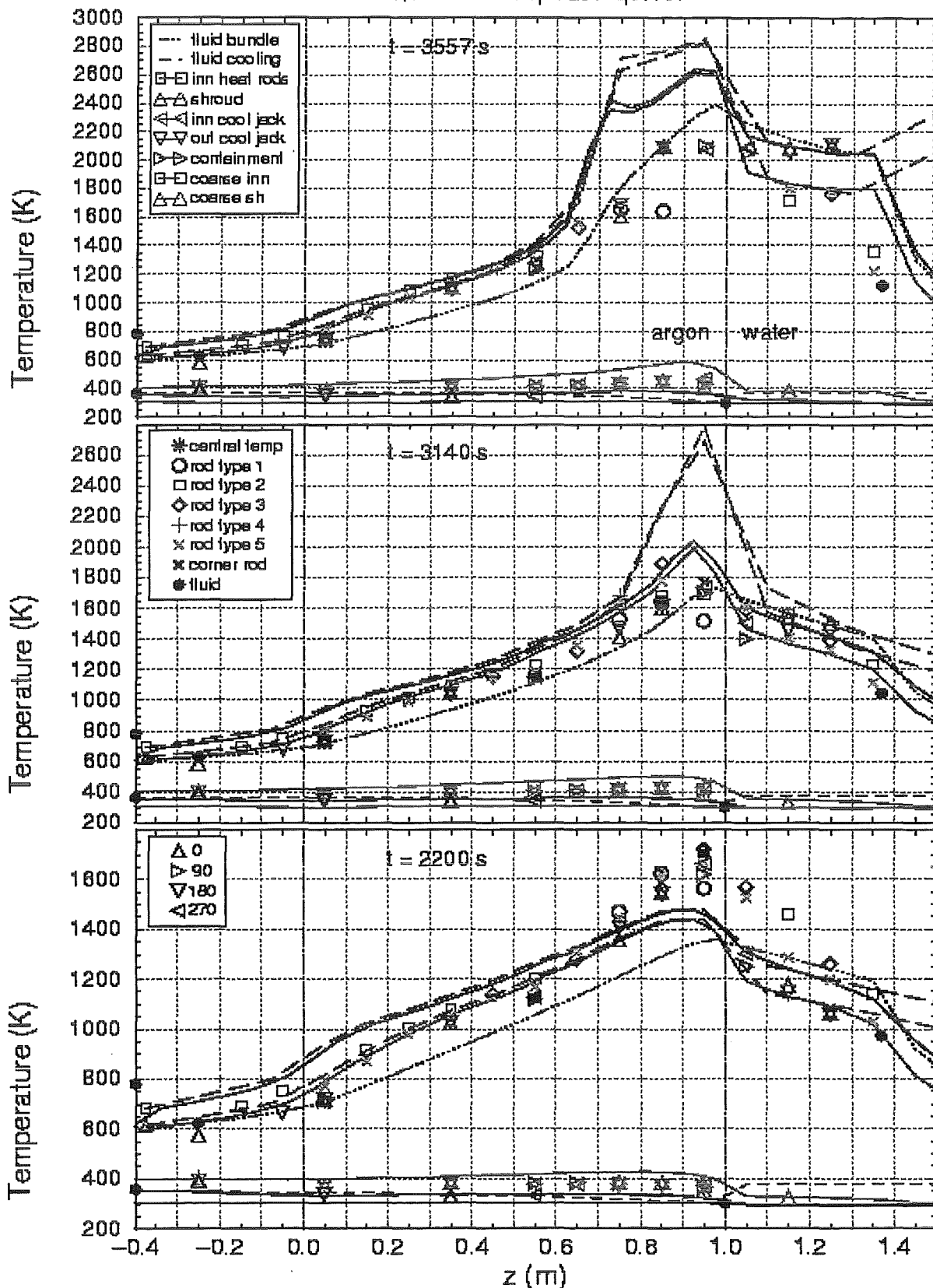


Mon Jan 28 17:31 03 2002

FZK/IRS Ch. Homann ar32.036i.x

Figure 4 Electrical and chemical power input, calculated clad temperatures and oxide layer thickness, and measured and calculated hydrogen production rate and cumulated mass for QUENCH-07

QUENCH-07 q07s01-q07r01

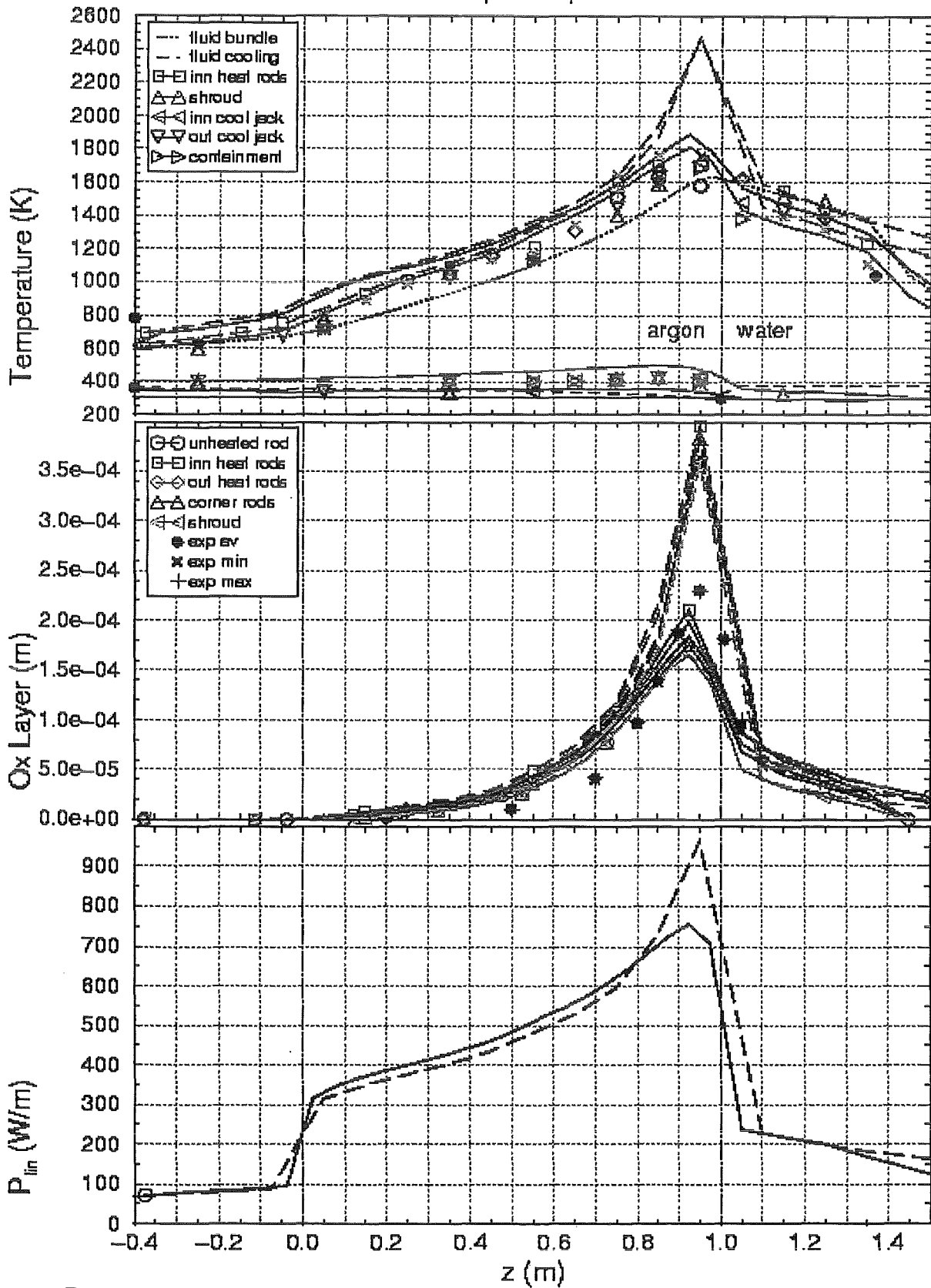


Mon Jan 28 16:48:21 2002

FZK/IRS Ch. Homann sr32.036i.x

Figure 5 Measured and calculated axial temperature profiles in various parts of the facility for QUENCH-07

QUENCH-07 q07s01-q07r01 t = 3090 s



Tue Feb 19 15:03:54 2002

FZK/IRS Ch. Homann a32.1036i.x

Figure 6 Measured and calculated axial temperature profiles and oxide layer thickness, and calculated linear power for QUENCH-07

A first post-test calculation gave larger differences for temperature histories and hence hydrogen production. Especially the first temperature increase is underestimated in the upper part of the bundle, and during the following oxidation at nearly constant temperature a temperature increase is calculated. In a first attempt to improve the results, the axial mesh lengths were halved for the whole facility as it has already been done in the simplified version used for post-test calculations for the quench phase of test QUENCH-06, where the parts of the facility outside the argon and water cooling were not modelled. This measure does not improve results for the first temperature transient, but gives better agreement with the experiment for higher temperatures as for the subsequent oxidation phase, predicts a later onset of temperature escalation and improves agreement in the upper electrode zone. The reasons for the remaining discrepancies are not yet identified. Comparison of measured temperatures in the upper half of the heated zone suggests that especially at level 11 physical or chemical processes occur, which are not yet understood.

#### 1.4 Literature

- /1/ The SCDAP/RELAP5 Development Team: SCDAP/RELAP5/MOD 3.2 Code Manual, NUREG/CR-6150, INEL-96/0422, Idaho Fall, Idaho, USA, 1997.
- /2/ Gonzales R., Chatelard D., Jacq F. ; ICARE2 Version 2 Mod 1, Description of physical models, Note Technique DRS/SEMAR 92/43, 1996.
- /3/ Hering, W., Homann C.; Improvement of the SCDAP/RELAP5 Simulator Model with respect to FZK Facilities, FZKA Report 6566, to be published 2002.
- /4/ Elias E., Sanchez V.H., Hering V.; Development and validation of a transition boiling model for RELAP5/MOD3 reflood simulations, NEDEA 183 177-332 (1998).
- /5/ Hering W., Homann Ch., Miassoedov A., Steinbrück M.; Specification of the International Standard Problem ISP-45 (QUENCH-06), Internal Report 3355, OECD/NEA/CSNI/ R(2001)1.
- /6/ Sepold L., Homann C., Miassoedov A., Piel D., Schanz G., Schmidt L., Stegmaier U., Steinbrück M.; Experimental and Calculation Results of the QUENCH-06 Test (OECD ISP-45), Wissenschaftliche Berichte, FZKA-6664, March 2002.
- /7/ Hering W., Homann C., Lamy J.-S.; Comparison Report on the Blind Phase of the OECD International Standard Problem No. 45 Exercise (QUENCH-06), FZKA-6677, March 2002.
- /8/ Hering W., Homann Ch., Lamy J.-S., Miassoedov A., Schanz G., Sepold L., Steinbrück M., Interpretation and Comparison Report of the OECD International Standard Problem No. 45 Exercise (QUENCH-06), OECD/NEA/CSNI/R(2002)2, FZKA-6722, to be published in 2002.

### **32.21.09 Entwicklung von Methoden zur Abschätzung und Minimierung der radiologischen Folgen von Reaktorunfällen**

(G. Benz\*, J. Ehrhardt, F. Fischer, Ch. Haller\*, I. Hasemann, E. Hesselschwerdt, C. Landman, A. Lorenz, J. Päsler-Sauer, M. Rafat\*, W. Raskob\*, T. Schichtel\*, IKET)

#### **Abstract**

The operational version PV4.0 of the decision support system RODOS has been further developed with respect to its operational functionalities with support from the European Commission by the RODOS Consortium of currently 15 R&D institutes in East and West Europe. The FZK activities have been concentrated on the preparation of a new web-based user interface and an improved meteorological pre-processor, and on the extension of the RODOS applicability to long lasting activity releases.

In parallel, the operation of RODOS at the Stabsstelle AR, Bundesamt für Strahlenschutz, has been expanded and the installation of RODOS in East European countries has been continued and supported. The evaluation of the operational experience within the DSSNET of developers and users of RODOS has been stimulated by common emergency exercises.

#### **Entwicklungsarbeiten zum Entscheidungshilfesystem RODOS**

Die operationelle Version PV4.0 des Echtzeit- und On-line- Entscheidungshilfesystems RODOS für den externen Notfallschutz nach kerntechnischen Unfällen wird mit Unterstützung der Europäischen Kommission im 5. Rahmenprogramm im Hinblick auf seine anwendungsorientierte Nutzung in Notfallschutzzentralen europäischer Länder sowohl inhaltlich als auch funktionell weiterentwickelt. Die entsprechenden Arbeiten werden derzeit im Rahmen von drei Verträgen mit insgesamt 15 europäischen Partnerinstituten durchgeführt.

---

\*Fa. D.T.I., Dr. Trippe Ingenieurgesellschaft m.b.H., Karlsruhe

Im Berichtszeitraum konzentrierten sich die Entwicklungsarbeiten auf die folgenden Punkte:

*a) Entwicklung einer neuen Web-basierten Benutzeroberfläche*

Die derzeitige X-Window Oberfläche für Benutzer der Kategorie A wird ergänzt durch eine auf der WWW Technologie basierenden Benutzeroberfläche, die einen plattform-unabhängigen Zugriff auf das RODOS System ermöglicht. Die zukünftigen Benutzer der Kategorie B können über die Web-Oberfläche die Eingabedaten für das RODOS System definieren, an das System weiterleiten und interaktive Rechenläufe durchführen lassen; berechtigten Benutzern der Kategorie C ist nur der passive Zugriff auf Rechenergebnisse der Benutzer der Kategorien A und B möglich. Die Inhalte der Benutzeroberflächen wurden in Abstimmung mit den RODOS Benutzern in Deutschland (s.u.) festgelegt und in standardisierter Form als Web-Fenster programmiert. Die Verknüpfungen zwischen der Kategorie C Oberfläche und dem RODOS System wurde in einer Prototypversion fertiggestellt. Die komplette Oberfläche für Benutzer der Kategorien B und C wird in der 2. Jahreshälfte 2002 fertiggestellt und freigegeben.

*b) Verbesserter meteorologischer Präprozessor*

Die Entwicklung eines verbesserten meteorologischen Präprozessors mit erweiterter Anwendbarkeit für ein weites Spektrum von gemessenen und prognostizierten meteorologischen Eingabedaten und für Ausbreitungsmodelle unterschiedlicher Komplexität und Parametrisierung (Puff- und Partikelmodelle) wurde in Zusammenarbeit mit dem Vertragspartner NCSR Demokritos, Griechenland) weitgehend abgeschlossen. Im Rahmen dieser Arbeiten wurde die Softwarestruktur der Modellkette für atmosphärische Ausbreitungsrechnungen im Nahbereich (LSMC) streng modularisiert, um eine breites Spektrum von Rechencodes einsetzen zu können und um die zukünftige Software-Pflege zu erleichtern. Die entsprechenden Software-Komponenten werden in die Version 5.0 des RODOS Systems (Mai 2002) integriert.

*c) Langanhaltende radioaktive Freisetzungen*

Die Anwendbarkeit des RODOS Systems wird für radioaktive Freisetzungen ertüchtigt, die sich über mehr als 12 Stunden bis zu 48 Tage erstrecken. Hierzu müssen sowohl die Eingabefenster für den Quellterm als auch Funktionen und Schnittstellen

des Quelltermmoduls sowie der Module zur Berechnung der atmosphärischen Ausbreitung, der Katastrophen- und Strahlenschutzvorsorgemaßnahmen und der Strahlendosen erweitert bzw. modifiziert werden. Die zugehörigen Arbeiten wurden in Zusammenarbeit mit den Vertragspartnern NRPB, UK, und GSF, Neuherberg, weitgehend abgeschlossen, die neue Funktionalität wird in der RODOS Version PV5.0 enthalten sein.

#### *d) Datenassimilation*

Die Einbeziehung von Messdaten zur Verbesserung der diagnostischen und prognostischen Modellrechnungen sind ein wesentlicher Entwicklungsbeitrag laufender RODOS Vorhaben. Die RODOS Version PV5.0 wird erstmals und als einziges Entscheidungshilfesystem Software-Module enthalten, in denen Messwerte von Aktivitätskonzentration und der Strahlendosis zur Verbesserung der Ergebnisse von Ausbreitungsrechnungen im Nahbereich, der Nahrungsmittelkonzentrationen und der Dosisabschätzungen benutzen. Die laufenden Softwareentwicklungen wurden im Hinblick auf die Integration in das RODOS System unterstützt.

#### *e) Datenaustausch zwischen Nachbarstaaten*

Der schnellen Daten- und Informationsaustausch zwischen Nachbarstaaten durch Netzwerkverbindungen zwischen den in ihren Notfallschutzzentralen operationell betriebenen Entscheidungshilfesystemen ist wesentlicher Bestandteil eines durch informationstechnische Hilfsmittel verbesserten Notfallschutzmanagements in Europa. Im Rahmen eines laufenden Vorhabens werden die informationstechnischen Voraussetzung zur Realisierung eines derartigen direkten Datenaustauschs geschaffen. Hierzu gehören die Festlegung der für die Entscheidungsfindung in Nachbarstaaten benötigten Daten und Informationen, sowie Format, Schnelligkeit und Häufigkeit ihrer Übertragung. Die Untersuchungen werden – auch durch Auswertung von Übungserfahrungen im DSSNET (s.u.) – unterstützt.

#### *f) Softwarepflege*

Der Bereitstellung eines operationellen Entscheidungshilfesystems erfordert die kontinuierliche Programmpflege; hierzu gehören u.a. Fehlerkorrekturen sowie Modifikationen und Erweiterungen der System- und Anwendungssoftware aufgrund von

Anforderungen der Benutzer. Die entsprechenden Entwicklungsarbeiten werden in der Regel nicht durch F&E-Vorhaben abgedeckt, sondern werden im Rahmen von Wartungs- und Pflegeverträgen mit den Benutzern durchgeführt. Im Berichtszeitraum wurden drei Software-Patches für die RODOS Version 4.0 mit Fehlerkorrekturen und Funktionserweiterungen erstellt und die RODOS Dokumentation in Form eines „RODOS Handbook“ einschließlich deutschem und englischem Benutzerhandbuch vervollständigt.

### **Installationen von RODOS zum operationellen Betrieb in Notfallschutzzentralen**

Im Auftrag des Bundesamtes für Strahlenschutz (BfS) wurde im Jahr 2000 das RODOS System zum operationellen Betrieb auf einem redundanten Server-Cluster installiert und konfiguriert. Im Januar 2001 wurden sämtliche Hardware- und Software-Komponenten zum zentralen Betrieb in der Stabsstelle AR des Bundesamtes für Strahlenschutz (BfS), Bonn, aufgebaut. In der Folge wurden die Netzwerkverbindungen zu den Bundesländern Schleswig-Holstein, Niedersachsen und Hessen sowie zum Deutsche Wetterdienst (DWD) hergestellt und getestet. Im Endausbau werden zunächst 10 Nutzer (die Einsatzzentralen von 7 Bundesländern, des BMU und des BfS sowie der DWD) auf das System zugreifen. Die RODOS Operateure des Bundes und der Länder wurden während eines im IKET entwickelten Trainingskurses im Oktober 2001 geschult, der in Zukunft nach Bedarf wiederholt wird.

Die Europäische Kommission fördert finanziell die Installation des RODOS Systems in Notfallschutzzentralen osteuropäischer Länder. Dies schließt die Beschaffung der notwendigen Hardware- und Software-Komponenten, die Einrichtung aller Netzwerkverbindungen zu Datenlieferanten und RODOS-Nutzern und die Anpassung des RODOS Systems an nationale Gegebenheiten ein. Die entsprechenden Arbeiten in Polen und der Slowakischen Republik wurden mit Unterstützung des IKET im Mai 2000 abgeschlossen. Die Projekte zur Installation in Ungarn und der Ukraine begannen im November 2000; die Arbeiten in Ungarn wurden im September 2001 abgeschlossen, die Arbeiten in der Ukraine werden im Mai 2002 beendet sein. Danach werden die Tschechische Republik und Slowenien in 2002 sowie später Rumänien und Bulgarien folgen. Die Installationen werden im Rahmen von Unteraufträgen vom IKET unterstützt. In einer Reihe von westeuropäischen Ländern ist die (test-) opera-

tionelle Installation des RODOS System bereits erfolgt bzw. befindet sich in Vorbereitung, wie z.B. Finnland, die Niederlande, Spanien, Portugal und Österreich.

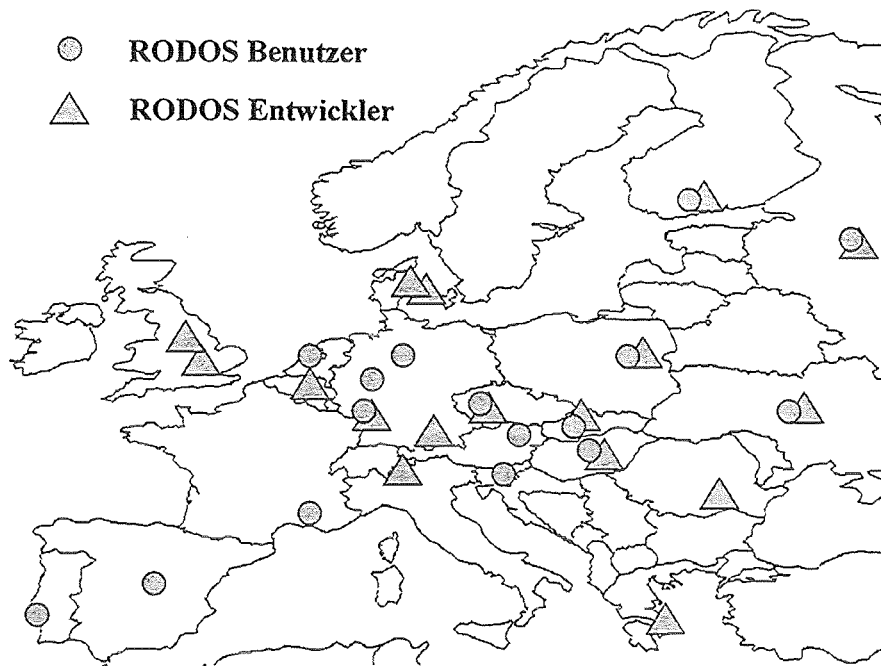
Ebenfalls mit Unterstützung der Europäischen Kommission wurde ein Trainingskurs für RODOS Operateure im europäischen Raum entwickelt und erstmals im Dezember 2000 im FTU durchgeführt. Zwei weitere Kurse wurden im März und November 2001 abgehalten. Die gesamten Kursunterlagen werden den Teilnehmern zur Verfügung gestellt als Basis zur Durchführung entsprechender Kurse in ihren Ländern.

### **Netzwerk von Benutzern und Entwicklern von Entscheidungshilfesystemen**

Im Rahmen des von der Europäischen Kommission finanzierten und vom IKET koordinierten Netzwerks DSSNET aus 35 Institutionen wird die Interaktion zwischen den an der Entwicklung beteiligten Instituten und den jetzigen und zukünftigen Benutzern der Entscheidungshilfesysteme RODOS und ARGOS organisiert, um durch gemeinsame Auswertung der Erfahrungen des operationellen Einsatzes Verbesserungen an den Systemen selbst und dem Notfallschutzmanagement generell zu initiieren. Hierzu werden jährliche Notfallschutzübungen mit den beteiligten Institutionen unter Einsatz der Entscheidungshilfesysteme durchgeführt und ausgewertet. Das Szenario und der Ablauf der ersten Übung wurden im IKET entwickelt; sie wurde im April 2001 unter Verwendung der EMERCON Meldeformulare über die DSSNET Homepage durchgeführt. Aufgrund der positiven Resonanz wird die Übung mit geänderten Bedingungen am 27. Februar 2002 wiederholt. Darüber hinaus ist das IKET für die Koordination und die Organisation des Netzwerks (Meetings des Advisory Committee und der Task Leader sowie aller Netzwerk-Mitglieder, Erstellung und Pflege der RODOS und DSSNET Homepages, Adresslisten, etc.) zuständig.

### **Sonstige Aktivitäten**

Im Rahmen eines Auftrags des Hahn-Meitner-Instituts, Berlin, wurden mit dem Programmsystem COSYMA probabilistische Abschätzungen zu den zu erwartenden Strahlenbelastungen und Katastrophenschutzmaßnahmen nach unfallbedingten Freisetzungen aus dem BER II durchgeführt und dokumentiert. Bei den Rechnungen wurden für die Fälle „trockene Kernschmelze“ (einstündige Freisetzung) und „Kernschmelze unter Wasser“ (Freisetzung über 168 Stunden) betrachtet.



Im DSSNET vertretene RODOS Benutzer und Entwickler

### 32.21.10 Beteiligung am PHEBUS-Projekt

#### I. Analytical Interpretation of Experimental Results

(W. Sengpiel, W. Hering, IRS)

#### **Abstract**

With the experiment PHEBUS FPT2 the fuel rod behavior during a severe LWR core melt accident is investigated. Contrary to the tests FPT0 and FPT1 in oxidizing atmosphere, FPT2 was performed under steam starved conditions. FPT2 has been analyzed with the code ICARE2 (V3 mod1.1). The comparison of calculated temperatures and cumulative hydrogen masses with the experimental data shows a good agreement up to the late high-temperature phase. The post-test analysis with ICARE2 for the final phase of the experiment with massive material relocation and pool formation is still underway.

#### **Zusammenfassung**

Das Experiment PHEBUS FPT2 simuliert das Brennstabverhalten im Verlauf eines LWR-Kernschmelzunfalles. Im Gegensatz zu den vorausgegangenen Experimenten FPT0 und FPT1 mit oxidierender Atmosphäre bei Dampfüberschuss wird in FPT2 das Brennstabverhalten in reduzierender Atmosphäre bei Dampfangel untersucht. FPT2 wurde mit dem Programm ICARE2 (V3 mod1.1) analysiert. Der Vergleich gemessener und gerechneter Temperaturen sowie der erzeugten Wasserstoffmassen zeigt gute Übereinstimmungen bis in die späte Hochtemperaturphase. Die ICARE2-Analyse der Endphase des Experiments mit massiven Materialverlagerungen und Poolbildung ist noch im Gange.

#### **Post-Test Analyses for the Experiment PHEBUS FPT2 with ICARE2 V3 mod1.1**

The experiment FPT2 is the third bundle degradation experiment performed in Cadarache, France, in the frame of the international PHEBUS FP project. After the tests FPT0 and FPT1 performed in steam-rich oxidizing atmosphere, FPT2 had been conducted to study the phenomena of bundle degradation under conditions with a pronounced steam starvation period. The bundle consisted of 18 irradiated fuel rods (burnup of 32 GWd/t) and 2 instrumented fresh fuel rods as well as of a central Ag-In-

Cd control rod, surrounded by an insulating shroud made of an inner Thoria layer and an outer Zirconia layer. The length of the fuel zone heated by nuclear power in the Phebus reactor was 1 m. The bundle was cooled by a constant steam flow rate of 0.5 g/s. Three phases have been distinguished during the course of the experiment: a low-temperature calibration phase, an oxidation phase including a pronounced steam starvation period, and a heat-up phase with fuel liquefaction and molten pool formation.

The post-test analyses have been performed with the latest version of the code ICARE2, i.e. ICARE2 V3 mod1.1, as previously done for the debris bed experiment FPT4 /1/ and for the FZK QUENCH-04 experiment /2/. The structure of the code input and the models used had been discussed and harmonized in cooperation with ICARE users from IPSN Cadarache as part of the PHEBUS Bundle Interpretation Circle. Figure 1 shows schematically the arrangement and material compositions of the bundle components as defined by the ICARE2 FPT2 model: an inner absorber rod, two representative irradiated fuel rods and 1 representative fresh fuel rod surrounded by the insulating shroud and an outer pressure tube. Figure 2 shows the nominal bundle power as deduced from reactor power measurements and the estimated so-called power coupling factor. The bundle power as used for the post-test analyses (fig. 2) had to be reduced by 18 % taking into account uncertainties affecting the bundle power.

Figures 3 - 6 demonstrate the course of fuel rod temperatures and shroud temperatures, respectively, as calculated for axial locations in the lower and higher bundle regions. The comparison with the experimental data (symbols, as far as available in the high-temperature period) shows a good agreement both qualitatively and quantitatively. However, the simulation with ICARE2 did not come to a regular end but failed at 18400 s (cp. figure 2); this is due to massive material relocation resulting in an extended blockage area and accordingly in numerical problems which will be overcome by slight modeling changes. Figure 7 presents the calculated hydrogen generation rates and the cumulative hydrogen mass. As foreseen in the experimental objectives and confirmed by the experimental findings, ICARE2 calculates a pronounced steam starvation interval of about 1100 s too. The cumulative hydrogen mass calculated lies in the experimental scatter band indicated in figure 7.

So far, the post-test analyses of PHEBUS FPT2 with ICARE2 have demonstrated that the course of a severe bundle degradation event can be reliably simulated up to

the occurrence of massive fuel relocation. The continuation of this study is dedicated to the detailed investigation of the late phase high-temperature phenomena including molten pool formation. Valuable information about the temperature evolution and hence about the mass relocation process is given by the measurement of the shroud temperatures. Figure 8 shows the evolution of axial profiles of late phase shroud temperatures as calculated with ICARE2 in comparison with experimental data. The gradual shift of high temperatures towards the lower part of the bundle reflecting fuel relocation as experimentally observed is confirmed by the calculation.

### **Perspective**

The post-test analyses for the PHEBUS FP bundle experiments will be continued including the application of the SCDAP/RELAP5 code. Beside FPT2 the test FPT1 will be considered in the frame of the international standard problem ISP-46.

### **References**

- [1] Programm Nukleare Sicherheitsforschung-Jahresbericht 2000, FZKA 6653, September 2001, p. 327-331
- [2] W.Sengpiel, W.Hering, Ch.Homann, C.Messainguiral,"Analyses of QUENCH and PHEBUS FP Experiments using ICARE2", in: Proceedings of the ICARE/CATHARE User's Club (1<sup>st</sup> Seminar), Cadarache, Nov. 19-20, 2000

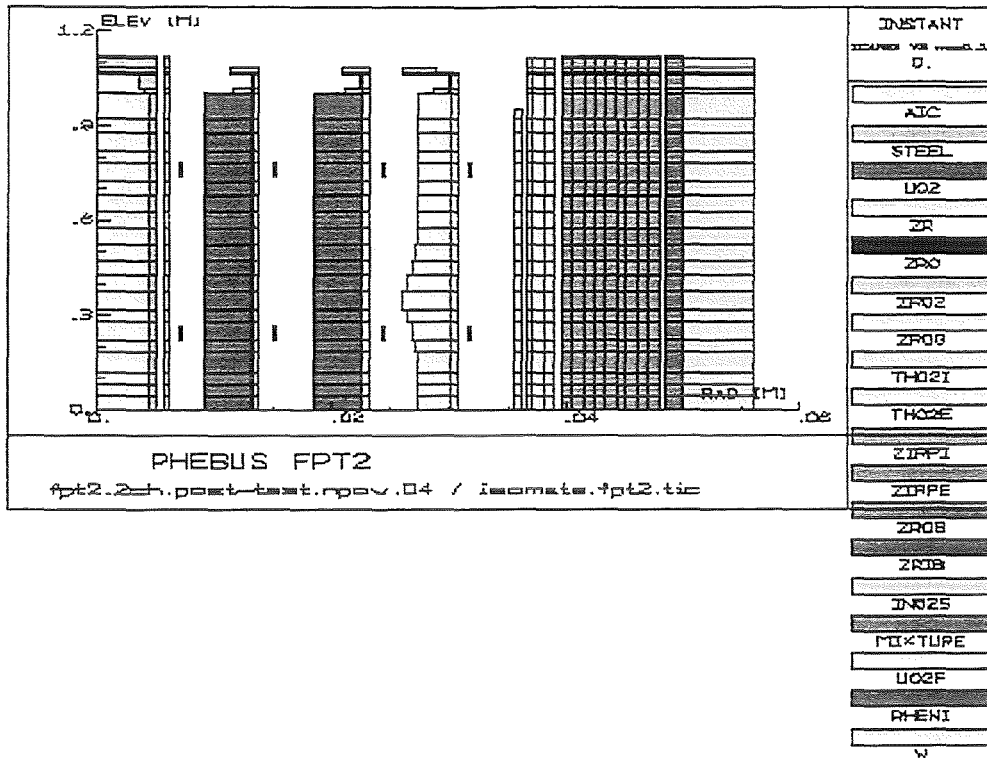


Fig. 1: Scheme of geometry and material arrangement as defined in the FPT2 input model of ICARE2: central Ag-In-Cd absorber rod, inner irradiated fuel rod, outer irradiated fuel rod, outer fresh fuel rod, stiffener, shroud (inner Thoria layer, outer Zirconia layer), pressure tube

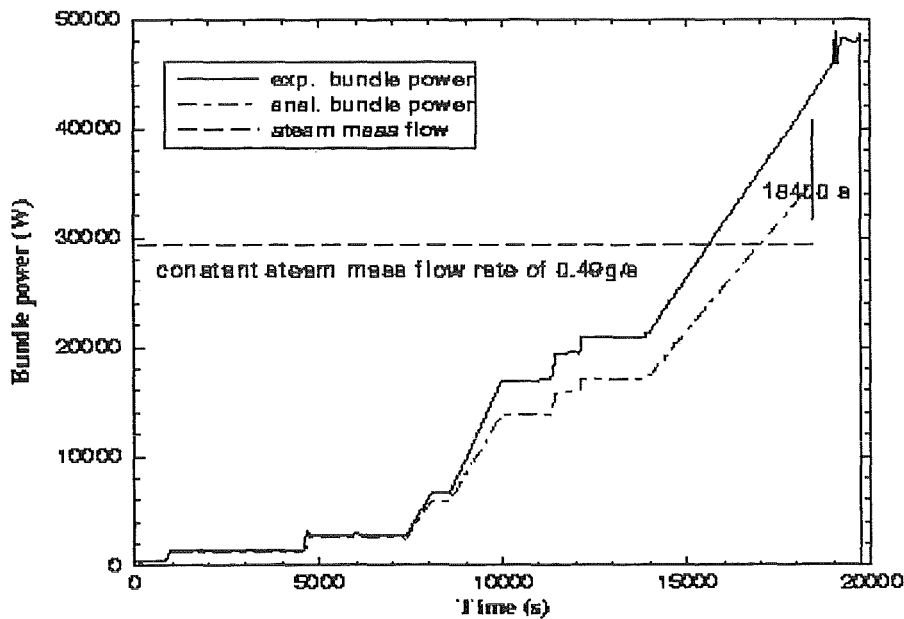


Fig. 2: Nominal experimental bundle power as deduced from reactor power and coupling factors (solid line) and reduced bundle power for FPT2 calculation with ICARE2 taking into account power uncertainties

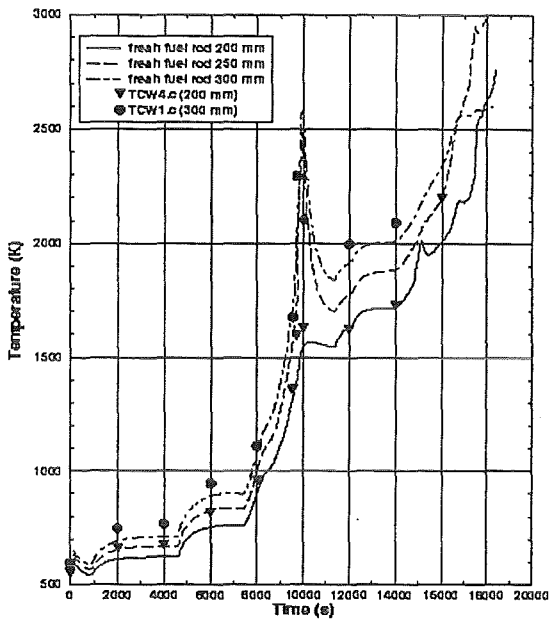


Fig. 3: Unirradiated fuel temperatures at 200 mm, 250 mm and 300 mm, calculated (lines) and measured (symbols)

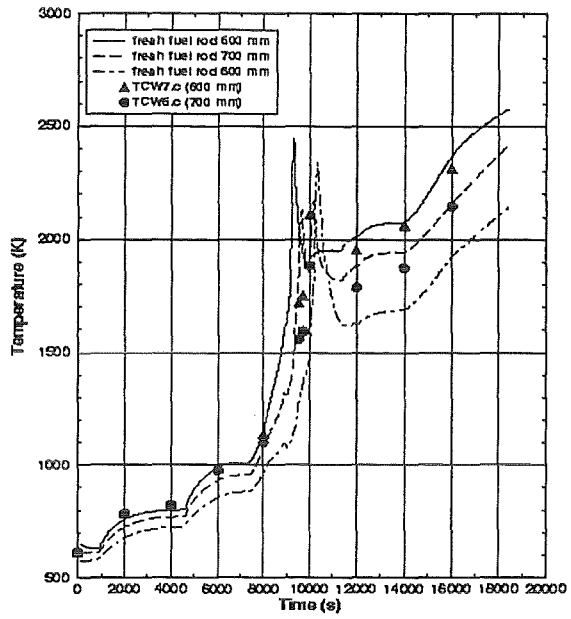


Fig. 4: Unirradiated fuel temperatures at 600 mm, 700 mm and 800 mm

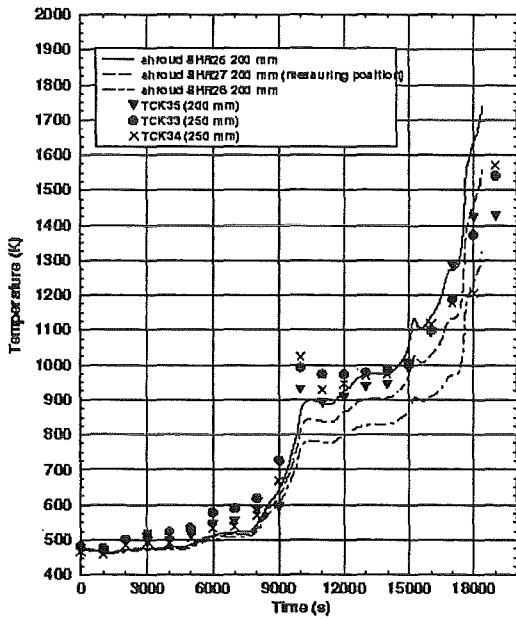


Fig. 5: Inner shroud temperatures at 200 mm elevation, calculated (lines) at radial measuring position (SHR27) and nearest inner (SHR26) and outer (SHR28) position; symbols are measured temperatures

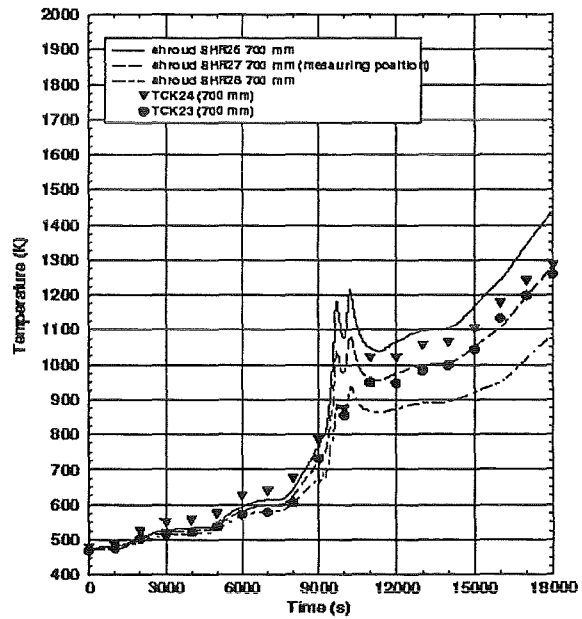


Fig. 6: Inner shroud temperatures at 700 mm elevation

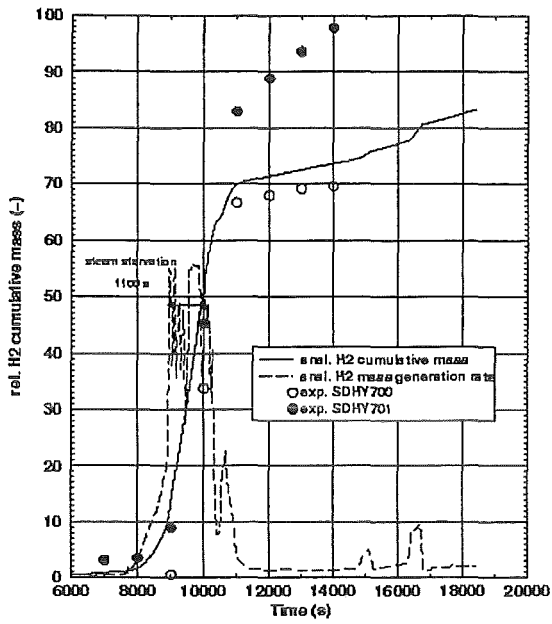


Fig. 7: Hydrogen masses calculated (lines) and measured (symbols) in relative units; the relative H2 production rates calculated are shown in dashed line

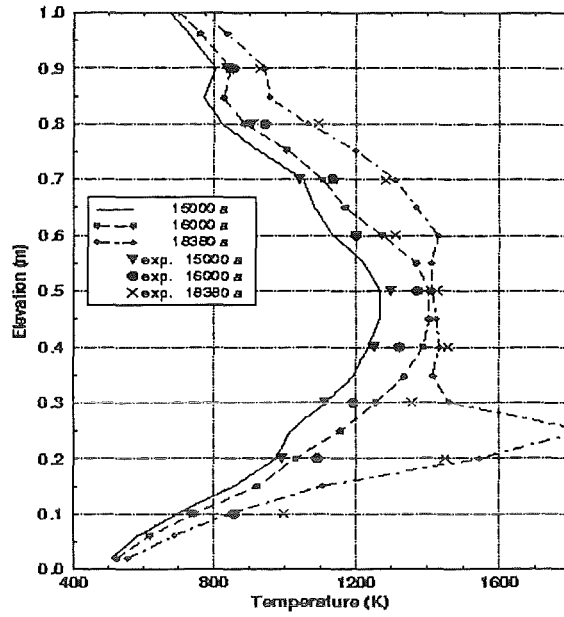


Fig. 8: Axial inner shroud temperatures at 15000 s, 16000 s and 18300 s, symbols represent measured data

## II. Deposition and Revaporisation of Fission Products

(G. Henneges, IKET)

### 1. Introduction

One of the objectives of the four-year FP5 PHEBEN2 project is to validate integral codes for LWR severe accident analysis versus available PHEBUS FPT data. This requires assessment criteria for integral codes based on the intended application in plant safety analysis, which is a second, parallel, objective. In order to meet this, a separate work package WP3 was defined. The objectives of the first two-year period of the project were to develop the criteria for integral code applications and to establish target uncertainties for their use in safety margin assessment, risk studies and other application areas. In the second two-year period of the project, the developed criteria will be applied and user guidelines will be developed for optimum code use to approach the target uncertainties as closely as possible.

Five key safety phenomena were selected which could be addressed by the PHEBUS FP programme: *Iodine chemical forms at circuit outlet, Iodine forms in containment, Aerosol behaviour inside containment, Deposition and revaporisation of fission products and Late phase H<sub>2</sub> production*. FZK agreed to be lead organisation for "Deposition and revaporisation of fission products".

### 2. Safety importance

Fission products are released during core degradation. The fission products sourced to the containment during confined sequences and the source to the auxiliary building or directly to the atmosphere during bypass sequences are found to have a high impact on the risk in PSA studies if the fission products are bound to aerosols being in suspension in the atmosphere or in gaseous form like I<sub>2</sub> or noble gases.

Besides of the mass of aerosol compounds or gases and the timing of the release many factors affect the behaviour of the fission products. These are mainly the physical and chemical forms of the species, the composition of the atmosphere, the structures of surfaces, temperatures and the mass flow regimes in the containment

building. For example Iodine which is bound in an insoluble form e.g. AgI, will deposit relatively fast on structures or can be washed out by containment sprays. Together with Cs it may react to CsI or another soluble species. Iodine in soluble form would again deposit, but could be re-released by radiochemical processes from the sump. In the case of basemat penetration or some other forms of containment leakage iodine-compounds or I<sup>-</sup> in the sump water could find its way into ground water and so enter the food chain. Deposited fission products can be revaporized by temperature changes, chemical reactions, radiochemical processes or changes of pH-values of the sump. Iodine is highly volatile and easily absorbed by inhalation or ingestion. Compared with other fission products it is only present in moderate quantities but it makes the major contribution to the short-term dose. Most hazardous is gaseous iodine, particularly in bypass sequences or for plants with high containment leak rates.

### **3. PSA assumptions**

A level 2 probabilistic safety analysis (PSA) requires studying complex physical and chemical processes for which only limited experimental data are available. Phenomena affecting the radionuclides during the accident and the transport of the radioactive material from the fuel through the containment to the environment are called "source term analysis". In the source term analysis the following issues are important:

- Inventories of radionuclides and structural materials in the core
- In-vessel radionuclide release and transport
- Iodine and caesium chemistry
- Chemistry of other fission products
- Retention and deposition of fission products inside the reactor coolant system (RCS)
- Ex-vessel radionuclide release and transport
- Aerosol behaviour inside the containment
- Deposition of aerosols and hosted fission products
- Revolatisation of aerosols and fission products
- Effect of energetic phenomena on in-containment fissions product behaviour
- Radionuclide release from containment or via bypass-scenario (Source Term).

Accident progression and containment performance analysis as well as source term calculation are strongly coupled. For example, the timing and the containment failure mode are important factors for the release from the containment to the environment, or the deposition of radionuclides in steam generator tubes or pressuriser surge line may create an extra hot spot which might fail the RCS at a particular location.

The radionuclide release and transport is dominated by "Iodine and caesium chemistry" in the short-term analysis, "Chemistry of other fission products" and "Deposition and resuspension of fission products inside the reactor" will be described in this section.

The term resuspension is also used for representing the following four phenomena:

*Resuspension:* Deposited aerosol or condensed materials on structure surface is suspended as fine fragments due to drag force by fluid flow or hydrogen burns.

*Revaporisation:* Chemical compound in the deposited aerosol or condensed material on the structure surface is vapourised when the vapour pressure at the surface is larger than the partial pressure in the gas due to, for example, fission product decay heating or heat by chemical reactions. It may also be initiated by a change of chemical conditions such as occurs when air from the containment enters the reactor coolant system.

*Reentrainment:* Chemical compound once dissolved in the liquid or deposited on walls is entrained as droplets by the boiling of liquid or steam flashing due to, for example, depressurisation.

*Revolatilisation:* Dissolved material in the pool water is evaporated due to conversion to volatile form by chemical reactions in particular by radiation field.

Besides of Cs and Iodine Tellurium exists in the fuel as  $Cs_2Te$ . It reacts with steam/hydrogen and forms  $TeO_2$ ,  $TeO$ , elemental Te and  $H_2Te$ . Elemental Te is more volatile than  $Cs_2Te$ . It can react with Zr and Sn producing tellurides and

zirconium, which are retained in the core debris up to about 2000°C. Vaporisation of structural and control rod materials also contributes to fission product releases, because these processes can make up the bulk of the aerosols which carry the fission products.

Barium and Strontium oxides in the fuel could react with zircalloy cladding to release volatile elemental Ba and Sr to the RCS relatively early. These would form hydroxides on contact with steam and behave similar like CsOH.

The fission products are carried along with steam and hydrogen, both as vapours and aerosols, or dissolved in any water retained in the circuit. Fission product vapours can condense on colder surfaces, as well as on other aerosol particles during their passage through the reactor coolant system to the containment. Fission product aerosols can agglomerate with other radioactive and nonactive aerosols to form larger particles which can deposit on structures.

Chemical interactions between fission products and metallic surfaces might lead to heatup due to decay heat content of deposits beyond the temperature required for re-vaporisation of previously deposited, chemically unbound volatile fission products. Also mechanisms like re-entrainment may cause re-volatilisation of previously deposited fission products.

In the primary system, the flow of liquid films on walls may be a major mechanism for the mass transport of deposited liquid droplets, and their subsequent re-injection into the containment atmosphere at the end of a broken pipe. Similarly, the transport of a large fraction of the solid particles deposited in the primary system may occur in the form of creep flow of the particles on the piping surfaces or saltation of particles close to surface.

Late in-vessel release of deposits will occur due to the decay heating of deposits in the reactor cooling system and produce temperatures sufficient to cause extensive re-vaporisation of volatile radionuclides such as caesium, iodine and perhaps tellurium and antimony. This re-vaporisation process can lead to protracted, low intensity release of radionuclides to the containment which could continue to

periods up to 50 hours. Thus, revaporisation can maintain risk significant concentrations of radionuclides in the reactor containment for very long times. Because of this, revaporisation is viewed as a more significant source term than resuspension of deposited radionuclides.

Ex-vessel phenomena in the long term phase depend on corium-concrete interactions, ex-vessel quenching, containment thermal hydraulics and eventually hydrogen combustion. After core melt/debris has fallen to the concrete at the bottom of the cavity it will heat up, begin to desintegrate and decompose chemically. As the bubbles of hydrogen, CO and CO<sub>2</sub> break up at the surface, aerosols are formed due to vapour condensation and film rupture. They contain radioactive fission products that contribute to the radiological source term. The volatility of the fission products carried away by the produced gases depends on the chemical conditions in the melt. In addition to this, the corium-concrete interaction may produce considerable amounts of non-radioactive aerosols, which may influence fission product transport at later times.

Volatile fission products, such as Cs, I and Te, which are volatile at the high temperatures of a degraded core either condense to form liquid or solid particles or combine chemically to form lower volatile species which then condense. The non-volatile fission products, together with the non-radioactive material, can be released during the hot corium-concrete interaction. These then become solid aerosols or absorb water vapour to become liquid aerosols. The behaviour of aerosols govern the rate of deposition of fission products in the containment. Deposition of aerosols are very important for removal of fission products from gases in severe accident scenarios.

Radioactive material deposited on surfaces or in water pools can, under certain circumstances, get airborne again. This resuspension process may occur if the gas flow across the surface increases, the temperature increases, the flashing or boiling in the pool occurs, or material in the pool is converted to volatile form.

#### **4. State of knowledge: experiments and calculations**

PHEBUS2 depends on other EU projects to provide input information for Phebus experiments and analysis. REVAP provided models to judge the contribution of revaporisation to circuit, while STORM gave valuable data on resuspension, which may have played a role in reducing the overall steam generator deposition. Revaporisation tests on samples from PHEBUS FPT1 fission products at ITU, Karlsruhe, AEA Technology, Winfrith and VTT, Espoo showed that kinetic barriers exist to revaporisation and the rerelease of caesium is slower than predicted by thermodynamics. The revaporisation of caesium is poorly predicted by current computer models. The TGT (thermal gradient tube) experiments at VTT with CsI and CsOH helped to design the TGT apparatus for revaporisation of FPT-1 samples. Models for revaporisation assume that the deposits are in chemical equilibrium and form an ideal mixture. Mass spectrometer studies of FPT-1 deposits have confirmed that caesium revaporisation occurs more slowly than would be expected from thermodynamics of Cs or CsO<sub>n</sub>, either due to diffusion effects or, perhaps due to interactions between Cs and other deposit materials. The Falcon experimental program at Winfrith and the small-scale VTT tests at Espoo showed that code calculations tend to overpredict rates of revaporisation and the total amounts revaporised. Better agreement between code analyses (SOPHAEROS and VICTORIA) was found than between code analyses and experimental results. This is on the side of conservatism. It seems that chemical reactions in the deposit and between the deposit and the substrate, which are not modelled in SOPHAEROS, may either decrease the quantities of fission products revaporised or increase the volatility of deposited fission products. The uncertainties in these experiments had proved to be very large and was not good for code validation.

There is a need for more and better revaporisation data before the models can be fully assessed and before proper extrapolation to reactor plant conditions can be made. To achieve greater confidence in application of the models in reactor studies further comparisons are necessary against both simple and, more importantly, realistic situations as may be generated by the Phebus FP experiments.

Analysis has shown that a large fraction of the fission products released during the early stages of a severe accident are deposited on reactor coolant surfaces due to

condensation, chemical interactions and aerosol deposition. The possible revaporisation of these deposits is probably the most significant uncertainty in the present understanding of fission product source terms. Models for revaporisation assume that the deposits are in chemical equilibrium and form an ideal mixture. This is not always true and has to be studied in more detail.

Fission product release from molten pools were carried out at AEAT, Winfrith (metallic melt) and ceramic melt experiments were conducted by LSK, Leningrad. The release of medium volatile fission products (Sr, Ba, Te) from molten pools during the late phase of severe accidents in light water reactors has been identified as being very important for source term calculations. A considerable mass of fuel melt (U) is likely to volatilise during a severe accident, if the melt is not cooled in the shortest time possible. Calculations with codes like RELOS.MOD2, GEMINI and MTDATA showed that the available experimental and theoretical database are incomplete. The RELOS.MOD2 analysis for U and Ba showed typical deviations of about one order of magnitude. The comparison of Sr releases showed significant differences of more than four orders of magnitude. GEMINI release rates for Sr, Ba and U were all overpredicted in ceramic environment whilst for the metallic melt tests the release of U, Ru and Zr were underpredicted. For Sr, Ba, Cs and Te the code overpredicted the release.

Resuspension processes are often characterised by low mass density rates but due to their long period (month, years) of activity they may be significant. The KAREX resuspension experiments at FZK, Karlsruhe study the resuspension of particles from liquids. Investigations on jet droplet formation due to bubble bursting at liquid surfaces are undertaken with different particle materials for many parameters. Numerical investigations and code developments for jet droplet formation are done with RESUS a code system developed at RUB (Ruhr Universität Bochum), Germany.

## **5. Lessons learned from the Phebus FP tests up to now**

The Phebus-FP experiments provide a unique opportunity to acquire samples of real deposited fission products. In the frame of the "Revaporisation Tests on Samples from Phebus Fission Products" (RVP) a detailed examination of re-

vaporisation phenomena, based on separate-effects studies with simulant fission product compounds and radiolabelled simulants, and integral validation of these studies with tests on samples from Phebus FPT1 was undertaken. They are described in detail in [BAN00] and [BRY98]. The test samples came from the upper vertical line (UVL) and the lower vertical line (LVL) in Phebus. The UVL samples, which had been deposited at about 500°C, were covered with a thick layer of aerosol particles and there was little oxidation of the metal substrate. The LVL samples had a much thinner layer of aerosol particles and oxidation happened beneath the aerosol layer. The LVL samples were deposited at about 700 °C. There was about 10 times more Cs on the UVL samples than the LVL samples. The Cs on the UVL sample was believed to be due to condensation of CsOH vapour and CsOH aerosol deposition. The Cs on the LVL sample was probably a mixture of condensed and chemiabsorbed CsOH, depending on the temperature history of the samples. The main constituents of the deposit layer were Re (from FPT-1 thermocouples), Ba and In although Cd, Ag, Sn, Zr, Mo, Sr and U were detected.

The main conclusions of the revaporisation tests on samples from Phebus FPT-1 studies were: When CsOH in hydrogen-steam atmospheres reacts with stainless steel above 500°C, a water soluble Cs-species is formed. This is followed by diffusion of Cs into oxide to form an insoluble Cs-species. Revaporisation of CsOH deposited at temperatures above 700 °C showed that the revaporisation rate of the chemiabsorbed soluble Cs-species, was controlled by kinetic factors and was considerably slower than would be expected from thermodynamics. This contradicts the assumption in the VICTORIA code that the soluble component of the chemiabsorbed CsOH can revaporise from the structure surface as easily as any other CsOH deposit. The revaporisation rate of the insoluble Cs-species was also controlled by kinetic factors, that is the desorption reaction and/or the diffusion of Cs through the oxide. The presence of steam appeared to increase the revaporisation rate of the soluble Cs-species, but the reasons are not yet understood.

The first 82% of the Cs on the UVL sample, and the first 45% of Cs on the LVL sample, revaporised in steam at the same rate as a CsOH radiotracer sample i.e. the revaporisation rate was initially controlled by thermodynamics, then by mass transfer rates. Hence, the revaporisation behaviour of CsOH condensed from the

gas phase or deposited as aerosol on the Phebus samples was not affected by the presence of other elements in the aerosol layer. This independence of the Cs revaporisation is highly significant as it enables one to predict Cs behaviour more easily under severe accident conditions. The basic assumption of codes such as VICTORIA, that deposit formed on structural surfaces behaves as an ideal mixture and that revaporisation of Cs can be modelled using thermodynamics and mass transfer considerations, is shown to be reasonable, at least at deposition temperatures below 500°C.

The last 15% of the Cs revaporised from the UVL sample, and the last 30 to 35% of Cs revaporised from the LVL sample, was released at a much slower rate than expected from thermodynamics and mass transfer considerations. The higher deposition temperature compared to the UVL sample seems the most likely explanation for the difference. This confirms the results of the separate-effects studies that kinetic effects are an important factor in the release of chemoabsorbed CsOH.

Significant revaporisation of Re, Ba, In and Ag occurred from the Phebus UVL sample during the revaporisation test in steam. Upon heating the UVL samples to 2400 °C in the Knudsen cell of a mass spectrometer the following species were released: Ag metal, In metal, Sn metal and oxides, Te metal, Re oxide, Mo oxides, W metal and oxides, and U metal and oxides. The revaporisation of the species was in reasonable agreement with thermodynamic predictions. However, Cs effused from the UVL samples at a much lower rate than that predicted under conditions of equilibrium partial pressure of Cs, CsOH or CsO<sub>n</sub>. This appears to contradict the revaporisation results for the UVL sample in steam. One explanation is that CsOH reacts with the aerosol layer to form a less volatile compound when the sample is heated in an atmosphere that contains water vapour.

A wave of Cs vapour (i.e. revaporisation or physical resuspension) occurred in the FPT-1 test directly after shutdown as fresh steam was passed through the circuit. The RVP results provide a plausible explanation for this effect, since the Phebus UVL and LVL samples displayed equilibrium with the CsOH vapour pressure in the steam in their initial exponential releases.

## 6. Preliminary indications for code use and code improvement

Present aerosol resuspension models are inadequate because existing models are based on different concepts and there is disagreement which are the important parameters that affect resuspension. Codes like SOPHAEROS, CAESAR, ECART, ART, VICTORIA used for ISP40 showed that even mechanistic codes tended to overpredict resuspension at high gas velocities and depended on unknown parameters. The simpler semi-empirical models suffer from the lack of a large database of experimental results, obtained under different test conditions, for different materials. The empirical coefficients used in those models were obtained by fitting a small number of experiments in a limited range of test conditions which are usually quite different from any reactor conditions. Much more data is needed before these models can obtain the degree of reliability of similar models for deposition calculations.

The potential of resuspension depends strongly on the characteristics of the deposit. The capability of codes to reproduce experimental results for aerosol resuspension is severely hindered by the lack of knowledge of physical characteristics of these deposits, namely the sizes of the resuspendable agglomerates and the porosity of the bed and surface. The size of the resuspended particles is crucial in determining whether they will re-deposit downstream or be carried into the containment or into the environment.

The focus in future must therefore be on errors due to the applied physical model; and the error due to the freedom in choice of model parameters, as allowed by current knowledge. These errors depend on the extent to which the model is valid for the range of conditions occurring in the applications. In case a correlation is used in a model, the range of validity of the correlation is critical.

Particular attention has to be paid to the aspect of scaling. Phebus is realistic (scaled 1:1 compared with a plant) for some aspects, but very much reduced in scale for others e.g volume to surface ratios. These aspects must be considered in detail.

## References

[ALL00] H.-J. Allelein et al, "Validation strategies for severe accident codes", Final Summary Report, EC contract FI14S-CT98-0054, GRS Cologne, 2000.

[ALL00] H.-J. Allelein (ed.), "Nuclear aerosols in reactor safety" - proceedings of an OECD/CSNI workshop 15-18<sup>th</sup> June 1998, Cologne, Germany". Report NEA/CSNI/R(98)4 , February 2000.

[BAN00] A. Benderson et al, "Revaporisation tests on samples from Phebus fission products", summary final report, ST.RVP(00)-P30, 2000.

[BRY98] C. J. Bryan et al, "Revaporisation: Simulant studies, final report", AEAT 3931 Issue 2, July 98

[BEN99] C. G. Benson et al, "Fission product release and speciation", EU Research in Reactor Safety, FISA 99 , Luxembourg, 29 November to 1 December 1999, pp 321.

[BEN99] C. G. Benson et al, "Fission product release from molten pools", EU Research in Reactor Safety, FISA 99 , Luxembourg, 29 November to 1 December 1999, pp 375.

[BOW85] B. R. Bowsher, "Fission product chemistry and aerosol behaviour in the primary circuit of a pressurised water reactor under severe accident conditions", UKAEA Report AEEW-R 1982, 1985.

[BOW99] B. R. Bowsher et al, "Revaporization tests on samples from Phebus fission products", EU Research in Reactor Safety, FISA 99 , Luxembourg, 29 November to 1 December 1999, pp 357.

[CAN99] L. Cantrel and L. van Wijk, "Iodine chemical kinetic study within the primary circuit under Phebus FPT0 conditions", JRC Technical Note No. I.99.188, Pheben document ST-PHEBEN(99)-D13, 1999.

[CAN01] L. Cantrel and E. Krausmann, Manuscript in preparation, 2001.

[CRO88] A. W. Cronenberg and D. J. Osetek, "Reaction kinetics of iodine and cesium in steam/hydrogen mixtures", Nucl. Technol. **81**, 1988, pp 347.

[DIC99] S. Dickinson et al, "Iodine chemistry", EU Research in Reactor Safety, Luxembourg, FISA 99 , 29 Nov. –1 Dec. 1999, pp 330.

[DIC00] S. Dickinson and H E Sims, "Development of the INSPECT model for the prediction of Iodine volatility from irradiated solutions", Nucl Techn. **129**, pp 374, 2000.

[DIC01] S. Dickinson et al, "Iodine chemistry and mitigation mechanisms", FISA-2001, EU Research in Reactor Safety, Luxembourg, 12-14 November 2001, pp 496.

[EVA96] G. J. Evans, "Measurement and modeling of Iodine volatility above irradiated Csl solutions", Nucl Techn. **116**, pp 293, 1996.

[FPT00] PHEBUS PF Team, "Final Report FPT1", CEA, issued by ABC Communication September 2000 (available on CD-ROM).

[GUN01] S. Guntay et al, "Radiolytic stability of Silver Iodide – PSI Phebus in-kind contribution", Phebus-FP Report TG-390, 2001

[HOB93] R. R. Hobbins, D A Petti and D L Hagrman, "Fission product release from fuel under severe accident conditions", Nucl Technol 101, pp 270, 1993.

[JAC00] D. Jacquemain et al, "FPT1 Final Report" IPSN Report PH-PF IP/00/479, December 2000.

[JON00] A. V. Jones et al, "Benchmark release, circuit and containment codes against Phebus FP", EU Research in Reactor Safety, Luxembourg, FISA 99 , Luxembourg, 29 Nov. –1 Dec. 1999, pp 394.

[JON00] A. V. Jones and M.P. Kissane, "Phebus FP: State of understanding of fission product transport in the circuit and of aerosol behaviour in the containment", JRC Tech. Note I.00.55, April 2000

[KRA01] E. Krausmann, "State of the art report on iodine chemistry and related mitigation mechanisms in the containment", Report EUR 19752 EN (2001)

[MAS99] P. K. Mason. "Preliminary assessment of boron carbide control rod release and consequences for fission products", NT SEMAR 98/129, February 1999.

[NEA97] OECD Nuclear Energy Agency. "Level2 PSA methodology and severe accident management, prepared by the CNRA working group on inspection practices (WGIP)", report OCDE/GD(97)198, 1997.

[NEA99] OECD Nuclear Energy Agency. "ISP 40, Aerosol deposition and resuspension", report NEA/CSNI/R(99)4 and EUR 18708EN, Feb. 1999.

[NEA00] OECD Nuclear Energy Agency. "Insights into the control of the release of iodine, caesium, strontium and other fission products in the containment by severe accident management", report NEA/CSNI/R(2000)9, March 2000.

[SCH99] M. Schwarz, B. Clement, A.V. Jones, "Applicability of Phebus-FP results to severe accident safety evaluations and management measures", EU Research in Reactor Safety, FISA 99 , Luxembourg, 29 November to 1 December, pp 311.

[SCH01] M. Schwarz, B. Clement, A.V. Jones, "Applicability of Phebus-FP results to severe accident safety evaluations and management measures", Nuclear Engineering and Design, V.209, pp 173, 2001.

[SMI99] P. N. Smith et al, "Source term leakage from containment", EU Research in Reactor Safety, FISA 99 , Luxembourg, 29 November to 1 December 1999, pp 410.

[TAG01] F. Taghipour and G. J. Evans, "Radioiodine volatilisation in the presence of organic compounds", Nucl Technol 134, pp 208, 2001.

[WIL99] D. A. Williams et al, "Assessment of models for fission product revaporisation", EU Research in Reactor Safety, FISA 99 , Luxembourg, 29 November to 1 December 1999, pp 366.

[VOS97] A. Voßnacke, M.K. Koch, H. Unger, "RECOM: A Code for the simulation of radionuclide resuspension at bubbling water pools surfaces", Proc. Of Annual Meeting on Nucl. Technol. 97, pp 206, 1997.

## **32.21.11 Untersuchungen zur Reaktor- und Anlagendynamik**

### Investigations on Reactor and Plant Dynamics

(D.C. Cacuci, M. Ionescu-Bujor, W. Hering, V.H. Sanchez, IRS)

#### **Abstract**

At the Institute for Reactor Safety (IRS) of the Forschungszentrum Karlsruhe (FZK) the thermohydraulic code system RELAP5 is validated and extended as part of the CAMP agreement. The Adjoint Sensitivity Analysis Procedure (ASAP) implemented in RELAP5 is under validation for single- and two-phase conditions. As part of the 5<sup>th</sup> EU framework program HPLWR, RELAP5 mod 3.3 was assessed to simulate correctly transient fluid conditions in the supercritical and in the transition to the two-phase flow regime.

#### **Zusammenfassung**

Am Institut für Reaktorsicherheit (IRS) des Forschungszentrums Karlsruhe (FZK) wird im Rahmen der CAMP-Vereinbarung das Thermohydraulik-Programm RELAP5 validiert und erweitert. Das in RELAP5 implementierte Verfahren "Adjoint Sensitivity Analysis Procedure" (ASAP) wird für ein- und zweiphasige Bedingungen erweitert und validiert. Als Beitrag zum HPLWR Programm im 5. Rahmenprogramm der EU wurde RELAP5 mod 3.3 in Bezug auf seine Eignung für transiente Analysen im überkritischen Bereich und beim Übergang in das Zweiphasengebiet untersucht.

#### **1.1 Status of the implementation of ASAP (Adjoint Sensitivity Analysis Procedure) within RELAP5**

The implementation of the Adjoint Sensitivity Analysis Procedure (ASAP) within the RELAP5/MOD3.2 reactor safety code system has been continued by developing the Adjoint Sensitivity Model for the heat structure equations and subsequently coupling it to the extant Adjoint Sensitivity Model for the two-fluid-flow equations. The validation of the numerical solution of the coupled two-fluid/heat structure adjoint models has been successfully performed using the experimental data of the QUENCH-04 experiment.

Current work on implementing the ASAP procedure within the RELAP5 code system focuses on obtaining sensitivities to the many hundreds of parameters pertaining to the two-fluid and heat structure equations. Currently, the parameters of interest are those associated with the geometry of the problem, system power, and heat conductivity. Many sensitivities of temperature profiles with respect to selected parameter at various axial and radial levels in the rod bundle of the QUENCH-04 experiment have been calculated and validated. The validation process involves comparison between ASAP-results and exact values obtained by recalculations.

The near-term goal of this research is to extend the ASAP to obtain sensitivities to additional parameters, such as those underlying correlation for the heat coefficients. Longer-term, it is planned to extend the ASAP to perform sensitivity analysis of transition phenomena between various flow regimes. Furthermore, the ASAP-modules will be revised and adapted to the final version of RELAP5/MOD3.3, as soon as this new code version is released to CAMP members /1/.

## **1.2 Status of the coupled code system RELAP5/PARCS**

The steady development of computer tools for safety evaluation of NPPs as well as the needs to improve the economics of LWR under operation keeping high safety levels make necessary the qualification and improvement of advanced safety analysis tools.

Hence best-estimate code systems with 3D-neutron kinetic capabilities are being qualified and validated at IRS by means of international benchmarks and data from power plants or experiments. FZK and Framatome ANP/Erlangen (former Siemens/KWU) participated on the OECD/NEA PWR Main Steam Line Break (MSLB)-Benchmark /2/ obtaining very good results with the code system RELAP5/PANBOX. PANBOX is a 3D-kinetics code system developed by Framatome ANP /3/.

In the frame of the international CAMP-program, the code system RELAP5/PARCS was installed at IRS and it is being tested. The neutronics code PARCS /4/, Purdue Analyse Reactor Core Simulator, is a 3D-kinetics system with few- and multi-group neutron diffusion capability for both square and hexagonal fuel assemblies, respectively. Its multi-group capability linked to the hexagonal fuel assembly is unique and it makes PARCS a appropriate candidate to assess the safety features not only of

Russian VVER-reactors but also of innovative systems like the HPLWR. Consequently a large number of transients in PWR and BWR can be analysed from a multi-dimensional point of view with the coupled system RELAP5/PARCS.

It is envisaged to use RELAP5/PARCS to simulate the OECD/NEA international benchmark devoted to the Kozloduy VVER-1000 NPP that will start in this year. In this connection the emphasis is paid on the qualification of the multidimensional capability for hexagonal fuel assemblies.

### **1.3 Evaluation of RELAP5 for innovative reactor concepts (HPLWR)**

In the frame of the 5<sup>th</sup> Framework Program of the EU the HPLWR-project, the design and safety features of the HPLWR are being investigated at IRS using several computer codes /7/,/8/.

Since RELAP5 was not developed for supercritical water conditions and hence never tested under such situations, investigations are focused on thermo-physical properties of water for the supercritical region, relevant heat transfer correlations and the simulation of selected transients.

It was demonstrated that the steam tables implemented in RELAP5, i.e. the ASME-IF-67 (optional) and IAPWS-IF95 (default) covers the sub-critical and the supercritical regions and that the thermo-physical properties are predicted in a consistent manner for steady state situations. In case of fast de-pressurization transients like the LB-LOCA, the interpolation scheme fails to predict the thermo-physical properties of the super-critical water especially around the critical point.

To check the appropriateness of RELAP5 to simulate the selected HPLWR-transients, a simplified plant model was developed. After some code modifications RELAP5/MOD3.2.2 $\psi$  was able to predict reasonable stationary plant conditions that serve as a starting point for following of analysis of transients. The model is based on the reference design /9/.

Coupling RELAP5 with the neutronic package KARBUS/KAPROS a more realistic axial power profile for the reference design was determined. Calculated power profile the main steady state parameters for the reference design were recalculated with RELAP5.

In Figure 1 a comparison of the assumed and of the predicted axial power profile for the reference design is given. Most of the power is concentrated in the lower core part. The resulting axial density distribution for the cosine-shaped and predicted power profile is shown in Figure 2. Further investigations are underway to analyse the HPLWR-behaviour under accidental conditions. Based on the performed studies can be already stated that the core neutronic is very tight linked with the thermal hydraulic plant behaviour.

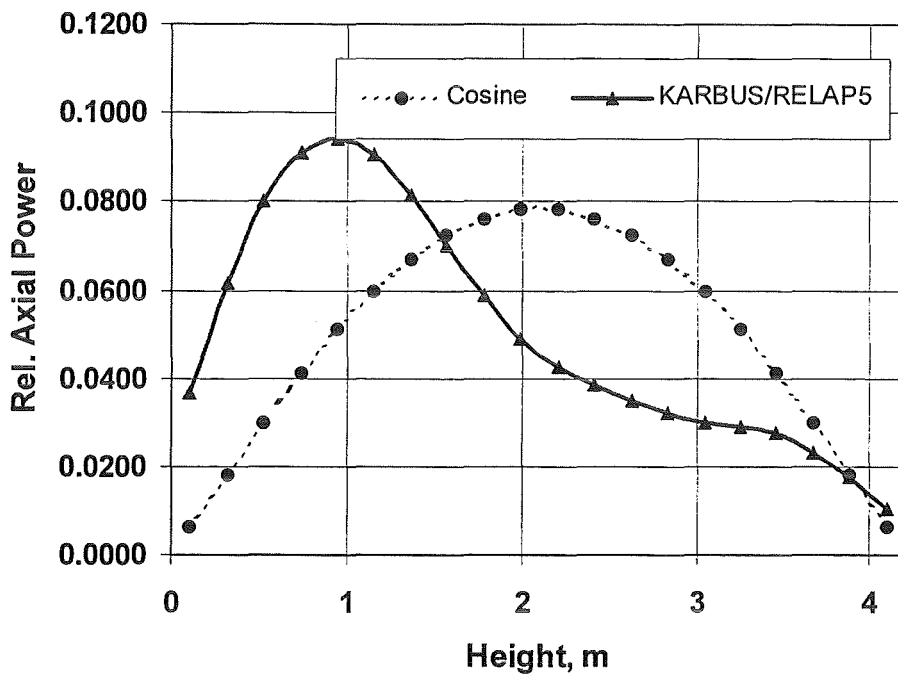


Figure 1 Comparison of the assumed (cosine shape) and predicted axial power profile for the reference design

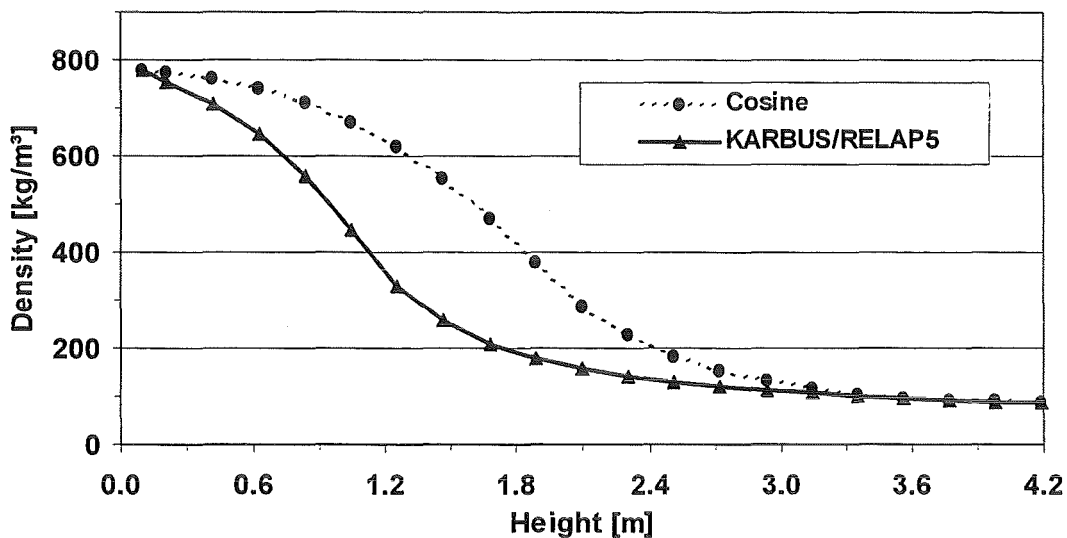


Figure 2 Predicted axial density distribution based on different axial power profiles

### 1.3.1 Literature

- /1/ Scientec Thermohydraulic Group, RELAP5/MOD3 Code Manuals Vol. 1-8, Formerly NUREG/CR-5535, June 1999.
- /2/ K. N. Ivanov, T. M. Beam and A. Baratta; Pressurised Water Reactor main Steam Line Break (MSLB) Benchmark. Volume 1: Final Specifications. NEA/NSC/DOC(99)8. April 1999.
- /3/ R. Böer, R. Böhm, H. Finneemann, R. Müller; The coupled neutronics and thermal hydraulics code system PANBOX for PWR safety analysis, Kerntechnik 57 (1992) No. 1, pp. 49-54.
- /4/ D. A. Barber, T. J. Downar, W. Wang; Final Completion of Report for the Coupled RELAP5/PARCS. Report PU/NE-98-31. November 1998.
- /5/ V. Sánchez, A. Knoll; Analyses of the International Main Steam Line Break (MSLB)-Benchmark with the Code System RELAP5/MOD3.2 using the Point Kinetics Option. Report FZK-6427, 2001.
- /6/ V. Sánchez, Ch. Homann, R. Böer, FZK/Siemens Investigations on MSLB-Phase 3 with the "Best-Estimate" Code System RELAP5/PANBOX . 16 Spring 2000 CAMP-Meeting. 17-19 April 2000. Sicily, Italy.
- /7/ G. Heusener, U. Müller, T. Schulenberg, D. Squarer; A European Development Program for a High Performance Light Water Reactor. , SCR-2000, Nov. 6-8, 2000
- /8/ Dobashi, K. Oka, Y., Koshizuka, S., Conceptual Design of a High Temperature Power Reactor Cooled And Moderated By Supercritical Light Water; ICONE-6, May 10-15, 1998, ASME, NY.
- /9/ Oka, Y. Koshizuka, S., Design Concept of Once-Through Cycle Supercritical-Pressure Light Water Cooled Reactors; SCR-2000, Nov. 6-8, 2000.

## 32.22 INNOVATIVE SYSTEME

### 32.22.03 Entwicklung von Methoden, physikalischen Modellen und Rechenprogrammen zur Zweiphasenströmung

#### I. Theoretische Untersuchungen

(M. Wörner, M. Ilic, G. Grötzbach, D.G. Cacuci, IRS)

#### **Abstract**

We discuss results of direct numerical simulations for the rise of an ellipsoidal bubble through liquid. In particular we perform a numerical study to assess the influence of the liquid-to-gas density ratio. Supposing the similarity of the Morton number and the Eötvös number, we have found that results obtained for steady bubble rise with density ratio of order  $O(10)$  can well be transferred to a density ratio of  $O(1000)$ , typical for practical situations. In addition, we used the DNS data to test and to rate several methods proposed in literature for evaluation of spectra from discontinuous liquid phase velocity signals.

#### **Zusammenfassung**

Es werden Ergebnisse von Direkten Numerischen Simulationen zum Aufstieg einer ellipsoiden Einzelblase diskutiert. Eine Studie zum Einfluss des Dichteverhältnisses zeigt, dass unter Beachtung der Ähnlichkeitsparameter Morton- und Eötvös-Zahl Ergebnisse für stationär aufsteigende Blasen mit einem Dichteverhältnis in der Größenordnung  $O(10)$  auf das in der Realität typische Dichteverhältnis  $O(1000)$  übertragbar sind. Basierend auf den DNS Ergebnissen werden verschiedene in der Literatur vorgeschlagene Methoden zur Auswertung des Spektrums der Geschwindigkeitsfluktuationen analysiert und bewertet.

#### **1. Introduction**

One important, but only partly understood, topic in two-phase flow research is the modification of the turbulence structure in the liquid phase due to the presence of bubbles and their relative motion. While turbulence modeling of single phase flows has now reached a certain level of maturity, reliable and general models for bubble induced turbulence (BIT) are still missing. In this context, our research concerns the

investigation of bubble induced turbulence using direct numerical simulation (DNS). Ultimately, the results shall contribute to the development of improved statistical models of BIT. The study of BIT by DNS offers a significant advantage, that is, the detailed information about the full three-dimensional velocity field and the interface topology is available. The DNS are performed with our in-house computer code TURBIT-VOF [1,2,3] which solves Navier-Stokes equations in formulation for incompressible gas and liquid phase and uses the volume-of-fluid method for tracking the gas-liquid interfaces. The DNS results presented below concern the rise of an ellipsoidal bubble through an initially still liquid. Firstly, we investigate the influence of the gas-liquid density ratio on the rise velocity of a single bubble in steady regime. Secondly, we consider the rise of a regular chain of ellipsoidal bubbles. We use these DNS results to test several methods proposed in literature how to bridge over the gaps in the discontinuous liquid phase velocity signal in order to provide the evaluation of the spectrum.

## 2. Influence of density ratio on bubble rise velocity

We consider the rise of a single bubble (equivalent diameter  $d$ , density  $\rho_g$ , viscosity  $\mu_g$ ) through quiescent liquid (density  $\rho_l$ , viscosity  $\mu_l$ , surface tension  $\sigma$ ) of infinite extent due to gravity ( $g$ ). By dimensional analysis one can show that for the terminal velocity  $U_B$  of the bubble a functional relationship  $Re_B = f(M, E\ddot{o}, \lambda, \eta)$  does exist [4]. Here,  $Re_B = \rho_l d U_B / \mu_l$  is the bubble Reynolds number,  $M = (\rho_l - \rho_g) g d^4 / (\rho_l^2 \sigma^3)$  is the Morton number,  $E\ddot{o} = (\rho_l - \rho_g) g d^2 / \sigma$  is the Eötvös number, and  $\lambda = \rho_l / \rho_g$  and  $\eta = \mu_l / \mu_g$  are the ratios of liquid-to-gas density and viscosity, respectively.

In the state-of-the-art literature only very few studies have been devoted to the influence of the density ratio on the non-dimensional bubble rise velocity, i.e. the bubble Reynolds number  $Re_B$ . In these studies, however, besides the density ratio  $M$  and  $E\ddot{o}$  are, also, varied. Associated with the development of advanced methods for direct numerical simulation of bubbles and the availability of more and more powerful computers there is, however, a certain interest to quantify the influence of  $\lambda$  on  $Re_B$ . In two-phase flow DNS is usually not performed for a density ratio of about 1000, as it is typical for air bubbles in water. Instead, to avoid numerical problems and to minimize the computational costs, often a value  $\lambda < 100$  is chosen. This raises the question to which extent results obtained from such simulations can be transferred to gas-liquid systems of higher  $\lambda$ .

We systematically investigated the influence of the density ratio on the bubble Reynolds number by a series of 3D direct numerical simulations. In Figure 1 a sketch of the computational domain is shown. It consists of a box of (non-dimensional) size  $L_x \times L_y \times L_z = 2 \times 1 \times 1$ , which is laterally confined by two rigid walls ( $z=0$  and  $z=1$ ). In vertical ( $x$ ) and spanwise direction ( $y$ ) periodic boundary conditions are applied. The domain is discretized by  $128 \times 64 \times 64$  uniform mesh cells. At time  $t=0$  a spherical bubble of diameter  $1/4$  is positioned at  $x = y = z = 0.5$ ; both gas and liquid are initially at rest. In all computations the Morton number was  $M = 3,09 \cdot 10^{-6}$ , the Eötvös number was  $E\ddot{o} = 3,06$ , and the viscosity ratio was  $\eta = 1$ . These values for  $M$  and  $E\ddot{o}$  correspond to an axisymmetric ellipsoidal bubble that rises along a rectilinear path. The values chosen for the density ratio in the different runs are  $\lambda = 2, 5, 10$  and  $50$ .

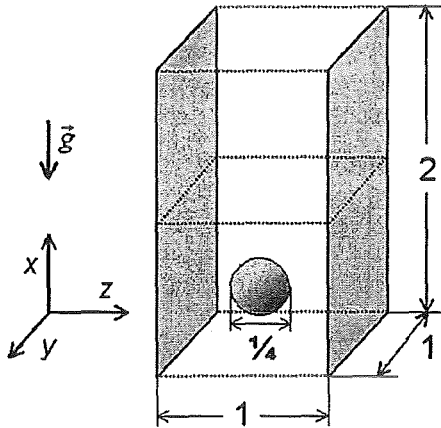


Fig. 1: Sketch of computational domain.

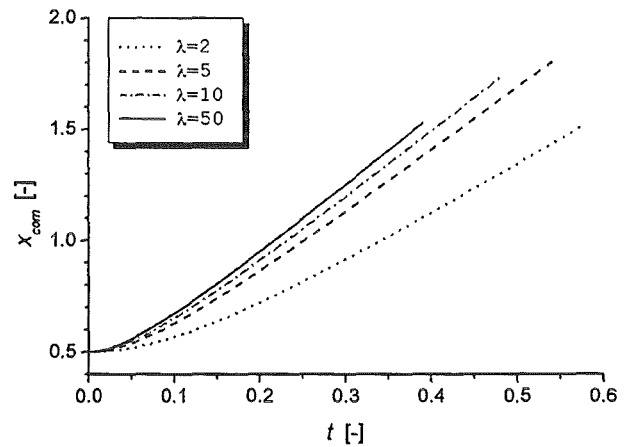
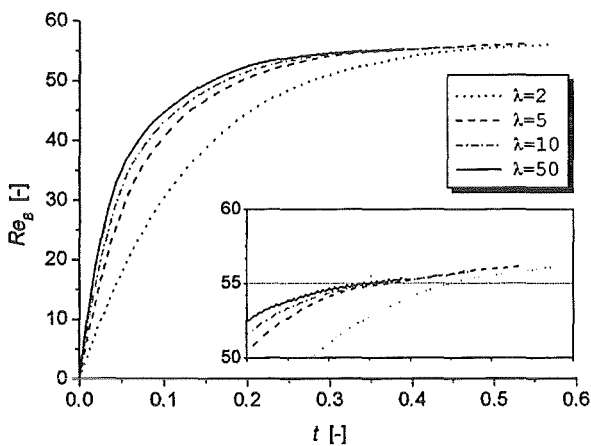


Fig. 2: Vertical position of bubble center of mass over time for different values of  $\lambda$ .

In the recent paper [5] we analyzed the simulation results regarding the influence of the density ratio on the bubble Reynolds number. In Figure 2 the vertical position of the bubble center of mass is shown as function of time for the different density ratios. It appears that the density ratio affects the intensity of bubble acceleration from rest towards its terminal velocity and, also, affects the terminal velocity as well. The influence of  $\lambda$  on the bubble acceleration can be explained by the added mass force [5]. Figure 3, however, shows that the terminal value of the bubble Reynolds number  $Re_B$  is obviously unaffected by the density ratio. The numerical value of  $Re_B$  is in good agreement with that of a correlation  $Re_B = f(M, E\ddot{o})$  obtained from two-phase wave theory.

The findings just discussed are based on the bubble velocity  $U_B$  which is essentially an integral velocity. We now analyze our DNS results regarding the influence of the density ratio on the *local* velocity field, in both the liquid and gas phase. For a reasonable comparison of the local velocity field obtained for the different density ratios we firstly select a certain instant in time. The vertical size of the computational domain is eight times the equivalent bubble diameter. To ensure that the influence of the periodic boundary conditions, i.e. that of the “leading” and “trailing” bubble, is sufficiently small we consider that instant in time when the vertical position of the bubble center of mass is at  $x_{com} = 1.5$  and thus the bubble has passed the distance equal exactly four times its initial diameter. As it can be seen in Figure 2 this time level differs for the different runs. We compare local velocity profiles along certain lines within our 3D flow domain. As an example in Figure 4 the vertical velocity component  $u$  normalized by the bubble velocity  $U_B$  is shown as function of the vertical co-ordinate  $x$  for fixed spanwise and wall-normal co-ordinates  $y = z = 0.5$ . Also shown in Figure 4 is the local profile of the liquid volumetric fraction  $f$ . In mesh cells filled with liquid  $f = 1$ , in cells filled with gas  $f = 0$ , while in cells that instantaneously contain both phases  $0 < f < 1$ . It can be seen that the curves for the different density ratios do almost collapse exactly to one single curve. Thus, when scaled with the bubble rise velocity, the local velocity both inside the bubble and in the liquid are identical and are invariant with respect to the density ratio.



**Fig. 3:** Bubble Reynolds number  $Re_B$  as function of time for different values of density ratio  $\lambda$ .

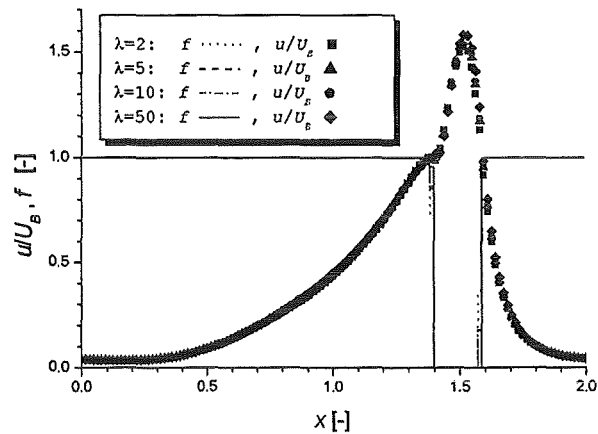


**Fig. 4:** Vertical profile of normalized vertical velocity  $u/U_B$  and liquid volume fraction  $f$  for position  $y = z = 0.5$ .

### 3. Analysis of spectrum of liquid phase velocity fluctuations

While the boundary and initial conditions are the same as in the previous section, in the simulation considered now the size of the computational domain is reduced to  $1 \times 1 \times 1$ . The grid consists of  $64 \times 64 \times 64$  uniform mesh cells. Also the Eötvös and Morton number are the same as before while the density ratio is 2. Using the time step width  $\Delta t = 0.0001$  in total 65,000 time steps are computed. Within this time the gas-liquid system has reached a quasi-steady state, where the mean velocity of the liquid phase and the bubble rise velocity can be considered as constant. In total the bubble passes 24 times the computational domain. In this simulation there is therefore a distinct influence due to the periodic boundary conditions and the flow is typical for a regular bubble chain instead for a single bubble, as it was the case in section 2. However, the bubble is still axisymmetric and of oblate ellipsoidal shape and rises along a rectilinear path.

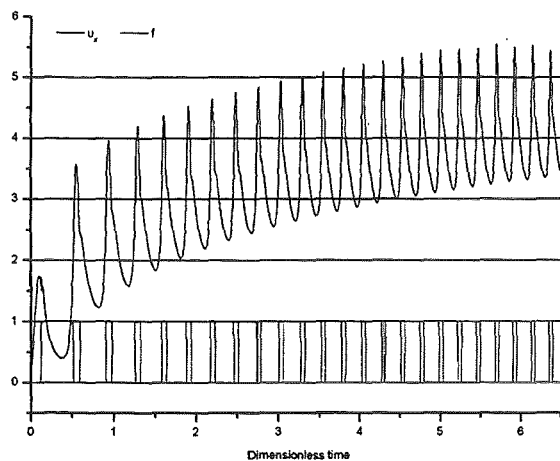


**Fig. 5:** Instantaneous vertical component,  $u_x$ , of center-of-mass velocity and liquid volume fraction,  $f$ , for position  $x = y = z = 0.5$ .

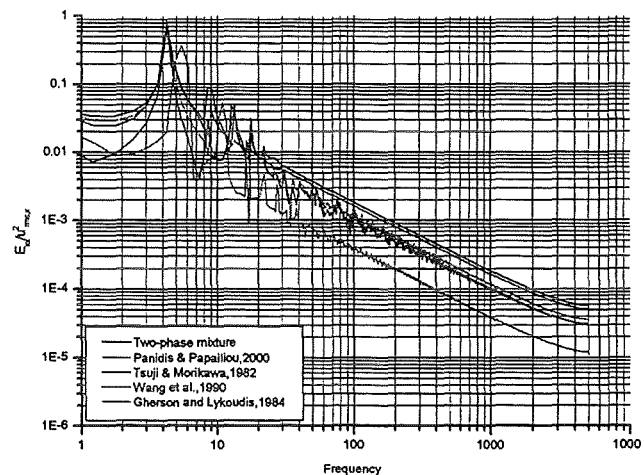


**Fig. 6:** Spectrum of kinetic energy of liquid phase velocity fluctuations for the different methodologies.

In Figure 5 values of the vertical component of the instantaneous center-of-mass velocity and liquid volumetric fraction,  $f$ , in the mesh cell with the center at  $x = y = z = 0.5$  are shown. When the cell is fully occupied by liquid then  $f = 1$  and the center-of-mass velocity is just the liquid velocity. Hence, from the signals displayed in Figure 5 the liquid phase velocity can be extracted. The instantaneous velocity signal for liquid phase is, however, discontinuous. Nevertheless, from this signal a mean velocity can be computed within a suitable time interval. Then the signal of the instantaneous velocity fluctuations can be computed, which is, also, discontinuous. From this signal

the following statistical quantities have been evaluated for different wall-normal positions: root-mean-square values of velocity components, kinetic energy of liquid velocity fluctuations, and components of the Reynolds stress tensor.

Due to the discontinuous character of the fluctuating liquid velocity signal the evaluation of autocorrelations and spectra is not straightforward. In literature various methodologies how to bridge the signal gaps due to bubble passages are proposed:

- Gherson & Lykoudis [6] suppressed parts of the signal concerning gas presence and simply patched together the successive liquid velocity records;
- Tsuji & Morikawa [7] replaced the defective parts of the signal by straight lines obtained by linear interpolation between the regular parts;
- Wang et al. [8] replaced the gaps in the signal with the values of the mean velocity;
- Panidis & Papailiou [9] introduced an indirect analytic continuity which essentially presumes that the void fraction parts of the signal are filled with segments having the same statistical properties as those of the continuous phase velocity signal.

As none of the methods proposed up to now has been accepted as definite one, we applied the above four methods to the discontinuous signal obtained from our DNS and computed the autocorrelation functions. Employing the Fast Fourier Transformation of these autocorrelation functions corresponding spectra are obtained. Figure 6 shows the spectrum of the kinetic energy of the liquid phase velocity fluctuations in time interval  $t = 4.8-6.5$  evaluated according to these four methods. For comparison, the spectrum obtained using the continuous center-of-mass velocity signal (i.e. the two-phase mixture) is, also, included in Figure 6. Further, we investigated the influence of the length of the time interval on the spectrum for the different methodologies.

From the results obtained the following conclusions can be drawn. The method of Gherson & Lykoudis [6] can not be recommended as it significantly overestimates the dominant frequency, while all the other methods do meet it correctly. Except of the low frequency part, the spectrum obtained by the method of Tsuji & Morikawa [7] is very close to that obtained for the two-phase mixture. Besides, the spectrum calculated by this method strongly depends on the length of the time interval

considered. The methods of Panidis & Papailiou [9] and Wang et al. [8] gave similar results, but the former one should be preferred since it showed weaker sensitivity on the length of the time interval.

#### 4. Conclusions and outlook

From the result presented above we conclude that under proper scaling the local velocity field induced by a bubble rising steadily through liquid is invariant under variation of the density ratio. Therefore, DNS results obtained for such bubbles using a density ratio of order 10-100 can well be transferred to gas-liquid systems with density ratio of order 1000, provided the similarity of  $E\ddot{o}_B$ ,  $M$  and  $\eta$  does hold. Furthermore, our results indicate that rather universal models for the turbulence induced by bubbles rising almost steadily in dilute gas-liquid flows may be derived in terms of  $E\ddot{o}_B$  and  $M$ . A key aspect for modelling of bubble-induced turbulence is the knowledge and understanding of statistical features of liquid phase velocity fluctuations. By analysis of the spectrum of liquid phase velocity fluctuations and further statistical data, not shown here, a first step toward this goal is undertaken. The next step will be the analysis of terms in the transport equation for the kinetic energy of liquid phase velocity fluctuations. In engineering computer codes the modelled form of this equations often forms the basis to account for bubble induced turbulence.

#### References

- [1] W. Sabisch: *Dreidimensionale numerische Simulation der Dynamik von aufsteigenden Einzelblasen und Blasenschwärmen mit einer Volume-of-Fluid-Methode*. Forschungszentrum Karlsruhe, Wissenschaftliche Berichte FZKA 6478, Juni 2000.
- [2] W. Sabisch, M. Wörner, G. Grötzbach, D.G. Cacuci: *3D Volume-of-Fluid Simulation of a Wobbling Bubble in a Gas-Liquid System of Low Morton Number*, 4<sup>th</sup> Int. Conf. on Multiphase Flow, New Orleans, USA, May 27 – June 1, 2001.
- [3] M. Wörner, W. Sabisch, G. Grötzbach, D.G. Cacuci: *Volume-averaged conservation equations for volume-of-fluid interface tracking*, 4<sup>th</sup> Int. Conf. on Multiphase Flow, New Orleans, USA, May 27 – June 1, 2001.

- [4] J.R. Grace: *Shapes and velocities of bubbles rising in infinite liquids*. Trans. Instn. Chem. Eng. **51** (1973) 116.
- [5] M. Wörner: *The influence of gas-liquid density ratio on shape and rise velocity of an ellipsoidal bubble: A numerical study by 3D volume-of-fluid computations*, Proc. 1<sup>st</sup> Workshop on Transport Phenomena with Moving Boundaries, October 11-12, 2001, Berlin, Germany, to appear.
- [6] P. Gherson, P.S. Lykoudis: *Local Measurements in Two-Phase Liquid-Metal Magneto-Fluid-Mechanistic Flow*, Journal of Fluid Mechanics **147** (1984) 81.
- [7] Y. Tsuji, Y. Morikawa: *LDV Measurements of an Air-Solid Two-Phase Flow in a Horizontal Pipe*, Journal of Fluid Mechanics **120** (1982) 385.
- [8] S.K. Wang, S.J. Lee, O.C. Jones, R.T. Lahey Jr.: *Statistical Analysis of Turbulent Two-Phase Pipe Flow*, Journal of Fluids Engineering **112** (1990) 89.
- [9] Th. Panidis, D.D. Papailiou: *The Structure of Two-Phase Grid Turbulence in a Rectangular Channel: an Experimental Study*, Int. J. Multiphase Flow **26** (2000) 1369.

- II. Experimentelle Untersuchungen zum Strömungsumfeld aufsteigender Gasblasen in ruhendem Fluid und dessen Wechselwirkung mit dem Aufstiegsverhalten der Blasen  
(V. Heinzl, H. Sauter, IRS)

### **Abstract**

In this report we characterize different types of flow around a single rising bubble for the validation of simulation model calculations by elaborating typical factors exercising the most intensive impacts on the wake. We used deionised water, sometimes mixed with a few percent of ethanol as a stagnant fluid in a test cell, and synthetic air as a gas. We produced small bubbles only, with limited deviations from a rectilinear rising path. For start up, we investigated the life time of the wake behind the bubble so that the requirement of rising "single" bubbles in quiescent water could be fulfilled. We used non-invasive optical methods like photographing and light-barrier measurements for speed and path observations as well as invasive methods to test the aptitude of hot wire anemometry. The slightly invasive, but very versatile and sensitive Schlierenmethod was applied to visualize details in inner and outer wake behaviour.

### **Zusammenfassung**

Es wird über die Messungen des Blasennachlaufzeitverhaltens in ruhendem Fluid bei kleinen Blasen berichtet. Die mit einer Heißfilmsonde gemessenen Zeitkonstanten sind konsistent mit Videoaufnahmen, bei denen der Nachlauf mit der Methode der Schlierenoptik visualisiert wurde. Zum Studium von Details im inneren und äußeren Nachlauf sind außer bei sehr kleinen Blasen mit völlig symmetrischer Umströmung Beobachtungen in zwei Dimensionen notwendig, deren Realisierung vorgestellt wird.

### **Introduction**

When giving experimental support to the understanding and numerical modelling of the behaviour of single bubbles rising in a quiescent fluid, as well as the near and far flow field around it, different methods of investigation are available. In this report, we

concentrate on optical methods such as photographing and measurements by light barriers, the hot wire anemometry and the Schlierenoptik.

### **Optical observation of rising velocities of a “single” air bubble in “quiescent” water – relationship between the rising velocity and the bubble diameter**

One method is, to observe the relationship between the bubble size, the bubble shape, the bubble path and the velocity depending on the fluid and gas properties by optical devices. This method is not invasive and allows a characterisation of relevant cases.

The relationships for “single” bubbles in a system with water and air are well depicted by H. Brauer [1], R. Clift et al [2] or U. Müller [3]. The results of our experiments are in good agreement. They reveal the influences of the physical characteristics of the liquid and of the gas on the ascent velocities. Also the impact from the experimental device, such as vibrations, ambient air blow or slip of the generator, could be demonstrated.

More detailed information can be drawn from investigations on the fluid motion around a rising bubble using invasive methods such as LDA, PIV, hot film sensor anemometry and Schlierenoptik. There is some evidence from literature study on experimental work, and even more from our investigations, that the above mentioned methods rather differ in their aptitude to examine different types or regions of the near and the far bubble flow regimes. LDA and PIV give good information about the potential flow and the outer wake flow. A hot wire sensor gives response to the wake far behind the bubble. Schlierenoptik, however, gives a good visualisation both of the inner wake and the shedding connected to bubble path and/or velocity changes in the far field. Above all, very fine hairpin-like structures can be seen very sharply. All those statements hold true for small bubbles with a moderate shape deformation and a nearly straight rising path in water.

### **Experimental device for investigating the near and far flow field around a rising bubble**

For more intensive investigations, we built a little pool (MINIFLEX) with a special optical design suited for 3-dimensional Schlierenoptik-takes with a large magnification, so that even the formation of tiny wakes can be registered. The bubble

generator allows for creating bubbles from 0.2 to 2.5 mm in diameter with a stable and adjustable periodicity, depending on the fluid in use. In order to avoid any disturbance causing the generation of pre-mature smaller bubbles or a triggered shedding, an actively damped breadboard carries the setup including the light source and the CCD-cameras. A time resolution may be achieved either by a high-speed video camera or by using the frame-straddling method.

### **Hot wire anemometry for wake lifetime measurement**

This set-up was well suited for a camera-coupled hot film anemometry near the bubble path, due to its ability to apply fine adjustment to the test vessel, the bubble generator, the sensor, the cameras and the illumination. We used a video-coupled multiple flashing as well as a sensor-coupled one. A number of preliminary tests with different fluids and bubble sizes showed different types of interaction of the bubbles at the sensor wire. They were similar to the pattern characterised by Serizawa [5] with some more detailed differentiation due to some more refined optical observation. However, in this work we were not looking for the signal identifying the type of interaction, but rather for a signal, i.e. a time dependent velocity following the passage of a bubble. It could be revealed, that a channel-like flow field exists behind the rising bubble with a lifetime from 1.5 to 3 seconds depending on the bubble size. The corresponding hot film sensor signal is well reproducible. It declines after the passage of the bubble with a time constant fairly independent from the very distance between the sensor and the bubble (fig. 1). In connection with earlier measurements rough estimations allow to regard the remaining flow speed in the case of short bubble intervals as additive to the single bubble speed – or the relative speed of the rising bubble in the surrounding liquid is constant and adds to the speed of the still existing wake of the preceding bubble. This is true for bubbles till a diameter of about 1.2 mm rising straight upward. W. Sabisch comes to a comparable result due to a direct numeric simulation [6] with a volume-of-fluid-method.

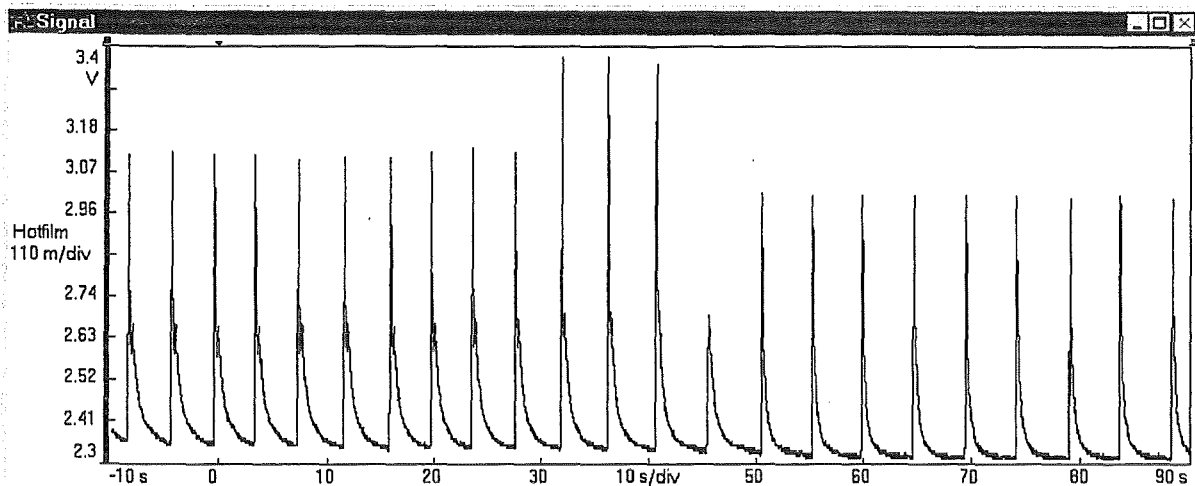


Fig. 1 Signals of a Hot Film Sensor near to the bubble path. As the bubble frequency decreases towards the end of the record, the baseline value also lowers. The decay time values, however, remain constant.

### Near and far wake field visualized by Schlierenoptic

In order to optimise the periodicity in the bubble-Schlierenexperiments, it was quite helpful to have the data about lifetimes of the bubble wakes available. Thus, an excessive transportation mixing of the two fluids necessary to produce different optical path lengths could largely be avoided. For most simplicity, we divided the test vessel into a lower, narrower section representing the bubble generator volume filled with NaCl-solution of a low concentration (selective cooling would be a different possibility) and a typical height above the generator of 10 to 15 bubble diameters.

The upper section measured 3x3x13 cm and was carefully filled up to 10/13 with deionised water at the start of an experimental run. The observation area was ca. 3x3 cm large and 3 cm underneath the surface of the fluid. Special care was taken when selecting the test vessel to have a minimum of Schlieren present in the wall material or in the boundary layer wall/fluid.

As a bubble event every three or six seconds is a rather rare event with respect to focussing and adjusting the set-ups, as well as to select the "good" events to be stored, two auxiliary software programmes were developed using LabVIEW-IMAQ as a platform. They can make use of external trigger signals likewise from a light barrier, of an alert circuitry or from an internal trigger fired by changes of the picture light distribution. Subsequently, they show a "pre-and post trigger series" of a number of

fields, which can be measured by a brightness-distribution histogram, or selected and numbered by automatic counting, and stored.

This procedure ensures a non-biased collection of events with a true distribution of different types of events in a bubbles wake rather than a selection of striking pictures by the experimentator.

In this way, an originating bubble develops its inner wake completely in the NaCl-solution and transports it – without visible losses – to the observation volume. Most mixing occurred near the inner wake when penetrating the concentration border and also in front of the bubble. Furthermore some traces seemed to follow the rims of the wake at a low and rapidly vanishing speed, thus remaining near the borderline.

The Schlieren were made visible according to (fig. 2). A laser beam was first expanded and then rendered parallel and divided into two rectangular beams traversing the volume of observation. Each beam hit an objective separately adjustable in 6 directions in order to align the optical axis relatively to each beam and having the focus of the undisturbed beam at the very place of the aperture. This one could be a central (bright field), a focal (dark field) or a half-cut one.

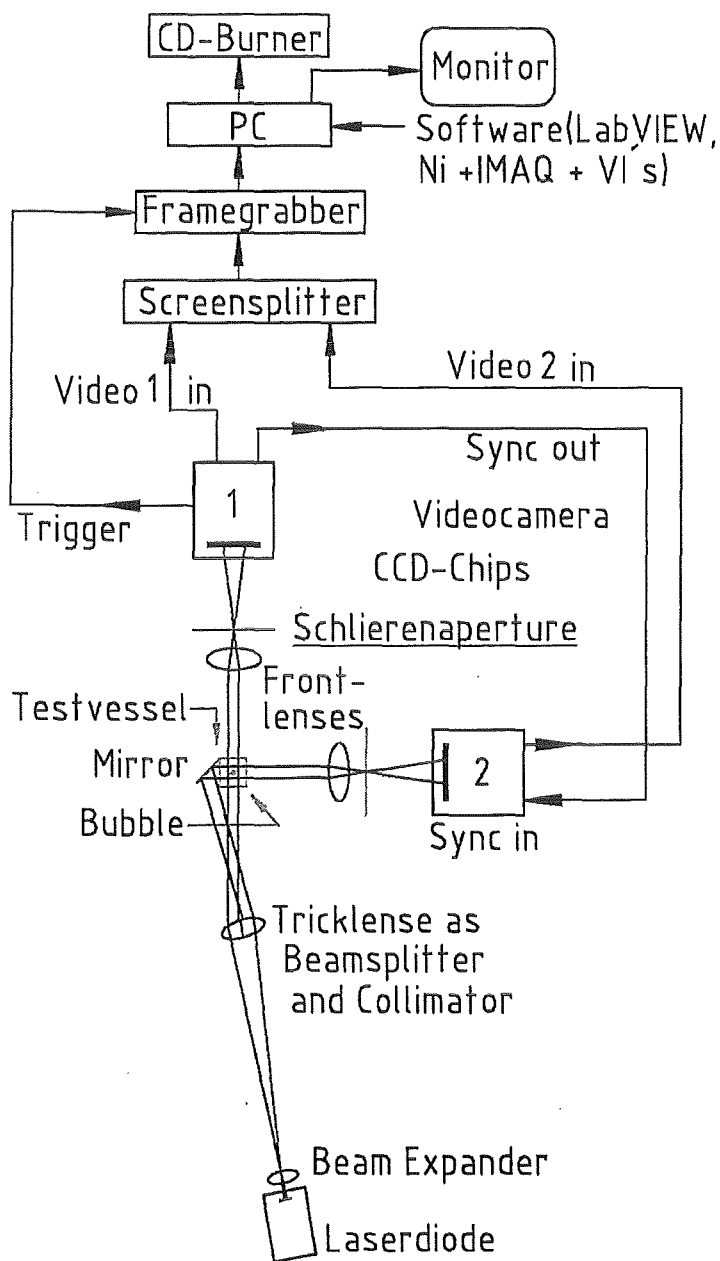


Fig. 2 Diagram of the experimental device for the Schlierenvisualization; old version with a screen splitter and a single frame grabber instead of the new dual one.

Sharp video-pictures were achieved by adjusting the cameras independently; thereby taking into account the settings of an electronic screen splitter, which combined both pictures into one field at the same time. As we used closed circuit cameras,

synchronisation of both cameras was available as well as an alert signal to trigger the frame grabbing procedure if the alert circuitry detected a change in the picture content e.g. by a rising bubble.

In practice, however, the performance of the screen splitter device turned out to deliver too poor a resolution especially of the internally stored half of the field, where no stable dark reference value could be maintained. The received pictures encouraged us to continue by using a dual frame grabber, which are commercially available by now.

### **Experimental findings**

We started our takes with one camera first, to avoid early alignment and balancing problems but rather to find out the most interesting fields of view to be combined later on by screening the different flow or wake patterns as a function of the bubbles size. We identified the scenarios to be investigated more in detail: the first onset of a wake at the increasing size of very tiny bubbles, the onset of wake asymmetries, the wake deformation in connection with bubble path and speed deviations, both spontaneous and triggered ablations of hairpin structures up to the complete tear-off and new build-up of the wake related to major path and speed changes.

The two-camera pictures with perpendicular view directions allowed a clear separation of the inner and outer wake for small bubbles. Remaining channel like flow fields could be measured by the hot film sensor (fig. 1) corresponding to the visualisation by the picture sequences as far as the lifetime is regarded.

Larger bubbles with their non symmetric inner wakes and with ablation procedures which can only be interpreted when investigating them in three dimensions due to their complex structures (fig. 3). With an improved resolution and a reliable contrast balance in the otherwise symmetric pair of observation paths future work will come to more obviously satisfying results.

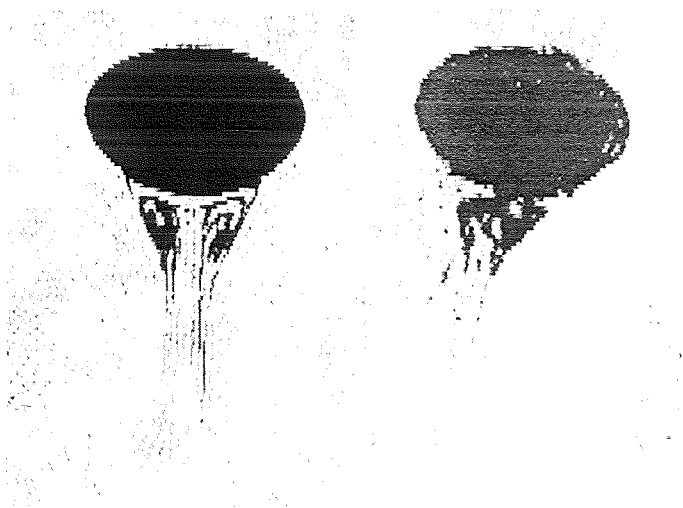


Fig. 3 One half field of a direct video camera take left hand and the corresponding 90°-half field from the memory of a screen splitter on the right hand. The bubble is somewhat larger than 1.2 mm and therefore oblate. It is slightly tilted in one direction, with the according asymmetric wake. This could not be seen in the left half of the picture only.

## References

- [1] H. Brauer, Grundlagen der Einphasen- und Mehrphasenströmungen, Verlag Sauerländer, Aarau und Frankfurt am Main, 1971, S. 294
- [2] R. Clift, J. R. Grace, M. E. Weber, Bubbles, Drops and Particles, Academic Press, 1978
- [3] U. Müller, Zweiphasenströmung mit Wärmeübertragung, Vorlesung an der Universität Karlsruhe, SS 1994 (unpublished)
- [4] H. Sauter, et al, Experimentelle Untersuchungen zum Strömungsfeld aufsteigender Gasblasen in ruhendem Fluid und dessen Wechselwirkung mit dem Aufstiegsverhalten der Blasen, PSF-Jahresbericht (FZKA 6480), p 527-540, 1999
- [5] A. Serizawa, I. Kataoka, I. Michiyoshi, Real-time measurement of two-phase flow turbulences using a dual-sensor anemometry, Proc. Symp. on Measuring Techniques in Gas-Liquid Two-Phase Flows, Nancy France, p. 495-523
- [6] W. Sabisch, Dreidimensionale numerische Simulation der Dynamik von aufsteigenden Einzelblasen und Blasenschwärme mit einer Volume-of-Fluid-Methode, FZKA 6478, Juni 2000

### 32.22.04 Strukturelle Integrität

#### I. Investigations to Size Effects on Deformation and Failure Behavior of Specimens Including a Center Hole

(J. Aktaa, M. Klotz, M. Pfeifenroth, R. Schmitt, IMF II)

In the European research project LISSAC (Limit Strains for Severe Accident Conditions) the size influence on material properties, e.g. failure strain, needed for the best possible assessment of components failure due to severe accident is investigated.

Tensile tests at room temperature with specimens of similar geometry and different sizes, cut from the wall of a real reactor vessel are performed. The investigations have been started with flat specimens including a central hole. The hole is incorporated to obtain inhomogeneous deformation with high strain gradients.

As a representative integral strain measure for the local deformation field, surrounding the hole, stress versus hole opening displacement is considered, shown in Figure 1 for specimens with different sizes. Therefrom it is obvious, that the curves show up to maximum stress no distinctive difference and therewith no size effects. In the decreasing path differences could be recognized even between the 4 and 20 mm thick specimens. The remarkable drop of the curves might be identified by the state of macro crack nucleation and local failure, respectively. According to this criterion a failure strain of 75, 61 and 48% (denoted by filled circles) can be determined for the 4, 20 and 80 mm thick specimens, respectively. Unfortunately, due to exceeding the measuring range at approx. 60 % with the 40 mm thick specimen there is a loss of information concerning the size effect.

In order to investigate the influence of strain gradient on the size effects observed additional tests with flat specimens including an increased central hole – lower gradient – and flat specimens including a slot – higher gradient – are in progress.

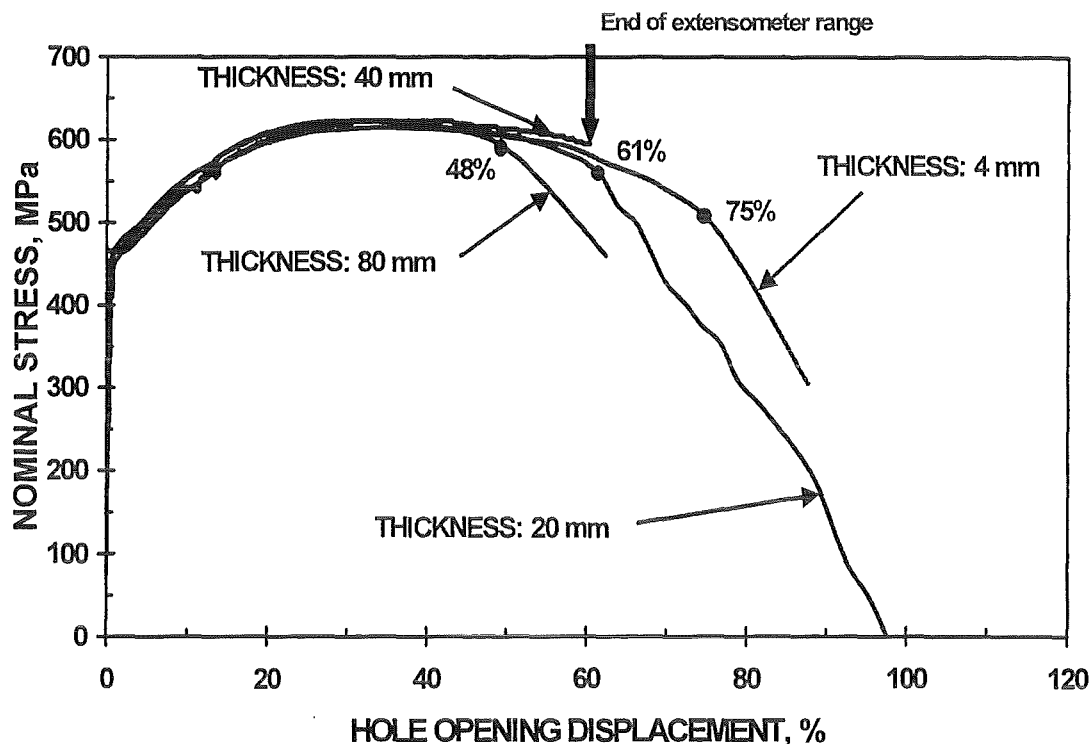


Fig. 1 Nominal stress vs. hole opening displacement for different sized specimens in comparison

## References

- Aktaa, J.; Klotz, M.; Pfeifenroth, M.; Schmitt, R.  
 Investigations to size effects on deformation and failure behavior of specimens including a center hole. Programm Nukleare Sicherheitsforschung. Jahresbericht 2000 Wissenschaftliche Berichte, FZKA-6653 (September 2001) S.357-58
- Aktaa, J.; Hädrich, H.J.; Julisch, P.; Klotz, M.; Schmitt, R.  
 Investigations to size effects on plastic deformation and failure behavior of inhomogeneously loaded structures. Matzen, V.C. [Hrsg.] Transactions of the 16th Internat. Conf. on Structural Mechanics in Reactor Technology (SMiRT 16), Washington, D.C., August 12-17, 2001 Madison, Wis.: Omnipress, 2001 CD-ROM Paper 1891
- Dolensky, B.; Jordan, T.; Krieg, R.; Malmberg, T.; Messemer, G.; Rieger, H.; Aktaa, J.; Diegele, E.; Schmitt, R.; Plitz, H.  
 Limit strains for severe accident conditions. Description of an European program and first results. Programm Nukleare Sicherheitsforschung. Jahresbericht 2000 Wissenschaftliche Berichte, FZKA-6653 (September 2001) S.197-211
- Krieg, R.; Jordan, T.; Dolensky, B.; Malmberg, T.; Aktaa, J.; Plitz, H.; Julisch, P.; Seidenfuss, M.; Talja, H.; Solomos, G.; Aifantis, E.; Cizelj, L.; Caroli, C.; Fokkens, J.; Bhandari, S.B.; Veron, P.; Trauth, M.  
 Limit strains for severe accident conditions, description of an European research program and first results. 16th Internat. Conf. on Structural Mechanics in Reactor Technology (SMiRT 16), Washington, D.C., August 12-17, 2001

- II. Material models for large deformation elasticity and plasticity theories  
(E. Diegele, R. Elsässer, D. Hofer, G. Rizzi, IMF II; Ch. Tsakmakis, TU Darmstadt)

### **Abstract**

Within the framework of the European Project LISSAC, material models incorporating size effects for large deformation have been developed for large deformation elasticity and plasticity theories. A local substructure is introduced at any material point of a body. Non local effects are generated in a natural way including spatial derivatives of the deformation gradient. Micromorphic and micropolar models are generated by allowing different degrees of freedom on the local structure. In a first step the purely elastic parts of the theories were implemented in the finite element code ABAQUS through the User supplied ELeMent option (UEL). Micropolar elasticity has been used for finite element analyses of four types of specimen with large local strain gradients as tested in the experimental part of the LISSAC programme.

### **Zusammenfassung**

Im Rahmen des EU-Projektes LISSAC wurden für große Verformungen Materialmodelle der Elastizität und Plastizität entwickelt, die Größeneffekte beschreiben. Jedem materiellen Punkt wird dabei eine lokale Substruktur zugeordnet. Nichtlokale Einflüsse erhält man durch die Berücksichtigung der räumlichen Ableitung des Deformationsgradienten für diese Substruktur. Durch geeignete Wahl der Freiheitsgrade für die lokale Verformung lassen sich verschiedene Modelle formulieren, z.B. "mikromorphe" Materialmodelle für eine beliebige Verformung oder "mikropolare" Modelle, falls nur eine Rotation erlaubt wird. In einem ersten Schritt wurden die rein elastischen Zweige der Theorien im FE Programm ABAQUS als benutzerdefinierte Elemente implementiert. Mit mikropolarer Elastizität wurden vier der in LISSAC getesteten Probenformen parametrisch untersucht. Es zeigte sich, dass das Modell Größeneffekte beschreiben kann.

## Part I: “Nonlocal elasticity theory on the basis of micromorphic continua”

E. Diégele<sup>1</sup>, D. Hofer<sup>1</sup>, Ch. Tsakmakis<sup>2</sup>

<sup>1</sup> Institut für Materialforschung II, Forschungszentrum Karlsruhe

<sup>2</sup> Institut für Mechanik, Technische Universität Darmstadt

### 1. Introduction

Size-dependent phenomena can be modelled using theories with intrinsic- or material-length-scales. In the case of elasticity, length scales enter the constitutive equations through the elastic strain energy function, which, in this case, depends on the deformation gradient  $\mathbf{F}$  and in addition to that on a deformation gradient of the microstructure  $\mathbf{f}$  and the gradient of  $\mathbf{f}$ .

This paper presents an elasticity theory for small deformations called micromorphic elasticity which has similarities with theories formulated by ERINGEN [1-3] and MINDLIN [4].

### 2. Preliminaries – decomposition of deformation

#### 2.1 Notation

In the following we consider isothermal deformations and write  $\dot{\varphi}(t)$  for the material time derivative of a function  $\varphi(t)$ , where  $t$  is the time. We use bold face letters for second order tensors. In particular  $\mathbf{1}$  represents the identity second order tensor and  $\mathbf{A}^T$  denotes the transpose of a second order tensor  $\mathbf{A}$ . We write  $\text{tr}\mathbf{A}$  for the trace of  $\mathbf{A}$ ,  $\mathbf{A}^D = \mathbf{A} - 1/3 (\text{tr}\mathbf{A})\mathbf{1}$  for the deviator of  $\mathbf{A}$  and  $\mathbf{A} \cdot \mathbf{B} = \text{tr}(\mathbf{A}\mathbf{B}^T) = \text{tr}(\mathbf{A}^T\mathbf{B})$  for the inner product of  $\mathbf{A}$  and  $\mathbf{B}$ . Also we use the notation  $\mathbf{A}^{T-1} = (\mathbf{A}^{-1})^T$  provided that  $\mathbf{A}^{-1}$  exists.

#### 2.2 Decomposition of deformation

Consider a material body  $\mathbf{B}$ , which occupies a region  $\mathbf{R}_R$  in the three dimensional Euclidean point space  $E$  in the reference configuration ( $t=0$ ). Each particle of the material body  $\mathbf{B}$  can be identified by a position vector  $\mathbf{X}$  to the place  $X$  in  $\mathbf{R}_R$  after having chosen a fixed point (origin) in  $E$ . A configuration at time  $t$  is called actual configuration  $\mathbf{R}_t$ . The position of a particle is identified by a position vector  $\mathbf{x}$  to the place  $x$  in this configuration.

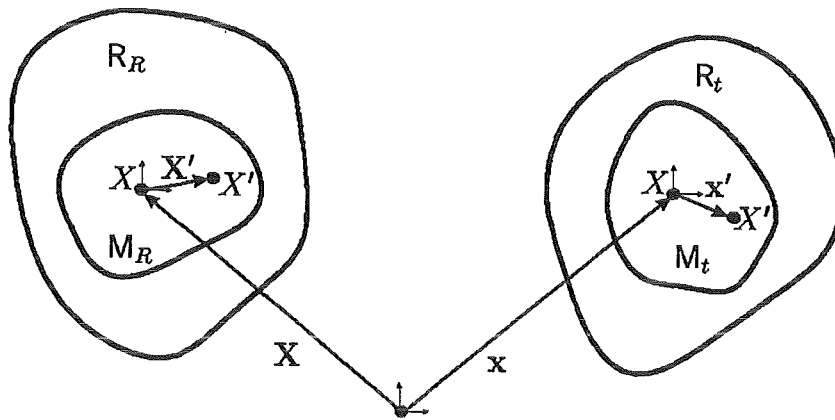


Fig. 1 Motion, reference and actual configuration

A motion is described by the equation

$$\mathbf{x} = \hat{\mathbf{x}}(\mathbf{X}, t) \quad (2.1)$$

The components of displacement of a material particle are defined as

$$\mathbf{u} = \mathbf{x} - \mathbf{X} \quad (2.2)$$

The deformation gradient tensor is denoted by

$$\mathbf{F} = \mathbf{F}(\mathbf{X}, t) = \frac{\partial \hat{\mathbf{x}}}{\partial \mathbf{X}} = \text{GRAD} \hat{\mathbf{x}} \quad (2.3)$$

For  $\mathbf{F}$  ( $\det \mathbf{F} > 0$ ) the polar decomposition

$$\mathbf{F} = \mathbf{R}\mathbf{U} = \mathbf{V}\mathbf{R}, \quad (2.4)$$

applies, where  $\mathbf{R}$  represents a proper orthogonal second-order tensor.

At each point  $X$  of the material body there is assumed to be a microstructure  $M$  in which  $X'$  and  $x'$  are the material and spatial position vectors, respectively. The origin of the coordinate system is fixed at the material point  $X$  and moves with the displacement  $\mathbf{u}$ .

Following ERINGEN et al. [1-3], (cf. also MINDLIN [4]), we introduce a micro-deformation gradient tensor  $\mathbf{f}$

$$\mathbf{f} = \mathbf{f}(\mathbf{X}', t) = \frac{\partial \hat{\mathbf{x}}'}{\partial \mathbf{X}'} \quad (2.5)$$

( $\det \mathbf{f} > 0$ ) for which the polar decomposition

$$\mathbf{f} = \mathbf{r}\mathbf{u} = \mathbf{v}\mathbf{r} \quad (2.6)$$

holds. A micro-displacement is defined by

$$\mathbf{u}' = \mathbf{x}' - \mathbf{X}' \quad (2.7)$$

An interpretation of the micro-deformation is given by MINDLIN [4]. Every point  $X$  is considered to possess three deformable directors, which represent the degrees of freedom arising from microdeformations. From this point of view a micromorphic continuum is a classical continuum endowed with extra degrees of freedom represented by the deformable directors  $\Phi_{(i)}$  and  $\varphi_{(i)}$ .

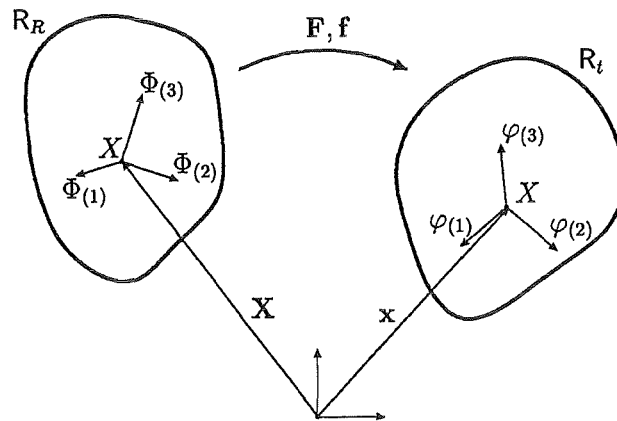


Fig. 2: Deformable directors

In order to introduce some strain measures we first concentrate on pure elasticity. In this case the specific free energy function  $\psi$  is supposed to depend on  $\mathbf{F}$ ,  $\mathbf{f}$  and  $\text{GRAD } \mathbf{f}$ :

$$\psi = \overline{\psi}(\mathbf{F}, \mathbf{f}, \text{GRAD}\mathbf{f}) \quad (2.8)$$

$\text{GRAD}\mathbf{f}$  introduces an internal length scale in the constitutive theory; with respect to convective coordinates, it is given by

$$\text{GRAD}\mathbf{f} = \frac{\partial \mathbf{f}}{\partial \theta^k} \otimes \mathbf{G}_k \quad (2.9)$$

so that  $\text{GRAD}\mathbf{f}$  represents a third order tensor. By using the principle of material objectivity, it is a routine matter to obtain the reduced form

$$\psi = \overline{\psi}(\tilde{\boldsymbol{\varepsilon}}, \tilde{\boldsymbol{\beta}}, \tilde{\mathbf{K}}) \quad (2.10)$$

where

$$\tilde{\boldsymbol{\varepsilon}} = \mathbf{f}^{-1}\mathbf{F} - \mathbf{1} \quad (2.11)$$

$$\tilde{\boldsymbol{\beta}} = \frac{1}{2}(\mathbf{u}^2 - \mathbf{1}) \quad (2.12)$$

$$\tilde{\mathbf{K}} = \mathbf{f}^{-1}\text{GRAD}\mathbf{f} \quad (2.13)$$

In these equations,  $\tilde{\boldsymbol{\beta}}$  is the classical Green strain tensor with respect to the reference configuration and the curvature tensor  $\tilde{\mathbf{K}}$  renders a nonlocality to the constitutive model.

### 2.3 Linearized theory

Displacement gradients are defined by

$$\mathbf{H} = \frac{\partial \mathbf{u}}{\partial \mathbf{X}} = \mathbf{F} - \mathbf{1}, \quad \mathbf{h} = \frac{\partial \mathbf{u}'}{\partial \mathbf{X}'} = \mathbf{f} - \mathbf{1} \quad (2.14)$$

The absolute value of  $\mathbf{H}$  and  $\mathbf{h}$  are assumed to be small in comparison with unity

$$\|\mathbf{H}\| \ll 1, \quad \|\mathbf{h}\| \ll 1 \quad (2.15)$$

so that we may write

$$\mathbf{H} = \frac{\partial \mathbf{u}}{\partial \mathbf{X}} \approx \frac{\partial \mathbf{u}}{\partial \mathbf{x}}, \quad \mathbf{h} = \frac{\partial \mathbf{u}'}{\partial \mathbf{X}'} \approx \frac{\partial \mathbf{u}'}{\partial \mathbf{x}'} \quad (2.16)$$

We use the relation

$$\mathbf{f}^{-1} \approx \mathbf{h}^{-1} \quad (2.17)$$

to linearize the strain tensors:

$$\begin{aligned} \tilde{\boldsymbol{\varepsilon}} &\approx \mathbf{H} - \mathbf{h} =: \bar{\boldsymbol{\varepsilon}} \\ \tilde{\boldsymbol{\beta}} &\approx \frac{1}{2}(\mathbf{h} + \mathbf{h}^T) =: \bar{\boldsymbol{\beta}} \\ \tilde{\mathbf{K}} &\approx \frac{\partial \mathbf{h}}{\partial \mathbf{X}} =: \bar{\mathbf{K}} \end{aligned} \quad (2.18)$$

In these equations,  $\bar{\boldsymbol{\varepsilon}}$ ,  $\bar{\boldsymbol{\beta}}$  and  $\bar{\mathbf{K}}$  are linearized strain and curvature tensors.

$\psi$  depends in the linearized theory on  $\bar{\boldsymbol{\varepsilon}}$ ,  $\bar{\boldsymbol{\beta}}$  and  $\bar{\mathbf{K}}$ :

$$\psi = \bar{\psi}(\bar{\boldsymbol{\varepsilon}}, \bar{\boldsymbol{\beta}}, \bar{\mathbf{K}}) \quad (2.19)$$

Using the above form of the strain energy, we are able to define the following stresses and couple stresses:

$$\begin{aligned} \boldsymbol{\sigma} &:= \frac{\partial \psi}{\partial \bar{\boldsymbol{\varepsilon}}} \\ \boldsymbol{\tau} &:= \frac{\partial \psi}{\partial \bar{\boldsymbol{\beta}}} = \boldsymbol{\tau}^T \\ \mathbf{M} &:= \frac{\partial \psi}{\partial \bar{\mathbf{K}}} \end{aligned} \quad (2.20)$$

### 3. Variational equation of motion

We formulate the variational principle for independent variations  $\delta \mathbf{u}$  and  $\delta \mathbf{h}$ :

$$\delta W_{(e)} = \delta W_{(i)} \quad , \quad (3.1)$$

where  $\delta W_{(e)}$  and  $\delta W_{(i)}$  are the variation of work done by external forces and potential energy, respectively:

$$\delta W_{(i)} = \int_V \delta \psi dV \quad . \quad (3.2)$$

From (2.20) and (3.2) we obtain (index notation)

$$\delta W_{(i)} = \int_V (\sigma_{ij} \delta \varepsilon_{ij} + \tau_{ij} \delta \beta_{ij} + M_{ijk} \delta K_{ijk}) dV \quad . \quad (3.3)$$

On the basis of (2.18) we get with  $\tau = \tau^T$  :

$$\delta W_{(i)} = \int_V [\sigma_{ij} \delta (u_{i,j} - h_{ij}) + \tau_{ij} \delta h_{ij} + M_{ijk} \delta h_{ij,k}] dV \quad . \quad (3.4)$$

Applying the divergence theorem, we find

$$\delta W_{(i)} = - \int_V \sigma_{ij,j} \delta u_i dV + \int_V (\tau_{ij} - \sigma_{ij} - M_{ijk,k}) \delta h_{ij} dV + \int_A \sigma_{ij} \delta u_i n_j dA + \int_A M_{ijk} \delta h_{ij} n_k dA \quad . \quad (3.5)$$

This equation is the motivation of the following form for the variation of work done by external forces:

$$\delta W_{(e)} = \int_V f_i \delta u_i dV + \int_V \phi_{ij} \delta h_{ij} dV + \int_A t_i \delta u_i dA + \int_A T_{ij} \delta h_{ij} dA \quad . \quad (3.6)$$

$f_i$  and  $t_i$  are the classical body and surface forces, respectively. An interpretation of  $\phi_{ij}$  and  $T_{ij}$  is given by MINDLIN [4]:

$\phi$  is to be interpreted as a double force per unit volume and  $T$  as a double force per unit area. The diagonal terms of  $\phi$  and  $T$  are double forces without moment

and the off-diagonal terms are double forces with moment. The antisymmetric part of the body double force is the body couple. The antisymmetric part of the double traction is the Cosserat couple-stress vector. In both  $\phi_{ij}$  and  $T_{ij}$  the first subscript gives the orientation of the lever arm between the forces and the second subscript gives the orientation of the forces. Across a surface with its outward normal in the positive direction, the force at the positive end of the lever arm acts in the positive direction. ("Positive" refers to the positive sense of the coordinate axis parallel to the lever arm or force). Across a surface with its outward normal in the negative direction, the directions of the forces are reversed.

Substituting (3.5) and (3.6) in (3.1), we obtain the variational equation of motion:

$$\int_V (f_i + \sigma_{ij,j}) \delta u_i dV + \int_V (\phi_{ij} - \tau_{ij} + \sigma_{ij} + M_{ijk,k}) \delta n_{ij} dV + \int_A (t_i - \sigma_{ij} n_j) \delta u_i dA + \int_A (T_{ij} - M_{ijk} n_k) \delta n_{ij} dA = 0 \quad (3.7)$$

From (3.7) there follow immediately the momentum principle

$$\sigma_{ij,j} + f_i = 0 \quad (3.8)$$

the moment of momentum principle

$$\phi_{ij} - \tau_{ij} + \sigma_{ij} + M_{ijk,k} = 0 \quad (3.9)$$

and the traction boundary conditions

$$\begin{aligned} t_i &= \sigma_{ij} n_j \\ T_{ij} &= M_{ijk} n_k \end{aligned} \quad (3.10)$$

These equations show that micromorphic theories are an extension of the classical theory. In classical theories, the moment of momentum principle does not furnish any new differential equation of motion.

#### 4. Constitutive equations

Constitutive equations for micromorphic continua are developed by MINDLIN [4] and IESAN [5]. It is assumed that the potential energy depends on a homogeneous, quadratic function of  $\bar{\epsilon}$ ,  $\bar{\beta}$  and  $\bar{K}$  (index notation):

$$\begin{aligned}\psi = & \frac{1}{2} E_{ijpq} \bar{\varepsilon}_{ij} \bar{\varepsilon}_{pq} + \frac{1}{2} A_{ijpq} \bar{\beta}_{ij} \bar{\beta}_{pq} + \frac{1}{2} B_{ijkpqr} \bar{K}_{ijk} \bar{K}_{pqr} + \\ & + \frac{1}{2} C_{ijpq} \bar{\varepsilon}_{ij} \bar{\beta}_{pq} + \frac{1}{2} D_{ijkpq} \bar{K}_{ijk} \bar{\beta}_{pq} + \frac{1}{2} F_{ijkpq} \bar{K}_{ijk} \bar{\varepsilon}_{pq}\end{aligned}\quad (4.1)$$

The theory depends in addition of the classical material tensor **E** on 5 material tensors **A**, **B**, **C**, **D**, and **F**. In case of an isotropic material the tensors of odd rank **D** and **F** must vanish [4]. We have the symmetry conditions:

$$\begin{aligned}E_{ijpq} &= E_{pqij} \\ A_{ijpq} &= A_{pqij} = A_{ijqp} \\ B_{ijkpqr} &= B_{pqrijk} \\ C_{ijpq} &= C_{ijqp}\end{aligned}\quad (4.2)$$

The material tensors are in case of isotropy homogeneous, linear functions of products of Kronecker deltas. There are three independent products of two Kronecker deltas and fifteen independent products of three Kronecker deltas. Using the symmetry conditions, we obtain:

$$\begin{aligned}E_{ijpq} &= \lambda \delta_{ij} \delta_{pq} + (\mu + \alpha) \delta_{ip} \delta_{jq} + (\mu - \alpha) \delta_{iq} \delta_{jp} \\ A_{ijpq} &= a_1 \delta_{ij} \delta_{pq} + a_2 (\delta_{ip} \delta_{jq} + \delta_{iq} \delta_{jp}) \\ B_{ijkpqr} &= b_1 \delta_{ij} \delta_{kp} \delta_{qr} + b_2 \delta_{ij} \delta_{kq} \delta_{rp} + b_3 \delta_{ij} \delta_{kr} \delta_{pq} + b_4 \delta_{jk} \delta_{ip} \delta_{qr} + b_5 \delta_{jk} \delta_{iq} \delta_{pr} + \\ &+ b_1 \delta_{jk} \delta_{ir} \delta_{pq} + b_5 \delta_{ki} \delta_{jp} \delta_{qr} + b_8 \delta_{ki} \delta_{jq} \delta_{rp} + b_2 \delta_{ki} \delta_{jr} \delta_{pq} + b_{10} \delta_{ip} \delta_{jq} \delta_{kr} + \\ &+ b_{11} \delta_{jp} \delta_{kq} \delta_{ir} + b_{11} \delta_{kp} \delta_{iq} \delta_{jr} + b_{13} \delta_{ip} \delta_{jr} \delta_{kq} + b_{14} \delta_{jp} \delta_{kr} \delta_{iq} + b_{15} \delta_{kp} \delta_{ir} \delta_{jq} + \\ C_{ijpq} &= c_1 \delta_{ij} \delta_{pq} + c_2 (\delta_{ip} \delta_{jq} + \delta_{iq} \delta_{jp})\end{aligned}\quad (4.3)$$

In case of isotropy the theory depends on eighteen independent coefficients. Using the definitions of stresses and couple stresses, we are able to obtain the following relations:

$$\begin{aligned}\sigma_{ij} &= E_{ijpq} \bar{\varepsilon}_{pq} + C_{ijpq} \bar{\beta}_{pq} \\ \tau_{ij} &= A_{ijpq} \bar{\beta}_{pq} + C_{pqij} \bar{\varepsilon}_{pq} \\ M_{ijk} &= B_{ijkpqr} \bar{K}_{pqr}\end{aligned}\quad (4.4)$$

## 5. Weak form

In order to implement the boundary value problem in a finite-element code we have to develop a weak form. The strong form consists of the momentum equation, moment of momentum equation and the traction boundary conditions. There are different ways to develop the weak form. The first way is to multiply equations (3.8) and (3.9) by the test functions  $\delta u_i$ ,  $\delta h_{ij}$  and to integrate over the domain of the body.

Another way is to start with equations (3.1) and (3.3):

$$0 = \delta W_{(e)} - \int_V (\sigma_{ij} \delta \varepsilon_{ij} + \tau_{ij} \delta \beta_{ij} + M_{ijk} \delta K_{ijk}) dV \quad (5.1)$$

Using (2.18) and the constitutive equations, we state the weak form

$$0 = \delta W_{(e)}(\delta u_i, \delta h_{ij}) - \int_V (\delta u_{i,j} E_{ijpq} u_{p,q} + \delta u_{i,j} G_{ijpq} h_{pq} + \delta h_{ij} G_{pqij} u_{p,q} + \delta h_{ij} H_{pqij} h_{pq} + \delta h_{ij,k} B_{ijkpqr} h_{p,q,r}) dV \quad (5.2)$$

The material tensors  $\mathbf{G}$  and  $\mathbf{H}$  are defined in the following way:

$$\begin{aligned} G_{ijpq} &:= C_{ijpq} - E_{ijpq} \\ H_{ijpq} &:= E_{ijpq} - C_{ijpq} - C_{pqij} + A_{ijpq} \end{aligned} \quad (5.3)$$

## 6. References

- [1] Eringen, A. C., *Microcontinuum Field Theories, I. Foundations and Solids*, Springer, New York, 1999.
- [2] Eringen, A. C., *Nonlinear Theory of Simple Micro-elastic Solids - I*, Int. J. Engng. Sci. Vol. 2, 189-203, 1964.
- [3] Suhubi, E. S., Eringen, A. C., *Nonlinear Theory of Simple Micro-elastic Solids - II*, Int. J. Engng. Sci. Vol. 2, 389-404, 1964.
- [4] Mindlin, R. D., *Micro-structure in Linear Elasticity*, Archs. Ration. Mech. Anal. Vol. 10, pp. 51-78 (1964).
- [5] Iesan, D., Nappa, L., *Extremum principles and existence results in micromorphic elasticity*, International Journal of Engineering Science Vol. 39, pp. 2051-2070 (2001).
- [6] Grammenoudis, P., Hofer, D., Tsakmakis, Ch., *Micromorphic plasticity with kinematic hardening*, private communication, unpublished

## Part II: "Finite element analysis of specimens with local strain concentration using micropolar elasticity"

E. Diegele, R. Elsässer, G. Rizzi

Institut für Materialforschung II, Forschungszentrum Karlsruhe

### 1. Introduction

In the previous part a complete formulation of the micromorphic elasticity was outlined. In the following, the theory of micropolar elasticity is shortly reviewed. The theory is based on micro deformations. However, in case of micropolar models the local deformations are restricted to rotational ones only.

The linearised theory was formulated in its weak form and implemented as User supplied ELEMENT (UEL) in the finite element code ABAQUS.

In the LISSAC project (Limit Strains for Severe Accident Conditions), the size effect on deformation and damage behaviour is studied. One work package is dedicated to the development and the application of models that are able to describe size effects. In a first step finite element analysis using micropolar elasticity is applied to a series of samples as tested within the project.

### 2. Summary of the theory of micropolar elasticity

#### 2.1 Linearised theory

The theory can be formulated with the displacement gradient  $\mathbf{H}$  and the micro gradient  $\phi$ , or equivalently, by an axial symmetrical vector  $\varphi$ :

$$\mathbf{F} = \mathbf{H} + \mathbf{1}, \quad \mathbf{f} = \mathbf{1} + \Phi$$

where  $\mathbf{f}^T = \mathbf{f}^{-1}$ ,  $\Phi^T = -\Phi$  and  $\Phi_{kl} = -\varepsilon_{klm} \varphi_m$ .

In case of small deformation, i.e. assuming the absolute values of  $\mathbf{H}$  and  $\phi$  are small in comparison with unity ( $\|\mathbf{H}\| \ll 1, \|\Phi\| \ll 1$ ). The linearised theory is formulated on the basis of three strain tensors,  $\mathbf{E}$  (classical Green strain tensor),  $\varepsilon$  and  $\Gamma$ , which are given by:

$$\mathbf{E} \approx \frac{1}{2}(\mathbf{H} + \mathbf{H}^T), \quad \varepsilon \approx (\Phi + \mathbf{H}^T) \text{ and } \Gamma \approx \frac{\partial \Phi}{\partial \mathbf{X}}.$$

## 2.2 Constitutive equations

Constitutive equations for micropolar continua are developed following the same approach, i.e. assuming that the potential energy depends on a: homogeneous, quadratic function of the strain tensors. This results in decoupled equations for the stress tensor  $\sigma$  and the momentum tensor  $\mathbf{M}$

$$\sigma_{ik} = \lambda \delta_{ik} \varepsilon_{rr} + (\mu + \alpha) \varepsilon_{ki} + (\mu - \alpha) \varepsilon_{ik} , \quad M_{ki} = \beta \delta_{ki} \varphi_{r,r} + (\gamma - \delta) \varphi_{k,i} + (\gamma + \delta) \varphi_{i,k} .$$

where  $\lambda, \mu$  are the constants of classical elasticity theory and  $\alpha, \beta, \delta, \gamma$ , are four additional constants. In two dimensional analysis, the three constants characterising the momentum stress tensor, i.e.  $\beta, \delta, \gamma$ , effectively reduce to one constant, which in the following is taken to be  $\gamma$ , whereas  $\beta, \delta$  are zero. It can be seen, that  $\alpha$  is the antisymmetric coupling between strain tensor and stress tensor and, that  $\gamma$  plays the role of a coupling constant for the momentum tensor. Moreover,  $\gamma$  has the dimensional quantity of an area. Varying  $\gamma$  is equivalent to a variation in length scale. Therefore, in the figures given in section 4 the axis is assigned  $\gamma$  as well as  $(L/L_0)^2$  as coordinate.

## 3. Specimens used in the LISSAC project

Size effects in mechanical testing are most pronounced under severe strain gradients. Therefore, specimens have been designed, that exhibit regions of strain and stress gradients of considerable size. The specimen types tested in LISSAC include notched plates (with inner and outer notches) and three point bend bars with notches of different depth and shape, as depicted in Figs 1 and 2, respectively. Both figures show only a symmetry part (with is a quarter for the plates and one half for the bend bars). In the figures the boundary conditions as applied in the FE simulations are indicated.

Specimens of the same shape but different overall dimensions are investigated . The relative size includes factors of 5, 10 and 50. The dimensions of the smallest specimens of each type are summarized in Table 1.

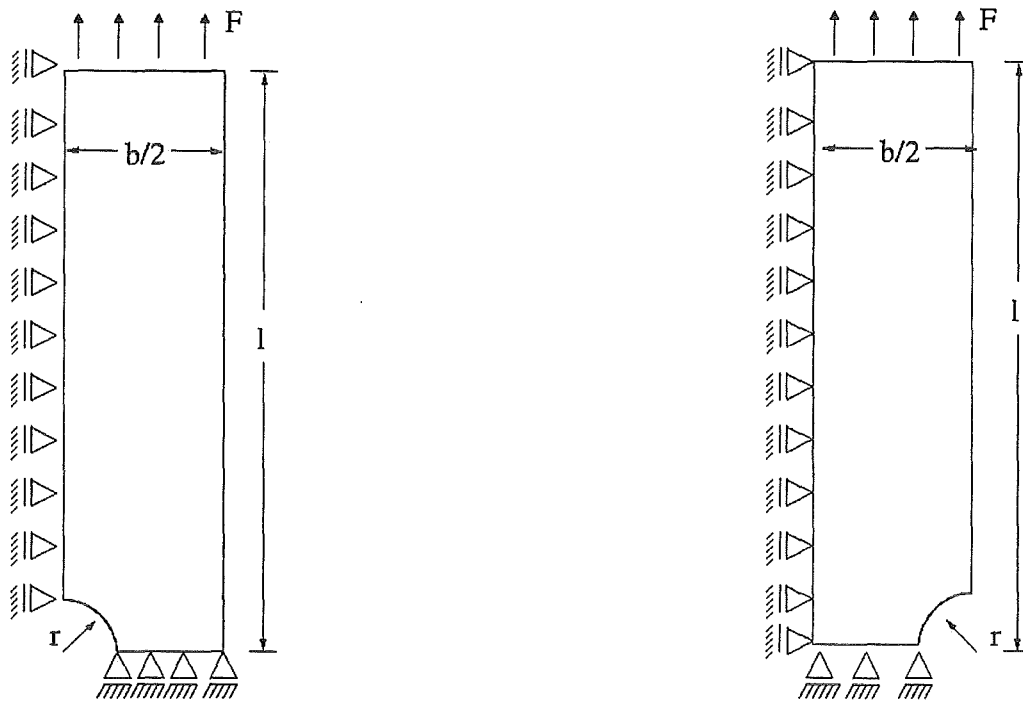


Fig. 1: Inner notched plate (left) outer notched plate (right).

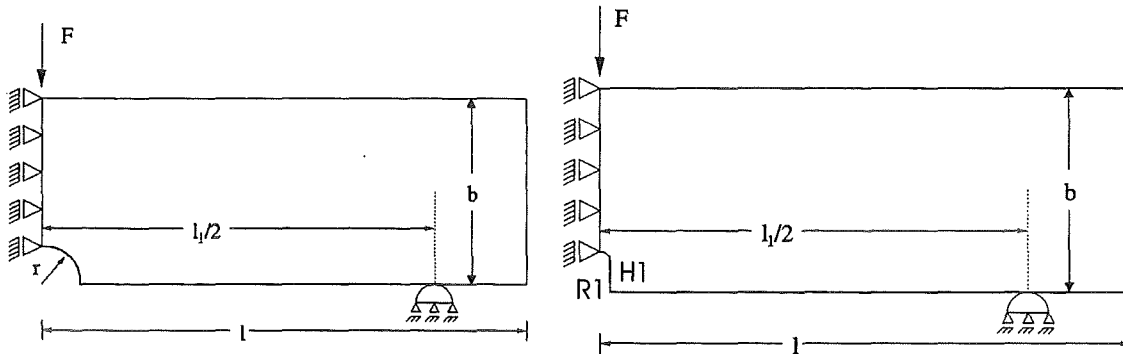


Fig. 2: Notched 3point bend specimen, (left: semicircle, right: deeply notched).

Inner Notch	$b=10$	$l=12$	$r=12$
Outer Notch	$b=10$	$l=1$	$r=1$
3PointBend -a	$b=5$	$l=13.75$ $l1=25$	$r=1$
3PointBend -a	$b=5$	$l=13.75$ $l1=25$	$R1=0.2$ $H1=1$

Table 1. Size of the specimens [mm] to be multiplied by factors of 1, 5, 10, 50 to get real specimen dimensions.

#### 4. Finite Element simulations

The LISSAC type specimen have been modelled in two dimensions assuming plane strain and plane stress, respectively. The 'non classical' material parameter of the theory, i.e.  $\gamma$  and  $\alpha$  under 2D conditions, are unknown, and, moreover their identification is by no means straightforward from experiment. Therefore, at the present stage the numerical analyses are simulations in order to study the influence of the model parameters.

From observation, for  $\alpha$ , which measures the antisymmetric part of the coupling between shear stress and strain, a small value compared to the Young's modulus  $E$  is reasonable. Therefore,  $\alpha$  parametrically was chosen as  $E/10$  and  $E/100$ . The parameter  $\gamma$ , which has a dimension of areas (compared to the Young's modulus), was varied within a range of ten decades. The parameter variation, finally is limited by numerical instabilities in solving FE equations. As will be shown,  $\alpha$  has a strong influence on results.

The notched plate was analysed for a series of parameter variations and with three different dimensions  $D$ , which differ by a factor of 10 relatively to each other. A measure for the size effect is the stress concentration, which is defined as maximum stress at the notch compared to the remote load. In Fig.3 the stress intensity factor is plotted for three different plate dimensions. It is demonstrated that increasing the overall dimensions by a factor of 10 results in the same change in stress concentration factor as changing the material parameter  $\gamma$  by a factor of 100 (length squared).

## Inner Notch - Plane Strain

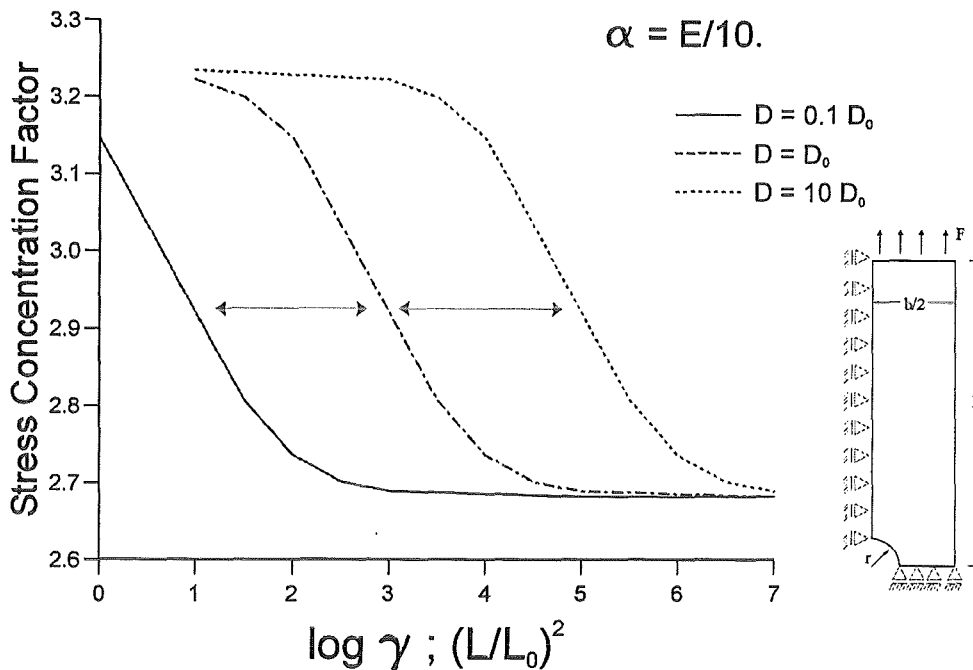


Fig. 3: Stress concentration factor for inner notched plate.

Thereafter, any of the four specimen types was analysed under both, plane stress and plane strain conditions. The results are depicted in Figs. 4 and 5 for the inner and outer notched plate and in Figs. 6 and 7 for the notched bend bars, respectively.

The common features of all simulations exhibit include:

For small values of  $\gamma$ : The results approach asymptotically the classical limit. For very large values of  $\gamma$ : The results asymptotically tend to a second limit (which is known as 'coupled-stress-theory').

A major influence of the parameter  $\alpha$  on the stress concentration factor is observed. As an example, for both types of notched plates, the size effect is limited to a few percent for  $\alpha=E/100$ . In case of  $\alpha=E/10$ , the size effect is up to some 20%. Changing plane stress to plane strain conditions as boundary condition has a minor influence.

A special result is observed for the bend bars. The stress concentration factor in the notch is found to be below 1 under some combination of material parameter. This means that as a results of increased bending stiffness the stress in the hole may even be lower than the outer fibre stress of the unnotched bar in the classical theory.

## Inner Notch - Plane Stress

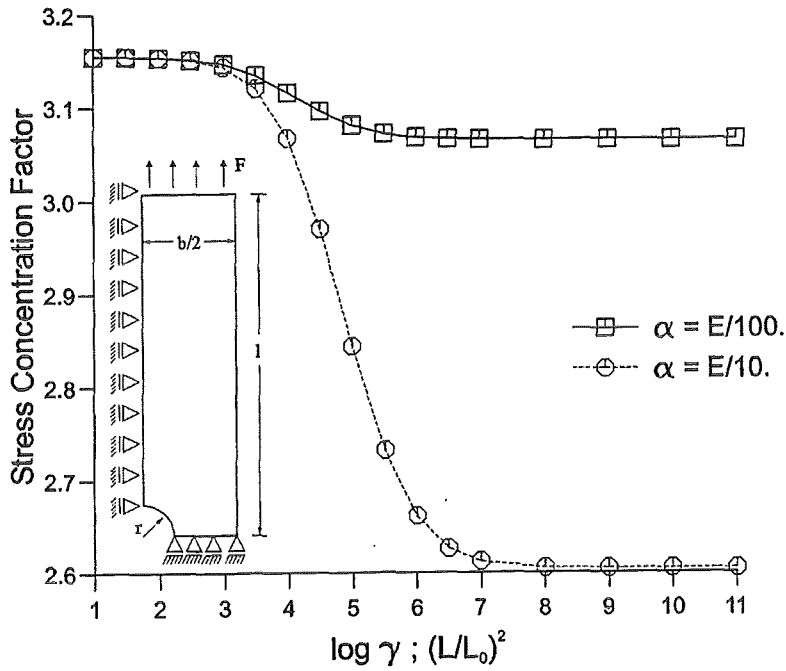


Fig. 4: Stress concentration factor for an inner notched plate under plane strain conditions as function of material parameter.

## Outer Notch - Plane stress

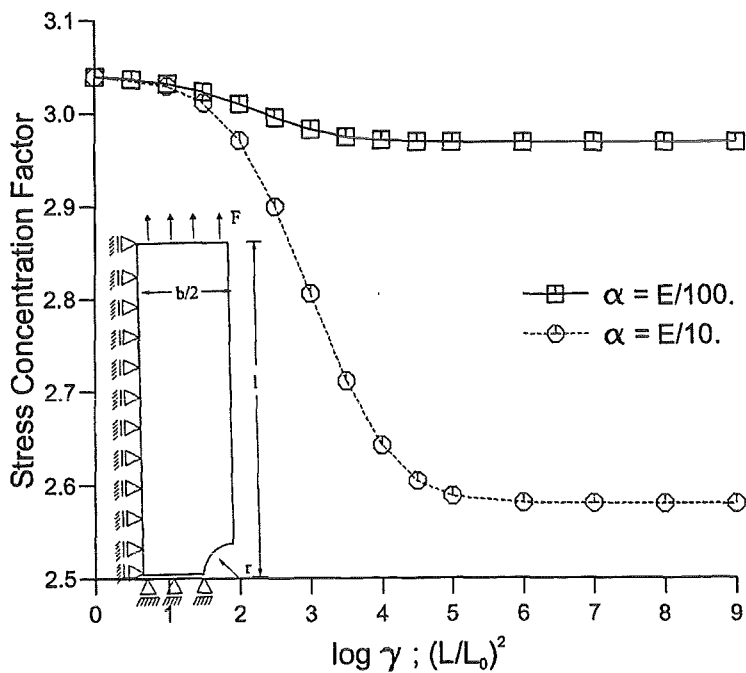


Fig. 5: Stress concentration factor for an outer notched plate under plane stress conditions as function of material parameter.

### 3-Point Bend - Plane Strain

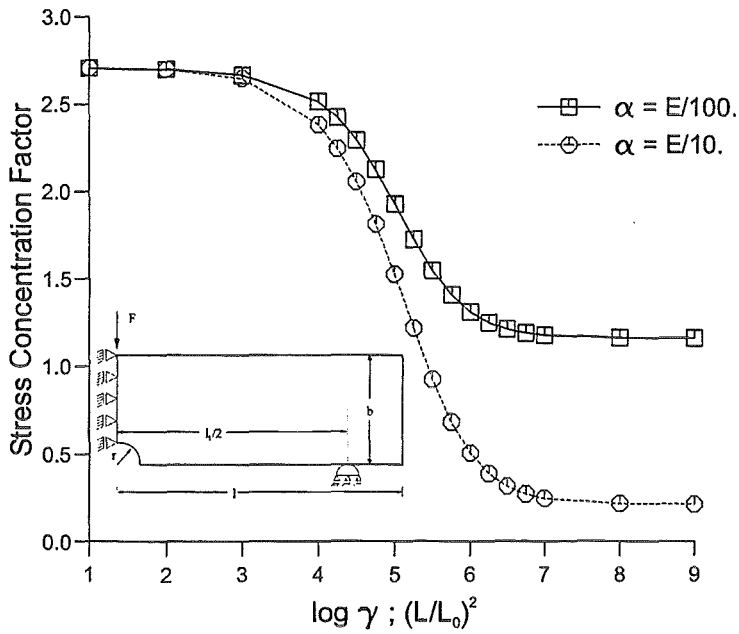


Fig. 6: Stress concentration factor for a 3 point bend specimen under plane strain conditions as function of material parameter.

### 3-Point Bend - Plane Strain

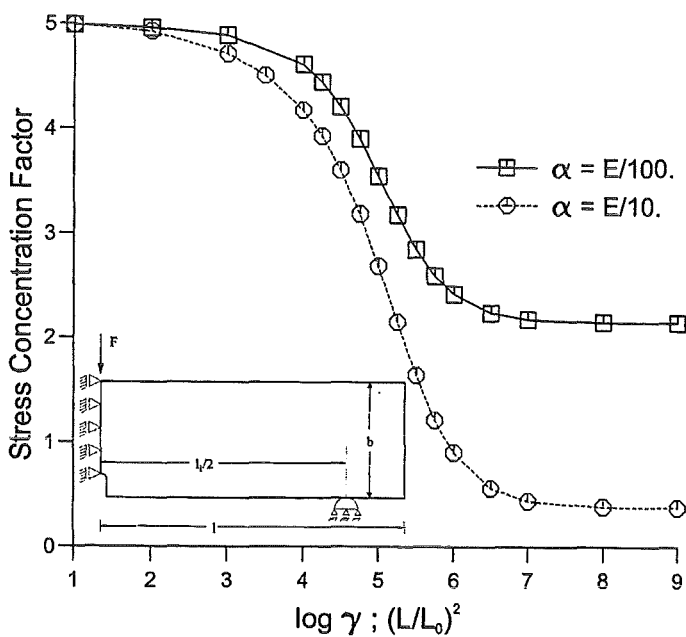


Fig. 7: Stress concentration factor for a deep notched 3 point bend specimen under plane strain conditions as function of material parameter.

### **32.22.06 Untersuchungen zum Brennstoff- und Brennstabverhalten innovativer Systeme**

#### **I. Instrumentierung für CABRI-Testeinsätze (P. Norajitra, D. Piel, L. Sepold, IMF III)**

Im Auftrag des IPSN Cadarache wurden weitere instrumentierte Abstandshalter-systeme für vorbestrahlte Brennstäbe und Hochtemperatur-Verlagerungsaufnehmer der bewährten Bauart für die laufenden CABRI-Experimente hergestellt und ausgeliefert. Zusätzlich wurden für die REP-Na-Versuche einzelne Brennstabspitzen zur axialen Wegmessung gefertigt und geliefert.

Die Mitarbeit für die Testinstrumentierung im Hinblick auf die geplanten RIA-Experimente im künftigen CABRI-Druckwasserloop wurde im Rahmen der „Instrumentation Working Group“ begonnen.

Für die Experimente im Druckwasserloop waren bereits Abstandshalterkäfige aus Zircaloy entwickelt worden. Die Finite-Elemente-Berechnungen für eine 2D-Spannungs- und Deformationsanalyse der Zircaloy-Ringe bei Temperaturen bis 700°C wurden abgeschlossen.

## II. Theoretical interpretation of results of CABRI-experiments

(D. Struwe, W. Pfrang, W. Zimmerer, IRS)

### **Pre-failure and post-failure in-pin fuel relocation**

Pre-failure and post-failure in-pin fuel relocation has been investigated in various experiments of the different CABRI programmes. Theoretical evaluation of the respective phenomena has been performed using the EJECT model of the newest SAS4A code version. The basic features of the EJECT model as implemented in the code version Ref-01 Rel-0 by IPSN were kept unchanged with only one exception. The originally supplied model assumes that the fuel released to the central hole maintains the enthalpy of the melting fuel reservoir adjacent to the solid fuel shell. This means that the enthalpy of the fuel entering the central hole initially is on an enthalpy level between the fuel solidus enthalpy and the fuel liquidus enthalpy but initially close to the solidus fuel enthalpy. Therefore, the mobility of this fuel is rather small initially due to the large dependence of the fuel viscosity from the fuel enthalpy level. In reality the fuel entering the central hole is on the fuel liquidus enthalpy and the still solid fuel of the reservoir fuel remains in the fuel reservoir. Upon release of a fraction of the fuel from the reservoir fuel with the liquidus enthalpy the average fuel enthalpy of the reservoir fuel becomes reduced.

The originally supplied model has been modified to take note of the above mentioned situation. As a consequence of this modification it became necessary to reformulate the actually established effective interface temperature and thus the heat transfer from the relocating fuel/fission gas mixture in the central hole to the solid fuel shell with the aim to choose a simpler and more straight forward approach than provided in the original formulation. Beyond this basic modification of the EJECT model a large variety of modifications in the different EJECT subroutines have been introduced which were developed at FZK during efforts to get an improved experimental qualification of the model in view of results obtained in the different CABRI programmes. The experiments used for the experimental qualification were the OPHELIE 6 experiments E9, E5, E7 and E8, the SCARABIX experiments MF2 and LT4 and the QUASAR experiments PF2 and LT2. Results of all these experiments could be represented in a satisfactory manner with the modified code version. The mass deviation errors in the calculations remained small i.e. below  $3 \cdot 10^{-5}$  with only a few exceptions in reactor case applications.

## 32.22.08 Oberflächenvergütung mit gepulsten Elektronen- und Ionenstrahlen

### I. Behandlung von MCrAlY-Schutzschichten und Grundlagenuntersuchungen zur Stahlerzeugung

(G. Müller, R. Huber, G. Schumacher, H. Bluhm, V. An, D. Strauß, F. Zimmermann, IHM; V. Engelko, Efremov Institute, St. Petersburg)

#### **Abstract**

Work on surface modification by GESA of turbine blade MCrAlY coatings for thermal barrier coatings is continued. Aim of this work is to influence the structure and morphology of the surface of the MCrAlY coating to achieve improved bonding properties for TBC's. A comprehensive test program was started to examine the stability of TBC's at temperatures of 950 and 1000 °C on air and the influence of the GESA treatment. As a result, GESA treatment improves the bonding stability and lowers  $\beta$ -depletion for the standard bond coating examined. With other bond coats possible melt drop formation at the surface has to be avoided to obtain the same positive results.

#### **Zusammenfassung**

Die Arbeit über Oberflächenmodifikation von MCrAlY beschichteten Turbinenschaufeln für kolumnar strukturierte Wärmedämmschichten (WDS) wird fortgesetzt. Ziel der Arbeit ist, die Struktur und Morphologie der Oberfläche so zu beeinflussen, dass eine Verbesserung der Haftungseigenschaften der WDS erreicht wird. Ein umfangreiches Test-Programm wurde gestartet, um die Stabilität der WDS bei Temperaturen vom 950 und 1000 °C an Luft zu untersuchen und den Einfluss der GESA-Behandlung zu ermitteln. Das Ergebnis ist, dass die GESA-Behandlung bei den untersuchten Standard Beschichtungen die Haftfestigkeit erhöht und die  $\beta$ -Verarmung reduziert. Bei anderen Haftvermittlerschichten muss eine mögliche Bildung von Schmelztropfen an der Oberfläche vermieden werden, um ähnlich positive Ergebnisse zu erzielen.

## **1. Einleitung**

In einem vorausgegangen Experiment an einer mit MCrAlY beschichteten Probe, deren Oberfläche vor der Beschichtung mit einer keramischen Wärmedämmschicht (WDS) mit GESA-behandelt wurde, konnte auch nach 10 000 Std. Auslagerung an Luft bei 950 °C kein Schaden an der WDS festgestellt werden. Das thermisch gewachsene Oxid (TGO) hatte nach dieser Zeit erst eine Dicke von 4 µm erreicht und die  $\beta$ -verarmte Zone war mit nur 20 µm noch entsprechend dünn. Diese Daten deuten darauf hin, dass die doppelte Standzeit, nämlich 20 000 Std. möglich ist. Das ist für den industriellen Einsatz eine interessante Marke.

Aufgrund der positiven Anfangsergebnisse wurde zusammen mit dem Industriepartner ein umfangreiches Versuchsprogramm gestartet, einmal um die ersten Ergebnisse statistisch abzusichern, zum anderen um neben der bisher untersuchten Standard-MCrAlY-Schicht auch neuere Entwicklungen auf ihre Eignung als Haftvermittlerschicht zu untersuchen.

## **2. Experimente**

Proben mit Wärmedämmschichten bestehend aus Zirkonoxid (stabilisiert mit Yttriumoxid) wurden stationär bei 950/1000 °C an Luft ausgelagert. Ein Teil der Proben war vor dem Beschichten nur mechanisch geglättet, ein anderer war mit der GESA behandelt. Die Proben wurden in Intervallen von 200 h aus dem Ofen entnommen, auf Raumtemperatur abgekühlt und visuell auf Abplatzungen untersucht. Außerdem wurden nach 300, 1000, 3000 und 5000 Stunden metallographische Untersuchungen an Querschliffen durchgeführt. Diese Untersuchungen hatten zum Ziel das zeitliche Anwachsen der thermisch gewachsenen Oxidschicht (TGO), der  $\beta$ -verarmten Zone und die Interdiffusion zu ermitteln. Neben der Standardschutzschicht mit 8 wt%-Al wurden auch zwei Neuentwicklungen mit 10-12 wt%-Al untersucht.

## **3. Versagensstatistik**

In Tab. 1 sind die Ergebnisse der visuellen Schadensinspektion dargestellt. Bei 950 °C sind, abgesehen von einzelnen Ausfallerscheinungen an einer GESA-behandelten (3800 h) und einer industriell präparierten Neuentwicklung (5000 h), alle

übrigen Proben noch intakt. Eine endgültige Bewertung der Ergebnisse bei 950 °C kann erst nach längeren Auslagerungszeiten gegeben werden.

Bei 1000 °C muss zwischen dem Verhalten der Standardschutzschicht und dem Verhalten der Neuentwicklungen unterschieden werden. Unabhängig von der Vorbehandlung (GESA oder industriell) verhalten sich die Neuentwicklungen statistisch identisch. Alle Proben zeigen erste Ausfälle zwischen ca. 600 und 800 h und weisen eine maximale Lebensdauer von ca. 3000 h auf. Die Standardschicht verhält sich weitaus günstiger. Es treten zwar nach 1000 h (industriell) bzw. 3624 h (GESA-Behandlung) auch einzelne Ausfälle auf, doch sind nach 5004 h alle übrigen Proben noch intakt. Aus den Auslagerungen bei 1000 °C lässt sich schließen, dass die Standardschicht gegenüber den neuentwickelten Schichten, deutlich höhere Standzeiten besitzt. Vergleicht man die Ergebnisse bei 950 °C mit denen bei 1000 °C, so lässt sich feststellen, dass bei 1000 °C die Neuentwicklungen völlig versagen, während die Standardschichten nur einen Ausfall von 15 % aufweisen.

		1000 °C		950 °C	
		min. [h]	max. [h]	min. [h]	max. [h]
Standardschicht	mech. gegl.	1000	>	>	>
	GESA beh.	3624	>	>	>
1. Neuentwicklung	mech. gegl.	804	3000	>	>
	GESA beh.	804	2854	3816	>
2. Neuentwicklung	mech. gegl.	660	3000	5004	>
	GESA beh.	660	2854	>	>

Tabelle 1: Zusammenfassende Darstellung der Ergebnisse bis zur aktuellen Auslagerungszeit von 5004 h. *min.* beschreibt den Zeitpunkt bei dem erste Ausfälle beobachtet wurden, während *max.* den Zeitpunkt angibt, bei dem alle Proben versagt haben (> heißt > 5004 h).

Die Abb. 1 und 2 zeigen die Ausfallstatistik der Standardprobe und einer Neuentwicklung. Die Balken geben jeweils die Zahl der intakten Proben nach der auf der Abszisse angegebenen Zeit wieder.

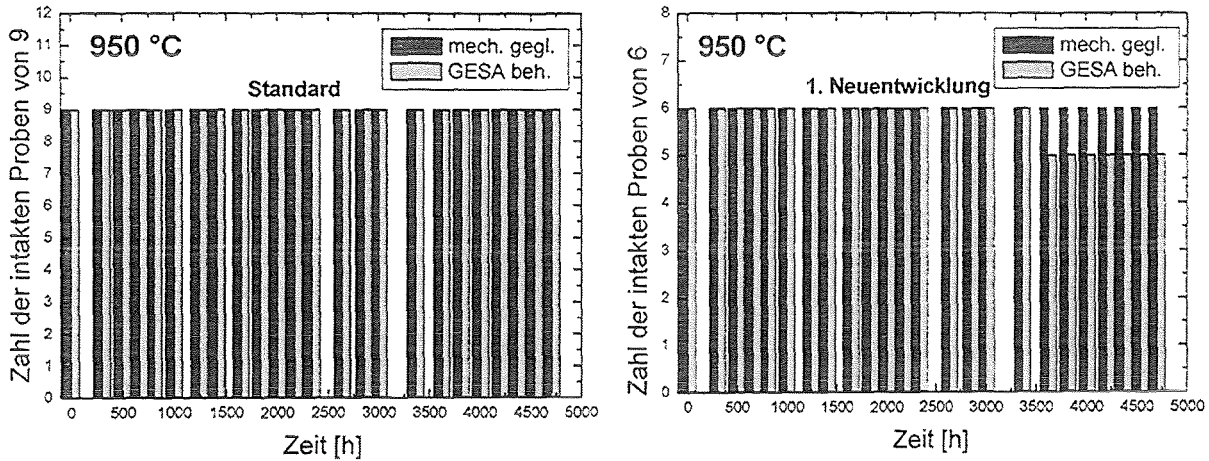


Abb. 1: Anzahl der intakten Proben mit u. ohne GESA-Behandlung in Abhängigkeit von der Auslagerungszeit bei 950 °C; links Standardschicht, rechts 1. Neuentwicklung.

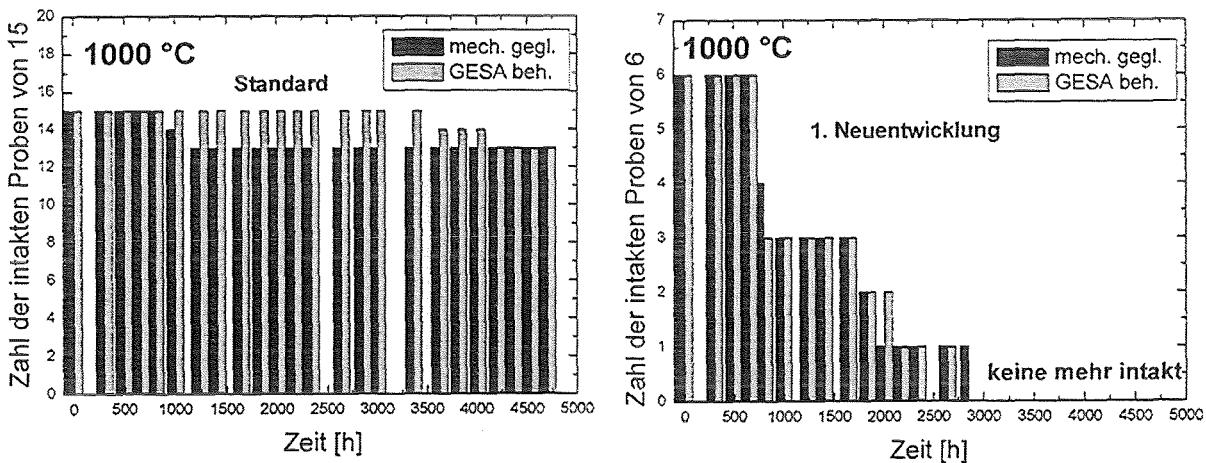


Abb. 2: Anzahl der intakten Proben mit u. ohne GESA-Behandlung in Abhängigkeit von der Auslagerungszeit bei 1000 °C; links Standardschicht, rechts 1. Neuentwicklung.

#### 4. Strukturveränderung

Die Strukturen der WDS und die der Oberflächenschicht der Proben, die nur mechanisch geglättet wurden, unterscheiden sich schon nach dem Beschichten wesentlich von den mit GESA-behandelten. In Abb. 3 sind REM (Raster-Elektronen-Mikroskopie)-Aufnahmen der Querschliffe zweier solcher Proben gegenüber gestellt. Die im herkömmlichen Verfahren mechanisch geglättete Oberfläche, Abb. 3 links, weist erhebliche Mikrorauhigkeiten auf, die das erwünschte regelmäßige Wachstum der Säulenkristalle der WDS nicht zulassen. Die Säulenachsen sind willkürlich gegeneinander geneigt, was zu frühzeitigem Abplatzen führen kann. Auf der mit GESA-behandelten glatten Oberfläche, Abb.3 rechts, wachsen die Säulenkristalle senkrecht

zur Oberfläche und bilden somit eine Struktur, die zu erheblich geringeren Wachstumsspannungen im TGO führen sollten. Wachstumsspannungen werden für das Abplatzen der WDS verantwortlich gemacht. Es ist auch zu erkennen, dass die GESA-behandelte Probe eine wesentlich homogenere Oberflächenstruktur besitzt, was sich positiv auf die Entwicklung der TGO-Schicht auswirkt, die zwischen Oberfläche und WDS entsteht und für die Anbindung der WDS an die MCrAlY-Oberfläche verantwortlich ist.

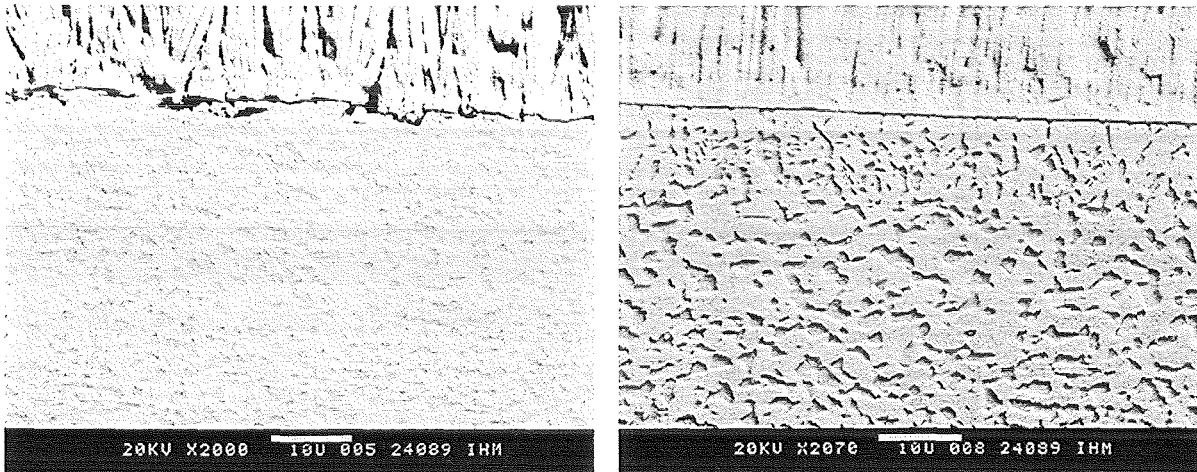


Abb. 3: Ausgangszustand nach der Beschichtung bei mechanisch geglätteter (links) und GESA-behandelter (rechts) Oberfläche von der Standardbeschichtung; oben mechanisch geglättet, unten GESA-behandelt.

Für die Neuentwicklung ergibt sich im Grunde der gleiche Befund. Auffällig ist hier nur, dass auf dem GESA-behandelten Oberflächen Schmelztröpfchen aus Yttrium-Aluminaten entstehen, die teilweise eine kritische Größe  $> 10 \mu\text{m}$  erreichen und beim Beschichten zu einem fächerförmigen Säulenwachstum an solchen Stellen führen, was dort die Stabilität schwächt. Diese Schmelztröpfchen haben einen ursächlichen Zusammenhang mit der Y-Konzentration. Sie entstehen, wenn diese über der Löslichkeitsgrenze von ca. 0,1 Gew.% liegt. Das primäre Ziel muss sein, MCrAlY-Schichten mit niedrigerer Y-Konzentration herzustellen. Andere Möglichkeiten zur Beseitigung der Tröpfchen sind Mehrfachpulse, die zur Verdampfung führen, oder mechanisches Abtragen.

Die Entwicklung der Strukturveränderungen während der Exposition bei hohen Temperaturen an Luft soll nun zunächst am Beispiel der Standardbeschichtung gezeigt werden. Nach 1000 h Auslagerung bei  $950 \text{ }^\circ\text{C}$  ist sehr gut zu sehen, welchen

positiven Einfluss die GESA-Behandlung auf die Struktur der TGO-Haftvermittlerschicht hat. Die heterogene Struktur der mechanisch geglätteten Oberfläche in Abb.

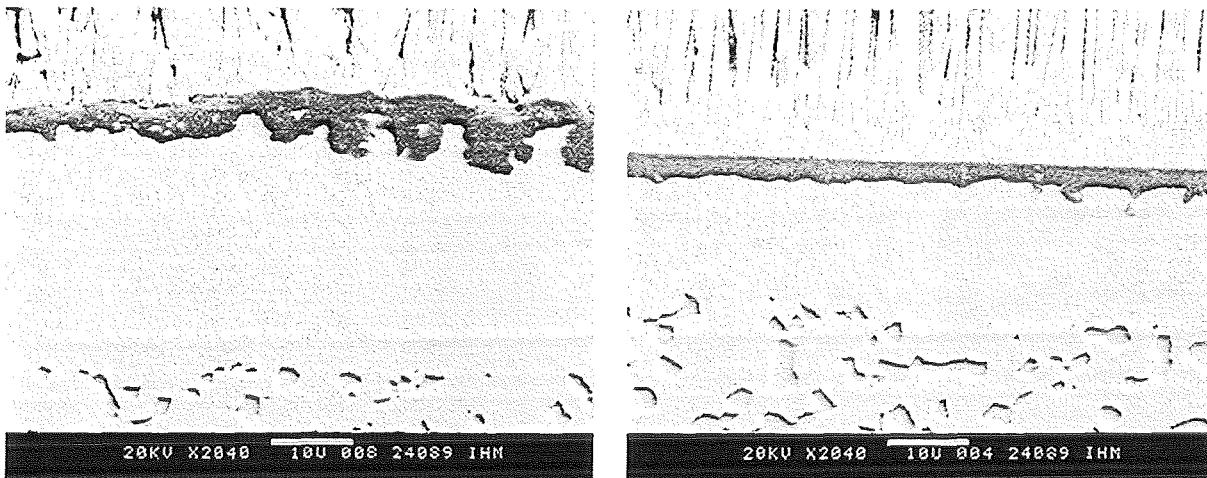


Abb. 4: Mechanisch geglättete (links) und GESA-behandelte (rechts) Standard Probe nach 1000 h Exposition bei 950 °C.

4 links führte zu einer weiteren Zerklüftung der Oberfläche durch eindringenden Sauerstoff und Ausbildung von sogenannten Oxidwurzeln mit hoher Konzentration von Yttriumaluminaten, sowie zu stärkerer  $\beta$ -Verarmung (breitere strukturlose Oberflächenzone) Die Oxidwurzeln werden im Fall einer Delamination durchtrennt und tragen nicht zu einer verbesserten Anbindung der WDS bei. Die Schicht auf der GESA-behandelten Oberfläche ist wesentlich homogener und stabiler. Bei 1000 °C sind die Unterschiede nicht so groß weil dort die Umwandlung der TGO zu  $\alpha$ - $\text{Al}_2\text{O}_3$  schneller vonstatten geht. Trotzdem neigt die WDS der mechanisch geglätteten Probe wegen des unregelmäßigen Säulenkristallwachstums zu früherem Abplatzen. Deutliche Unterschiede sind jedoch in der Statistik bis 5004 h noch nicht aufgetreten. Die noch laufenden Experimente werden erst nach längeren Zeiten eine Auskunft über die Standzeit geben.

Bei den Neuentwicklungen, deren  $\text{MCrAlY}$ -Schicht 10-12 Gew.% Al enthält, ist nach 1000 h bei 950 °C ein ähnliches Verhalten zu beobachten, Abb. 5. Die unregelmäßige Säulenkristallstruktur hatte aber bei der mechanisch geglätteten Probe, Abb. 6 links, offenbar aufgrund von Wachstumsspannungen, bei der Präparation zum Ablösen der WDS geführt. Beachten sollte man die geringe  $\beta$ -Verarmung, die allerdings aufgrund der hohen Al-Konzentration und des langsamen Wachstums der TGO zu erwarten ist.

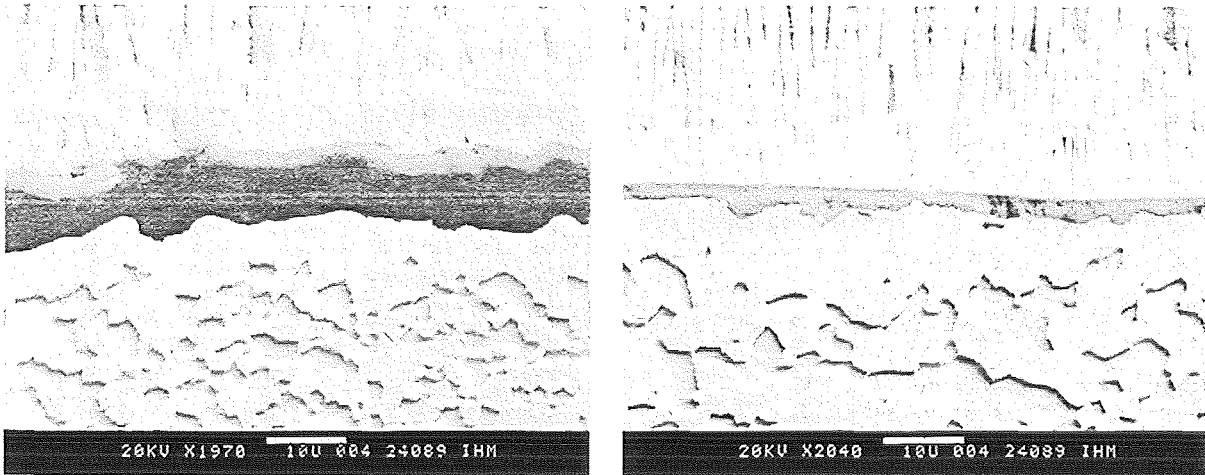


Abb. 5: Mechanisch geglättete (links) und GESA-behandelte (rechts) Standard Probe nach 1000 h Exposition bei 950 °C.

Warum sich auf den Proben mit neu entwickelter MCrAlY-Schicht die WDS trotz GESA-Behandlung und homogener TGO ablöst zeigt Abb. 6. Hier hat sich die WDS um einen überkritischen Schmelztropfen herum abgelöst. Unten sieht man die immer noch glatte GESA-behandelte Oberfläche.

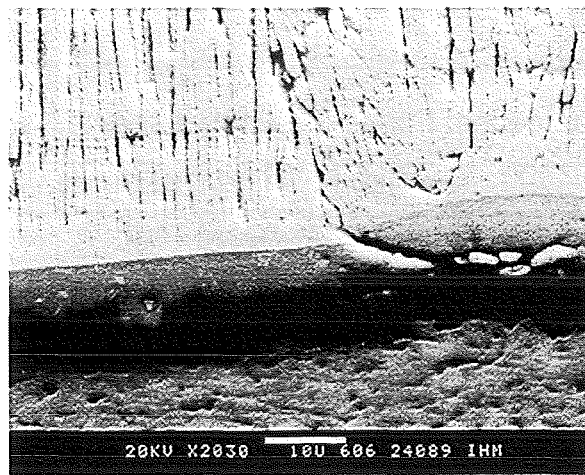


Abb. 6: GESA-behandelte Probe mit neuentwickelter MCrAlY-Schicht nach 3000 h Exposition bei 1000 °C. Die TGO hat sich im Experiment abgelöst.

## 5. Interdiffusion und $\beta$ -Verarmung

Die  $\beta$ -verarmte Zone wurde aus der Strukturentwicklung anhand von REM-Aufnahmen der Querschnitte senkrecht zur Oberfläche bestimmt. Es ergab sich, dass bei 950 °C die Entwicklung der  $\beta$ -verarmten Zone stark von der vorausgegangenen GESA-Behandlung beeinflusst wird, Abb. 7.

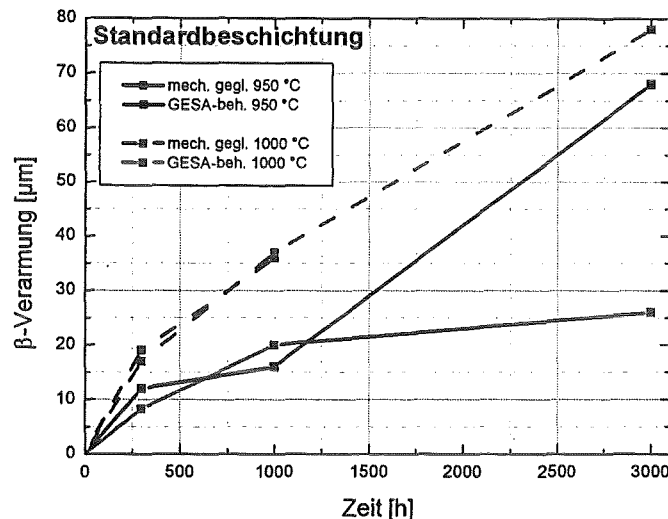


Abb. 7:  $\beta$ -Verarmung Standardbeschichtung

Nach der GESA-Behandlung der Standard-Probe ergibt sich eine um mehr als die Hälfte verringerte  $\beta$ -Verarmung. Für die neuentwickelten Schichten sind diese Unterschiede gering. Bei 1000 °C sind keine Unterschiede vorhanden wegen der schnelleren Umwandlung der TGO zu  $\alpha$ -Al<sub>2</sub>O<sub>3</sub> bei 1000 °C.

Die Interdiffusionszone wird erwartungsgemäß nicht von der GESA-Behandlung beeinflusst. Sie hängt nur von der Beschaffenheit der MCrAlY-Schicht ab.

## 6. Industrielle Anwendung

Zur Durchführung eines Regenbogentests (verschiedene Testschaufeln werden in einer Gasturbine unter realistischen Betriebsbedingungen eingesetzt) wurden zunächst mehrere ganze Turbinenschaufeln umgeschmolzen und anhand von Qualifizierungsschnitten untersucht und für den Einsatz im Regenbogentest zugelassen. Danach wurden 5 Schaufeln GESA-behandelt und dem Industriepartner übergeben, Abb. 8.

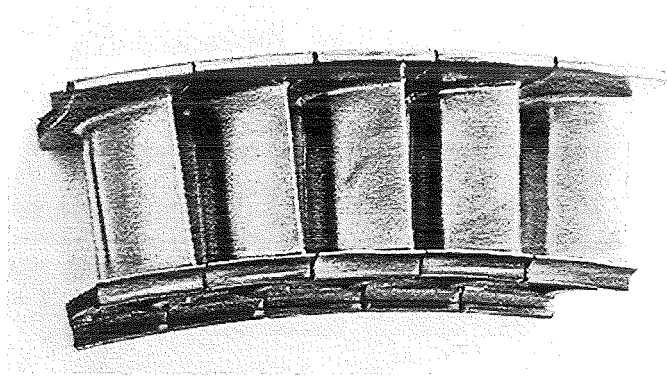


Abb. 8: Turbinenschaufeln für den Regenbogentest in einer stationären Gasturbine nach der GESA-Behandlung.

Der Regenbogentest soll Anfang nächsten Jahres beginnen.

Eine Designstudie für eine industrielle GESA-Anlage zur Behandlung von Turbinenschaufeln wurde begonnen. Diese Anlage soll eine Bearbeitungskapazität von 3000 – 5000 Schaufeln pro Jahr haben.

## 7. Strahlqualität

Für manche Anwendungen z.B. auf dem Gebiet der Oberflächenhärtung und Bruchfestigkeitsverbesserung ist die Homogenität der Elektronenstromdichte auf dem zu behandelnden Werkstück von ausschlaggebender Bedeutung. Daher wurden im Berichtszeitraum weiterhin eine Reihe von experimentellen- und theoretischen Grundlagenuntersuchungen zur Strahlerzeugung und zur Verbesserung der Strahlhomogenität durchgeführt. Die Ergebnisse lassen sich wie folgt zusammenfassen:

- Zur Beschreibung der Expansion des Targetplasmas, das sich bei der Wechselwirkung des Elektronenstrahls mit dem Werkstück bildet und hauptsächlich für die Raumladungskompensation des Elektronenstrahls verantwortlich ist, wurde ein analytisches Modell entwickelt. Die Voraussagen des Modells wurden experimentell durch Messung der zeitlichen Entwicklung des Elektronenstrahlpotentials mittels einer kapazitiven Sonde bestätigt. Für typische GESA Parameter bildet sich das Plasma nach ca. 4  $\mu\text{s}$  und breitet sich mit zunehmender Geschwindigkeit in Richtung Kathode aus.
- Zur Messung der orts- und zeitaufgelösten Leistungsdichteverteilung am Target wurde eine neue Röntgenstrahl Diagnostik entwickelt, die sich gegenüber der bisherigen direkten Messung der Stromdichteverteilung mittels

Faradaybechern durch eine um eine Größenordnung höhere Ortsauflösung auszeichnet. Außerdem ist das Messsignal während der gesamten Pulsdauer von bis zu 40  $\mu\text{s}$  auswertbar während die Signale der Faradaybecher nach wenigen  $\mu\text{s}$  durch Plasmabildung gestört werden. Die Diagnostik basiert auf der Konversion des Elektronenstrahls in Röntgenstrahlung mit Hilfe eines dünnen Metallblechs aus einem Material hoher Ordnungszahl. Der Konverter befindet sich in engem Kontakt mit einer Szintillatorscheibe in der die Röntgenstrahlung in Licht gewandelt wird, das mit Hilfe einer Optik auf die Photokathode einer Streak-Framing-Kamera abgebildet wird, Abb. 9.

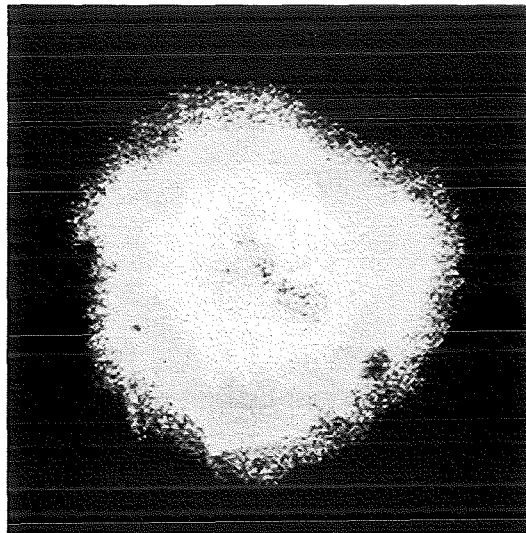


Abb. 9: Momentaufnahme der Leistungsdichteverteilung am Target aufgenommen mit der neuen Röntgenstrahldiagnostik. Die Bildbreite entspricht 10 cm.

Diese Diagnostik soll in Zukunft als Standardmessmethode zur Bestimmung der Strahlhomogenität eingesetzt werden. Sie ermöglicht die direkte Überprüfung der Wirksamkeit von Maßnahmen zur Verbesserung der Strahlhomogenität in der Diode oder im Driftröhre.

## II. Mikromechanische Modellierung von Wärmedämmschichten

(K. Sfar, J. Aktaa, IMF II)

Ziel der mikromechanischen Modellierung von Wärmedämmschichten ist die Bestimmung des Versagensverhaltens des Verbundsystems und die Aufstellung eines Lebensdauermodells. Ausgehend von einer umfassenden Spannungsanalyse wurden kritische Versagensbereiche identifiziert. Es ist nicht möglich das Versagenverhalten der Wärmedämmschichtsysteme allein aufgrund Eigenspannungsanalysen zu untersuchen, sondern viel mehr werden geeignete Methoden der Rissmodellierung und der Rissbewertung eingesetzt. Da die untersuchten Risskonfigurationen eine sehr starke Modeabhängigkeit aufwiesen, wurde die modifizierte Rissschließungsmethode eingesetzt. Diese Rissbewertungsmethode liefert die einzelnen Komponenten der Energiefreisetzungsrate  $G_I$  und  $G_{II}$ . Die Modellierung von Rissen in der Keramikschiicht, in der Oxidschiicht und an der Grenzfläche Haftvermittlerschiicht / Oxidschiicht ermöglichte die Untersuchung der folgenden Versagensmechanismen:

- Versagen durch Rissausbreitung in der Keramikschiicht
- Versagen durch Rissausbreitung in der Oxidschiicht
- Versagen ausgehend von einer Ablösung an der Grenzfläche zwischen Haftvermittlerschiicht und Oxidschiicht.

Es wurde gezeigt, dass bei allen drei Versagensmechanismen der Oxidationsprozess die wichtigste Systembelastung ist. Gleichzeitig stellt die Oxidation der Haftvermittlerschiicht die notwendige treibende Kraft für das Risswachstum bereit. Es wurde eindeutig gezeigt, dass das Schichtwachstum (verursacht durch die Oxidation) für die Zunahme der Mode-II-Belastung an der Risspitze und gleichzeitig für die Abnahme der Mode-I-Komponente verantwortlich ist. Als die Oxidation der Haftvermittlerschiicht vernachlässigt wurde, wurde die Mode-I-Belastung dominierend und die Mode-II-Komponente vernachlässigbar klein. Es wird festgehalten, dass das Risswachstum hauptsächlich in Mode II stattfindet. Dieser Sachverhalt wurde bei allen oben aufgelisteten Versagensmechanismen festgestellt.

Die bereitgestellten numerischen Werkzeuge dienen als Grundbaustein für ein gesamtes numerisches Lebensdauermodell. Die Bestimmung der Mode-abhängigen bruchmechanischen Parameter kombiniert mit den kritischen Werkstoffparametern ermöglicht die Untersuchung des Rissausbreitungsverhaltens. Damit ist die Voraus-

setzung für eine inkrementelle und iterative Rissausbreitungssimulation erfüllt. Als Endergebnis dieses Verfahrens sollte die Lebensdauer (je nach Bedarf z.B. eine kritische Risslänge, kritische Oxidationszeit, kritische Oxidschichtdicke etc.) des Verbundes erhalten werden. Das numerische Verfahren kann weiterhin ausgebaut werden, um weitere Aspekte des Wärmedämmschichtsystems zu berücksichtigen. Dieses Verfahren wird als zuverlässiges Werkzeug für Optimierungs- und Validierungszwecke eingesetzt.

## 32.22.09 High Performance Light Water Reactor (HPLWR)

- I. Thermal-Hydraulic Analysis of Supercritical Pressure Light Water Reactors  
(X. Cheng, H. Jacobs, T. Schulenberg, D. Squarer, IKET)

### Abstract

The innovative HPLWR concept is mainly understood as a challenging training field for young engineers in the field of light water reactor (LWR) technologies. One of the important items in this project is to develop comprehensive knowledge of heat transfer at the HPLWR condition, which differs strongly from that at sub-critical pressure conditions. In the present study, a thorough literature review on heat transfer in supercritical water is performed. Some heat transfer correlations available in the literature are assessed. A new sub-channel analysis code (STAR-SC) is developed to determine the flow condition in the sub-channels of a HPLWR fuel assembly. A design analysis was carried out using the STAR-SC code for a previous design concept of a supercritical LWR.

### Kurzfassung

Das innovative HPLWR-Konzept wird hauptsächlich verfolgt, um jungen Ingenieuren ein anspruchsvolles Studienobjekt im Bereich Leichtwasserreaktoren (LWR) bieten zu können. Eine der wichtigen Aufgaben in diesem Projekt ist die Gewinnung umfangreicher Kenntnisse bezüglich des Wärmeübergangsverhaltens unter den Bedingungen eines HPLWR, das offensichtlich von dem unter unterkritischen Drücken sehr verschieden ist. In der vorhandenen Arbeit wird eine gründliche Literaturstudie über den Wärmeübergang bei überkritischen Drücken durchgeführt. Einige vorhandene Wärmeübergangskorrelationen wurden bewertet und analysiert. Ein neues Rechenprogramm (STAR-SC) wurde entwickelt, um die Strömungsparameter in den Unterkämen eines HPLWR-Brennelements zu ermitteln. Mit diesem Programm wurde eine Auslegungsstudie für ein bereits vorhandenes Konzept des überkritischen LWR durchgeführt.

## **1 Introduction**

The European project 'high performance light water reactor (HPLWR)' has been launched with the main objective to assess the technical and economic feasibility of a high efficiency LWR operating at supercritical pressure [1]. The main technical contribution of IKET to this project consists of the following tasks:

- Assessment of the existing knowledge on thermal-hydraulic behavior of supercritical water
- Preliminary design analysis of fuel assemblies of a HPLWR
- Definition of the safety requirements and assessment of basic safety properties
- Analysis of the economics of a nuclear power plant with an HPLWR.

In the reporting period, a thorough literature review has been carried out on the thermal-hydraulic behavior of supercritical water. Design analysis of fuel assemblies of HPLWR has been performed using the sub-channel analysis code STAR-SC. Contribution has been made to the economics analysis, which should be documented in a future report. The present report summarizes the main results achieved so far related to the first two technical tasks.

## **2 Literature review on heat transfer at supercritical pressures**

Heat transfer at supercritical pressure is mainly characterized by the thermal-physical properties of water which vary strongly with temperature. Figures 1 and 2 show the specific heat and the density versus temperature at two different pressure values. The condition, at which the specific heat has its maximum value, is the so-called pseudo-critical condition.

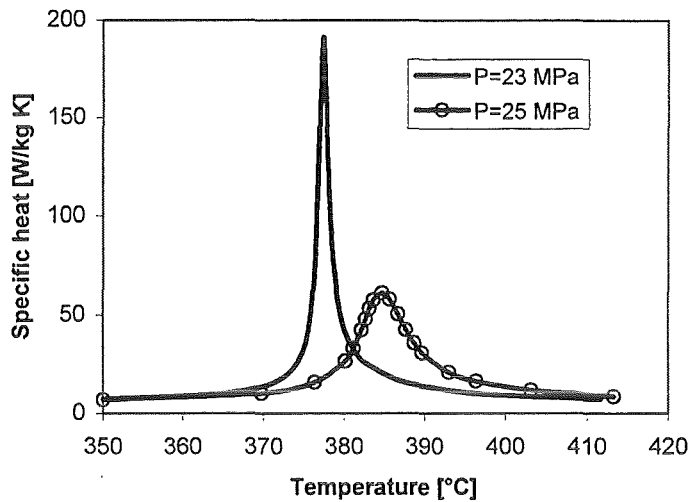


Figure 1: Specific heat of supercritical water

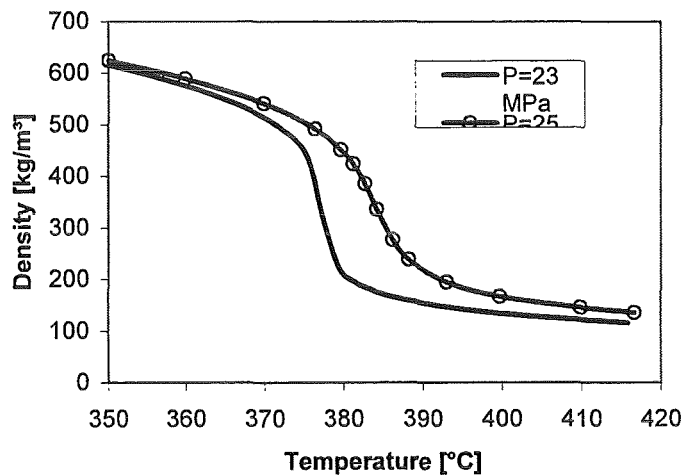


Figure 2: Density of supercritical water

The variation of the specific heat as well as the density is strong at super-critical pressure condition, especially in the vicinity of the pseudo-critical condition. Taking into account the Dittus-Boelter equation

$$Nu = 0.023 \cdot Re^{0.8} \cdot Pr^{1/3}$$

for turbulent water flow, the heat transfer coefficient shows a strong change, when the temperature approaches the pseudo-critical value. The closer the pressure to the critical point is, the higher is the peak of the heat transfer coefficient. However, the real heat transfer coefficient deviates from the Dittus-Boelter equation, especially near the pseudo-critical condition [3]. At low heat fluxes, heat transfer coefficient is

higher than the values predicted by the Dittus-Boelter equation. This phenomenon is called heat transfer enhancement. At high heat fluxes, the heat transfer coefficient is lower than that computed by the Dittus-Boelter equation. Under some specific conditions, a sharp decrease in the heat transfer coefficient may occur. This phenomenon is referred to 'heat transfer deterioration'.

A thorough literature review has pointed out that the experimental works available in the open literature are mainly restricted to the circular tube geometry. Large deviation was obtained between the Dittus-Boelter equation and the test data with the bulk temperature or the wall temperature near the pseudo-critical values. Figure 3 compares the heat transfer coefficients calculated using different correlations. The flow parameters selected correspond well to the condition of a supercritical LWR. A large deviation is obtained between different correlations, especially at a coolant temperature close to the pseudo-critical value.

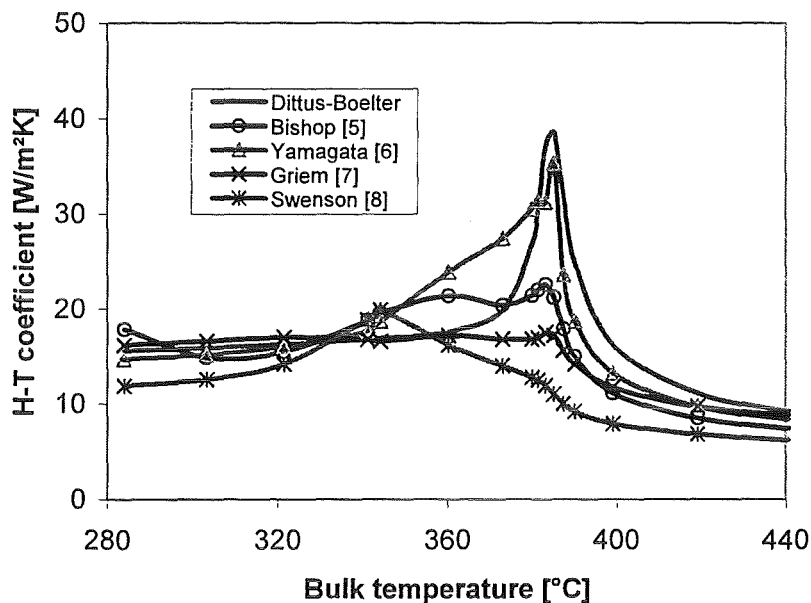


Figure 3: Heat transfer coefficient according to different correlations:  $P=25\text{MPa}$ ,  
 $G=1000\text{kg/m}^2\text{s}$ ,  $q=10^6\text{W/m}^2$

Figure 4 shows the critical heat flux for the onset of heat transfer deterioration in a tube with an inner diameter of 4 mm at a pressure of 25 MPa. A large deviation between different correlations is obtained. Both empirical correlations of Yamagata [6] and of Styrikovich [9] give much smaller critical heat fluxes than the semi-empirical correlations of Petrukhv [10] and Jackson [11]. It has to be pointed out that in the literature, there is still no unique definition for the onset of heat transfer

deterioration, because the reduction in the heat transfer coefficient, or the increase in the wall temperature behaves rather smoothly, compared to the behavior of boiling crisis that is observed at subcritical pressure and at which a much sharper increase in the wall temperature takes place. This is one of the reasons for the large deviation between different correlations. However, it is well agreed that heat transfer deterioration is expected to occur only in case that the bulk temperature is below the pseudo critical value and the wall temperature exceeds the pseudo-critical temperature. All the correlations mentioned above do not take this limitation into consideration. Furthermore, the increase in the heated wall temperature at the onset of heat transfer deterioration is limited and does normally not lead to an excessively high temperature of the heated wall. Therefore, in some design proposals of supercritical LWRs heat transfer deterioration is not taken as a design criterion. Efforts should be made to predict the heat transfer coefficient in the heat transfer deterioration region.

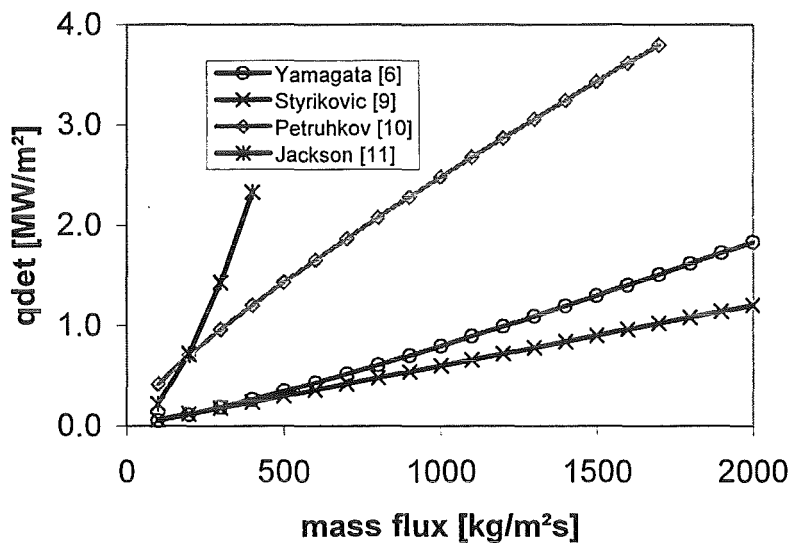


Figure 4: Onset of heat transfer deterioration according to different correlations:  
 $P=25\text{MPa}$ ,  $d=4\text{ mm}$

The correlations of heat transfer and of the onset of heat transfer deterioration mentioned above have been assessed based on their data base and their valid parameter ranges [4]. The heat transfer correlation of Bishop [5] and the correlation of Yamagata [6] for the onset of heat transfer deterioration have been recommended

for the condition of a supercritical LWR, until more reliable test data and correlations are available.

### 3 Sub-channel analysis

The sub-channel analysis code STAR-SC has been developed for the thermal-hydraulic design of the fuel assembly of a supercritical LWR [4]. The main features of the STAR-SC code are: (a) a high feasibility for different geometric configuration of the fuel assembly. This is of crucial importance for applying the code to fuel assemblies of a supercritical LWR, where large amount of irregular sub-channels might exist due to some specific design requirements, e.g. moderator tubes [2]; (b) the capability of the macro sub-channel approach, which combines a number of similar sub-channels into one group, the so-called macro sub-channel. This approach would significantly reduce the computational expenditure. With a proper selection of the macro sub-channels, the impact of the macro sub-channel approach on the thermal-hydraulic conditions in the individual sub-channels, especially in the hot sub-channel, can be negligibly small. This method is highly useful in the stage of the conceptual design of a fuel assembly, where a wide range of design parameters, e.g. geometric configurations, needs to be investigated. The STAR-SC code has been applied to the design of Dobashi [2]. Some technical specifications and operating parameters of this design are summarized as below:

Thermal power:	3568 MW
System pressure:	25 MPa
Height of the active core:	4.20 m
Number of fuel assemblies:	211
Number of fuel rods in one fuel assembly:	258
Diameter of fuel rods:	8.0 mm
Pitch to diameter ratio:	1.19
Average specific power:	15.6 kW/m
Coolant inlet/outlet temperature:	280°C/508°C
Feed water flow rate:	1816 kg/s

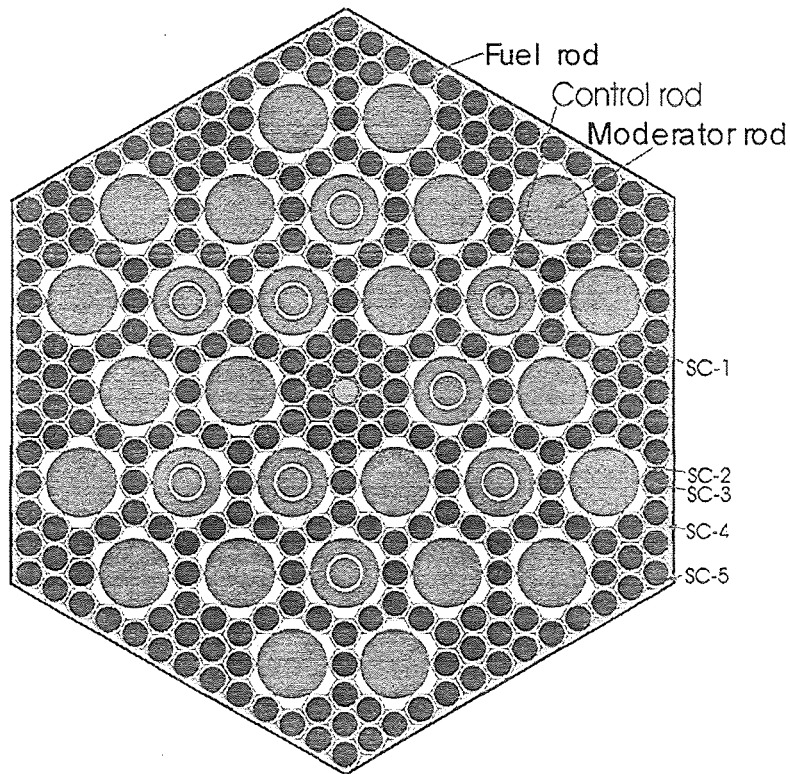


Figure 5: Cross section of the fuel assembly of a supercritical LWR [2]

Figure 5 shows schematically the fuel assembly. It consists of 258 fuel rods and 30 moderator rods. The fuel rods have an outer diameter of 8 mm and are arranged hexagonally with a pitch of 9.5 mm. The wall clearance  $\delta$ , i.e. the distance between the duct wall and the fuel rods, is varied from 0.5 mm to 1.5 mm with the reference value of 1.0 mm. Nine of the 30 moderator rods contain a control rod in their central part. For simplicity, the control rods are neglected in this thermal-hydraulic study. All 30 moderator rods are considered as a single type.

One moderator rod replaces 7 fuel rods and consists of a moderator tube and six moderator boxes, as indicated in figure 6. In this design proposal, the feed water is divided into two parts after entering the pressure vessel. One part flows through the moderator tube downward, and the other goes through the down-comer to the bottom of the reactor core, where it merges with the moderator flow. Afterwards, the total feed water flows as coolant through the fuel assemblies. The mass flow rate through the moderator tube has been varied according to neutron-physical requirements. To study the effect of the moderator flow rate on the sub-channel condition, the moderator mass flow rate changes from about 10 % to 90 % of the total feed water flow rate. The reference value is 50 %.

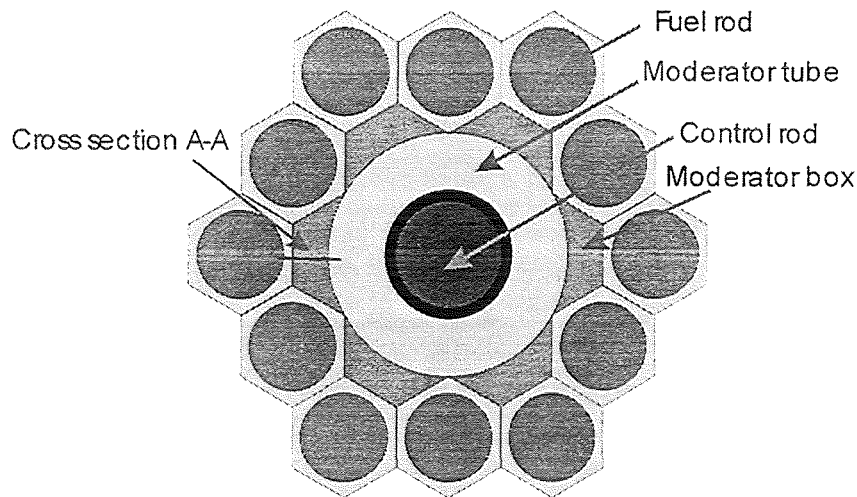


Figure 6: moderator rod and its surroundings [2]

The moderator tube is surrounded by six moderator boxes, which contain stagnant water. Along the core height, the moderator box is divided into many small zones by using plates with a spacing of about 2 cm. It was expected that a strong natural convection of water in the moderator box should be avoided. This way, the heat transfer between the coolant and the moderator inside the moderator tube would be minimized. For a proper analysis, the heat transfer through the stagnant water in the moderator box was determined using the CFX-4.3 code [4]. Based on this systematic analysis, a look-up table of heat transfer coefficient was derived which is used for the present sub-channel analysis.

To present the results, flow conditions in five different sub-channels are selected and discussed. Each selected sub-channel represents one sub-channel group in the fuel assembly (see figure 5). Sub-channel No.1 (SC-1) is called a normal sub-channel and located between three fuel rods. Sub-channels No.4 (SC-4) and No.5 (SC-5) are adjacent to the duct wall and called wall sub-channel and corner sub-channel. Sub-channel No.2 (SC-2) and No.3 (SC-3) are located next to the moderator rods.

### 3.1 Reference case

Figure 7 shows the mass flux in the five sub-channels at the reference condition, i.e. the turbulent mixing coefficient  $\beta=0.002$ , the wall clearance  $\delta=1.0$  mm and the mass flow ratio  $f_m=50$  %. A strongly non-uniform distribution of mass flux in the fuel assembly is obtained. Due to the small hydraulic diameter, the mass flux in the sub-channels No.2 and No.3 is much lower than the ones in other sub-channels. After

each grid spacer a re-distribution of the mass flux occurs. The non-uniformity of the mass flux distribution becomes stronger, as the distance from the grid spacers increases. Above an axial elevation of about 2 m, the coolant temperature in some sub-channels reaches the pseudo-critical value (figure 8), the density in these sub-channels decreases sharply. This causes a further reduction in the mass flux in these sub-channels, and subsequently a greater non-uniformity of the mass flux distribution in the fuel assembly. At the upper end of the core active height, the mass flux in the sub-channel No.3 is about  $800 \text{ kg/m}^2\text{s}$ , only 50 % of that in the sub-channel No.4.

Figure 8 shows the coolant temperature in the five sub-channels. The coolant temperature in the sub-channels 2 and 3 is much higher than that in the other sub-channels. Therefore, both the sub-channel 2 and 3 are considered as the hot sub-channels. Although the mass flux in the sub-channel No.3 is much lower than that in the sub-channel No.1, the equivalent heated diameter (related to the heated perimeter) of the sub-channel No.3 is much larger. Both effects compensate each other, so that the coolant temperature distribution is well uniform in the lower part of the fuel assembly. When the coolant temperature in the hot sub-channels exceeds the pseudo-critical value, both the density and the specific heat decrease rapidly (see figures 1 & 2). A reduction in the density leads to a reduction in the mass flux, and subsequently to a stronger increase in the coolant enthalpy, which, combined with a low specific heat, causes a rapid increase in the coolant temperature. Therefore, in the upper part of the fuel assembly, a strong non-uniform distribution of the coolant temperature occurs.

The difference of the coolant temperature between sub-channels is as high as  $180^\circ\text{C}$  at the axial elevation 3.5 m. Due to the heat transfer between the coolant and the moderator, the coolant temperature in the sub-channels 2 & 3 decreases slightly by approaching the upper end of the fuel active length. It has been found that the water temperature in the moderator tubes increases from  $280^\circ\text{C}$  to about  $340^\circ\text{C}$ , i.e. 1.3 MW heat is transferred from the coolant in the sub-channels to the moderator in each fuel assembly.

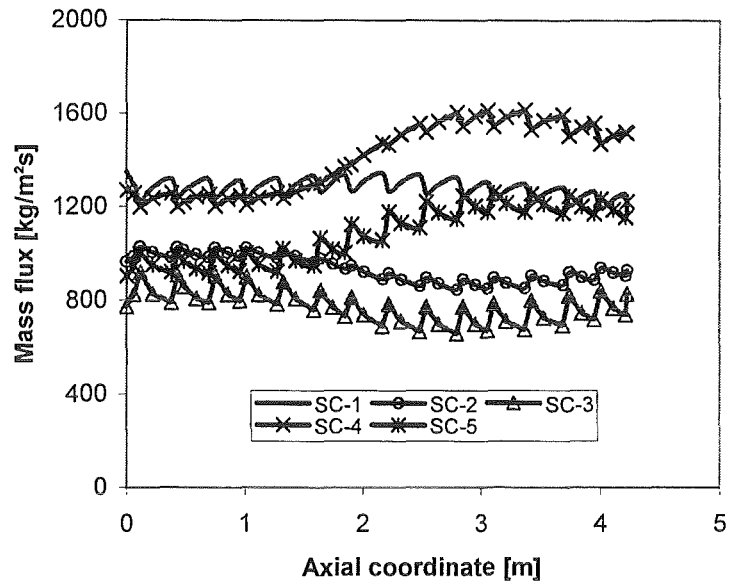


Figure 7: Mass flux in sub-channels

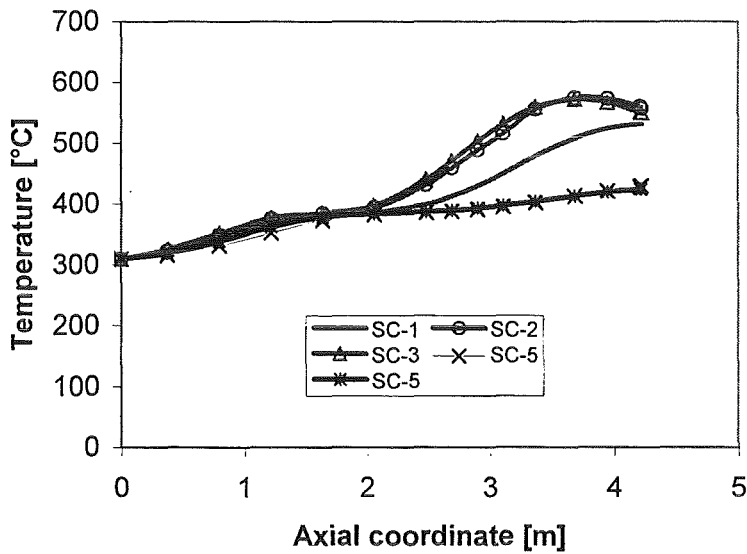


Figure 8: Coolant temperature in sub-channels

Figure 9 shows the water density averaged over the axial cross section. It is well known that the water density affects directly the moderation and, subsequently, the neutronic performance. The water density in the present design varies between  $430 \text{ kg/m}^3$  and  $690 \text{ kg/m}^3$ .

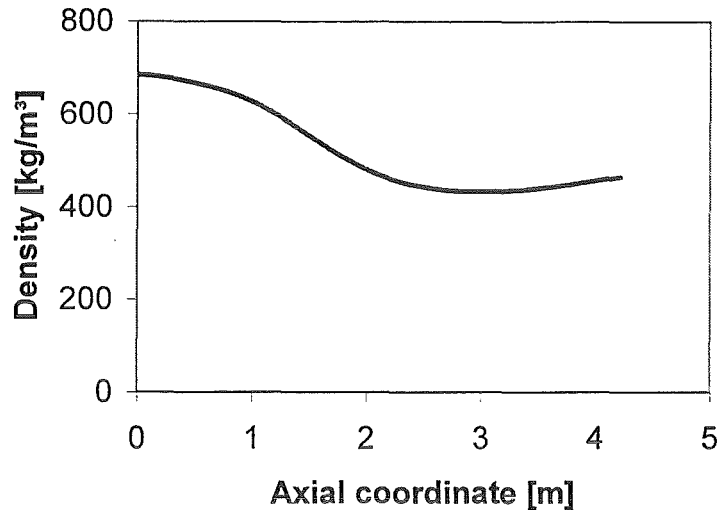


Figure 9: Average water density in fuel assembly

### 3.2 Parametric studies

Figures 10 and 11 show the effect of different heat transfer coefficients between the moderator tubes and the coolant in the sub-channels on the coolant temperature in the hot sub-channel (SC-3) and on the average density of water. In case that the moderator tubes are thermally insulated from the sub-channels, the coolant temperature at the sub-channel inlet is only 280°C, much lower than in the case without the stagnant water layer (conducting case). In the conducting case, on the other hand, the coolant temperature exceeds the pseudo-critical temperature already at a lower axial elevation. Due to the heat transfer to the moderator, the increase in the coolant temperature is much lower than in the insulating case, so that the maximum coolant temperature is more than 100°C lower.

However, in the insulating case, the average water density is much higher than that in the conducting case. Therefore, an under-moderation is expected in the case without thermal insulation of the moderator tubes.

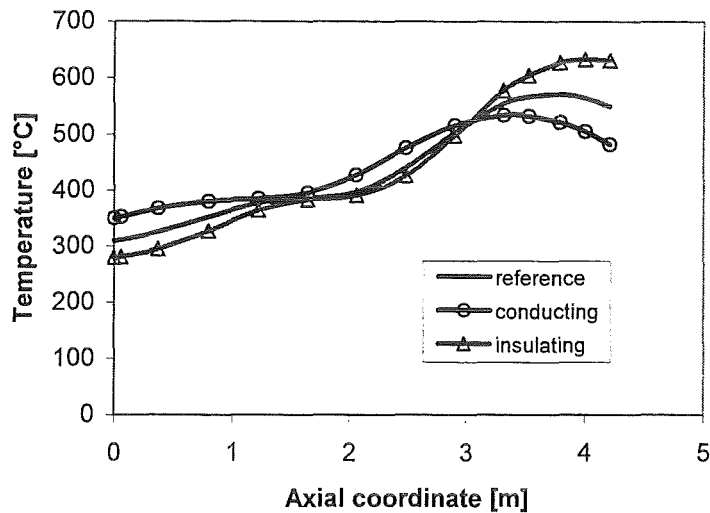


Figure 10: Effect of the heat transfer to the moderator tubes on the coolant temperature

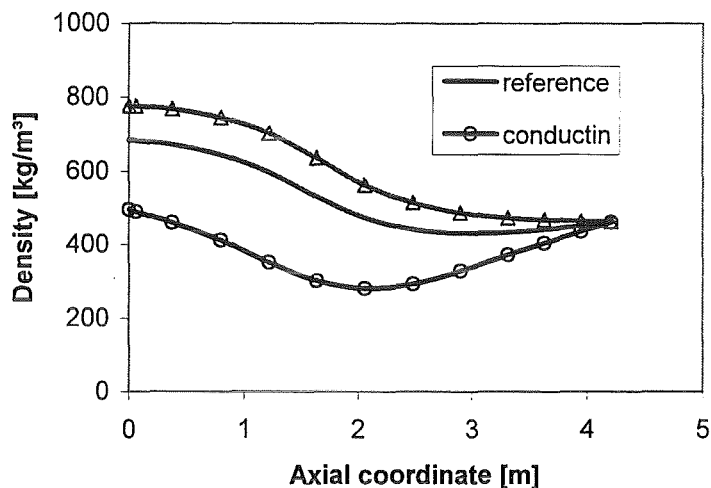


Figure 11: Effect of the heat transfer to the moderator tubes on the water density

Table I summarizes the effect of different parameters on the maximum coolant temperature in the hot sub-channel (SC-3). The accuracy of the turbulent mixing coefficient has a strong impact on the sub-channel condition. A higher turbulent mixing ( $\beta=0.004$ ) leads to a more uniform temperature distribution in the fuel assembly and, subsequently, to a reduction in the coolant temperature in the hot sub-channel. The wall clearance is a sensitive parameter. A reduction in the wall clearance from 1.0 mm to 0.5 mm causes a decrease in the coolant temperature in the hot sub-channel of about 40°C. The higher the moderator mass flow rate is, the lower is the coolant temperature in the hot sub-channels.

Table I: Effect of different parameters on the maximum coolant temperature in the hot sub-channel

Cases	$T_{\max}$
Reference	572.3
$\beta = 0.0$	636.2
$\beta = 0.004$	555.2
$\delta = 0.5$ mm	532.6
$\delta = 1.5$ mm	612.2
$f_m = 10$ %	607.5
$f_m = 90$ %	559.0

#### 4 Summary

The main purpose of the common European project HPLWR, joined by European research institutions, industrial partners and the University of Tokyo, is to assess the technical and economic feasibility of a supercritical pressure light water reactor. It is well agreed that heat transfer is one of the important items affecting the design of the reactor core. To gather a deeper knowledge about the heat transfer at supercritical pressures, a thorough literature survey has been carried out. Although a large amount of experimental and theoretical work is available in the open literature, there exists a large discrepancy related to the prediction of the heat transfer coefficient and the onset of heat transfer deterioration. Moreover, all of these works are restricted to simple flow channels, e.g. circular tubes. Quantitatively, these results can not be directly extrapolated to the reactor relevant condition. Further research activities are thus required.

The sub-channel analysis code STAR-SC has been developed with a high numerical efficiency and a high applicability for different kinds of fuel assembly configurations. Application of this code to the design proposal of the University of Tokyo reveals that due to the presence of the moderator tubes, a strongly non-uniform distribution of the mass flux and of the coolant temperature occurs in the fuel assembly. The parametric studies show that the maximum coolant temperature is sensitive to the mixing coefficient, the wall clearance and the mass flow ratio. This suggests that such

parameters should be carefully designed and optimized to enhance the reactor performance.

## 5 References

- [1] G. Heusener, U. Müller, T. Schulenberg, D. Squarer, A European development program for a high performance light water reactor (HPLWR), *Proc. of SCR-2000, Nov.6-8, 2000, Tokyo, pp.23-28*
- [2] K. Dobashi, Y. Oka, S. Koshizuka, Conceptual design of a high temperature power reactor cooled and moderated by supercritical light water, *ICONE6, May 10-15, 1998*
- [3] B.S. Petuhkov, Heat transfer and friction in turbulent pipe flow, *Advances in Heat Transfer, Vol.6, 1970, 511-564*
- [4] X. Cheng, T. Schulenberg, Heat Transfer at Supercritical Pressures – Literature Review and Application to an HPLWR, *Wissenschaftliche Berichte FZKA 6609, Forschungszentrum Karlsruhe, May 2001*
- [5] A.A. Bishop, R.O. Sandberg, L.S. Tong, Forced convection heat transfer to water at near critical temperatures and supercritical pressures, *WCAP-2056-P, Part-III-B, February, 1964*
- [6] Yamagata, K., Nishikawa, K., Hasegawa, S., Fujii, T. and Yoshida, S.: *Forced Convection Heat Transfer to Supercritical Water Flowing in Tubes, Int. J. Heat Mass Transfer 15, 2575-2593 (1972)*
- [7] H. Griem, W. Köhler, H. Schmidt, Heat transfer, pressure drop and stresses in evaporator water walls, *VGB Power Tech 79, January 1999, pp.26-35 [2]*
- [8] H.S. Swenson, J.R. Caever, C.R. Kakarala, Heat transfer to supercritical water in smooth-bore tube, *Journal of Heat Transfer, Vol. (1965), pp.477-484*
- [9] M.A. Styrikovich, T.K. Margulova, Z.L. Miropolskiy  
Problem in the development of designs of supercritical boilers, *Teploenergetika, Vol.14, No.6, 1967, pp.4-7*
- [10] B.S. Petuhkov, V.A. Kurganov, Heat transfer and flow resistance un the turbulent pipe flow of a fluid with near-critical state parameters, *Teplofizika Vysokikh Temperature, Vol.21, No.1, pp.92-100, Jan. 1983*

- [11] J.D. Jackson, W.B. Hall, Influences of Buoyancy on heat transfer to fluids in vertical tubes under turbulent conditions, *In Turbulent Forced Convection in Channels and Bundles, Vol.2, pp.613-640, Hemisphere, New York,*
- [12] B.S. Shiralkar, P. Griffith, Deterioration in heat transfer to fluids at supercritical pressure and high heat fluxes, *Journal of heat transfer, Feb. 1969, pp.27-36*
- [13] V.A. Kurganov, V.B. Ankudinov, Calculation of normal and deterioration heat transfer in tubes with turbulent flow of liquids in the near-critical and vapour region of state, *Teploenergetika, Vol.32 (6), 1985, pp.53-57*

## II. Validation of Coupled Neutron Physics and Thermohydraulics Analysis for HPLWR

(C.H.M. Broeders, V. Sanchez, A. Travleyev, IRS; E. Stein, IKET)

### **Abstract**

The utilization of supercritical water pressure in the High Performance LWR (HPLWR) leads to a strong axial variation of the water density in the coolant channels of the fuel assemblies. The actual reference design based on work of Oka et. al. [1] contains in each fuel assembly a number of moderator rods to enhance the over-all mean water density and three radial and three axial zone enrichments for power flattening. This leads to a very complicated neutron physics behavior of the reactor. The validation of applied calculation procedures is mandatory for such new core concepts. In a first exploratory step validation with Monte Carlo simulations seems to be adequate. A specific feature of the actual HPLWR design is the strong feedback between the neutron physics and the thermohydraulics calculations. For the coupling with thermohydraulic codes deterministic multi-group neutron physics calculations are needed. In the following in a first step two- and three-dimensional models for Monte Carlo calculations with MCNP are developed. Comparisons of different MCNP models give confidence in the results and show some sensitivities, e.g. with respect to the treatment of the isolation wrappers around the moderator rods. The second step involves the development of a super-cell model for the fuel assembly for deterministic multi-group calculations. Here the comparison with the results of Monte Carlo calculations with MCNP shows the applicability of the super-cell model. Finally, on the basis of this super-cell model a coupling with the thermohydraulic code RELAP5 is realized. First results from the coupled calculations are given.

### **Zusammenfassung**

Die Nutzung von Wasser mit superkritischem Druck im "High Performance LWR" (HPLWR) führt zu starken Änderungen in der axialen Verteilung der Kühlmitteldichte. Der aktuelle Referenzentwurf (basierend auf Arbeiten von Oka et.al. [1]) enthält Moderatorröhren um die mittlere Wasserdichte zu erhöhen und drei radiale und drei axiale Anreicherungsstufen des Brennstoffs um besseren Leistungsverteilungen zu erreichen. Dies führt zu einem sehr komplizierten neutronenphysikalischen Verhalten

des Reaktors und die angewandten Rechenverfahren müssen für diese Anwendung validiert werden. In dem jetzigen Stadium der Untersuchungen sind Monte Carlo Verfahren dazu gut geeignet. Eine zusätzliche Komplikation liefert die starke Rückkopplung zwischen den thermohydraulischen und neutronenphysikalischen Rechnungen. Für diese Kopplung sind deterministische Multi-Gruppen Reaktor Rechnungen erforderlich. Im folgenden werden in einem ersten Schritt zwei- und dreidimensionale Modelle für Monte Carlo Rechnungen mit MCNP entwickelt. Der Vergleich von Ergebnisse mit verschiedenen MCNP Modellen zeigt dabei gute Übereinstimmung und deckt einigen Sensitivitäten auf, wie z.B. den Einfluss der Behandlung der thermischen Isolierung um die Moderatorröhren. Der zweite Schritt befasst sich mit der Entwicklung eines Super-Zelle Modells für das Brennelement für die deterministischen Multi-Gruppen Rechnungen. Hier zeigt der Vergleich mit Monte Carlo Rechnungen die Anwendbarkeit des entwickelten Modells. Die Kopplung dieses Super-Zelle Modells für Neutronik Rechnungen mit dem Code RELAP5 für Thermo-hydraulik Rechnungen wurde realisiert. Erste Ergebnisse dieser gekoppelten Rechnungen werden zum Schluss präsentiert.

## **1. Introduction**

The utilization of supercritical water pressure in the High Performance LWR (HPLWR) under consideration in the 5 Framework Program of the EC leads to a strong axial variation of the water density in the fuel assemblies. The actual reference design based on work of Oka et. al. [1] contains in each fuel assembly a number of moderator rods to enhance the over-all mean water density and three radial and three axial zone enrichments for power flattening. Together with the strong axial density variation, this leads to a very complicated neutron physics behavior of the reactor. The validation of applied calculation procedures is mandatory for such new reactor concepts. Although experimental validation will be required for a final design, in an intermediate step validation with Monte Carlo simulations seems to be a good approach. Modern Monte Carlo procedures like MCNP are very powerful for the description of complicated nuclear reactor systems. Important drawbacks are still the required large computing times and the lack of continuous temperature variations of the fuel. Moreover, the utilization of the supercritical water pressure leads to a very strong feedback between neutron physics and thermohydraulics behavior, making

coupled calculations mandatory. For this purpose models with comparable levels of discretization for neutronics and thermohydraulics calculations have to be selected. In the present note the thermohydraulic calculations are based on a complete reactor system with one core channel with 20 axial nodes. For this model neutronics calculations for one fuel assembly in an infinite array are adequate. Multichannel thermohydraulic core calculations are planned and need full core neutronic calculations. In the second section of the present note the validation of a simplified fuel assembly model is described. The work starts with a slice model of the fuel assembly as defined for the HPLWR benchmark investigations [3]. Complimentary to the 30° model of VTT, Finland, at FZK full two-dimensional MCNP models were developed and compared. After validation, the simplest full 2-D model could be extended to three dimensions. These MCNP models are the basis for the qualification of simplified geometrical models for deterministic multi-group calculations with the code system KAPROS/KARBUS, described in the third section. In the fourth section the automatic coupling of the validated simplified deterministic calculation procedures of KAPROS/KARBUS with thermodynamics calculations with the code RELAP5 are described.

## **2. Model description for the MCNP calculations**

The geometry of the current model is based on data supplied in [2]. There are four different materials used in the model - fuel, Ni-based alloy, stainless steel and water. Fuel is uranium dioxide with oxygen-uranium ratio equal to 1,98. According to [1], the fuel enrichment is profiled in radial and axial direction and, therefore, fuel is represented by nine material compositions (three radial and three axial regions), which differ only for the U5/U8 ratio.

The water within the assembly is divided into three zones on the basis of its density and temperature behavior in axial direction: "moderator", "stagnant water" and "coolant". "Moderator" represents water inside water rods. The water in this region has almost constant axial density, equal to that of the inlet water. "Stagnant water" fills regions, surrounded by flower-shaped walls, i.e. this is a layer between hot "coolant" and cold "moderator". Water referred to as "coolant" is any other water except "stagnant water" and "moderator" within the assembly; mainly, this is water, which surrounds fuel pins. The density of the "coolant" changes very strongly with the

height. The space between assemblies has been also taken into account in the current model. This space has been filled with the "coolant".

### 2.1 Creation of MCNP models for HPLWR fuel assembly slices

In a first approach a MCNP model for HPLWR fuel assembly slices was developed with the help of a PERL script. This automatized procedure lead to a quite large input data set FZK-S. Subsequently an alternative specification method resulted in a more compact input data set FZK-T. A systematic comparison of the results of  $K_{\infty}$  calculations with these models is summarized in table 1.

Table 1.  $K_{\text{eff}}$ , obtained from different geometry models

Description	$K_{\text{eff}}$
VTT geometry ( $30^{\circ}$ )	1.1730 $\pm$ 0.0006
FZK-S model ( $360^{\circ}$ )	1.1783 $\pm$ 0.0005
FZK-T model ( $360^{\circ}$ )	1.1790 $\pm$ 0.0010
FZK-T-mod, same guide tube modeling as VTT	1.1737 $\pm$ 0.0006

We may observe good agreement between the FZK-S and FZK-T model. The comparison of FZK-T, FZK-T-mod and VTT shows that the exact treatment of the guide tubes in the moderator rods leads to  $\approx 0.5\%$  difference in  $K_{\text{eff}}$ . The agreement between FZK-T-mod and VTT is good.

### 2.2 Creation of three-dimensional MCNP models for a HPLWR fuel assembly

In order to specify accurately the axial water density distribution, all water zones, mentioned above, are divided into several axial planes. To simplify this splitting, some auxiliary code was developed. This code uses a manually created input MCNP "template" file that contains two-dimensional description of the assembly, and an additional file, which contains information about the axial subdivision, and produces a 3-D input model for MCNP. This procedure allows preparing automatically an MCNP input file and enables the specification of different fuel enrichments in the assembly. An initial guess for the "coolant" and "moderator" densities and temperatures was obtained in [5] with the RELAP5 code with the assumption of a cosine axial heat distribution and full thermal isolation between "coolant" and "moderator". Properties of

"stagnant water" were taken to be similar to "coolant" in the first case, or to "moderator" temperature and densities in the second case.

In order to apply the density and temperature data obtained from RELAP5, the fuel assembly is divided into 20 axial subregions.

The temperature for each cell is approximated by the application of data libraries with different temperatures, evaluated by VTT and by appropriate "TMP" input cards for MCNP for thermal scattering. The data library, prepared at 600K was applied for Ni-based alloy, stainless steel and for water. For fuel the 1200K data were used. For more accurate modelling of thermal neutrons transport in water, the S(a,b) treatment for water was included into the calculations. The corresponding S(a,b) table, prepared at 600K also has been taken from VTT.

### **3. Axial power distribution calculation with MCNP**

On the basis of the 3-D model of the HPLWR fuel assembly, the axial power distribution due to fissions was obtained with MCNP. These calculations were performed for two assumptions for the "stagnant water" density and temperature:

- Equal to properties of "coolant" water,
- Equal to properties of "moderator" water.

The intermediate and final results for both cases (stagnant as coolant and stagnant as moderator) are presented in figure1.

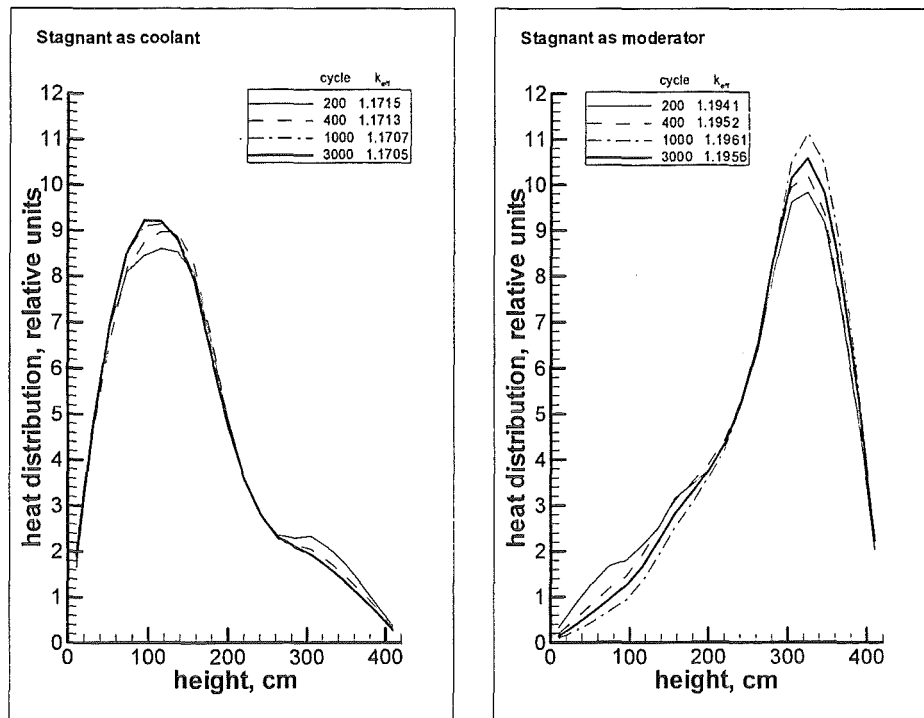


Fig. 1 Comparison of axial power shapes in a HPLWR fuel assembly for different treatments of the stagnant water. The evaluation of the results for  $K_{\infty}$  and the power shape for increasing number of neutron cycles is also shown.

One can observe a big difference in the axial power distribution depending on the treatment of the stagnant water (despite the fact, that stagnant water only represents 17% of the water in the assembly horizontal cross section). Therefore, for accurate calculations of axial power distributions one should supply the water densities for stagnant water also. On the other hand it has to be noted that the current calculations are based on a thermo-hydraulic model with full isolation between moderator and coolant, which, of course, is not the case for a real system.

#### 4. Development of HPLWR fuel assembly models for deterministic calculations

Based on the experiences for tight lattice LWR investigations in reference [4] a 1-dim. super-cell model for the complicated HPLWR fuel assembly was developed. This model consists of a moderator rod and its surroundings. In the radial direction the model has four zones: moderator, rod, isolation wrapper with stagnant water and an equivalent fuel zone. The radius of this fuel zone is determined by the volume of the fuel cells per moderator rod and the inter subassembly space. The mean cross sections in the fuel are determined from appropriate cell calculations. Using reflective boundary conditions for bottom and top of this model one can perform 1-dim. calcu-

lations for fuel assembly slices. Extension to a 2-dim. (R-Z) model easily can be done by the introduction of axial zones and modified boundary conditions on bottom and top. In a first step validation calculations were performed for benchmark specifications for fuel assembly slices from reference [3]. Here good agreement could be observed for the comparison of the deterministic benchmark solutions of FZK and of the solutions of other participants with MCNP, see figure 2.

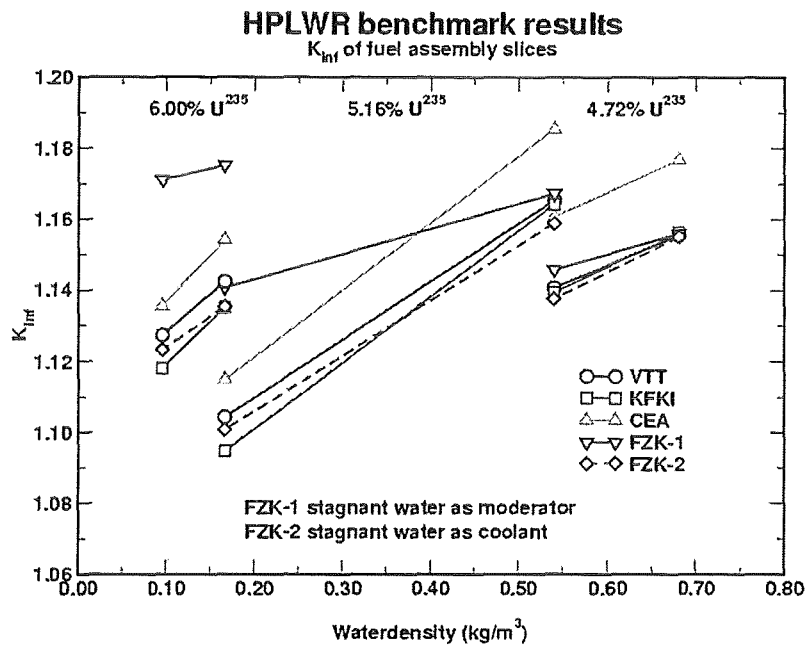


Fig. 2: Comparison of  $K_{\infty}$  values for HPLWR fuel assembly slices from FZK super-cell calculations with Monte Carlo results from VTT, Finland, and FFKI, Hungary. The difference between FZK-1 and FZK-2 is only the treatment of the isolation wrapper. Fuel enrichment and water density are varied corresponding to benchmark specifications by CEA.

The differences between the FZK-1 and FZK-2 results are remarkable. Obviously, the observations in section 3 that the treatment of the isolation wrapper has strong influence are confirmed.

After these encouraging results for slice calculations, the deterministic super-cell model was applied for a full height fuel assembly with the same material and geometry specifications as for the Monte Carlo calculations of section 3. The same fuel temperatures and water densities were applied. For the radial fuel enrichments a mean values is used. The comparison of the results of Monte Carlo MCNP and deterministic TWODANT calculations is shown in figure 3.

Arbitrary units for the power are used. The mean slice data is normalized to the same maximum value 1. Very good agreement may be observed.

### Comparison of Axial Power Distributions in HPLWR

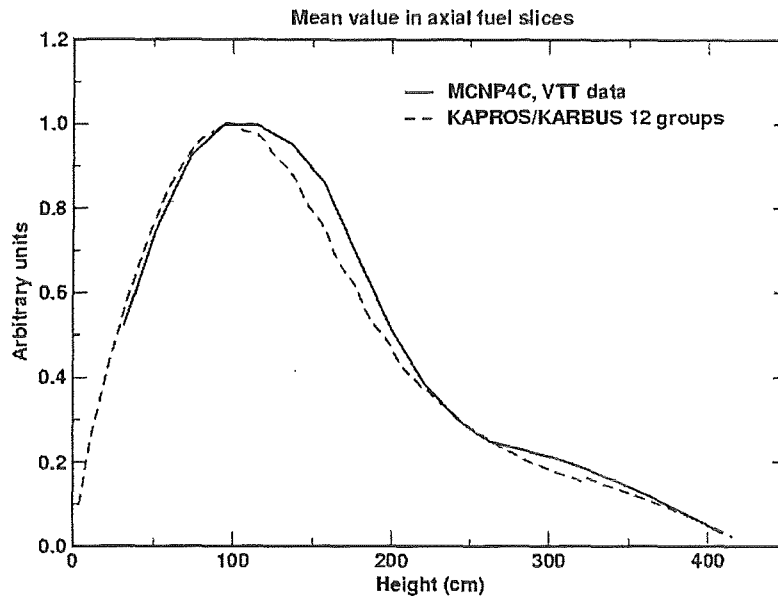


Fig.3: Comparison of axial power distributions in a HPLWR fuel assembly. MCNP4C results are obtained with temperature dependent data libraries from VTT, Finland. KAPROS/KARBUS results are obtained with TWODANT super-cell calculations with 12 energy groups from a library generated with COLLIB [5].

## 5. Coupling of KAPROS/KARBUS with RELAP5

A specific feature of the actual HPLWR design is the strong feedback between the neutron physics and the thermohydraulics calculations, making the coupling of these calculations mandatory. As a first step for coupled neutronics and thermohydraulic investigations, the super-cell model in the KAPROS/KARBUS code is coupled with the thermohydraulic system code RELAP5, being improved for HPLWR applications, see reference [5]. The RELAP5 input model describes the whole reactor system, including a one-channel representation for the core. In this case the fuel assembly model for the neutron physics calculations seems to be adequate.

The coupled calculations start with a cosine shape estimate for the power distribution in 20 axial zones in the RELAP5 core model. The resulting axial distributions of the fuel and coolant densities and of the fuel, clad and coolant temperatures in these 20 zones of the model are extracted from the RELAP5 output and processed to input for the KAPROS/KARBUS cross section generation. These cross sections are used for the calculation of an axial power distribution in the super-cell fuel assembly model with the TWODANT code. The feedback of this new axial power distribution to the RELAP5 calculation may be repeated as many times as desired by input. The coupling of these codes RELAP5, KARBUS and TWODANT is organised within the

KAPROS system in a new procedure R5PROC. Using appropriate mixing of the new axial power distribution with the previous one (relaxation factor), this procedure proves to converge after 8 to 10 iterations. First preliminary results with a RELAP5 model with full isolation between moderator and coolant are shown in the figures 4 to 6. In figure 4 the criticality is given as a function of the number of iterations for 4, 12 and 69 energy groups. In figure 4 the criticality is given as a function of the number of iterations for 4, 12 and 69 energy groups.

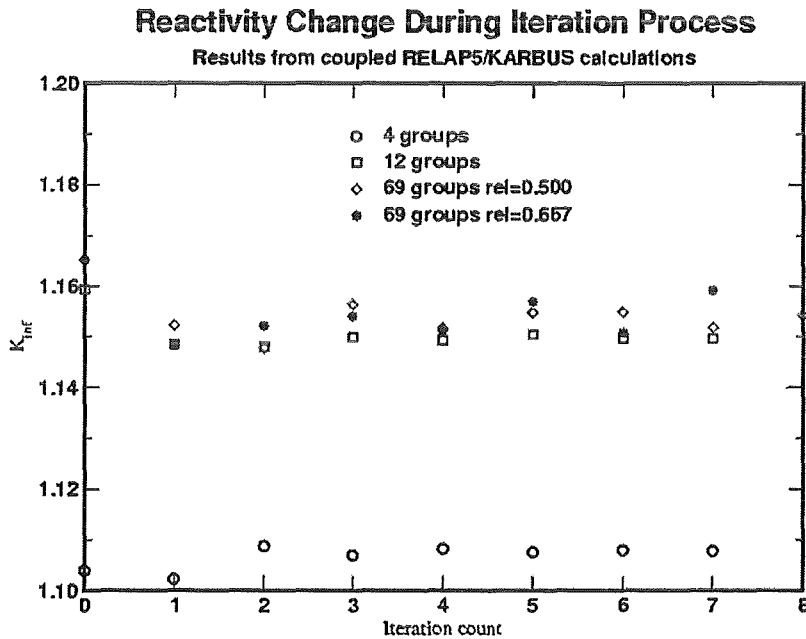


Fig. 4: Reactivity changes during iteration steps for coupled RELAP5/KARBUS calculations with different number of energy groups. The relaxation factors were rel=0.667 for 4, 12 and 69 groups and in addition rel=0.5 for 69 groups

The calculations with 69 groups proved to be sensitive to the relaxation factor. In the case of rel=0.667 no convergence for the criticality is observed. For rel=0.5 the criticality converges and satisfactory agreement may be observed with the 12 group solution. The 4 group results show good convergence behavior, but the deviation from 69 groups is not acceptable. In figures 5 and 6 the axial water density and the mean fuel temperature after 8 iterations are shown for the same energy group cases as in figure 4.

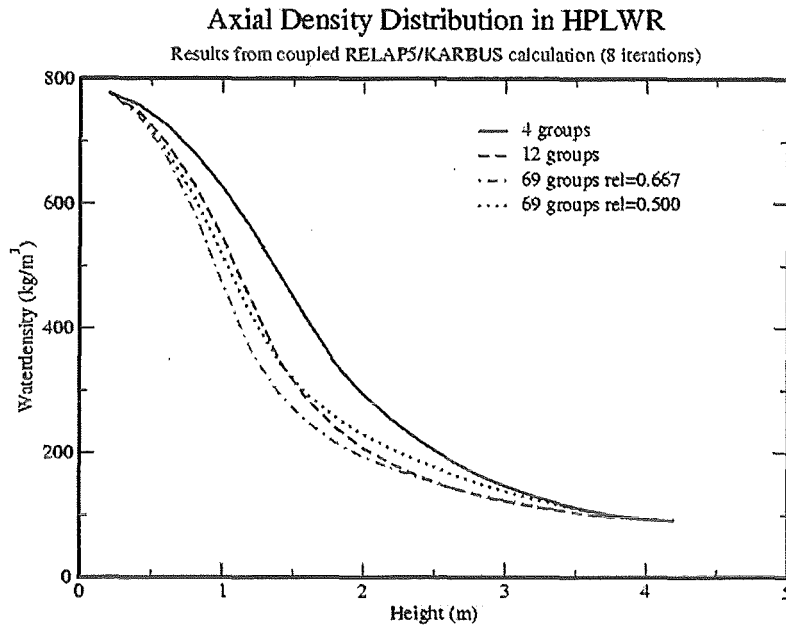


Fig. 5: Axial distributions of the water density after 8 iteration steps of coupled RELAP5/KARBUS calculations. The same cases are plotted as in figure 4.

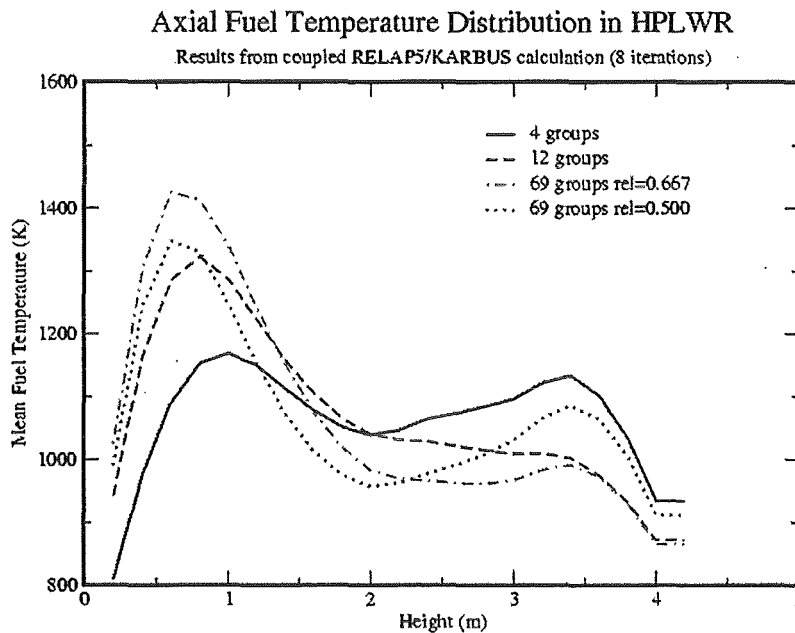


Fig.6: Axial distributions of the mean fuel temperature after 8 iteration steps of coupled RELAP5/KARBUS calculations. The same cases are plotted as in figure 4.

We may observe good agreement for the water density for the 12 and 69 group,  $rel=0.5$ , solutions. The mean fuel temperature behaves quite sensitive.

These first results of coupled calculations show the sensitivity of the coupling for the actual HPLWR reference design. Also the modelling of design details like isolation wrappers and stagnant water must be considered carefully.

## 6. References

- [1] K. Dobashi, Y. Oka, S. Koshizuka, "Conceptual design of a high temperature power reactor cooled and moderated by supercritical light water", 6th International Conference on Nuclear Engineering may 10-15, 1998
- [2] "VTT's contribution to the HPLWR neutronics studies". Paper presented in the HPLWR project meeting at PSI on august 27-30, 2001
- [3] G. Rimpault, P. Dumaz, "HPLWR WP2 tentative work programme", Private communication (2001)
- [4] C.H.M. Broeders, „Entwicklungsarbeiten für die neutronenphysikalische Auslegung von Fortschrittlichen Druckwasserreaktoren (FDWR) mit kompakten Dreiecksgittern in hexagonalen Brennelementen“, KfK 5072 (1992)
- [5] V. Sanchez-Espinoza, D. Struwe, "RELAP5 investigations for the HPLWR - evaluation of the code capabilities", Third HPLWR project meeting at PSI-Würenlingen, Switzerland. August 27-30, 2001.
- [6] C.H.M. Broeders, R. Dagan, "Generation of coarse group libraries with the KAPROS procedure COLLIB", this volume

III. Water Chemistry of BWR's, PWR's and Supercritical Fossil Fuel Power Plants

(J. Konys, K. Ehrlich, S. Leistikow, IMF)

**Abstract**

Within the EU-funded HPLWR project, the feasibility of a new reactor design, cooled with supercritical water, has to be evaluated. Based on Prof. Oka's ideas, new concepts for the core of such a reactor, including the fuel elements and for the peripheral parts (turbines etc.) have to be considered and compared regarding their technical relevance.

One of the major issues for the realization of a HPLWR is the availability of appropriate in- and ex-core materials. Besides the mechanical and irradiation properties of potential materials like steels, the corrosion behavior under supercritical conditions is of key interest. Learning from the operation of existing BWR's and PWR's, the water chemistry of the cooling circuit has a great influence on the corrosivity of the coolant. Due to the lack of experimental data of supercritical operated power plants, only an outlook regarding the possible operational windows for the major parameters can be given.

**Zusammenfassung**

Innerhalb des von der EU geförderten HPLWR-Projekts soll die Machbarkeit dieses neuen Reaktordesigns nachgewiesen werden. Ausgehend von den ursprünglichen Ideen von Prof. Oka sollen neue Konzepte für den Reaktorkern, die Brennelemente bzw. für die externen Bereiche wie Turbinen erarbeitet und auf ihre technische Relevanz hin überprüft werden.

Einer der kritischsten Punkte bei der Realisierung eines HPLWR ist die Verfügbarkeit geeigneter in- bzw. ex-core Werkstoffe. Neben den mechanischen bzw. den Bestrahlungseigenschaften potentieller Werkstoffe wie Stähle ist das Korrosionsverhalten unter überkritischen Bedingungen von entscheidender Bedeutung. Aus dem Betrieb bestehender BWR- bzw. PWR-Reaktoren hat man gelernt, dass die Wasserchemie des Kühlkreislaufs sehr großen Einfluss auf das Korrosionsverhalten der verwendeten Materialien besitzt. Da aber zur Zeit nur wenige belastbare Daten von überkritisch betriebenen Reaktoren vorliegen, kann nur ein Ausblick auf die Wasserchemie eines zukünftigen HPLWR's gegeben werden.

## **1. Introduction**

Feedwater for BWR, PWR and once-through cycles of future HPLWR's must meet specific quality requirements, both to ensure a safe and economic operation. If the water/steam is circulated in a closed cycle (PWR, HPLWR), the quality of circulating water and steam must be suitable for all components in the water/steam cycle. This leads to more strict specifications than the individual plant components would demand.

The purpose of a controlled water chemistry in a water/steam cycle of a water-cooled Nuclear Reactor is:

- The minimization of corrosion of structural materials
- To avoid deposits within the water/steam cycle
- To minimize the mass transport of corrosion products within the water/steam cycle

Besides the basic principles of power plant chemistry to reach the objectives, like using demineralized water, limiting the ingress of impurities to the water/steam cycle and controlling the pH-value, the different reactor concepts require a special adapted water chemistry to ensure a safe operation [1, 2].

### **1.1 Formation of protective oxide layers**

The oxidation is controlled by the steel composition, as reviewed earlier in HPLWR IV reports, and by the temperature. The corrosion attack of water/steam/fluid is leading to the formation of iron oxides. The corrosion rate is limited by the formation of a superficial protective uniform oxide layer. The only natural oxide that can exist in direct contact is magnetite. The basic chemical reaction between steel and water leads to iron dissolution within several reaction stages: redox from Fe(II) to Fe(III) and condensation stages (Schikorr reaction), leading to the formation of magnetite. Based on these interactions, water/steam cycles in power plants can be divided into two areas:

- the temperature range up to 200°C Schikorr reaction assures that the steel surface in contact with water remains active in respect of iron dissolution and
- the hot water area above 200°C, where magnetite protective layer forms spontaneously.

## 1.2 Mass transport of corrosion products

Due to the decrease of solubility with temperature of iron in hot water, magnetite tends to precipitate out from aqueous solutions above 200°C. This can lead to dramatic reductions in cross-sections and in a distinct change of heat transfer conditions of steam generating tubing.

Other undissolved corrosion products will be carried along the water/steam cycle and can be deposited on thermally high stressed tube walls like boilers. This can have a detrimental effect on the stability of such components. On the one hand, the formation of thermally insulating layers can lead to an increase in temperature and thereby to a reduction in mechanical strength due to overheating. On the other hand, under deposits, dissolved electrolytes can be enriched, hence initiating a chemical attack on both, the metallic tube material and the protective layer.

## 1.3 Impurities

Impurities in water/steam have to be strictly controlled because they can cause corrosion and deposits on components of a water/steam cycle (table 1). Looking at these values from Garzarolli [3] with the levels for “normal operation condition” given in the 1996 revision of VGB\_R 401 J [2] it is obvious, that the newer VGB-values are more on the conservative side, with narrower ranges of variation, especially for the feedwater, compared to the reactor water.

In view of the inhibiting effect of **oxygen** on steel in demineralized water/steam, special care has to be taken on the concentration by means of different “*oxygen chemistries*”. However, if the specified conductivity for demineralized water ( $< 0.2 \mu\text{S}/\text{cm}$ ) is exceeded due to system leakages, it is necessary to stay at a lower oxygen level of about 0.02 mg/l for a short period of time.

**Iron and copper** concentrations in the water/steam are an indicator of the efficiency of conditioning. Their values give information about the corrosion/deposition processes in the water/steam cycle, respectively in the boiler and turbine. Both levels should therefore be maintained in the wppb-range.

**Silica** concentrations in once-through boilers may not exceed certain values due to the specification for turbine operation. When operating with fully demineralized water, the silica content will be far below the specified level. Some problems can arise when colloidal silica is present in the feed water and was thereby not retained during the water treatment processes.

Reactor type	pH	Conductivity μS/cm	Li wppm	B wppm	H wppm	O wppb	Fe wppb	Cu wppb	Solids wppb
BWR	5.5	0.1-0.3	-	-	0.025	200	0.5-10	0.1-1	1-10
PWR	6.9- 7.3	*	1-2	0- 1500	2-4	<1	1-10	-	1-10

\*: Depending on B (and Li) concentration

**Table 1:** Water chemistry in BWR's and PWR's (normal condition) after Garzarolli et.al. [3]

## 2. Water chemistry in BWR, PWR and HPLWR

**BWR's** have an open cycle, operate at system pressures of 70 bars at typical temperatures of 285°C and form steam in the core. The water is separated from the steam within the pressure vessel and the steam is taken directly to the turbine and to the condenser. Due to the corrosion of structural components, about 10-100 kg of crud are deposited on the fuel elements per full power year. These deposits contain mainly iron and in some plants copper, too.

Another important aspect of BWR's is the water radiolysis in the core, which leads to oxygen concentrations of 200 to 300 wppb in the water and 20 to 30 wppm in the steam. The corrosion potential at an oxygen level of 200 wppb lies in the range of -0.4 and 0 V (SHE). In some BWR's, hydrogen is added to reduce the oxygen content in the feedwater (HWC). However, the radiolytic oxygen in the core cannot be suppressed by such hydrogen addition. Under such conditions, the hydrogen becomes stripped off from the water to the steam phase. The normal water chemistry is called NWC, whereas the hydrogen modified one is termed HWC.

**PWR's** have a closed cycle. The water is pressurized up to about 150 bars and is circulating through a steam generator and back to the core. The core entrance temperatures range from 280 to 295°C and reach values between 300 to 340°C at the exit of the core. The water chemistry is controlled by additives (see table 1). Boric acid is added for controlling the reactivity and hydrogen for suppressing the formation of radiolytic oxygen. Numerical considerations have shown, that hydrogen concentrations above 0.5 wppm are enough to control the radiolytic oxygen. As a consequence, hydrogen is kept usually between 2 to 4 wppm. To maintain the pH at an appropriate level, lithium as LiOH, is added in the wppm-range.

No data for water chemistry are available for HPLWR's because this reactor type is at a conceptual level at the moment. Nevertheless, experiences from BWR, PWR and SCFPP can be used when discussing the special conditions of water chemistry for HPLWR's. Due to the fact that in a HPLWR, the coolant water remains in a single-phase condition (water → steam → supercritical water) along the whole once-through cycle, a control of the oxygen by adding of hydrogen, like in the PWR's, seems to be very likely. Therefore it is obvious, that the water chemistry of *Supercritical Fossil Power Plants* could equally be used to define specific conditions for a HPLWR (see table 2). In this case, a strong support from the reactor industry and utilities that have extensive experience is required.

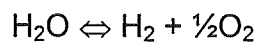
Process type	Boiler Water [5]	Boiler Water [4] (normal operation values)
<b>POWER GENERATING UNIT</b>		
Turbine inlet pressure, MPa	19.7	13.6 for alkalizing conditions
Water Chemistry type	Hydrazine-ammonia (NH <sub>3</sub> /N <sub>2</sub> H <sub>4</sub> )	Hydrazine-ammonia (NH <sub>3</sub> /N <sub>2</sub> H <sub>4</sub> )
<b>FEEDWATER</b>		
Electric conductivity μS/cm - cation	< 0.2	0.1
Composition, wppb		
total Fe		10
total Cu		1
Silica		5
Na		2
Oxygen		< 100
pH	9.2 - 9.6	9 - 10
<b>BOILER WATER</b>		
Electric conductivity, μS/cm - cation	1.0	< 50

<b>pH</b>		9.5 - 10
<b>Composition, wppb</b>		
Na	300	2
Chlorides	111	-
Silicides	52	-
Hydrazine	-	-
Sulfates	14	-
Phosphates	-	-
total Fe	-	10
total Cu	-	1
Silica	-	5
<b>SATURATED STEAM: STEAM DOWNSTREAM OF THE REHEATER</b>		
<b>Electric conductivity, <math>\mu\text{S}/\text{cm}</math></b>		
- cation	< 0.15	0.1
<b>Composition, wppb</b>		
Na	< 3	2
Chlorides	< 3	-
Silicides	< 10	-
Sulfates	< 3	-
Total organic concentration	< 100	-
Silica	-	5
total Fe	-	5
total Cu	-	1

**Table 2:** Main water chemistry characteristics of fossil fuel power generating units

Regarding the radiolysis of supercritical cores, no data are available. Nevertheless, some statements concerning the expected conditions can be made:

- The production rate of oxygen in the core is independent of temperature and pressure and only depending on the radiation dose
- The transport properties of the produced oxygen in the supercritical water are depending on temperature and pressure
- Due to the change from sub- to supercritical in the core, physical properties of the water like the density are changing. This will influence the flow parameters of the dissolved oxygen, but not the concentration in the water.
- The oxygen concentration in the water phase of a BWR (200-300 wppb) can be considered as the "base level" for the content of radiolytic oxygen. For the conditions of a HPLWR these values are seen as the upper limit, because a) an increase of the pressure from 70 to 250 bar will suppress the decomposition of water and will therefore shift the



equilibrium more to the left side of this equation and b) the possibility of adding hydrogen (like for PWR's) will furthermore control the radiolytic oxygen on a low level.

### **3. Corrosion related to water chemistry**

The corrosion of structural materials in supercritical water is extensively investigated in high-oxygenated water in the frame of the research for the Supercritical Water Oxidation Process (SCWO). Although the conditions in a future HPLWR are different regarding the oxygen content, some principal issues are maybe of general validity.

For materials like steels and nickel-based alloys the principal corrosion rate as a function of pressure and temperature is as shown in figure 1.

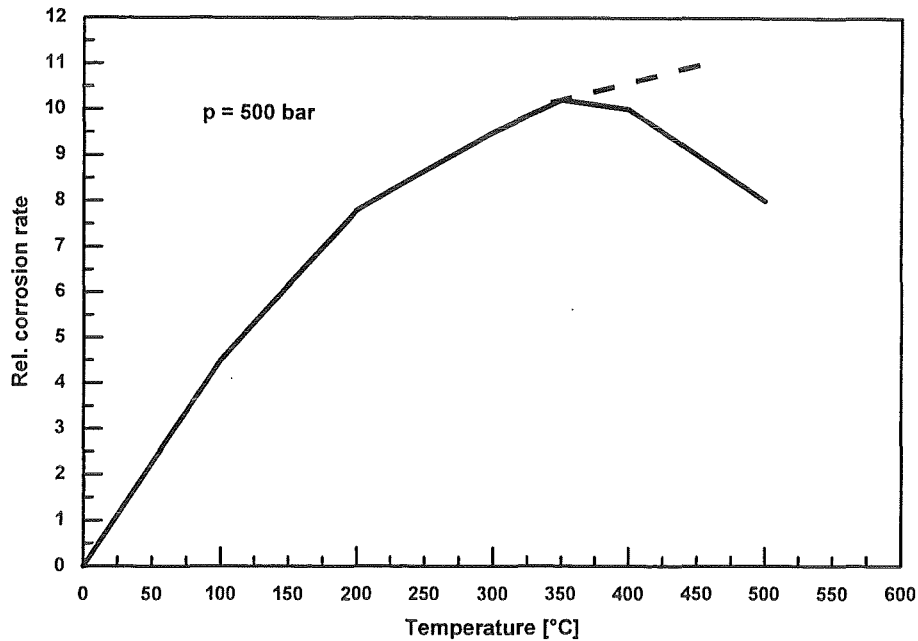


**Figure 1:** Relative corrosion rate of alloys in high-oxygen/chloride water at 500 bars (oxygen is in great excess)

It is obvious, that the corrosion rate is higher in the sub- than in the supercritical range. The maximum of the curve is a result of a) the increase of the corrosion rate with temperature (Arrhenius-type) and b) the decrease of the dissociation constant and the density of water with temperature ( $c_{H^+}$  becomes lower). Whether the maximum of the corrosion rate around the critical point of water (ca. 374°C) is typical for very low-oxygen water or the increase of the corrosion rate far into the supercritical range, as indicated by the dashed line in figure 1, is true, has to be validated by further investigations. For a conservative assessment of the corrosion rate, it is therefore agreed to rely on existing subcritical data.

Experimental data of Boyd et.al. [6] on the corrosion of different materials in low-oxygen, demineralized supercritical water (see table 3) supported the corrosion behavior, expressed by the dashed line in figure 1.

Materials	Rate constant at 426°C mg/dm <sup>2</sup> ·d	Rate constant at 537°C mg/dm <sup>2</sup> ·d	Rate constant at 732°C mg/dm <sup>2</sup> ·d
SS 410	0.05	0.1	1.2
AMS 5616	0.2	0.3	0.39
SS 302	0.1	0.66	4.7
SS 347	0.01	0.26	9.83
SS 309	0.073	0.29	0.83
SS 310	0.11	0.17	0.87
Armco 17-4 PH	0.1	-	0.3
Armco 17-7 PH	0.033	0.067	0.48
Allegheny A-286	0.07	0.18	9.3
Inconel X	0.011	0.97	6.7
Hastelloy F	0.011	0.22	0.39
Hastelloy X	0.024	0.31	1.8

**Table 3:** Corrosion rate in supercritical water at 344 bar after [6]

It seems that with low-oxygen/chloride containing water, the corrosion rate increases beyond 400°C, which is in contrary to high-oxygen/chloride water, as shown by the maximum of the rate in figure 1. Further experiments have to prove, if the corrosion of potential alloys like steels is increasing when changing from subcritical water/steam to supercritical conditions.

#### 4. References

- [1] VGB-Richtlinie für das Wasser in Kernkraftwerken mit Leichtwasserreaktoren, VGB-R 401 J, 2<sup>nd</sup> edition 1985, Verlag technisch-wissenschaftlicher Schriften, Essen, Germany
- [2] Revision der VGB-Richtlinie für das Wasser in Kernkraftwerken mit Leichtwasserreaktoren (VGB-R 401 J), VGB Kraftwerkstechnik 76 (1996), Heft 3

- [3] F. Garzarolli, R. Holzer, Waterside corrosion performance of light water power reactor fuel, Nucl. Energy 31, No. 1 (1992) 65
- [4] VGB Guidelines for boiler feedwater, boiler water and steam of steam generators with a permissible operating pressure > 68 bar, VGB-R 450 Le, edition 1995, Verlag technisch-wissenschaftlicher Schriften, Essen, Germany
- [5] EPRI target values: Thermal Engineering Vol 4777 pp 606- 611, ME Shitsman: EPRI TR-105041, 1996.
- [6] W. K. Boyd, H. A. Pray, Corrosion of stainless steels in supercritical water, Corrosion NACE, Vol. 13 (1957) 375

#### IV. Untersuchungen an Strukturmaterialien der Kerntechnik

(M. Schirra, P. Graf, A. Falkenstein, S. Heger, E. Materna-Morris, IMF I;  
L. Heikinheimo, GW)

##### **Abstract**

This title comprises several research activities. The test program creep behaviour of the austenitic steel 316-L(N) on low stress level at 550° and 600°C was finished (85 000 hrs) and documented. In an EU-study contract for a High-Performance Light Water Reactor the mechanical and corrosion long-term behaviour of martensitic and austenitic steels and Ni-base alloys was evaluated as potential structure material. Characterisation of ADS-alloys (EUROFER + <sup>10</sup>Bor) and irradiation conditions in different ADS-irradiation arrangements (SPIRE-program).

##### **Zusammenfassung**

In diesem Arbeitsgebiet sind mehrere Aktivitäten zusammengefasst: Das Untersuchungsprogramm zum Kriechverhalten des martensitischen Stahles 316-L (N) bei 550° und 600°C im auslegungsrelevanten Spannungsbereich wurde bei 8500 h beendet und dokumentiert. Für die EU-Studie zu einem fortgeschrittenen Leichtwasserreaktor (HPLWR) wurde das Potential von martensitischen und austenitischen Stählen und Ni-Basis-Legierungen bezüglich der mechanischen Langzeiteigenschaften und des Korrosionsverhaltens bewertet. Charakterisierung von ADS-Legierungen (EUROFER + <sup>10</sup>B) und Bestrahlungsbedingungen in Bestrahlungseinsätzen von verschiedenen ADS-Anordnungen (SPIRE-Programm).

##### **1. Langzeitkriechversuche am Strukturwerkstoff 316 L(N)**

Im vorangegangenen Jahresbericht '99 (FZKA 6480) ist über das Versuchsprogramm bis zum Stand 70 000 h ausführlich berichtet worden. In der Zwischenzeit sind die Versuche bis 85 000 h weitergeführt und qualifiziert abgeschlossen worden. Die Versuchsergebnisse sind im FZKA 6699 (Febr. 2002) zusammengestellt. Wesentliches Ergebnis ist, dass im auslegungsrelevanten niedrigen Spannungsbereich < 150 MPa bei 550° und 600°C sich die deutliche Änderung in der Spannungsabhängigkeit der minimalen Kriechgeschwindigkeit zur nichtkonservativen Seite bestätigt hat, die im FZKA 6480 noch als vorläufig dargestellt wurde (Bild 1). Auch für die technisch wichtigen Dehngrenzen (0,01-1%) liegt im unteren Spannungsbereich

eine geänderte Spannungsabhängigkeit vor. Die wesentliche Ursache ist, dass alle bisher durchgeführten Versuche (auch weltweit) sich aus versuchstechnischen Gründen bei Spannungen  $> 150$  MPa durchgeführt wurden. D.h., diese Versuchsspannungen liegen oberhalb der Streckgrenze, bei Versuchsbeginn tritt eine plastische Verformung auf, und das Kriechverhalten bezieht sich auf einen Werkstoffzustand lösungsgeglüht und verformt. Die Langzeitkriechversuche bei  $\sigma < 150$  MPa dagegen erfassen das Verhalten des in der Praxis vorliegenden lösungsgeglühten Zustandes.

Ergänzend wird im FZKA 6699 [2] noch das Kriechverhalten von Versuchen mit ansteigender Spannung ( $2,5 \rightarrow 15$  MPa/t) im Vergleich zu den zuvor erwähnten Langzeitkriechversuchen mit konstanter Last beschrieben. Der Vergleich ergibt bei allen Spannungsniveaus bis 150 MPa, dass der Gesamtkriechbetrag bei stufenweiser Spannungserhöhung immer niedriger ist als bei Versuchen mit entsprechender konstanter Versuchsspannung von Anbeginn an.

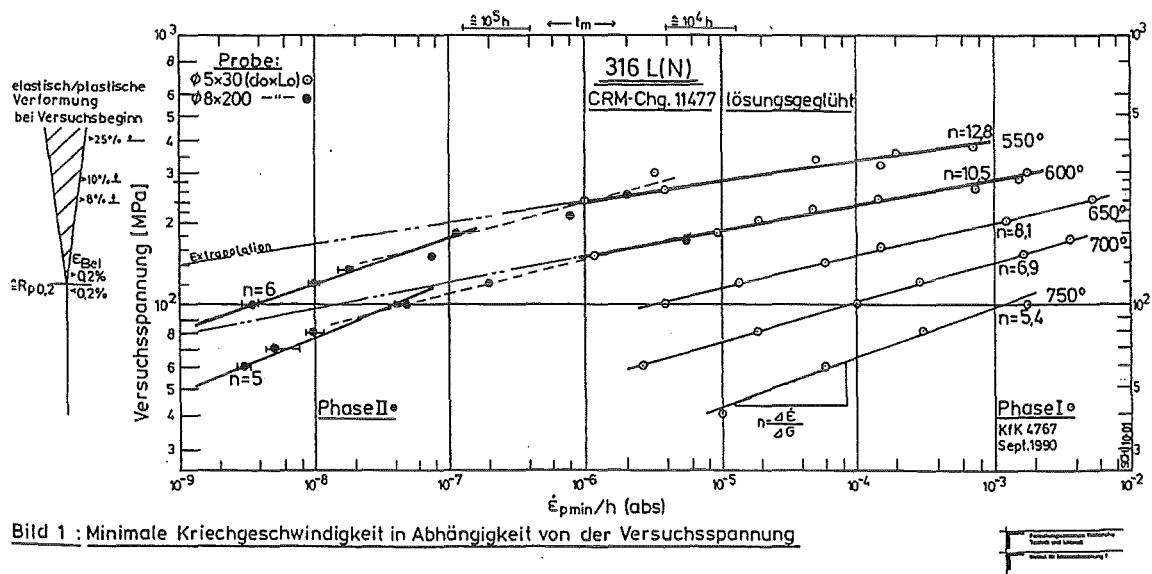


Bild 1 : Minimale Kriechgeschwindigkeit in Abhängigkeit von der Versuchsspannung

## Literatur:

[1] M. Schirra

"Long-term studies on the creep behaviour of the structure material 316 L (N) in the low stress range at 550 and 500°C".

9<sup>th</sup> Int. Conf. on Creep and Fracture Engineering Materials, Swansea, 1.-6. April 2001

[2] M. Schirra, A. Falkenstein, S. Heger

"Experimentelle Ergebnisse zum Kriechverhalten des Strukturwerkstoffes 316 L (N)-DIN 1.4909 im niedrigen Spannungsbereich bei 550° und 600°C (Abschlussbericht). FZKA 6699, Febr. 2002

## 2. HPLWR

Die im August 2000 begonnene EU-Studie über einen fortgeschrittenen Leichtwasserreaktor mit überkritischen Dampfparametern wurde im Rahmen einer Zusammenarbeit mit CEA-Saclay, VTT-Otaniemo und Framatome-Erlangen weitergeführt. Dabei wurden zunächst mit den Auslegern die zu erwartenden Betriebsdaten und Belastungsbedingungen für die In- und Ex-Core Komponenten festgelegt, wobei Anschluss an die bestehenden Kraftwerke mit überkritischen Dampfbedingungen gesucht werden sollte. Gegenwärtig werden in solchen Anlagen ferritisch-martensitische 9-12%Cr Stähle bis ca. 600°C verwendet und darüber hinaus sollen austenitische Stähle zum Einsatz kommen. Für eine Reihe von Werkstoffen die in solchen konventionellen Anlagen und zum Teil auch in Kernkraftwerken angewendet werden, wurden deshalb die mechanischen Langzeitdaten und das Korrosionsverhalten für den interessierenden Temperatur-Spannungsbereich zusammengestellt und ausgewertet und eine erste orientierende Aussage zu dem möglichen Einsatzbereich für die Gruppe der f/m-Stähle, der austenitischen Stähle und der Nickellegierungen unter vereinfachenden Annahmen gemacht. Des Weiteren wurden insbesondere die noch weitgehend offenen Fragen zum Verhalten dieser Werkstoffe unter dem gleichzeitigen Einfluss von Bestrahlung und dem überkritischem Kühlmittel Wasser auf hohem Spannungsniveau diskutiert. Die möglichen Auswirkungen auf Korrosion, Spannungsrisskorrosion und die mechanischen Eigenschaften bedürfen weiterer Erörterungen und in einer nächsten Phase der Studie der experimentellen Untersuchung. Die bisherigen Ergebnisse sind in einem internen Arbeitsbericht zusammengefasst [1].

### Literatur:

[1] K. Ehrlich, L. Heikinheimo, M. Schirra, S. Leistikow, J. Konys and P. Arnoux; HPLWR Annual Technical Report 2001, Work Package IV-Materials and Corrosion, FZK-Report Nuklear-3363, Oktober 2001

## **32.23     STUDIEN ZUR ACTINIDENUMWANDLUNG**

### **32.23.01 Neutronenphysikalische Untersuchungen zur Transmutation von Actiniden und Spaltprodukten**

Status und Weiterentwicklung des Inventarcodes KORIGEN, der Szenariocodes KORREC und SOLEQ sowie des Nachwärmecodes CALOR

(H.W. Wiese, IKET)

#### **1. Einleitung**

Zur quantitativen Analyse von Transmutationsszenarien hinsichtlich der Verbrennung von Pu und minoren Actiniden (Np, Am, Cm) bei Mehrfachzyklisierung dieser Elemente in thermischen und schnellen Reaktoren ist das Abbrand- und Zerfallsprogramm KORIGEN verfügbar. Eine Visualisierung der Ergebnisse kann mit dem Rechenprogramm KORMOT vorgenommen werden.

Die zur Reduzierung des langlebigen radioaktiven Abfalls aus dem Betrieb von Leistungsreaktoren ins Auge gefassten Transmutationsmaschinen einschließlich Beschleuniger getriebener, unterkritischer Anlagen erfordern eine frühzeitige Bewertung ihres Abfallreduktionspotenzials. Zu diesem Zweck wurden die Szenariocodes SOLEQ und KORREC entwickelt. Die Einsatzfähigkeit der genannten Rechenprogramme wurde in vorangegangenen Arbeiten demonstriert /1, 2, 3, 4/.

Das Rechenprogramm CALOR zur Bestimmung der Zerfallsleistungen von LWR-MOX-Brennstoffen erwuchs aus der Mitarbeit des Verfassers im Ausschuss „Zerfallsleistung“ des Deutschen Instituts für Normung, DIN.

#### **2. Abbrand- und Zerfallscode KORIGEN einschließlich Visualisierung von Ergebnissen mit KORMOT**

KORIGEN /5, 6/ wurde zur Erleichterung der Eingabeerstellung mit dem problemorientierten Eingabeprozessor POKI ausgerüstet. Mit diesem Preprozessor können interaktiv mit der Möglichkeit der sofortigen Korrektur bei von POKI erkannten Fehl-

eingaben für alle KORIGEN-Optionen Eingaben für Inventarrechnungen erstellt werden. Die bisher für gelegentliche Benutzer oft schwierige Wahl der zum Problem passenden Wirkungsquerschnittssätze wird durch ein vorsortiertes Angebot erleichtert.

Beim Starten von KORIGEN mit einer vorhandenen, eventuell modifizierten Eingabe besorgt POKI das Anhängen der Wirkungsquerschnittssätze.

Mit dem von D. Woll entwickelten Programm KORMOT (Korigen Motion) /7, 8/ wird ein visueller Überblick über KORIGEN-Ergebnisse in Form statischer Kurven, z.B. des Plutoniumaufbaus im LWR als Funktion der Standzeit des Brennstoffs im Reaktor, oder in Form von sich mit der Zerfallszeit ändernden Balkendiagrammen und Nuklidkartenausschnitten ermöglicht (Film).

Das in KORMOT enthaltene KORINT ermöglicht die Erstellung von KORIGEN-Eingaben für einfache, orientierende Anwendungen. Es steht jedoch auch der POKI-KORIGEN-Pfad für detaillierte Eingaben zur Verfügung.

### **3. Szenariocodes KORREC**

KORREC und SOLEQ analysieren die Massenströme in Parks gekoppelter Leistungs- und Brennerreaktoren und ermitteln die ins Endlager gehenden, akkumulierenden Abfälle, insbesondere ihre Radiotoxizität im Vergleich zu einem äquivalenten Park von Leistungsreaktoren mit direkter Abfall-Endlagerung.

KORREC (KORIGEN for RECycling) startet mit einem Park von Leistungsreaktoren (LWR), in welchem sukzessive bis zum Erreichen des Gleichgewichts zwischen Abfall erzeugenden und Abfall vernichtenden Reaktoren unter Erhaltung der Parkleistung LWRs durch Brennerreaktoren ersetzt werden. KORIGEN ist wesentlicher Bestandteil von KORREC. Ausführlich dokumentierte Anwendungsrechnungen sind in /1/ und /3/ zu finden.

### **4. Gleichgewichts-Szenariocode SOLEQ**

SOLEQ (SOLve Equilibrium equations) berechnet mit Hilfe eines vom Verfasser zur iterativen Lösung des Nuklidgleichgewichts entwickelten Verfahrens /4/ bei vorgegebenen Typen von Actinidenerzeugungsreaktoren und Brennerreaktoren das Ver-

hältnis dieser Reaktoren (Support Ratio) im Gleichgewicht. KORIGEN ist wesentlicher Bestandteil von SOLEQ.

## **5. Nachwärmecode CALOR**

Die Berechnung der in bestrahlten Brennelementen wegen der in ihnen enthaltenen radioaktiven Spaltprodukte und Actiniden freigesetzten Zerfallsleistung ist eine der KORIGEN-Optionen. Auf Grund der im Brennstoffkreislauf interessierenden maximalen Zerfallszeit von 30 Jahren und der in diesem Zeitbereich in Uranbrennstoff dominierenden und einfach zu beschreibenden Spaltprodukte war es jedoch schon früh möglich, für Uranbrennstoff einen einfachen und für einen weiten Bereich von BE-Typen einsetzbaren Ersatzformalismus zu entwickeln (Uran-Norm). Mit zunehmendem Einsatz von MOX-BE in Leichtwasserreaktoren entstand bei Reaktorbetreibern und Überwachungsbehörden der Wunsch nach einer entsprechenden einfachen MOX-Norm. Im Rahmen der von FZK geförderten Mitarbeit des Verfassers im Ausschuss „Zerfallsleistung“ des DIN entstand bei FZK der Rechencode CALOR, der die Dominanz der Actiniden bei längeren Zerfallszeiten beinhaltet und mittels 3d-Interpolation in fünfzehn Querschnittsdateien einen breiten Anwendungsbereich überdeckt.

## **6. Einsatz der Codes und Ausblick**

KORIGEN wird im FZK sowie von der Industrie, von Reaktorbetreibern und Überwachungsbehörden zur Berechnung des nuklearen Inventars von Leistungsreaktoren eingesetzt. Seine nuklearen Basisdaten müssen dem Stand von Wissenschaft und Technik folgen und dementsprechend aktualisiert werden.

Bei Sonderanwendungen und Detailfragen erwarten die Anwender, die den Code z.T. käuflich von FZK bezogen haben, kompetente Beratung und gegebenenfalls Rechenunterstützung. Dies sollte nach Ausscheiden des Verfassers gewährleistet sein.

Desgleichen ist es nach Dafürhalten des Verfassers zur Bewertung von Transmutationsszenarien nötig, zumindest den in /4/ in seinen Grundlagen umfassend dokumentierten Code SOLEQ weiterhin einsatzfähig zu halten.

Der im wesentlichen abgeschlossene und Drittmittel trachtige Code CALOR wird in 2002 dokumentiert. Seine Erweiterung auf Uranbrennstoff wird ins Auge gefasst.

## Literatur

- /1/ H.W. Wiese, B. Krieg: Comparative Analysis of Actinide Burning in multiple-recycling FBRs and PWRs  
Proc. of Int. Conf. on Future Nuclear Systems, GLOBAL'93, Seattle, USA, 1993, S. 908
- /2/ H.W. Wiese, B. Krieg: Sensitivity of the Support Ratio in Fast Reactor Incineration Calculations  
Proc. of Int. Nuclear Congress – Atoms for Energy, ENC'94, 1994, Lyon, Frankreich, S. 384
- /3/ H.W. Wiese, B. Krieg: Actinide Transmutation Properties of Thermal and Fast Fission Reactors including multiple Recycling  
Proc. of Int. Conf. Actinides'97, Baden-Baden, 1997, in J. of Alloys and Compounds, 271-273, 118, S. 522
- /4/ H.W. Wiese: Equilibrium in Pools of PWRs and Burner Reactors with homogeneous Recycling of Plutonium and minor Actinides  
Proc. of F. Joliot – O. Hahn Summer School in Reactor Physics, Karlsruhe, 1999, S. 237
- /5/ U. Fischer, H.W. Wiese: Verbesserte konsistente Bestimmung des Inventars von Druckwasserreaktoren auf der Basis von Zell-Abbrand-Verfahren mit KORIGEN  
KFK 3014, 1983, ORNL-tr-5043
- /6/ H.W. Wiese, B. Krieg: Erweiterung der KORIGEN Datenbibliotheken und Berucksichtigung der Spaltprodukte aus Spontanspaltungen  
Interner Bericht INR 1941, PSF 3253
- /7/ D. Woll: Darstellungen der zeitlichen Veranderungen von Massen und Radiotoxizitatsindizes von Kernbrennstoffen bei Bestrahlung und Zerfall  
Interner Bericht IKET 2/02, NUKLEAR 3368
- /8/ H.W. Wiese, D. Woll: Determination of Changes of Nuclear Fuel during Irradiation and Decay with KORIGEN and associated Visualization of Masses and Radiotoxicities  
Interner Bericht IKET 3/02, NUKLEAR 3371

## 32.23.02 Abtrennverfahren für Actiniden aus hochradioaktiven Abfällen

(A. Geist, M. Weigl, U. Müllich, K. Gompper, INE)

### Zusammenfassung

Die bislang zur Abtrennung der Minoren Actiniden von den Lanthaniden eingesetzte Hohlfaser-Extraktionsanlage erforderte Feedvolumina von einigen Litern. Deshalb wurde begonnen, eine Hohlfaser-Microplant aufzubauen, mit der Extraktionsversuche auch in Heißen Zellen durchgeführt werden können. Dazu wurden miniaturisierte Hohlfasermodule gefertigt und getestet. Diese Module ermöglichen die Durchführung von Extraktionstests mit Feedvolumina von einigen 10 ml. In einem solchen Modul wurden erste Versuche durchgeführt. Beispielsweise konnte in einem Versuch zur Americium-Lanthaniden-Trennung Americium zu 99,95 % abgetrennt werden, bei geringer Lanthaniden-Koextraktion.

### 1 Einleitung

Die Langzeitradiotoxizität abgebrannter Kernbrennstoffe wird über einen Zeitraum von einigen  $10^5$  Jahren durch den Gehalt an Plutonium und Minoren Actiniden (Neptunium, Americium, Curium) bestimmt (Abb. 1a). Mit der Partitioning & Transmutation-Strategie (P&T) [1] kann die Langzeitradiotoxizität deutlich vermindert werden, indem diese Elemente abgetrennt (Partitioning) und anschließend zu kurzlebigen und schließlich stabilen Nukliden umgewandelt werden (Transmutation) (Abb. 1b). Eine weitere Option besteht darin, die abgetrennten langlebigen Radionuklide in speziellen, auf ihre Eigenschaften abgestimmten, hoch langzeitbeständigen Matrices (z.B. Keramik) einzubauen und getrennt von den kürzerlebigen Abfällen endzulagern (Partitioning&Conditioning).

Die Abtrennung der dreiwertigen Minoren Actiniden Americium und Curium von den Spaltlanthaniden ist dabei ein Schlüsselschritt. Diese Trennung ist wegen der Wirkung einiger Spaltlanthaniden als Neutronengift und aufgrund ihres hohen Massenüberschusses den Actiniden gegenüber erforderlich. Sie ist aber wegen der chemischen Ähnlichkeit der Gruppen schwierig und stellt hohe Anforderungen an die Trennchemie und den Trennprozess.

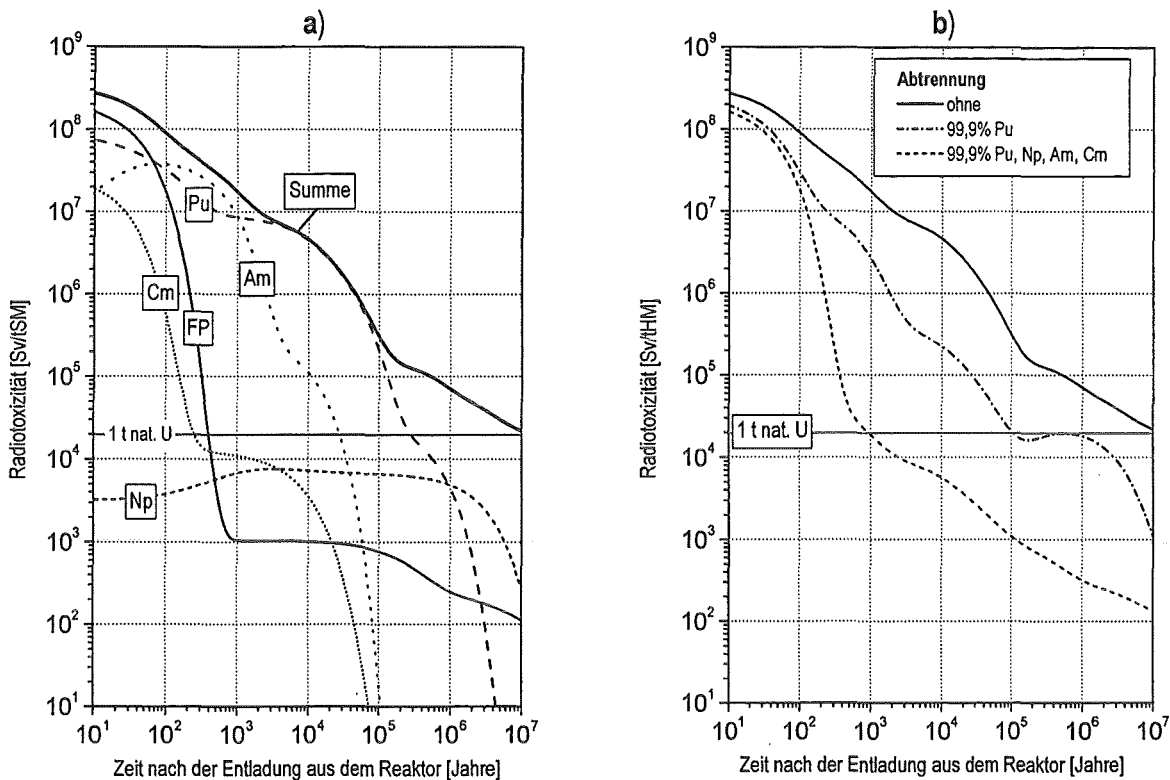


Abb. 1: Radiotoxizität von 1 Tonne abgebranntem Kernbrennstoff als Funktion der Zeit; Anreicherung 4,2% U-235, Abbrand: 50 GWd/t  
 a) Beitrag der Actiniden und Spaltprodukte zur Radiotoxizität  
 b) Einfluß verschiedener Abtrennszenarien auf den zeitlichen Verlauf der Radiotoxizität  
 (zum Vergleich ist die Radiotoxizität von 1 t Uran natürlicher Isotopenzusammensetzung angegeben)

Vor diesem Hintergrund werden im Rahmen des EU-Projekts PARTNEW Arbeiten zur Actiniden(III)-Lanthaniden-Trennung mittels chemischer Flüssig-flüssig-Extraktion durchgeführt. Die Arbeiten umfassen drei Teilbereiche:

1. Synthese neuer stickstoffhaltiger Extraktionsmittel zur selektiven Abtrennung dreiwertiger Actiniden
2. Untersuchung der Stoffaustauschkinetik relevanter Extraktionssysteme
3. Einsatz von Hohlfasermodulen als Flüssig-flüssig-Phasenkontakoren.

Im Berichtszeitraum wurden annähernd 20 neue N-Donor-Komplexbildner synthetisiert, die potentiell für diese Trennung geeignet sind [2]. Weiterhin wurden die kinetischen Untersuchungen fortgesetzt, worauf hier nicht eingegangen wird. Außerdem

wurden Versuche zur Americium(III)-Lanthaniden-Trennung in miniaturisierten Hohl-fasermodule durchgeführt, welche im Folgenden beschrieben werden.

## 2 Entwicklung einer Hohlfaser-Microplant

Zur Durchführung eines vollständigen Trennprozesses mittels Flüssig-flüssig-Extraktion werden üblicherweise die drei Teilschritte Extraktion, Scrubbing und Stripping (Rückextraktion) gekoppelt (siehe Abb. 2). Im Extraktionsschritt wird die Hauptkomponente A und etwas Nebenkompone nte B aus der Feedphase in die organische Phase, welche einen geeigneten Komplexbildner enthält, überführt. Die koextrahierte Menge B wird im Scrubbing-Schritt wieder ins Raffinat rückextrahiert. Die nun exklusiv in der organischen Phase vorliegende Hauptkomponente A wird im Stripping-Schritt ins wässrige Produkt überführt. Dadurch kann die regenerierte organische Phase wieder eingesetzt werden. Die Komponenten A und B liegen nun getrennt in Produkt und Raffinat vor.

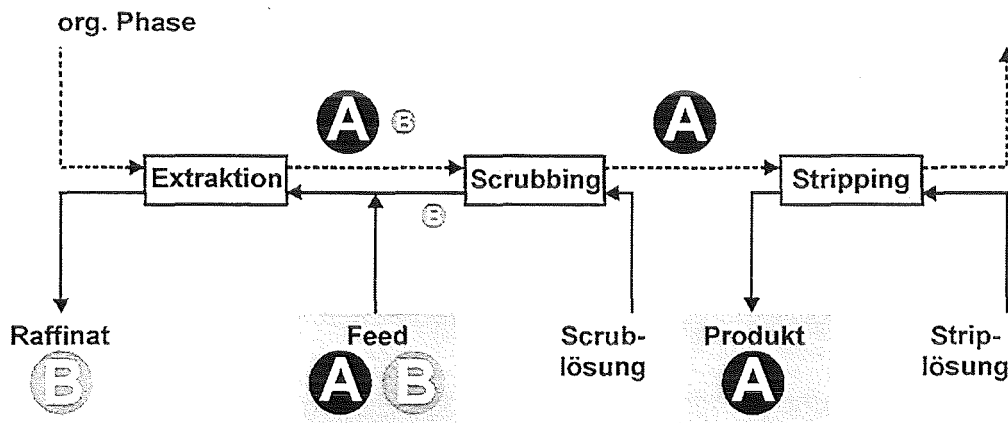


Abb. 2: Typische Verschaltung der drei Stufen Extraktion, Scrubbing und Stripping (Rückextraktion) zur extraktiven Trennung zweier Komponenten A und B.

Das stationäre Betreiben einer solchen Anlage erfordert hohe Feedvolumina. Dies ist unvorteilhaft, da die zum Einsatz kommenden Komplexbildner – teils aufwendig – synthetisiert werden müssen. Um dennoch stationäre Versuche mit vertretbarem Feedvolumen und Aktivitätsinventar betreiben zu können, wurden verkleinerte Hohl-fasermodule hergestellt (siehe Abb. 3). Dazu wurden 50-100 Hohlfasern (im Gegen-satz zu 10000 bei den bisher eingesetzten [3] käuflichen Modulen in ein Mantelrohr eingeklebt. Die verwendeten Hohlfasern entsprechen denen, die in den käuflichen Modulen eingebaut sind. Anschließend wurde eine Hohlfaser-Microplant aufgebaut, in der drei Module entsprechend Abb. 4 verschaltet sind.

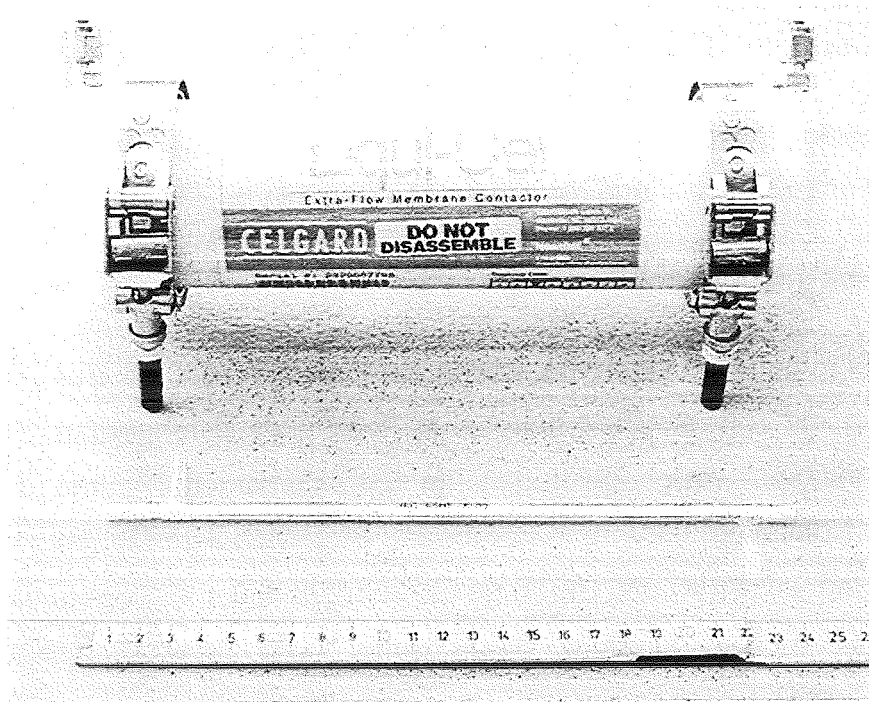


Abb. 3: Vergleich eines hergestellten Mini-Moduls (unten, 55 Hohlfasern, aktive Länge 0,2 m) mit einem erhältlichen Modul (10000 Fasern, 0,15 m).

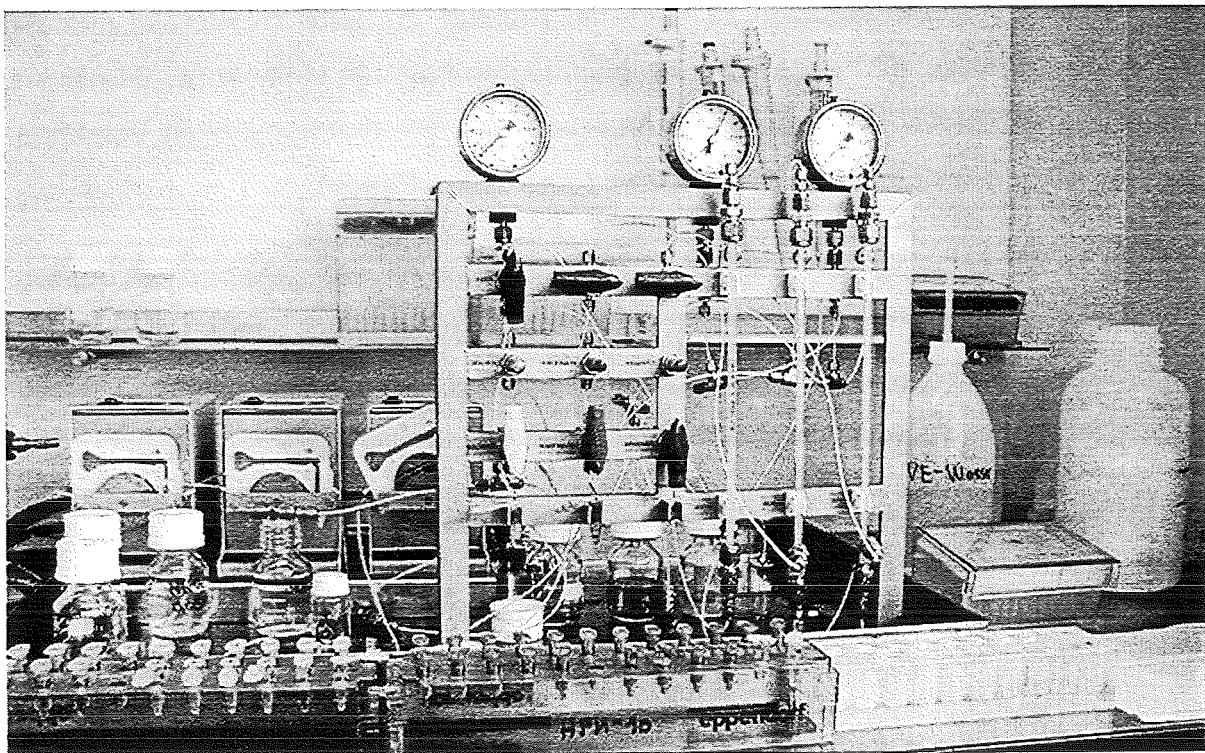


Abb.4: Hohlfaser-Microplant.

### 3 Durchgeführte Versuche

Es wurden bislang sowohl Einzelmodul-Versuche als auch gekoppelte Versuche mit drei Modulen unter Verwendung der neuen Mini-Module durchgeführt.

#### 3.1 Europium-Praseodym-Trennung

Um erste Erfahrungen zu sammeln, wurde ein inaktiver Test zur Europium-Praseodym-Trennung mit Di(2-ethylhexyl)phosphat (D2EHPA) durchgeführt. Drei Module mit je 55 Hohlfasern waren gekoppelt. Im Extraktionsmodul wurde die wässrige Phase in den Hohlfasern geführt, in Scrub- und Strip-Modul im Mantelraum [4]. Feed war eine Lösung von Pr(III) und Eu(III) (je ca. 95 mg/l) in 0,1 M Salpetersäure, Scrub-Lösung war 0,2 M Salpetersäure, Strip-Lösung 1,0 M Salpetersäure. Organische Phase war 0,1 M D2EHPA in Kerosin. Der Feed-Volumenstrom betrug 1,9 ml/h, der Scrub-Volumenstrom 1,4 ml/h, der Strip-Volumenstrom 1,9 ml/h und der Volumenstrom der organischen Phase 2,6 ml/h.

Der Versuch war nach einer Betriebszeit von 5,5 Stunden noch nicht ganz stationär. Nach dieser Zeit lag Praseodym zu 104% im Raffinat, zu 3,2% im Produkt und zu 0,3% in der organischen Phase vor. Europium lag zu 1,8% im Raffinat, zu 84,4% im Produkt und zu 14,4% in der organischen Phase vor. Die durchgesetzten Volumina lagen bei 10,5 ml (Feedphase) bzw. 14,3 ml (organische Phase).

Da noch keine verlässlichen Stoffaustauschrechnungen für den gekoppelten Betrieb verfügbar waren, konnte der Versuch nicht optimal geplant werden. Bei entsprechender Einstellung der Volumenströme sollte eine bessere Trennung sowie Regenerierung der organischen Phase ohne Weiteres möglich sein.

#### 3.2 Americium(III)-Lanthaniden-Trennung: n-Pr-BTP

Es wurde ein Versuch zur Americium(III)-Lanthaniden-Trennung mit 2,6-Bis-(5,6-dipropyl-1,2,4-triazin-3-yl)pyridin (n-Pr-BTP) [5] durchgeführt. Dazu wurde ein einzelnes Modul (105 Hohlfasern) verwendet. Die wässrige Phase (3,7 MBq/l Am-241 und inaktive Lanthaniden, La-Gd + Y, insgesamt 2,5 g/l in 1 M Salpetersäure) wurde in den Hohlfasern geführt, die organische Phase (0,04 M n-Pr-BTP in Kerosin/1-Octanol, 70:30 vol.) im Gegenstrom im Mantelraum. Die Volumenströme (wässrig = organisch) wurden zwischen 0,72 ml/h und 1,43 ml/h variiert.

Die Massenbilanzen lagen bei  $(100 \pm 5)\%$ . Bei einem Volumenstrom von 0,72 ml/h konnte Americium zu 99,95% extrahiert werden (vgl. Abb. 5), entsprechend einem Dekontaminationsfaktor von 2000. Dies bedeutet eine wesentliche Verbesserung gegenüber einem früher mit einem großen Modul durchgeführten Versuch [6, 7], bei dem Americium lediglich zu 94% in die organische Phase überführt werden konnte.

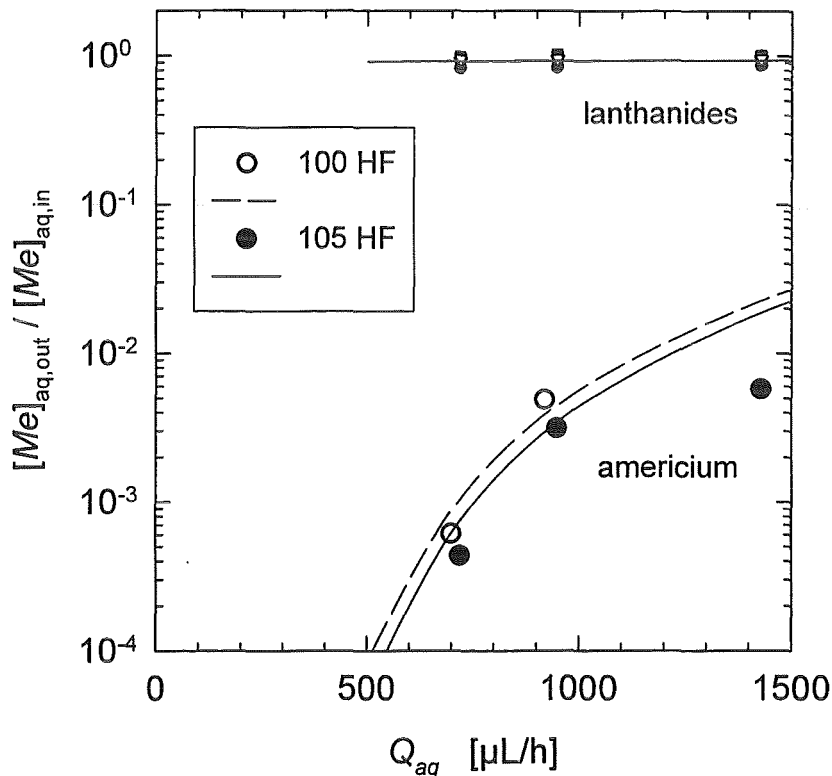


Abb. 5: Am(III)-Ln(III)-Trennung mit n-Pr-BTP, relative wässrige Austrittskonzentrationen. Wässrige Phase, in HF: Am-241 + Ln in 1 M HNO<sub>3</sub>. Organische Phase: 0,04 M n-Pr-BTP in Kerosin/1-Octanol (70:30 vol). Module: 105 bzw. 100 HF.

Von den Lanthaniden wurden 21 mg/l, d.h. weniger als 1% koextrahiert, was in Abb. 5 nicht zu erkennen ist. Dies entspricht einem Dekontaminationsfaktor von 120, und zwar bereits ohne Lanthanidenscrubbing. Der Anteil der einzelnen Lanthaniden in der organischen Phase ist deshalb in Abb. 6 gezeigt.

Der Versuch wurde schließlich reproduziert, allerdings diesmal in einem 100 Hohlfasern enthaltenden Modul (offene Punkte in Abb. 5). Die Ergebnisse aus den beiden Versuchen stimmen gut überein; hinsichtlich der Lanthaniden zeigte sich im Rahmen der Fehler kein Unterschied.

Daraus lässt sich also schließen, dass Module reproduzierbarer Qualität gefertigt werden können.

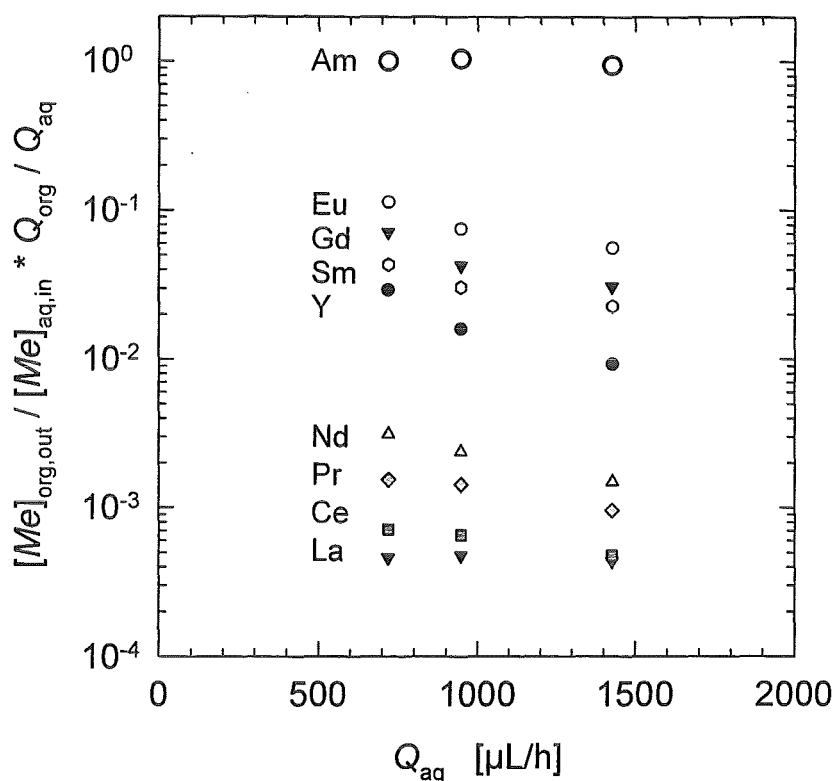


Abb. 6: Am(III)-Ln(III)-Trennung mit n-Pr-BTP, relative organische Austrittskonzentrationen. Modul: 105 HF. Weitere Versuchsbedingungen siehe Abb. 5.

### 3.3 Europium-Extraktion: D2EHPA

Derzeit werden Versuche zur – nicht gekoppelten – Extraktion und Rückextraktion von Europium mit D2EHPA in Kerosin in einem Einzelmodul durchgeführt. Diese dienen insbesondere zur Überprüfung der Tragfähigkeit der eingesetzten Stoffaustauschrechnungen. Da diese Versuche noch nicht abgeschlossen sind, wird auf eine Darstellung von Ergebnissen verzichtet.

## 4 Schlussfolgerung

Um den Aufbau eines kontinuierlichen Extraktionsprozesses mit Hohlfasermodulen mit vertretbarem Aufwand, d.h. geringen Volumina an Feedphasen, zu ermöglichen, wurden miniaturisierte Hohlfasermodule angefertigt. Der volumenbezogene Skalierungsfaktor betrug rund 1/100, d.h., Versuche können bereits mit einigen 10 ml an Feedphasen durchgeführt werden.

Die bislang durchgeführten Versuche zeigen die Eignung der neuen Module. Insbesondere die erfolgreiche Abtrennung von Americium zu 99,95% mit n-Pr-BTP belegt dies eindrucksvoll.

## Literatur

- 1 *Actinide and Fission Product Partitioning and Transmutation, Status and Assessment Report*. OECD-NEA, Paris (1999).
- 2 M. Weigl, U. Müllich, A. Geist, K. Gompper, H. Stephan, T. Zevaco, *Alkyl-substituted 2,6-Di(oxadiazolyl)-pyridines as Selective Extractants for Trivalent Actinides* (in Vorbereitung).
- 3 A. Geist, M. Weigl, U. Müllich, K. Gompper, *Abtrennverfahren für Aktiniden aus hochradioaktiven Abfällen*. Projekt Nukleare Sicherheitsforschung, Jahresbericht 2000. Wissenschaftliche Berichte, FZKA-6653 (September 2001) S. 387.
- 4 A. Geist, M. Weigl, K. Gompper, *Actinide(III)/Lanthanide(III) Separation in a Hollow Fiber Module with a Synergistic Mixture of bis(Chlorophenyl)dithiophosphinic Acid and TOPO*. Paper 049, Proceedings of the International Conference on: Back End of the Fuel Cycle: From Research to Solutions (GLOBAL 2001), September 9-13, 2001, Paris, France.
- 5 Z. Kolarik, U. Müllich and F. Gassner, *Extraction of Am(III) and Eu(III) Nitrates by 2,6-Di(5,6-dipropyl-1,2,4-triazin-3-yl)pyridine*, *Solv. Extr. Ion Exch.* 17(5), 1155 (1999).
- 6 A. Geist, M. Weigl, U. Müllich, K. Gompper, *Abtrennverfahren für Aktiniden aus hochradioaktiven Abfällen*. Projekt Nukleare Sicherheitsforschung, Jahresbericht 1999. Wissenschaftliche Berichte, FZKA-6480 (August 2000) S. 593.
- 7 A. Geist, M. Weigl, K. Gompper, *Actinide(III)/Lanthanide(III) Separation in a Hollow Fiber Module with a Synergistic Mixture of bis(Chlorophenyl)dithiophosphinic Acid and TOPO*. Paper 049, Proceedings of the International Conference on: Back End of the Fuel Cycle: From Research to Solutions (GLOBAL 2001), September 9-13, 2001, Paris, France.

### 32.23.03 Sicherheitsuntersuchungen zum dynamischen Verhalten von Kernen mit Actinidenanteil

#### I. Improvements of Passive Safety Features of Accelerator Driven Transmutation Systems

(W. Maschek, A. Rineiski, S. Wang, X. Chen, M. Mori, E. Wiegner, W. Götzmann, IKET; M. Flad, D.T.I. GmbH)

#### 1. Introduction

Safety studies have been extended for ADSs with dedicated fuel with the mission of waste transmutation/incineration /1-4/. The key issue is the high minor actinide content of these fuels with the simultaneous lack of the classical fertile materials as U238 or Th232 for maximizing incineration rates /5/. Both the high MA load and the lack of fertile material may have a significant impact on the fuel behavior itself, and will also influence the safety performance of the entire core. Especially the reactivity potentials of the core materials could be high and mitigating effects like the prompt negative feedback (Doppler) could be rather small. In addition, the use of dedicated fuels may lead to a strong deterioration of the kinetics quantities as neutron generation time and  $\beta_{\text{eff}}$ . The implications of these features become apparent especially under design extension conditions (DEC), in the severe transient and accident range (traditionally: beyond design basis accidents, BDBA). A rearrangement of the core material configuration could increase the reactivity level or even eliminate the subcriticality of the ADS. In such a case the deteriorated safety parameters would dominate the outcome of the accident scenario. To cope with such conditions a safety strategy is proposed with the ultimate goal to eliminate any severe accident scenario with core destruction and additionally remove the potential for high energetics in the beyond design region. The safety strategy heavily relies on inherent and passive safety measures and concentrates on preserving the subcriticality level and eliminating cliff-edge effects. To perform safety assessments for ADS, mainly the SIMMER-III code /6/ in its ADS version has been applied /7, 8/. SIMMER-III, a coupled fluid-dynamics, thermal-hydraulics, space-time neutron dynamics accident code is developed by JNC (Japan Nuclear Cycle Development Institute, O-arai Engineering Center) in cooperation with Forschungszentrum Karlsruhe and CEA (Commissariat à l'Énergie

Atomique, CE Grenoble and CE Cadarache). Recently also IPSN (Institut de Protection et Sûreté Nucléaire) has joined the SIMMER-club.

## 2. Some Safety Investigations for Dedicated Cores

In /3, 4/ first generic analyses for a lead cooled ADS with 'dedicated' nitride and oxide fuels have been presented. A dedicated fuel with a very high MA load has been chosen for the analyses. The background strategy scenario of this fuel is a double stratum concept with a first stratum global reactor fleet of UOX-PWR, (MOX1+MOX2)-PWR and LMFBRs, delivering MAs (and Pu if needed for operational purposes) into a second stratum ADS fleet for final incineration /9/. For the safety analysis, starting from steady state conditions and entering a transient, an ADS with a thermal power of 1200 MW and a subcriticality level of  $k_{\text{eff}} = 0.98$  has been defined. Static neutronic calculations for this specific core gave a Doppler constant of about -100 pcm, a  $\beta_{\text{eff}}$  of ~150 pcm and a very short neutron generation time of  $\Lambda \sim 2.0 \cdot 10^{-7}$  s. A considerable core void has been calculated with about 5000 pcm. The available reactivity potentials from lead voiding could eliminate the subcriticality margin built into the core. The coolant voiding problem is relieved by the high boiling point of Pb or Pb/Bi, however, core voiding could take place by a gas release from breached pins and a gas blow-down from the plena. The criticality potential of the fuel is large with about 60 available critical masses. Any local subassembly melting with subsequent fuel compaction processes could drive the core towards critical.

For investigating the dedicated core behavior under severe accident conditions, mechanistic code calculations, finally ending in core destruction and/or melting, have been performed. The main intention of the analyses were to test the 'response' of the core to different accidental conditions and scenarios. In the case entering more severe transients or even the accident regime, the following issues might cause problems /3, 4/ in dedicated cores:

- The high intrinsic material reactivity worth
- Mechanisms that could lead to a core material rearrangement and eliminate the built-in subcriticality level
- The lack of sufficient negative feedback and the deteriorated kinetics parameters

An unprotected loss of flow (ULOF) has been investigated as an initiator with the potential of core damage. A scenario leading to a ULOF may be caused by a beam-trip which is followed by a pump-coast down for prevention/mitigation of thermal-shocks. After the pump run-down, the beam is suddenly reinstalled. In the course of the accident, clad melting triggers a blow-down of helium together with fission gases leading to a sufficient addition of void reactivity to drive a power excursion /10, 11/. According to the analyses, a type of *cliff edge effect* could exist for dedicated cores with the implication of severe power transients. The lack of an impeding negative reactivity feedback, as the Doppler effect, in company with deteriorated kinetics parameters leads to a significant increase of the potential for accident energetics. The results of the investigations on dedicated cores showed the necessity to integrate measures against severe accidents into the safety strategy for an ADS - not relying solely on the subcriticality of the system.

### **3. A Possible Safety Strategy for Transmuters**

A safety strategy, especially suited for new innovative systems, where e.g. accident potentials and failure rates of components are not well known or even unknown, is the concept of 'lines of defense' (LOD) /12/. This method is compatible with the classical barrier and defense in depth concept. The proposal for safety improvements heavily relies on inherent and passive measures. Developing an ADS safety strategy /10, 11/ one could first resort to 'critical' fast reactors, as e.g. to the CAPRA/CADRA waste burner reactors /13, 14/ and the EFR (European Fast Reactor) /15/, because of certain similarities. A waste burning ADS, similar to a fast critical reactor, will not be in its neutronically most critical configuration, thus any rearrangement of core materials implies the (theoretical) possibility to achieve critical or even superprompt-critical configurations. A fundamental issue of the safety approach is therefore the preservation of subcriticality and the assurance of a safe 'nuclear shutdown' (Fig. 1).

Shut-down in an ADS in the first line corresponds to a shut-off of the external neutron source. Source (beam) shut-off reliability will mainly depend on the monitoring and detection systems. From analyses it is known /1/ that the shut-down of the source might not lead to decay heat levels. Therefore one could think of installing additional 'conventional' absorber rods. These shut-down measures together resemble the redundant and diverse shut-down devices of critical fast reactor systems. In the

framework of the EFR development and later applied for the CAPRA/CADRA waste burner reactors /13/ an additional line of defense, the so-called third shut-down level has been developed and introduced. This 3rd shutdown-level mainly relies on passive measures/systems, which break the logic (deterministic) chains to core disruption. In its basic concept the 3<sup>rd</sup> shutdown-level for 'critical' reactors relies on negative reactivity effects which overcome any positive reactivity addition.

Ultimately, the classical initiators for a core disruption, as the ULOF, UTOP (unprotected over power), ULOHS (unprotected loss of heat sink) are eliminated from design.

For the ADS, a similar strategy could be adopted and a 3<sup>rd</sup> shut-down level could also be installed. This 3<sup>rd</sup> shut-down level relies on passive measures related to optimization of the subcriticality level, the core safety coefficients and interruption of the beam. In the ADS, in addition to the transients caused from the 'core side', transients initiated from the external neutron source (e.g. the UTOC, the *unprotected*

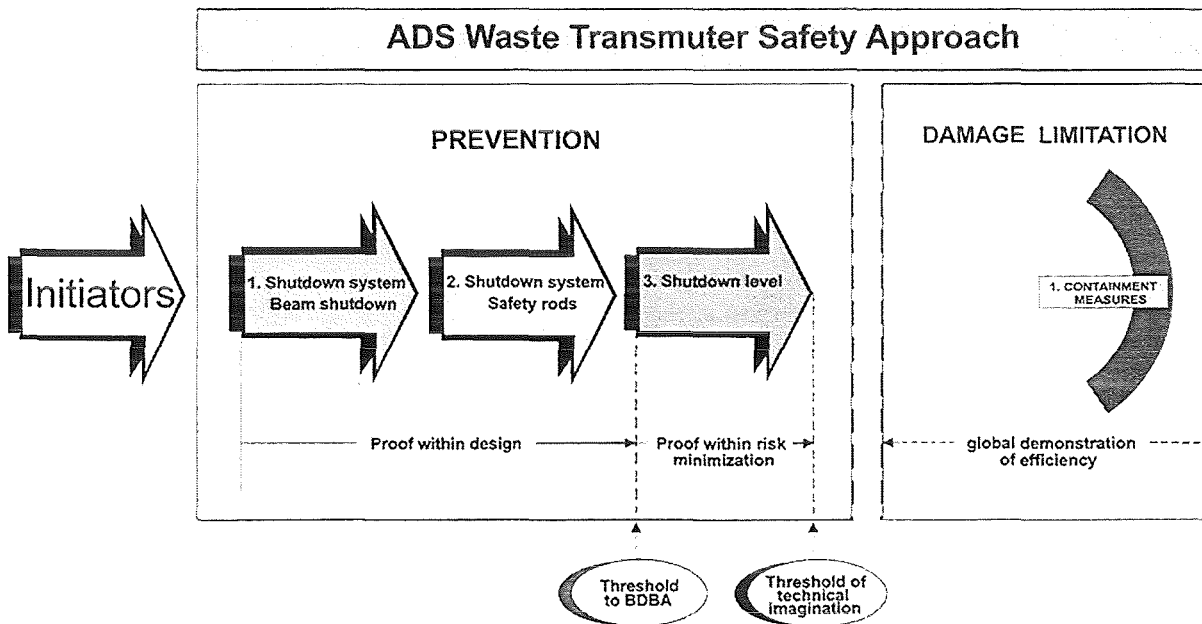


Fig. 1 A safety strategy for ADS waste burners

*transient over current*) will have to be taken into account. In the left box of Fig. 1 the different measures are grouped together and represent the prevention level in the ADS safety strategy. The intention of this strategy is, that for an ADS, severe core disruptive accidents can be 'designed out'. The prevention level in Fig. 1 is displayed as a *closed* box without any link towards the 'damage limitation' region. The 'damage limitation region' nevertheless plays a significant role in the overall safety strategy. Though there might not exist any deterministic/mechanistic link from the prevention to

the damage limitation region and the initiators for core disruption have been designed out, the residual risk for core disruption scenarios involving energetics still has to be considered. The basic problems as 'the limit of human understanding', or the 'proof of completeness' in the region of preventive safety still remain and consequently additional mitigative measures have to be introduced as provisions against the unforeseeable. Thus mitigative, damage limiting measures (containment) are required within this safety strategy.

The key essence of the overall safety strategy is to relegate core disruptive accidents with energetics to the extreme outer edge of the residual risk. The provisions made on the preventive level should exclude any deterministic path into a core-meltdown. Additionally, the core and reactor system should be designed in a way that severe accident scenarios with high energetics can be excluded. The safety approach relies on active measures, but additionally to a large extent on integrated inherent and passive safety features. In the following, improvements referring to inherent preventive measures are discussed in detail.

#### **4. Improvement of Inherent Safety Measures**

Inherent safety improvements for dedicated cores will have implications on the different lines of defense. From the analyses performed in /3, 4, 10, 11/ some general inherent safety requirements and reasonable improvements can be deduced:

- Limitation of the fuel worth (fuel worth of single subassembly)
- Stability of the fuel matrix (prevention of separation/segregation processes)
- Limitation of the coolant void worth
- Respecting the clad worth
- Assuring a prompt negative feedback effect (Doppler, thermal expansion)
- Assuring reasonable kinetics parameters (neutron generation time)
- Respecting the Am/Cm content in fuels to limit He pressure build-up

Complying with these proposals both influences the 3<sup>rd</sup> shut-down level and also helps to eliminate cliff-edge effects and the potential for severe energetics under accident conditions. The subcriticality level, which is linked in first place to operational and design needs could be directly correlated to specific and defined safety requirements.

To realize the above safety proposals, a useful measure would be the integration of Th232/U233 into the fuel matrix. Introduction of fissile increases the probability of nuclear fission and, therefore, the neutron importance in the resonance (keV) energy range. Consequently, the absolute value of the coolant density/void effects decreases and the generation time increases. Moreover, a higher "resonance" neutron importance results in a larger (absolute value of) Doppler constant provided that a sufficient amount of resonance absorber nuclei exists in the reactor. Introduction of Th232 provides the resonance absorber nuclei to "improve" the Doppler constant, compensates a criticality variation due to adding of U233 and may (partly) compensate the burn-up of U233 during reactor operation (due to breeding). The integration of resonance absorbers as e.g. hafnium could also be discussed, but this measure will not fully solve the problem of low neutron importance in the resonance region. Finally, by the introduction of thorium the recriticality potentials will also be reduced.

The general procedure for improving safety parameters in a MA fueled core could thus be summarized as:

- Provision of a resonance absorber
- Provision of fissionable material to increase the neutron importance

In the following, some preliminary analyses on the impact of introducing Th232 (in company with U233) on the core disruption behavior are given. By increasing the negative Doppler feedback the functional dependency of excursion energetics on the neutron generation time is also changed resulting in reduced energetics levels. In Fig. 2 a typical power transient of a snap-shot analysis is displayed in the dedicated core with and without fertile fuel material. The power transient is triggered by a postulated fuel compaction process resulting in approximately the same ramp rate, given in  $\$/s$ ,

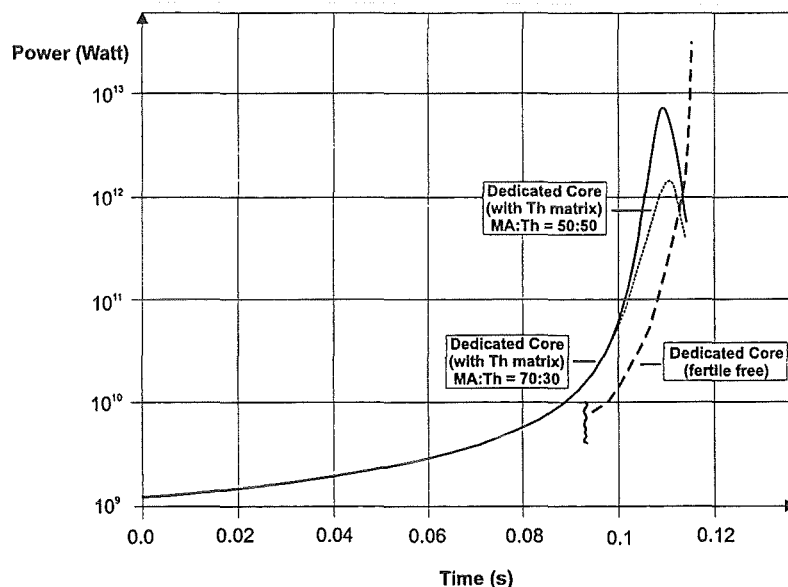
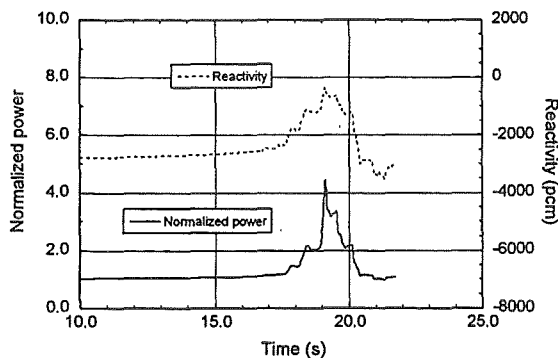


Fig. 2 Snap-shot analysis of a reactivity transient in a core with pure dedicated fuel and a core with thorium integration.

in both cores. Note that in the dedicated fuel core (without Th232) the  $\beta_{\text{eff}}$  is about a factor of 2 smaller than in the core with thorium. The main purpose is to test the general impact of the different core material configurations and their response to reactivity insertions. To match the transients of the fertile free with the 'thorium cores' the time-scale in Fig. 2 had to be shifted.

The impact of fertile material on the postulated power transients is significant and shows the desired trend towards lower energetics. For the core with 30% thorium in the fuel matrix also mechanistic calculations with the SIMMER-III code have been performed, simulating a ULOF transient. The results in Fig. 3 show, that a severe power excursion is absent and the accident, though leading to core disruption, takes a mild path. This indicates, that the undesired cliff-edge effect /3, 4/could be eliminated by design measures. The introduction of some fertile fuel effectively helps to curb severe neutronic activity and excursion behavior. Though there naturally exists a large uncertainty in the modeling of such fuels, the general trends seem to be consistent and logical.



*Fig. 3 Mechanistic simulation and nuclear power trace of an un-protected (beam-on) LOF in a dedicated oxide core with 30% thorium in the fuel matrix*

Along the same lines the Pu content relative to the MAs (no fertile fuel as U238 or Th232 is introduced) could be increased. This measure will influence the Doppler, the void and the kinetics data. The main effect of the Pu dominance is a shift of the spectrum and the increase of the neutron importance in the resonance range /16/. Both proposals – inserting fertile fuel or increasing the Pu content – lead to a moderate re-

duction of the MA incineration potential in the second stratum. As conclusion one could state that to achieve the safety goals, the mass of MAs loaded into an ADS has to be limited, however in a much less restrictive way compared to a critical waste burning reactor.

## 5. Measures for Accident Prevention

The 3<sup>rd</sup> shut-down level measures should rely on a bundle of passive measures to guarantee both a safe shutdown of the proton beam in case of any power to flow mismatch and a sufficiently negative reactivity margin. The following measures could be proposed:

- An adequate subcriticality level.
- A limited variability of the source
- The possibility of passively shutting down the beam. In /17/ and in /18/ beam stopper devices are proposed. In /17/ the lead expansion during heat-up is utilized in an overflow device to stop the beam. In /18/ a melt-rupture disk in the side-wall of the proton guide tube is proposed, which would fail and flood the vacuum tube with heavy liquid metal. Ideas have to be elaborated into a direction of passively stopping the beam without lead filling of the vacuum tube
- Passive source feedback – in analogy to the passive reactivity feedback – might be exploited /19/
- ‘Classical’ reactivity oriented shut-down measures /15/

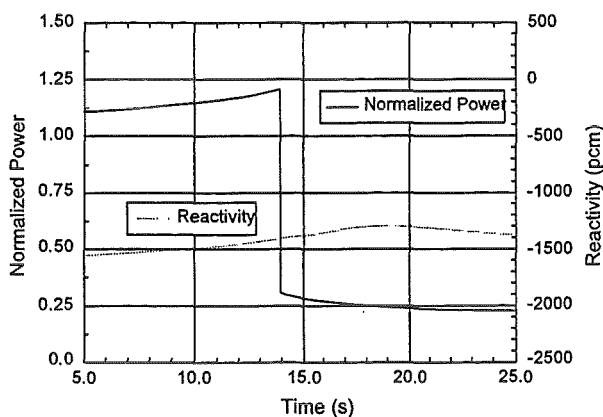


Fig. 4 Mechanistic simulation and nuclear power trace of an originally un-protected (beam-on) LOF in a dedicated oxide core with a later beam-trip

The importance of a beam trip in time, is demonstrated in Fig. 4. Though already under loss of flow conditions, the beam-trip leads to a sufficient drop of the power level. Early pin failures, damage propagation and the short-term excursion behavior is prevented. The power still stays around 20% of nominal after the beam trip. To achieve decay heat levels additional negative reactivity has to be introduced into the reactor core.

In a further calculation (Fig. 5), the effect of a control rod scram without a beam shut-off has been investigated. For the same transient as in Fig. 3 at ~15 s a negative reactivity worth of  $-15 \text{ \$}$  has been introduced. This does not lead to the desired effect. The power level is still high at around 60 % after the scram. Cooling conditions are

insufficient and the core degradation process is inevitable. This confirms, that in an ADS beam shut-down has the first priority and should logically be accompanied by an absorber rod scram [1, 20].

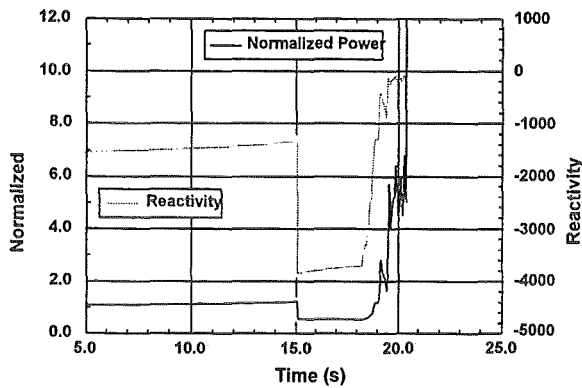


Fig. 5 Mechanistic simulation and nuclear power trace of an un-protected (beam-on) LOF in a dedicated oxide core with a later reactor scram

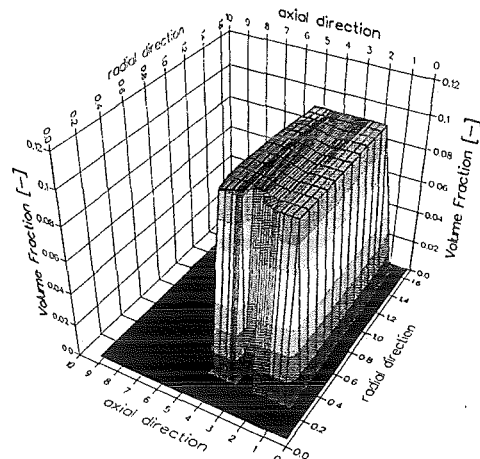


Fig. 6 Volume fraction of clad with central damage region opposite to the target

In Fig. 6 it can be observed that in the above simulation with SIMMER-III clad damage has occurred around the beam target region, initiating a gas blow-down and further propagation of the accident.

## 6. Final Remarks

For maximizing incineration rates, dedicated fuels and dedicated cores are under discussion. As characteristics, these fuels/cores have a very high MA content accompanied by the elimination of the classical fertile materials as U238 or Th232. Investigations of the transient and accident behavior in dedicated cores revealed potential safety problems, especially for core-melt and core disruptive accident conditions. Basically, two major – interrelated – problem areas exist. The high reactivity potential of the dedicated fuel (irrespective of the type of fuel) can overcome the built-in subcriticality of an ADS in case of any local fuel rearrangement and compaction. Any nuclear excursion, triggered under such neutronicly ‘critical’ conditions will not be hampered by an effective prompt negative feedback (e.g. Doppler effect). In addition, the kinetics parameters, as e.g. the neutron generation time are very small. This all together could lead to a classical *cliff edge effect* behavior, where

benign transients may turn into severe accidents and/or classes of accidents exist with the release of significant thermal and mechanical energy.

An overall safety strategy based on the lines of defense concept with a bundle of preventive and mitigative measures is proposed. Basic inherent safety measures are discussed, which have a direct impact on the different lines and could lay the ground for a benign core behavior also under severe perturbations and accident conditions. In this strategy, the subcriticality level of the ADS is directly related to the safety requirements, besides the conditions coming from normal operation. The safe and assured shut-down of the beam is the primary goal. Shut-down rods will complement the beam-shutdown devices on the prevention level. In the damage limitation region, which still has its place because of the 'limits in human understanding', classical containment measures have to be foreseen. The ultimate goal of all measures is the elimination of any severe accident scenario from the design and the removal of cliff-edge effects and severe energetics.

Some direct measures are proposed to improve the inherent safety behavior of a dedicated oxide fuel core, as e.g. the implementation of fertile materials, reduction of the minor actinide content or changing the plutonium to minor actinide ratio. These proposals violate the principle of maximization of incineration rates. The consequences would be a moderately increased recycling effort, a larger ADS fleet and/or with the introduction of thorium – another fuel cycle. However, constraints on the dedicated fuel cycle 'efficiency' have to be expected anyway, coming from fuel fabrication, design, performance and operational requirements.

## 7. References

- /1/ W. Maschek, B. Merk, H. U. Wider, Some Safety Studies for Accelerator Driven Subcritical Systems, AccApp'98, Gatlinburg, USA (1998)
- /2/ W. Maschek, A. Rineiski, K. Morita, E. Kiefhaber, G. Buckel, M. Flad, P. Coste, S. Pigny, G. Rimpault, J. Louvet, T. Cadiou, S. Kondo, Y. Tobita, T. Suzuki, H. Yamano, S. Fujita, SIMMER-III, a Code for Analyzing Transients and Accidents in ADS, AccApp'00, Washington D.C., USA (2000)
- /3/ W. Maschek, A. Rineiski, K. Morita, E. M. Flad, G. Mühling, R.J.M. Konings, Safety Analyses for ADS Cores with Dedicated Fuel and Proposals for Safety Improvements, IAEA TCM Meeting, Argonne, USA (2000)

- /4/ K. Morita, A. Rineiski, E. Kiefhaber, W. Maschek; M. Flad, G. Rimpault, P. Coste, S. Pigny, Sa. Kondo, Y. Tobita, S. Fujita, Mechanistic SIMMER-III Analyses of Severe Transients in Accelerator Driven Systems (ADS), ICONE-9, Nice, France (2001)
- /5/ Report of the Fuel Fabrication and Processing Subgroup of the Technical Working Group on ADS (2000)
- /6/ S. Kondo, K. Morita, Y. Tobita, N. Shirakawa: SIMMER-III : An Advanced Computer Program for LMFBR Severe Accident Analysis, ANP'92, Tokyo, Japan (1992)
- /7/ R. Rineiski, B. Merk, W. Maschek: ADS Related Extension of the Neutronics Module in the Accident Analysis Code SIMMER-III, ADDTA'99, Praha, Czech Rep. (1999)
- /8/ R. Rineiski, E. Kiefhaber, B. Merk, W. Maschek, M. Flad: Neutron Kinetics Develop. of the SIMMER-III Safety Code for ADS Appl.ication, OECD/NEA Workshop on the Utilization and Reliability of High Power Proton Accelerators, Cadarache, France (1999)
- /9/ M. Salvatores, I. Slessarev, G. Ritter, P. Fougeras, A. Tchistiakkov, G. Youinou, A Zaetta, Long-lived radioactive waste transmutation and the role of accelerator driven hybrid systems, Nucl. Instruments and Methods in Physics Research A, 414, 5 (1998)
- /10/ W. Maschek, A. Rineiski, S. Wang, M. Flad, K. Morita), Safety Improvements for ADS Transmuters with Dedicated Fuel, AccApp'01 and ADDTA'01, Reno, USA (2001)
- /11/ W. Maschek, A. Rineiski, K. Morita, M. Flad, Inherent and Passive Safety Measures in Accelerator Driven Safety Systems: A Safety Strategy for ADS, GLOBAL 2001, Paris, France (2001)
- /12/ J.D. Griffith, J. Graham, P. Greebler, R.T. Lancet, Safety Considerations for Large Fast Breeder Plants, Int. Mtg. On Fast Reactor Safety and Related Physics, Chicago, USA (1976)
- /13/ A. Languille, A., Garnier, J.C., Lo Pinto, P., Na, B.C., Verrier, D., Duplaix, J., Allan, P., Sunderland, R.E., Kiefhaber, E., Maschek, W., Struwe, D., 1995. CAPRA Core Studies - the Oxide Ref. Option, GLOBAL '95, Paris, France (1995)
- /14/ W. Maschek, D. Struwe, Accident analyses and passive measures reducing the consequences of a core-melt in CAPRA/CADRA reactor cores, Nucl. Eng. and Design 202, 311 (2000)
- /15/ H. Vossebrecker, H., Considerations. on Risk Reduction for Future Breeder Reactors, IA Ident.-35.026027 (1990)
- /16/ W. Seifritz, Skizze eines zukünftigen Neptunium-Brenners, Kerntechnik 56, 3, 167 (1991)
- /17/ Rubbia, C., Rubio, J.A., 1996, A Tentative Progr. tow. a Full Scale Energy Ampl., CERN/LCH/96-11 (EET)
- /18/ Wider, H.U., Schönherr, H., Beam Pipe with Safety Function for Accelerator-Driven Nuclear Systems, European patent, No 9811339.7 (1999)

- /19/ D. C. Wade, Safety Considerations in Design of Fast Spectrum ADS for Transuranic or Minor Actinide Burning. A Status Report on Activities of the OECD-NEA Expert Group, 6th Inform. Mtg. On Actinide and Fission Product P&T, Madrid, Spain (2000).
- /20/ M. Schikkor, Generic Issues of Dyn. Resp. of ADS, CAPRA/CADRA Meeting, Cadarache, France (2001)

## II. Investigation of Neutron Kinetics Models For ADS Transient Analyses (A. Rineiski, W. Maschek, IKET)

### **Abstract**

Within the framework of the SIMMER code development, neutron kinetics models for simulating transients and hypothetical accidents in advanced reactor systems, in particular in Accelerator Driven Systems (ADSs), have been recently developed. SIMMER is a fluid-dynamics/thermal-hydraulics code, coupled with a structure model and a space-, time- and energy-dependent neutronics module for analyzing transients and accidents. The advanced kinetics models have also been implemented into KIN3D, a module of the VARIANT/TGV code (stand-alone neutron kinetics) for broadening application and for testing and benchmarking.

In the paper, a short review of the SIMMER and KIN3D neutron kinetics models is given. Some typical transients related to ADS perturbations are analyzed. The general models of SIMMER and KIN3D are compared with more simple techniques developed in the context of this work to get a better understanding of the specifics of transients in subcritical systems and to estimate the performance of different kinetics options. These comparisons may also help in elaborating new models and extending existing computation tools for ADS transient analyses.

### **1. Introduction**

For incinerating/transmuting plutonium and Minor Actinides (MAs), Accelerator Driven Systems (ADSs) are of special interest as they inherently offer a larger flexibility in design and operation and for coping with safety problems. To perform the safety assessment for ADSs, accident codes for critical reactor systems, as the SIMMER-III code (Kondo, 1992), should therefore be utilized and adapted to describe the specific ADS features. In particular, the corresponding neutron kinetics models should properly take into account the impact of the strong external neutron source on transient power distribution. Such kinetics models are also needed for analyzing the experiments performed to support the ADS studies, these analyses being done by employing neutronic code systems as ERANOS (Doriath, 1993).

Two kinetics models for simulating transients and hypothetical accidents in advanced reactor systems, in particular in ADSs, have been developed at FZK/IKET in cooperation with CEA Cadarache. These models are implemented in SIMMER (Rineiski, 1999) and in

the KIN3D (Rineiski, 1997) module of the VARIANT/TGV code (Lewis, 1997), a part of ERANOS.

These ADS-related kinetics options are based essentially on the extensions of the schemes developed mainly for critical system analyses. Therefore, their verification is important. Currently, however, the experience in ADS transient analyses is significantly smaller compared to that one existing for critical reactors. That is why a corresponding benchmark has been recently proposed (Rineiski, 2000).

There is also another way to get an impression about the performance of the developed techniques: to analyze rather simple cases in detail and to create suitable simplified models. Agreement (which we hope to reach) between simplified models and more general schemes of SIMMER and KIN3D would provide an additional proof of the validity of the general schemes. On the other hand, comparisons between different models may give a better understanding of neutron kinetics phenomena in ADSs and provide a basis for elaborating new efficient computation techniques.

In this paper, a short review of the SIMMER and KIN3D kinetics models is given. The advanced computation techniques are described. Some typical reactor perturbations for subcritical systems driven by external source are analyzed. Conclusions on the performance of point-kinetics and quasistatic options for relatively "smooth" perturbations are drawn.

## 2. Kinetics model of SIMMER

To analyze severe transients and hypothetical core disruptive accidents in nuclear reactors, the SIMMER-III code (Kondo, 1992) is under development at JNC (Japan Nuclear Cycle Development Institute, O-arai Engineering Center) with cooperation of Forschungszentrum Karlsruhe and CEA (Commissariat à l'Énergie Atomique, CE Grenoble and CE Cadarache). SIMMER-III is a two-dimensional, three-velocity-field, multi-phase, multi-component, Eulerian, fluid-dynamics code coupled with a fuel-pin model and a space-, time- and energy-dependent neutron dynamics model.

The SIMMER neutronics model was originally developed for critical systems. Recently new features were included to make possible ADS transient analyses (Rineiski, 1999). The thermal-hydraulics part was also extended for new coolants (lead, lead/bismuth) and fuels (Maschek, 2000). Recently the first full scale analyses of an ULOF event in lead-cooled ADSs with thorium and so called dedicated (consisting mainly of MAs and Pu) fuel were performed with SIMMER (Maschek, 2001)

In SIMMER the time-dependent multigroup neutron transport equation (in the following, only one family of delayed neutrons is considered for simplicity,  $x$  denotes a space-angular position,  $\Phi, Q, v, \chi_p, \chi_d$  are "multigroup" vectors  $\chi = \{1 - \beta\} \chi_p + \beta \chi_d$ ;  $M$  and  $F$  are operators having their standard meaning (Ott, 1985): neutron "leakage, absorption, and scattering" and "generation",  $\gamma_0$  is a user-defined parameter for adjusting the initial reactivity level):

$$\frac{1}{v} \frac{\partial \Phi(x,t)}{\partial t} + M(t)\Phi(x,t) = \frac{1}{\gamma_0} (1-\beta)\chi_p F(t)\Phi(x,t) + \chi_d \lambda C(x,t) + Q(x,t), \quad (1)$$

$$\frac{\partial C(x,t)}{\partial t} = \frac{1}{\gamma_0} \beta F(t)\Phi(x,t) - \lambda C(x,t); \quad (2)$$

is solved by employing the quasistatic scheme (Ott, 1985). Space-time factorization is employed for each shape step assuming that

$$\Phi(x,t) = N(t)\psi(x,t), \quad (3)$$

$$\langle W(x), \frac{1}{v} \psi(x,t) \rangle = \gamma = 1, \quad (4)$$

where  $N(t=0)=N_0$  (amplitude at  $t=0$ ) is usually set to the fraction of total power which does not include decay heat. In SIMMER (and KIN3D), the time-independent weighting vector-function  $W$  is by default assumed to be the (quasi-) critical adjoint flux computed at  $t=0$ :

$$M(0)W(x) = \frac{1}{k_{eff}} \frac{1}{\gamma_0} \chi F(0)W(x). \quad (5)$$

Another option is discussed later. The shape equations (time-dependence is omitted hereafter in this section for  $N$ ,  $M$ ,  $F$  and all point-kinetics parameters, we assume that  $\gamma_0=1$  hereafter):

$$\frac{1}{v} \frac{\partial \psi(x,t)}{\partial t} + \frac{1}{vN} \frac{dN}{dt} \psi(x,t) + M\psi(x,t) = (1-\beta)\chi_p F\psi(x,t) + \frac{1}{N} \chi_d \lambda C(x,t) + \frac{1}{N} Q(x,t), \quad (6)$$

$$\frac{\partial C(x,t)}{\partial t} = N\beta F\psi(x,t) - \lambda C(x,t), \quad (7)$$

are solved relatively seldom (shape steps) compared to the more frequently solved point-kinetics equations for the amplitude

$$\frac{dN}{dt} = \left( \frac{\rho - \beta_{eff}}{\Lambda} \right) N + \lambda c + q_{eff}, \quad (8)$$

$$\frac{\partial c}{\partial t} = \frac{\beta_{eff}}{\Lambda} N - \lambda c, \quad (9)$$

where the reactivity, generation time, and effective source (the definitions of other point-kinetics parameters can be found e. g. in (Ott, 1985);  $\langle \dots \rangle$  means phase-space integration) are:

$$\rho = \frac{1}{\langle W, \chi F \psi(x,t) \rangle} \langle W(x), (\chi F - M)\psi(x,t) \rangle, \quad (10)$$

$$\Lambda = \frac{1}{\langle W(x), \chi F \psi(x,t) \rangle} \langle W(x), \frac{1}{v} \psi(x,t) \rangle, \quad (11)$$

$$q_{eff} = \frac{1}{\langle W(x), \chi F \psi(x,t) \rangle} \langle W(x), Q(x,t) \rangle. \quad (12)$$

Eqs. (6), (7) are transformed to a sequence of steady-state-like equations by employing the first-order implicit scheme and assuming the flux shape being linear (vs. time) within a shape step. The cross-sections and external source terms involved in these steady-state-like equations include "kinetics corrections". For example, the source term "correction" for a shape step  $(t_{n-1}, t_n)$  is

$$\Delta Q(x,t) = \frac{\psi(x, t_{n-1})}{v(t_n - t_{n-1})}. \quad (13)$$

The steady-state-like shape equations are solved by the TWODANT (Alcouffe, 1995)  $S_n$ -neutron transport code package, which was extended (Buckel, 1999) for taking into account the source and cross-sections "kinetics corrections". Inclusion of the THREEDANT (Alcouffe, 1995) code package in SIMMER version IV for 3D calculations is under implementation.

Since Eq. (6) contains the factors  $1/N$  and  $(dN/dt)/vN$ , the flux shape depends upon the amplitude behavior within a shape step. On the other hand, the point-kinetics parameters (which determine the amplitude) may depend upon the flux shape. Therefore, iteration is performed at each shape step till the convergence (to a certain limit) of the left-hand part of Eq. (4) is reached. If this limit differs appreciably from unity, one has to employ smaller shape steps and/or tighter flux convergence criteria.

SIMMER computes some additional values which may help in transient analyses:  $k_{\text{source}}$ , source effectiveness  $\phi^*$ , and source multiplication  $f_{\text{source}}$ :

$$k_{\text{source}}(t) = \frac{\langle I, \chi F \psi(x, t) \rangle}{\langle I, M \psi(x, t) \rangle}, \quad (14)$$

$$\phi^*(t) = \frac{\langle W(x), Q(x, t) \rangle}{\langle W(x), \chi F \psi(x, t) \rangle} / \frac{\langle I, Q(x, t) \rangle}{\langle I, \chi F \psi(x, t) \rangle} = \frac{\langle W(x), Q(x, t) \rangle \langle I, \chi F \psi(x, t) \rangle}{\langle I, Q(x, t) \rangle \langle W(x), \chi F \psi(x, t) \rangle} \quad (15)$$

$$f_{\text{source}}(t) = \frac{\langle I, \chi F \psi(x, t) \rangle + \langle I, \frac{1}{N} Q(x, t) \rangle}{\langle I, \frac{1}{N} Q(x, t) \rangle}, \quad (16)$$

where  $I$  is the unity vector. The source effectiveness is computed only if  $W$  is the critical adjoint flux. One may note that using of the unity weighting function in Eq. (10) is equivalent to computing the reactivity as  $\rho = 1 - 1/k_{\text{source}}(t)$  (if a particular weighting function is chosen for calculating the reactivity, the same function should be certainly employed for computing the generation time and other kinetics parameters).

### 3. Kinetics model of KIN3D

KIN3D, a kinetics and perturbation extension of the VARIANT 3D nodal transport (the angular expansion order is provided by the user, the lowest order corresponds to the diffusion approximation) code, includes 4 different kinetics options: direct, improved quasistatic, adiabatic and point-kinetics. The transient cross-sections and external source are to be provided by the user. VARIANT/KIN3D is also referenced as VARIANT-K.

The quasistatic models of SIMMER and KIN3D are quite similar in many respects. That is why the results of verification and performance analyses are useful for the amelioration of the **both** codes. A specific feature of the current KIN3D version is that only the even-parity (with respect to angle) components of the external source are taken into account. Consequently, only the "even-parity" cross-section and source "kinetics corrections" are introduced for the direct and quasistatic options. Therefore extremely fast phenomena such as propagation of neutron waves (which are usually not relevant for accident analyses) cannot be treated completely accurately (for the moment) in KIN3D. That corresponds to

the common (for diffusion models) practice of assuming the Fick's law being valid during transients. This avoids treatment of "artificial" (i.e. related to "kinetics corrections") anisotropy and simplifies the computation scheme. This feature will become optional in the next KIN3D version (currently under development, another major extension planned is to allow precursor movement).

The calculations of reactivity and other kinetics parameters are based on the perturbation theory technique. For example, the mean generation time is expressed as

$$\Lambda = \frac{\langle W^+(x), \frac{1}{v} \Phi^+(x,t) \rangle - \langle \Omega \nabla W^+, \frac{1}{v \sigma(0) \sigma(t)} \Omega \nabla \Phi^+(x,t) \rangle}{\langle W^+(x), \chi^F \Phi^+(x,t) \rangle}, \quad (17)$$

where the plus superscript denotes the even-parity components of the flux and weighting function. The "gradient" (second) term in the denominator of Eq. (17) takes into account impact of the odd-parity moments on the generation time. This term can be optionally omitted:

$$\Lambda_{\text{even-parity}} = \frac{\langle W^+(x), \frac{1}{v} \Phi^+(x,t) \rangle}{\langle W^+(x), \chi^F \Phi^+(x,t) \rangle}, \quad (18)$$

that may slightly change the generation time (usually by a few percents) and bring closer agreement between the left-hand and right-hand parts of Eq. (4). The reason is that using of Eq. (18) corresponds to ignoring the odd-parity cross-sections and source "kinetics corrections".

For the cases investigated by now, the two different options of computing the generation time have not influenced significantly the results of the calculations, indirectly confirming that ignoring the cross-section and source odd-parity "kinetics corrections" does not introduce a significant error. On the other hand, employing of the "even-parity" neutron generation option may improve the numerical performance. In the following we will always assume this option being employed in KIN3D; the results are usually quite accurate if the computed at  $t=0$   $\Lambda_{\text{even-parity}}$  and reactivity are made equal to "best estimate" static  $\Lambda$  and reactivity values by adjusting the velocities and  $\gamma_0$ .

#### 4. Two time-scales in ADS kinetics

In ADS transient simulations, the flux shape may vary appreciably even if the material configuration does not change significantly.

Unlike conventional (initially) critical systems, for which reaction rates are usually to be accurately computed only at near-zero reactivity levels (otherwise the system explodes or shuts down), much greater reactivity variations are of interest in ADSs.

These variations change contributions from the fission and external sources to the total neutron source. Therefore the flux shape may change significantly as shown in Fig. 1 (the results shown in Fig. 1 and 2 are obtained for an ADS with Th/U fuel, this system is described later). Source variations may also change contributions from the external and fission (prompt and delayed) sources to the total neutron source. Therefore, a few ms after a source breakdown the neutron flux shape may deviate from a “source on” shape in a manner shown in Fig. 2.

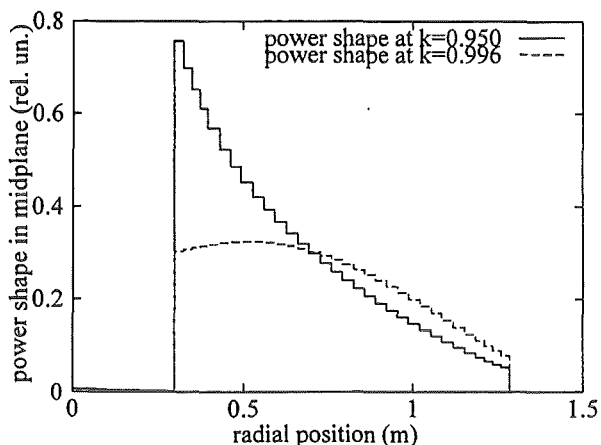


Fig. 1 Power shapes at two criticality levels

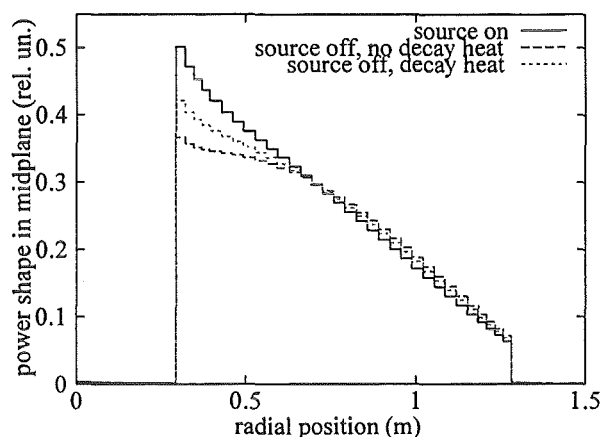


Fig. 2 Power shapes before and after (10 ms) a source breakdown

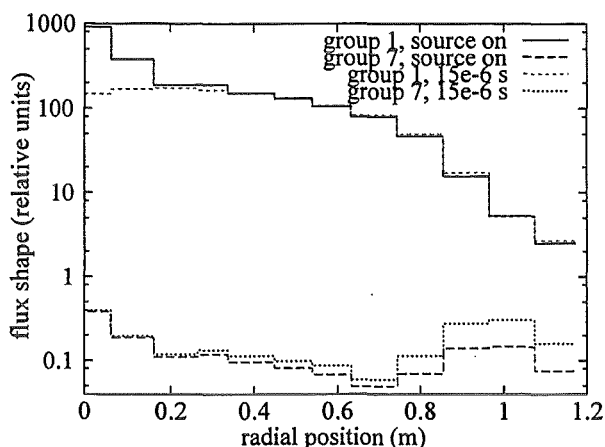


Fig. 3 Fast and thermal flux in the core and reflector (3 last radial meshes) before and after (15  $\mu$ s) the source breakdown.

In the above cases we considered “long-time-scale” events of the order of ms or s. Short-time-scale (comparable to generation time) phenomena are related e.g. to fast beam trips. Just after an almost prompt source variation, the flux (especially in the low energy domain) may change faster in the central core region than in the reflector. For example, in Fig. 3 one can see flux changes in the first and last energy groups after a source breakdown in a fast system with MOX fuel and steel reflector (see (Rineiski, 1999) for more details).

In the following, we employ SIMMER for simulating long-time-scale phenomena (relevant for ADS accident analysis, therefore we use a dynamics code) and KIN3D for short-time-scale phenomena (important for experimental analyses and diagnostics, therefore a kinetics code).

## 5. Weighting functions

In addition to “critical adjoint” (the default option), we use “ $\alpha$ -adjoint” (solutions of adjoint  $\alpha$ -eigenvalue problems) weighting functions for analyzing short-time-scale phenomena. Currently “ $\alpha$ -adjoint” can be used in the SIMMER and KIN3D point-kinetics calculations. Since  $\alpha$ -eigenvalue problems are sometimes difficult to solve with VARIANT, one may also

employ some approximations to “ $\alpha$ -adjoint” in KIN3D. We experienced originally problems in computing “ $\alpha$ -adjoint” with SIMMER too, but recently the situation has been improved significantly (Kiefhaber, 1999).

It is known (Ott, 1985) that critical adjoint weighting functions provide the least sensitive (to possible computation flux errors) reactivity values for small perturbations in a critical reactor. Therefore this is usually the best option for the critical systems. Since up to now weighting functions in SIMMER and KIN3D are time independent, there is a strong incentive to keep the “critical adjoint” available also for (initially) subcritical systems: in case of an accident the system may reach criticality, then using of this weighting function may be preferable. We will investigate in the following the performance of the “critical adjoint” weighting for a few representative cases.

One can easily see that  $\alpha$ -adjoint weighting gives the least sensitive (to flux) variations  $\rho/\Lambda$  ratios. The corresponding amplitude is the most slowly varying one (for short-time-scale phenomena related to beam trips). Therefore, the corresponding results may help in evaluating possible first order errors of “fast” transient simulations (by making comparisons with the results related to the “critical adjoint” weighting scheme).

We have not tried to employ more complicated weighting functions. An attempt to find a “proper” weighting function usually implies the assumption that one may take into account a major part of flux variations within each shape step by space-time factorization. If this assumption is valid, (i.e. the flux shape changes much slower than the amplitude during the transient) the main source of possible computation errors comes from possible inaccuracies in the amplitude calculations depending upon a few time-dependent parameters. Therefore, one may look for an “optimal” weighting function and corresponding kinetics parameters that reduce these inaccuracies to a lowest possible level.

If this assumption is not valid (i.e. different reaction rates vary in a rather different manner) the “optimal” weighting function may not exist. The reason is that the computed amplitude may be accurate with respect to one reaction rate, but rather inaccurate for another one.

Small perturbations are usually not of great importance in ADS kinetics: unlike the critical case, they cannot push an ADS far out of equilibrium, just slightly changing the nuclear reaction rates. On the other hand, strong perturbations - which may really pose problems for their simulation - may give rise to significant flux shape changes, comparable to amplitude variations. That is why in ADS transient analysis, the “optimal” weighting function can be frequently chosen only with respect to a particular reaction rate. Moreover, it may even vary (for a given rate) if the criticality level varies.

Certainly one may employ several weighting functions and produce several amplitudes, accurate for different reaction rates at different stages of transient. This approach, however, is rather complicated. This complication may not be needed for the quasistatic scheme: with any “reasonable” weighting function, the quasistatic results are converging to the same limit, provided that shape step decreases. Therefore while employing a non-optimal (with respect

to a particular reaction rate) weighting function, one may often opt for smaller shape steps (or this can be done automatically by a shape-step controller).

With the point-kinetics option, the related (to non-optimal weighting) errors cannot be compensated in this way (there is no shape recalculation). Therefore, it is interesting to analyze possible inaccuracies of the standard (critical adjoint weighting) point-kinetics option for a few typical cases and create simple models that would allow to explain (or correct) the observed deviations from the "spatial kinetics" results. That would also confirm the validity of the employed spatial kinetics models.

## 6. Correction factors for reaction rates computed with point-kinetics models

In the following we will always assume that the space-energy-angular shape of the external source remains unchanged during the transient, but the source amplitude may vary:

$$Q(x, t) = q(t)Q(x, 0). \quad (19)$$

It follows from Eq. (19) that  $q(0)=1$ . Let us consider (for the beginning) a very slow transient (so that the precursors are always in equilibrium with the fission source) and assume that during this transient the system is always subcritical. Under these conditions, the shape equations are transformed into

$$M(t)\psi(x, t) = \chi F(t)\psi(x, t) + \frac{1}{N(t)}q(t)Q(x, 0), \quad (20)$$

the flux amplitude being computed as

$$N(t) = q(t) \frac{\langle W(x), Q(x, 0) \rangle}{\langle W(x), (\chi F(t) - M(t))\psi(x, t) \rangle}. \quad (21)$$

A relative reaction rate variation is defined as

$$R(t) / R(0) = \frac{N(t) \langle I, \sigma(x, t)\psi(x, t) \rangle}{N(0) \langle I, \sigma(x, t)\psi(x, 0) \rangle}, \quad (22)$$

where  $\sigma(x, t)$  is the corresponding cross-section (if the reaction rate is computed for a particular node,  $\sigma(x, t)=0$  outside this node). Employing Eq. (21) one can get the following amplitude ratio:

$$N(t) / N(0) = q(t) \frac{\langle W(x), (\chi F(0) - M(0))\psi(x, 0) \rangle}{\langle W(x), (\chi F(t) - M(t))\psi(x, t) \rangle}. \quad (23)$$

If the shape is calculated only at  $t=0$ , the following "point-kinetics" amplitude ratio is computed on the basis of the first order perturbation theory (PT):

$$\{N(t) / N(0)\}_{point} = q(t) \frac{\langle W(x), (\chi F(0) - M(0))\psi(x, 0) \rangle}{\langle W(x), (\chi F(t) - M(t))\psi(x, 0) \rangle}. \quad (24)$$

To get the exact variation of the detector rate, one should multiply this ratio by a correction factor (defined "with respect to the initial conditions"):

$$f_{\sigma}(t,0) = \frac{\langle I, \sigma(x,t)\psi(x,t) \rangle \langle W, (\chi^F(t) - M(t))\psi(x,0) \rangle}{\langle I, \sigma(x,t)\psi(x,0) \rangle \langle W, (\chi^F(t) - M(t))\psi(x,t) \rangle} \quad (25)$$

For example, one can consider a perturbation related to a neutron production cross-section variation while all other properties of the system remain unchanged (i.e. the nubar varies only):

$$\chi^F(t) - M(t) = \frac{\|\chi^F(t)\|}{\|\chi^F(0)\|} \chi^F(0) - M(0). \quad (26)$$

Introduction in this manner of a so-called "external" reactivity is a usual way to model a perturbation that is difficult to take into account directly by varying the cross-sections (e.g. radial expansion of the core). In case of critical adjoint weighting Eq. (25) is reduced to

$$f_{\sigma,external}(t,0) = \frac{\langle I, \sigma(t)\psi(t) \rangle \langle W, \chi^F(0)\psi(x,0) \rangle}{\langle I, \sigma(t)\psi(0) \rangle \langle W, \chi^F(0)\psi(x,t) \rangle} \quad (27)$$

If the reactivity tables - employed in a point-kinetics model - are prepared to reproduce "exact PT" reactivity effects and the generation time is considered to be time-independent, the "exact PT" correction factors "with respect to the initial conditions" can be obtained by taking into account that

$$R(t) = \langle I, \sigma(t)\psi(t) \rangle N(t) = q(t) \frac{\langle I, \sigma(t)\psi(t) \rangle \langle W, Q(x,0) \rangle}{\langle W, (\chi^F(t) - M(t))\psi(x,t) \rangle}, \quad (28)$$

$$\{N(t)/N(0)\}_{point,exact\_PT} = q(t) \frac{\langle W(x), (\chi^F(0) - M(0))\psi(x,0) \rangle \langle W(x), (\chi^F(t)\psi(x,t)) \rangle}{\langle W(x), (\chi^F(t) - M(t))\psi(x,t) \rangle \langle W(x), \chi^F(0)\psi(x,0) \rangle}. \quad (29)$$

Therefore

$$f_{\sigma,exact}(t,0) = \frac{\langle I, \sigma(t)\psi(t) \rangle \langle W, \chi^F(0)\psi(x,0) \rangle}{\langle I, \sigma(t)\psi(0) \rangle \langle W, \chi^F(t)\psi(x,t) \rangle}. \quad (30)$$

This looks quite similar to the "external" correction factors. It is interesting to note that the correction factors (30) for the total fission rate (that is usually quite similar to the total power rate) should be close (equal for the one-energy-group case) to unity if  $W=1$  (constant weighting function) and  $\chi^F(t)$  is constant. In the following we will apply "first order PT" correction factors to explain the deviations between the point and spatial kinetics models.

The point-kinetics model is involved in the quasistatic scheme within each shape step: until the flux shape is calculated at the end of a shape step, the previous flux shape is used and the relative reaction rates changes (such as power production) are computed with a point-kinetics model (the real scheme is usually more complicated and involves some extrapolations to reduce the errors). Therefore, the ratios of the correction factors at the

beginning and end of a shape step give us an indication about the accuracy of the quasistatic scheme.

One may note that in the general case we are interested in ratios of correction factors. When these ratios are computed, it is not relevant whether the correction factors were calculated with respect to the initial conditions or with respect to some other conditions. Instead of using the correction factors defined by Eq. (25), one can employ, for example, the following ones (computed with respect to the quasi-critical initial flux):

$$f_{\sigma}(t) = \frac{\langle I, \sigma(x,t) \psi(x,t) \rangle \langle W, (\chi F(t) - M(t)) \tilde{\psi}(x) \rangle}{\langle I, \sigma(x,t) \tilde{\psi}(x) \rangle \langle W, (\chi F(t) - M(t)) \psi(x,t) \rangle} \quad (31)$$

where

$$M(0) \tilde{\psi}(x) = \frac{1}{k_{eff}} \chi F(0) \tilde{\psi}(x). \quad (32)$$

Then

$$f_{\sigma}(t,0) = f_{\sigma}(t) / f_{\sigma}(0). \quad (33)$$

The power (i.e. related to the power density) correction factors defined similarly to Eq. (31) may have an interesting application. If they can be approximated sufficiently well for each reactor node and possible transient state, one can use them together with corresponding (i.e. computed for the same quasi-critical configuration) "critical" power and reactivity worth distributions in a point-kinetics model to calculate the power distributions for slow (at subcritical level) transients. An obvious difficulty in implementing this approach is that the correction factors should be known for all possible perturbed reactor states. If for a certain set of different perturbations the shape changes are mainly related to variations of the criticality level, the number of the correction factors (to be computed in advance) may decrease. For taking these perturbations into account, one can interpolate the values from a table of the "external" correction factors computed at different criticality levels.

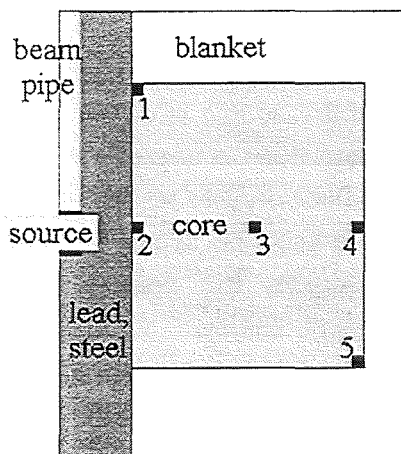


Fig. 4 ADS model in R-Z geometry, locations of nodes 1 - 5 are shown

To provide a numerical example, the "external" power correction factors (with respect to the quasi-critical initial flux) were computed for a 1200 MWt ADS model with Th/U fuel and lead coolant (Maschek, 2000) at 4 subcritical states. The unperturbed state corresponds to the reactivity level of -3050 pcm (critical adjoint weighting hereafter is assumed), i.e.  $k_{eff} \approx 0.97$ . The calculations were performed for 5 nodes and for the total power (the ADS model and the nodes are shown in Fig. 4). The results are presented in Table 1 and Fig. 5.

Table 1. "External" power correction factors for the core nodes and total power

Reactivity(pcm)	node 1	node 2	node 3	node 4	node 5	total
-100	1.010	1.014	0.998	0.994	0.994	0.999
-3050	1.294	1.390	0.932	0.847	0.841	0.971
-6145	1.546	1.736	0.874	0.727	0.717	0.948
-9241	1.765	2.044	0.824	0.631	0.620	0.929

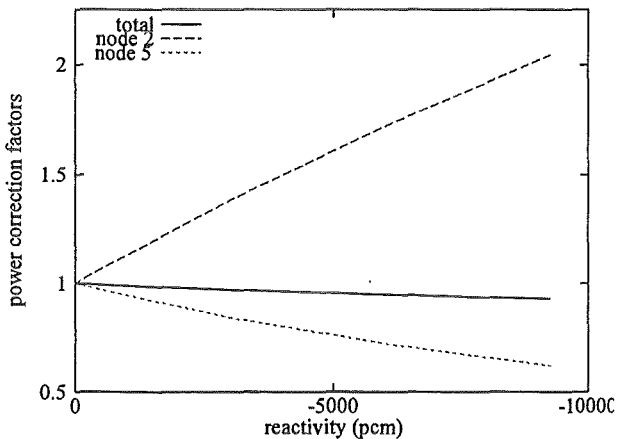


Fig. 5 "External" power correction factors for the core nodes and total power

The correction factors shown in Fig. 5 depend upon the reactivity level almost linearly. One may also conclude that there exists a location for which the correction factors are practically equal to unity (within the given reactivity range). If another time-independent weighting function is employed, this location may change. One may try, for example, to find a weighting function that would give closer to unity correction factors for the total power (try e. g. the unity weighting function instead of the adjoint one).

However, a ratio of two correction factors (at the same reactivity level) does not depend upon the weighting function. Therefore, an optimal - with respect to the total power - weighting procedure would give correction factors more deviating from unity (compared to Table 1) e.g. for node 2 (the hottest spot at most subcritical levels).

The results of Table 1 allow the following interpretation. Let us assume, for example, that the reactivity changes from -3050 pcm to -9241 pcm (i.e. introducing the external reactivity of about -20\$, here  $1\$\approx 345$  pcm), the transient is slow, and the source is constant. For a "zero-power" reactor (without feed-backs) the point-kinetics amplitude is decreased by about factor of 3. The point-kinetics option underestimates the power density at the end of the transient (in the following we do not take the decay heat into account) at node 1 by about 27% ( $1.294/1.765$ ). At node 2 (core mid-plane, near source) the power density is underestimated by about 32%. At node 3 (core, or ADS blanket, center) it is overestimated by about 13%; at node 4 (core mid-plane, right) it is overestimated by about 34%, at node 5 (lower right corner) it is overestimated by about 36%. The total power is overestimated by about 4.5%.

Using the quasistatic scheme and restricting the reactivity variation per shape step to 1\$ (we take only one of several available shape-step-control criteria for the reason of simplicity), one recalculates the shape about 20 times. Therefore, the maximum error (in power) reached at the end of each shape step would be about 20 times smaller than in the point-kinetics case. The average error (a half of the maximum error) in power production per each shape step

would be then about -0.7%, -0.8%, 0.3%, 0.8%, 0.9% at nodes 1 - 5 and about 0.1% in the total power.

If the reactivity changes from -3050 pcm to -100 pcm (i.e. introducing the external reactivity of about 10\$), the transient is slow, and the source is constant, the point-kinetics amplitude increases by a factor of 30. The power at node 1 is then overestimated by about 28%; at node 2 is overestimated by about 37%; at node 3 is underestimated by about 7%; at node 4 is underestimated by about 15%; at node 5 is underestimated by about 15%. The total power is underestimated by about 2.8%. If the quasistatic scheme is used with the same restriction of reactivity variation per shape step (of 1\$), at least 10 shape recalculations are performed. Average errors in power production per each shape step are (very roughly) then about 1.4%, 1.8%, -0.4%, -0.8%, -0.8% at nodes 1 – 5; and about 0.1% in the total power. These errors can be reduced: (for example, halved) by using a tighter reactivity variation limit per shape step (i.e. of 0.5\$).

One should remember that the above correction factors correspond to a particular reaction rate and a certain source location and energy spectrum (which approximates the spallation source). If, for example, the external source space-energy distribution is similar to the “precursor” source, the deviations of the correction factors from unity are (very roughly) about one order lower (for the same reactivity level) than shown in Table 1.

## 7. Application of correction factors for reactivity transients

In this section we analyze the results of two simplified (to make the analyses easier) transient SIMMER simulations caused by reactivity variations for the ADS shown in Fig. 4. The first transient is initiated by a postulated (forced by the user) variation of the fuel temperature from 900K to 3300K within a time interval of 1 s. The power distributions were computed by employing the point-kinetics (the shape recalculations were omitted) and quasistatic options, the results are shown in Fig. 6 for node 2, node 5 and for the total power.

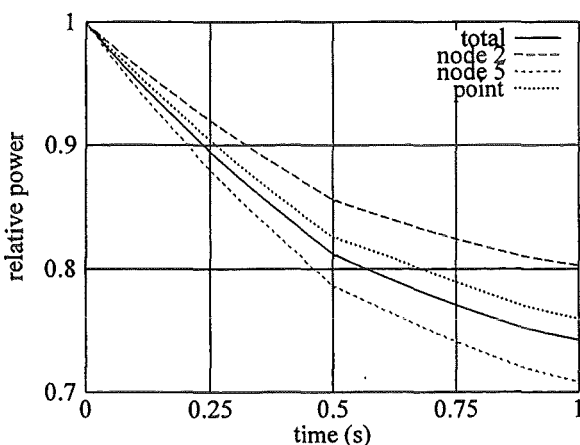


Fig. 6 “Fuel temperature variation” transient

The reactivity at  $t=0$  is about -2780 pcm. This is higher than -3050 pcm that corresponds to the nominal level with a higher in average fuel temperature. At  $t=1$  the reactivity is about -3755 pcm (the point and spatial kinetics models give slightly different values because during the transient the power distributions are different and therefore e.g. coolant temperature distributions differ). In the first row of Table 2 the ratios of power rates produced by the spatial and point-kinetics options are given.

At  $t=1$  the power density at node 2 is underestimated (by the point-kinetics option) by about 6%, at node 5 it is overestimated by about 7%, the total power is underestimated by about 2%. In the second row of Table 2 the “external” correction factor ratios obtained by

interpolating the values of Table 1 for the initial and final reactivity levels are given. They are in qualitative agreement with the power ratios of the first row. The correction factor ratios - computed at static conditions for two reactor states, with fuel temperature of 900K and 3300K - are given in the third row. They are naturally closer to the power ratios of the first row than the "external" correction factor ratios.

Certainly, exact agreement cannot be reached: the temperature and material distributions at  $t=1$  cannot be exactly reproduced at the initial stationary conditions for which the correction factors were computed. Besides, the transient is not very slow. Therefore the precursors are not in equilibrium with the fission source (we will address this problem later).

One can note that the "external" and "Doppler" correction factor ratios are in certain agreement. That means that the main reason for shape variations due to "Doppler" perturbations is a variation of the criticality level.

Table 2 Power rate and correction factor ratios for the "fuel temperature variation" transient

Ratio	node2	node5	total
Spatial kinetics to point-kinetics power at $t=1$	1.057	0.933	0.977
$f(-3755)/f(-2780)$	1.066	0.951	0.992
$f(t=3300K)/f(t=900K)$	1.056	0.937	0.991

As another example, in Fig. 7 one can see power curves (similarly to the previous case, the decay heat is ignored) for a transient caused by inserting the "external" reactivity into the Th/U ADS with the initial reactivity level of  $-3050$  pcm. The external reactivity increases linearly (with a rate of  $5100$  pcm/s) during the first time interval of  $0.5$  s, then remains constant for the same time interval, and then decreases linearly to zero.

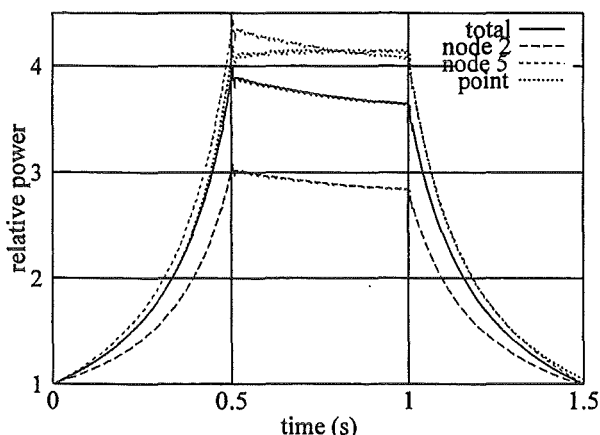


Fig. 7 "External reactivity" transient

In Table 3 the "spatial-to-point" ratios for  $t=0.5$  (row 1) are compared with the correction factor ratios (row 2). The major contribution to the difference is due to rather different reactivity levels ( $-557$  pcm and  $-495$  pcm) at  $t=0.5$  for the spatial and point models. The reactivity deviations are related to a significant error in transient power distribution at  $t < 0.5$  provided by the point model that gives rise to rather inaccurate material and temperature distributions for this model at  $t=0.5$

Thus, the correction factors should be applied permanently (at each thermal-hydraulics step) to properly take into account the reactor feedbacks. The figures presented in the last row include the factor that takes into account the mentioned reactivity deviations. Therefore better agreement with the "spatial-to-point" ratios is reached, but the remaining differences

are still significant (scaling the results cannot exclude completely the influence of different temperatures and densities).

Table 3 Power rate and correction factor ratios for the “external reactivity variation” transient

Ratio	node2	node5	total
Spatial kinetics to point-kinetics power at t=0.5	0.739	1.059	0.950
f(-495)/f(-3050)	0.766	1.158	1.025
The same as above, but divided by (557/495)	0.681	1.029	0.911

To make the situation more transparent (for validation of the correction factor technique) we rerun the case **without** taking into account the feedback effects (i.e. using constant macroscopic cross-sections and varying only the macroscopic “nubar” value to introduce the external reactivity). The reactivity ramp was slightly reduced to get a similar effective reactivity level at t=0.5 (that is about 534 pcm for this case).

The corresponding results show (in the first and second row of Table 4) much closer correspondence between the power and (obtained from Table 1) correction factor ratios. The remaining differences are related to non-equilibrium of the precursors. One may try to take this effect into account by assuming that the precursor source (with respect to the power shape) can be considered approximately equivalent to the fission source (we have mentioned above that the “precursor” correction factors are close to unity).

Table 4 Power rate and correction factor ratios for the “external reactivity variation” transient, without feedbacks

Ratio	node2	node5	total
Spatial kinetics to point-kinetics power at t≈0.5	0.797	1.138	1.024
f(-534)/f(-3050)	0.769	1.155	1.025
f(-781)/f(-3050)	0.792	1.140	1.022

Since at t=0.5 the precursor concentrations are not in equilibrium, one can try to find an “equivalent” (with respect to the contribution of the delayed and prompt fission neutrons to the total neutron source) reactivity value, for which the correction factors should be interpolated. In this case the initial to final reactivity ratio is about 5.712. The final to initial total power ratio is about 3.907. The difference is related to smaller precursor and (corresponding to the precursors) prompt fission sources. Therefore, the total (delayed and prompt) fission source corresponds to a reactivity level of  $(534 \cdot 5.712 / 3.907 =) 781$  pcm. Since we decide not to distinguish between the delayed and prompt fission sources (with respect to the correction factors), one should use at t=0.5 the correction factor interpolated for 781 pcm. The corresponding ratios are given in the last row of Table 4. They are in rather good agreement with the power ratios of row 1 thus giving a proof of the correctness of our technique (minor differences are probably related to interpolation errors and numerical errors related to the transient simulation). The point-kinetics option overestimates the power at node 2 by about 25%, overestimates it at node 5 by about 12% and in total by about 2%.

An interesting question is whether for all perturbations of interest the same “external” correction factors can ameliorate the point-kinetics model performance. For this ADS model we have observed that the “external correction factors” can improve the situation significantly if the fuel temperature changes while all other reactor parameters remain unchanged (i.e. if only the Doppler effect feedback is important).

The differences between “external” and “real” (i.e. computed for real perturbations) correction factors for “voided” states (obtained due to voiding of the whole core and core sub-regions) are significantly larger than for the Doppler case. However, the deviations of the factors from unity are of the same order. Therefore, our rough estimations of the performance of the quasistatic option (made at the end of the previous section) are valid for all types of perturbations in this ADS model. For correcting the point-kinetics results in the general case, one should use several tables that would describe sufficiently accurately all possible perturbed configurations. Therefore, for analyzing severe transients in ADSs, which involve gross core material configuration changes, one can hardly avoid using of space-time kinetics methods, this holds similarly for critical reactor systems.

### 8. Application of correction factors for slow source transients

For a few seconds the precursor term in Eq. (1) can be considered as an “external-like” source (with an appropriate efficiency). If the transient is not too slow, a relative ratio of the “precursor” source to the external one may deviate significantly from the corresponding steady-state value. That makes using of the correction factors technique a little bit tricky (as in the last case). To make this using simpler, one can split the total flux into the “prompt” and “delayed” components. The corresponding equations are as follows:

$$\frac{1}{v} \frac{\partial \Phi_p}{\partial t} + M(t) \Phi_p(x, t) = (1 - \beta) \chi_p F(t) \Phi_p(x, t) + Q(x, t), \quad (34)$$

$$\frac{\partial C_p(x, t)}{\partial t} = \beta F(t) \Phi_p(x, t) - \lambda C_p(x, t). \quad (35)$$

$$\frac{1}{v} \frac{\partial \Phi_d}{\partial t} + M(t) \Phi_d(x, t) = (1 - \beta) \chi_p F(t) \Phi_d(x, t) + \chi_d \lambda C_d(x, t) + \chi_d \lambda C_p(x, t), \quad (36)$$

$$\frac{\partial C_d(x, t)}{\partial t} = \beta F(t) \Phi_d(x, t) - \lambda C_d(x, t), \quad (37)$$

Eq. (34) can be solved independently from Eqs. (35) – (37) if the cross-sections are known. Then the “prompt” precursor concentrations can be found from Eq. (35) (since the “prompt” flux is already known) and can be used as an “artificial” external source in Eq. (36). Space-time factorization can be applied to Eqs. (34)- (35) and to Eqs. (36) – (37) separately:

$$\Phi(x, t) = N_p \psi_p(x, t) + N_d \psi_d(x, t), \quad (38)$$

The correction factors can be computed separately for these two flux components. For the delayed flux component, the factors are certainly close to unity. Therefore, for some transients (if reactivity is constant), it may be sufficient to take into account only the difference between the “prompt” and “total” flux shapes by using “external” correction factors.

To give an illustration, let us consider relatively slow harmonic source oscillations (without feedbacks):

$$q(t) = q + \Delta q \sin(\omega t), \quad (39)$$

$$\lambda \ll \omega \ll \frac{\rho - \beta_{\text{eff}}}{\Lambda}. \quad (40)$$

Following (Carta, 1999) one obtains that the point-kinetics option gives the (maximum) amplitude “deviation-to-average” ratio as

$$\frac{\Delta N}{N} \approx \frac{\rho}{\rho - \beta_{\text{eff}}} \frac{\Delta q}{q}. \quad (41)$$

To take into account spatial kinetics effects without transient shape recalculations, it was proposed (Carta, 1999) that at any time  $t$  the solution  $\Phi$  may be expanded in terms of the flux eigenfunctions (of a homogeneous time-independent problem) which are assumed to form a complete basis. In this section we suggest an alternative way of solving this problem.

Let us employ the two-shape model. Following (Carta, 1999), one can easily get that

$$\frac{\Delta N_p}{N_p} = \frac{\Delta q}{q}. \quad (42)$$

The corresponding ratio for the delayed amplitude is approximately equal to zero. Therefore

$$\Phi(x, t) \sim \psi_p(x) + \psi_d(x) + \frac{\Delta q}{q} \psi_p(x) \sin(\omega t) = \psi(x) + \frac{\Delta q}{q} \psi_p(x) \sin(\omega t), \quad (43)$$

the corresponding shapes being defined at steady-state conditions. A reaction rate related to the “prompt” shape can be approximately calculated as a product of (1) the rate related to the “total” shape, (2) a ratio of the actual and reduced (by effective delayed neutron fraction) reactivity values, and (3) an inverse ratio of the “external” correction factors at these values. Therefore for relatively slow harmonic source oscillations, the relative reaction rate variations calculated on the basis of the point kinetics model should be multiplied by the mentioned inverse ratio of the correction factors.

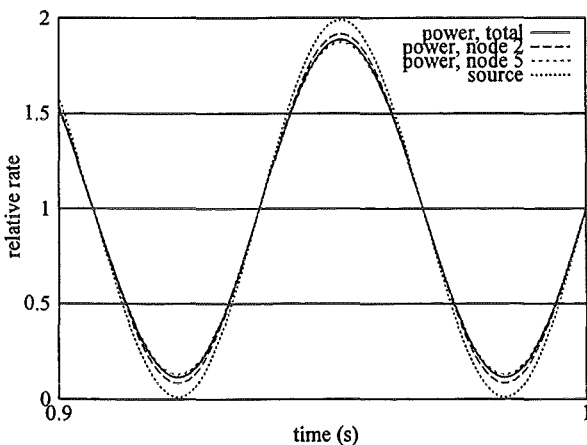


Fig. 8 Slow harmonic source oscillations

Let us consider a numerical example. For the ADS model (shown in Fig. 4) we evaluate the spatial kinetics effects for power production in nodes 2, 5 and in total. We simulate the source oscillation with a frequency of 16 Hz and  $\Delta q/q=0.99$ . The results are presented in Fig. 8. The corresponding relative power variation (spatial kinetics) to amplitude variation (point-kinetics) ratios and (interpolated from Table 1) correction factor ratios are given in Table 5 and show good agreement.

Table 5 Power rate and correction factor ratios for the slow harmonic source oscillations

Ratio	node2	node5	total
$(\Delta P/P)_{\text{spatial}}/(\Delta N/N)_{\text{point}}$ at $t \approx 0.953$	1.028	0.980	0.995
$f(-3050-345)/f(-3050)$	1.028	0.984	0.997

### 9. Prompt mode expansion method for fast transients related to beam trips

Until now we could neglect the first (time derivative) term in the left-hand part of Eq. (1). For simulating short fast beam-trip induced transients taking into account this term is important, while the cross-sections and precursor concentrations may be considered constant. If  $M$  and  $F$  are time-independent (i.e. time-dependence is restricted to  $Q$  and  $\Phi$ ), one can rewrite Eq. (34) as

$$L\Phi_p(x,t) = Q(x,t) + \partial L\Phi_p(x,t), \quad (44)$$

where  $L$  and  $\partial L$  are linear operators:

$$L = M - (1 - \beta)\chi_p F, \quad (45)$$

$$\partial L = -\frac{1}{v} \frac{\partial}{\partial t}. \quad (46)$$

One can split the "prompt" flux:

$$\Phi_p(x,t) = \Phi_0(x,t) + \tilde{\Phi}_1(x,t), \quad (47)$$

in a way that Eq. (44) is split into

$$L\Phi_0(x,t) = Q(x,t), \quad (48)$$

$$L\Phi_{1,a}(x,t) = \partial L\Phi_0(x,t) + \partial L\tilde{\Phi}_1(x,t). \quad (49)$$

Repeating the procedure several times yields

$$\Phi_p(x,t) = \Phi_0(x,t) + \Phi_1(x,t) + \Phi_2(x,t) + \Phi_3(x,t) + \dots + \Phi_n(x,t) + \tilde{\Phi}_{n+1}(x,t), \quad (50)$$

where

$$L\Phi_{i+1}(x,t) = \partial L\Phi_i(x,t), \quad i = 0, 1, 2, \dots, n-1, \quad (51)$$

$$L\Phi_{n+1,a}(x,t) = \partial L\Phi_n(x,t) + \partial L\tilde{\Phi}_{n+1}(x,t). \quad (52)$$

If Eq. (19) is valid and the source amplitude,  $q(t)$ , has  $n+1$  continuous derivatives, then

$$\Phi_p(x,t) = q(t)\psi_0(x) - q'(t)\psi_1(x) + q''(t)\psi_2(x) + \dots + (-1)^n q^{(n)}(t)\psi_n(x) + \tilde{\Phi}_{n+1}(x,t) \quad (53)$$

where

$$L\psi_0(x) = Q(x,0), \quad (54)$$

$$L\psi_{i+1}(x) = \frac{1}{v}\psi_i(x), i = 0, 1, 2, \dots, n-1, \quad (55)$$

$$\frac{1}{v}\frac{\partial}{\partial t}\tilde{\Phi}_{n+1}(x,t) + L\tilde{\Phi}_{n+1}(x,t) = (-1)^{n+1}q^{(n+1)}(t)\frac{1}{v}\psi_n(x). \quad (56)$$

Eq. (56) has the same structure as Eq. (3). However solving of Eqs. (54) – (56) may be preferable (compared to Eq. (3)) in some cases. We discuss these cases later.

By integrating Eq. (55) over the phase-space (with a weighting function) one obtains expressions “resembling” reactivity (left-hand side) and generation time (right-hand side). Therefore if the shapes  $\psi_i(x)$  and  $\psi_{i+1}(x)$  do not differ too much, their amplitudes ratio is close to the reactivity-to-generation-time ratio (that is  $\alpha$ ). Thus the right-hand part of Eq. (53) should converge faster for lower  $k_{\text{eff}}$  values.

Employing Eqs. (54) – (56) one obtains for fast harmonic oscillations (see Eq. (39)) that the prompt flux can be expanded (convergence criteria are not discussed here) as:

$$\begin{aligned} \Phi_p(x,t) = & q\psi_0(x) + \Delta q \sin(\omega t) \{ \psi_0(x) - \omega^2\psi_2(x) + \omega^2\psi_4(x) - \dots \} + \\ & \Delta q \cos(\omega t) \{ -\omega\psi_1(x) + \omega^3\psi_3(x) - \omega^5\psi_5(x) - \dots \} \end{aligned} \quad (57)$$

Another interesting example is the case when the source amplitude is constant before  $t=0$  and then starts to increase linearly. Let  $n=1$  in Eqs. (54) – (56). Then for  $t>0$

$$\Phi_p(x,t) = q(t)\psi_0(x) - q'(t)\psi_1(x) + \tilde{\Phi}_2(x,t) \quad (58)$$

$$\frac{1}{v}\frac{\partial}{\partial t}\tilde{\Phi}_2(x,t) + L\tilde{\Phi}_2(x,t) = q^{(2)}(t)\frac{1}{v}\psi_1(x). \quad (59)$$

Integrating Eq. (59) for a very small time interval  $(0,\varepsilon)$  and taking into account that  $\tilde{\Phi}_2(x,-0) = 0$  yields (hereafter one should consider generalized functions and derivatives, one can avoid it by considering very small “interface” time intervals where the “steps” and “delta-functions” can be replaced by “normal” functions)

$$\frac{1}{v}\tilde{\Phi}_2(x,\varepsilon) + \int_0^\varepsilon L\tilde{\Phi}_2(x,t)dt = q^{(1)}(\varepsilon)\frac{1}{v}\psi_1(x). \quad (60)$$

Since  $\varepsilon$  is very small, the integral in the left-hand part of Eq. (60) can be neglected:

$$\tilde{\Phi}_2(x,\varepsilon) = q'(\varepsilon)\psi_1(x). \quad (61)$$

For  $t>\varepsilon$  the right hand part of Eq. (60) is equal to zero. Since  $\varepsilon$  is arbitrary, one has for  $t>0$

$$\tilde{\Phi}_2(x,t) = G(x,t) * q'(\varepsilon), \quad (62)$$

where

$$\frac{1}{v} \frac{\partial}{\partial t} G(x,t) + LG(x,t) = (1 - H(t)) \frac{1}{v} \psi_0(x). \quad (63)$$

$H(t)$  is the unit step (Heaviside) function ( $H(t)=0$  at  $t \leq 0$ ,  $H(t)=1$  at  $t > 0$ ). The above equation defines  $G(x,t)$  for all values of  $t$ . It is obvious that for  $t \leq 0$  one has:  $G(x,t) = \psi_1(x)$ .

If the  $\alpha$ -eigenfunctions form a full basis (in a certain space of functions to which  $G(x,t)$  belongs), one has for  $t > 0$

$$G(x,t) = \sum_i c_i(x) \exp(\alpha_i t). \quad (64)$$

If only one exponent dominates and the other ones can be neglected, for  $t > 0$

$$G(x,t) \approx \exp(\alpha_0 t) \psi_1(x), \quad (65)$$

therefore

$$\Phi_p(x,t) \approx q(t) \psi_0(x) - q'(+0)(1 - \exp(\alpha_0 t)) \psi_1(x). \quad (66)$$

If all exponents should be taken into account,

$$\Phi_p(x,t) = q(t) \psi_0(x) + q'(+0) \{G(x,t) - \psi_1(x)\}. \quad (67)$$

$G(x,t)$  can be seen as a decay trace of the first prompt mode  $\psi_1(x)$  after shut-down of the "source" (see the right-hand part of Eq. (63)). For computing  $G(x,t)$  one can specify a very short time interval during which the source term is switched off. One can also note that the "fraction" of higher  $\alpha$ -eigenfunctions should be smaller in  $G(x,0)$  than in  $\Phi(x,0)$  due to another source term.

It is interesting to note that  $G(x,t)$  can be considered as a kind of Green's function in the sense that it can be used to describe any source induced transient without solving any kinetics equation (just assuming constant cross-sections): if  $q(t)$  in Eq. (19) can be represented as a piecewise linear function (the source amplitude derivative changes at  $t=0$ ,  $t_1$ ,  $t_2$ , ...):

$$q(t) = q(0) + q'(+0) \max(t,0) + (q'(+t_1) - q'(+0)) \max(t - t_1, 0) + (q'(+t_2) - q'(+t_1)) \max(t - t_2, 0) + \dots \quad (68)$$

then

$$\Phi_p(x,t) = q(t) \psi_0(x) + q'(+0) \{G(x,t) - \psi_1(x)\} + (q'(+t_1) - q'(+0)) \{G(x,t - t_1) - \psi_1(x)\} + (q'(+t_2) - q'(+t_1)) \{G(x,t - t_2) - \psi_1(x)\} + \dots \quad (69)$$

## 10. Application of the prompt mode expansion method

To give a numerical example, we analyzed a beam-trip transient for a model shown in Fig.9.

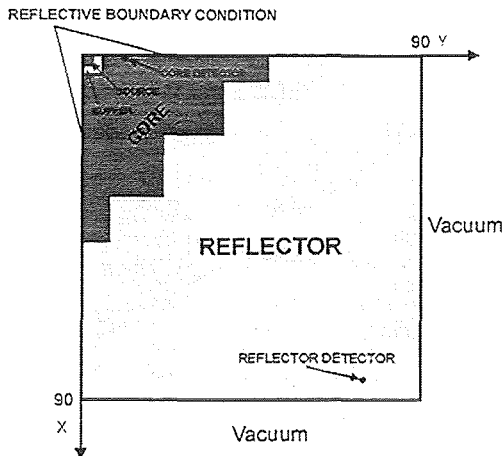


Fig. 9 2D XY model

The reactivity is about -4500 pcm. This is a quite simplified model of an experimental fast system (Salvatores, 1996). More accurate 3D models of this system are currently used in Cadarache for simulating beam-trip transients (Aliberti, 2001). We have observed that many phenomena are similar in these 2D and 3D models. In the following we will show some results of using the prompt mode expansion method.

We solved Eq. (34) by employing the prompt mode expansion technique and standard KIN3D options.

While using standard options, the fission source is multiplied by a factor of  $1-\beta$ , the delayed neutron fractions are assumed to be zero, and the prompt fission spectrum is the same as the fission spectrum. The last approximation (for the prompt fission spectrum) is not completely accurate, but introducing the same approximation for the new and standard options does not influence possible deviations between them.

To investigate the "prompt mode" properties, we computed first 10 functions  $\psi_i(x)$  by solving Eqs. (54), (55) with VARIANT/KIN3D (only even-parity components of the right-hand part of Eq. (55) were taken into account). Then we computed corresponding detector rates (by integrating the products of these modes and U-235 fission cross-sections) for two detectors shown in Fig. 9. The ("core" and "reflector") detector rate ratios related to two subsequent modes are plotted in Fig. 10 together with the corresponding absolute reciprocal  $\alpha$  (prompt reactor period) values. These values were obtained by substituting  $\psi_i(x)$  (instead of  $\Phi$ ) into Eq. (18). Then we computed the reactivity to generation time ratios. The ("core" and "reflector") detector rate ratios and the prompt reactor period values show (in Fig. 10) a tendency to converge to the same limit that - according to the theory - is the absolute reciprocal  $\alpha_0$  value. Certainly, if we used the  $\alpha$ -adjoint, the prompt period in Fig. 10 would be close to a constant. or the same 2D XY model we also computed the  $G(x,t)$  functions in two ways: numerically (by solving Eq. (63) with KIN3D) and analytically (according to Eq. (65), using asymptotic  $\alpha_0$ ). The corresponding detector rates are shown in Fig. 11. One can see that the derivative for the core detector rate is quite different from the corresponding analytical value at the very beginning, but, after some time, approaches this value earlier than that one related to the reflector detector (in correspondence with the results shown in Fig. 10).

If  $q(t)$  varies linearly from  $q(0)=1$  to  $q(T)$  and then back to  $q(2T) = 1$  (so that the  $q(t)$  plot would resemble a saw-tooth), one may get from Eq. (69) that

$$\Phi_p(x,t) = s(t)\psi_0(x) + q'(t) \{G(x,t) - 2G(x,t-T) + G(x,t-2T)\} \quad (70)$$

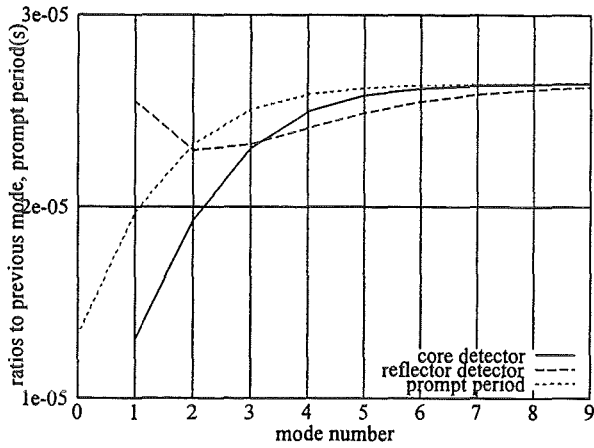


Fig. 10 Detector rate (corresponding to modes) ratios for two subsequent modes, reciprocal  $\alpha$  (prompt reactor period) values

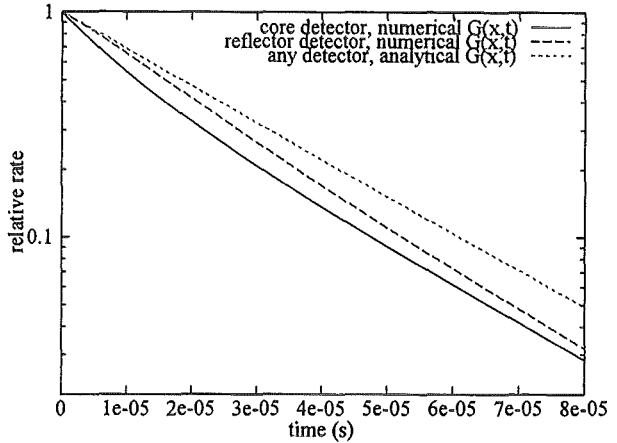


Fig. 12 Beam-trip transient

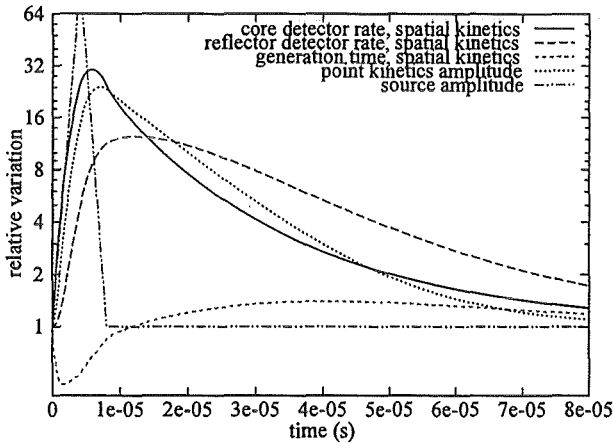


Fig. 11 detector rates corresponding to numerical and analytical g-functions

An example is given in Fig. 12. The core and reflector detector rates were computed with the spatial and point-kinetics options. The source amplitude is shown to  $(q(T)=100, T=4e-6)$ . The pronounced deviations between spatial and point-kinetics rates are related to the "derivative" term of Eq. (44) that can be seen as a component of the "total" external source. One can also see appreciable variations (reflecting different neutron lifetimes in the core and reflector regions) of the transient mean generation time.

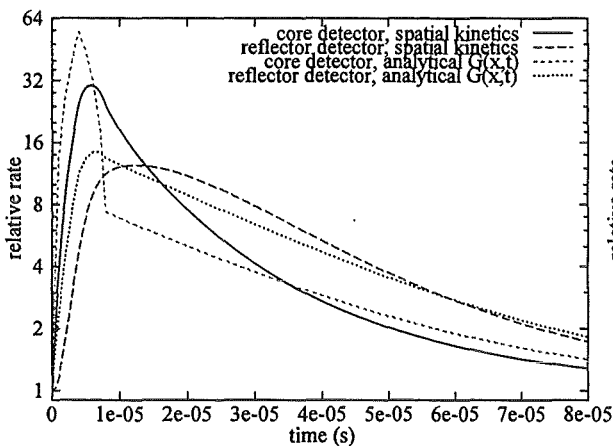


Fig. 13 Reference and computed with "analytical" G-functions detector rates.

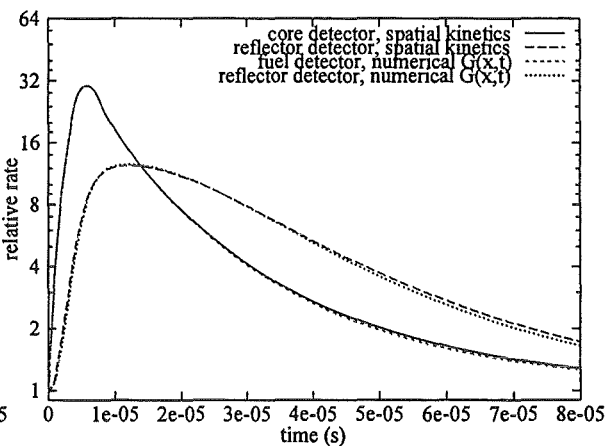


Fig. 14 Reference and computed with "numerical" G-functions detector rates

In Figs. 13 and 14 the detector rates - computed according to Eq. (70), with "analytical" and "numerical" functions  $G(x,t)$  - are shown and compared with the corresponding spatial kinetics (reference) results. The curves related to "analytical"  $G(x,t)$  already give a feeling about possible differences between the core and reflector detector rates, but cannot

reproduce the reference results. The curves related to the “numerical” functions  $G(x,t)$  are very close to the reference results.

To get these reference results, we had to employ rather fine time steps. That made difficult using of higher (than diffusion) angular approximation for routine analyses of the considered and similar (Aliberti, 2001) cases. The prompt mode expansion technique may facilitate the corresponding computations.

## 11. Conclusion

The traditional point-kinetics model may give rather inaccurate transient reaction rates in an ADS even if the material configuration does not change significantly. This is not related to the problem of choosing a “right” weighting function: the point-kinetics model with any weighting function cannot take into account pronounced flux shape variations related to possible significant changes in the criticality level or to fast beam trips.

To improve the accuracy of the point-kinetics option for slow transients, we have introduced a correction factor technique. The related analyses give a better understanding of “long-time-scale” kinetics phenomena in the subcritical domain and help to evaluate the performance of the quasistatic scheme. Though the performance of point-kinetics can be insufficient in the subcritical case, the quasistatic approach is still valid if the shape steps are chosen properly. It is worthwhile to mention that in combination with properly computed correction factor tables, one can use the reactivity and power distributions obtained for “critical” reactor models; this approach can simplify ADS-related application of conventional accident analyses codes (developed in the past for transient analyses of critical reactors).

For simulating fast beam-trip induced transients we have presented a prompt mode expansion method that offers an option to avoid solving the kinetics equations by using instead pre-computed Green’s-like functions. We had to employ, however, rather fine time steps for related spatial kinetics analyses that made difficult using of higher (than diffusion) angular approximations. In the future we will consider possible implementations of the proposed prompt mode expansion method as well as other known ways for accelerating the routine spatial kinetics computations based on the transport option of VARIANT/KIN3D.

The developed fast “simple” (without flux/shape recalculations during the transient) techniques are in good agreement with more general spatial kinetics schemes of SIMMER and KIN3D. That proves that the performance of these schemes for the analyzed cases is acceptable (though optimizations are possible) and offers new options for employing simple kinetics models in ADS transient analyses.

## ACKNOWLEDGMENTS

The authors thank Dr. E. Kiefhaber/FZK for useful suggestions and comments.

## 12. References

- Alcouffe, R. et al.: DANTSYS: A Diffusion Accelerated Neutral Particle Transport Code System, LA-12969, USA (1995)
- Aliberti, G., Rimpault G., Private communication (2001)
- Buckel, G., Hesselschwerdt E., Kiefhaber E., Kleinheins, S., Maschek W., A new SIMMER-III version with improved neutronics solution algorithms, FZKA 6290 (1999)
- Carta, M. and D'Angelo, A. Subcriticality-Level Evaluation in Accelerator-Driven Systems by Harmonic Modulation of External Source, *Nucl. Sci. Eng.* 133, 282
- Doriath, J. Y., McCallien, C. W., Kiefhaber, E., Wehmann, U., Rieunier, J.M., "ERANOS 1: The Advanced European System of Codes for Reactor Physics Calculations", Proc. Int. Conf., Karlsruhe, (1993).
- Kiefhaber, E., Private communication (1999)
- Kondo, S., Morita, K., Tobita Y., Shirakawa, N., SIMMER-III : An Advanced Computer Program for LMFBR Severe Accident Analysis, ANP'92, Tokyo, Japan (1992)
- Lewis, E.E., Carrico, C.B., Palmiotti, G., 1996. Variational Nodal Formulation for the Spherical Harmonics Equations. *Nucl. Sci. Eng.* 122, 194
- Maschek, W., Rineiski, A., Morita, K., Kiefhaber, E., et al., SIMMER-III, a Code for Analyzing Transients and Accidents in Accelerator Driven Systems (ADS), AccApp'00, Washington D.C., USA (2000)
- Maschek, W., Rineiski, A., et al., Safety Improvements for ADS Transmuters with Dedicated Fuel, submitted to AccApp'01, Reno, USA (2001)
- Ott, K., et al.: Introductory Nuclear Reactor Dynamics, La Grange Park, IL, USA (1985)
- Rineiski, A., Doriath J.Y., 1997. Time-Dependent Neutron Transport with Variational Nodal Method, Proc. Joint Int. Conf. on Math. Methods and Supercomputing for Nuclear Applications, Saratoga Springs, New York, p. 1661
- Rineiski, A., Kiefhaber, E., Merk, B., Maschek, W., Flad, M., Neutron Kinetics Developments of the SIMMER-III Safety Code for ADS Application, OECD/NEA Workshop on the Utilization and Reliability of High Power Proton Accelerators, Aix-en-Provence, France (1999)
- Rineiski, A., Maschek, W., Proposal of a Kinetics / Dynamics Benchmark for ADS, TCM, ANL, USA, Nov/Dec 2000
- Salvatores, M., Martini, M., Slessarev, I., Soule, R. et al., "MUSE-1: A First Experiment at MASURCA to Validate the Physics of Sub-Critical Multiplying Systems Relevant to ADS", Proc 2nd Int. Conf on ADTTA, Kalmar, Sweden, Vol 1, p 513 (1996)

### III. Improvements in the SIMMER-III/IV Neutronics Module

(G. Buckel, E. Kiefhaber, A. Rineiski, W. Götzmann, IKET)

The neutronics part of SIMMER has been further improved following the standard procedures established in the past for producing a new code version. Recent extensions, model upgrades and corrections developed at FZK were sent to the Japanese partner JNC for inclusion into the new SIMMER III version 2J. JNC integrates the changes into the overall code framework, checks the formal correctness and compatibility to various computer systems and, finally, tests the newly prepared SIMMER version by means of a set of well-established model problems.

During the tests of the latest correction sets that were sent by FZK some difficulties were observed at JNC in SIMMER version S3-T2 (2D - SIMMER and 2D neutronics part based on TWODANT) during the convergence process in a typical LWR-problem (STN-LWR) which so far was not available at FZK. Similar types of convergence difficulties have been observed during the preparation of the extension of the SIMMER neutronics part from two to three spatial dimensions when replacing the 2D-code TWODANT by the 3D-code THREEDANT of the program system DANTSYS. Such problems appeared using the international benchmarks KRITZ-2:19 and C5G7MOX considering neutron upscattering in big moderator regions outside the core zones.

These difficulties have been investigated more carefully using the stand-alone versions of the computer codes TWODANT/THREEDANT in order to extend the future applications of S3-T2 and S4-T3 (3D-SIMMER and 3D-neutronics part based on THREEDANT) and to enable an efficient treatment of such problems. The difficulties could be completely removed by substantial improved adaptations of the interval sizes in the mesh grids and by some carefully directed revisions of the program flow. In that way an operational version of S3-T2 and an upgraded version of THREEDANT could be established.

Some parameters that are essential for controlling the iteration processes are fixed empirically. They direct the transfer from the so-called inner iterations for the solution

of the calculations of the neutron fluxes within the energy groups to the outer iterations for the solution of the total system (power distribution and criticality factor). For this purpose the convergence criteria are successively refined during the iteration process until the values given by the user in the input are achieved. In addition, the allowed number of inner iterations during an outer is intentionally kept very small and is only slightly increased until the end of the iteration process when the desired accuracy is nearly achieved. Several acceleration procedures also interfere in this continuous interplay of inner/outer iterations. The so-called dsa (diffusion synthetic acceleration) is characteristic for the codes of the DANTSYS family. With this method the solution of the neutron transport equation in the inner iteration for the energy-group- and angular-dependent neutron fluxes will be accelerated by inserting solutions of the less computing time consuming, problem-adjusted neutron diffusion equation for the angular independent neutron flux. The necessary coefficients are calculated by using the available angular neutron fluxes. In the so-called outer iteration, a new neutron source distribution is calculated for application in the following outer iteration by using the neutron fluxes of all energy groups that have been determined in the inner iterations. The calculation of this neutron source distribution is additionally accelerated by further diffusion calculations (so-called sub-outers) in order to provide an improved spatial- and energy-dependent neutron flux distribution. At the beginning of the iteration process a fairly exact solution of the accompanying neutron diffusion equation does not lead to a significant advantage as long as the coefficients from the neutron transport equation are rather inaccurate especially in problems with neutron upscattering. Therefore, a modified iteration strategy has been developed for those problems. The number of allowed diffusion iterations is increased appropriately during the calculation.

Convergence could be achieved in all investigated cases by a suitable choice of the empirically fixed parameters and the formulation of proper decision criteria. In some cases, a considerable gain of computing time could be obtained, too, compared to cases using the standard iteration strategy.

## II. Erstellung einer neuen Referenzversion des Programms SAS4A

(D. Struwe, W. Pfrang, W. Zimmerer, IRS)

Die Sicherheitsuntersuchungen zu Kernen mit Aktinidenanteil und Flüssigmetallkühlung werden mit dem Programm SAS4A durchgeführt, das in internationaler Zusammenarbeit mit dem französischen IPSN, dem japanischen JNC und dem amerikanischen ANL entwickelt wird. Anfang 2002 wurde von dem japanischen JNC als derzeitigem Programm-Manager der internationalen Programmentwicklung eine neue Referenzversion des Programms SAS4A erstellt. Diese Programmversion wurde durch weiterführende Modellverbesserungen und Fehlerkorrekturen ergänzt, die im Forschungszentrum Karlsruhe entwickelt wurden. Die derart erweiterte Programmversion wurde durch Nachrechnung einer Vielzahl von Experimenten der unterschiedlichen CABRI Programme erneut experimentell qualifiziert.

Die so erweiterten Programmversion bildete die Grundlage dafür, eine Reihe von Entwurfsmerkmalen fortgeschrittener Kernentwurfsvarianten zu untersuchen mit dem Ziel, die Auswirkungen kernzerstörender Unfälle in der Einleitungsphase des Störfalls zu begrenzen. Im besonderen wurde die Auswirkung von unterschiedlichen Auslegungen der Spaltgasplena und der Brennstabtablettchen auf den Unfallverlauf eines unkontrollierten Kühlmitteldurchsatzstörfalls analysiert. Es konnte gezeigt werden, dass es von Vorteil ist, sowohl im aktiven Kernbereich als auch im Brutmantelbereich Hohltabletten zu verwenden, und dass es in gleicher Weise von Vorteil ist, das obere Spaltgasplenum klein zu halten.

### 32.23.04 Bestrahlungsexperimente zur Transmutation von Actiniden im HFR

(H. Plitz, NUKLEAR)

FZK is participating in the international CAPRA programme where the main objective is to evaluate the best possibilities in nuclear technology to burn plutonium and to burn or transmute long-living actinides. An enrichment of up to 45 % plutonium was chosen to remain compatible with current fuel cycle technology (dry route fabrication Purex process).

In order to demonstrate the good performance of such a CAPRA mixed oxide fuel pin an irradiation programme has been launched. The High Flux Reactor (HFR) at Petten (NL) was chosen to perform an experimental irradiation programme within specially designed irradiation devices called TRABANT (Transmutation And Burning of Actinides iN TRIOX) which can contain 3 fuel pins which are independently cooled.

In cooperation with the Commissariat à l'Energie Atomique (CEA), Forschungszentrum Karlsruhe and the Institute for Transuranium Elements (ITU), the TRABANT 1 three fuel pins have been designed, specified and manufactured and irradiated in the core of the HFR.

The failure of pin 1/1 has been traced back to local overpower conditions caused by evaporation/condensation processes of Pu in the central channel of the hollow fuel column, leading to a local increase of Pu and thus to overpower conditions and lastly to clad failure /1/. But in spite of this pin 11 defect, it has been concluded that the CAPRA reference fuel pin concept is feasible and in consequence another irradiation experiment TRABANT 2 was decided, aiming at lower heat ratings during irradiation, however.

The TRABANT 2 irradiation vehicle was ordered early in 1998. 3 CAPRA type pins, all with annular pellets, were manufactured at ITU, using both mechanical mixing (MM) of powders and the SOL-GEL method. The main data are given in Table I.

**Table I: Fuels prepared for the TRABANT2 irradiation experiment**

Pin No.	Fuel	Fabrication Process	Pu content Pu / (U+Pu)	O/M	Density (% t.d.)
2/1	(U,Pu)O <sub>2</sub>	MM	0.40	1.971	94.18
2/2	(U,Pu)O <sub>2</sub>	MM	0.40	1.995	93.40
2/3	(U,Pu)O <sub>2</sub>	SOL-GEL	0.45	1.990	86.36

The MM (mechanical mixing of powders) process is commonly used at CEA Cadarache, but the hybrid SOL-GEL process has some advantages /2/. Unlike the MM route the SOL-GEL route ensures the formation of an ideal solid solution.

The transport of these TRABANT 2 fuel pins was rather delayed. As pin 2/3 has a low fuel density and thus a poor thermal conductivity leading to high fuel temperature, it was decided to mount only the pins 2/1 and 2/2 into the TRABANT 2 capsule in autumn 2000. Due to various circumstances the irradiation of TRABANT 2 started late on 30 November 2001 with max. linear powers in the range of 410-425 W/cm. This will be kept for some reactor cycles.

Another fuel pin is being specified for manufacturing at ITU. The irradiation of this new fuel pin may start mid 2002 in the third (free) leg of the TRIOX-TRABANT 2 capsule. This new fuel pin will consist of two solid pellet columns, one half pin column in ZrO<sub>2</sub> matrix, yttrium stabilized with 1.1 g Pu/cm<sup>3</sup> homogeneously distributed, and another half pin column with Fe-based CERMET fuel.

## References

- /1/ E. Picard, H. Noirot, H. Plitz  
High Plutonium Content Oxide Fuel for Pu Burning in Fast Reactors. CAPRA Irradiation Programme and First In-pile Experimental Results.  
Global '97, Oct. 5-10, 1997, Yokohama, Japan, Proc. Vol. 1, 528-536.
- /2/ P. Gerontopolous, C. Cogliati, K. Richter  
Nuclear Power Option for the World.  
Trans SNS, 31(1979) 175d.

### **32.23.05 Untersuchungen zu Beschleuniger getriebenen, unterkritischen Anordnungen (ADS)**

#### **Abstract**

Transmutation is considered a promising technology worldwide for significantly reducing the amount and, thereby, the long-term radiotoxicity of high active waste (HAW) produced by the operation of nuclear power plants such as light water reactors (LWR). The maximum reduction of radiotoxicity could be by a factor of about 100. Transmutation is thus an alternative to the direct deposition of large volumes of highly radioactive waste. Transmutation presents the possibility of closing the fuel cycle including the minor actinides. Plutonium, minor actinides and long-lived fission products can be transmuted in a so called Accelerator Driven Sub-critical System (ADS), which consists of an accelerator, a target module and a subcritical blanket.

This article describes the work performed at Forschungszentrum Karlsruhe which is critically evaluating an ADS mainly with respect to its potential for transmuting minor actinides, to its feasibility and to safety aspects. The work is being done in the area of core design, neutronics, safety, system analyses, materials and corrosion.

An accelerator driven system (ADS) consists of three main parts: an accelerator for primary particles (protons), a spallation target (or target module) in which the protons produce free nucleons (neutrons) in a spallation reaction (external neutron source), and a subcritical blanket in which, first, the fission reaction, producing fission neutrons (internal neutron source) and thermal energy, and second, the transmutation reaction occur. The protons are injected into the spallation target through a vacuum beam pipe, the beam pipe being closed by a window at the end. The target is a heavy liquid metal (e.g. lead Pb or eutectic lead-bismuth Pb-Bi). The spallation neutrons produced in the spallation target are completely independent of the subcritical blanket. A shut-down of the accelerator or an interruption of the proton beam immediately stops the fission reaction. Safety aspects of such a subcritical system are discussed in 32.23.03. A sketch of an ADS is given in the figure below.

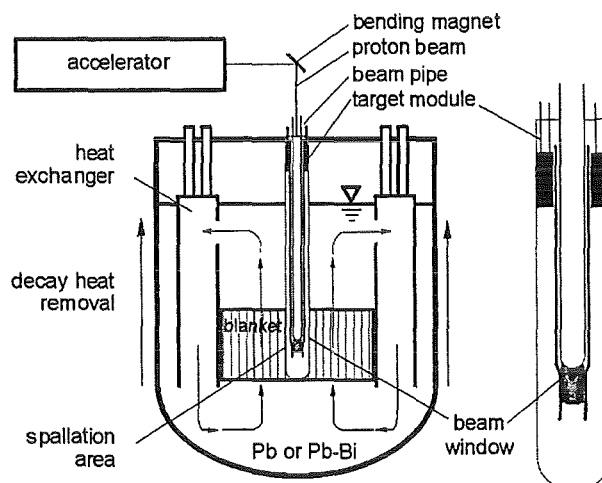
#### **Kurzfassung**

Transmutation wird weltweit als eine vielversprechende Technologie angesehen, um die Menge und gleichzeitig die Langzeitradiotoxizität des hochradioaktiven Abfalls, der beim Betrieb von Kernkraftwerken entsteht, entscheidend zu verringern. Die

maximale Verringerung ist etwa um den Faktor 100. Transmutation ist eine Alternative zur direkten Endlagerung großer Mengen an hochradioaktive Abfall und eröffnet die Möglichkeit, den Kernbrennstoffkreislauf einschließlich der minoren Actiniden zu schließen. Plutonium, minore Actiniden und langlebige Spaltprodukte können in einem Beschleuniger getriebenen System (ADS) transmutiert werden, der aus einem Beschleuniger, einem Spallationstarget und einem unterkritischen Blanket besteht.

Dieser Beitrag beschreibt die am Forschungszentrum Karlsruhe durchgeführten Arbeiten, die einen ADS kritisch hinsichtlich seines Potenzials zur Transmutation von minoren Actiniden, seiner Machbarkeit und seiner Sicherheitseigenschaften beleuchtet. Die Arbeiten werden für die Bereiche Kernausslegung, Neutronenphysik, Sicherheit, Systemanalyse, Material und Korrosion durchgeführt.

Ein Beschleuniger getriebenes System (ADS) besteht aus drei Komponenten: einem Beschleuniger für Primärteilchen (Protonen), einem Spallationstarget (oder Targetmodul), in welchem die Protonen in einer Spallationsreaktion (externe Neutronenquelle) freie Teilchen (Neutronen) erzeugen, und einem unterkritischen Blanket, in welchem zum einen eine Spaltungsreaktion und damit die Erzeugung von Spaltneutronen (interne Neutronenquelle) stattfindet und in welchem gleichzeitig die Transmutationsreaktionen ablaufen. Die Protonen werden durch ein evakuiertes Strahlrohr, das am Ende durch ein Strahlfenster verschlossen ist, in das Spallationstarget eingebracht. Das Target ist ein schweres Flüssigmetall (z.B. Blei Pb oder eutektisches Blei-Wismut Pb-Bi). Die Spallationsneutronen, die im Spallationstarget erzeugt werden, sind vollständig unabhängig vom unterkritischen Blanket. Ein Abschalten des Beschleunigers oder eine Unterbrechung des Protonenstrahls unterbricht sofort die Spaltungsreaktionen. Sicherheitsaspekte eines solchen unterkritischen Systems werden in 32.23.03 diskutiert.



Sketch of an accelerator driven system (ADS).

Skizze eines Beschleuniger getriebenen Systems (ADS).

- I. Thermalhydraulic Investigations into Blanket and Target Design  
(J.U. Knebel, X. Cheng, R. Stieglitz, M. Daubner, K.J. Mack, F. Fellmoser, C. Pettan, S. Gnieser, IKET)
  
1. Dynamic Behaviour of the ADTF Facility at ANL  
(X. Cheng, IKET, presently delegated to ANL)

### Introduction

One of the main objectives of the Accelerator-Driven Test Facility (ADTF) at Argonne National Laboratory (ANL) is the demonstration of the feasibility of the accelerator-based transmutation of nuclear waste. For this purpose, an accelerator-driven sub-critical reactor is designed with a thermal power of 100 MW. At the present pre-conceptual design phase, some options are still open related to the design of the reactor core and the primary loop. Analysis of the dynamic behavior of the ADTF is carried out in the frame of a bilateral collaboration between Forschungszentrum Karlsruhe GmbH and Argonne National Laboratory (ANL), applying the safety analysis code SAS-4A is applied.

### System configurations

The present studies put the main emphasis on the effect of different system configurations on the dynamic behavior of such a test facility. Five system configurations are taken into consideration with different types of fuel and different types of coolant. Table 1 summarizes the system configurations studied. Some neutron-physical data for the systems S1 and S3 were taken from [2]. Assumptions were made to generate the neutron-physical data required for the other systems. Table 2 summarizes the reactivity feedback data for different systems.

The entire primary loop, which is considered in the SAS calculation, is schematically shown in figure 1. The intermediate loop is neglected by using a pre-defined temperature drop over the heat exchangers. Two independent loops are proposed. Each loop contains one intermediate heat exchanger and one pump, technically specified as is [3]. The entire system is divided into 10 liquid segments, i.e. channels, 4 bypasses, 2 hot legs, 2 cold legs and 1 leakage path. The thermal power released in the reactor core and in the spallation target are 100 MW and 3.5 MW, respectively.

The total mass flow rate is determined, so that the average temperature rise of coolant over the reactor core is 100 K.

Table 1: System configurations studied.

System	S1	S2	S3	S4	S5
Fuel	Metallic	Metallic	Oxide	Metallic	Oxide
Coolant	Sodium	Sodium	Sodium	Pb-Bi	Pb-Bi
Sub-assembly configuration	EBR-2	FFTF	FFTF	ATW/ FFTF	ATW/ FFTF
No. of SA's	120	64	64	64	64
No. of pins in one SA	61	217	217	217	217
Pin diameter [mm]	5.842	5.842	5.842	5.80	5.80
Pin pitch [mm]	6.909	7.264	7.264	9.80	9.80
Clad thickness [mm]	0.381	0.381	0.381	0.70	0.70
Gap size [mm]	0.381	0.381	0.070	0.20	0.050
Fuel length [mm]	342.9	917.9	917.9	917.9	917.9
Total mass flow rate [kg/s]	798	798	798	7103	7103

Table 2: Reactivity feedback data for different systems.

System No.	Doppler [pcm]	Void [pcm/kg]	Fuel worth [pcm/kg]	Cladding worth [pcm/kg]
S1	-70	-49.5	69.6	-3.40
S2	-70	-5.04	10.3	-0.95
S3	-422	-5.04	15.2	-0.95

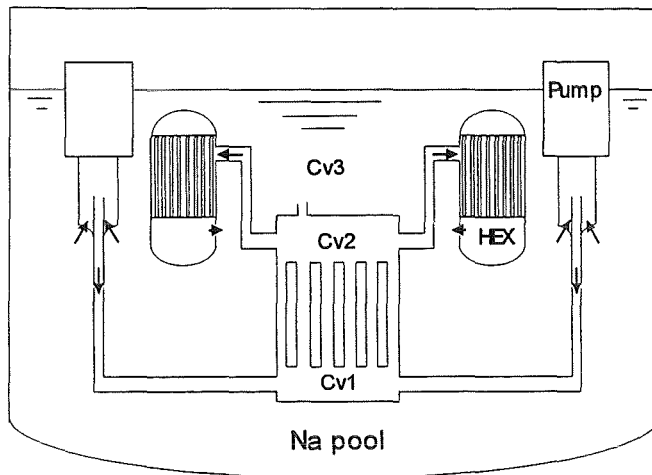


Figure 1: Scheme of the primary loop.

## Results

The analysis has been carried out for the first three systems with three different transient scenarios, i.e. doubled external source, unprotected loss of flow and unprotected loss of heat sink. Here, results from both the systems S1 and S3 are presented. All the results presented are restricted to the unprotected loss-of-flow

scenario, which shows the most serious concern of the safety behavior. The coast-down behavior of both pumps is taken from [1].

*System S1:* Figure 2 shows the behavior of different parameters in the system S1. During the coast-down of the pump, the temperatures of fuel, cladding and coolant (at the elevation of the upper end of the fuel pin) increase rapidly. The coolant temperature reaches the boiling point in about 8.5 s.

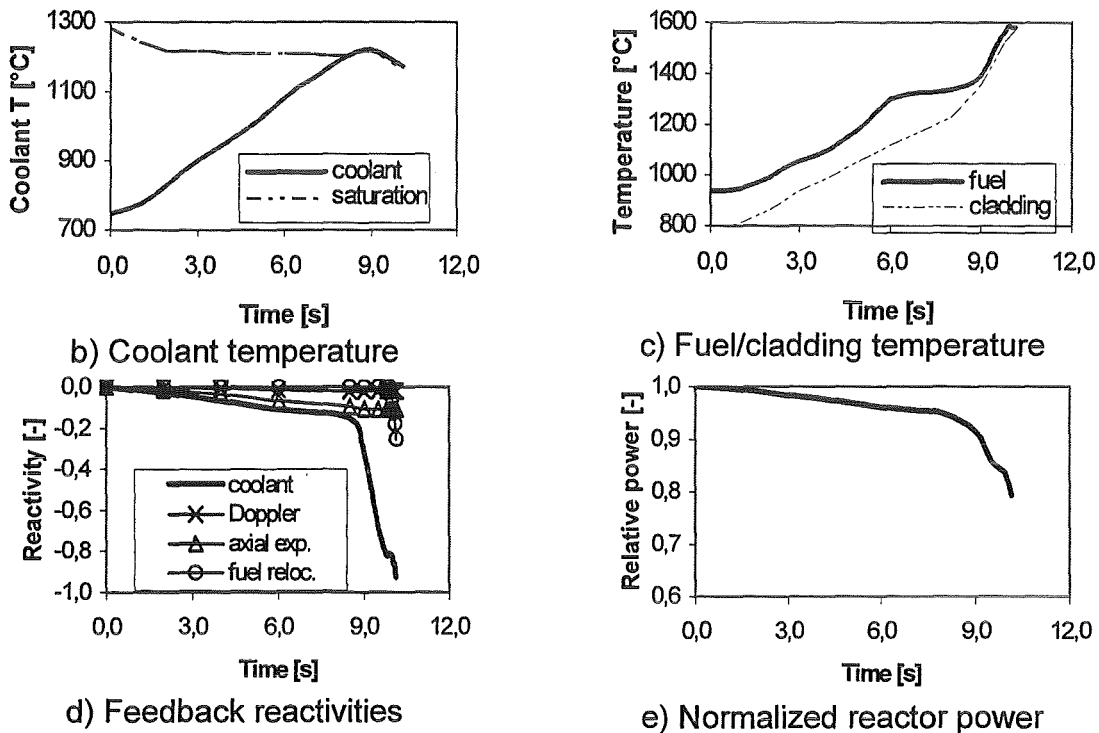


Figure 2: Results for the system S1

Table 3: Time point [in seconds] for the onset of boiling, cladding failure and molten fuel injection into the channel.

Channel No.	1	2	3	4	5
Boiling	8.45	8.50	8.81	9.00	9.01
Cladding failure	9.19	9.25	9.52	9.79	9.79
Molten fuel injection	9.80	9.89			

Table 3 gives the time, at which the onset of boiling, cladding failure and molten fuel injection occurs at different channels. After the onset of boiling, the coolant temperature reduces slightly due to the reduction in the pressure and, subsequently, in the saturation temperature. Obviously, boiling of sodium leads to a reduction in the heat transfer from the cladding to the coolant. The cladding temperature increases sharply. After a short delay, a sharp increase in the fuel temperature occurs. Due to

the eutectic formation of the metallic fuel (Uranium) with the cladding material, cladding is dissolved and becomes thinner. Cladding failure due to Hoop stress takes place prior to the cladding temperature reaches its melting point. First injection of the molten fuel into the coolant channel happens at a time point of 9.80 s.

The coolant boiling causes a large negative feedback reactivity, which leads to a strong reduction in the reactor power. The molten fuel injection causes fuel relocation, and subsequently, leads to a negative feedback reactivity. The Doppler feedback reactivity is small compared to the other reactivity feedback terms.

*System S3:* Figure 3 shows the results for the system S3. Coolant temperature and mass flow behavior is similar to that in the system S2, whereas the behavior of the cladding temperature and the fuel temperature is completely different. Due to the high melting point of the oxide fuel, the fuel is still kept in solid state. Cladding failure occurs due to the cladding melting. The melting of the cladding results in a large positive feedback reactivity, which compensates the negative feedback reactivity caused by coolant boiling. The net reactivity and subsequently the change in the reactor power are kept small.

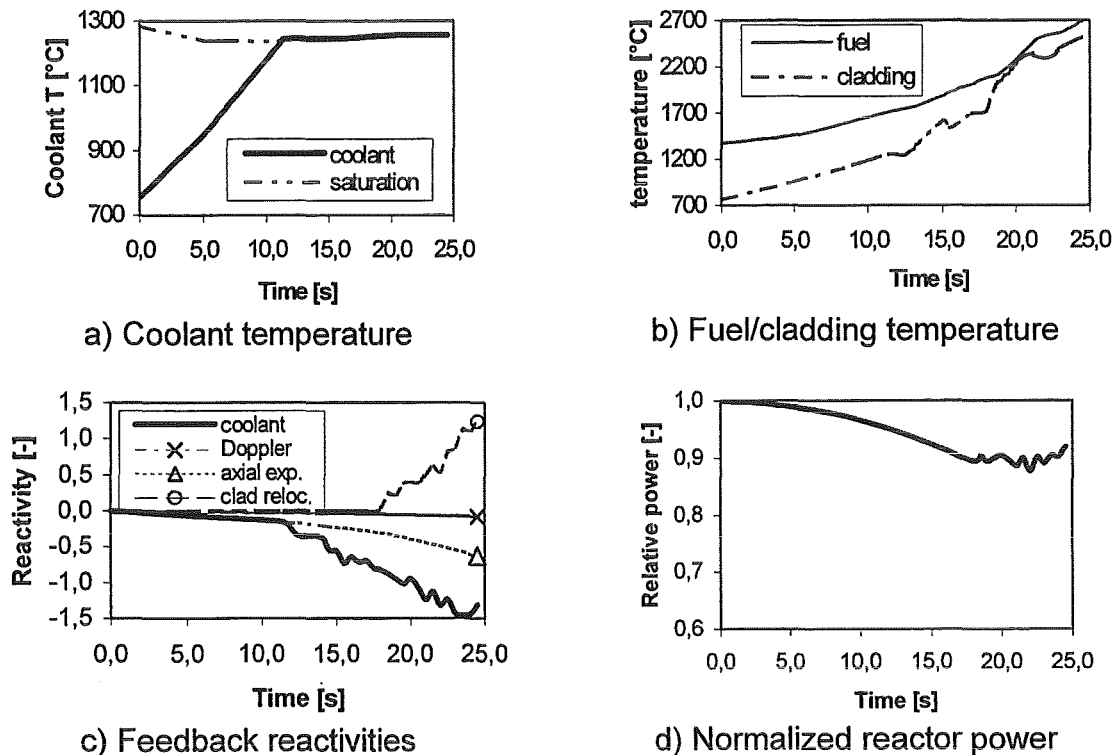


Figure 3: Results for the system S3

## Summary

Preliminary analysis of the dynamic behavior of the ADTF facility has been carried out using the SAS-4A code. The transient behavior under unprotected loss-of-flow scenario shows a serious safety concern. As long as the external source is switched on, LOF will lead to an overheating of coolant, cladding and fuel. Boiling of coolant, cladding failure and molten fuel injection take place just in several seconds after the coast-down of the pump. The analysis of the dynamic behavior using the SAS4A code will be continued in the next time period. The work will be focused on a) system configurations: S1, S2, S3, S4, S5, b) Transient cases: TOP, ULOF, ULOHS, and c) initial sub-criticality:  $0.97 < k_{eff} < 1.0$ .

## Acknowledgement

Scientific discussions with Mr. J.E. Cahalan and Mr. F.E. Dunn from Argonne National Laboratory have made an important contribution to this work.

## References

- [1] ADTF Design Team, Private Communication, ANL, May – November 2001
- [2] J.P. Herzog, SASSYS/EBR-II, Primary and Secondary System Models, ANL-FRA-173, Argonne National Laboratory, July 1993
- [3] L. Mercatali, Preliminary Neutron-Physics Analysis of Two SCM-100 Models, Intra-Laboratory MEMO, November 7, 2001
- [4] M. G. Stevenson, W.R. Bohl, L.L. Smith, Report on the Analysis of the Initiating Phase of a Loss of Flow (without Scram) accident in the FTR, ANL/RAS 74-24, Argonne national Laboratory, September 1974
- [5] C.P. Cabell, A Summary Description of the Fast Flux Test Facility, HEDL-400, Hanford Engineering Development Laboratory, December 1980
- [6] R.N. Hill, H.S. Khalil, Draft Report on Sodium Cooled ATW Blanket Development, Intra Laboratory MEMO, ANL, July 21, 2000
- [7] J.E. Cahalan, et al., The SAS4A/SASSYS-1, LMR Analysis Code System, ANL-FRA-1996-3, Volume 1 to 6, Argonne National Laboratory, August 1996

## 2. Dynamic Behavior of the Heat Removal System of the MEGAPIE Target (X. Cheng, J.U. Knebel, IKET)

### Introduction

The Forschungszentrum Karlsruhe is making a contribution to the design of the MEGAPIE target, covering design, neutronics, thermalhydraulics and material issues. The thermalhydraulics tasks consist mainly of the design optimization of the active part of the target, and the analysis of the dynamic behavior of the target cooling system. Here, the main results related to the analysis of the dynamic behavior of the target cooling system is reported.

### Target system and transient cases

The entire heat removal system consists of three loops, i.e. the primary loop, the intermediate loop and the third loop, as schematically indicated in figure 1. In the primary loop, lead-bismuth is circulated with two EM-pumps, cools down the beam window and the spallation zone and enters the target heat exchanger, where heat is transferred to the intermediate loop. The nominal flow rate of Pb-Bi is 4 l/s. The thermal power released in the spallation target is about 650 kW. The target heat exchanger consists of 12 cooling pins. In the intermediate loop, the organic fluid (Diphyl THT from Bayer AG) is used to keep the operating pressure in the intermediate loop as low as possible (<10 bar). The nominal flow rate of the organic fluid is about 10 l/s. An expansion accumulator tank with hot fluid is connected to the loop. This provides one option to avoid freezing of Pb-Bi in the case of the beam interrupt transient. Another option to avoid freezing is the activation (opening) of control valve CV2, and at the same time the closure of control valve CV3. The effectiveness of these options needs to be investigated.

The third loop is an existing heavy water loop at the SINQ facility. The nominal flow rate is 10 l/s, the temperature of D2O entering the second heat exchanger is 30 °C.

The transient cases analyzed here are summarized in table 1. The first three cases are related to the loss of the pump head (LoPH) in different loops, leading to an increase of the fluid temperature.

An excessive temperature of lead-bismuth in the primary loop leads to a damage of the structure material, e.g. the beam window. An excessive temperature in the

intermediate loop or in the third loop may result in a high loop pressure. In case of beam interrupt, the temperature of lead-bismuth in the primary loop has to be kept above the freezing point, to avoid a blockage of the flow path and, subsequently, a damage of the primary loop.

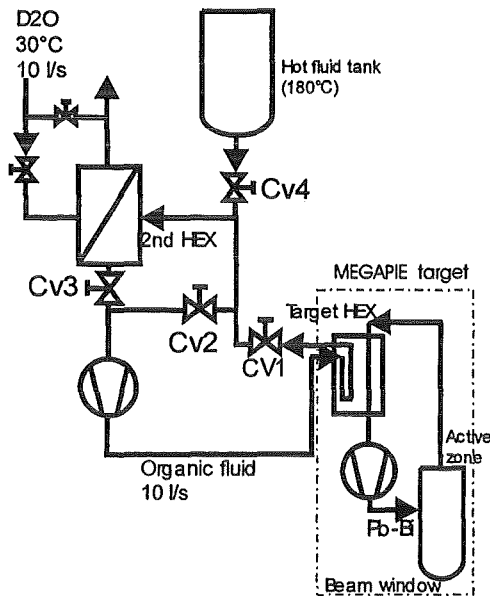


Figure 1: Schema of the MEGAPIE heat removal system.

Table 1: Transient cases analyzed.

Transient cases	Main phenomena	Safety concerns
Loss of pump head (LoPH) in the primary loop	Reduced flow and increased temperature of Pb-Bi	Excessive hot spot in the primary loop
Loss of pump head (LoPH) in the intermediate loop	Reduced heat removal capability of the target HEX	Excessive hot spot in the primary and the intermediate loop
Loss of pump head (LoPH) in the third loop	Reduced heat removal capability of the second HEX	Excessive hot spot in all three loops
Beam interrupt	Reduced thermal power & coolant temperature	Freezing of Pb-Bi in the primary loop

### Main Results

For the numerical analysis of the dynamic behavior of the MEGAPIE target system, the one-dimensional code HETRAF is applied. In HETRAF, the thermal and hydraulic characteristics of each individual flow cell can be modeled. This enables the simulation of any kind of distribution of heat source and flow resistance in the flow domain. The code is capable of simulating a multi-loops system with thermal coupling between loops. There are modules taking into account different components, e.g.

pump and bypass. In the frame of the MEGAPIE project, the HETRAF code has been extended to cooling systems with liquid lead-bismuth eutectic (LBE).

*Steady state condition:* Figure 2 shows the temperature distribution of the coolant in the primary loop and in the intermediate loop under the steady state condition. At the entrance of the target heat exchanger (starting point of the flow path of the primary loop), the temperature of LBE is 335 °C. Through the heat exchanger it is cooled down to 245 °C. Due to the heat transfer through the guide tube, lead-bismuth in the annular gap is warmed up for about 25 K. About 100 K temperature rise is obtained in the spallation zone. The maximum Pb-Bi temperature in the spallation zone is about 370 °C. Through the heat exchanger, the organic fluid is heated up from 115 °C up to 150 °C. These results agree well with the previous assessments.

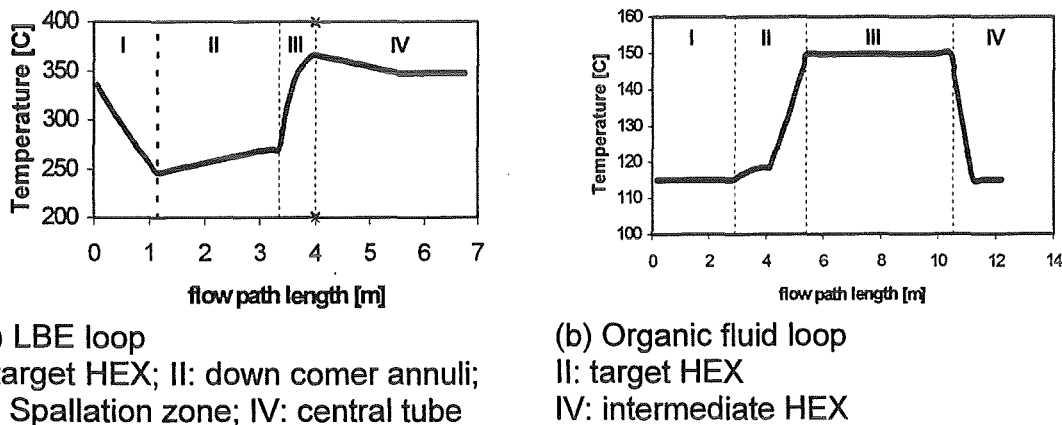


Figure 2: Coolant temperature at the steady state condition

*Loss of the pump head in the primary loop:* Figure 3 shows the normalized mass flow rate of LBE in case of the loss of the pump head in the primary loop. The mass flow rate reduces quickly and reaches in about 5 s its minimum value, which is about 50% of the nominal value. After then the mass flow rate increases again due to the enhanced buoyancy effect. Under the steady state natural convection condition the mass flow rate is about 60 % of the nominal value. The temperature of LBE in the spallation zone, as shown in figure 4, increases rapidly and reaches its maximum in about 5 s. Due to the increase in the mass flow rate, the temperature of LBE in the spallation zone decreases again from 465 °C down to about 440 °C, which is about 70 K higher than that under the normal operating condition. The short-term coolability of the beam window needs to be analyzed for the case that the main flow pump losses its pump head and the bypass injection pump is still in its full operation.

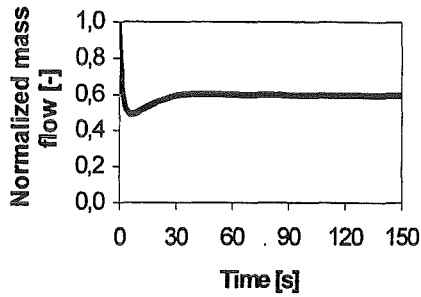


Figure 3: Mass flow rate of LBE under LoPH in the primary loop.

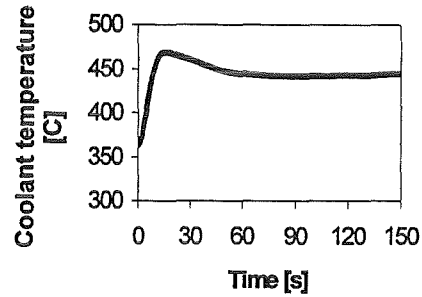


Figure 4: Temperature of LBE in active zone under LoPH in primary loop.

*Loss of the pump head in the intermediate loop:* Figures 5 and 6 show the transient results in case that the pump in the intermediate loop loses its pump head (LoPH). Three curves in figure 6 present the temperature of LBE in the spallation zone, the organic fluid and the wall temperature at the exit of the target heat exchanger, respectively. These calculations assume that no boiling of the organic fluid takes place. After the loss of the pump head, the mass flow rate in the intermediate loop reduces down to 1% in about 10 s (figure 5). The reduction in the mass flow rate and, subsequently, in the heat removal capability of the heat exchanger, leads to an increase in the LBE temperature in the primary loop. In the first 20 s the temperature in the spallation zone is hardly affected. After then it increases and reaches about 600 °C in 5 minutes. Obviously, safety measures have to be activated, to avoid the failure of the beam window. An increase of more than 200 °C in the temperature of the organic fluid at the exit of the target heat exchanger is obtained in 5 minutes. A possible onset of boiling of the organic fluid has to be checked. In case that boiling takes place, the pressure in the intermediate loop will increase significantly. Safety measures are, therefore, required to limit the pressure in the intermediate loop.

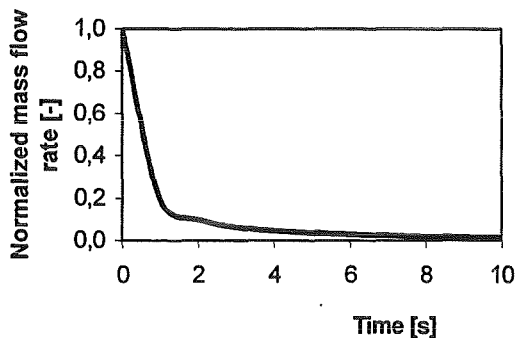


Figure 5: Mass flow rate under LoPH in the intermediate loop.

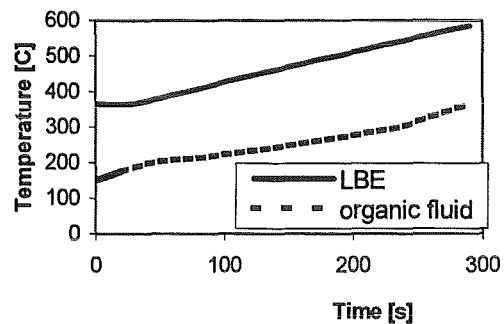


Figure 6: Temperature behavior under LoPH in the intermediate loop. LBE: in the spallation zone; organic fluid: at the exit of the target HEX.

*Loss of the pump head in the third loop:* Due to the deficiency in the technical data provided, the third loop is not completely simulated. For this transient, it is assumed that the inlet temperature of D<sub>2</sub>O into the intermediate heat exchanger is kept at 30 °C. The mass flow rate is exponentially reduced down to 1 % (with a time constant of 3 s) and then kept at 1 %.

The results show that the coolant temperature in all three loops increases continuously. The most concern in this case would be the third loop, in which the heavy water temperature reaches 200 °C in about 120 s after the begin of the transient. Due to the onset of boiling, a strong increase in the loop pressure is expected. Therefore, safety measures have to be made to avoid overpressure in the loops.

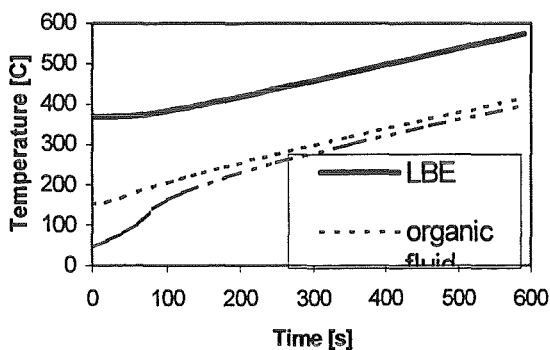


Figure 7: Temperature behavior under LoPH in the third loop. Pb-Bi: in the spallation zone; organic fluid: at the exit of the target HEX; D<sub>2</sub>O: at the exit of the intermediate HEX.

*Single beam trip:* The operation record of the SINQ accelerator of PSI shows that the proton beam can be interrupted frequently. The duration of the beam interrupts varies in a large range, from milliseconds to several minutes. In case of a beam interrupt, heat source is reduced (close) to zero. The temperature of LBE in the primary loop decreases. If necessary, safety measures have to be activated to keep the LBE temperature above the freezing point (123 °C), to avoid blockage of the flow path, subsequently, the damage of the target. Figure 8 shows the temperature of lead-bismuth at the exit of the target heat exchanger, where the LBE temperature has the lowest value in the primary loop. The temperature reaches the freezing point in about 4 minutes. Therefore, safety measures have to be activated in case of a beam interrupt with a duration larger than 4 minutes.

*Multi beam trips:* Figure 9 shows the LBE temperature at the exit of the target heat exchanger in case of multi-interrupts of the proton beam. The duration of each interrupt is one minute. The time interval between two beam interrupts is also one minute. It is seen that after five beam interrupts, the LBE temperature goes down to about 150°C. It is expected that after further five beam interrupts, the lead-bismuth temperature will approach the freezing point.

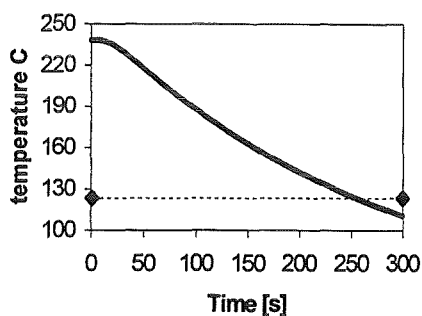


Figure 8: LBE temperature at the exit of the target HEX under the single beam interrupt transient.

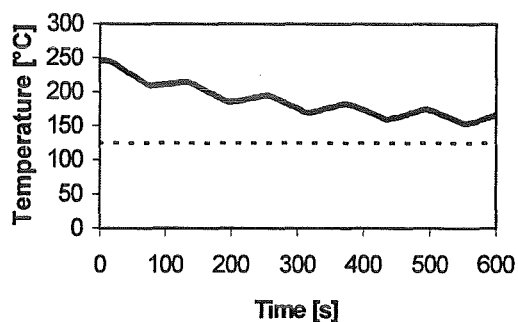


Figure 9: Temperature behavior under a multi beam interrupt transient. Interrupt duration: 60 s, Interrupt interval: 60 s.

Analysis of some special transient cases is required by the MEGAPIE design team. During the transient, the behavior of the beam power and the mass flow rate of LBE is controlled. One of the examples is shown in figure 10. In this case, the behavior of the LBE temperature is similar to the case shown in figure 9. The controlled reduction in the mass flow rate does not improve the temperature behavior, at least for the first two beam interrupts.

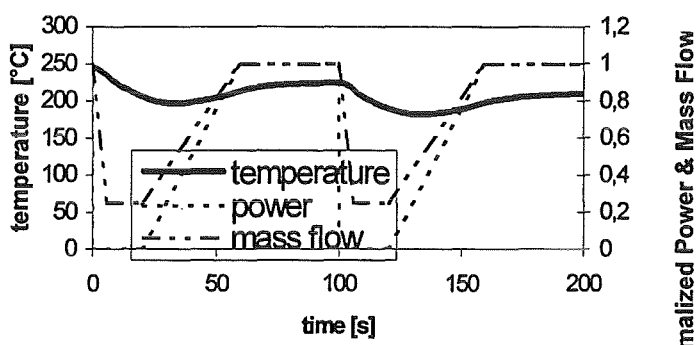


Figure 10: Temperature behavior under a transient with pre-controlled beam power and mass flow.

*Beam interrupt with protection:* One of the safety measures, to avoid the freezing of LBE in the primary loop, is to open the bypass valve CV2 and at the same time to close the control valve CV3 (see figure 1). Figure 11 shows the LBE temperature at the exit of the target heat exchanger and in the spallation zone. In this example, it is assumed that the opening of the valve CV2 begins 5 s after the beam interrupt. The valve opening procedure takes 5 s. The control valve CV3 begins to close 10 s after the beam interrupt. The closing procedure takes another 5 s, i.e. 15 s after the beam interrupt, the valve CV3 is completely closed. It is seen that the temperature in the spallation zone decreases sharply in the first few seconds. The temperature at the exit of the target heat exchanger increases sharply after the control valve CV3 is completely closed. It takes about 10 s, until the temperature in the spallation zone

increases again. After then, both temperatures decrease slowly. Steady state condition is reached in about 10 minutes with a LBE temperature of about 270 °C, which is much higher than the freezing point.

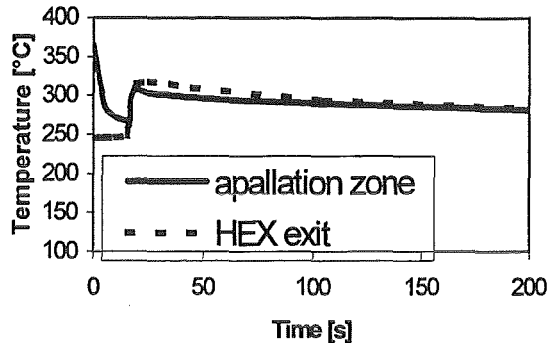


Figure 11: Temperature behavior in case of the protected beam interrupt transient.

### Summary

The main conclusions achieved are summarized as below:

- The HETRAF code is extended to the application to LBE systems. It is suited to analyze the dynamic behavior of the heat removal system of the MEGAPIE target, and to provide basic information for designing the safety system.
- Under the loss of the pump head in the primary loop, the mass flow of lead-bismuth is reduced to about 60 % of the nominal value. The temperature of LBE remains at an acceptable level. The main concern is the cooling of the beam window, which needs to be checked.
- Under the loss of the pump head in the intermediate loop, both the temperatures of LBE and the organic fluid increase continuously. Safety measures, e.g. shut down of the beam, are required to avoid an excessive temperature in the primary loop and an overpressure in the intermediate loop.
- Under the loss of the pump head in the third loop, the main safety concern would be the onset of local boiling of the heavy water, which could lead to an overpressure in the third loop.
- For a beam interrupt with a duration longer than four minutes, safety measures are necessary to avoid the freezing of LBE. The activation of both control valves (opening CV2 and closing CV3) seems to be an effective measure to achieve the safety goal.

3. KILOPIE and MEGAPIE Experiments in THEADES Loop of KALLA  
(R. Stieglitz, M. Daubner, F. Fellmoser, K.J. Mack, J.U. Knebel, IKET)

In a collaborative effort, the MEGAPIE Initiative founding members CEA, FZK, PSI together with their partners CNRS, DOE, ENEA, JAERI, KAERI, SCK-CEN, and SUBATECH agreed to design, build, operate, explore and decommission an exploratory liquid lead-bismuth spallation target for 1 MW of beam power, taking advantage of the existing spallation neutron facility and accelerator complex SINQ, [1]. In addition, this work is supported by the Euratom 5th Framework Programme (FP5): the MEGAPIE-TEST Project (MEGAWatt Pilot Experiment - TESTing) aims at the development and comprehensive testing of the spallation target both under beam-off and beam-on conditions, and at the set up of a handbook on the design of a neutron spallation source in general. The operation of MEGAPIE is envisaged in 2005. MEGAPIE is a first decisive step to realize a liquid metal spallation target in Europe.

All single-effect user-oriented experiments on MEGAPIE will be performed in the Thermohydraulic Loop THEADES of the KALLA laboratory. Detailed data about KALLA is available at <http://www.kalla.fzk.de>. The intention of the user experiment is to qualify a specific geometric design of the beam window and the target itself with respect to the thermohydraulic performance and the viability in a technical arrangement.

The MEGAPIE beam window has to withstand surface heat fluxes up to  $140 \text{ W/cm}^2$  and in case of miscellaneous beam focusing up to  $200 \text{ W/cm}^2$ . Although this is only a minor part (<10 %) of the total heat released in the target it represents one of the most critical issues of the liquid metal cooled target. The beam window is a 2.5 mm thin martensitic steel sheet (T91 being 9Cr-1MoVNb).

As the simulation of a 1:1 heat production scenario as in SINQ is hardly feasible out of pile, two issues have to be experimentally solved in the MEGAPIE test experiments, in order to set-up a data base and to validate CFD codes:

- The turbulent mixing of cold and hot fluid with low molecular Prandtl number,
- Simulation of the coolability of the beam window at similar surface heat fluxes.

The first issue can be easily investigated within the THEADES loop by injecting overheated lead bismuth ( $350 \text{ }^\circ\text{C}$ ) via a bypass tube into the relatively cold ( $300 \text{ }^\circ\text{C}$ ) main flow. In this configuration (Heated Jet Experiment) the window hemispheres

thickness can be in the order of 5 mm. The specific instrumentation for this experiment is the same as for the later on described KILOPIE experiment except for the thermocouple instrumentation in the hemisphere. A sketch of the thermocouple array is depicted in figure 1. The thermocouples being used are mantled NiCr-Ni elements with an outer diameter of 0.5 mm. This experiment is also aimed to qualify new pressure sensors and velocity sensors in lead bismuth.

The second issue will be investigated within the KILOPIE Experiment. In order to simulate a MEGAPIE relevant surface heat flux, an electric resistance heating system HETSS has been developed at PSI, which is capable to attain surface heat fluxes up to  $140 \text{ W/cm}^2$ . It consists of a  $50 \mu\text{m}$  thick nickel foil, which is glued to a dish and DC current heated. Attached to the nickel foils are spring loaded needles, with which local potential differences can be acquired. The measured local potential differences correspond to local heat transfer coefficients and are reflecting the local temperatures. Using the HETSS heating technique different proton beam footprints can be simulated and investigated. A sketch of the HETSS experimental set-up is illustrated in figure 2.

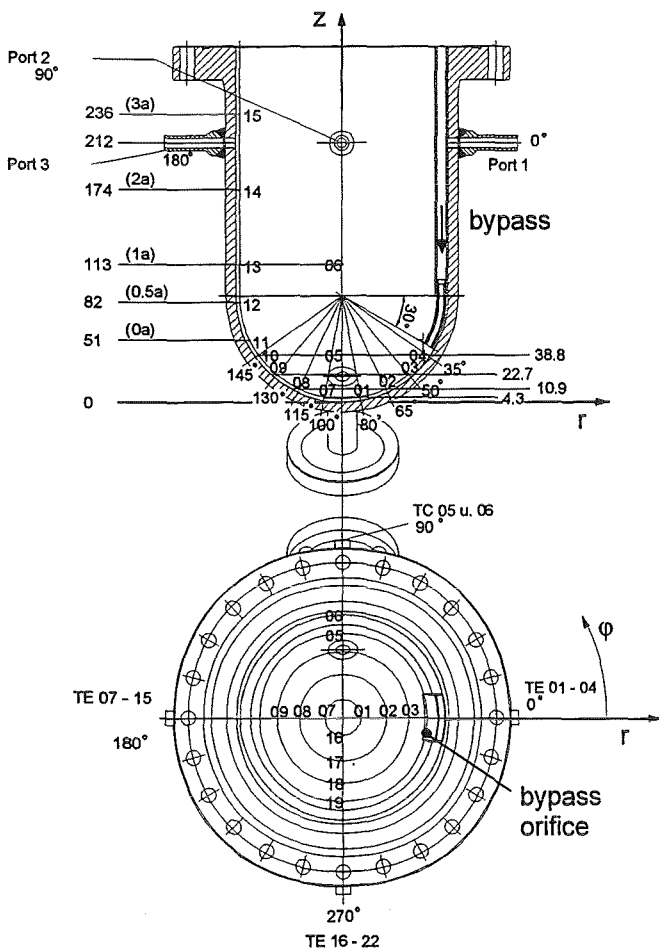


Figure 1: Used coordinate system and thermocouple (TE) instrumentation of the heated jet experiment being performed in the THEADES loop of KALLA (dimensions in characteristic length a and mm).

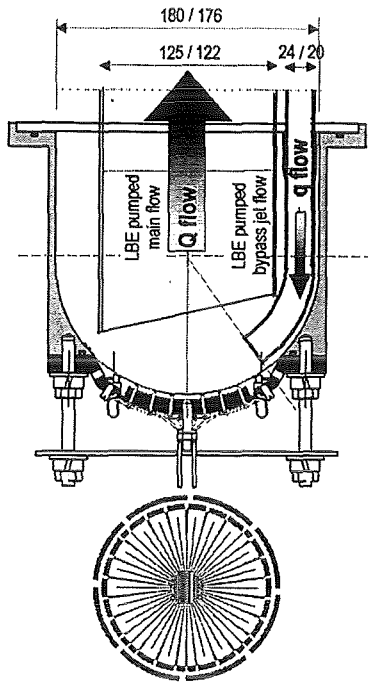


Figure 2: 2D HETSS experiment test section set-up, geometrical flow configuration and shape of Nickel heating foil, from PSI.

The change from the Heated Jet Experiment and the KILOPIE Experiment can be easily performed by exchanging the lower flange, shown in figure 3, and mounting the KILOPIE test part, see figure 2. The other environment especially regarding the pressure sensors, the velocity sensor and the connections to the THEADES loop are the same. The dimensions of the entire window test module correspond to the MEGAPIE geometry, including the instrumentation rod. Instead of a neutron flux measurement device as foreseen for the real in-pile module, a combined pressure and velocity sensor is installed. The total instrumentation MEGAPIE module test excluding the HETSS experiment amounts to 96 thermocouples, 4 pressure transducers (resolution  $\pm 3$  mbar) and 2 velocity sensors.

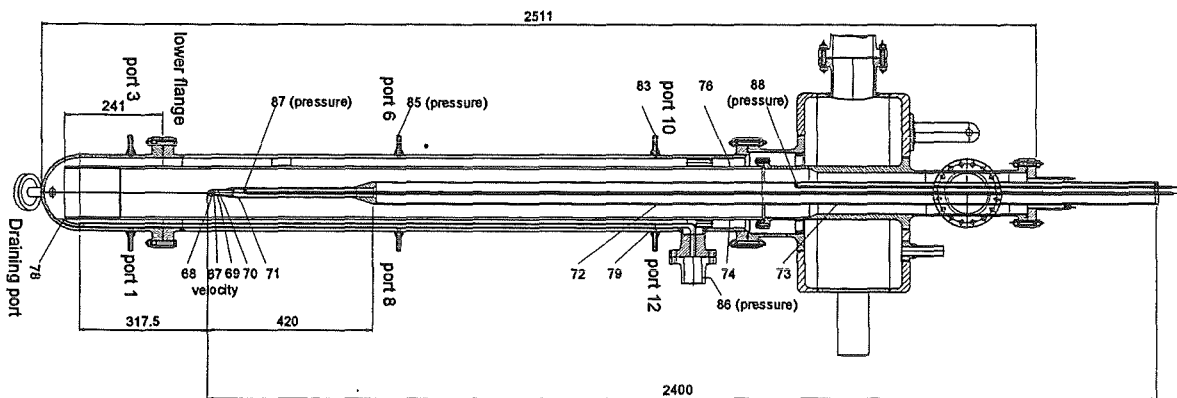


Figure 3: MEGAPIE window test module currently being set-up in the THEADES loop of the KALLA facility at FZK.

## Summary

In the Thermalhydraulic Loop THEADES of KALLA, the thermalhydraulic experiments on fluid mixing (Heated Jet Experiment) and on beam window cooling (KILOPIE Experiment) are performed. The test section is currently being set up. The experimental campaign is foreseen in summer 2002. The experiment is done in close cooperation with the International MEGAPIE Initiative. Guest scientists from KAERI Republic of Korea, IPUL Latvia, and PSI Switzerland are present at KALLA during the experiments. Thus, KALLA is developing well into being an international user lab and center of excellence in heavy liquid metal technologies.

Further information about lead-bismuth technologies can be found in 32.23.06.

## II. Liquid metal corrosion

(G. Müller, A. Heinzl, A. Weisenburger, IHM; J. Konys, O. Wedemeyer, IMF III, A. Rusanov, IPPE, V. Markov, PROMETHEY)

### **Abstract**

Corrosion tests were carried out on austenitic AISI 316L and 1.4970 steels and on MANET steel up to 2000 h of exposure to flowing (up to 2 m/s) Pb/Bi. The concentration of oxygen in the liquid alloy was controlled at  $10^{-6}$  wt%. Specimens consisted of tube and rod sections in original state and after alloying of Al into the surface. After 2000 h of exposure at 420 and 550 °C the specimen surfaces were covered with an intact oxide layer which provided a good protection against corrosion attack of the liquid Pb/Bi alloy. After the same time corrosion attack at 600 °C was severe at the original AISI 316L steel specimens. The alloyed specimens containing FeAl on the surface of the alloyed layer still maintained an intact oxide layer with good corrosion protection up to 600 °C.

### **Zusammenfassung**

Korrosionstests an den austenitischen Stählen AISI 316L und 1.4970 sowie an MANET Stahl wurden durch 2000 Std. Auslagerung in fließendem (bis zu 2 m/s) Pb/Bi durchgeführt. Die Sauerstoffkonzentration in der flüssigen Legierung wurde bei  $10^{-6}$  Gew.% gehalten. Die Proben bestanden aus Rohr- und Stahlabschnitten im originalen Zustand und solchen mit einlegiertem Al in die Oberflächen. Nach 2000 Std. Auslagerung bei 420 und 550 °C waren die Proben mit einer Oxidschicht bedeckt, die sie vor dem Lösungsangriff durch die flüssige Pb/Bi-Legierung schützte. Bei 600 °C nach derselben Auslagerungszeit gab es einen schweren Korrosionsangriff auf die AISI 316L-Stahlproben. Legierte Proben mit einer FeAl-Phase an der Oberfläche behielten eine intakte Oxidschicht mit gutem Korrosionsschutz bis 600 °C.

### **1. Introduction**

Steel corrosion by the eutectic liquid Pb/Bi alloy is one of the problems that appear in accelerator driven subcritical systems (ADS) [1] where the eutectic alloy is intended to be used as a coolant and target material. Corrosion effects in the 100 µm range

are reported on ferritic Fe-Cr steels between 575 and 750 °C after 3250 h exposure to liquid lead [2]. Steel components are soluble in liquid lead in the range of  $10^{-3}$  – 0.1 at% in this temperature region [3]. An exception exists for Ni, which has a solubility of 2 at% at 600 °C in lead [4].

Since all the solubilities vary with temperature, transport processes will take place which live from the higher solubility at high temperatures and precipitation at low temperatures. A temperature difference of about 150 °C is typical for lead cooling loops. Therefore already small solubilities can lead to heavy corrosion effects with high flow velocities, in the range of 1 m/s, and long in pile times.

These problems are increased by using the eutectic Pb/Bi alloy instead of Pb. Table 1 shows a comparison of solubilities in Pb and Bi. It is to be expected that Pb/Bi alloys are much more corrosive than Pb.

Early experiments with liquid Pb and Pb/Bi revealed that stable oxide scales on steel surfaces, consisting of magnetite and FeCr-spinels, prevent the dissolution attack if oxygen is dissolved in the liquid metal with a concentration of  $10^{-6}$  at% [6, 7]. Recent investigations of corrosion effects in stagnant liquid lead give an overview on the corrosion processes and its prevention by oxide scale formation on steel [8, 9]. Stable oxide layers are formed in liquid lead at 550 °C with a controlled oxygen concentration of  $8 \cdot 10^{-6}$  at% [8] as well as with saturated oxygen concentration of  $3 \cdot 10^{-3}$  at% [9]. The scale thickness including a magnetite layer on top and a spinel layer underneath amounts to 20 – 30  $\mu\text{m}$  after 3000 h of exposure.

Table 1: Solubilities in Pb and Bi at 600 °C [4, 5].

	Pb [at%]	Bi [at%]
Ni	2	17
Al	1	11
Cr	0.02	0.56
Fe	0.01	0.017

This may impose a new problem at much longer time scales because the corrosion on steel turns from the dissolution attack to that of oxidation. A way out of this dilemma is alloying of Al into the steel surface. The alloyed Al causes formation of a thin protective alumina layer that grows very slowly and prevents also extensive oxidation of the steel [8, 9]. Earlier experiments on Fe-Cr alloys containing 8 at% Al show also alumina scale formation in liquid lead at low oxygen potential [10].

Other experiments [11] employing a Fe-aluminide layer on MANET steel, which was oxidized before the experiment, resulted in no corrosion attack in liquid Pb-17Li after 10000 h at 450 °C. Thermodynamic investigation of Al-Fe alloys [12] showed that a self-healing of the alumina scale can take place in Pb-17Li if the kinetics of the process is high enough.

Although the temperatures of Pb/Bi in a proposed DEMO-ADS [13] can be kept below 400°C because of the low melting point of the eutectic alloy, it must be expected that at some places like at the beam window or in the core (on the claddings) the temperatures increase well above this value. Therefore, in the experiments the requirements of a real energy amplifier with high energy fluxes have to be considered. There, surface temperatures in the range of 600 °C can occur. Thus the experiments conducted in this work are extended up to 600 °C. To examine the influence of Bi in the alloy the Pb/Bi eutectic alloy is used in the experiments conducted in the liquid metal loops of IPPE, Obninsk and PROMETHEY, St. Petersburg in Russia.

## **2. Experimental**

### **2.1 Loop tests**

The corrosion tests were carried out in two different non-isothermal forced lead-bismuth loops at IPPE, Obninsk and at PROMETHEY, St. Petersburg. Both loops consist of a main heater, a cooler, a hot and a cold section, an electromechanical pump, a purification system, a flow meter and oxygen meters. In the IPPE loop two test sections are available, one at 420 °C the other at 600 °C. In case of the PROMETHEY loop the experiments are performed in the hot test section at 550 °C. The volume of the liquid Pb/Bi in both loops is about 60 l. The temperature is maintained by a electrical resistance heater which is positioned just in front of the hot test section. A cooler is placed directly before the cold test section. The oxygen activity in the liquid Pb/Bi containing  $10^{-6}$  at% oxygen is measured by electrochemical cells. Test parameters for both loops are listed in table 2.

The main difference between the two loops is in the flow velocities of the liquid metal, which is with 2 m/s four times higher in the IPPE loop. The still running corrosion experiments are foreseen for exposure times up to 5000 h. This paper deals with the results after the first stop of the loops at 2000 h.

Table 2: Loop test parameters.

	IPPE	PROMETEY
Liquid medium	Pb/Bi	Pb/Bi
T <sub>cold leg</sub> [°C]	420	-
T <sub>hot leg</sub> [°C]	600	550
Duration [h]	1000, <b>2000</b> , 5000	1000, <b>2000</b> , 5000
Velocity [m/s]	2	0.5
O <sub>2</sub> [w%]	1x10 <sup>-6</sup>	1x10 <sup>-6</sup>

## 2.2 Evaluation

Specimens were washed of in 180 °C oil after exposure to remove residues of lead-bismuth. The Analysis consisted of metallurgical examination by light and scanning electron microscopy (SEM) and energy dispersive x-ray analysis (EDX) on the cross section of the specimens.

## 2.3 Materials

Materials used in the experiments are cylindrical tubes and rods of AISI 316, 1.4970 and MANET steel of 8 mm diameter. The chemical composition of the steels is listed in table 3.

Table 3: Chemical composition of steels in wt%.

sign	steel	C	Si	Mn	P	S	Cr	Ni	Mo	Ti
A	AISI 316L	0.02	0.35	1.8	0.19	0.0005	17.3	12.1	2.31	-
B	1.4970	0.46	0.89	1.91	0.012	0.009	16.5	13.8	0.66	0.43
C	MANET	0.11	-	0.78	0.003	-	10.3	0.68	0.61	-

A surface layer of 10 – 100 µm is alloyed with aluminium (Al) in one part of the specimens signed with the number 2, 3. The other part is just smoothed and signed with the number 1. The specimen signatures are listed in table 4.

Aluminium alloying was achieved by two different procedures. The first (2) was done by wrapping Al-foil around the tube and heating at 1040 °C for 0.5 h, the second by hot dipping aluminization and annealing [14]. The hot-dipping process for the austenitic steels is performed in an Al-melt containing 12 at% of Si and consecutive annealing at 550 °C for 0.5 h. The low annealing temperature for the austenitic steels was necessary because severe embrittlement and crack formation in the aluminized layer on this steels.

Table 4: Specimen signatures.

steel	surface smoothed	surface alloyed	
		Al-foil	Al melt dipping
AISI 316L	A 1	A 2 (1040)	A 3 (550)
1.4970	B 1	B 2 (1040)	B 3 (550)
MANET	C 1	-	-

(..) = annealing temperature of alloyed steels in °C

A typical cross section of an Al alloy layer obtained by wrapping the tube sample and annealing is shown in Fig. 1. On top of the original surface there is a FeAl layer which forms by diffusion of iron into the liquid Al layer during annealing. The diffusion zone of 25 µm depth below the surface contains Al dissolved in Fe and NiAl precipitations, while the interface some µm thick contains NiAl created by Ni diffusion.

The hot dipped austenitic specimens A3 and B3 have a 50 µm layer consisting of Al with 12 at% of Si. The cross section of the layer on specimen A3 is shown in Fig. 2. This layer contains only a small amount of dissolved Fe because the annealing temperature was too low for a sufficient interdiffusion of Fe and Al. Silicon is not homogeneously distributed throughout the whole layer, it appears mainly in Silicon rich precipitations with up to 65 wt% Si.

The specimens were stacked together and fixed by an internal rod. The arrangement is completely immersed in the test sections of the loops.

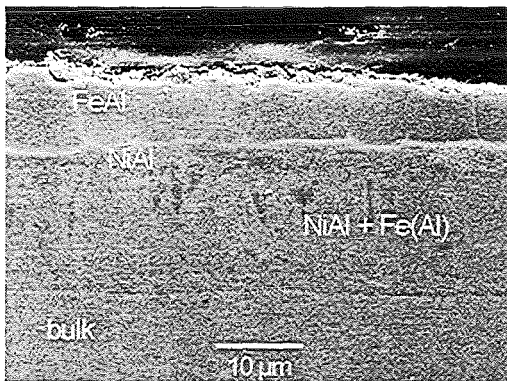


Fig.1: SEM cross section of 1.4970 specimen B2 after alloying by Al-foil wrapping and annealed at 1040 °C for 0.5 h.

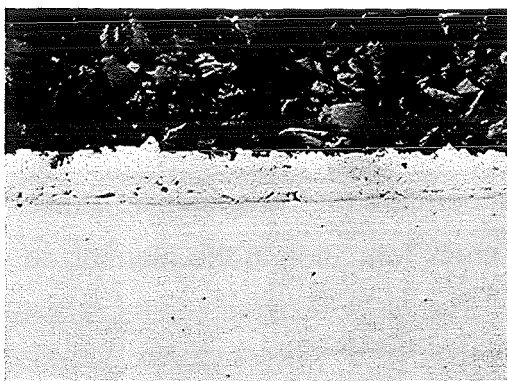


Fig. 2: SEM cross section of AISI 316L specimen A3 dipped in AlSi10 at 700 °C and annealed at 550 °C for 2 h.

### 3. Results

All the reported results are obtained from specimens which were taken out of the loop test sections after 2000 h at 420, 550 and 600 °C. In the following, the results of the examinations are described in a separate chapter for each one of the specimen types listed in Tab. 4. The behavior of the austenitic steel specimens A2 and B2 is described by the example of the AISI 316 L specimen A2 only, because there is no significant difference visible for both specimens.

In Fig. 3 a bundle of steel specimens can be seen that were exposed in the liquid Pb/Bi loop at 600 °C. Both AISI 316L specimens shown in the upper bundle are heavily corroded. The specimens consist of rods that are tapered at both ends to align them at one end in the mounting of the bundle and at the end side in the next specimen. Sample (a) shows a large area separation of material at the circumference of the rod. The tapering of sample (b) was entirely dissolved. The specimen was cut at the left border of the dissolved area and prepared for analysis.

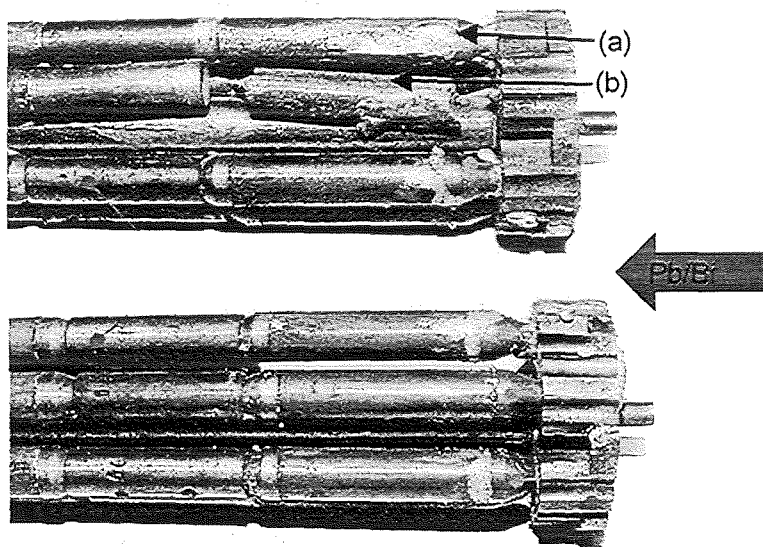


Fig. 3: Upper part of a bundle of specimens after 2000 h exposure in the Pb/Bi – loop containing 10-6 wt% oxygen at 600 °C, flow velocity  $v = 1.3$  m/s.

#### 3.1 AISI 316 L specimen A1

The effect of liquid Pb/Bi on the steel specimen of type A1 after 2000 h of exposure is shown in Fig. 4. No attack on the surface can be seen at the SEM cross section of specimen A1 after exposure to 420 °C. The EDX analysis indicates that the steel composition is not changed in the vicinity of the surface. This points out that no dissolution took place. Probably, a thin oxide scale protects the material from dissolution attack.

During exposure to 550 °C specimen A1 develops partly thick oxide scales consisting of a magnetite and a spinel zone underneath. The thin oxide layer observed after exposure to 420 °C is maintained on the other parts of the surface. In any case no dissolution attack took place. The concentration of the steel components below the oxide layer is also not changed.

Deep liquid metal penetration and massive ablation of material by erosion is observed at 600 °C on steel specimen A1 in the lower part of Fig. 4. Bright inclusions consist of Pb/Bi alloy enriched in Bi. The penetration zone is depleted in Ni down to 1 at%.

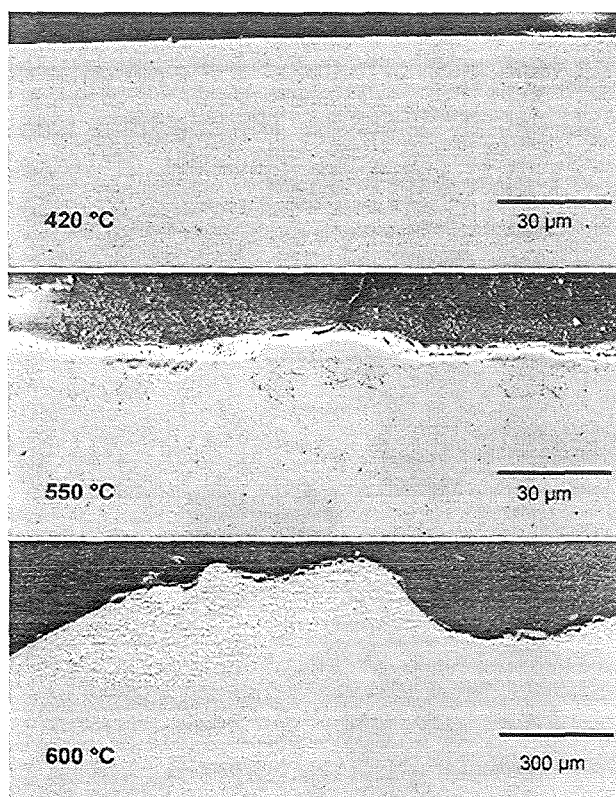


Fig. 4: SEM cross section of AISI 316 L specimens A1 after 2000 h of exposure.

### 3.2 1.4970 specimen B1

Corrosion effects of liquid Pb/Bi on the steel specimen of type B1 after 2000 h of exposure are shown in Fig. 5. The specimen has the same appearance at 420 °C like specimen A1 with no signs of corrosion attack. At 550 °C, however, large parts of the surface are covered by a continuous magnetite scale with a spinel zone underneath. On about half of the specimen the thin oxide layer observed for 420 °C is, however, still maintained. This behavior did not change at 600 °C. At 550 and 600 °C precipitation of chromium oxide is observed in the grain boundaries of the spinel zone represented by the dark network in the bulk material.

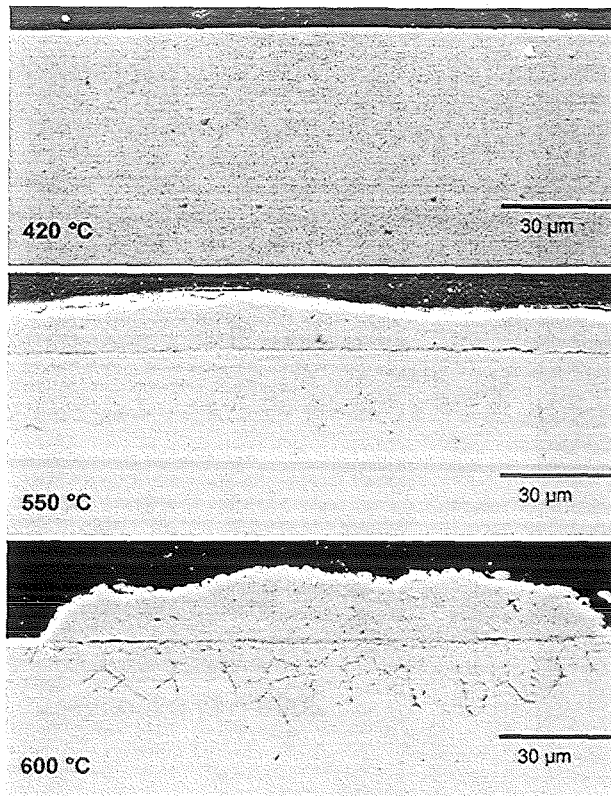


Fig. 5: SEM cross section of 1.4970 specimens B1 after 2000 h of exposure.

### 3.3 MANET specimen C1

The behavior of the MANET specimen C1 was examined at 420 °C and 550 °C only because this steel is not designed for higher temperatures. As expected from earlier experiments in stagnant lead [8] on martensitic steels a protective oxide formation takes place with a magnetite scale on top and a spinel layer below the specimen surface. It grows strongly with increasing temperatures.

### 3.4 Austenitic specimens A2 and B2, diffusion alloyed by Al-foil wrapping

The specimens show good corrosion resistance at all temperatures. This is demonstrated by the SEM cross sections and the overview picture for the example of AISI 316 L specimen A2 in Fig. 6. The only difference between the specimens is the appearance of some pores in the NiAl interface layer between the FeAl and the Fe(Al) dissolved region of 316 L on specimens exposed to 550 and 600 °C because of outward diffusion of iron into Fe(Al) layer. Specimen B2 consisting of 1.4970 steel has a dense NiAl interface layer. The FeAl layer on top of the specimens is maintained with the original thickness. No dissolution attack or liquid metal penetration is visible also at 600 °C on both specimens.

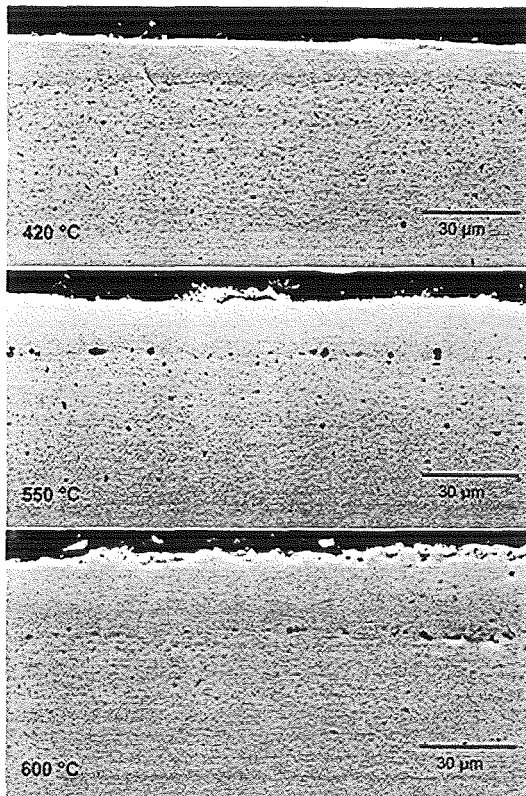


Fig. 6: SEM cross section of AISI 316 L specimens A2 after 2000 h of exposure.

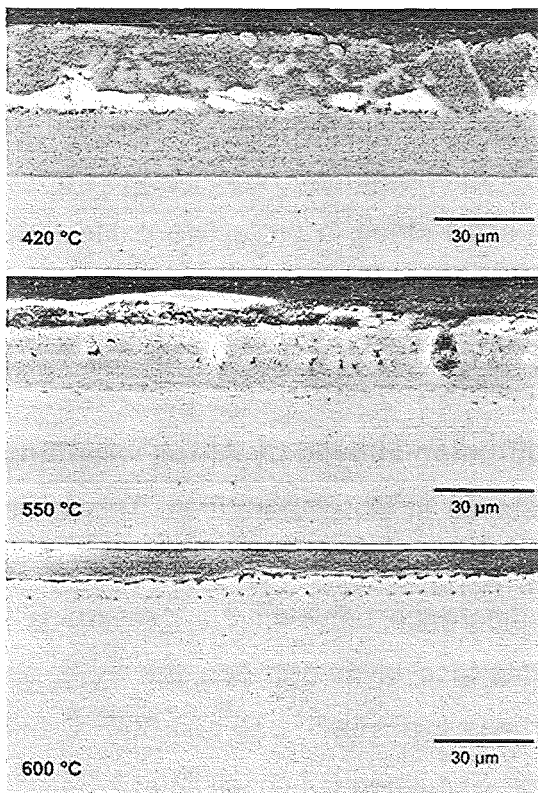


Fig. 7: SEM cross section of AISI 316 L specimens A3 alloyed by Al-hot-dipping.

### 3.5 AISI 316 L specimen A3, diffusion alloyed by Al-hot-dipping

Severe attack and penetration of the liquid metal is observed in the upper part of the Al layer already at 420 °C after 2000 h as shown in Fig. 7. This part consists only of

Al Si rich precipitations which appear as slightly brighter inclusions. The lower part of the layer contains additionally up to 10 at% iron. The sharp line represents the original steel surface. At 550 °C also the lower part of the Al layer containing some iron is corroded and penetrated by liquid metal. The specimen exposed to 600 °C has no Al layer any more. A small protective layer of a few microns only is observed on the surface. This layer consists now of FeAl. Since this phase was not existent in the beginning it must have been formed during the tests.

### 3.6 1.4970 specimen B3, diffusion alloyed by Al-hot-dipping

The layer on specimen B3 shows a similar structure like that on A3. At 420 and 550 °C, Fig. 8, in principle the same type of attack occurs as observed for the hot-dipped 316 L specimen A3. However at 600 °C the remaining small interdiffusion zone has no protective behavior. This zone contains less than 8 at% Al. The liquid metal penetrated the steel surface and caused dissolution on Ni partly through the whole tube wall of 400 µm thickness. By looking at the specimen surface it is noticed that large parts of the tube wall disappeared.

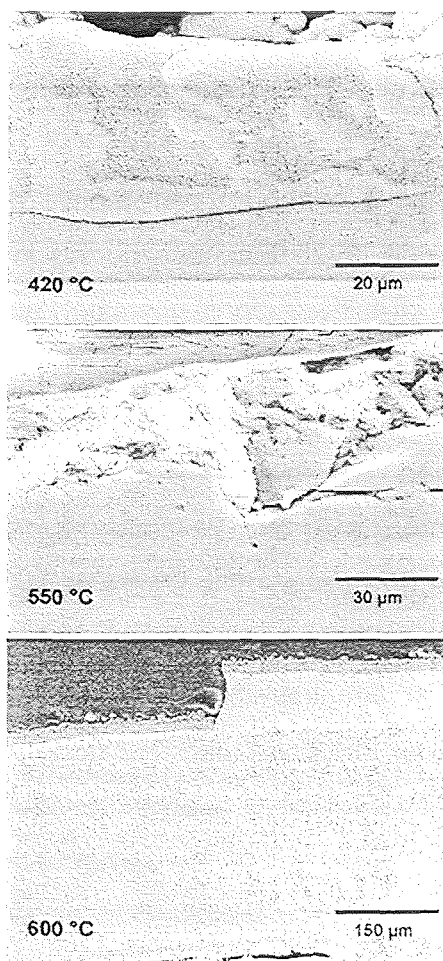


Fig. 8: SEM cross section of 1.4970 specimens B3 alloyed by Al-hot-dipping after 2000 h of exposure.

#### 4. Discussion

The formation of stable dense oxide layers protects steel from dissolution attack by liquid Pb/Bi at temperature below 600 °C. It is necessary therefore, to add oxygen and control its concentration in the liquid metal alloy to prevent oxide degradation. The oxygen concentration of  $10^{-6}$  at% applied in the loop test is sufficient for formation of oxide scales [8].

The austenitic and martensitic steels develop and maintain protective oxides at the surface that avoid the contact between the liquid metal alloy and the metallic steel. However, locally disintegration of the protective scale starts at 600 °C. This is the reason for onset of a partially severe solution attack, as observed for the AISI 316 L specimen A1. Once the liquid metal permeates the protective scale, its oxygen supply out of the liquid metal bulk is strongly reduced and with it the possibility of oxide formation at the front of penetrating Pb/Bi. The liquid metal inside the deep reaction zone in specimen A1 after exposure to 600 °C for 2000 h is highly enriched in Bi, represented by the bright phase. The remaining steel structures in this zone are highly reduced in Ni to less than 1 at%. The other austenitic specimen B1 of 1.4970 steel does not show this severe dissolution attack. The reason for this different behavior is not yet clear. The oxide layer on 1.4970 should be more stable than that one on 316L.

The oxide scale on MANET steel specimen C1 has a continuous protective oxide layer up to 550 °C. However, further increased oxide layer thickness during longer exposure times could impose a problem as well. A consideration of corrosion effects of this steel at 600 °C is not useful because of the insufficient mechanical stability at this temperature.

Steels with alloy formation at the surface have a good resistance against dissolution attack of liquid Pb/Bi up to 600 °C on condition that the Al and Fe concentration is high enough to allow FeAl formation at the surface. Both austenitic steels alloyed by Al-foil wrapping and annealing have an about 15 µm thick FeAl layer on top of the steel surface which is created by diffusion of iron into the liquid Al layer during annealing at 1040 °C. On the other hand Al diffuses into the bulk steel body, such forming a Fe(Al) solution zone. The surface layer develops a stable thin alumina layer in oxygenated liquid Pb/Bi which constitutes an effective barrier against dissolution and further oxidation. The same positive result is obtained in an earlier

work with stagnant lead [8] by alloying Al into the steel surface using the GESA facility [15].

Specimens A3 and B3 are alloyed by hot-dipping of austenitic steel into liquid Al and subsequent annealing. The steels examined have no stable surface alloy. It consists of Al with 12 at% Si and a few at% of iron only, because the annealing temperature is as low as 550 °C in this case. The silicon is an addition to the Al bath. Already at 420 °C the dissolution of the Al layer starts and is completed at 600 °C. After 2000 h of exposure only a few  $\mu\text{m}$  thick FeAl layer in the interdiffusion zone at the AISI 316 L steel surface still hinders the penetration of Pb/Bi at 600 °C. On the 1.4970 specimen B3, this barrier is already broken after 2000 h at 600 °C with a catastrophic dissolution attack as a consequence. The high carbon content in 1.4970 and observed precipitations of TiC and other impurities, mainly sulfur of up to 5  $\mu\text{m}$  extension may be the reason for a forced penetration through the steel surface.

The fact that FeAl layers form stable oxide scales and Al layers get dissolved shows the important role of the activity of Al in protective layer formation. The activity of Al must be drastically lowered e.g. by FeAl formation to favor oxide formation against the dissolution attack. Because of the high solubility of Al in Bi the dissolution attack of Pb/Bi on Al is so fast that no oxide scale can be formed. Therefore an Al compound is required at the surface which is stable enough to minimize the high dissolution attack of Bi. This problem does not appear with pure Pb melts in which the solubility is much lower [8].

## 5. Conclusions

In general, the original steels without surface alloying are suitable for application in liquid Pb/Bi up to temperatures of 550 °C at oxygen concentrations of  $10^{-6}$  at% and higher. The austenitic A2 and B2 specimens, surface alloyed by Al with formation of FeAl at the surface, have no signs of any corrosion even at 600 °C. They are protected by a thin alumina layer which remains stable.

Austenitic specimens A3 and B3 hot-dipped in Al and annealed at 550 °C only, with no FeAl formation at the surface, are not able to develop protective oxide scales.

In liquid Pb/Bi the activity of Al at the surface must be low enough to minimize the solution rate of Al in Pb/Bi and allow oxide scale formation. FeAl at the surface fulfills this requirement.

## 6. References

- [1] C. Rubbia, J.A.Rubio, S. Buono, F. Carminati, Conceptual Design of a Fast Neutron Operated High Power Energy Amplifier, CERN/AT/95-44 (ET), September 29, 1995.
- [2] G. Y. Lai, 'High Temperature Corrosion of Engineering Alloys', ASM Int. (1990).
- [3] R. P. Elliot, 'Constitution of Binary Alloys', First Supplement, McGraw-Hill Book Company.
- [4] T.B. Massalski, Editor, 'Binary Phase Diagrams' ASM Int. (1990).
- [5] O. Madelung, Editor, Landolt-Börnstein New Series IV, 5 (1995).
- [6] B. F. Gromov, Yu. I. Orlov, P. N. Martynov, K. D. Ivanov, V. A. Gulevski in 'Liquid Metal Systems', Edited by H. U. Borgstedt and G. Frees, Plenum Press (1995) 339.
- [7] I. V. Gorynin, G. P. Karzov, V. Markov, V. S. Lavrukhin, V. A. Yakovlev, Proceedings of the Conference HLMC 98, Obninsk: SSC RF – IPPE, 1999. – Volume 1 120-132.
- [8] G. Müller, G. Schumacher, F. Zimmermann, J. Nucl. Mater., 278 (2000) 85-95.
- [9] G. Benamati, P. Buttol, V. Imbeni, C. Martini, G. Palombarini, J. Nucl. Mater., 278 (2000) 308-316.
- [10] R. C. Asher, D. Davies, S. A. Beetham, Corrosion Science, 17 (1977) 545.
- [11] H. U. Borgstedt, H. Glasbrenner, Fusion Eng. Des. 27 (1995) 659.
- [12] H. Kleykamp, H. Glasbrenner, Z. Metallkd. 88 (1997) 3.
- [13] L. Cinotti et al. ANSALDO, 'the EAP 80 status of development' this journal
- [14] H. Glasbrenner, J. Konys, K. Stein-Fechner, O. Wedemeyer, J. Nucl. Mater. 258-263 (1998) 1173
- [15] G. Müller, G. Schumacher, D. Strauss, V. Engelko, A. Andreev, O. Komarov, N. Schegolichin, Proc. 11<sup>th</sup> Int. Conf. High Power Particle Beams (Prague, 1996), Vol. I, 267.

III. Generation of coarse group libraries with the KAPROS procedure COLLIB  
(C.H.M. Broeders, R. Dagan, IRS)

**Abstract**

Dynamic reactor simulations may need numerous repetitive cross section evaluations. Although computer resources are still developing fast, the application of multi-group calculations with a moderate number of groups ( $\approx 10$ ) seems to be reasonable for the near future. In this contribution a new KAPROS procedure COLLIB for the generation of microscopic group constant libraries with a reduced number of groups is presented. Starting from a well-validated master library, COLLIB may create a collapsed project library with the same data structures as the master library. The project library may be based on an arbitrary weighting spectrum. An arbitrary number of groups with arbitrary coarse group boundaries within the structure of the master library can be applied. The number of reactor materials on the project library may be restricted to the actually needed ones. First results from the applications ADS and HPLWR are presented.

**Zusammenfassung**

Für die dynamische Simulation von Kernreaktoren kann eine sehr häufige Neurechnung von Neutronenwirkungsquerschnitten erforderlich sein. Trotz schneller Weiterentwicklung der Computerressourcen kann man erwarten, dass in absehbarer Zukunft die Anwendung von Multigruppen Rechnungen mit etwa 10 Gruppen beibehalten wird. In diesem Beitrag wird eine neue KAPROS Prozedur COLLIB für die Erzeugung von Gruppenkonstanten Bibliotheken mit reduzierter Gruppenzahl vorgestellt. COLLIB kann, ausgehend von einer gut validierten Master-Bibliothek, eine Projekt-Bibliothek mit beliebiger Gruppenzahl mit beliebigen Gruppengrenzen innerhalb der Struktur des Master-Bibliotheks, unter Verwendung eines beliebigen Wichtungsspektrums erzeugen. Die Zahl der Materialien auf dieser Projekt-Bibliothek kann auf die aktuell benötigten beschränkt werden. Erste Ergebnisse für die Anwendungen ADS und HPLWR werden präsentiert.

## 1. Introduction

The coupling of thermal hydraulic and neutronic codes for dynamic simulations leads to numerous repetitive cross section evaluations. For conventional operating core designs it is convenient to generate these group constants by interpolating in pre-calculated tables of microscopic cross sections as a function of temperature, density, etc. For new core design concepts like ADS and HPLWR adequate tabulation and interpolation schemes are not known a priori and it is recommended to evaluate the cross section data each full time step where a neutronic and a thermal-hydraulic calculation are performed. Neutronic calculations start usually from well-validated multi-group libraries with typically 26, up to 2000 groups. These large group numbers lead to impractical long computing times and adequate group collapsing procedures are mandatory. These collapsing procedures may be based both on microscopic and on macroscopic level. In the following a KAPROS module COLLIB (COLLapsing LIBraries) and first applications are presented. COLLIB is a two stage collapsing procedure starting from a well validated more general applicable many-group **master** library and creating a system dependent coarse-group **project** library with the same organisation as the master library. The master library for the following investigations has the well-known 69 WIMS group structure.

## 2. Characteristics of the master library

The multi-group master library is generated from evaluated nuclear data files. At FZK the first applied evaluated nuclear data files were generated in the so-called KEDAK format and could be processed with the MIGROS code to multi-group libraries in GRUBA format, see e.g. KFK5072 [1] for more details. The FZK multi-group master libraries are partially still based on those developments. In the mean time the ENDF/B format is standard for evaluated nuclear data files and the group constant calculations are mainly performed with the NJOY processing code. The code system NJOY uses the ENDF data files to create the so-called PENDF (Point Evaluated Nuclear Data files). Those files are temperature dependent and are collapsed to a final number of energy groups for macroscopic calculations. The group structure and group number may be different from one system to another, based on the neutron energy spectrum

of the anticipated application. However, the WIMS library with 69 groups proves to be an adequate solution for the analysis of a broad range of fission reactor applications. Some care is required for application to ADS problems due to the upper energy limit of 10 MeV. For the calculation of mean group values in NJOY adequate user-defined weighting functions are required. The consequences of the choice of the spectrum become less important at larger number of energy groups. For most NJOY calculations with the WIMS energy group structure the NJOY standard spectrum of a LWR was applied. The FZK multi-group libraries in GRUBA format are based on the narrow-resonance approximation for resonance cross-sections. Cross sections are stored for infinite dilution and as self-shielding tables relative to these values (f-factors). The GRUBA format is very flexible and enables accurate representation of all data needed for deterministic neutron transport calculations for fast, epithermal and thermal reactor systems. Available libraries are well validated for a broad range of applications.

### **3. Application of coarse-group libraries**

For reducing the computing time of the cross section evaluation during transient calculations it is evident that the time consuming many-group calculations, followed by a collapsing procedure for each reactor zone, has to be modified.

One possible solution, applied in the SIMMER code [2], is the use of a multi-group library with the rather small number of 11 groups, evaluated in advance with the NJOY code or with other procedures.

An alternative solution, here realised in the new procedure COLLIB, is the collapsing of a 69 group master library. This means that the cross sections, f-factors, transfer matrices and other data have to be weighted in a proper manner and collapsed to the prescribed small number of groups. The spectrum chosen for such an evaluation is strictly problem dependent as the number of the groups is significantly reduced. Thereafter zones, which differ strongly from the original chosen spectrum for the collapsing procedure, may have inaccurate cross section values. From the above it is obvious that one should collapse the 69-group library in an optimized manner to account for as much as possible wide range peculiar issues concerned with the coarse group library generation. In particular, the group boundaries have to be carefully selected with respect to f-factors and threshold reaction characteristics. The collapsing

procedures are straightforward with some complications for f-factors if the storage mode (description of background-, temperature- dependencies) is not the same in all fine sub-groups of the coarse group system.

#### 4. Validation of the COLLIB procedure

##### 4.1 Application for fast energy spectrum ADS

For a fast energy spectrum ADS system, where the possibility of large voids within the core is to be excluded at least for the early stage of kinetic calculations, it was found that a collapsed 9 group library, based on a temperature and density averaged spectrum, results in acceptable accuracy in comparison with the time consuming 69 group master library. The comparisons were performed for the criticality and for the void- and Doppler- effects.

The zero dimensional (fundamental mode)  $K_{\infty}$  and  $K_{eff}$  (with constant buckling) were investigated for different number of groups. The results in table 1 show that the 9-group structure is sufficiently close to the 69-group case, whereas the 4-group case deviates from the reference 69-group solution significantly.

Table 1. Fundamental mode calculations with and without buckling for selected number of groups: master library 69 groups, COLLIB libraries 9 and 4 groups

Number of groups	69	9	4
$K_{eff}$	1.1403	1.1419	1.1451
$K_{eff}$	1.0241	1.0262	1.0311

The efficiency and accuracy of the 9 coarse group library generated by the COLLIB module was investigated for the FZK multiple source benchmark problem [3] with THO2/UO2 fuel and lead cooling. Macroscopic cross sections were calculated for each of the 187 core zones. The computation time was reduced by a factor of 5 using the new coarse library generated by COLLIB. Table 2 presents the results for the discrepancies in the criticality values for several types of perturbation.

Table 2. Validation results for a COLLIB library with 9 groups. The overall core criticality deviation for the FZK THO2/UO2 ADS design  $(K_{ref}-K_{collib})/K_{ref}$  amounts 0.47 %

Type of perturbation	Relative error $(\Delta K_{ref}-\Delta K_{collib})/\Delta K_{ref}$	Absolute error $(\Delta K_{ref}-\Delta K_{collib})/K_{ref}$
10% less fuel in center zone	1%	0.00007
50% of coolant density in core center zones	25%	0.00005
1000 <sup>0</sup> K increase in center core zones (from 1400K)	12%	0.00006
1000 <sup>0</sup> K decrease in center core zones (from 1400K)	12%	0.00019

The overall change in criticality was only 0.47% compared to the referenced 69 groups. Four extreme scenarios are investigated. The absolute error is of negligible importance, which indicates that for the specific case the chosen 9-group library is reliable. On the other hand the relative error points out the necessity of new validation tests for cores where the coolant density changes are more pronounced.

#### 4.2 Application for HPLWR investigations

For the high performance light water reactor (HPLWR) transport calculations with supercell models have been performed in order to evaluate the axial power distributions in the fuel assemblies to be used for coupling with thermohydraulic codes. For these calculations it was found that an HPLWR specific 12-group library was required.

The comparison in figure 1 of the results of  $K_{\infty}$  calculations for fuel assembly slices with this 12-group library, with the 69-group master library and with Monte Carlo calculations, show good agreement. On the basis of these results coupled calculations were performed with the thermodynamic code RELAP5 [4].

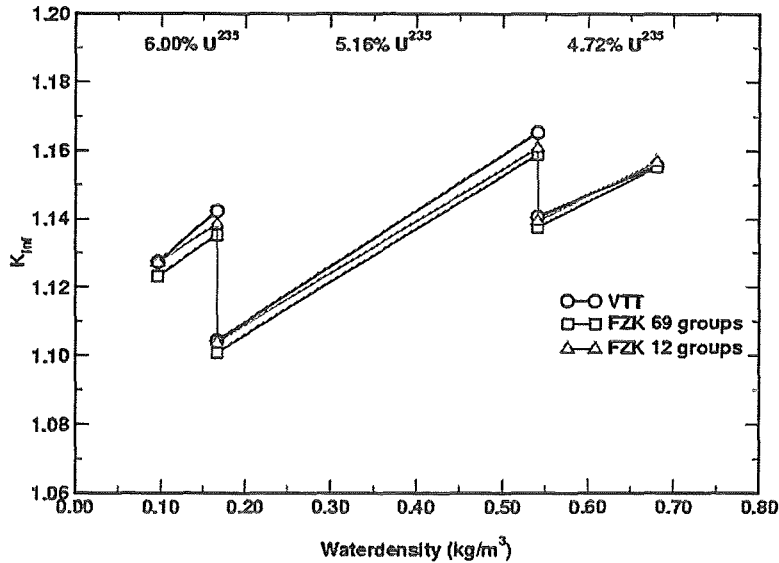


Figure 1. Comparison of  $K_{\infty}$  results of a 12-group COLLIB library with 69 group master library and with MCNP solution of VTT for fuel assembly slices of HPLWR benchmark. Fuel enrichment and waterdensity are varied.

#### 4.3 Application for the COSMO benchmark in the MUSE project

It is intended to validate proven calculation routes for the analysis of ADS in the MUSE project, being part of the 5. Framework Program of the EC. For this purpose dedicated experiments are in progress at the MASURCA reactor in Cadarache. Several benchmarks have been defined in order to evaluate the available calculation tools. For one of these benchmarks, the COSMO specification for a slightly simplified model of the critical reference system, some investigations were performed to validate the collapsing procedures in the KAPROS system. The calculations were carried out with the THREEDANT (X-Y-Z) transport code with  $S_8$  approximation. The results are summarized in table 3.

We observe a difference of about 1.3%  $\Delta K$  between the 69 group master library and 12 group solutions. Good agreement is found between cases 3 and 4, being alternative collapsing procedures in KAPROS with about a factor of 5 different computing times. The differences between 69 and 12 group calculations have to be analysed in more detail. Earlier observations already showed the high sensitivity of the treatment of the large blankets of the MASURCA reactor.

Table 3:  $K_{\text{eff}}$  results with THREEDANT (X-Y-Z)  $S_8$  approx. for MUSE COSMO benchmark

Method	COLLIB library			Collapsing from 69 groups		
Case	1	2	3	4	5	6
Groups	69	12	12	12	6	4
Mesh	coarse	fine	coarse	coarse	coarse	coarse
$K_{\text{eff}}$	0.99328	1.00112	1.00669	1.00650	1.007792	1.01213
cpu-time <sup>*)</sup>	≈156 min	≈275 min	≈5 min	≈24 min	≈15 min	≈7 min

Coarse mesh: 38x38x39 points (≈4 cm)  
 Fine mesh: 85x85x80 points (≈2 cm)  
 cpu-times are obtained on 1 GHz Pentium-III with LINUX OS

## 6. References

- [1] C.H.M. Broeders, „Entwicklungsarbeiten für die neutronenphysikalische Auslegung von Fortschrittlichen Druckwasserreaktoren (FDWR) mit kompakten Dreiecksgittern in hexagonalen Brennelementen“, KfK 5072 (1992)
- [2] E. Kiefhaber, „Updating of an 11-Groups Nuclear Cross Section Set for Transmutation Applications“, FZKA6480 (2000)
- [3] R. Dagan, C.H.M. Broeders, D. Struwe, „Modifications of the Code SAS4A for Simulation of ADS Designs“, FZKA 6334 (2000)
- [4] C.H.M. Broeders, V. Sanchez, E. Stein, A. Travleyev „Coupled Neutron Physics and Thermohydraulics Analysis of HPLWR fuel assemblies“, This volume

IV. Entwicklung des Rechenprogramms FLUTAN für thermo- und fluid-dynamische Anwendungen – Numerical analysis of MEGAPIE related thermal and fluid-dynamical problems

(G. Grötzbach, C. Panefresco, IKET; L.N. Carteciano, B. Dorr, W. Olbrich, IRS)

**Abstract**

The development and application of the thermal and fluid-dynamical code FLUTAN to ADS problems, especially to the MEGAPIE project, had to be stopped due to considerable changes in the team. The status of the reached code development is summarized. Meanwhile a new team at IKET has started. It is currently preparing additional numerical investigations by means of the commercial code CFX 4.4 for the design of MEGAPIE and for a benchmark to assess the numerical and physical modeling chosen by the different teams involved and to assess their different code results.

**Kurzfassung**

Die Weiterentwicklung und Anwendung des thermo- und fluiddynamischen Rechenprogramms FLUTAN auf Aufgaben aus dem ADS-Bereich und insbesondere aus dem MEGAPIE-Projekt mussten wegen personeller Veränderungen im IRS-Team beendet werden. Der Stand der erreichten Entwicklung des Codes wird kurz zusammengefasst. Inzwischen wurde am IKET ein neues Team in die Nutzung des kommerziellen CFD-Programms CFX 4.4 eingearbeitet. Es wurden die notwendigen Eingaben für weitere Analysen des MEGAPIE-Designs und für ein vom MEGAPIE-Target abgeleitetes Benchmark vorbereitet, mit dem die von den verschiedenen beteiligten internationalen Teams gewählten numerischen und physikalischen Modellierungen und ihre Codes bewertet werden sollen.

**1. Introduction**

The development of a spallation target for an ADS reactor requires the experimental and numerical investigation of the cooling of thin-walled thermally highly-loaded surfaces. In parallel to the HGF-project of 32.23.06 which concentrates here at FZK

on this topic, there is at PSI Würenlingen the MEGAPIE project ongoing in which a modeled target is developed for an ADS [2]. The target shall be irradiated in the SINQ radiation source [16]. The results gained from the design, construction, operation, analysis, and decommissioning of that target will provide a valuable basis for the development of an ADS target.

The thermal- and fluid-dynamical design of such a target is widely basing on numerical tools like on CFD codes. As the system is rather complex, powerful codes with recent physical modeling, numerical schemes, and pre- and post-processing tools are required. Up to mid of 2001 our numerical work at IRS on the MEGAPIE project and the related code development was basing on the FLUTAN code [17]. Due to major personal changes a new team had to be build up at IKET. The development and application work in this team is now basing on the commercial CFD code CFX 4.4 from AEA Technologies. Here we will shortly report on the status of the FLUTAN code development as it was finally achieved and on the ongoing preparations for new applications with the code CFX 4.4 to the MEGAPIE related investigations.

## **2. Final status of FLUTAN work**

FLUTAN is a highly vectorized computer code for 3d fluid-dynamic and thermal-hydraulic analyses in Cartesian or cylinder coordinates [16]. It was developed at FZK in order to simulate single phase flows with small compressibility. The conservation equations for mass, momentum, energy, and turbulence quantities are discretized on a structured grid by a finite volume method. A staggered grid is used for the velocities. The discretization of the diffusive terms is performed by a central difference scheme. A first order upwind or one of two second order upwind methods (QUICK [15] and LECUSSO [11]) can be chosen for the convective terms. Several Poisson solvers are available for pressure calculation, e.g. the highly vectorized CRESOR solver [4]. A first order implicit Euler-method is used for time discretization. Recently developed and implemented numerical features are achieving a larger numerical efficiency and an improved numerical accuracy: One is an explicitly treated static local grid refinement method for the Cartesian grid [1]. The other one is a new method to use body fitted coordinates in a code basing on a staggered grid: the conservation equations are transformed from the Cartesian to a general curvilinear system by keeping the physical Cartesian velocity components as dependent

variables and by defining three Cartesian velocity components on every cell surface [12].

Several turbulence models are available in FLUTAN. The most important one is the Turbulence Model for Buoyant Flows (TMBF) which consists of a first order  $k$ - $\epsilon$  model in a low-Reynolds number formulation and a second order five-equations turbulent heat flux model [6]. With specially developed model extensions deduced theoretically and calibrated by using Direct Numerical Simulation data the model capabilities were extended to liquid metal flows with heat transfer [7]. In several benchmarks it turned out that the TMBF in its current development status is a powerful tool at least for forced and mixed convection for a wide range of fluids including liquid metals with very small Prandtl numbers [3].

Special thermal boundary conditions are available like a heat exchanger model, a 1d wall model, and a model for heat radiation from solid surfaces [8]. A 3d heat conduction model for the structures was developed for the investigation of the SUCOS experiments [9], [10]. This is necessary for simulating solid structures with internal non-uniform transport of heat. The structure temperatures are discretized on an own grid on which the heat conduction equation is solved in all dimensions independent of the solution of the corresponding equation in the fluid domain. Accurate coupling of the radiation model and of the 3d structure model to the energy in the fluid is achieved by implementing both models within the outer iteration loop.

A modern graphical user interface was developed in which most of the existing programs for pre- and post-processing, solving the equations, data conversion, and maintenance of the FLUTAN code system were implemented. This user interface, as well as the ONLIVIS program for the local online visualization of results from a FLUTAN calculation running on an other computer system is based on the program language Tcl/Tk; thus, it can be used on Windows and on UNIX-based systems [5].

In order to verify the numerics and the physical modeling in the code, a large number of fundamental laminar and turbulent flows were recalculated, as well as a large number of numerical tests have been performed using flows with analytical solutions to check the consistency and accuracy of the results; see most of the references given here on the code. Applying the code to many different convective heat transfer problems and experiment interpretations showed the reliability of FLUTAN and its models.

Recent contributions of FLUTAN to the development of an ADS target or to the MEGAPIE model target were the following:

The COULI benchmark was thought to investigate the reliability of available CFD codes for the adiabatic flow through a target. In blind predictions, research as well as commercial codes provided qualitatively different results, with different positions of areas where separated flow occurs. Unfortunately, the experimental results from CEA Grenoble which became available up to now suffered from some experimental difficulties and do not allow for final conclusions. In this context FLUTAN was also used to find a modified target flow guide geometry which should ensure flow without separation [13].

Detailed analyses of the window area of the MEGAPIE target with commercial codes require boundary conditions for the limited computational domain. With the more efficient FLUTAN code a fully 3d analysis of a simplified version of the complete MEGAPIE module was analyzed. It was found that either the use of case specific inlet conditions in small domain calculations are required, or that it is required to use a full length representation of the complete target area below the heat exchanger. In using the 3d heat conduction model for the guide tube it was also found, that in a typical forced convection case about one quarter of the heat introduced by the beam is transferred from the hot fluid rising inside the guide tube through this tube to the cold down coming fluid outside the guide tube. This increases the temperature of the coolant near the window and therefore increases also the window temperature [5]. Thus, detailed analyses have to include the modeling of thermal interaction of the coolant with the internal structures inside the fluid domain.

The performance and accuracy of the turbulence models used in FLUTAN were recently investigated by participating in the TEFLU benchmark. As many of the colleagues in Europe participating in this recalculation of a heated sodium jet experiment [14] we also found that standard turbulent heat flux models basing on Reynolds analogy cannot well reproduce the thermal mixing within the liquid metal. From the results with the TMBF model we can predict an approximate spatial distribution of the turbulent Prandtl number; it turned out that this calculated value strongly depends on flow parameters and on the position in the flow domain, and that it varies between two and five [13]. This explains, why some colleagues achieved best results by just neglecting the turbulent contribution to the heat flux, which corresponds to use a infinite turbulent Prandtl number. These results will further be

evaluated within the ASCHLIM project to assess the currently available CFD tools for liquid metal heat transfer.

Due to changes in staff the FLUTAN code is no longer been used at FZK. The code has been archived at FZK/IKET, most of the pre- and post-processing tools are archived at FZK/IRS. Some of the ADS relevant models, like the TMBF, are planned to be made available by means of user specified subroutines to the CFX 4.4 code.

### **3. Preparations for MEGAPIE specific thermal and fluid-dynamical investigations**

Since summer 2001 a new team was built up for the ADS specific activities. In a first step, the team started to get acquainted to the CFX 4.4 code by developing first analyses for some of the basic research experiments from KALLA, see contribution to 32.23.06. Unfortunately, major problems occurred and additional activities were required in implementing the latest code version in the hardware environment of the IKET computers. In parallel, we were involved in the discussions of the ongoing work on the detailed design of the MEGAPIE target experiment. To prepare contributions to the project by making full use of our special physical modeling knowledge, we developed a first 3d block structured geometry input for the code representing the window area of the experiment up to the lower end of the heat exchanger. In Fig. 1 a detail of the block structure for the hemispherical window area is shown which includes a guide tube with a horizontal lower end and a bypass jet nozzle with a slanted lower end. The permanently changing design details provided from the MEGAPIE design team seem to converge now so that our input will be adapted to it and detailed numerical analyses of the final cooling concept of MEGAPIE are to come soon.

To assess the different codes used in the project together with the teams doing the numerical analyses, a benchmark specification was developed together with the other partners within the thermal-hydraulic activities in the MEGAPIE Initiative. The specified cases are near to the current design concept. Currently we are preparing the block structured geometry input for these calculations. The comparison and discussion of the results to come will help to identify weaknesses of the chosen modeling and will help to specify requirements for reliable predictions for the final MEGAPIE design and for an accurate interpretation of the related experiments.

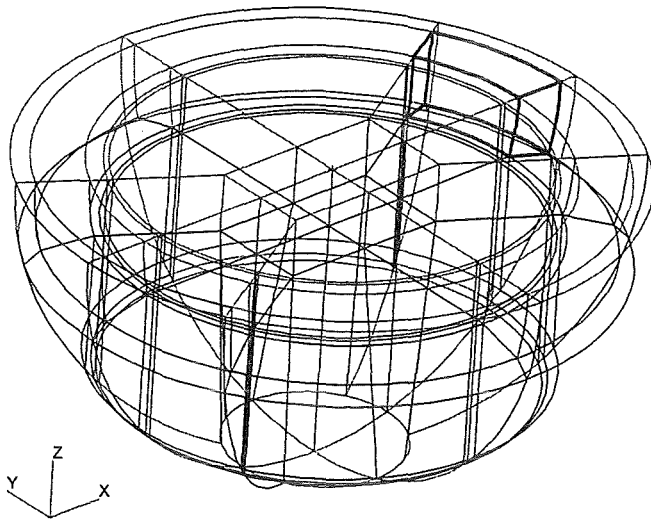


Fig.1: Detail of a CFX 4.4 input with the block structure in the window area. MEGAPIE geometry with a guide tube with a horizontal lower end and with a slanted jet nozzle (thick lines) with a rectangular cross section for the bypass flow across the hemispherical window.

#### 4. Conclusions

Up to the year 2001 we used in the ADS project the commercial code CFX at IKET and the FZK-code FLUTAN at IRS for thermal and fluid-dynamical investigations. The physical models in FLUTAN were widely adapted to the special problems of liquid metal heat transfer. As the key developers and users from the FLUTAN team left FZK, this development was stopped and the code and its tools were archived. The status of the finally achieved code status is shortly summarized. A new team had to be build up at IKET instead which is meanwhile introduced roughly in the application methods of CFX 4.4. Ongoing work is related to the preparation of numerical analyses for some open problems related to the detailed MEGAPIE design and for a benchmark basing on a MEGAPIE related geometry to assess the numerical modeling by the different teams involved in the project and by their codes.

#### References

1. Ammann, T., Entwicklung eines impliziten Verfahrens zur lokalen Verfeinerung eines strukturierten Gitters. Dissertation, Universität Karlsruhe (1997) FZKA 5864
2. Bauer, G., Salvatores, M., Heusener, G., The MEGAPIE initiative – Executive Outline and Status as per November 1999, Paul Scherrer Institut, Würenlingen, Switzerland
3. Baumann, W., Carteciano, L., Weinberg, D., Thermal propagation effects in a vertical turbulent flow behind a jet block - A benchmark exercise. J. of Hydraulics Research 35 (1997) pp. 843-864
4. Borgwaldt, H., CRESOR, A Robust Vectorized Poisson Solver Implemented in the COMMIX-2(V) Thermal-Hydraulic Code. Int. Conf. On Supercomputing in Nuclear Applications (SNA 90). Mito City, Japan, March 12-16 (1990) pp. 346-351

5. Carteciano, L., Dorr, B., Grötzbach, G., Olbrich, W., Jin, X., Two- and three-dimensional thermal and fluid-dynamical analysis of the complete MEGAPIE-module with the computer code FLUTAN. Programm Nukleare Sicherheitsforschung, Jahresbericht 2000, Forschungszentrum Karlsruhe, FZKA 6653 (2001) pp. 443 – 458
6. Carteciano L.N., Weinberg D., Müller U., Development and Analysis of a Turbulence Model for Buoyant Flows. 4th World Conf. on Experimental Heat Transfer, Fluid Mechanics and Thermodynamics, Bruxelles, Belgium (1997) 3 Pisa Edition ETS, pp. 1339-46
7. Carteciano, L. N., Wörner, M., Grötzbach, G., Erweiterte Turbulenzmodelle für technische Anwendungen von FLUTAN auf Naturkonvektion. Jahrestagung Kerntechnik 1999, Kerntechnische Gesellschaft e.V., INFORUM Bonn (1999) S. 129 - 134
8. Cheng, X., Müller, U., Turbulent Natural Convection Coupled with Thermal Radiation in Large Vertical Channels with Asymmetric Heating. Int. J. Heat Mass Transfer 41 (1998) pp. 1681-1692
9. Grötzbach, G., Peculiarities of natural convective heat removal from complex pools. A. Wada, H. Ninokata (Ed.), Flow Modeling and Turbulence Measurements, World Scientific Publishing Co. Pte. Ltd., Singapore (2002)
10. Grötzbach, G., Carteciano, L.N., Dorr, B., Jin, X., Analysis of an LWR Sump Cooling Concept. 29th IAHR Congress, Special Seminar on "Advances in Industrial Hydraulics and Applications to Energy Production", Beijing, China (2001)
11. Günther, C., Fortgeschrittene Upwind-Differenzen-Verfahren zur numerischen Lösung der Konvektions-Diffusionsgleichung. Habilitation, Universität Karlsruhe (1992) KfK 4697
12. Jin, X., Rechenverfahren zur Diskretisierung von Strömungen in komplexer Geometrie mittels körperangepasster Gitter. Dissertation, Universität Karlsruhe (2001) FZKA 6596
13. Knebel, J.U., Cheng, X., Müller, G., Schumacher, G., Konys, J., Wedemeyer, O., Grötzbach, G., Carteciano, L., Thermalhydraulic and Material Specific Investigations into the Realisation of an Accelerator Driven System (ADS) to Transmute Minor Actinides – 2000 Status Report. Forschungszentrum Karlsruhe (2001) FZKA 6618
14. Knebel, J.U., Krebs, L., Müller, U., Axcell, B.P., Experimental investigations of a confined heated sodium jet in a co-flow. J. Fluid Mech., 368 (1998) pp. 51-79
15. Leonard, B. P., A Stable and Accurate Convective Modelling Procedure Based on Quadratic Upstream Interpolation. Computer Methods in Applied Mechanics & Engineering 19 (1979) p. 59
16. PSI Annual Report 1997. Annex IIIA, Paul Scherrer Institut, Würenlingen, Switzerland
17. Willerding, G., Baumann, W., FLUTAN 2.0 Input Specifications (1996) FZKA 5712

## V. Werkstoffkundliche Bewertung des Strahlfensters

(E. Materna-Morris, A. Möslang, D. Preininger, P. Vladimirov, IMF I)

### **Abstract**

For the selection of an appropriate structural material as target window for MEGAPIE a first assessment of the observed radiation hardening and embrittlement in ferritic/martensitic steels has been made based on reactor irradiations ( $< 5$  dpa) in the temperature range RT to 400 °C. Taking into account helium effects, two approaches used in the assessment came to similar results regarding the most likely DBTT shift in the 9Cr1Mo steel after MEGAPIE irradiation to 10 dpa in the temperature range 250-300°C. For these conditions both, the "saturation model" and the "radiation hardening model" predict a DBTT shift in the range  $160 \pm 25$ °C. This means that the initial criterion can be just fulfilled. In addition, based on a combination of different codes (MCNP-X, NJOY, BOLT) calculations have started to get a 3D distribution of material specific loading conditions.

### **Zusammenfassung**

Zur Auswahl eines geeigneten Strukturmaterials für ein MEGAPIE-Targetfenster wurde eine erste Beurteilung vorgenommen für eine Reihe ferritisch-martensitischer Stähle auf der Basis von Reatorbestrahlungen ( $< 5$  dpa, Bestrahlungstemperatur RT bis 400 °C) unter besonderer Berücksichtigung potentieller Heliumeffekte. Zwei unterschiedliche Modelle, das „Sättigungsmodell“ und das „Bestrahlungshärtungsmodell“ kommen zu ähnlichen Aussagen. Demzufolge kann z. B. für einen 9Cr1Mo-Stahl nach 6-monatiger MEGAPIE-Bestrahlung (10 dpa,  $T_{irr} = 250-300$  °C) eine Sprödbruchübergangstemperatur von  $160 \pm 25$ °C vorausgesagt werden, welche die Mindestanforderungen gerade noch erfüllen würde. Des Weiteren sind zur Bestimmung der räumlichen Verteilung wesentlicher Werkstoffkennwerte Berechnungen (MCNP-X, NJOY, BOLT) angelaufen.

### **Loading conditions for the target window and assessment methodology**

The target window of the forthcoming MEGAPIE experiment that serves as interface between the vacuum proton beam line and the liquid Pb-Bi spallation target has to withstand high energy mixed proton/neutron irradiation and accumulates at rather low irradiation temperatures (150-250 °C) within 0.5 years a total displacement

damage of ~10 dpa and a significant amount of transmutation products (e.g. 500 appm He, 9000 appm H). It is expected that the combination of relatively low irradiation temperature and a large amount of transmutation products will lead to significant irradiation hardening, loss of ductility and embrittlement. In order to achieve safe operation conditions and overall structural integrity of the beam window, the ductile brittle transition temperature DBTT must be kept below the coolant inlet temperature. Thus, a DBTT <150 °C after irradiation is presently considered as the major design criteria.

Two different ways of extrapolation have been adopted: The first extrapolation is based on an earlier analysis of the development of DBTT for MANET I [1], which describes the observed shift  $\Delta DBTT$  of the Ductile-to-Brittle-Transition-Temperature at 300 °C up to 15 dpa by a formula and which is adapted to the very few data of the 9Cr1Mo mod steel. The second approach is based on a model which correlates observed radiation hardening with  $\Delta DBTT$  [ 2,3] and allows to estimate a possible additional effect of high helium generation on the DBTT shift.

### **Analyses of neutron irradiated 7-12% Cr-steels with low helium content**

As a first step, a direct extrapolation of DBTT from Charpy specimen tests has been performed. Based on Charpy-V-tests of specimens that had been irradiated between 250 - 475 °C in the HFR reactor a phenomenological formula description of the irradiation effects for MANET I was made [1]. The underlying procedure is based on a variety of equations that have been fitted to the experimental data using least square fit algorithm. As a result, it has been found that at a given irradiation temperature  $T_{irr}$  an exponential behavior fits best the DBTT increase as function of the dpa dose. Fig. 1 shows the experimental data (symbols) of MANET I and other f/m steels of the irradiation induced shift  $\Delta DBTT$  as function of dpa dose for different f/m steels [3-6]. These data have been fitted (curves) by the equations  $DBTT = DBTT_0 + \Delta DBTT$  and  $\Delta DBTT = T_s (1 - \exp(-AN_{dpa}))$  which implies saturation with fluence.  $DBTT_0$  is the ductile to brittle transition temperature before irradiation,  $\Delta DBTT$  the irradiation induced shift,  $T_s$  the saturation value of  $\Delta DBTT$ ,  $A$  is a dose constant at which the exponential term arrives at 1/e and  $N_{dpa}$  the irradiation dose. A reliable fit of  $A$  and  $N_{dpa}$  covering the dose of a MEGAPIE window was only possible

for the MANET I steel that had been irradiated at 300 °C up to 15 dpa. All other steels were irradiated to 2.4 dpa.

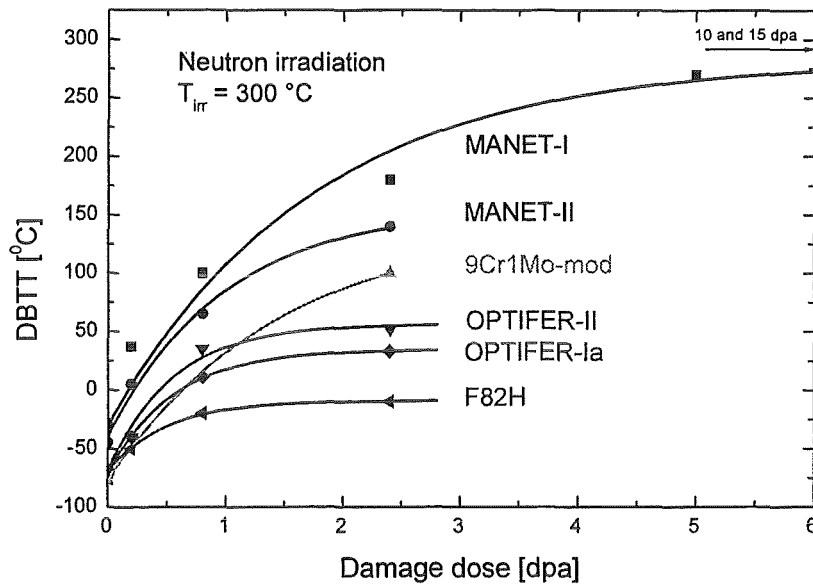


Fig. 1: DBTT of several ferritic-martensitic steels irradiated in the HFR at 300 °C.

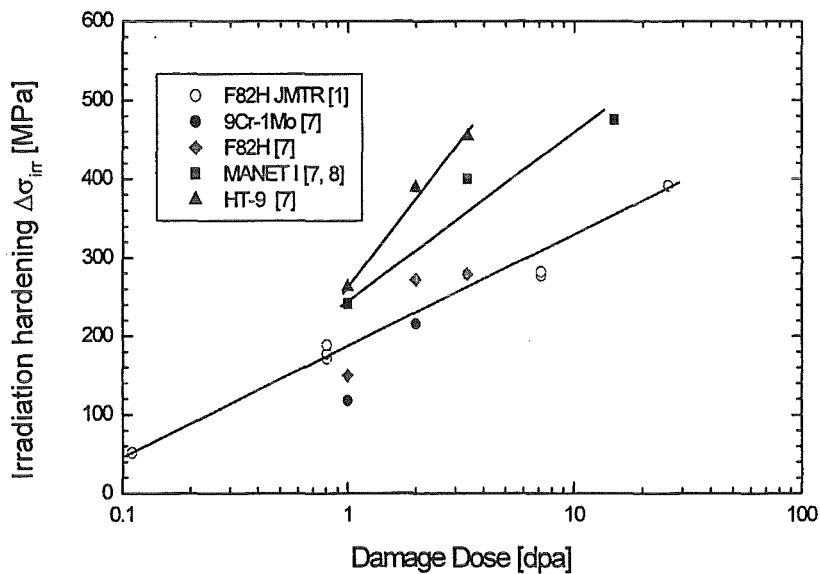


Fig. 2: Radiation induced hardening  $\Delta\sigma_{irr}$  versus damage dose at 300 °C in HFR.

The outcome of this methodology clearly shows that among the conventional steels only the 9Cr1Mo-mod comes close to the requirement of a DBTT below about 150 °C. One reason for this finding could be the lower initial  $DBTT_0$ -value for the 9CrMo mod. alloy, another reason could be the difference in the boron content of the conventional alloys and hence the produced helium during the irradiation in HFR. All RA 7-10%CrWVTa steels are well below that limit. However, helium embrittlement is

hardly taken into account because the helium concentration in all steels investigated is below about 60 appm, in the F82H-mod even below about 10 appm. As shown later, an additional DBTT increase of about 34 °C has been evaluated for a helium concentration of 500 appm in this temperature range. That is, all RA 7-10CrWVTa steels would still meet the requirement of  $DBTT_{10 \text{ dpa}} \leq 150 \text{ °C}$ , assuming saturation in DBTT.

In a second step, a correlation of the irradiation induced shift  $\Delta DBTT$  with radiation hardening  $\Delta\sigma_{irr}$  has been made. Such a correlation is derived from a model [3] which describes the dynamic brittle fracture of f/m steels by stress induced propagation of micro-cracks, taking into account radiation induced hardening as well as void or bubble formation. A specific feature of this correlation is the proportionality between  $\Delta DBTT/DBTT_0$  and  $\Delta\sigma_{irr}$  for a given fracture stress. Fig. 2 shows for typical f/m steels the irradiation induced hardening  $\Delta\sigma_{irr}$  as function of the displacement damage following neutron irradiation at 300 °C in the HFIR [4,5] and JMTR [6]. Quantitatively the irradiation induced hardening  $\Delta\sigma_{irr}$  can be described for F82H and all other alloys by an equation of type  $\Delta\sigma_{irr} = A + B \ln(dpa)$  without saturation below 26 dpa. An extrapolation to 10dpa gives at 300°C for F82H a radiation hardening of 330 MPa and for the 9Cr1Mo mod 355MPa. Within the frame of the underlying approach this DBTT-value is shown to be quite reliable [3,7]. With this dose dependence the DBTT after an exposure of 10 dpa can be calculated individually for the given materials.

### Helium effects on DBTT

In the HFR irradiated steels between about 10 and 60 appm helium are generated within the early irradiation phase ( $\leq 1$  dpa) due to the different contents of the boron, especially the isotope  $^{10}\text{B}$ . This moderate helium concentration is already included in the findings of the above chapter. At helium concentrations of 300 appm experimental data mainly based on MANET-1 and F82H irradiations have demonstrated [3] that under dynamic loading conditions helium can contribute to the cleavage fracture embrittlement of martensitic steels. While in neutron irradiated specimens (low He/dpa ratio) the DBTT increase is mainly caused through hardening induced displacement damage, a significant fraction of the additional DBTT shift in helium implanted specimens (higher He/dpa ratio) can be attributed to fracture stress reduction due helium segregation at fracture surfaces.

A phenomenological model has been proposed [3] that correlates the dynamic quasi-cleavage fracture of martensitic steels with irradiation induced changes of strength and fracture stress. Although micro-mechanical and microstructural features are not yet included in detail, the model is able to distinguish quantitatively between helium and damage-induced embrittlement. It predicts that the relative shift in the ductile-brittle-transition temperature  $\Delta DBTT/DBTT_0$  should be basically proportional to the square root of the dpa dose and, in an additive manner, also to the square root of the helium content. That is, if the effect of 300 appm helium results at an irradiation temperature of 300 °C in a  $\Delta DBTT$  shift of 26 °C, 500 appm helium would produce a shift of approximately 34 °C. This shift comes practically on top to the displacement damage induced  $\Delta DBTT$  shifts discussed in the previous chapters.

## Conclusions

Table 1 summarizes the findings of the evaluation described above, taking into account the effect of helium on hardening and consequently on DBTT increase. The extrapolations of both models used in this assessment come to similar results regarding the DBTT in the 9Cr1Mo mod steel after irradiation to 10 dpa in the temperature range 250-300°C and predict under this conditions a transition temperature of  $DBTT = 160 \pm 25^\circ\text{C}$ . This means that the initial strong criterion based on DBTT can be almost fulfilled. However, one should mention that the fracture strength at this temperature is still well above a critical value. In addition, an evaluation of stabilized austenitic steels to high displacement doses is reported in [8].

Finally, transport code calculations (MCNP-X, NJOY, BOLT) have been started more recently within the European SPIRE programme in order to characterise the 3D distribution of material specific loading conditions.

Table 1: Relevant data, derived from the correlation of  $\Delta$ DBTT with irradiation hardening  $\Delta\sigma_{irr}$ .

Material	$\Delta\sigma_{irr}$ [MPa]	DBTT $\sigma_0$ [°C]	DBTT at 10 dpa & 10-60 appm He [°C]	DBTT at 10 dpa & 500 appm He [°C]
MANET-II	480	-45	218	249
HT-9	618	~-45	295	326
F82H	330	-70	131	165
9Cr1Mo	355	-80	128	161

## References

- [1] M. Rieth, B. Dafferner, H.D. Röhrig, C. Wassilew, Fusion Engineering and Design 29 (1995) 365-370.
- [2] M. Rieth, B. Dafferner, H.D. Röhrig, Journ. Nucl. Mater 258-263 (1998) 1147
- [3] R. Lindau, A. Möslang, D. Preininger, M. Rieth, H.D. Röhrig, J. Nucl. Mater. 272&272 (1999) 450-454.
- [3] M.G. Horsten, E.V. van Osch, D.S. Gelles, M.L. Hamilton, „Effects of radiation on Materials“; 19<sup>th</sup> Internat. Symposium ASTM STP 1366, Eds: M.L. Hamilton, A.-S. Kumar, S.T Rosinski and M.L. Grossbeck, West Conshohocken, PA 1999, p. 597 and p. 612
- [4] A. Alamo, M. Horsten, X. Averty, E.I. Materna-Morris, M. Rieth, J.C. Brachet, J. Nucl. Mater 283-287 (2000) 353
- [5] E. Materna-Morris, M. Rieth and K. Ehrlich, „Effects of radiation on Materials“; 19<sup>th</sup> Internat. Symposium ASTM STP 1366, Eds: M.L. Hamilton, A.-S. Kumar, S.T Rosinski and M.L. Grossbeck, West Conshohocken, PA 1999, p.597
- [6] K. Shiba and A. Hishinuma, Journ. Nucl. Mater. 283-287 (2000) 474
- [7] D. Preininger, A. Möslang and K. Ehrlich; *Assessment of irradiation hardening and embrittlement in ferritic/martensitic steels*; Internal working document MEGAPIE, June 2000
- [8] R. Hübner und K. Ehrlich; Untersuchungen an Hüll- und Strukturmaterialien für ADS; FZKA 6480; August 2000

### **32.23.06 HGF-Strategy Fund Project 99/16: Thermalhydraulic and Material Specific Investigations into the Realization of an Accelerator Driven System (ADS) to Transmute Minor Actinides**

(J.U. Knebel IKET, G. Müller IHM, J. Konys IMF III, KALLA Team)

#### **Abstract**

The objective of this HGF Strategy Fund Project is the development of new methods and technologies to design and manufacture thin-walled and thermally highly-loaded surfaces which are cooled by a corrosive heavy liquid metal (lead-bismuth eutectic). Such a surface is the beam window which is a vital component of the spallation target of an accelerator driven system (ADS).

The results of this project will provide the scientific-technical basis which allows the conception and the design of an ADS spallation target and later on a European Demonstrator of an ADS system. The work performed at Forschungszentrum Karlsruhe is embedded in the Euratom 5<sup>th</sup> Framework Programme on ADS systems.

The project is divided in three sub-projects:

*Sub-Project SP1: Thermalhydraulic Investigations*

*Sub-Project SP2: Material Specific Investigations*

*Sub-Project SP3: Oxygen Control System*

The experimental investigations are performed in the KARlsruhe Lead Laboratory KALLA. KALLA is an international user laboratory.

This report gives the main results achieved during the year 2001.

#### **Kurzfassung**

Ziel dieses HGF-Strategiefondsprojektes ist es, neue Methoden und Technologien zur Auslegung und Herstellung dünnwandiger, thermisch hochbelasteter Oberflächen, die von einem korrosiven schweren Flüssigmetall (eutektisches Blei-Wismut) gekühlt werden, zu entwickeln. Eine solche Oberfläche ist das Strahlfenster, das eine entscheidende Komponente eines Spallationstargets für eine Beschleuniger getriebene Anordnung (ADS) bildet.

Das Ergebnis dieses Projektes ist ein wissenschaftlich-technisches Instrumentarium zur Konzeption und zur detaillierten Auslegung zunächst eines Spallationstargets und später einer Europäischen Demonstrationsanlage eines ADS. Die Arbeiten am Forschungszentrum sind in das Euratom 5. Rahmenprogramm zu Beschleuniger getriebenen Anordnungen (ADS) eingebunden.

Das Projekt gliedert sich in drei Teilprojekte:

Teilprojekt 1: Thermohydraulische Untersuchungen

Teilprojekt 2: Materialspezifische Untersuchungen

Teilprojekt 3: Sauerstoffkontrolle

Die experimentellen Untersuchungen werden im Flüssigmetalllabor KALLA (Karlsruhe Lead Laboratory) durchgeführt. KALLA ist ein internationales Anwenderlabor. Dieser Bericht gibt die wesentlichen im Jahr 2001 erzielten Ergebnisse wieder.

## 1. INTRODUCTION AND OBJECTIVES

The long-term strategy of the European research and development programme in the area of the peaceful utilization of nuclear energy for electricity production is based on scenarios, which consider the importance of the CO<sub>2</sub> emissions and the emission of other greenhouse gases, and the importance of the reduction of fossil fuel. These scenarios are balancing all possible energy resources. Supposing that nuclear energy shall provide a considerable amount of the electric energy produced in Europe, criteria such as energy security, economic efficiency and environmental sustainability are important.

To face facts, the nuclear waste is already existing in large quantities and will be produced continuously in the operating nuclear power plants. This is independent of the future of nuclear energy. As a consequence projects on fundamental actinide research, *partitioning and transmutation (P&T)*, spent fuel behaviour and fuel storage safety evaluations are required.

*Transmutation* is considered a promising technology worldwide for significantly reducing the amount and, thereby, the long-term radiotoxicity of highly active waste (HAW). Transmutation is the treatment of nuclear waste with an intense neutron flux in order to transmute transuranium (TRU) isotopes (plutonium and minor actinides) and long-lived fission products into short-lived radioisotopes or stable nuclei. The

maximum reduction of radiotoxicity could be by a factor of about 100. Transmutation is thus an alternative to the direct deposition of large volumes of highly radioactive waste. Transmutation presents the possibility of closing the fuel cycle including the minor actinides. Plutonium, minor actinides and long-lived fission products can be transmuted in a so called *Accelerator Driven System (ADS)*, which consists of an accelerator, a target module and a subcritical blanket.

The *target module* for ADS application is a technologically new component, the technical feasibility of which has to be assessed and experimentally proved. This project is concentrating on the development of a spallation target and on the solution of accompanying questions.

The *short-term objective of this HGF Strategy Fund Project* is the development of new methods and technologies to design and manufacture thin-walled and thermally highly-loaded components which are cooled by a corrosive heavy liquid metal. Such a component is the beam window which is cooled by liquid lead-bismuth eutectic. The beam window is a vital component of an ADS spallation target and thus of an Accelerator Driven System (ADS).

The project is divided in three sub-projects (SP):

- SP1: Thermalhydraulic investigations  
Thermalhydraulic investigations of thin-walled, thermally highly-loaded surfaces (beam window) with liquid lead-bismuth (Pb-Bi) as coolant,
- SP2: Material specific investigations  
Investigation of corrosion mechanisms and development of an instruction to condition metals in flowing lead-bismuth,
- SP3: Oxygen control system  
Oxygen concentration measurement and oxygen control in Pb-Bi loops.

The strategy of the project is based both on a theoretical / numerical approach and on an experimental approach.

The *medium-term objective of this HGF Strategy Fund Project* is the participation in the MEGAPIE Initiative which aims at the development and operation of the exploratory heavy liquid metal spallation target MEGAPIE with a beam power of 1 MW. MEGAPIE will be implemented in the existing spallation neutron source SINQ at Paul Scherrer Institute (PSI), Switzerland.

The *long-term objective of this HGF Strategy Fund Project* is – on the basis of the newly developed methods and technologies – to provide the scientific-technical tool which allows, now, the conceptual design and, at a later stage, the detailed design of a European Experimental Demonstrator of an ADS. The Experimental Demonstrator with a thermal power of about 80 to 100 MW(th) is a milestone towards the long-term realization of a prototypical ADS with a thermal power of about 1500 MW(th).

An *accelerator driven system (ADS)* consists of three main parts: an accelerator for primary particles (protons), a spallation target (or target module) in which the protons produce free nucleons (neutrons) in a spallation reaction (external neutron source), and a subcritical blanket in which, first, the fission reaction, producing fission neutrons (internal neutron source) and thermal energy, and second, the transmutation reaction occur. The protons are injected into the spallation target through a vacuum beam pipe, the beam pipe being closed by a window at the end. The target is a heavy liquid metal (e.g. lead Pb or eutectic lead-bismuth Pb-Bi). The spallation neutrons produced in the spallation target are completely independent of the subcritical blanket. A shut-down of the accelerator or an interruption of the proton beam immediately stops the fission reaction. Safety aspects of such a subcritical system are discussed in 32.23.03.

## **2. RESULTS DURING 2001**

Here, only a brief overview of the main results is given. A detailed description of the achieved results is given in the 2001 status report from Knebel et al., Forschungszentrum Karlsruhe, Wissenschaftliche Berichte FZKA 6618, 2002.

### **2.1 KARlsruhe Lead LABORatory KALLA**

The KARlsruhe Lead LABORatory KALLA summarizes all experimental activities at Forschungszentrum Karlsruhe which use the fluid lead-bismuth eutectic. The involved institutes are Institute for Nuclear and Energy Technologies (IKET), Institute for Pulsed Power and Microwave Technology (IHM), Institute for Materials Research I and III (IMF I and III).

The experimental activities of KALLA can be divided in two groups:

- Stagnant experiments:
  - COSTA 1 to 6 (CORrosion test stand for STagnant liquid lead Alloys)
  - KOSIMA 1 to 6 (Karlsruhe Oxygen Sensor In Molten Alloys)
  - KOCOS (Kinetics of Oxygen COntrol Systems)
- Loop experiments:
  - THESYS (Technologies for HEavy metal SYStems)
  - THEADES (THErmalhydraulics and Ads DESign)
  - CORRIDA (CORROsion In Dynamic lead Alloys)
  - K4T (planned) (Karlsruhe 4 MW Target experiment)

With the KARlsruhe Lead LABORatory KALLA at Forschungszentrum Karlsruhe there will be a strategic focal point in the field of lead-bismuth technologies in Germany, [http:// www.kalla.fzk.de](http://www.kalla.fzk.de). KALLA is an open user laboratory for experiments which are relevant for ADS applications. KALLA enhances international collaboration and encourages scientific staff exchange. In addition, young scientists are educated and trained in heavy liquid metal technologies and applications. This is in agreement with the new direction of EURATOM research in the Framework Program 2002-2006, which will strengthen both Integrated Projects and Networks of Excellence. Parallel to the lead-bismuth experiments in KALLA, model experiments with water as fluid are performed in the well-instrumented and flexible test facility HYTAS (HYdraulic behaviour in spallation TArget Systems).

## 2.2 Sub-Project SP1: Thermalhydraulic Investigations

A three steps strategy has been proposed for the research activities accompanying the spallation target design.

In the *first step* a numerical analysis is carried out with available CFD codes (the commercial codes CFX and FIDAP, and the Forschungszentrum Karlsruhe code FLUTAN), to provide a fundamental knowledge about the steady-state and transient thermalhydraulic behaviour of a spallation target, and to develop evaluation criteria which are to be applied to a design selection procedure at a later stage.

In the *second step* model experiments are performed, to provide an experimental data base for physical model development and code improvement and validation. At

the present stage a deficiency in applied Pb-Bi technology exists so that experimental investigations both with a model fluid, e.g. water, and with the realistic coolant, Pb-Bi eutectic, are recommended. A model experiment using water as fluid allows to both perform a systematical study of the physical phenomena involved and to apply sophisticated measurement techniques. The results obtained in a water model experiment cannot be directly transferred to the prototype conditions as far as heat transfer characteristics and buoyancy effects are concerned.

In the *third step* experimental studies in liquid Pb-Bi are performed in the KARlsruhe Lead Laboratory KALLA for the final design of a beam window. The design of the complete spallation target module is done numerically first. The experimental investigations of a target module in the integral experiment K4T is beyond the scope of this HGF Strategy Fund Project, it is envisaged within Euratom 6<sup>th</sup> Framework Programme.

Here, some selected results are discussed.

### 2.2.1 HYTAS Water Experiments on Beam Window Design

(C. Pettan, S. Gnieser, R. Stieglitz, J.U. Knebel, IKET)

The liquid metal experiment on the beam window of the MEGAPIE spallation target described in 32.23.05 is accompanied by a water experiment of nearly exact the same dimensions. The water experiment, performed in the test facility HYTAS, allows to measure the velocity distribution and the fluctuations at several discrete points, which are not accessible in the lead-bismuth experiment, and at the same hydraulic Reynolds number in order to study the kinetic energy transfer. The obtained results serve as data base for numerical models currently developed.

The HYTAS test module, manufactured completely of plexiglass, is shown with all its geometrical dimensions in figure 1. At the top of the module a flow straightener is installed in order to produce a homogeneous grid turbulence at the inlet of the annular gap. Within the HYTAS program Laser Light Sheet (LLS), Laser Doppler Anemometer (LDA) and Ultrasonic Doppler measurements (UVP) are performed. The range of Reynolds numbers  $Re$ , which is investigated in seven planes, is  $Re = 10^4, 2 \times 10^4, 4 \times 10^4, 6 \times 10^4$ , where  $Re$  is built with the hydraulic diameter of the annular gap. Measured within the LDA program are the mean axial velocity  $u_z$ , the mean circumferential velocity  $u_\varphi$  as well as fluctuations  $u_z'$  and  $u_\varphi'$  and RMS-values.

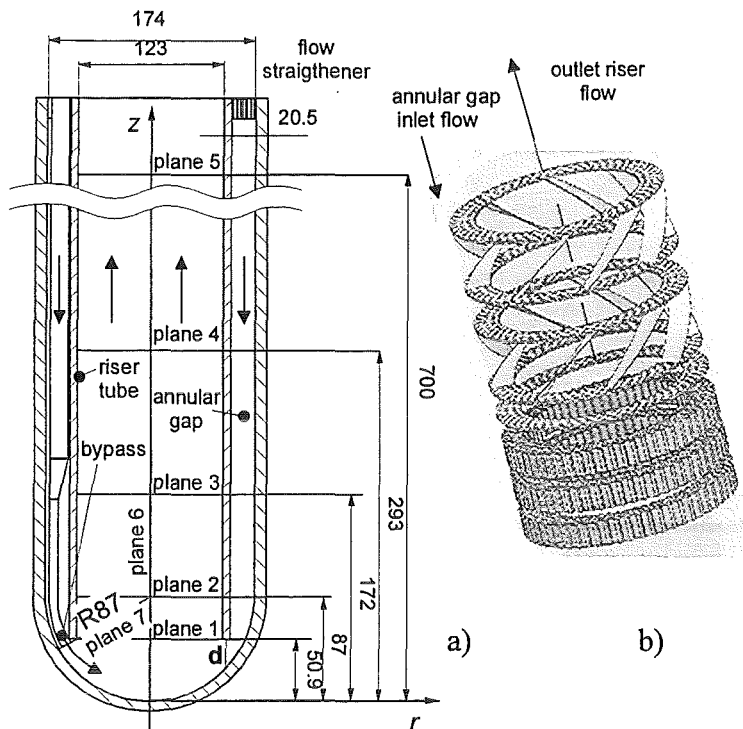


Figure 1: (a) Geometrical dimensions of the HYTAS test module and the coordinate system. (b) Design of the flow straightener in HYTAS.

In the so-called base case no bypass is installed, whereas in two other cases curved rectangular bypass orifices of  $20 \times 10 \text{ mm}^2$  and  $40 \times 5 \text{ mm}^2$  are studied.

Additionally, two different cases of the distance  $d$  between riser tube and beam window are studied. Finally, setups, in which the riser tube are slanted by 15 mm and 25 mm with respect to the radial coordinate  $r$ , are planned. This design is aimed at preventing a stagnation point in the bottom center of the window. In all bypass cases the flow rate ratio of bypass to main flow is 1:15.

First measurements for a base case without additional bypass show that smallest geometric deviations from concentricity immediately lead to a non-negligible swirl motion, which is persistent throughout the whole test module. In figure 2 a LLS of the lower window part is shown at a Reynolds number of  $Re = 5.4 \times 10^4$  and for an illumination time of 196 ms. At the expansion from guide tube to riser, a large recirculation area appears which leads to an intense kinetic energy exchange.

The actual experiments show that above Reynolds numbers of  $Re = 4 \times 10^4$  the stagnation point is not steadily positioned in the center/lowest point of the beam window; it is rather travelling thereby. Further measurements with a bypass flow and different riser geometries will be performed.

In figure 3 the normalized axial velocity  $u/u_z$  is shown as a function of the radial coordinate  $r/R$  in a height of  $z/R = 7.78$  for two different turbulent Reynolds

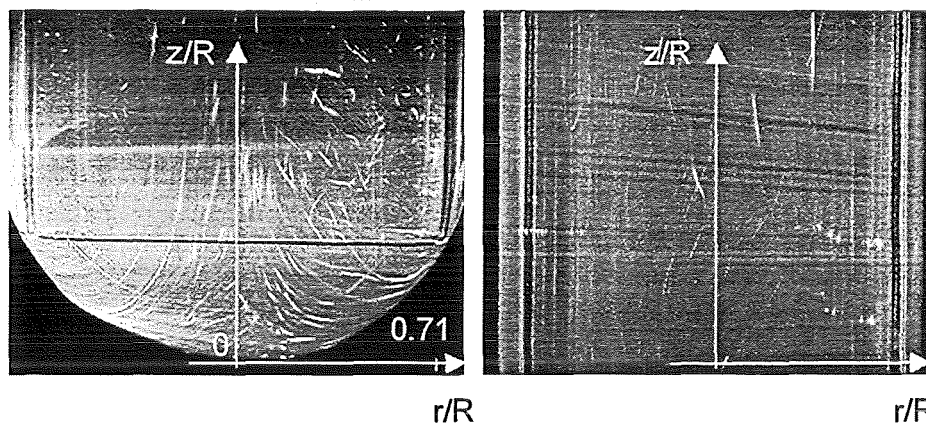


Figure 2: (left) LLS at the lower part of the beam window at  $Re = 5.4 \times 10^4$ . (right) LLS at  $6.5 \leq z/R \leq 8$ . In both photographs the illumination time is 196 ms.

numbers. Here, all geometric scales are normalized by the inner radius  $R$  of the window and the velocities are scaled by the mean velocity  $u_z$ . The inflow in the annular gap ( $0.76 \leq r/R \leq 1$ ) is rather homogeneous up to  $Re = 4 \times 10^4$  with a flat velocity profile close to unity; then the profile tends to decrease towards the outer wall at  $r/R = 1$ , indicating that the experimental set-up is not providing completely hydraulic symmetrical conditions.

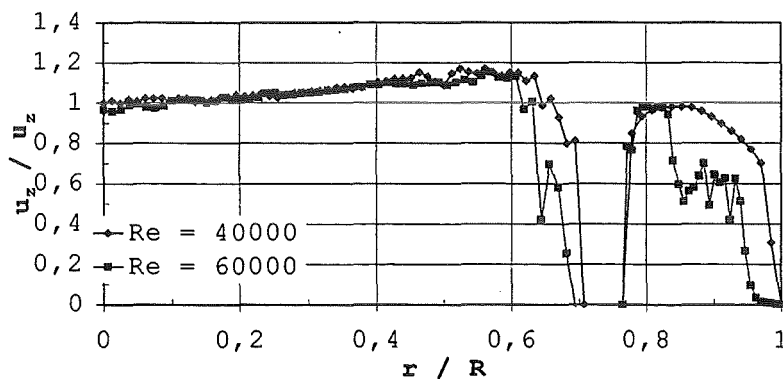


Figure 3: Normalized axial velocity  $u/u_z$  versus radius  $r/R$  at axial height  $z/R = 7.78$ .

## 2.2.2 Practical Experience on the Operation of a Lead-Bismuth Loop

(C.H. Lefhalm, M. Daubner, K.J. Mack, F. Fellmoser, H. Piecha, J.U. Knebel, IKET)

### Introduction

The Technology Loop THESYS (Technology for Heavy metal SYStems) in the Karlsruhe Lead LABoratory (KALLA) has been successfully operated since August 2000 without major shutdown phases. This part summarizes the experience in

handling liquid Pb-Bi and gives a survey of three experimental results: the conditioning of the loop before and during operation (cf. also sub-project SP3), methods for the accurate measurement of the flow rate, and an outlook on the measurement of velocity and temperature profiles in a developed pipe flow.

### Technology Loop THESYS

Figure 4 shows a scheme of the Technology Loop THESYS. The main components are an EM pump with a power up to 15 kW, a filter section, two test sections, the Karlsruhe Oxygen Control System (OCS), cf. SP3, and a heat exchanger.

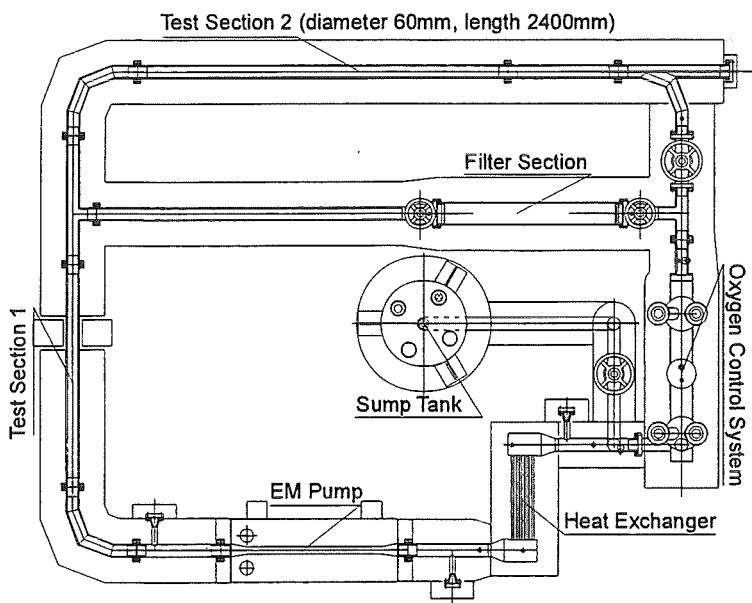


Figure 4: Scheme of the Technology Loop THESYS at Karlsruhe Lead Laboratory KALLA.

### Material Conditioning

About 100 liters of lead-bismuth were liquefied in the crucible under Argon cover gas atmosphere and filled into the sump tank. Before the first filling process of the pipe system, the loop was pre-oxidized by heating under air atmosphere. By this means the formation of a protective oxide layer on the pipe walls is assured before the first contact to Pb-Bi. During operation the Karlsruhe OCS is used to sustain the protective oxide scale. The pipe wall at the pump is periodically observed by ultrasonic measurement and additionally after half a year and one year, samples were taken from the test section pipes to check for corrosion attack. However, over the whole operation time, no liquid metal or other corrosion was detected.

## Flow Rate Measurement Techniques

An essential parameter for a loop system is the total flow rate of the fluid. For a liquid metal, due to its conductivity, one possibility is a magnetic inductive device: The measured induced voltage is proportional to the vector product of the magnetic field and the velocity of the moving fluid. At the Technology Loop a permanent magnet is installed perpendicular to the flow and the measured values show the expected linear dependency on the pump power. The absolute voltage is very low and turns out to be dependent on the temperature of the medium at the magnet. So, one has to calibrate the magnet flow meter with another measurement technique before each experiment in order to get an absolute value for the flow rate. One technique is a turbine flowmeter which is installed in the first test section. In figure 5 the measured flow rate is plotted versus the EM pump power. Due to its mechanical properties the blade frequency of the rotating turbine in the flow is a measure for the velocity of the fluid. Because of the rather small flow velocity a turbine with a small diameter had to be chosen. The pressure loss imposed by the turbine leads to a lower flow rate compared to the experiments with the magnetic inductive flowmeter. A calibration is possible for velocities in a range up to  $1 \text{ m}^3/\text{h}$ .

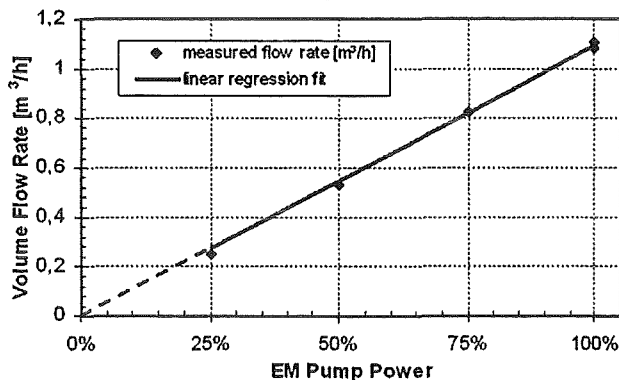


Figure 5: Measured flow rate in THESYS by means of a turbine flowmeter.

A commercial ultrasonic transient time flow measurement system from Panametrics, Inc. (XMT868) is installed in test section 2 of the Technology Loop THESYS. Two transducers are mounted face to face on the pipe under an angle of  $45^\circ$  to the flow, so that ultrasonic pulses can be sent in direction and towards the flow direction. The faster the flow, the higher is the transient time difference, which is evaluated out of the correlated signals. Thus, the mean flow velocity can be calculated. Figure 6 shows the absolute calibration curve of the ultrasonic transient

time flowmeter, where a flow velocity of 0.26 m/s corresponds to a flow rate of about 2.6 m<sup>3</sup>/h in the given pipe geometry.

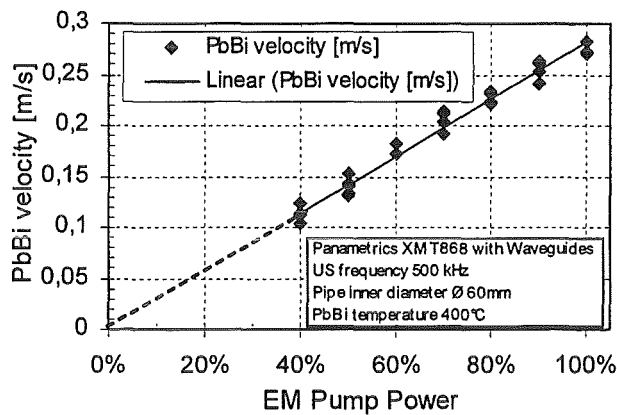


Figure 6: Measured Pb-Bi flow velocity in THESYS by means of an ultrasonic transient time flowmeter.

Unfortunately, the use of the ultrasonic measurement techniques with liquid metal flow is difficult: one difficulty is the high temperature, because the piezo crystal transducers endure only temperatures up to 200°C under short-term and 150°C under long-term load. For application in lead-bismuth at temperature up to 600°C so called waveguides are used, which are specially designed interfaces guiding the ultrasonic waves. The hot side of the waveguide immerses directly into the liquid metal; the cold side, where the transducer is mounted, is cooled by air.

Another difficulty is related to the coupling of the ultrasonic waves through the steel pipes into the liquid metal. This is directly linked to the wetting problem between the lead-bismuth and the steel wall, because, without wetting, no coupling of the ultrasonic waves is possible at all. To ensure perfect conditions at the coupling surface of the waveguide, it has to be treated by chemical processes to support wetting. Additionally, the oxygen content of the liquid metal has to be controlled in the measurement region to prevent too much oxidation of the coupling surface.

### Velocity and Temperature Profile Measurement

For local measurements of velocity or temperature two techniques are in development.

The first technique is the Miniature Permanent magnet flow meter Probe (MPP) which is installed on a traverse path at the end of test section 2. This probe (outer diameter 2.5 mm) consists of two thermocouples at the sides of a small permanent magnet and is used for local temperature and velocity measurement. Figure 7

shows the temperature profile at the end of test section 2, downstream of the high power heater. The velocity measurement with the MPP is well known in liquid sodium and will be adapted to lead-bismuth applications in a next step.

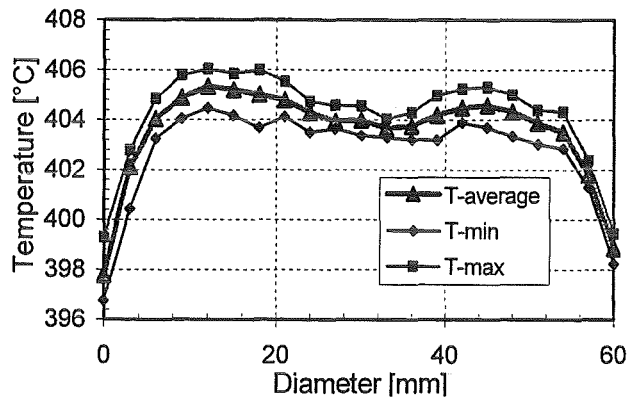


Figure 7: Temperature profile at the end of Test Section 2 (heater installed) at 100% pump power.

The second technique is the ultrasonic Doppler method. For technical applications in lead-bismuth this method has not been used before and a solution is not available for a high temperature liquid metal environment yet. Preliminary water experiments are in progress and waveguides for high temperature liquid metal ultrasonic Doppler measurements are in development at Forschungszentrum Rossendorf.

### Conclusions

The Technology Loop THESYS of KALLA could be successfully operated for more than one year. The conditioning of the steel piping and the liquid Pb-Bi itself is possible with a suitable expense: there are no indications of corrosion problems at operation temperatures around 400°C when applying the Karlsruhe Oxygen Control System (OCS).

The development of a reliable, absolute flow measurement technique is the basis for a thermohydraulic experiment. A relative flow measurement technique is the magnetic inductive flowmeter, however, a method for absolute calibration has still to be validated. One promising solution is the ultrasonic transient time measurement technique, which is successful operated in combination with waveguides to make up the high temperature of the liquid Pb-Bi.

Future work is directed in applying the waveguide technique to the ultrasonic Doppler method to measure local velocities in liquid lead-bismuth at temperatures up to or even above 400°C.

### 2.2.3 Fundamental Experiments in Liquid Lead-Bismuth on Heat Transfer and Model Development / Model Validation

(G. Grötzbach, A. Batta, R. Drummond, I. Otić, C. Panefresco, IKET)

#### Introduction

In order to determine the structure temperatures in a spallation target with sufficient accuracy, adequate turbulence models are required to predict the temperature field in the cooling fluid. Standard models, which are used in commercial codes, are not suitable for the simulation of convective heat transfer in heavy liquid metals, with buoyancy effects being important: the models using a turbulent Prandtl number to describe the turbulent heat transport assume the Reynolds analogy between the convective transport of momentum and heat. This assumption is not valid for liquid metals because the momentum field is mainly turbulence dominated and has only thin viscous wall layers, whereas the temperature field is less turbulence dominated and has thick wall layers governed by molecular conduction.

Improved turbulent heat transfer modelling for liquid metals requires more sophisticated methods. Additional transport equations have to be used which characterize the statistics of the temperature fluctuations which have a completely different time scale than the velocity fluctuations. The TMBF turbulence model consists of a combination of a low Reynolds number  $k$ - $\epsilon$  model and a second order 5-equation heat flux model. Certain model extensions for liquid metal flows were developed and implemented in the TMBF based on the analysis of data from direct numerical turbulence simulations.

The promising results for the TEFLU benchmark by the FLUTAN code using the TMBF model show that a further development of the TMBF model has still to be carried out as the radial profiles of the temperature variance  $\overline{\theta^2}$  in the plume regime are overestimated. In fact, a new modeling depending on the Peclet number should be developed for the transport equation of the destruction of the temperature variance  $\epsilon_\theta$ . Further validation of the TMBF model for heavy liquid metals has to be carried out for flow regimes in which the velocity field is influenced greatly by turbulent heat transport and buoyancy. As FLUTAN is no longer in use at FZK (see 32.23.05), the TMBF or a similar model has to be made available in the CFX code.

The objective of the past year activity was to introduce a new team at IKET to the code CFX 4.4 and in turbulence modeling. First applications with standard turbulence models concentrated on the begin of a numerical interpretation of two experiments from KALLA, these are the heated pipe test for which some calculations have already been performed and the heated rod test, both in the THESYS loop, for which calculations are in preparation. In parallel, theoretical work within a DFG-project has started to deduce by analytical means improved model terms for the TMBF and to provide turbulence data by direct numerical simulations with the TURBIT code to determine the corresponding model coefficients.

Heated pipe experiment in THESYS

The first example which is being investigated in more detail is an experiment with a flow in a circular tube after a 90° bend, which has been performed in the THESYS loop of the KALLA laboratory using lead bismuth as operating fluid, Figure 8. The average inlet temperature 250 mm before the bend is 354°C at a hydraulic Reynolds number of  $Re = 40.000$  corresponding to a mean velocity of  $v=0.09m/s$ . In a distance of 360 m after the bend a surface heater is circumferentially attached to the tube providing a heat flux of  $q'' = 8.03 W/cm^2$ . The measurement plane, in which a Ni-CrNi thermocouple is traversed from  $-0.5 \leq r/D \leq 0.5$ , is located 674 mm behind the outlet of the heater.

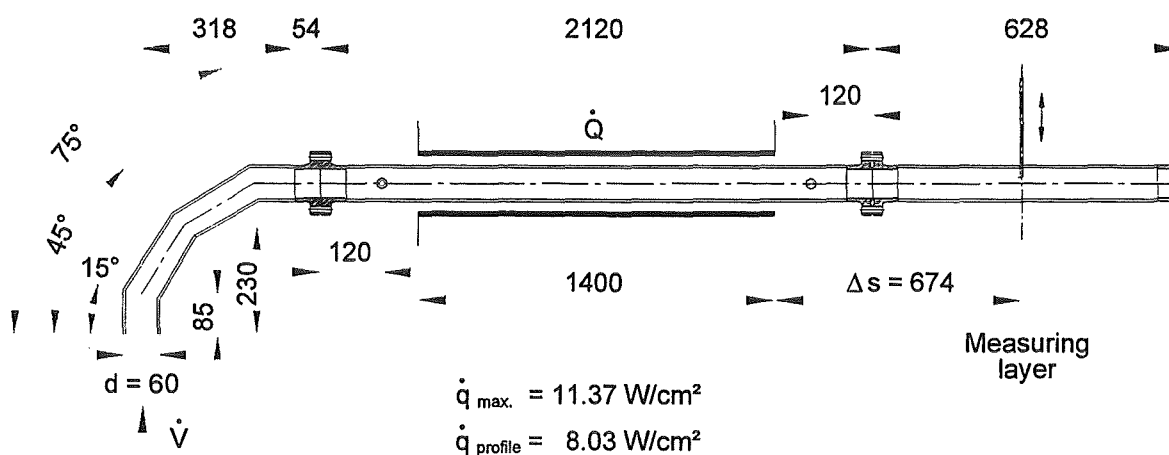


Figure 8: Geometric specifications for the heated pipe experiment in the Technology Loop THESYS of the KALLA laboratory.

The complete area shown in figure 8 including the 90° bend has been modeled in the input for CFX 4.4. The numerical model does not only record the fluid domain,

but also all channel walls, the detailed grooves for the 9 electrical heaters in the wall and the insulation around the piping. The heat input is not modeled by a specified surface heat flux, but by prescribing in total 18.8 kW to the spatially resolved electrical heaters in the grooves. This allows to record the azimuthal variation of the heat flux through the pipe wall into the fluid. For the first screening studies a rather coarse grid is applied; by using 81 axial cells and 72 azimuthal cells the o-grid in the fluid domain results in about 50.000 fluid cells; about 80.000 cells are used in the solid structures. The turbulent fluxes are calculated using a standard k-ε model and by a standard value of 0.9 for the turbulent Prandtl number.

Examples from the results of this screening calculation are given in figure 9. The centrifugal forces in the bend cause the well known pattern of secondary currents in the plane perpendicular to the mean flow. Over most of the cross section the flow is pointing outwards, but further away from the bend the flow pattern becomes more symmetrical. The cross-stream velocities reach directly downstream of the bend values up to about 10% of the mean velocity, whereas near the exit from the computational domain the secondary currents are reduced to about 0.4%.

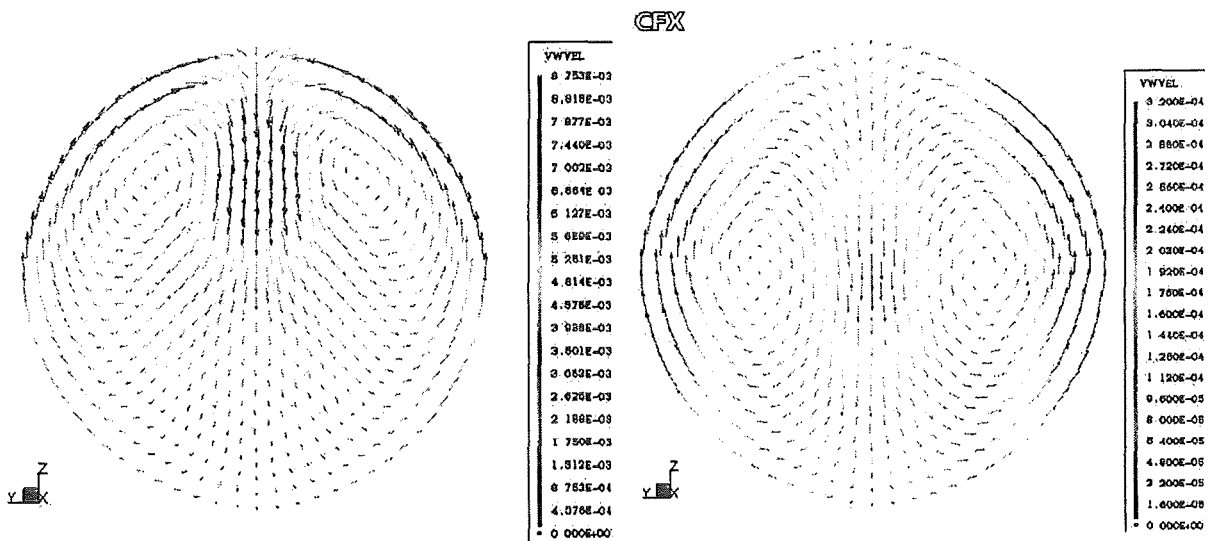


Figure 9: Secondary currents in planes downstream of the bend and in the measuring plane downstream of the heater.

The calculated radial profiles of the axial mean velocity in the same planes are strongly influenced by the secondary currents, figure 10. The fluid is faster near the outside of the bend, whereas the slower fluid which is transported by the secondary currents along the walls retards the fluid on the inside where the slow fluid is mixed into the mean flow. At the measuring plane the radial profile of the axial mean

velocity is still non-symmetrical. In the future it will be necessary to investigate how this prediction depends on the turbulence modelling and on the wall condition formulation used.

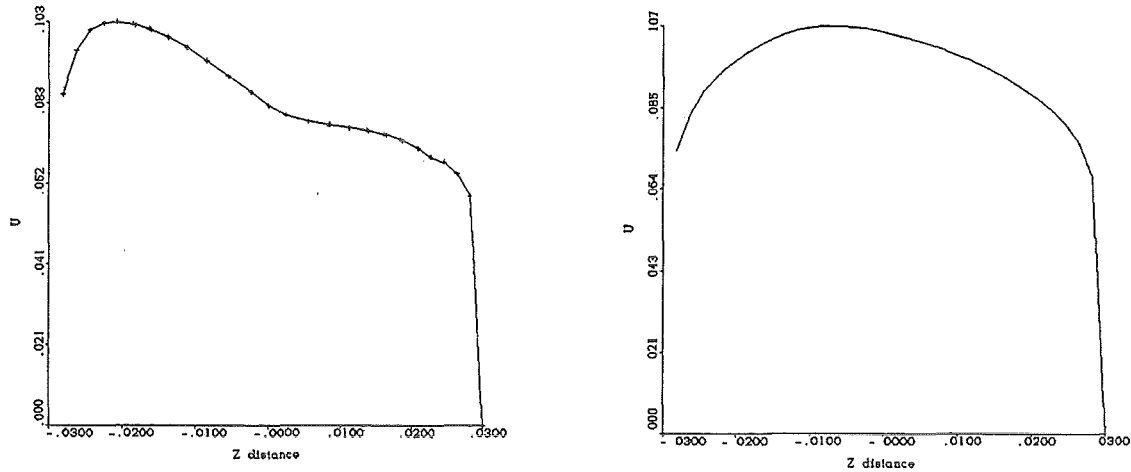


Figure 10: Consequences of the calculated secondary currents on the calculated axial mean velocity field in the planes just behind the bend and in the measuring plane downstream of the heater.

The corresponding temperature profiles also show such asymmetries, figure 11. The profile downstream of the bend has the maximum temperature on the outside of the bend. The reason for this is that the secondary current transports fluid along the wall which is cooled down by the heat losses through the insulation and mixes this colder fluid into the hotter core. The calculated heat losses are roughly one third of those occurring in the experiment. This means that it is not sufficient to use the material property data for the insulation alone, but that also heat losses through structural material which is going through the insulation should be included in the calculation. The temperature profile downstream of the heater is not yet fully mixed. Still higher temperatures occur near both walls. Here, we have the maximum temperature at the position where the secondary current detaches from the wall, that is, where the hot fluid from the up-streams heated boundary layer is pushed together. In the calculation we also included the heat conduction from the heater in the axial direction inside the pipe wall; this partly compensates the heat losses through the insulation at the measuring plane. Therefore, the temperature is only slightly reduced at the wall. In case of a modified thermal conductivity in the insulation material the radial temperature profile in the measuring plane may look qualitatively different.

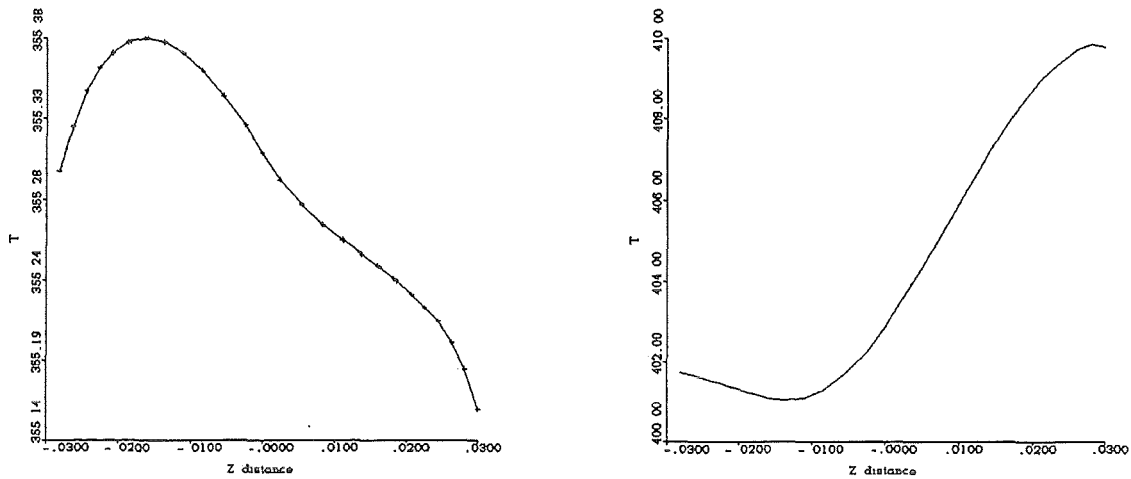


Figure 11: Consequences of the calculated secondary currents on the calculated temperature field in the planes just behind the bend and in the measuring plane downstream of the heater.

The numerical investigation of this experiment will in the next steps concentrate on the local adaptation of the grids, on the modelling of some boundary conditions and on a better representation of the insulation material including the structural material going through it, on investigating the influence of measuring devices on the results, and on the influence of the turbulence models on the secondary current and on the turbulent heat transfer. Finally, a validation of the calculation will be performed on the basis of the experimental results.

#### Concept for an improved turbulence model

The results of the TMBF model for the TEFLU benchmark are promising; nevertheless it becomes obvious that some of the calculated turbulence data for the temperature field which are calculated by the model are locally erroneous. This means, the model needs improvement in some of its modelled transport equations. Detailed information for the development of the required models will partly become available from experiments in THESYS; most detailed information will be provided by direct numerical simulations which are performed in a DFG project. Within the 'Interdisciplinary Turbulence Initiative' we are using direct numerical simulation data for Rayleigh-Bénard convection in liquid metals to develop subgrid scale models for large eddy simulations of such flows. These data will also be used to analyse improvements of the TMBF model for ADS applications.

As a by-product of this work an improved modelling is widely deduced by analytical means. The TMBF model is using transport equations not only for  $k$  and  $\varepsilon$ , but also for the three turbulent heat fluxes and for the temperature variance  $\overline{\theta^2}$  and in some cases also for its dissipation  $\varepsilon_\theta$ . The latter two equations are important to allow for a separate time scale in the temperature field and for a better modelling of buoyant flows.

Using the two-point correlation technique developed by Burgers (1953) and Kolovandin & Vatutin (1972), the thermal dissipation rate  $\varepsilon_\theta$ , which is given as

$$\varepsilon_\theta = \overline{\frac{\partial \theta}{\partial x_i} \frac{\partial \theta}{\partial x_i}},$$

can be decomposed in an inhomogeneous part  $\varepsilon_{\theta,ih}$  and a homogeneous part  $\varepsilon_{\theta,h}$ :

$$\varepsilon_\theta = \underbrace{\frac{1}{4} \alpha \Delta_x \overline{\theta^2}}_{\varepsilon_{\theta,ih}} - \underbrace{\alpha (\Delta_\xi \overline{\theta \theta'})}_0}_{\varepsilon_{\theta,h}}.$$

Here  $\alpha$  is the thermal diffusivity;  $\Delta_x = \partial^2 / \partial x_i \partial x_i$  is the Laplace operator with respect to  $x$ ;  $\xi$  represents a local coordinate system relative to two arbitrary points. Prime ' indicates the value of the two-point correlation function and subscript  $0$  represents the zero separation between two points. While  $\varepsilon_{\theta,ih}$  is known by the second moment closure of the temperature variance equation only the term  $\varepsilon_{\theta,h}$  needs to be modeled for closure of the thermal dissipation rate equation.

The homogeneous thermal dissipation rate  $\varepsilon_{\theta,h}$  can be approximated by the following modified form of the usually applied modeled equation:

$$\frac{D\varepsilon_{\theta,h}}{Dt} = \varepsilon_{\theta,h} \left( C_{P1} \frac{\varepsilon_h}{2R_h k} \overline{u_i \theta} \frac{\partial T}{\partial x_i} + C_{P2} \frac{\overline{u_i u_j}}{k} \frac{\partial U}{\partial x_j} \right) - \varepsilon_{\theta,h} \left( C_{D1} \frac{\varepsilon_h}{2R_h k} + C_{D2} \frac{\varepsilon_h}{\theta^2} \right).$$

$\varepsilon_h$  is the homogeneous part of the dissipation rate  $\varepsilon = \nu \overline{\frac{\partial u_i \partial u_j}{\partial x_j \partial x_j}}$ :

$$\varepsilon_h = \varepsilon - \frac{1}{4} \nu \Delta_x k.$$

Thus, a homogeneous thermal to mechanical time scale ratio  $R_h$  can be defined as

$$R_h = \frac{\overline{\theta^2} \varepsilon_h}{2\varepsilon_{\theta,h} k}.$$

The coefficients  $C_{P1}$ ,  $C_{P2}$ ,  $C_{D1}$ ,  $C_{D2}$  are functions of the Prandtl number, Reynolds number, and of the anisotropy invariant. They will be determined from the already existing simulation results and from new ones for higher Rayleigh numbers.

The advantages of this model are that a modeling of the diffusion terms in the equation for  $\varepsilon_\theta$  is not required, because these terms cancel out; further on a simplified modeling in the near-wall area is sufficient, because inhomogeneity effects are formally included in the equation for  $\varepsilon_{\theta,ih}$ ; thus, the usually required numerous wall approximations are not necessary here; and, the modeling is widely independent on the local inhomogeneity, but the dependence on the local anisotropy, which is important in buoyant flows, is still included.

The required direct numerical simulation data are not yet fully available because liquid metal simulations need extremely fine grids to resolve the small scales in the velocity field and to record a large computational domain because flow structures with long wavelengths also exist in this flow type. The available direct numerical simulations for liquid metal convection did not reach sufficiently high Rayleigh numbers to be in a fully developed turbulent regime. Starting from earlier simulations by Bunk & Wörner (1998) and Ghidersa (2000) we currently use the VPP5000 supercomputer to run a simulation of turbulent Rayleigh-Bénard convection in mercury ( $Pr = 0.025$ ) with  $Ra = 100\ 000$  with the TURBIT code. The underlying grid consists of  $400 \times 400 \times 75$  mesh cells and uses a periodic computational box of  $8 \times 8 \times 1$  (normalized by the channel height). First analyses of the simulation show that this and even somewhat higher Rayleigh numbers can be achieved with the current computer system and that the convection at this Rayleigh number gets now closer to the required fully turbulent regime.

## Conclusions

A new team is introduced at IKET into the CFD of ADS typical flows and its modeling. With first numerical results we started interpreting qualitative peculiarities of the heated pipe experiment from the Technology Loop THESYS of KALLA. Further investigations of this experiment are ongoing. The numerical analysis of the heated rod experiment is in preparation. This will be the basis in the future to check the relevance of new turbulence model improvements. A new model improvement

for the TMBF was deduced. It will be analysed and calibrated on the basis of the recent direct numerical simulation results.

### Literature

Bunk, M., Wörner, M., Direkte numerische Simulation turbulenter Rayleigh-Bénard-Konvektion in Quecksilber. FZKA 5915, Forschungszentrum Karlsruhe, April (1998)

Burgers J.M. Some considerations on turbulent flow with shear. In Proc. K. Ned. Akad. Wet., ser. B, vol. 56 (1953)

Ghidrsa, B., personal information (2000)

Kolovandin B.A. and Vatutin I.A. Statistical transfer theory in non-homogeneous turbulence. Int. J. Heat Mass Transfer, 15 (1972) pp. 2371-2383

## **2.2.4 Design of a Closed 4 MW Spallation Target With Heat Removal Chain for an Accelerator Driven System**

(H.J. Neitzel, J.U. Knebel, IKET)

### Introduction

One technologically new component of an ADS is the heavy liquid metal spallation target. Here, the development of the geometrical design of such a spallation target of 4 MW of proton beam power, which is characteristic for an Experimental ADS Demonstration Facility, is given. For the target module and the heat removal chain, the main components such as spallation area, heat exchangers and stack are designed, and the relevant parameters such as temperatures, pressure drops, driving heights and heat transfer characteristics are calculated using the as one-dimensional ADS\_CLS code.

It is shown that the heat removal is technically feasible for normal steady-state operational conditions.

### Investigated Coupled Loop System

The heat removal chain of a closed spallation target consists of three coupled loops as is sketched in figure 12. The primary loop (index  $i=1$ ) is the spallation target, the spallation area / beam window being the heat source  $\dot{Q}$  and the heat exchanger WT12 being the heat sink. In the secondary loop (index  $i=2$ ) the heat sink is the air

cooler WT23, which removes the heat via an open tertiary loop and a stack (index  $i=3$ ) to the environment.

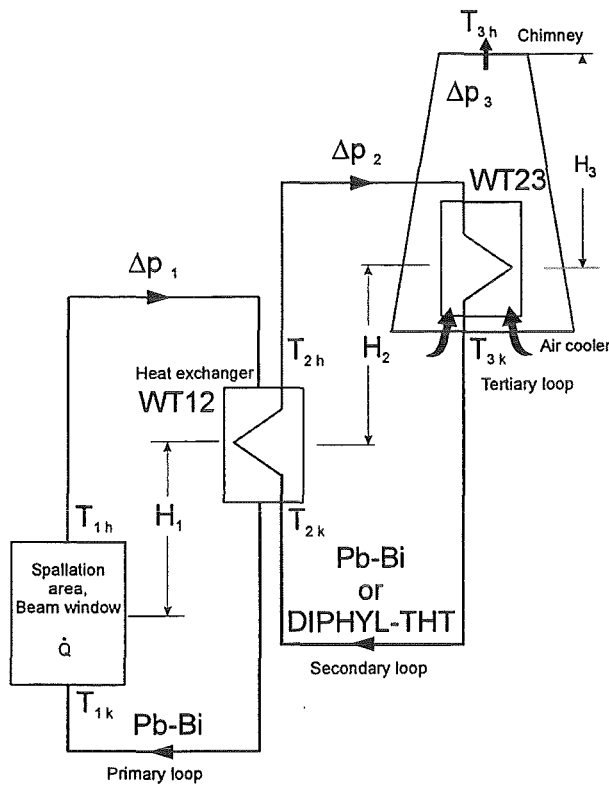


Figure 12: Sketch of the spallation target with heat removal chain.

and outlet annular plenums, the secondary side fluid flows in the pipes, and a stack, figure 14.

Here, three different cases are discussed, with Case A being the reference case. It is envisaged to design the heat transfer solely by natural circulation.

**Case A:** - Fluid in primary loop: lead-bismuth (Pb-Bi) at high temperature level

$$T_{1h} = 500^{\circ}\text{C} \text{ (hot riser)}, T_{1k} = 350^{\circ}\text{C} \text{ (cold downcomer)}$$

- Fluid in secondary loop: lead-bismuth (Pb-Bi)

For the two other cases the temperature level of the primary loop is lowered by 50 K. For Case B the fluid in the secondary loop is lead-bismuth, for Case C the fluid is an organic fluid (Diphyl THT of Bayer AG). The lowering of the temperature level is favourable in order to reduce both the high thermal loads on the beam window and the increasing corrosion attack to structure and beam window materials. Corrosion is a serious problem above about  $400^{\circ}\text{C}$  unless precautions

The relevant parameters such as temperatures  $T_i$ , pressure drops  $\Delta p_i$ , and driving heights  $H_i$  are indicated in figure 12.

The main components are:

- the spallation module itself, consisting of the spallation area within the funnel neck and the beam window, the riser and the downcomer (figure 13),
- the primary-secondary heat exchanger, being a straight tube heat exchanger working in counter-current mode, the primary side fluid flows in the pipes, figure 13,
- circular air cooler with inlet

such as an oxygen control system [1] and some surface treatment (thermal restructuring of and aluminium alloying into the top surface layer [1]) is applied. The use of an organic fluid in the secondary loop is cheap and technically simple to handle, however, boiling of the organic oil has to be omitted in order not to deteriorate the heat transfer characteristics of the oil.

**Case B:** - Fluid in primary loop: lead-bismuth (Pb-Bi) at low temperature level

$$T_{1h} = 450^{\circ}\text{C} \text{ (hot riser)}, T_{1k} = 300^{\circ}\text{C} \text{ (cold downcomer)}$$

- Fluid in secondary loop: lead-bismuth (Pb-Bi)

**Case C:** - Fluid in primary loop: lead-bismuth (Pb-Bi) at low temperature level

$$T_{1h} = 450^{\circ}\text{C} \text{ (hot riser)}, T_{1k} = 300^{\circ}\text{C} \text{ (cold downcomer)}$$

- Fluid in secondary loop: organic oil Diphyl THT

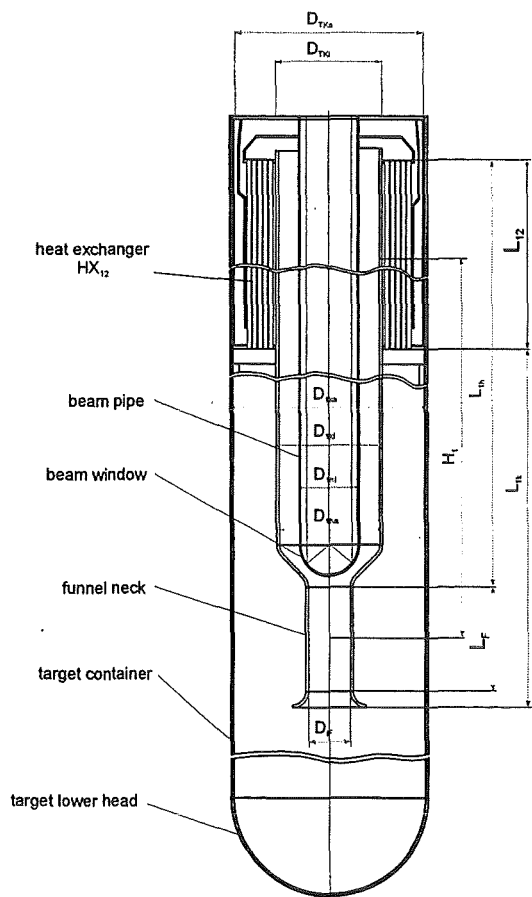


Figure 13: Spallation target module with primary-secondary heat exchanger WT12.

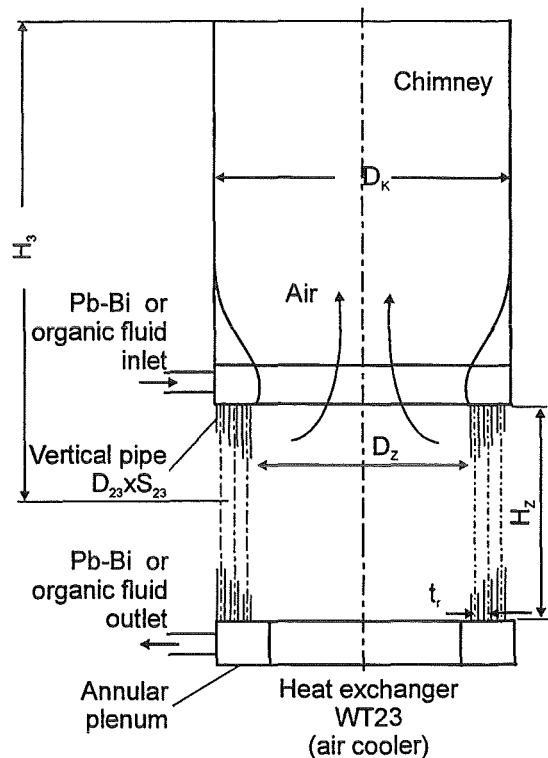


Figure 14: Secondary-tertiary heat exchanger WT23 with stack.

In all three cases, the lead-bismuth has a maximum heat-up span of  $150\text{ K}$  in order to prevent liquid metal corrosion effects due to leaching out of steel components in the hot regions and deposition in the cold regions of the loops. The air inlet

temperature in the air cooler is set to  $T_{3k} = 30^{\circ}\text{C}$ . When changing the fluid of the secondary loop, the dimensions of the heat exchangers WT12 and WT23 were both kept the same. This is important in order to keep the costs for a future integral experiment as low as possible.

## Results

Supposing a spallation heat of  $\dot{Q} = 4 \text{ MW}$ , which has to be removed from the spallation target to the environment, the results for the main parameters such as temperatures  $T_i$ , driving heights  $H_i$ , pressure drops  $\Delta p_i$ , flow rate  $V_i$ , and length of the heat exchangers  $L_{ij}$ , are given in table 1.

Lowering the temperature level of the primary loop and thus the driving temperature difference between primary and secondary side of the heat exchanger, results in a longer primary-secondary heat exchanger. The effective length  $L_{12}$  for Case B is increased by a factor of 1.52 compared to Case A. This increases the total flow resistance, so that the required natural circulation driving heights of the primary and secondary loop and Case B are increased slightly by a factor of 1.07 and 1.08 respectively.

In order to set the same heat transfer coefficient on the primary side for Case C as was calculated for Case B, the Diphyl THT flow rate in the secondary loop has to be significantly increased by a factor of 11.5 in comparison to the flow rate required for Pb-Bi. Then, the temperature increase of the Diphyl THT results in 10 K only. A comparison between Case B and Case C shows that the length of the heat exchanger pipes has to be increase only by 25 % and 4 % for the primary-secondary and the secondary-tertiary heat exchanger respectively.

The required natural circulation driving height for the primary loop which result in 6.02 m, 6.44 m and 6.76 m for the three cases, are realistic for an ADS application. For Case C, however, a natural circulation heat removal in the secondary loop is no longer possible ( $H_2 = 744 \text{ m}$ ). The high pressure drop and the flow rate of 713 m<sup>3</sup>/h can only be provided by a pump.

The stack has a height of  $H_3 = 4.78 \text{ m}$  for Cases A and B and of 5.64 m for Case C, which is reasonable when thinking of a technical realisation.

Besides the integral layout of the spallation target, the local cooling of the beam window has to be investigated in detail using three-dimensional CFD codes.

According to [2] the calculated integral primary side flow rate of  $63 \text{ m}^3/\text{h}$  for all three cases is sufficient to allow a cooling of the beam window which has its hottest spot in the stagnation point (supposing a parabolic radial power profile of the proton beam). The stagnation point is located at the lowest position of the beam window.

Tables 2 and 3 give the heat transfer characteristics of the heat exchangers WT12 and WT23 respectively. All relevant heat transfer correlations are taken from [3, 4].

When substituting the Pb-Bi in the secondary loop by the organic oil Diphyl THT, the flow rate has to be increased by a factor of  $11.4$  in order to achieve the same order of magnitude heat transfer coefficient on the secondary side of heat exchanger WT12. The velocity of the primary side Pb-Bi in the heat exchanger pipes is below  $0.5 \text{ m/s}$  so that erosion effects are of no importance. The flow both on the primary and on the secondary side of the heat exchanger is highly turbulent. The heat transfer coefficient on the Diphyl THT side of the heat exchanger WT12 and Case C results only in  $2370 \text{ W}/(\text{m}^2 \text{ K})$  which is lower than the values of  $2680 \text{ W}/(\text{m}^2 \text{ K})$  and  $2640 \text{ W}/(\text{m}^2 \text{ K})$  for Cases A and B respectively. This is despite the fact that the Nusselt number on the Diphyl THT side is larger than the Nusselt number on the Pb-Bi side by a factor of  $92$ . Here, the effect of the thermal conductivity is obvious which is two orders of magnitude lower for Diphyl THT in comparison to Pb-Bi.

With heat exchanger WT23 the over-all heat transfer coefficient results to about  $71 \text{ W}/(\text{m}^2 \text{ K})$  for all three cases. This is due to the comparatively low heat transfer on the air side, having a heat transfer coefficient of about  $65 \text{ W}/(\text{m}^2 \text{ K})$  for all three cases, which is limiting the overall performance of the heat exchanger.

### Summary

The heat removal from a  $4 \text{ MW}$  spallation target for an Experimental ADS Demonstrator Facility, as is foreseen within the European Project PDS-XADS, is technically feasible under steady-state natural circulation conditions, if lead-bismuth is used as fluid in the primary and in the secondary loop. If the secondary loop is operated with the organic oil Diphyl THT a pump is needed due to the required high flow rate and thus high flow resistance.

Future investigations have to be directed towards the transient behaviour of the coupled loop system and further local three-dimensional CFD calculations for the

cooling of the beam window. Finally, an integral experiment to validate the theoretical findings has to be developed.

Table 1: Results for the main parameters.

symbol	unit	Case A	CASE B	Case C
		Fluid 1: Pb-Bi $T_{1h} = 500^\circ\text{C}$ Fluid 2: Pb-Bi	Fluid 1: Pb-Bi $T_{1h} = 450^\circ\text{C}$ Fluid 2: Pb-Bi	Fluid 1: Pb-Bi $T_{1h} = 450^\circ\text{C}$ Fluid 2: Diphyl THT
$Q$	MW	4.0	4.0	4.0
$T_{1k}, T_{1h}$	$^\circ\text{C}$	350, 500	300, 450	300, 450
$T_{2k}, T_{2h}$	$^\circ\text{C}$	200, 350	200, 350	263, 273
$T_{3k}, T_{3h}$	$^\circ\text{C}$	30, 150	30, 150	30, 140
$H_1$	M	6.02	6.44	6.76
$H_2$	m	2.61	2.80	744.5
$H_3$	m	4.78	4.78	5.64
$\Delta p_1$	Pa	10623	11379	11941
$\Delta p_2$	Pa	4860	5226	47472
$\Delta p_3$	Pa	15	15	17
$V_1$	$\text{m}^3/\text{h}$	63.4	63.0	63.0
$V_2$	$\text{m}^3/\text{h}$	62.3	62.3	713.4
$V_3$	$\text{m}^3/\text{h}$	103200	103200	112600
$L_{12}$	m	0.615	0.936	1.17
$L_{23}$	m	4.88	4.88	5.07
$Q$	spallation heat		$V$	flow rate
$T$	temperatur		$L_{12}, L_{23}$	length of heat exchanger pipes
$H$	driving height		index 1, 2, 3	primary, secondary, tertiary
$\Delta p$	total pressure drop		index k, h	downcomer, riser

Table 2: Heat transfer characteristics of the heat exchangers WT12.  
 $Re$  Reynolds number,  $Nu$  Nusselt number,  $\alpha$  heat transfer coefficient.

symbol	unit	Case A	CASE B	Case C
Primary side: fluid 1 flows in heat exchanger pipes.				
$Re_{12i}$	-	34020	31250	31250
$Nu_{12i}$	-	6.694	6.766	6.766
$\alpha_{12i}$	$\text{W}/(\text{m}^2\text{K})$	8489	8242	8242
Secondary side: fluid 2 flows in free volume between heat exchanger pipes.				
$Re_{12a}$	-	18700	18700	70320
$Nu_{12a}$	-	6.375	6.375	584.7
$\alpha_{12a}$	$\text{W}/(\text{m}^2\text{K})$	6265	6265	4735
Over-all heat transfer coefficient:				
$k_{12}$	$\text{W}/(\text{m}^2\text{K})$	2682	2644	2367

Table 3: Heat transfer characteristics of the heat exchangers WT23.  
 $Re$  Reynolds number,  $Nu$  Nusselt number,  $\alpha$  heat transfer coefficient.

<i>symbol</i>	unit	Case A	CASE B	Case C
Secondary side: fluid 2 flows in heat exchanger pipes.				
$Re_{23i}$	-	6414	6414	24120
$Nu_{23i}$	-	5.297	5.297	217.1
$\alpha_{23i}$	$W/(m^2K)$	6280	6280	2121
Tertiary side: fluid 3 flows perpendicular to pipes.				
$Re_{23a}$	-	1874	1874	1989
$Nu_{23a}$	-	43.75	43.75	45.23
$\alpha_{23a}$	$W/(m^2K)$	64.15	64.15	65.56
Over-all heat transfer coefficient:				
$k_{23}$	$W/(m^2K)$	71.22	71.22	70.92

### 2.3 Sub-Project SP2: Material Specific Investigations

This sub-project systematically describes the mechanisms of corrosion, concentrating on dynamic experiments in flowing lead under defined oxygen control. The applied techniques and methods for the improvement of corrosion resistivity by surface protection and the surface modification using the pulsed electron beam facility GESA are dealt with. The applied oxygen control system (OCS) is explained in detail in sub-project SP3.

#### 2.3.1 Investigation of the Corrosion and Erosion of Structure and Window Materials in Flowing Lead-Bismuth

(G. Müller, A. Heinzl, A. Weisenburger, IHM)

##### Introduction

Corrosion tests of steels in liquid lead-bismuth have shown that only stable oxide scales can protect the steel surface against a dissolution attack. Therefore the control of the oxygen concentration in the liquid metal alloy is of great importance, see sub-project SP3. Oxide scales can be generated either from steel components or from special oxidants alloyed into the steel surface, like aluminium or silicon. Both methods are investigated in corrosion tests, in particular the temperature is determined up to which the generated oxide scales retain stable.

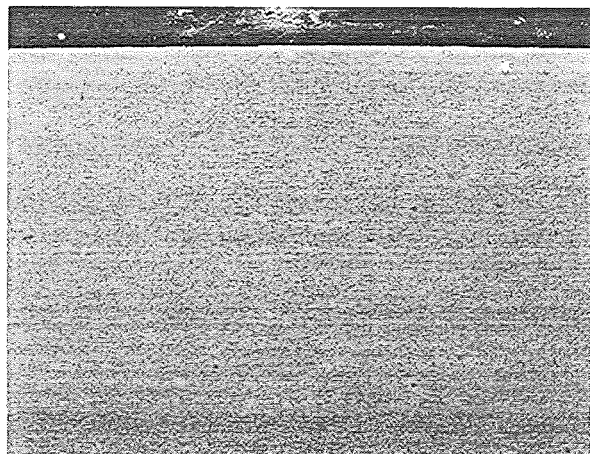
## Results

The behavior of steels in original state that form oxide scales from own components and of steels aluminum (Al) alloyed at the surface with GESA was investigated systematically. The temperature of the liquid Pb-Bi in the corrosion-loops varied between 420 to 600°C, the oxygen concentration was  $10^{-6}$  wt%.

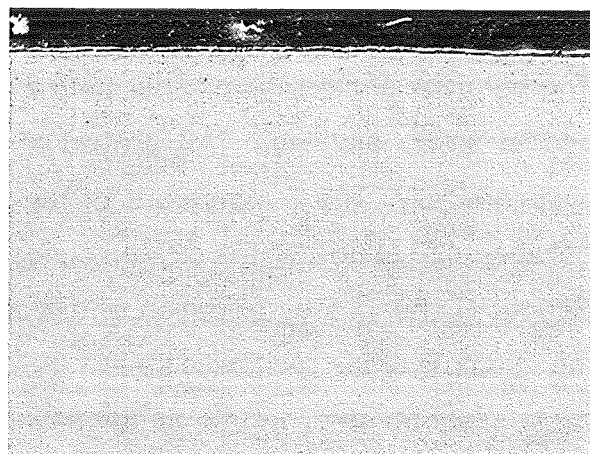
Structural changes by oxidation or dissolution attack by Pb-Bi will be described for the example of the austenitic steel 1.4970. Figure 15 shows the development of the oxide scale on steel 1.4970 as a function of temperature after 2000 h of exposure. At temperatures up to 550°C a homogenous covering oxide scale develops. It is very thin at 420°C. Only at higher temperatures an external magnetite scale develops, which is well distinct at 550°C. Underneath a Cr-spinel zone is formed. This structure is disturbed at 600°C. Thin oxide scales alternate with the formerly described structure of the oxide scale. An explanation for this behavior is still missing. Up to 600°C and 2000 h of exposure protection against dissolution attack exist. In contrast catastrophic dissolution attack occurred on Steel AISI 316L after 2000 h of exposure at 600°C.

Looking at Figure 16 makes it clear that tests up to 2000 h of exposure don't allow any recommendation on the suitability of a specific steel. Already at 550°C after 4000 h of exposure dissolution attack starts by penetrating of Pb/Bi underneath the oxide scale. At 600°C the attack reaches catastrophic dimensions. Bright inclusions consist of Pb-Bi. The penetration zone is entirely depleted in nickel.

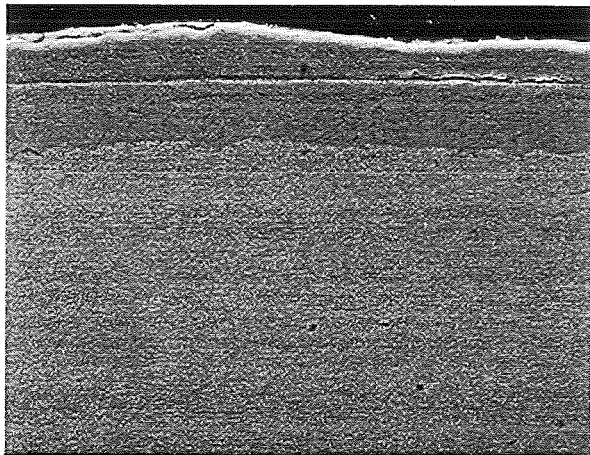
A completely different behavior is observed for the steel 1.4970 surface alloyed with GESA to a depth up to 30  $\mu\text{m}$ , Figure 17. Even after 4000 h at 600°C no sign of corrosion attack can be observed. A 1-2  $\mu\text{m}$  thick  $\text{Al}_2\text{O}_3$ -oxide scale protects the steel against dissolution attack. Screening tests show that the Al-content alloyed into the steel surface has to be at least 8 wt% to allow the formation of protective layers of  $\text{Al}_2\text{O}_3$ . If the Al-content is lower magnetite and FeCrAl-spinel are formed and the oxidation behavior differs only little compared to untreated steels. The maximum tolerable Al content is in the range of 20 to 30 wt.%, depending on the type of steel because of weakened structure due to cracks after GESA-treatment. For the best possible corrosion protection of steel in liquid Pb-Bi the Al content in the steel surface should be in the range of 8 to 15 wt%.



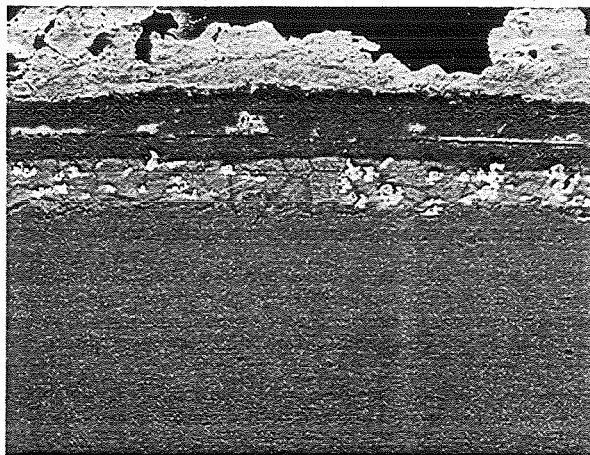
1.4970 original PbBi-Loop 420°C/2000h\_1000 30 μm



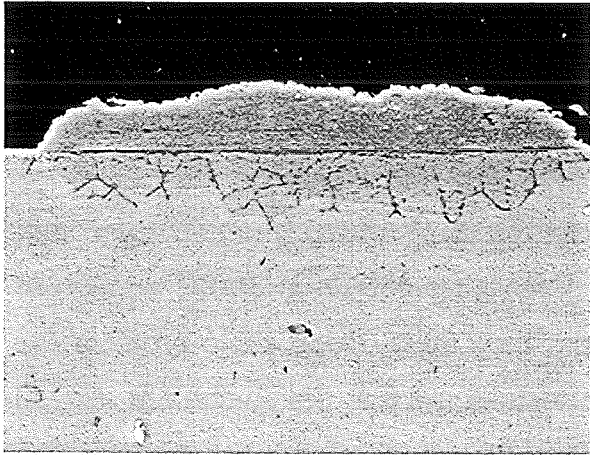
20KV 1000 X 1.4979 original 420 °C 4000h 20 μm



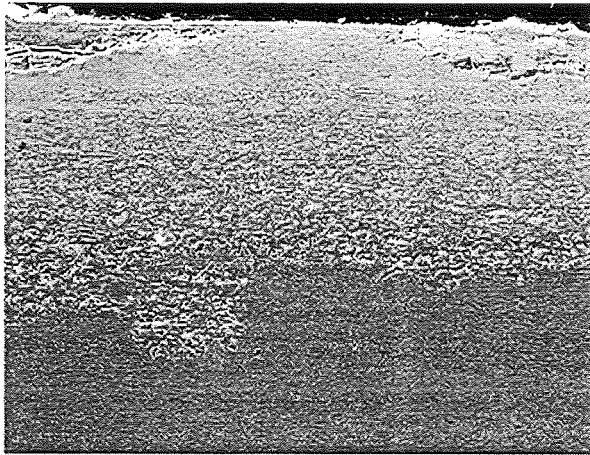
1.4970 original, PbBi-Loop, 550°C-2000h 30 μm



20KV 1000 X 1.4970 original 550°C 4300h Loop 20 μm



1.4970 original 600°C-2000h- 1000x 30 μm



20KV 500 X 1.4970 original 600 °C 4000h 50 μm

Figure 15: SEM cross-section of steel 1.4970 after 2000 h of exposure to Pb-Bi at 420 to 600°C containing  $10^{-6}$  wt% oxygen: Formation of oxide scale.

Figure 16: SEM cross-section of steel 1.4970 after 4000 h of exposure to Pb-Bi at 420 to 600°C containing  $10^{-6}$  wt% oxygen: Formation of oxide scale and dissolution attack.

Conclusions:

Table 4 gives an overview of the behavior of the examined steels in Pb-Bi. It is clearly visible that only the steels alloyed with Al at the surface can be used at higher temperatures and longer times of exposure. The use of original steels that

form oxide scales from their components seems to be restricted at temperatures below 500°C.

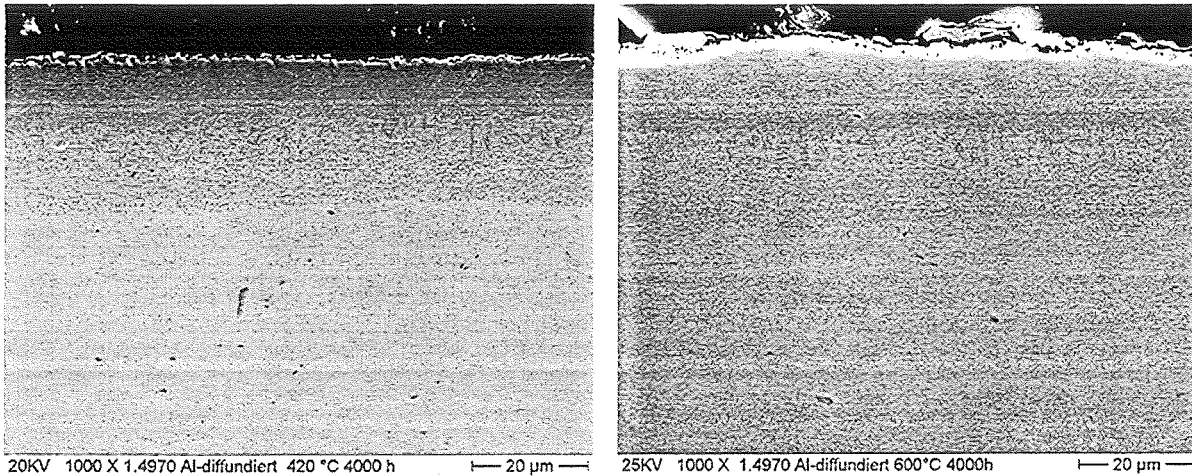


Figure 17: SEM cross-section of steel 1.4970 surface alloyed with GESA up to 30 µm depth after 4000 h of exposure to Pb-Bi at 420 to 600 °C containing 10<sup>-6</sup> wt% oxygen: formation of oxide scale.

Table 4: Overview of the behavior of original steels and steels alloyed with Al at the surface in liquid Pb-Bi loop tests.

steel		420°C		550°C		600°C	
		2000h	4000h	2000h	4000h	2000h	4000h
316	original	+	+	+	-	-	-
	Al-alloyed	+	+	+	+	+	+
1.4970	original	+	+	+	-	+	-
	Al-alloyed	+	+	+	+	+	+
Manet	Original	+	+	+	-		

## 2.4 Sub-Project SP3: Oxygen Control System

### 2.4.1 Work Package WP1:

#### Oxygen measurement in lead-bismuth

(J. Konys, Z. Voss, O. Wedemeyer, H. Muscher, W. Krauss, IMF III)

#### Introduction

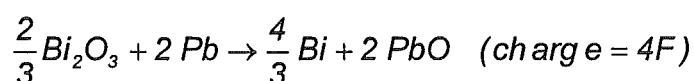
A detailed technical description of the theoretical background of electrochemical oxygen probes and in particular of the reference electrodes and the sensor design is given in the 2000 report. During 2001, new approaches of calibration and new

testing techniques and experimental procedures in the area of oxygen measurement and control in liquid lead bismuth at elevated temperatures has been made. First results of the EMF-temperature dependency (cooling curves obtained using oxygen meters with Bi/Bi<sub>2</sub>O<sub>3</sub> reference electrodes) and further recordings with the Pt/air and In/In<sub>2</sub>O<sub>3</sub> systems, successfully employed before, have shown that the theoretical predictions are fulfilled for both oxygen saturated and nearly oxygen-free liquid lead-bismuth. The interpretation of the measured values in terms of the thermodynamic theory proposed in 2000 is now accepted, adopted and widely spread in the community as a useful tool in oxygen cell calibration and a new LEBD validation method.

Here, results on the response behavior of the EMF signal versus changes in the oxygen concentration in the eutectic lead-bismuth and data on the long-term stability of the EMF signal as well as the discussion and quantitative evaluation of experimental uncertainties at lower temperatures is presented. The experiments were performed under stagnant conditions in the test facility KOSIMA.

#### Thermodynamic considerations of the Bi/Bi<sub>2</sub>O<sub>3</sub>-reference electrode

The thermodynamic calculations for the reference system Bi/Bi<sub>2</sub>O<sub>3</sub> were fulfilled in accordance to the scheme presented earlier in case of the In/In<sub>2</sub>O<sub>3</sub> system. There is only one important difference: the opposite reaction path (affinity  $A > 0$ ), which is here the following:



The affinity of that unidirectional reaction (formation of lead oxide) is  $A > 0$ . The RED and the OX parts of the global REDOX process are given as (the oxidation or anodic process, being the left side of the galvanic cell scheme):



the reduction or cathodic process, being the right side of the galvanic cell scheme, is consequently:



Thus, the galvanic cell scheme has the form:

(-) SS, Pb, PbO | YSZ |, Bi, Bi<sub>2</sub>O<sub>3</sub>, Mo (+)

In this system oxygen ions as such have no influence on the potential, if only the liquid metal is saturated with dissolved oxygen. According to the stoichiometry of the bismuth sesquioxide formation one obtains (dimension: J/ mol oxide):

$$\Delta G_{ref}^0 = RT \ln p_{O_2}^{ref} = \frac{2}{3} \Delta_f G^0 Bi_2O_3 \quad [J / mol \text{ oxide}]$$

In the case of equilibrium in oxygen saturated solution of PbBi one obtains:

$$\Delta G_{sample}^0 = RT \ln p_{O_2}^{sample} = 2 \Delta_f G^0 PbO - 2 RT \ln a_{Pb} \quad [J / mol \text{ oxide}]$$

And finally for the case of an equilibrium in an oxygen unsaturated solution one obtains:

$$\Delta G_{sample}^0 = RT \ln p_{O_2}^{sample} = 2 \Delta_f G^0 PbO - 2 RT \ln a_{Pb} + 2 RT \ln \frac{C_O}{C_O^{sat}} \quad [J / mol \text{ oxide}]$$

Using Gibbs free energy of bismuth oxide and lead oxide formation data is:

$$\Delta G_{PbO}^0 = -436850 + 197.991 T \quad [J / mol O_2]$$

$$\Delta G_{Bi_2O_3}^0 = -386790 + 188.95 T \quad [J / mol O_2]$$

The EMF for oxygen saturated PbBi can be calculated as:

$$\Delta G_{global} = \Delta G_{right} - \Delta G_{left}$$

$$E^0 = -\frac{1}{4F} \left( \frac{2}{3} \Delta_f G_{Bi_2O_3}^0 - 2 \Delta_f G_{PbO}^0 \right)$$

$$E(V) = 0.1297 - 5.33 \cdot 10^{-5} T (K)$$

In case of unsaturated solutions of oxygen in PbBi, the EMF of the cell can also be estimated as

$$E = -\frac{1}{4F} \left( \frac{2}{3} \Delta_f G_{Bi_2O_3}^0 - 2 \Delta_f G_{PbO}^0 - 2 RT \ln \frac{C_O}{C_O^{sat}} + 2 RT \ln a_{Pb} \right)$$

by using the temperature-dependent solubility data as:

$$E(V) = -0.2075 + 4.62 \cdot 10^{-4} T (K) - 4.308 \cdot 10^{-5} T (K) \ln c_{O,PbBi}$$

## Results

Oxygen probes with Bi/Bi<sub>2</sub>O<sub>3</sub> type reference electrodes were tested in liquid Pb-Bi with varying amounts of dissolved oxygen. The oxygen-saturated solutions were prepared by bubbling of dry air through the liquid Pb-Bi eutectic as a dispersed bubble flow. For the purpose of producing nearly oxygen-free lead bismuth, Ar+5% H<sub>2</sub> gas was bubbled through the melt until saturation conditions were reached. In figure 18, the results of the EMF-measurements are compared with the expected dependencies of the EMF on temperature and concentration of oxygen dissolved in PbBi, according to theoretical calculations. The dashed lines represent the theoretical temperature dependency of the EMF for unsaturated solutions of oxygen in the liquid Pb-Bi eutectic corresponding to the indicated oxygen concentrations, given in wppm, whereas the full line gives the EMF (T/K) dependency for oxygen saturated Pb-Bi. For the plots of theoretical dependencies of EMF (T/K), the assumption was made that the activity of lead in the Pb-Bi eutectic can be described by a numerical value close to 0.5, which is a sufficient approximation.

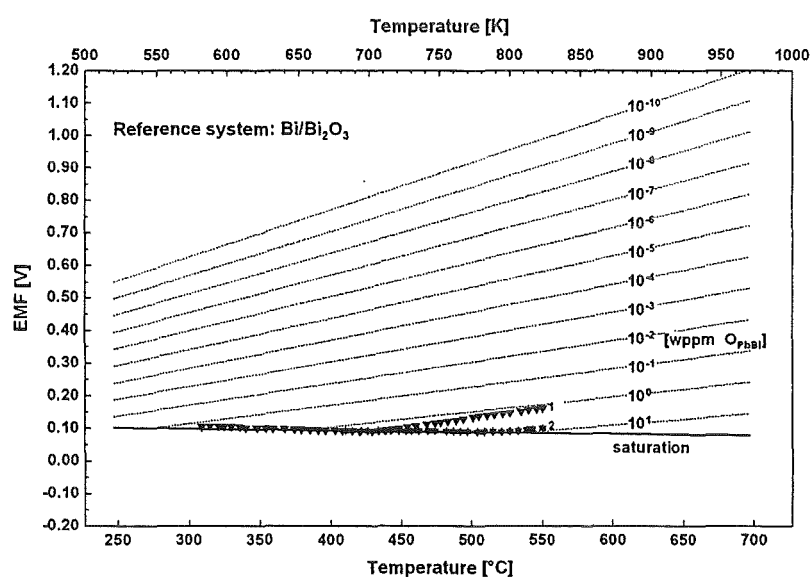


Figure 18: Comparison of calculated and measured EMF's for a cell with Bi/Bi<sub>2</sub>O<sub>3</sub> reference system.

For the Bi/Bi<sub>2</sub>O<sub>3</sub> system coming from the unsaturated state (high temperature range), the point of coincidence of the cooling curve with the theoretically expected EMF (T) line for the oxygen-saturated state is reached at about 470 to 460°C. At lower temperatures both lines are in excellent agreement for the whole temperature range of about 150°C down to even about 300°C. This is a temperature value only slightly higher than the melting point of bismuth. It is obvious that during the cooling down / warming up cycles of no. 1 and 2 with continuous air bubbling, the oxygen

concentration (and activity) values in the liquid Pb-Bi melt increased from no. 1 to no. 2 until nearly saturation was reached within the whole temperature range (no. 2). A very important experimental finding is that the LEBD of our oxygen probes based on the Bi/Bi<sub>2</sub>O<sub>3</sub> reference system is found out to be very low – about 310°C. For loops like THESYS, which is operated at low temperatures, this oxygen probes with Bi/Bi<sub>2</sub>O<sub>3</sub> reference are able to measure the oxygen activities more correctly than sensors with Pt/air reference.

Figure 19 describes the kinetic response of an oxygen meter with Bi/Bi<sub>2</sub>O<sub>3</sub> reference system during bubbling of reducing and oxidizing gases through the Pb-Bi melt. Starting at nearly oxygen saturated conditions first air was injected (p<sub>O2</sub> = 0.21 bar), and then subsequently Ar+5%H<sub>2</sub> bubbling was performed. The rate of the meter response to oxygen activity changes in the Pb-Bi has been found to be very rapid, similar to the previous experiments with the Pt/air and In/In<sub>2</sub>O<sub>3</sub> systems. The results are also verified by other research groups (e.g. LANL), during their kinetic studies with Pt/air oxygen probes. The fast transient response to step changes of the oxygen activity in Pb-Bi exhibit no unusual behavior. The excellent time response of the EMF values after replacing of the Ar+5%H<sub>2</sub> by air bubbling and vice versa, there is nearly no time delay observed. The kinetics of the Bi/Bi<sub>2</sub>O<sub>3</sub> oxygen probes is better than the In/In<sub>2</sub>O<sub>3</sub> system adopted previously. The intrinsic temperature fluctuations in the second part of the temperature-on-time-curve (figure 19) could be due to the reaction enthalpy of oxide scales degradation of the structure material

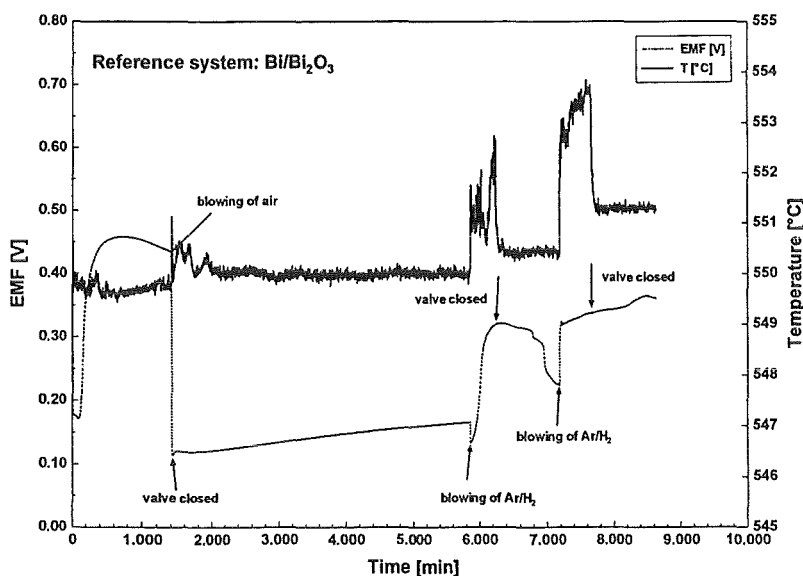


Figure 19: Changes of EMF for a cell with Bi/Bi<sub>2</sub>O<sub>3</sub> reference system due to bubbling of reducing and oxidizing gases through the Pb-Bi melt.

(i.e. the wall, where the dissolved oxygen is removed by blowing Ar+5%H<sub>2</sub> through the melt). After closing the valve of Ar+5%H<sub>2</sub> and during air bubbling, the mean value of the temperature becomes constant very soon, and only a small rms-value is measured. The EMF versus time curves are very smooth, no low-frequency voltage noise could be detected here at the usual time resolution digit. However, the presence of any kHz-electrochemical EMF voltage noise sources could not be excluded yet without time-zooming applying spectral density analysis.

Figure 19 shows also the good stability of the EMF values of a cell with Bi/Bi<sub>2</sub>O<sub>3</sub> reference electrode immersed into a oxygen saturated Pb-Bi melt at about 550°C over about 100 hours of continuous data monitoring. Before blowing of air (the kinetic experiment starts at oxygen "fairly unsaturated", low level conditions, easy to recognize by the relative high, positive EMF magnitude) the rapid change from reducing to oxidizing conditions causes a stepwise change (rapid descending) of the EMF-response of minus 330 mV towards the saturation value expected from the theory. Regardless of the following slight, very, very flat ascending of the EMF during the "blowing of air"-period (i.e. a kind of an "equilibration"-period) -the trend gives a shift of about 50 mV over 75 hours - the close vicinity of the EMF oxygen saturation line is kept nearly constant. This stability within a small range of mV over days –and this without any intermittencies/ periodicities or noise seems to be a very good experimental proof of the thermo chemical oxide data (Gibbs free enthalpies of oxide formation) both for PbO and Bi<sub>2</sub>O<sub>3</sub>, which were needed for the calculations. Switching towards Ar+5%H<sub>2</sub> bubbling exhibited promptly a strong increasing towards highly positive EMF values. Of course, it takes some time before the melt reaches a state, where the analytic amount of dissolved oxygen in the liquid metal bulk becomes very low and the corresponding oxygen activity values are those of a strong oxygen-depleted solution. Surely, the meter response is faster than the changes of the potential–giving oxygen activity values in the melt. On the other hand, transients, as in figure 19, give us the experimental evidence, that the Bi/Bi<sub>2</sub>O<sub>3</sub> meter reacts precisely and selective on oxygen activity changes in the melt. The ascending of the EMF at the beginning of the experiment was due to the chemical reaction of the primarily dissolved oxygen (as an impurity in the liquid metal) with the steel of the container wall.

## Conclusions

The successful performance of oxygen sensors has been demonstrated in a number of stagnant experiments. Calibration slopes EMF versus temperature fit the theoretical straight lines very well. Similar results have been obtained previously for oxygen meters with Pt/air and In/In<sub>2</sub>O<sub>3</sub> reference systems. Sensors with Bi/Bi<sub>2</sub>O<sub>3</sub> reference electrodes revealed a very good response to changes in the oxygen activity of the Pb-Bi. The response time for significant reactions of the EMF was in the range of minutes. The reproducibility of this behavior was very good for cells with Bi/Bi<sub>2</sub>O<sub>3</sub> reference system, when cycling between reducing and oxidizing gases.

The results from the EMF-temperature dependency tests have shown, that the minimum operational temperature of the oxygen sensor is about 300°C for Bi/Bi<sub>2</sub>O<sub>3</sub>. This is much lower than the measured about 380°C for Pt/air and the 480°C for In/In<sub>2</sub>O<sub>3</sub>. The reason for such differences could be due to higher internal resistances of the Pt/air resp. the In/In<sub>2</sub>O<sub>3</sub> electrode.

### **2.4.2 Work Package WP2: Oxygen control in flowing lead-bismuth**

(G. Müller, G. Schumacher, A. Weisenburger, IHM, C.H. Lefhalm, IKET)

#### Introduction

The control of the oxygen concentration in the liquid metal alloy (lead-bismuth) is of great importance and a definite prerequisite, in order to form stable oxide scales on the steel surface, which then can protect the steel against the dissolution attack [1]. The control of a defined H<sub>2</sub>/H<sub>2</sub>O ratio is the method of choice to adjust continuously the oxygen potential of the melt which is necessary to retain stable oxide scales over long time scales. In general, oxide scales can be generated either from steel components or from special oxidants alloyed into the steel surface, like aluminium or silicon.

#### Oxygen control System

During the reporting period the control of the oxygen activity in liquid Pb-Bi, developed at IHM was tested at the Technology Loop THESYS of KALLA. The

adjustment of the oxygen activity in a liquid metal is based on the exchange with a gas phase having a defined oxygen partial pressure above the free surface of the liquid metal. The oxygen activity was measured using electrolytic probes developed at IMF III. The principal task was to measure the dynamics of the establishment of equilibrium between the gas phase and the liquid metal.

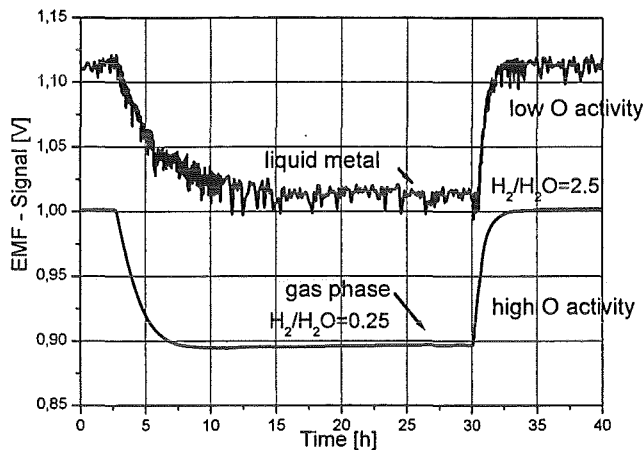


Figure 20: Establishment of equilibrium between gas phase and liquid Pb-Bi after altering the oxygen activity of the gas phase in the Technology Loop THESYS.

It can be seen that the oxygen activity in the liquid melt follows quite closely any change of the activity in the gas phase (figure 20). Reaching a new equilibrium of the oxygen activity in Pb-Bi one order of magnitude higher in THESYS (50 l Pb-Bi, liquid metal velocity: 0.2 m/s, exchange area: 0.14 m<sup>2</sup>) takes about 5 h. The reduction of the activity to the former value took instead only about half of the time. This difference in the establishment of equilibrium between loading of the liquid metal by oxygen and unloading can be explained by the specific experimental set-up and by the mechanism of the equilibrium process, especially the release of hydrogen dissolved in Pb-Bi. Additionally the exchange rate and therefore the velocity of the establishment of equilibrium increases with increasing velocity of the liquid metal and the exchange area available.

### Oxygen activity in Pb-Bi

Because almost no relevant data from literature for the system Pb-Bi-O is available, several thermodynamic calculations were performed to determine the saturation solubility of oxygen in Pb-Bi. One starts with a formulation in which the partial free molar enthalpy in pure Pb and Bi and the free excess mixing enthalpy of alloy is determined [2].

$$\overline{\Delta G_{O_2}}(Pb/Bi) = \frac{X_{Pb}}{X_{Pb} + X_{Bi}} \overline{\Delta G_{O_2}}(Pb) + \frac{X_{Bi}}{X_{Pb} + X_{Bi}} \overline{\Delta G_{O_2}}(Bi) - 2 \cdot \Delta G^{x\delta}(Pb/Bi)$$

Significant differences (factor 3) compared with the few data from literature arise from the calculations, figure 21.

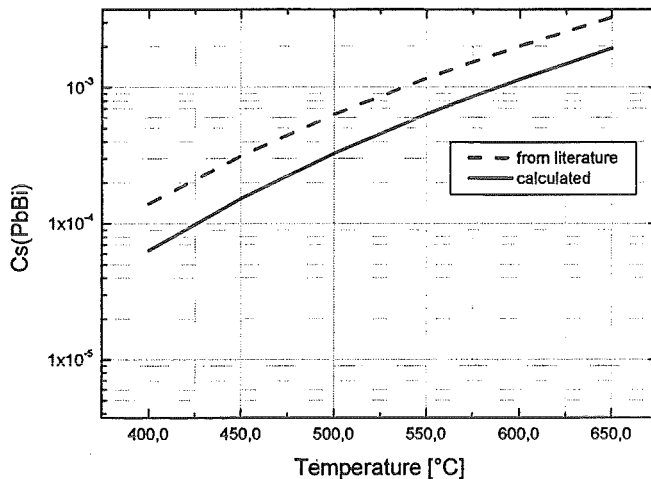


Figure 21: Comparison between data from literature [3] and calculation.

To determine experimentally the temperature dependent solubility limit of oxygen in Pb-Bi a new experimental set-up was built and went into operation. Using this experimental set-up also the dependency of the activity coefficient on the concentration can be measured as precise as possible. This might not be attainable for the lower oxidation limit, but should be achievable 1-2 orders below the solubility limit. Using these values the temperature dependency of the activity coefficient could be extrapolated to the whole range of interest. At present the activity coefficient is assumed to be constant over the whole range. First results are expected at the beginning of next year.

### Summary

This strategy fund project enabled Forschungszentrum Karlsruhe to develop an Oxygen Control System (OCS) which is reliably working on a liquid lead-bismuth loop as a stand-alone instrument. Right now, there are several requests from international laboratories to purchase this OCS.

The next step is to apply the OCS to a larger scale system such as the Thermalhydraulic Loop THEADES. Another application could be the large-scale pool-type test facility CIRCE at ENEA, which provides operational conditions very similar to an ADS Demonstrator.

### 3. OVERALL CONCLUSIONS AND PERSPECTIVES

The objective of the HGF Project is to provide the scientific-technical basis which allows the conception and the design of a spallation target. The application of a spallation target is in the fields of, first, spallation neutron source for material investigations and, second, transmutation of highly radioactive waste.

The HGF Strategy Fund Project is divided into three sub-projects: thermalhydraulic investigations, material specific investigations, and Oxygen control system.

The major results are:

- **KALLA:**  
The stagnant experiments COSTA, KOSIMA and KOCOS are in operation. The loop experiment THESYS is in operation; THEADES and CORRIDA are being commissioned.
- **SP1: Thermalhydraulic investigations**  
Experimental (HYTAS test facility) and numerical (CFX) results for a beam window with water as the model fluid are provided for the MEGAPIE spallation target. The numerical optimization and the detailed design of a beam window in Pb-Bi is in progress.  
Two fundamental liquid metal heat transfer experiments are performed, a numerical simulation using CFX is in progress.  
A stepwise numerical analysis of a complete spallation target is in progress. The general technical feasibility of the heat removal chain is demonstrated. The integral experiment K4T is designed in order to simulate the thermal-hydraulic behaviour of a spallation target including the heat removal chain. The next step is to integrate K4T in FP6 of the European Community.
- **SP2: Material specific investigations**  
Experimental investigations prove that only the steels alloyed with aluminium at the surface (GESA treatment) can be used at higher temperatures and longer times of exposure in liquid Pb-Bi. The use of original steels that form oxide scales from their components is restricted at temperatures below 500°C. However, an oxygen control system is required for all operational conditions.

- SP3: Oxygen control system (OCS)

It is successfully demonstrated that electrochemical oxygen meters with three different reference systems (Pt/air, In/In<sub>2</sub>O<sub>3</sub>, and Bi/Bi<sub>2</sub>O<sub>3</sub>) are an in-situ device to measure the chemical activity of dissolved oxygen in liquid lead or lead-bismuth. The response time is in the range of minutes. The results from the EMF-temperature dependency shows that the minimum operational temperature of the oxygen sensor is about 300°C for Bi/Bi<sub>2</sub>O<sub>3</sub>, being much lower than 380°C and 480°C for Pt/air and In/In<sub>2</sub>O<sub>3</sub>, respectively.

The oxygen control system (OCS) is successfully applied to the small-scale loop experiment THESYS with flowing lead-bismuth. The next step is the application of the large-scale THEADES loop system. OCS is a stand-alone system which is ready to be sold to other institutions.

#### 4. LITERATURE

A complete list of references is given in „Thermalhydraulic and Material Specific Investigations into the Realization of an Accelerator Driven System (ADS) to Transmute Minor Actinides, 2001 Status Report“, Forschungszentrum Karlsruhe, Wissenschaftliche Berichte FZKA 6719, 2002 by J.U. Knebel, X. Cheng, G. Grötzbach, R. Stieglitz, G. Müller, G. Schumacher, J. Konys, O. Wedemeyer.

#### 5. ACKNOWLEDGEMENTS

The co-authors and co-workers, who significantly contributed to this work, are listed together with the institute in alphabetical order:

Institut für Kern- und Energietechnik (IKET): A. Batta, X. Cheng, M. Daubner, F. Doule, R. Drummond, F. Fellmoser, S. Gnieser, G. Grötzbach, J.U. Knebel, V. Krieger, C.H. Lefhalm, K.J. Mack, P. Miodek, H.J. Neitzel, I. Otić, C. Panefresco, C. Pettan, H. Piecha, R. Stieglitz, R. Vollmer

Institut für Hochleistungsimpuls- und Mikrowellentechnik (IHM): A. Heinzel, R. Huber, G. Müller, G. Schumacher, A. Weisenburger, F. Zimmermann

Institut für Materialforschung I and III (IMF I and III): C. Adelhelm, H. Glasbrenner, J. Konys, W. Krauss, H. Muscher, J. Novotny, Z. Voss, O. Wedemeyer